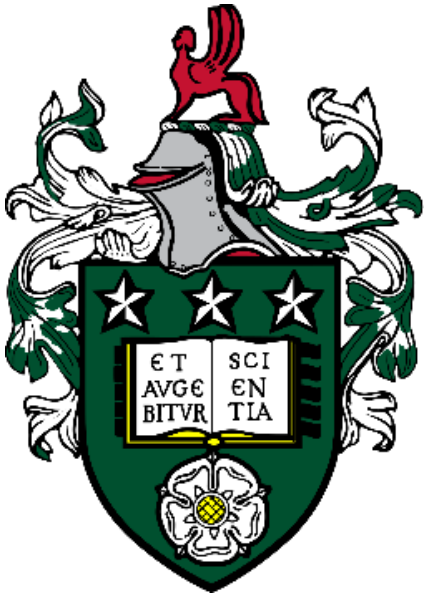

Optimal sizing of hybrid renewable systems to improve electricity supply reliability in Iraqi domestic dwellings.

By
Hussain Ali Hatam Alshamri

The University of Leeds
School of Chemical and Process Engineering

October 2019

Declaration

The candidate confirms that the work submitted is his own, except where work formed jointly-authored publication has been included. The contribution of the candidate and other authors to this work has been explicitly indicated overleaf. The candidate confirms that appropriate credit has been given within the thesis where reference has been made to the work of others. This copy has been supplied on the understanding that it is copyright material and that no quotation from the thesis may be published without proper acknowledgement.

© 2019 The University of Leeds, Hussain Ali Hatam Alshamri

WORK APPEARING IN JOINTLY AUTHORED PUBLICATIONS

Peer Reviewed Conference Proceedings and Poster

1. H. Alshamri, T. Cockerill, Alison S. Tomlin, " An Optimal Sizing Method For Wind-Pv-Battery Hybrid Power System For Unreliable Electricity Supply," in Energy Leeds PhD network conference 25th June, University of Leeds, UK, 25th June 2019. (Poster)

ACKNOWLEDGEMENTS

Foremost, I would like to express my sincere gratitude to my main supervisor Professor Tim Cockerill for all the support and encouragement of my Ph.D study and research, for his patience, motivation, enthusiasm, and immense knowledge. His guidance helped me throughout my time of research and in the writing of this thesis. I could not have imagined having a better advisor and mentor for my Ph.D study during the long months I spent undertaking my PhD work.

In addition, I would like to say a very big thank you to my second supervisor Professor Alison S. Tomlin for all her continuous guidance, support and immense knowledge that she gave me during the long months I spent undertaking my field work. Without her guidance and constant feedback, this PhD would not have been achievable.

My sincere thanks also goes to Dr. Andrew Pimm for all his support, encouragement and insightful comments

I would like to thank my family. First of all, my mother and father for giving birth to me at the first place and supporting me spiritually throughout my life. In addition, I would like to give big thank you to my wife and children for their help, support, encouragement and patience during the years of my study.

I am very proud to graduate from the University of Leeds and would like to extend my thanks and gratitude to all of its staff and all the friends I have made during my time here.

Finally, I would like to thank the Iraqi Ministry of Higher Education and Scientific Research (MOHE) for giving me the chance to study in the UK.

ABSTRACT

This project aims to evaluate wind and solar power availability in Iraq in order to support and design an optimized hybrid renewables system for use in domestic sectors. The unreliable energy supply is one of the main challenges that the residential sector faces in Iraq. This project assessed to what extent the investment in Hybrid Renewable Energy System (HRES) is feasible and efficient to overcome the problem of unreliable supply at reasonable cost. Several researchers have tried to assess wind and solar resources in Iraq using low-resolution databases from a limited number of weather stations, but they were unable to produce a comprehensive evaluation of renewable energy in Iraq.

This research identified and developed techniques that allow more accurate mapping of wind resources in Iraq than has been possible previously. In addition, the thesis developed a unique technique to optimize the best design of HRES that has sufficient flexibility to deal with various climatic conditions and economic challenges using wind turbines, solar panels, and rechargeable batteries.

In order to assess the potential wind power in Iraq, many wind resource evaluation techniques based on the spatial and temporal microscale and mesoscale were reviewed. In addition, the availability of several wind data resources was considered and discussed using observed and estimated data. To evaluate wind resources for the whole of Iraq, a downscaling model using reanalysis data from Modern-era retrospective analysis for research and applications (MERRA) and a land-use map as the basis of the surface roughness map for the whole of the country has been developed. Following this, a power curve model was used to estimate potential wind power production from several types of small wind turbines.

The most fundamental techniques were used to evaluate and calculate solar power production. In addition, the most important solar databases were used to evaluate the solar radiation for the whole of Iraq. To evaluate solar resources in Iraq, the most validated solar dataset was employed to evaluate annual solar energy production for the whole of the country. In addition, the hourly solar energy production model based on wind speed and ambient temperature impact (HSEP-WT model) was developed to estimate the hourly solar system output, combining the effects of wind speed with the impact of ambient temperature on cell temperature, aiming to make the solar power evaluation more realistic.

The hybrid system, which has multiple renewable technologies, is considered the most useful approach to satisfy energy demand in the residential sector. Accordingly, several methodologies to size and optimize a hybrid system in terms of reliability and cost parameters were reviewed. Consequently, a novel computational model has been designed to size and optimize HRES, which is deemed suitable to maintain supply in domestic

properties that suffer continually from unscheduled outages from the national grid**.** The process of optimization examined several energy flow strategies and economical solutions to decrease the total cost of a project and to increase the reliability of HRES.

The results of this thesis have shown, that the downscaling model succeeded in increasing the resolution and accuracy of estimated wind speed and confirmed that the model should be applied, based on the local variables of the boundary layer. In addition, the wind power production demonstrated that the most productive locations in Iraq are concentrated above the water surfaces and the area that extends from central to east and south-east of Iraq. Also, these areas have shown low cost of energy and a payback period lower than eight years. Furthermore, solar power production confirmed that the most productive locations are located in the west of Iraq. Also, most places in Iraq have shown low cost of energy and a short payback period.

Finally, the optimized technique for identifying optimal combinations of wind, solar and battery technologies for domestic scale renewable energy provision was developed in an unique design using MATLAB by integrating an on-grid and off-grid system (On-off-grid Op-HRES). This system has been developed to resolve the problem of frequent and unscheduled outage for some hours per day from the national grid. The On-off-grid Op-HRES system is examined according to different scenarios of grid Increasing Block Tariffs (IBT) prices, strategies of energy flow management (discharge and without discharge battery in case of on-grid) and based on different land covers and various weather conditions (wind speed and solar radiation). The On-off-grid Op-HRES system was successful in reducing the cost of energy and increasing the reliability of the system when using HRES in areas that have high wind speed and high solar radiation. In addition, when applying the strategy of non-discharging the storage system when connected to the grid as well as using relatively high electricity prices from the national grid, HRES has shown excellent performance in terms of cost and reliability by reducing the Levelized Cost of Energy (LCE), Payback Period (PBP), Loss of Power Supply Probability (LPSP) and Grid Power Absorption Probability (GPAP). Lastly, the availability of wind speed has played an exceptional role in terms of increasing reliability of HRES, even in areas that have low solar radiation.

TABLE OF CONTENTS

LIST OF FIGURES

LIST OF TABLES

NOMENCLATURE

Symbol	Quantity	SI Unit
$\bar{u}$	Mean wind speed	m/s
u	Actual instantaneous velocity	m/s
$u^{'}$	Turbulent part of wind speed	m/s
$\bar{u}(z)$	Mean wind speed of an air mass at height z	m/s
u_*	Friction velocity	m/s
l	Prandtl mixing length	m
$w^{'}$	Ertical velocity	m/s
z_o	Roughness length of the surface	m
$\overline{u'w'}$	Momentum flux in the kinematic	-
τ	Shear stress (Reynolds stress)	-
C_h	Canopy height	m
d	Displacement height	m
Z_{bh}	Blending height	m
z_{0eff}	Effective local roughness	m
k_v	Von Karman constant.	-
k	Weibull shape factor	-
c	Weibull scale factor	m/s
$f(v)$	Probability density function	-
Γ	Gamma function	-
E_k	kinetic energy	Watt
$P(v)$	power electricity converted by turbine	Watt
$P_w(v)$	Wind power	Watt
ρ	Air density	kg/m^3
A	Area of a turbine rotor	m^2
C_p	Power coefficient of the turbine	-
$q(v)$	Non-linear relationship between wind speed and power.	-
v_{ci}	Cut-in: wind turbine starts to generate energy	m/s
v_r	Wind speed that produces the highest power in Wind turbine.	m/s
v_{co}	Cut-out wind speed in wind turbine	m/s
Z_{bh}	Blending height	m
u_{hh}	Wind speed at hub height at target site	m/s
u_{10}	Reference wind climatology at 10 m	m/s
Z_h	Hub height at reference site	m
Z_{ref}	Reference height	m
$z_{o\,ref}$	Surface roughness of the reference site	m
d_{eff}	Effective displacement height of the region	m
$z_{o\,eff}$	Effective local roughness of the upwind fetch	m
d	Displacement height	m
$z_{0\,urban}$	Surface roughness of the target site in the urban area	m
u_{ch}	Wind speed at the canopy height.	m/s
u_{ref}	Wind speed at the reference height.	m/s
u_{bh}	Wind speed at the blending height.	m/s
d_{urban}	Displacement height at urban area	m

Z_{hh}	Hub height at target site	m
λ_f	Frontal surface area of an obstacle to the wind flow	-
d_{ref}	Displacement height of the reference site	m
L_p	Variability scale.	-
f_i	Spatial fraction of each roughness length patch within the upwind fetch.	-
L_d	Length scale	m
$\max du$	Maximum likely speed change	m/s
$\overline{du(z_{o,t})}$	Average likely speed change	m/s
$z_{o,t}$	Surface roughness over the upwind fetch	m
$z_{0,i}$	Roughness length of each patch.	m
N	Number of patches within upwind fetch.	-
$P\ mean$	Average of power production.	watt
$p(v_i)$	Power production for each wind speed	Watt
$f(v_i)$	Frequency for each wind speed	-
k	Shape factor	-
c	Scale factor	m/s
Γ	Gamma function.	-
$\bar{v}$	Average of wind speed	m/s
k_s	Initial shape factor value at surface level	-
z_s	Surface level of the initial shape factor	m
z_r	Reversal height	m
k_z	Shape factor at a target height	m
c_k	Experimental coefficient	-
k_{50}	Initial shape factor at 50 m	-
$F(v)$	Cumulative density function of Weibull distribution	-
P_r	Rated power for any wind turbine sizes	watt
$Capex$	Capital expenditure	£
OMC	Operation and Maintenance Cost	£
OMC_0	Initial cost of operation and maintenance for the First year of project	£
C_{nom}	Nominal capacity of a replacement unit in	watt.
C_{unit}	Price of replacement unit.	£
N_{rep}	Number of replacement	-
PVS	Present value of scrap	£
SV	Value of scrap	£
TCOP	Total cost of project	£
LAC	Levelized annual costs	£/kWh
MEP	Monthly energy production	kWh/month
MD_i	Monthly demand	kWh/month
ND_i	Number of days for each month in a year	
Hh_i	Typical average of daily global solar radiation on a horizontal surface	Wh/m^2/day
P	Actual power for each time step 1hr	Watt.
z	Sun's zenith angle.	degree
α	Elevation angle or altitude angle	degree
δ	Declination angle.	degree

d	Number of days since the start of a year	-
P_{pk}	Nominal peak power,	Watt
eff_{nom}	Nominal efficiency at standard test condition	-
eff_{rel}	Relative efficiency	-
G	Global solar radiation, insolation	W/m^2
T_a	Ambient temperature	°C
I_{cc}	Short-circuit current	Amp
T_m	PV module temperature.	°C
$ASEP$	Annual solar energy production	kWh/year
$InverterC$	Inverter cost	£
ICF	Installation, Civil work and Foundation cost of the solar system	£
γ	Irradiance coefficients	
β_o	Temperature coefficients	
P_{PV}	PV energy production	Wh
Y_{PV}	Rated capacity of the solar system	kW
f_{PV}	PV derating factor	
$\bar{G}_T$	Solar radiation incident on the solar module	kW/m^2
$\bar{G}_{T,STC}$	Incident radiation at standard test conditions STC	Watt/m^2
α_P	Temperature coefficient of power -0.41	%/°C
T_c	Denotes the PV cell temperature [°C] in the current time step	°C
$T_{c,STC}$	The cell temperature under Standard Test Conditions STC 25°C	°C
$\bar{G}_b$	Direct beam radiation.	Watt/m^2
$\bar{G}_d$	Diffuse radiation	Watt/m^2
$\bar{G}$	Global solar radiation	Watt/m^2
β	The slope of the surface	degree
ρ_g	Ground reflectance	%
f	Horizon brightening	-
A_i	Anisotropy index	-
$\bar{G}_o$	Extra-terrestrial horizontal radiation averaged over the time step	Watt/m^2
δ	Solar declination	degree
ω	Hour angle	degree
θ	Angle of incidence	degree
θz	Zenith angle	degree
R_b	Ratio of direct radiation on the sloped surface to direct radiation on the horizontal surface	%
t_s	Solar time	Minutes
t_c	Civil time or local time zone in hours	Minutes
L_{st}	Standard meridian for local time zone	degree
L_{loc}	Location longitude in degrees $0^o < L < 360^o$	degree
E	Equation of time which represents the difference between solar time and mean solar time.	hour
Z_s	The azimuth of the surface	degree
$\emptyset$	Latitude of a location	degree

G_{sc}	Solar constant	
ω_1	Hour angles at the beginning (sunrise) of the time step	degree
ω_2	Hour angles at the end (sunset) of the time step	degree
R_b	Ratio of direct radiation on the sloped surface to direct radiation on the horizontal surface	%
T_a	Ambient temperature	°C
v	Hourly wind speed	m/s
η_{STC}	Module efficiency at STC	-
β_{STC}	Temperature coefficient of maximal power	-
τ	Solar transmittance of any cover over the PV array 0.9%.	%
$h_w(v)$	Wind convection coefficient	m/s
I_{NOCT}	800W/m² the Irradiance at normal operating cell temperature	W/m²
T_{NOCT}	Temperature at nominal operating cell temperature	°C
$h_{w,NOCT}$	Wind convection coefficient for wind speed according to NOCT conditions, i.e. v_w= 1 m/s	m/s
v_w	Local wind speed close to the module at 2.5 m or 2 m height	m/s
LPS (t)	Loss of power supply at the time step (t)	Watt
$E_{load}(t)$	Load demand at the time step (t)	Watt
$E_{GP}(t)$	Grid purchased energy at the time step (t)	Watt
$E_{DG}(t)$	Energy by diesel generators at the time step (t)	Watt
AEP	Annual energy production	kWh/year
T	Lifetime of project	years
r	Net interest rate	%
i	Inflation rate	%
$C_{bat\ n}$	Nominal storage capacity	watt
DOD	Depth of discharge	%
$C_{bat\ max}$	Maximum allowable storage capacity	%
$C_{bat\ min}$	Minimum allowable storage capacity	%
σ	Self-discharge rate	-
$(E_{pv}(t))$	Energies produced by the PV	kWh
$E_w(t)$	Energies produced by wind turbine	kWh
$E_{load}(t)$	Energy flow from the DC bus to the load	kWh
η_{inv}	Inverter efficiency	%
$D(t)$	Equivalent DC load demand corresponding to the inverter input	kWh
$Max.P_{charg}$	Maximum power charge	kW
$E_{RE}(t)$	Total renewable energy generated by the HRES	kWh
$E_{Ex}(t)$	Excess electricity	kWh
Δt	Times step	hour
$P_{discharg}(t)$	Amount of power discharging	kW
$E_{DG}(t))$	Energy from the diesel generator purchased for period	kWh
η_{bc}	Battery charge efficiency	%
η_{bd}	Battery discharge efficiency	%
AE_{GP}	Annual grid purchase	kWh

AE_{DG}	Annual diesel generator supply	kWh
AE_{load}	Off-grid and on-grid demand over 8760 hours)	kWh
$AEload$	Annual energy load	kWh
$AnnSavCost$	Annual saving cost strategy	£/year
$CostMD_i$	Cost of monthly demand based on provider price	£/month
$CostMD_i\ on\ grid$	Cost of monthly on-grid demand	£/month
$CostMD_i\ off\ grid$	Cost of monthly off-grid demand	£/month
$Cost\ MNetgrid_i$	Cost of monthly net grid trade	£/month
$E_{sp}(t)$	Surplus electricity	kWh
$E_{GP}(t)$	Grid purchases	kWh
$TCOP_{WT}$,	Total cost of the project for a wind turbine	£
$TCOP_{Batt}$	Total cost of the project for a solar system	£
$TCOP_{inv}$	Total cost of the project for a battery and inverter	£

Abbreviations

3DVAR	Three-dimensional variational data assimilation
AC	Alternating current
AEP	Annual energy production
AEZ	Agro-ecological zoning
AMSU-A	Advanced Microwave Sounding Unit-A
a-Si	The non-crystalline form of silicon
BG	Baghdad house
BGW	Baghdad international airport weather station
BS	Basra house
CdTe	PV cadmium telluride
CF	Capacity factor
CFD	Computational fluid dynamic
CFSR	Climate forecast system reanalysis
CIGS	Copper indium gallium selenide solar cell
CM-SAF	Satellite application facility on climate monitoring
CRF	Capital recovery factor
DC	Direct current
DS	Downscaling Square
DSM	Downscaling model
EA	Evolutionary algorithms
ECMWF	European centre for medium-range weather forecasts
EENS	Expected energy not supplied
EIR	Energy index of reliability
EU	European Union
ERS	European Remote Sensing Satellite
FOB	Free on board
GA	Genetic algorithm
GCM	General circulation model
GEOS-5 DAS	Goddard earth observing system data assimilation system version 5
GOES	Geostationary Operational Environmental Satellite
GES DISC	Goddard earth sciences data and information services centre
GHI	Global horizontal irradiation

GPAP	Grid Power Absorption Probability
GRI	Graphical results inter-face
GSI	Grid-point statistical interpolation scheme
GUI	Graphical user interface
HOGA	Hybrid optimization by genetic algorithms
Homer	Hybrid optimization model for electric renewables
HRES	Hybrid renewable energy system
HSEP-WT model	Hourly solar energy production model based on wind speed and ambient temperature impact
HIRS	High Resolution Infrared Radiation
IAN	Iraqi agrometeorological network
IAU	Incremental analysis update
IBT	Increasing block tariffs
ICF	Installation cost, civil work and foundation
IMOS	Iraqi meteorological organization and seismology
IPCC	Intergovernmental panel on climate change
JRC	Joint research centre
JMA	Japan Meteorological Agency.
KR	Karbala house
LAC	Levelized annual costs
LCE	Levelized cost of energy
LCI	Land cover institute
LCM	Land cover map
LPS	Losses of power supply
LPSP	Loss of power supply probability
LR	Longwave Radiation
LST	The local solar time
MAE	Mean absolute error
MAPE	Mean absolute percentage error
MBE	Mean bias error
MCP	Measure-correlate-predict
MDISC	MERRA Data and Information Services Center
MERRA	Modern-era retrospective analysis for research and applications
MM5	Fifth-generation mesoscale model
MMM	Mesoscale and microscale meteorology
MSG	Meteosat Second Generation satellite images
MODIS	Moderate Resolution Imaging Spectroradiometer
MDISC	Modeling Data and Information Services Center
MSU	Microwave Sounding Unit
NASA	National aeronautics and space administration
NCAR	National centre for atmospheric research
NCEP	National centres for environmental prediction
NERC	North american electric reliability council
NetCDF	Network Common Data Form file format
NGAS-II	Fast elitist non-dominated sorting genetic algorithm
NOAA	National oceanic and atmospheric administration's
NPC	Net present cost

NREL	National renewable energy laboratory
NWP	Numerical weather prediction
NCDC	National Climatic Data Center
Obs	Observation data
OI	Optimum Interpolation
OMC	Operation and maintenance Cost
OPEC	Organization of petroleum exporting countries
PBL	Planetary boundary layer
PBP	Payback period
PSD	Percentage self-demand
PSO	Particle swarm optimization
PV	Photovoltaic technology
PVGIS	Photovoltaic geographical information system
PVS	Present value of scrap
RD	Rotor diameter of the wind turbine
RF	Renewable energy fraction
RI	Repeated insertion
RL	Roughness layer
RMSE	Root mean square error
RSC	Replacement and spare part
SARAH	The surface solar radiation data set - heliosat
SLTC	Sea and land transport plus customs cost
SLTCm	Sea and land transport + customs cost per $1m^3$ of shipment
SPEA	Strength pareto evolutionary algorithm
SR	Shortwave Radiation
SSI	Solar Surface Irradiation
STC	Standard test conditions
SSU	Stratospheric Sounding Unit
SSM/I	Special Sensor Microwave/Imager
TCOP	Total cost of project
TPV	Total present value
TSL	Turbulent surface layer
TSR	Time series raob (NCAR format for upper-air data)
UNEP	The united nations environment programme
UNGA	United nations general assembly
UTC	Coordinated Universal Time
WMO	World organization meteorology
WRF	Weather research and forecasting
WT	Wind turbine
WTC	Cost of the wind turbine
VC	Variable cost

Chapter 1 **INTRODUCTION**

1.1 **Background**

Although Iraq is one of the major oil-producing countries in the world, there is still an urgent need to overcome the increased demand for electricity and cover the extensive shortage of electricity supply for residential, commercial and industrial sectors in Iraq. Energy security in Iraq has represented the most central challenge facing people and government and threatens political and economic stability due to climate change that led to extreme temperatures. Accordingly, there is an urgent and increased need to introduce renewable energies as a part of the global trend towards reducing greenhouse effects and resolve the issue of energy security.

The increased use of fossil fuels in all industrial sectors including electricity generation has played a crucial role in the rise of pollution and global warming. The use of renewable energy and sustainable development are considered the most important solutions to reduce the emission of pollutants, reducing the dependence on fossil fuels, reducing the climate change phenomenon in the world, reducing the cost of electricity generation and to cover the growing demand for energy.

Renewable energy sources, such as solar, wind, biomass, geothermal energy and hydro-energy, which have recently become more prevalent in use, have started to replace fossil fuels as it became apparent that the Earth's resources are not inexhaustible.

Recently, there have been vigorous efforts by the international community to resolve the problems of pollution, climate change and energy security. The United Nations General Assembly (UNGA) declared that 2014 -2024 should be a period of sustainable energy for all, through preparation of the post-2015 development schedule designed to supply affordable electricity and economically viable energy [1]. In addition, the European Union (EU) has planned for a new power strategy based on energy security, sustainable development and a low-carbon economy. In 2009, the EU Parliament set targets to increase renewable energy production to 20% of the total energy demand by 2020 and also has planned to produce around 27% of total electricity supply by 2030 in order to encourage private investment in low-carbon technologies [2].

Hybrid renewable energy systems (HRES) using a small wind turbine, solar panels and rechargeable batteries have become increasingly prevalent in response to global challenges such as energy security and climate change [3]. In order to invest in renewable energies optimally, a number of challenges must be overcome. One of the most important is to develop suitable techniques for evaluating wind and solar power resource accurately. The

assessment of wind and solar resources is crucial for predicting the likely power yield at any site [4].

1.1.1 Climate Change

The greenhouse effect and air pollution are considered significant threats not only to human health but also to plants and to animals [5]. Thirty years ago, the risk of increasing pollution and environmental deterioration became a serious problem [6]. The Intergovernmental Panel on Climate Change (IPCC) was established in 1988, aiming to provide the world with a scientific assessment of the reasons for - and effects of - climate change [7]. The fifth IPCC evaluation report in 2013 showed evidence that during the period 1850 - 2000, the global mean surface layer temperature and mean sea and oceans levels increased because of an increasing concentration of greenhouse gas emissions [7]. Also, the report stated that the emission of greenhouse gases has grown rapidly during the period between 1970 and 2000 to around 70%, [7] due to human activities and increasing consumption of fossil fuels [8]. Furthermore, a large quantity of greenhouse gas emissions are produced from the use of fossil fuels used for power generation. In addition, the IPCC reported that global surface layer temperatures are calculated to increase 3°C by 2100 [9]. Such an increase in global surface temperatures will lead to an increase in severe weather events, affect water supplies and global food and human habitats [8].

1.1.2 Energy Security

Energy security has presented the second serious challenge for fossil fuel consuming countries since 1973, due to the growing concerns about the fluctuation of oil prices, political tensions and instability in the Middle East [10]. These problems and increased demand for oil have raised the critical question of how to resolve the issue of energy supply. Renewable energy investment is one of the most significant solutions for the problem of energy, such as energy security and climate change. One of the most significant advantages of renewable energy is that it is considered an active contributor to reducing dependence on imported fossil fuels [10].

1.1.3 The Problem of Energy Supply in Iraq

Iraq is the second-biggest oil producer of Organization of the Petroleum Exporting Countries (OPEC) and has the second-biggest oil reserves in the world [11]. Yet Iraqi people have suffered from massive shortages of electricity supply since 1990 for various reasons. Firstly, Iraq has seen a dramatic increase in population over the past 40 years as shown in Figure 1-1a, which has rapidly led to increased demand for electricity supply as shown in Figure 1-1c [12]. Also, the national electricity grid was suffering from neglect, severe

damage and poor maintenance due to the military operations and economic sanctions for the period between 1990, 2003 and 2014 [13]. Iraq's power sector faces substantial challenges. Outages remain an everyday occurrence for most households, as rising generating capacity has been outrun by growing demand for electricity, in particular by high demand for cooling in the hot summer season. Between 2013 to 2018, the size of the gap between the maximum grid supply of power and peak electricity demand has widened, even when the available supply has increased by one-third [14] as shown in Figure 1-1b [12].

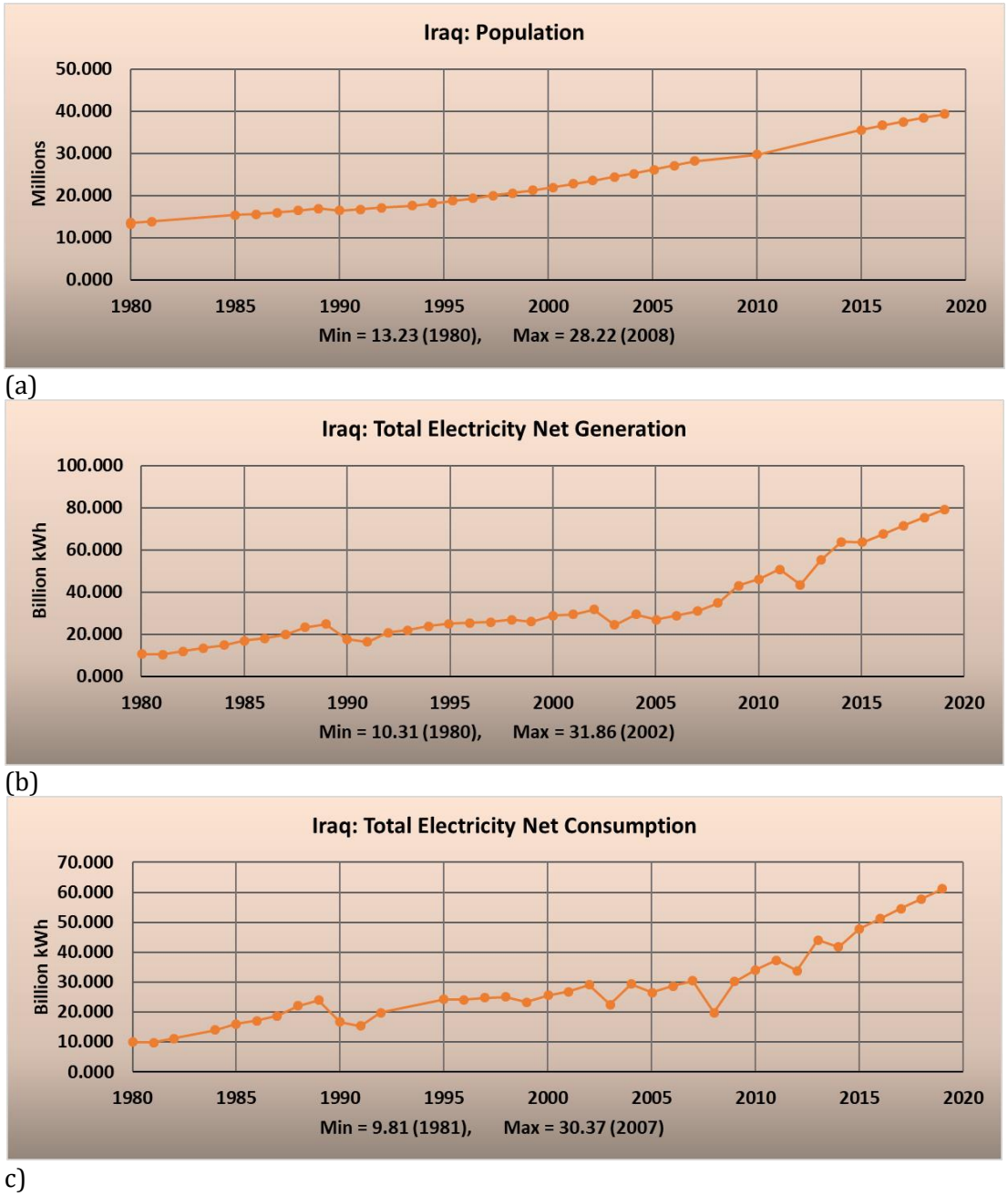

Figure 1-1. Increase of population (a), total electricity net generation (b) and consumption (c) in Iraq [12].

The electricity demand trend is characterised by two peaks during a year: the biggest one during the summer months of June/July/August and the small peak appears over the winter

months of December/January/ February, as shown in Figure 1-2. The calculated electricity demand for the summer in 2004 was about 7,200 MW and 8,800 MW in 2005. While power production was calculated to be about 3,400 MW in 2004 and increased to 4,000 MW in 2005, it is possible to note that the general trend of energy demand increased dramatically during 2004 and 2005 with an apparent deficit in generating capacity of about 56% [13]. For these reasons, the quota of Iraqi citizens is approximately 12 hours per day of electricity supply from the national grid. Electricity production increased by nearly 90% between 2012 and 2018, but the gap between peak demand and supply is broader today than in 2012. Especially in the summer months, energy supply to meet peak demand is weak, and this is a primary concern for citizens across the country [14].

Hence, they are additionally depending on private small electricity generators using petrol, or buying energy from local medium diesel generators within small communities in order to acquire the necessary energy. In reality, there are many disadvantages associated with this procedure, such as increasing air pollution, waste motor oil, noise pollution, high fuel prices, lack of fuel supply, low quality of generators, increasing faults during summer months due to increasing temperature and increasing maintenance costs. In fact, renewable energy investment within small communities or housing units could be the perfect solution to meet future increases in energy demand to cover the shortage of electricity supply and successful business in rural, suburban and urban areas across Iraq. An assessment of wind and solar resources is therefore required to facilitate investment in renewable energy in Iraq.

1.1.4 **Renewable Energy in Iraq**

Several studies have tried to assess wind and solar resources in Iraq, but none of them has produced a high-resolution wind resource map, because most of these studies were based on observed data from a limited number of weather stations in Iraq. For instance, Darwish, et al. [15] has evaluated wind power in Iraq using Weibull distributions based on monthly average wind speeds for 15 locations for eleven years. It was found that one-sixth of Iraq has annual wind speeds higher than 5 m/s. Khalifa, [16] mentioned that twenty-three weather stations were selected for analysis. The daily model for wind speed has the most significant values in the midst of the day and the early morning. These highest values ranged from 5 to 10 m/s. The wind speed in summer months is higher than in winter months. The demands on energy also increase in summer compared with winter, due to increased cooling and air-conditioning loads. Ahmed, [17] has divided Iraq into three territories. The first one covers about 48% of Iraq and has monthly average wind speeds ranging between 2 to 3 m/s. The second area (covering about 35% of Iraq) has monthly average wind speeds ranging between 3.1 to 4.9 m/s. The third region, which represents 8% of Iraq has high wind

speeds of higher than 5m/s. Ahmed, [17] estimated the energy densities for wind regions were 174 W/m^2 in Al-Amarra, 337 W/m^2 in Al-Kout, 194 W/m^2 in Al-Nekhaib, 353 W/m^2 in Ana, and 378 W/m^2 in Al-Naseria. Concerning the solar assessment, Borja, et al. [18] produced a monthly and yearly solar energy map for the radiation periods of 24 weather stations across Iraq. Dihrab, et al. [19] suggested a hybrid solar and wind systems of electricity generation for a connected grid in three cities in Iraq. Results revealed that it was feasible for Iraq to use solar and wind power to generate enough energy for many villages in the desert or rural areas.

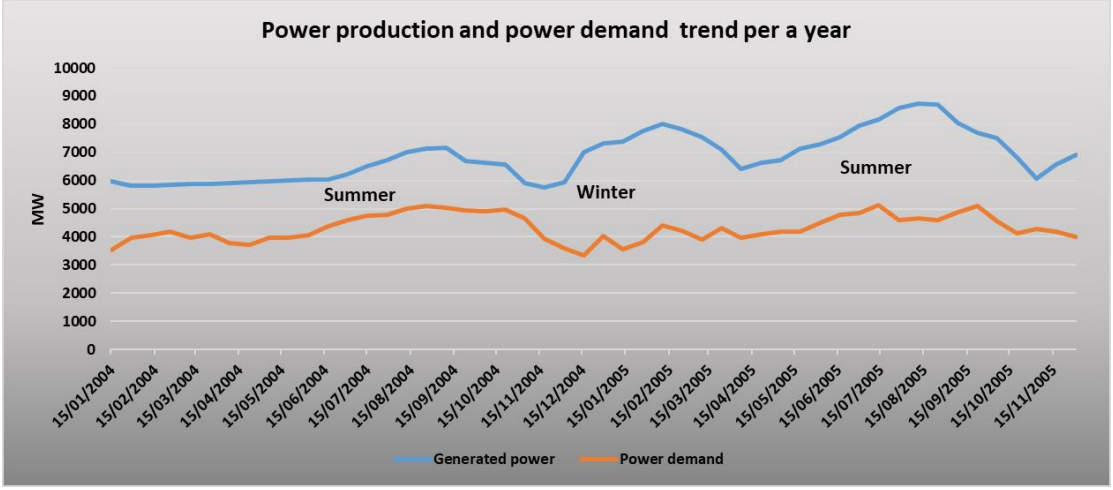

Figure 1-2. Fluctuation of electricity demand trend is characterised per year [13].

1.2 Aim and objectives

The main aim of this thesis is to develop a unique method of optimizing a HRES to control energy flow to meet house electricity demand which is suffering from unscheduled outage from the national grid. HRES will generate energy using small wind turbines, solar panels and rechargeable batteries based on the power availability in Iraq and energy demand that recorded from several housing units in different places in Iraq. In addition, this project aims to assess the wind and solar power availability in Iraq to estimate the potential power production from renewables.

The following objectives were identified to answer several main research questions that are related to the wind and solar resources assessment as well as the feasibility of using an optimized HRES for housing units in Iraq:

1. To improve the wind resource assessment methodology (the downscaling model (DSM)) to create a wind resource map for the whole of Iraq using global modeling data (Modern-Era Retrospective analysis for Research and Applications (MERRA)), Land

Cover Map (LCM) as roughness map and local observation data for validation. This objective tries to answer three research questions:

- To what extent is the wind speed prediction using the developed the DSM accurate for Iraq?
- What are the disadvantages of the implementation of a DSM using MERRA data?
- To what extent is the DSM useful in improving the wind resources assessment in Iraq using MERRA data?

2. To estimate the annual potential energy production by wind and solar systems, based on wind and solar resource assessment for the whole of Iraq and evaluate the hourly energy production from different sizes of these systems for any locations in Iraq. This objective tries to answer the following research questions:
   - To what extent is the wind and solar resources assessment in Iraq helpful to determine the spatial distribution of power production?
   - To what extent do the wind speed and temperature affect the performance and efficiency of the solar system?
3. To evaluate the cost of wind and solar systems and determine their efficiency and feasibility based on a renewables assessment and economical technique, aiming to cover the shortage of information about this kind of investment in Iraq. In addition, this objective tries to answer the following research question:
   - To what extent is the investment in solar and wind systems feasible in Iraq?
4. To examine the impact of different climate conditions, land cover categories and different techniques of optimized HRES, using wind turbines, solar panels and rechargeable batteries to cover the energy demands and to reduce energy costs in housing units for different locations in Iraq. Again, this vital objective tries to answer the following research questions:
   - To what extent will an optimization system succeed in covering the energy demand based on wind and solar power availability in Iraq?
   - To what extent will the optimized hybrid renewables system be feasible and economical for household consumers in terms of on-grid and off-grid in Iraq?
   - To what extent does the land cover category have an effect on the efficiency of the solar system, wind system and hybrid system?
   - To what exyent are these methods and results novel, and what is the key contribution to knowledge?

1.3 Thesis structure

Chapter 2 reviews literature related to the fundamental physics of the wind flow in the boundary layer and wind speed distributions. Different wind resource assessment technologies are reviewed according to various spatial and temporal. Furthermore, the available data sources that can be used to achieve wind resource assessment for the whole of Iraq are outlined and discussed.

Chapter 3 explains the importance of solar power and presents techniques that can be used to evaluate solar power production. An overview of the most important solar database used to assess solar radiation and solar power production is provided.

Chapter 4 presents a general literature review of methods for determining the optimal sizes of HRES according to the concepts of reliability and economic assessment of HRES performance. An overview of the merits and demerits of software available and used for examining the optimal sizes of HRES and simulating the hybrid system is also set out.

Chapter 5 illustrates the main steps of the DSM using MERRA data as sources of reference wind data. A second step reviews the broad spectrum of parameterization of the surface aerodynamics, which is developed, based on a land-use map of Iraq. Sensitivity analysis is used to study the impact of proposed parameters when applying the DSM. This approach involves developing a technique to achieve better outcomes of wind speed against observation data. The DSM performance is evaluated by validating the results with observed data previously obtained from several sites.

In Chapter 6, several potential techniques to estimate the Annual Energy Production (AEP) for the whole of Iraq map are discussed. Estimation of the factors of a Weibull distribution and evaluation of the values of the shape factor with height is explained.

In Chapter 7, the capital cost of a wind turbine project is estimated, based on reliable sources of information, together with the variable cost. The electricity pricing system in Iraq Increasing Block Tariffs (IBT) is described. The Levelized Cost of Energy and payback period are used to evaluate the feasibility of a wind turbine project based on a saving strategy and on different levels of energy demand.

Chapter 8 presents the methodology used to evaluate the annual energy production from different sizes of PV system for the whole of Iraq, the economic methodology for estimating the cost of a solar project, and the cost of energy and the payback period. This chapter presents the method of developing the Hourly Solar Energy Production by integration the effect of Wind and Temperature (HSEP-WT model), which involves combining the effects of wind speed and ambient temperature on cell temperature, to calculate the hourly solar energy production from different sizes of solar system at any location in Iraq.

Chapter 9 presents an overview of optimization methodology and energy management in HRES, which includes a demonstration of the component of HRES configuration in this project. This involves explaining the modeling of system components (wind turbine and solar system) and the sources of data that are used in this project. The mathematical model, of the storage system and energy flow management for different scenarios, are demonstrated. Modeling of system reliability and system economic are also demonstrated. Validation and the analysis of the results of optimization for various locations in Iraq are presented.

Chapter 2 **WIND FUNDAMENTALS AND WIND RESOURCES ASSESSMENT METHODS**

2.1 Introduction

One of the main aims of this project is to assess the availability of wind power in Iraq and to estimate the potential power production from small wind turbines size. To determine the potential power production of a wind turbine, the wind power availability within a prospective site must be estimated. In order to evaluate the potential power, a suitable wind resource assessment methodology must be conducted, which should take into consideration the power availability of close-surface wind flow at the planetary boundary layer [20]. The role of wind resources assessment is vital to determine the best sites for wind farms and, if it is accurate enough, it will increase the accuracy of estimations of power production.

In this chapter, an overview of the fundamental physics of the wind flow and the fundamentals of boundary layer wind flow will be presented in sections 2.2 and 2.2.1. In addition, a description of the wind speed frequency distribution will be presented in section 2.3. An overview of different wind resources assessments according to various spatial scale and temporal scale is outlined in section 2.4. Furthermore, a description of the wind power curve model for wind power production is present in section 2.5. Finally, there is an overview of available data sources that could be used to achieve wind resource assessment all of Iraq in section 2.6.

2.2 Wind Physics

Investment in wind power requires the development of a wind resource assessment methodology for a specific site. A wide range of physical and meteorological factors should be taken into consideration to develop wind resource assessment methods. Furthermore, the fundamental physics of the wind flow and factors that influence wind flow at a specific site are required. In addition, meteorological information plays an essential role in the assessment of wind resources. To achieve a precise evaluation for wind resources at a particular location requires the researcher to estimate the variability of the wind speed at a location for a long time, in order to forecast wind energy production over the long term [21, 22]. With respect to the forecasting of wind power production, the fundamentals of wind power production and the methods for describing spatial and temporal variability should be understood, so as to develop and improve a wind resource assessment. A comprehensive

understanding of the physical and climatic properties of the atmosphere is necessary to assess wind resources [23]. The difference in atmospheric pressure above the Earth's surface will lead to generate wind flow from high pressure to low pressure [24]. The differential heating in the surface layer creates convection above the hot surface which leads to rising air in the region of low pressure, while above the cold area the air will be heavy, which leads it to go down. For this reason, the air mass will move from the area of high pressure to the area of low pressure to create wind flow [24]. Variation of the wind speed is generated by diurnal, synoptic and turbulent factors [25]. The atmosphere of the Earth consists of many layers. For example, the troposphere is the closest to the Earth's surface. In the troposphere, the drag effects of the surface grow near to the surface, which affects movements and processes in the boundary layer [26]. Boundary layer depth ranges from 1 km high during the day, to 100 m at night, based on the atmospheric conditions [25, 26]. The boundary layer consists of several layers, such as the planetary boundary layer (PBL), the turbulent surface layer (TSL) and roughness layer (RL), as shown in Figure 2-2 [25]. The geostrophic wind is active within the free atmosphere layer, which is located above the boundary layer. This wind controls the movements of synoptic weather systems [25] and is affected by Coriolis force more than roughness factors at the surface [27]. The movement of synoptic weather systems leads to annual and seasonal variation of the wind speed [23]. Within the TSL, wind flow is highly affected by roughness length (z_o) in the RL [27]. Wind speed within TSL is affected by the drag force of surface roughness, which is exerted on the wind flow. The drag force of surface roughness forms shear stress (τ), which lead to reducing momentum of wind flow near the surface, until the wind speed is zero [25, 26]. In addition, the roughness length in the RL causes turbulennce in wind flow within TSL [25]. Furthermore, the daily variability of wind speeds is created by heat flux from the Earth's surface. The quantity of heat flux changes throughout the day; the strongest occur during periods of highest solar radiation [26]. The heat transfer from the surface leads to an increasing temperature of an air parcel, which rises due to buoyancy forces, which causes a pressure differential at the surface [28]. The variation of thermal capacities between land and water leads to differing buoyancy forces over these surfaces, which in turn, leads to increasing differentials in the wind speed [23].

The greatest interaction between Earth's surface and atmosphere occurs within the troposphere layer, which represents the lowest 11 km of the atmosphere [25]. The most atmospheric transportation processes such as wind flow and turbulence happen within the boundary layer which represents the lowest layer of troposphere, ranging from 100m to 3000m, depending on the weather condition, while the remainder of the troposphere is generally called the free atmosphere layer, as shown in Figure 2-1 [26]. The boundary layer has been defined as the lowest part of the troposphere, which is directly affected by the

existence of the Earth's surface and responds to surface effects during the time scale within the limits of a hour or less [26].

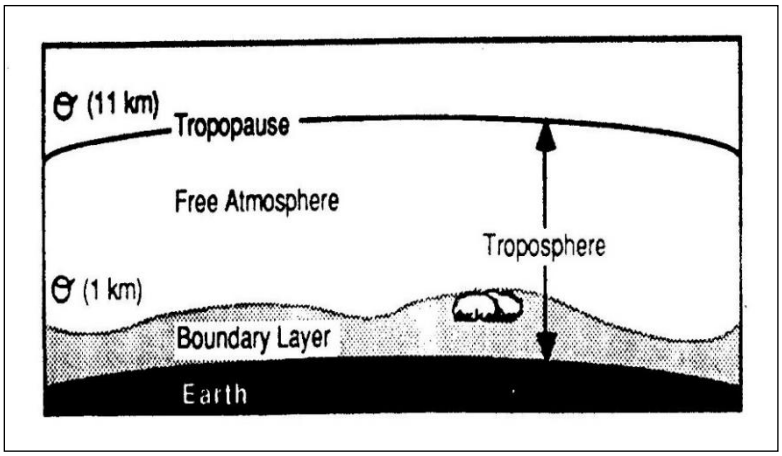

Figure 2-1. The troposphere layer, which includes the boundary layer and free atmosphere [26].

These effects involve a wide variety of physical elements, such as friction drag, heat transfer, rough and rigid surface, pollutant emission, evaporation and transpiration [25, 26]. The previously mentioned physical factors generally cause turbulence in wind flow that, in turn, leads to changes in the vertical wind profile and also causes significant variation of the wind speed [29]. The boundary layer has several significant layers: TSL; PBL and RL, which are shown in Figure 2-2 [26, 27].

2.2.1 **Similarity Theory**

The Monin-Obukhov similarity theory has been used to describe the variation of wind speed with height, within the TSL, by using empirical data. In addition, similarity theory described the logarithmic vertical profile for mean wind speed within neutral conditions in the boundary layer [26, 29]. Firstly, to define the turbulent part of the wind speed within a logarithmic vertical profile, we should understand the structure of mean wind speed. (u) is the actual instantaneous velocity that includes: mean wind speed ($\bar{u}$) at any time interval about one hour and the turbulent part of wind speed (u') . To get the value of u'we should follow Equation 2-1 [26].

$$u' = u - \bar{u} \qquad \text{Equation 2-1}$$

Similarity theory has been used to describe mean wind speed within the TSL based on the assumption that ($\bar{u}(z)$) represents the mean wind speed of an air mass at height z based on friction velocity (u_*) and roughness length of the surface (z_o) [29]. The roughness length represents the height where wind speed equals zero [26]. The friction velocity u_* is defined

as “the turbulent momentum flux close to the surface” [30]. If an air parcel at height z with mean wind speed $\bar{u}(z)$ has been displaced by vertical distance (Prandtl mixing length l) to height $(z-l)$, the wind speed will be increased to be $\bar{u}(z-l)$. Based on Equation 2-1, it is possible to estimate the value of u', as expressed in Equation 2-2 [26] and as shown in Figure 2-3 [31].

$$u' = \bar{u}(z-l) - \bar{u}(z) = -l\frac{d\bar{u}}{dz} \qquad \text{Equation 2-2}$$

The variation in the wind speed component with many levels can be described using the l. When the air parcel at a height z that goes upward and mixes with the fluid at height $(z-l)$, the quantity of momentum amounting $(\rho u')$ will add to the fluid in the $(z-l)$ where the vertical velocity for fluid is (w').

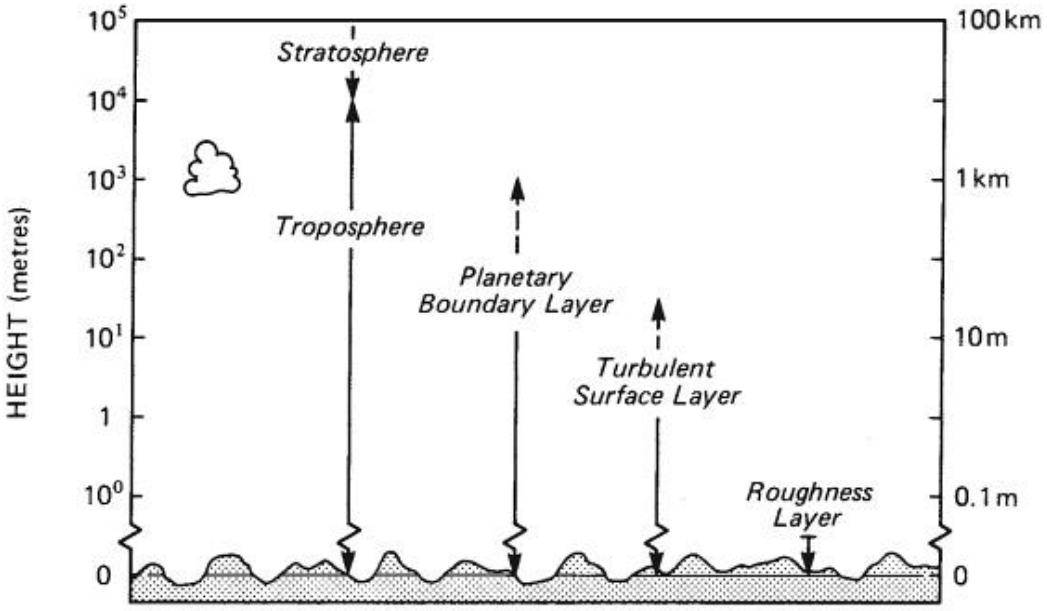

Figure 2-2. Schematic of significant layers within the Boundary layer [25].

The average transfer of momentum to the area unit is called the shear stress (Reynolds stress), as appears in Equation 2-3 [26, 31];

$$\tau = \rho u' w' \qquad \text{Equation 2-3}$$

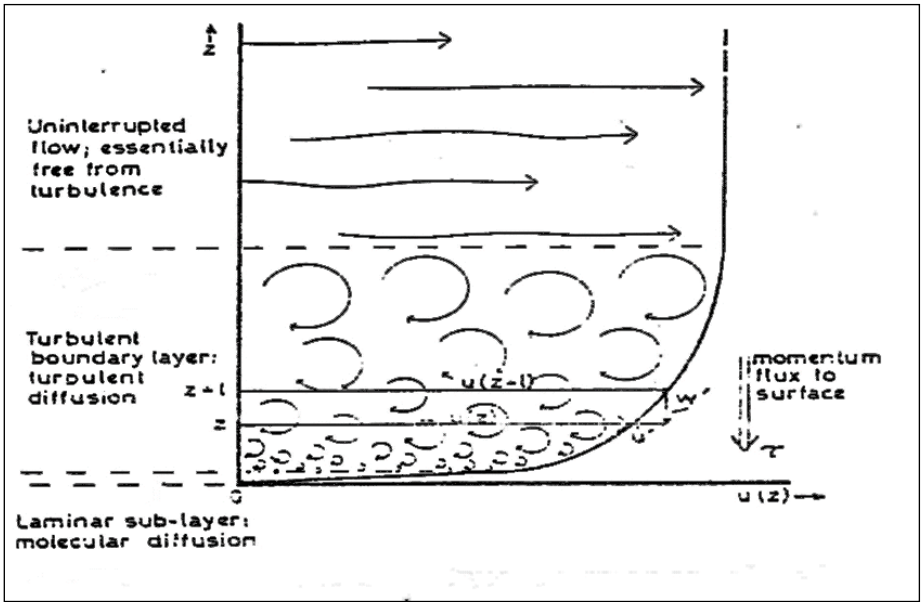

Figure 2-3. Schematic of wind speed with different layers within the boundary layer [31].

The shear stress (τ) is defined in terms of friction velocity in Equation 2-4 [26];

$$\tau = \rho u_*^2 \qquad \text{Equation 2-4}$$

Furthermore, the shear stress (Reynolds stress) is often evaluated in terms of the friction velocity from Equation 2-3 and Equation 2-4. It is possible to calculate the value u_* as expressed in Equation 2-5

$$u_*^2 = \overline{u' \; w'} \qquad \text{Equation 2-5}$$

The momentum flux in the kinematic units is $\overline{u'w'}$; it will be constant through the level where the momentum is constant too. Assuming that $u' = w'$ it is possible to consider that u_* represents the value of turbulent $u' = w' = u_*$ within a turbulent flow. In this way, it is possible to compensate for the value of u_* rather than u' in Equation 2-2 to get Equation 2-6

$$u_* = -l\frac{d\bar{u}}{dz} \qquad \text{Equation 2-6}$$

The variation in a vertical speed component w' can be added, as expressed in Equation 2-7.

$$\overline{u' \; w'} = -l^2 \frac{d\bar{u}^2}{dz} \qquad \text{Equation 2-7}$$

The shear stress in Equation 2-4 represents the turbulent motion of fluid for an average of velocity components v', u' and w' vertically and horizontally and the density of the air ρ.

In addition, the shear stress can be described, based on Prandtl mixing length using the von Karman constant k_v = 0.41, as expressed in Equation 2-8 [25] because Prandtl mixing length is directly proportional to the height from the surface z, as in Equation 2-8 [32].

$$l = k\,z \qquad \text{Equation 2-8}$$

$$\tau = -\overline{\rho u' w'} = -\rho {k_v}^2 z^2 \frac{d\bar{u}^2}{dz} \qquad \text{Equation 2-9}$$

It becomes possible to define the equation of wind shear in terms of describing the velocity fluctuation by combining the Prandtl mixing length and the friction velocity equation, as expressed in Equation 2-10.

$$\frac{d\bar{u}^2}{dz} = \frac{-\overline{\rho u' w'}}{-\rho k^2 z^2} \equiv \frac{du}{dz} = \frac{u_*}{kz} \qquad \text{Equation 2-10}$$

A new value for mean wind speed $\bar{u}(z)$ will be found when integrating the wind shear equation (Equation 2-9) between the surface and height z, based on Equation 2-10 to get Equation 2-11 [26, 28].

$$\int_0^u du = \frac{u_*}{k_v} \int_{z_o}^{z} \frac{dz}{z} \qquad \text{Equation 2-11}$$

When applying Equation 2-11 it is found that when the $z = 0$ the wind speed will be given by $\bar{u}(z) = -\infty$. Therefore the Equation 2-11 will be applicable when the height $z = z_o$ and also for this reason the value of mean wind speed will be $\bar{u}(z_o) = 0$, where z_o represents the roughness length for the surface. Therefore Equation 2-11 after integration will produce Equation 2-12 [25-27].

$$\bar{u}(z) = \frac{u_*}{k_v} log \frac{z}{z_o} \qquad \text{Equation 2-12}$$

From this equation, it is clear that when the surface roughness z_o is increased, the wind speed that was required to generate certain shear stress will reduce also. Consequently, it is possible to rewrite Equation 2-12 as the following formula in Equation 2-13 [32];

$$ln\,(z) = \frac{k_v}{u_*} \bar{u}(z) + ln\, z_o \qquad \text{Equation 2-13}$$

Wind speed has a mean logarithmic profile within a neutral boundary layer based on u_*, the height z, the z_o and the k_v [25]. In addition, it is possible to assess the stability situation by drawing a relationship between $\bar{u}(z)$ and z. This relationship will produce a logarithmic curve with a gradient that equal k_v/u_* within neutral stability conditions. Within unstable conditions, however, the wind profile will deviate from the logarithmic relationship, to form a concave curve; whereas, the wind profile will be a convex curve, within a stable boundary layer, as shown in Figure 2-4 [26].

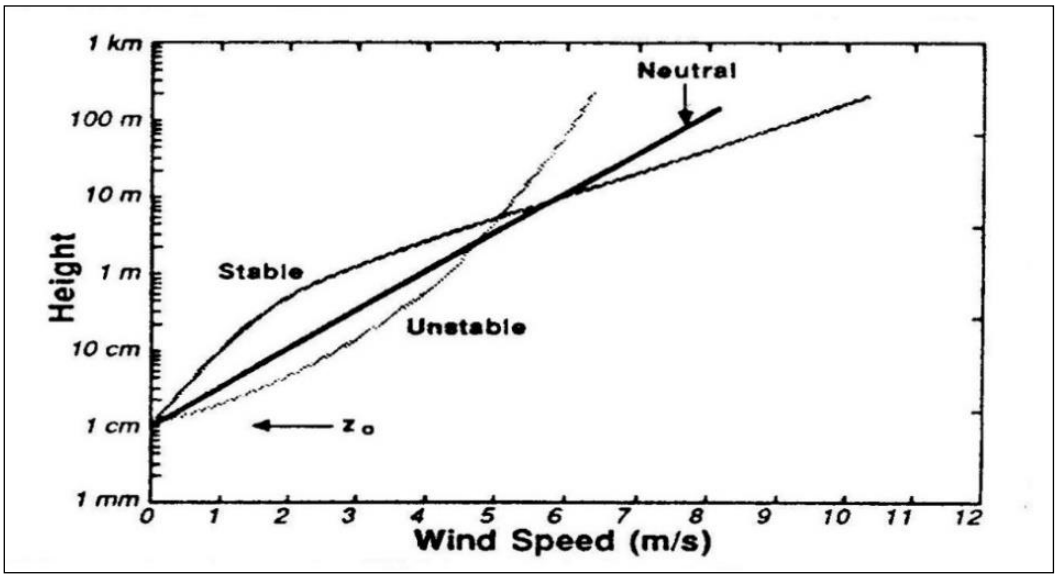

Figure 2-4. Different wind profiles based on a logarithmic relationship for different weather conditions [26].

2.2.2 Aerodynamic Properties in The Boundary Layer

Variation in the roughness length of the surface is one of the factors that play a significant role in changing the wind speed from one region to another. The change in surface roughness elements causes a drag force on wind speed, which leads to reduced wind speed near the surface and a variation in wind speed with height. In addition, the roughness length represents aerodynamic properties to the surface that affect the wind speed. Buildings in urban and suburban areas, forest and orography, represent the surface roughness that affects the momentum of the wind flow within the boundary layer. Several aerodynamic properties are connected with each terrain of the earth's surface;

- z_o is the height above the surface, where the mean wind speed arrives at zero within the surface boundary layer, because of the effect of the surface roughness characterizations on wind flow for a particular surface area [26].
- Canopy height (C_h) is the mean height of the highest trees above ground level in the forest and buildings in the urban area [28]. It is the average elevation of the roughness

elements in a certain area [33]. The canopy height can be expressed as $C_h \approx 10\, z_o$ [28, 33].

- Zero plane displacement height (d) is the height, where the wind speed is equal to zero, because of the presence of several roughness components, rather than a single element. The displacement height is widespread in regions that are regarded as highly rough surfaces, such as suburban and urban areas. The displacement height is approximated as $d \approx {}^{2}/_{3}\ C_h$ [33].

Both the canopy height and displacement height are built on mean empirical data. This empirical data should be collected from weather stations, wind farms, or wind tunnel experiments to get approximated values for canopy height and displacement height [33]. Approximations of the displacement and canopy height are essential to developing the estimations of surface roughness. The approximations of the displacement and canopy height vary from one area to another, based on differing land covers [33, 34]. Furthermore, the approximations are effective for the assessment of the aerodynamics and will be applied in this project [25, 33]. From the foregoing, it is possible to rewrite Equation 2-12 to estimate mean wind speed to the urban or suburban areas within the boundary layer using displacement height, as expressed in Equation 2-14 [34-37];

$$\bar{u}(z) = \frac{u_*}{k_v} log\left(\frac{z-d}{z_o}\right) \qquad \text{Equation 2-14}$$

The difference in aerodynamic properties over regions which are located upwind of a site will affect wind speed. The aerodynamic properties in each area should be determined [36], to estimate different upwind aerodynamic properties. The aerodynamic properties of the region located in the upwind fetch should be determined to account for the effects of roughness length on wind speed; usually, this region is about two kilometers from a site or is dependent on the hub height of a proposed turbine. Additionally, the characteristics of the upwind area can be averaged to define the regional aerodynamics such as;

- Blending height (Z_{bh}), which is the elevation that represents the frictional effects of individual roughness components at the region's surface even to become homogeneous [28, 36].
- Effective local roughness (z_{0eff}) represents the roughness length of all surface components upwind of the site.

2.3 Probability Wind Speed Distribution.

The wind speed frequency distribution is regarded as a very significant factor in terms of assessing the characteristics of wind speed variations [23, 38]. The easiest and most practical way to evaluate the variation of wind speeds is to use probability distribution [38-42], which is the most useful and flexible method to describe many wind regimes over a long period of time and an important part of designing wind farms [38, 43-46]. In recent decades, the Weibull distribution function has been one of the most commonly used statistical distributions that could present a very useful method to estimate wind speed data [38-40, 42, 45, 47-49]. In fact, several studies have pointed out a number of reasons why the Weibull distribution is the best method to represent the distribution of wind speed. Furthermore, it provides more accurate forecasts of average wind velocity and wind power density than the Rayleigh distribution at an altitude of 10 m [44]. However, there is an essential weakness in the Weibull distribution function: it cannot precisely represent probabilities of observing very low wind velocity and zero [40, 42]. Nevertheless, Weibull distribution represents the best model to assess the variation of wind speed because the aim of estimating observed wind speed is generating power from wind turbines and low wind speeds (between 2.5 and 3.5 m/s) are not sufficient for generating power in this way. Many studies have utilized the Weibull distribution, which has a two factor function, where (k) is the Weibull shape factor (dimensionless factor), (c) is the Weibull scale factor and (v) is the wind speed [23, 42, 44, 45, 47, 50-56]. The Weibull distribution if it is the probability density function $f(v)$, for wind speed is defined by Equation 2-15 [39, 40, 42, 44-50, 52, 53, 55, 57];

$$f(v) = \left(\frac{k}{c}\right)\left(\frac{v}{c}\right)^{k-1} \exp^{-\left(\frac{v}{c}\right)^{k}} \qquad \text{Equation 2-15}$$

While the cumulative density function of Weibull distribution $F(v)$ is expressed by Equation 2-16 [42, 45, 46, 48-50, 52, 53, 55, 57, 58];

$$F(v) = 1 - \exp^{-\left(\frac{v}{c}\right)^{k}} \qquad \text{Equation 2-16}$$

The aim of using these equations is to supply more information to improve the understanding of wind speed distribution in several places, where the scale factor has a close relationship with the mean wind speed, as shown in Equation 2-20, while the shape factor measures the width of density distribution. If yearly and monthly average wind speeds only are available, the factors of Weibull distribution are capable of characterizing the hourly change of wind speed in any region [48]. For example, generally, the value of k is

located between 1.5 and 3, according to the variability of the wind speed. If the value of k is around 2.5 or 3, it refers to a hourly wind speed that diverges from the average wind speed by a small value. However, if the value of k is around 1.5, it indicates that the hourly wind velocity deviates far from the mean wind speed by large values [23, 48]. Weibull distribution is equivalent to the Rayleigh distribution when k =2 which corresponds to a normal wind speed distribution [23, 48, 53, 57, 58]. Furthermore, the lower value of k refers to a wind profile with a great deal of turbulence and also indicates an extensive distribution of wind velocity around the mean wind speed, as presented in Figure 2-5 [23].

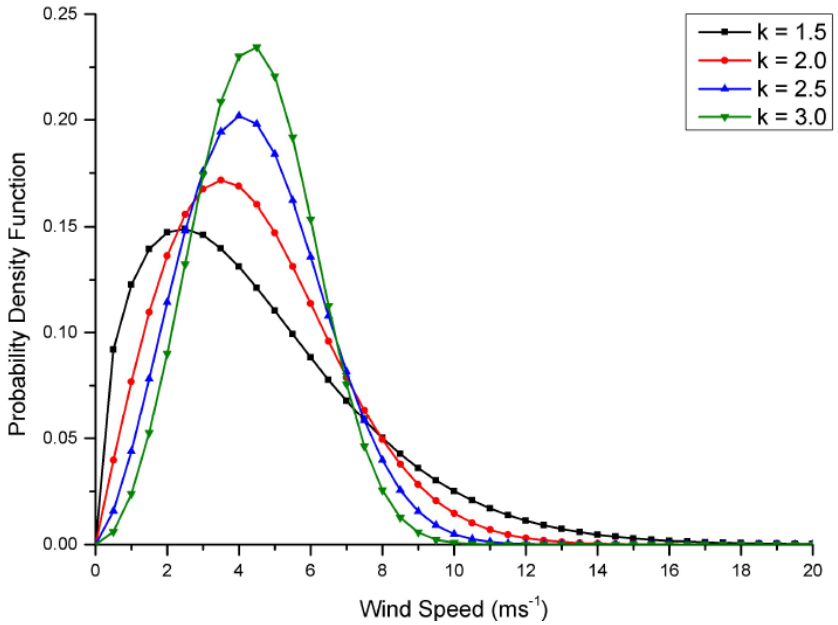

Figure 2-5. This graph shows number of probabilities density distribution, representing the varying shape factors value for Weibull distribution. Reproduced from [23].

In fact, several methods have been developed to estimate Weibull distribution factors using wind speed data [53, 57]. However, the three most commonly used methods to estimate Weibull distribution factors are:

- The Regression method [46-49].
- The Maximum likelihood method [41, 45, 48-50, 57].
- The Moments method [45, 46, 50, 57].

Some of these methods have been known by other names, such as the regression method, graphic method or linear method. Originally, the titles of this method were derived from the Weibull cumulative density distribution function, which can be represented by a linear equation by taking twice the logarithm of cumulative distribution function $F(v)$ Equation 2-17 as follows;

$$\ln[-\ln[1-F(v)]] = k\ln(v) - k\ln c \qquad \text{Equation 2-17}$$

This equation can be presented graphically to define the shape and scale factors of the Weibull distribution [45, 48]. Where $\ln[-\ln[1-F(v)]]$ setting as Y-axis while ln(v) represent X, the graphic relationship $y = k\,x - k\ln c$ will be represented by a straight line, the gradient of this line is k, and the intercept with the Y-axis, is $(k \ln c)$ [47, 48]

Secondly, the Maximum Likelihood method has been considered to be one of the most significant methods to estimate the Weibull distribution factors. In fact, this method requires wide numerical iteration of wind velocity data, taking into consideration of nonzero wind speeds. Where the wind speed is v_i during number nonzero data n. The two Weibull factors k and c can be estimated as follows in Equation 2-18 and Equation 2-19 [48, 49, 59];

$$k = \left(\frac{\sum_{i=1}^{n} v_i^k \ln(v_i)}{\sum_{i=1}^{n} v_i^k} - \frac{\sum_{i=1}^{n} \ln(v_i)}{n} \right)^{-1} \qquad \text{Equation 2-18}$$

$$c = \left(\frac{\sum_{i=1}^{n} (v_i)^k}{n} \right)^{1/k} \qquad \text{Equation 2-19}$$

The value of the shape factor is usually influenced by the variance in wind velocity [23]. It is possible to represent the variance of wind speed using a standard deviation [42]. Finally, one of the common methods that can measure the factors of Weibull distribution using the equation standard deviation and the mean wind speed is shown in Equation 2-20 and Equation 2-21 [41, 42, 46, 49, 51, 52, 59];

$$\bar{v} = c\,\Gamma\left(1 + \frac{1}{k}\right) \qquad \text{Equation 2-20}$$

$$\sigma = c\left[\Gamma\left(1 + \frac{2}{k}\right) - \Gamma^2\left(1 + \frac{1}{k}\right) \right]^{\frac{1}{2}} \qquad \text{Equation 2-21}$$

Where the average wind speed $\bar{v}$ is as shown in Equation 2-22.

$$\bar{v} = \frac{1}{n}\sum_{i=1}^{n} v_i \qquad \text{Equation 2-22}$$

$$\sigma = \left[\frac{1}{n-1}\sum_{i=1}^{n} (v_i - \bar{v})^2 \right]^{1/2} \qquad \text{Equation 2-23}$$

2.4 Wind Resources Assessment

Renewable energies, especially wind energy, play an essential role in resolving the worsening problems of climate change, pollution and the increase in electricity demand, and can contribute to the achievement of a more sustainable energy future for many countries. Wind resource assessment has become the first basic phase for any wind power project to maximize the advantages of using wind power. The role of wind resources assessment is vital to determine the best sites for wind farms and, if it is accurate enough, it will increase the accuracy of estimations in power production. In addition, it is useful for assessing the financial viability of the wind farm project.

Regarding the accurate assessment of wind resources, if there is a 1 percent error in wind velocity measurement, it leads to a 3 percent error in the production of power [60]. Gathering all of the factors affecting variation in wind speed is important to increase the accuracy of wind resource assessment.

Most wind resources assessment models are subject to the classification of spatial and temporal scale, but there is no clear agreement or explicit formula about the spatial and time scale for each significant category [61]. Wind resources assessment models have been divided into three classifications [62], depending on the spatial resolution of coverage area and timescale [63], as presented in Table 2-1.

Table 2-1. Description of spatial resolution and temporal resolution for each of the Microscale, Mesoscale and Macroscale

	Microscale	Mesoscale	Macroscale
Spatial description	Local or site coverage	National or regional coverage	Global coverage
Space scale	From 10 m – 100 m	From 5 km and above	From 50 – 200 km
Temporal scale	Seconds to minutes	Minutes to hours	Hours to days

Each project has several objectives, as well as specific information and datasets from different sources according to the available data and information related to the location of the proposed site [64]. For these reasons, a suitable model should be selected, which caters to the objectives of the project and is capable of dealing with the available data. A number of wind resources assessment techniques will be reviewed. Some of those that belong to the microscale resolution will be discussed in section 2.4.1 (on-site measurement, measure-correlate-predict (MCP), Computational Fluid Dynamic (CFD) and statistical power assessment and analytical boundary layer scaling models). In addition, mesoscale wind resources assessment models will be reviewed in section 2.4.2, such as the Fifth-generation mesoscale model (MM5) weather model, Weather Research and Forecasting (WRF) models. The advantages and disadvantages of each wind resource assessment technique will be discussed, based on site-specific project objectives and available data.

2.4.1 Micro-Scale Resource Assessment Techniques

2.4.1.1 On-Site Measurement

One of the most accurate methods to assess wind power resources at a proposed site is the on-site measurement. Also, the observation data from this method has been regarded as being very significant in estimating and predicting the amount of power that will be produced from the proposed wind farm [60, 65]. Monitoring equipment should be installed in on-site measurements, such as that found in any standard weather station. This station must be installed on-site to measure data for a period usually ranging between at least one to five years [64]. There are two kinds of weather station: the first type has been installed in airports, or near urban settings for climatic and research purposes; the second type is connected to wind measurement programs to evaluate the wind resource in the proposed site for wind farms [64, 66].

The time scale and spatial scale of measuring wind data on-site have been classified as a micro-scale resolution method. The time-step of the recommended sampling period of this method ranged from 10 to 30 minutes, as well as one hour to measure the average wind speed [64, 65]. This method requires a spatial scale ranging from 10 times the elevation of the nearest obstruction or at least more than 100 m [64, 67]. The standard elevation for the anemometer and wind vanes for a standard weather station is ten meters above the ground, according to the standard criteria for the World Meteorology Organization (WMO) [64, 67]. A number of anemometers at different levels up to 100 m above the ground should be installed, to measure the vertical wind speed profile [64].

The method of on-site measurement has various pros and cons. For instance, the on-site measurement is considered the most accurate way to evaluate the wind resource on-site. Furthermore, the observation data from this method might be used as a reference for verification of the Numerical Weather Prediction (NWP) technique and re-analysis of the data. On the other hand, this method requires a long time to observe the data and is the most costly way to gather data. The average cost for a signal station with a 40 m tower which operates over two years ranges from $25,000 to 40,000 [66]. In the context of this project, the high cost and a significant amount of time needed for observing data would be fruitless for the following reasons:

- Wind resources assessment for the whole of Iraq would require an enormous number of weather stations throughout Iraq with a high resolution.
- It requires high funding, which is not available for this research.
- This method needs a lot of time, a vast number of weather stations and two years to conduct the observations, all of which are not available for this project.

Therefore, the production of a wind resources assessment for the whole of Iraq using the on-site measurement method is unachievable.

2.4.1.2 **Measure-correlate-predict**

One of the most common wind resources assessment methods is measure-correlate-predict (MCP). This statistical technique has been used for several years to predict mean wind speed for the long term at the potential site [68, 69]. The strategy of this method supposes a linear regression relationship between wind data for a candidate site in the short-term, with a long-term measurement at a reference location to evaluate the wind speed resource in the candidate site [60, 70]. The procedure of this method can be summarized by observing wind speed and direction for a potential site over a period of up to one year (short-term). This measurement should be gathered simultaneously with the measurement of wind data at the reference site (meteorology station) for a long period, ranging from five to ten years (long-term) [68, 71]. The potential site should be located near to the reference site to achieve a high accuracy assessment. The MCP aims to apply a regression equation to measure wind speed for each wind direction sector for both the reference and potential sites at the same time [72]. The linear regression will draw a straight line to represent the relationship of wind speed between the candidate site y, and the reference site x, as expressed in Equation 2-24 [60, 73]:

$$\mathrm{y} = m\mathrm{x} + c \qquad \text{Equation 2-24}$$

MCP should be applied for one year, which has been suggested to extrapolate the long term wind speed at the candidate site, based on matching similar wind speed data for the same direction sector between the candidate and reference. Then, based on the gradient m and c, it should be possible to predict wind speed at the candidate site for the long term only based on wind data of the reference site [68]. One advantage of applying this methodology is that it is more accurate than other analytical models because it depends on observation data from the candidate site. In addition, this method is more economical than on-site measurement, because it will reduce the lifespan of the candidate station to just one year or less [69], and will decrease the operational costs between $ 13,000 and 20,000 for each station per year, which is drastically less than the price of on-site measurement for five years. Practically, the MCP model does not meet the requirements of this project for the following reasons:

- Firstly, this method is still costly and the funding available for this project is minimal.
- Secondly, this method requires a large number of temporary weather stations to cover all of Iraq.

- This method needs a long time to install a vast number of stations, and it requires considerable time for gathering data, which is not available for this project.
- Finally, most of the meteorology stations which might play the role of reference sites are currently out of service.

2.4.1.3 **Computational Fluid Dynamic**

Exponential developments in the computing field have allowed for complicated mathematical models to be utilized for microscale modeling. One of these complex mathematical methodologies is computational fluid dynamic (CFD) for wind resources assessment. CFD is used to enhance the prediction precision of wind flow, particularly in complex topographies, as well as in urban areas [71, 74]. The CFD technique is able to output high-resolution information about the wind flow and provides a clear description of the interaction of the wind flow with geographical, topographical features and roughness at the location of the wind farm [75, 76].

CFD is a wind model which is used to evaluate wind resources above complex terrains, within a micro-scale resolution, using non-linear solvers of fluid flow equations, as represented by the Reynolds-Averaged Navier–Stokes equations [71, 74, 76]. These equations consist of the following [75]:

- The law of conservation of mass.
- Newton's second law
- The law of conservation of energy.

CFD has several features and advantages. Firstly, this technique can be a faster method of assessing wind resources at the potential wind farm, for example, CFD is faster than MCP and on-site measurement based on the period of measuring data, as well as a less expensive wind resources assessment as this technique works within a micro-scale or urban area. Furthermore, it provides an accurate description of turbulent wind flow in urban areas, within neutral stability conditions in the surface boundary layer [74, 77, 78]. Fundamentally, the required input data to run the CFD technique should be observation data from an on-site measurement. To obtain accurate results using CFD requires highly accurate wind climatology, neutral surface boundary layer and isothermal condition as an operating environment [79], including wind direction at three dimensions over the long term (one year without missing data), a suitable location that ranges from 50 m to 100 m around the mast and a standard elevation above the ground (10 m, 30 m, 50 m) [75]. However, the CFD model is not a suitable choice to achieve the objectives of this project for the following reasons:

- CFD techniques require a massive amount of high-resolution climatology data for each potential site for the whole of Iraq. Practically, this kind of data is limited because few weather stations measure hourly data.
- This methodology necessitates the installation of more than one station at the candidate site to measure wind data for one year at least. But the funding of this project is too limited to cover the cost of this modeling throughout Iraq.
- This project does not have enough time available to install a vast number of stations, or to gather data for one year at least, for all of Iraq.
- This modeling requires an enormous amount of information about the topography, geography and roughness elements for a large number of potential sites throughout Iraq which are unavailable currently.

Therefore, the production of a wind resources assessment for all of Iraq using CFD techniques is unachievable.

2.4.1.4 Analytical Boundary Layer Scaling Models

One of the most significant wind resources assessment techniques that gathers the advantages of both microscale and mesoscale models is the downscaling model (the boundary layer scaling model) [28, 80, 81]. It should be noted that the downscaling model can calculate the wind speed at the desired height by vertically scaling the reference of wind climatology based on roughness elements of the surface, which in turn can lead to varying the wind speed vertically [25].

The downscaling model (DSM) has been derived from the Monin-Obukhov similarity theory using a logarithmic wind profile, which was explained in section 2.2.1. The first step in this method requires scaling up a wind speed at a reference height above a reference wind climatology, where wind flow becomes homogeneous due to that the roughness of a regional and local surface is beyond the scope of influence [36]. Secondly, wind speed can be downscaled from the reference height to the blending height, where the wind speed has a horizontally homogenous flow when the effect of surface patches roughness is spatially averaged. Thirdly, the wind speed at blending height can also be downscaled to the hub height, depending on the local roughness of the surface elements [28]. In addition, an accurate wind climatology and local roughness for fetches surrounding the area are required to achieve the DSM calculation [35]. Furthermore, the raw wind climatology data that cover a large scale spatial area can be corrected using the effect of site elements roughness using the DSM [82]. Here it is also evident that boundary-layer stability and terrain-roughness have a significant impact on characteristics of wind flow profile within the boundary layer.

For these reasons, highly accurate data about these factors limit the application of boundary layer scaling models [81]. For example, different kinds of roughness, which represent the texture of the surface ranging from grass, trees and farmhouses, buildings in suburban and urban areas, will decrease the wind speed due to the drag force of roughness elements of the ground, while the intensity of drag force depends on the density of roughness elements above the surface. The drag of these elements will reduce the wind speed near the ground and then the wind speed will increase with height until blending height, when the flow of wind speed becomes more homogenous, and the change of wind speed with elevation will be small, as shown in Figure 2-6 [36].

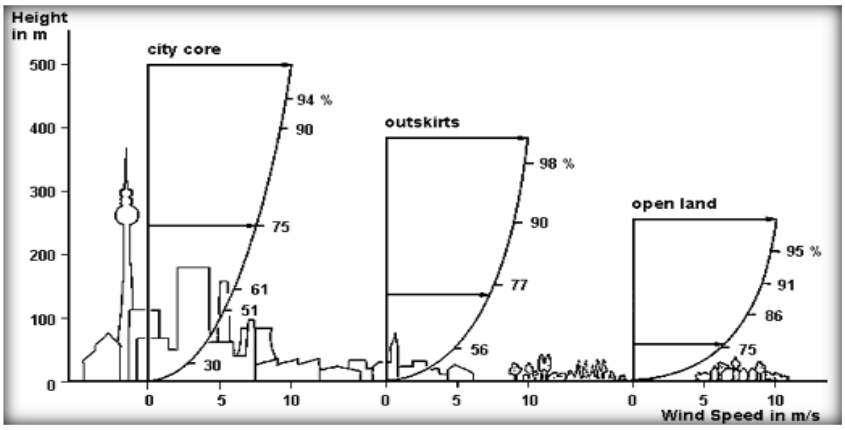

Figure 2-6. Effect of surface roughness elements on wind flow through the boundary layer [36].

In addition, the stability of the surface boundary layer plays an essential role when increasing or decreasing the intensity of changing wind speed with height. For instance, the wind speed variation with height is larger when the surface boundary layer is stable, while the variation of wind speed with height is smaller due to an unstable surface boundary layer, as shown in Figure 2-7 [26].

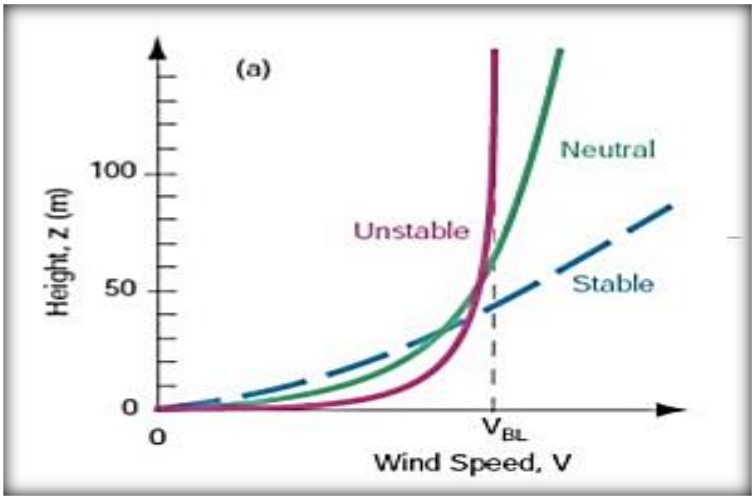

Figure 2-7. wind speed variation with height in the surface layer with the different conditions of stability [83].

As with any other model used to assess wind resources, there are several advantages and disadvantages to the performance of DSM. Generally, the DSM is regarded as one of the most suitable applications for the microgeneration of wind turbines in a wide range of surface roughnesses such as those found in rural, suburban and urban areas [36]. In addition, this technique has been considered the cheapest model to assess wind resources because it only requires wind speed data for different levels and roughness length data for the site. In general, most reference climatology centers provide observation data or reanalysis data.
Furthermore, the DSM is a suitable technique for producing a wind resource map of Iraq in this project. Currently, data scarcity for the whole of Iraq, such as hourly wind speed data for several levels, is considered one of the most significant barriers to assessing wind resources in Iraq..
On the other hand, a number of disadvantages are related to applying the DSM, such as the accuracy of wind data and the roughness length of a site surface. If this technique has been provided by weak data, it will produce a high level of uncertainty regarding the output, according to the rule that any error in wind speed will multiply the error in production power by three times [60].

- Firstly, most reference climatology centers provide wind data suffering from low accuracy, because the interpolation procedure does not take into consideration the impact of elements of roughness and the orography of the region on wind flow at the candidate site.
- Secondly, several reference climatology centers supply wind data without direction information, leading to poor assessment for upwind surface roughness.

A comparison reveals an overview of the advantages and disadvantages of microscale wind resources evaluation models, as shown in Table 2-2

2.4.2 Mesoscale Resource Assessment Techniques

2.4.2.1 MM5 Weather Model

Many researchers have noted that the fifth-generation mesoscale model (MM5) is one of the most common mesoscale prediction techniques to be used to describe and produce large scale wind resources assessment maps [71, 84, 85]. This technique employs equations to describe the atmosphere state and it can simulate weather conditions and show how the atmosphere varies with height [86]. The resolution resolved by MM5 ranges from 100 to 1 km [84]. Generally, MM5 uses National Centres for Environmental Prediction (NCEP) data with 24 levels vertically [86], in addition to other sources of global NWP data [87], such as the European Centre for Medium-Range Weather Forecasts (ECMWF) [88]. This model has been designed to reproduce observed climatology data with a high degree of realism [88].

In addition, a wide range of time series for observation data has been reproduced by MM5, ranging from hours to months, with a broad range of climate elements near the surface, such as temperature and wind speed [86, 88]. Studies have found that MM5 has shown a proportion of uncertainty for prediction data approximately 4% at 10 m and 100 m above the surface, while it reviewed an accurate correspondence to measurement at low elevations in particular at 30 and 40 m [86]. It is worth mentioning that a number of basic equations that describe the movement in the atmosphere have been used, including Newton's second law of motion (momentum conservation), the continuity equation (mass conservation), the first law of thermodynamics (energy conservation), the water conservation equation and the equation of state [89]. With respect to the resolution data, MM5 divides the atmosphere into three-dimensional cubes as shown in 4a in Figure 2-8; note that the climate elements, represented by grid points, are located in the centre of each cube [86].

Table 2-2. Advantages and disadvantages of each wind resources assessment model

Microscale	Advantages	Disadvantages
On-site Measurement	• The most accurate way to evaluate the wind resource on-site. • The observation data from this method can be used as a reference for verification of the NWP technique and re-analysis data.	• This method requires a large number of weather stations throughout Iraq for high resolution. • This plan requires extensive funding, which is not available for this project. • This method needs a long time to determine the place and install a lot of weather stations. • Two years for observation are not available for this project.
Measure-correlate predict (MCP)	• This method is more accurate than other analytical models. • More economical than on-site measurement. • The lifespan of candidate station until one year.	• This method is too expensive and also the funding of this project is very limited. • This method requires large number of temporary weather stations. • This method needs a lot of time to install a huge number of stations. • Long time for gathering data is not available to this project. • Most weather stations which might play the role of reference sites are currently out of service.
Computational Fluid Dynamic	• This model can be a faster method to assess the wind resources at the potential wind farm. • Most accurate description of the turbulent wind flow at the urban areas.	• This model requires a huge amount of high resolution data for each potential site in Iraq. • This method needs to install more than one station at a candidate site. • The funding of this project is too limited to cover the cost of this modeling throughout Iraq. • This project does not have sufficient timescale to install a huge number of station and to gather data for one year at least, for whole of Iraq. • This modeling requires a great deal of information about the topography, geography and roughness elements for a large number of each potential sites.
Downscaling Model (MDS)	• This technique is the most suitable application for micro generation of wind turbine in wide range of surface roughness areas, such as rural, suburban and urban. • The cheapest model to assess wind resources • This model is typical technique to produce a wind resource map of Iraq in this project. • Most reference climatology centres provide observation and reanalysis data.	• Most reference climatology centres provides wind data with low resolution. • The accuracy of wind speed, wind direction and roughness parameters play a crucial role to produce high accuracy output data.

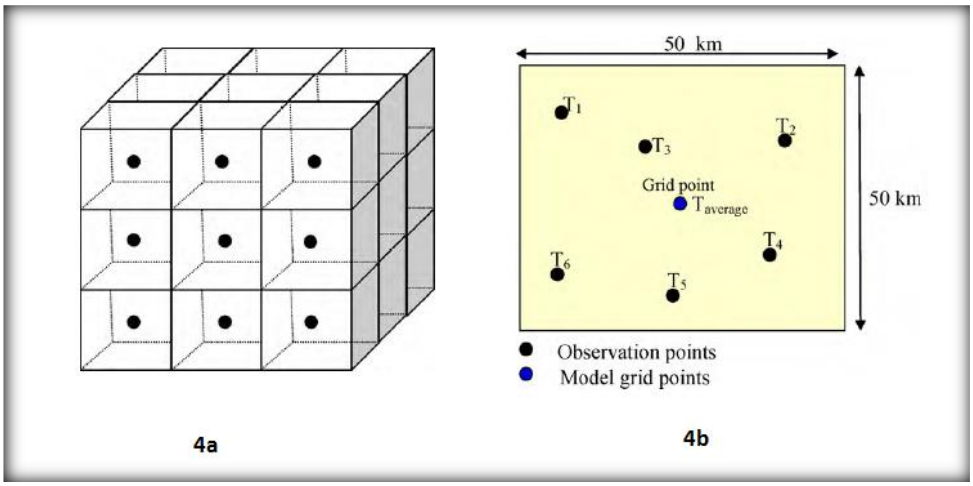

Figure 2-8. The shape 4a represents 3D-cubes of the atmosphere used by NWP models and Figure 4b shows a 50 km grid box, which represents an area of 2500 km2 [86].

MM5 solves weather equations for each climate factor at each grid point. Consequently, the grid cubes will contain the value of variables that MM5 has interpolated in the 3D grid. In the same way, the short distance between the close points forms the high resolution horizontally, as shown in Figure 2-8 part 4b [90]. Furthermore, to increase the resolution horizontally, MM5 uses nested fields for different levels of resolution, according to a rate of 1:3 between the small and the large domains [91]. In the same context, it divides the atmosphere into high numbers of layers vertically, which will increase the resolution in the lower troposphere and allow MM5 to determine boundary layer processes and features. This procedure leads to a significant contribution to understanding the climate elements' behaviour, such as turbulence, temperature, low level winds and stability [86].

Consequently, observation data is interpolated to predict average hourly wind speed at a specific wind park [87]. MM5 has a number of advantages due to several solutions and improvements which have been adopted to develop this model:

- MM5 can simulate a realistic daily cycle for the surface layer variables [88].
- One of the most significant features of the MM5 technique is nesting between different domains of integration [92].

However, NWP models attempt to be close to reality. Generally, MM5 has a number of disadvantages :

- Firstly, MM5 output has a ratio of uncertainty regarding wind speed bias ranging from 0.25 above the flat surface and 2.5 over complex ground [86].
- Secondly, MM5 has shown a proportion of uncertainty for prediction data approximately 4% at 10 m and 100 m above the surface while it corresponds to measurement at low elevations in particular 30 and 40 m [84].

- Thirdly, a high number of errors have been observed regarding the prediction of air temperature near the surface, related to the slow wind speed within a condition of high stability.
- MM5 has difficulty distinguishing accurately turbulent fluxes in the surface layer with strong static stability [88].
- Finally, NCEP and National Centre for Atmospheric Research (NCAR) are wind resources of global data that MM5 model depends on. These wind resources have less accuracy than MERRA reanalysis wind data [93]. NCEP/NCAR have a low spatial resolution of 2.5° latitude × 2.5° longitude, which represents 280 × 170 km every 6 hours, while MERRA data has high spatial resolution data of 1/2° latitude × 2/3° longitude, which represents 56 × 45 km with hourly temporal resolution [28, 94, 95].

Therefore, in spite of the many features of the MM5 technique, this model is not a suitable NWP technique to use in this project for the above reasons.

2.4.2.2 **Weather Research and Forecasting Model (WRF)**

The non-hydrostatic Weather Research and Forecasting (WRF) model has been developed for atmospheric research and operational prediction. The WRF model is regarded as the next-generation in mesoscale forecast techniques and data assimilation systems, after MM5 [96]. WRF has been designed by multi-agency: the NCAR; the National Oceanic and Atmospheric Administration's (NOAA); Mesoscale and Microscale Meteorology (MMM) and the NCEP [97-99]. Generally, WRF has a lot of flexibility in terms of processing a wide spectrum of atmospheric data from many database centres, as well as creating a wide range of horizontal grid and vertical layers. It also predicts a broad range of output data with short periods of prediction. WRF has the ability to simulate the atmospheric situation depending on observation and analyses of data, or using idealized conditions. Currently, most of the data being used by WRF in operational prediction is provided by NCEP and other database centres [99]. Interestingly, WRF is used to supply predictions in real-time and for the next 36 hours for domains WRF4 at 4km and WRF10 at 10 km [100]. In addition, this model is designed to fit a resolution for horizontal grids, ranging from 10 to 100 km [101]. In other case studies, the WRF model is designed to meet high-resolution horizontal grids, ranging from 1 to 10 km [98]. Several studies operated the WRF model at different horizontal grids, such as 4 and 10 km, covering domains WRF4 and WRF10 [100] as well as a horizontal grid equally 25, 50 and 100 km which refer to WRF25, WRF50 and WRF100 [101].

In addition to the horizontal resolution, the WRF model has varying degrees of vertical resolution, which is dependent on the requirement of each study or project. There are two ways to classify the vertical resolution for the WRF model. The first uses the geometric

elevation for the vertical coordinate, while the second uses the hydrostatic pressure gradient as the vertical coordinate [97, 98]. For example, the vertical resolution of one study was divided into 40 vertical layers, starting from 10-hPa at the top and also included 10 levels in the lowest 1 km near the surface [101]. Version 1.3 of WRF had 35 vertical levels with 250m space between each in the lowest 1 km close to the surface and 1 km space above 14 km; this vertical resolution is for domains WRF4 and WRF10 [100]. Another study has 43 vertical levels, starting from 50 hPa from the top with 17 layers between 1000 and 800 hPa [102]. In general, each NWP model has several advantages and disadvantages, based on the performance and the accuracy of predictions. The WRF technique has a wide range of advantages related to the mesoscale assessment:

- WRF has horizontal resolutions ranging from 1 to 100 km grid [98, 101].
- WRF has high-resolution simulation and is similar to the realistic wind for WRF10 [101].
- WRF is very useful for predicting and describing atmospheric components in the oceans and the Arctic by simulating idealized conditions [96].

However, WRF models are considered the latest state-of-the-art mesoscale NWP system that is close to reality. However, WRF has several disadvantages which prevent the model from being used in this project:

- Firstly, use of a simulation procedure to predict atmospheric condition using idealized conditions will not produce high quality outcomes.
- Secondly, the WRF model does not provide a climate data archive for Iraq.

Lastly, in spite of the many features of the WRF technique, this model is not a suitable NWP technique for use in this project for the reasons stated above. In respect to selecting a suitable wind resources assessment technique for this project, it is useful to create a comparison among mesoscale NWP models and Analytical Boundary Layer Scaling Models, in order to reveal an overview of the advantages and disadvantages of each technique, as shown in Table 2-3.

Table 2-3. Comparison between the advantages and disadvantages of each Mesoscale wind resources assessment

Mesoscale	Advantages	Disadvantages
MM5 Weather Model	• MM5 has the ability to simulate a realistic daily cycle for surface layer variables. • One of the most significant features of the MM5 technique is nesting between different domains of integration. • MM5 has been shown to be accurate, compared to measurements taken at low elevations in particular 30 and 40 m.	• MM5 output has a ratio of uncertainty regarding wind speed bias, ranging from 0.25 to 2.5 • MM5 has shown a proportion of uncertainty for prediction data: 4% at 10 m and 100 m above the surface. • A great number of errors regarding the prediction of air temperature near the surface have been observed. • MM5 has difficulty distinguishing accurately turbulent fluxes in the surface layer with strong static stability. • NCEP and NCAR are wind resources of global data that the MM5 model depends on; these wind resources are less accurate than MERRA reanalysis wind data.
Weather Research and Forecasting (WRF) Model	• WRF has wide range of horizontal resolution ranging from 1 to 100 km grid. • WRF has high resolution simulation and is similar to the realistic wind for WRF10. • WRF model is very useful for predicting and describing the atmospheric component in the oceans and the Arctic by simulating idealized conditions.	• Simulation procedure to predict atmospheric condition by using idealized conditions will not produce high quality of outcomes. • The WRF model does not provide climate and weather data archive for IRAQ. • NCEP/NCAR are wind resources of global data that MM5 model depends on; these wind resources are less accurate than MERRA reanalysis wind data.
Downscaling Model (DSM)	• This technique is the most suitable application for micro generation of wind turbines in a wide range of surface roughness, such as rural, suburban and urban area. • It is the cheapest model to assess wind resources. • This model is a typical technique to produce a wind resource map of Iraq in this project. • Most reference climatology centres provide observation and reanalysis data. • This model reveals better description for wind flow near the surface, compared to others.	• This technique is unable to predict these wind speed distributions. • Most reference climatology centres provide wind data with low accuracy. • The accuracy of wind speed, wind direction and roughness parameters play a crucial role to produce high accuracy output data.

2.5 Wind Turbine Power Production and Power Curve Modeling

It is a well-known fact that the wind has kinetic energy which is converted to electrical energy by rotating the blades of a wind turbine; in turn, this produces electricity that comes from a rotating magnetic flux inside the wind turbine generator [28]. In fact, there are two ways to calculate production power from a wind turbine:

2.5.1 The First Method

The first method built was based on the principle of kinetic energy (E_k) for a mass in motion as given by the expression in Equation 2-25 [28]:

$$E_k = \frac{1}{2} m \mathrm{v}^2 \qquad \text{Equation 2-25}$$

This basic physical principles have been applied in wind turbine through calculating the amount power that can be gained from the available wind speed by the blade sweep area of the wind turbine [103]. In this case, the wind turbine works by using a transducer that converts mechanical power in the wind speed that has been captured by the wind rotor into electricity energy. The output power represents a cubic of wind speed through the relationship below, as expressed in Equation 2-26 [72, 104]

$$\mathrm{P(v)} = \frac{1}{2} C_p \, \rho A \mathrm{v}^3 \qquad \text{Equation 2-26}$$

The theoretical wind power that is obtainable from the air mass flow is obtained from Equation 2-27 [105].

$$\mathrm{P_w(v)} = \frac{1}{2} \rho A \mathrm{v}^3 \qquad \text{Equation 2-27}$$

- P(v) represents the power electricity which is converted by turbine per unit of time,
- $\mathrm{P_w(v)}$ represents the wind power, usually measured in Kilowatts.
- (ρ) is the air density kg/m^3.
- (A) represents the area of a turbine rotor in m^2.
- (v) refers to the wind speed which is measured in m/s.
- (C_p) represents the power coefficient of the turbine [72, 104].

One of the important aspects related to the behaviour of typical wind turbines is the power coefficient. It is difficult to transduce a maximum amount of wind power into electricity power for a variety of reasons: blade design, the tip angle, air density, the kind of relationship between wind speed and rotor speed, location of turbine, wind direction, and

wind speed distribution. In addition C_p represents the ratio of theoretical power output compared to the actual wind power available. Theoretically, the maximum value of C_p will not exceed 0.593 (it is known as the Betz limit) [106, 107]. In fact, the value of power coefficient for small wind turbines is typically below 0.5; in addition, Drew (2011) has stated that the majority of power coefficient values varies with wind speed, and in general there are peaks between 5 and 10 m/s [108]. The power coefficient can be calculated by using Equation 2-28 [37, 109]:

$$C_p = \frac{\mathrm{P(v)}}{\frac{1}{2}\rho A \mathrm{V}^3} = \frac{8\mathrm{P(v)}}{\pi\rho d^2\,\mathrm{V}^3} \qquad \text{Equation 2-28}$$

A is the rotor swept area, d the rotor diameter. The wind power output of a wind turbine depends on various wind speeds over a long period, location weather patterns, terrain types and seasonal variations [104]. The electricity power output of a wind turbine has been classified according to the variance of wind speed [105, 107]. Any typical power curve of a wind turbine has three key characteristic speeds:

- ($\mathrm{v_{ci}}$) cut-in is defined as the wind speed at which the wind turbine starts to generate power, when the wind velocity arrives at the cut-in level. Cut-in wind speed depends on the kind of wind turbine [23, 106].
- ($\mathrm{v_r}$) the rated speed is the wind speed that produces the highest power the potential turbine is able to generate. Produced power by wind turbine increases side by side with the wind speed until it reaches the rated speed[23].
- ($\mathrm{v_{co}}$) cut-out wind speed. If wind speed continues increasing, it will reach a point when the wind turbine shuts down power production to prevent damage and defects in the wind turbine machine [23, 106] Figure 2-9 shows the mechanism of power curve for a typical wind turbine.

The three key characteristics of the power curve of a wind turbine represent the common relationship between power production and wind speed that is defined in Equation 2-29 [107, 110]:

$$\mathrm{P(v)} = \begin{cases} \mathrm{P_{r,}} & \mathrm{v_r < v \le v_{co,}} \\ \mathrm{q(v)} & \mathrm{v_{ci} < v \le v_{r,}} \\ 0, & \mathrm{v \le v_{ci}\ or\ v > v_{co,}} \end{cases} \qquad \text{Equation 2-29}$$

- $\mathrm{P_r}$ represents the rated power in wind turbine,
- q(v) refers to the non-linear relationship between wind speed and power.

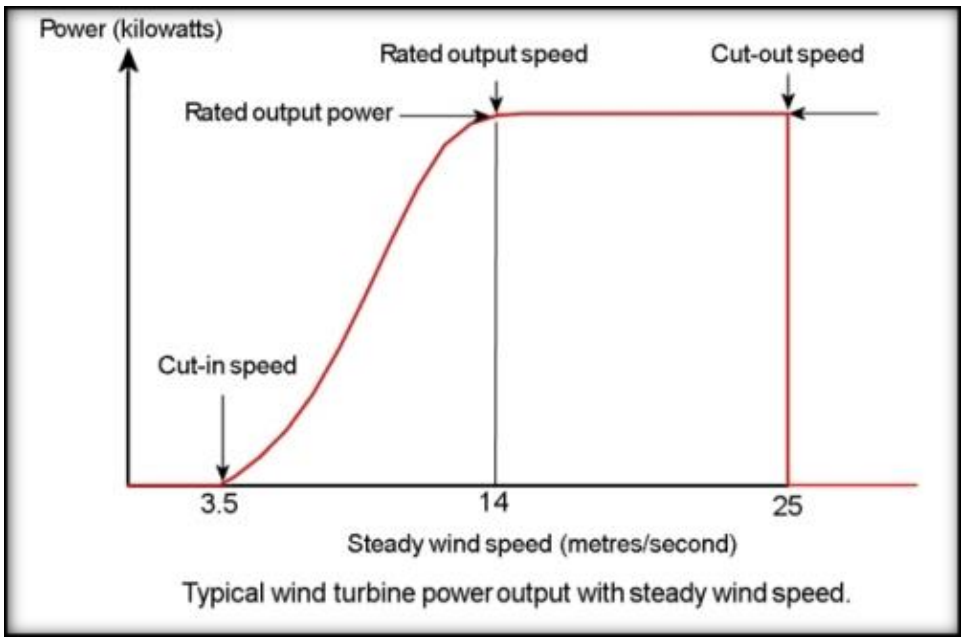

Figure 2-9. Behaviour of a typical wind turbine with wind speed, which shows the three levels of wind speed cut-in, rated wind speed and cut-out [111].

2.5.2 The Second Method

The wind power curve model is regarded as one of the essential tools to assess wind power production within the microscale [105]. This technique estimates wind power production by an individual wind turbine or wind farm at the potential site, aiming to evaluate the performance and determine the uncertainty of a single wind turbine [105, 112]. A wind turbine power curve represents a nonlinear relationship between wind speed and wind power output that is produced by the wind turbine [23, 105, 113]. To achieve high accuracy estimation for output power of wind turbines the power curve method is recommended [108]. The power output from a wind turbine is generated over a wide range of wind speeds that usually range from 1 to 25 m/s . It is possible to draw a power curve that represents the real relationship between observed wind speed and generated power from a specific wind turbine. This power curve normally is provided by the turbine manufacturer based on real data from different sites [108]. The shape of a power curve is affected by a number of factors and features, such as the rotor area, the shape of a blade, number of blades, speed of rotation, the blade shape, the cut-in, rated power and cut-out for wind speeds and also whether the blade pitch control is fixed or moving [37, 108]. Figure 2-9 shows a typical power curve for a wind turbine. At the low wind speed (generally between 0 to 3 m/s) the wind turbine does not work. Nonetheless, the wind turbine will start to generate power from cut-in speed at 3.5 m/s and when the wind speed is increased further the amount of the power output is also increased, until it has reached the rated wind speed to generate the rated power. At this level, the turbine's generated power stays

constant, until the wind speed arrives at the cut-out speed at 25 m/s. At this wind speed the wind turbine will shut down to prevent wind turbine damage [5].

The power curve method has been used in this project because it is more precise than Equation 2-26, since the amount of C_p varies with wind speed as previously mentioned. In this project, the power curve information that comes with the wind turbine specification sheet has been used in the form of a curve or table. In addition, MATLAB was used to calculate the potential power output by applying a polynomial function from a curve fitting tool.

2.6 Data Sources Available

2.6.1 Observational Data From IMOS

Observation data in Iraq is taken from a network of reference weather stations, which are distributed across the country and kept in the Iraqi Meteorological Organization and Seismology (IMOS). There are 51 weather stations in Iraq as shown in Figure 2-10; they provide climate observation data from 1970 until now; this data represents the full range of elements that describe the climate regime above the surface, such as wind speed, direction, temperature, solar radiation etc. [114]. All these weather stations provide IMOS with 8 observations of meteorology data every 3 hours per day [32]. Most weather stations measure the wind speed and direction at the height of 10 m while the weather stations in some airports measure the wind speed, direction data and other climate elements at different elevations within the boundary layer twice a day at 00 and 12 GMT using the radiosonde. The weather station at Baghdad international airport, code number 650, provides hourly surface observation data as well as upper-air data using the radiosonde. This weather station is located 31.7 m above sea level; Latitude: 33° 15' 46" N and Longitude: 44° 14' 7" E [32]. All upper-air and surface weather stations which are associated with IMOS are subject to the criteria of the WMO [32, 114]. High-resolution observation data - such as hourly data - is required to enhance the performance of wind resource assessment models through an increase in the accuracy of the production of wind power density [23] and high-resolution data is necessary for verification purposes. For these reasons, hourly observations of wind speed and solar irradiation data from many weather stations in Iraq are required. Unfortunately, hourly observational data sets in Iraq are scarce and cannot be used directly for resource estimation for several reasons, such as that the observation system is old in most weather stations and measures data every 3 hours. Some of the weather stations do not work because of security concerns and some are already out of service. The only hourly data is provided by Baghdad International airport weather station (BGW), which is associated with IMOS [114]. Even though the weather

station of BGW provides hourly wind speed, direction and temperature long term (from 2004 to 2014), there is missing data for three years: 2009, 2010 and 2011. Furthermore, there are other data collection sources that provide weather observation data in Iraq.

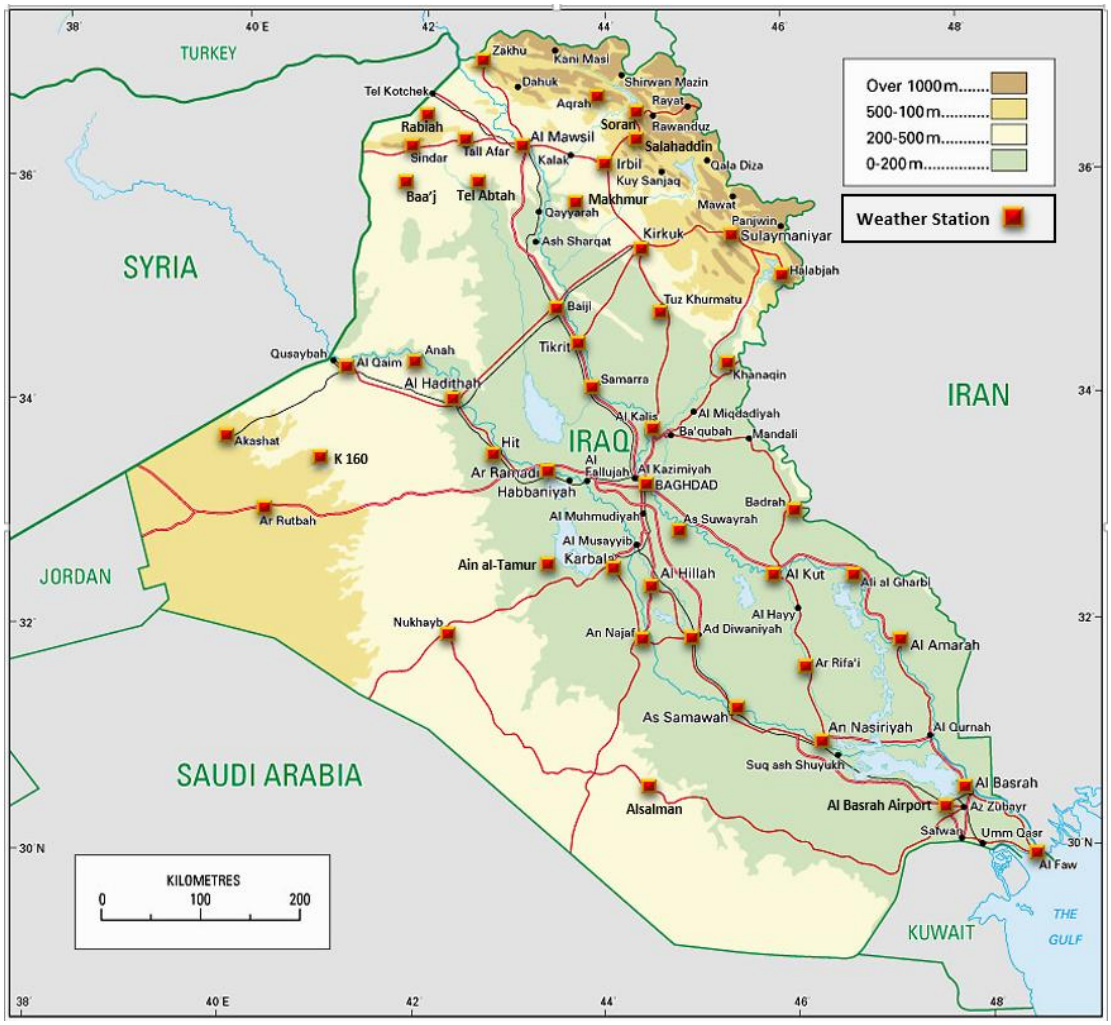

Figure 2-10. Weather stations across Iraq adapted from [114].

2.6.2 Observational data from Iraqi agrometeorological network (IAN).

The Iraqi Agrometeorological Network (IAN) is a specialised department for gathering weather data for agricultural purposes, related to the Ministry of Agriculture. This department has 53 automatic weather stations distributed across the country to provide average monthly, weekly and daily weather data, such as wind speed and direction at the height of 3 m, average solar radiation and other weather data, as shown in Figure 2-11 [115]. Currently, just 7 of these are out of service, so this project will have the advantage of observation data of solar radiation, while wind speed data from these weather stations are not useful, as the wind speed is measured at the height of 3 m above the ground. Finally, observation data from IAN is available online [115].

Figure 2-11. Automatic weather stations associated with the Iraqi Agrometeorological Network (IAN) [115].

2.6.3 Wind Resource Map Data

One of the most important data resources style is wind resource maps which provide estimations of the average wind speed for all of the world or several countries [24]. In the same context, one of the objectives of this project is to establish a general map of wind speed variation throughout Iraq to supply long term mean wind speed - for at least ten years [23] to be a reference for wind resource assessment in Iraq. There are two ways to create a wind resource map: either using observed wind data with high resolution according to spatial interpolation [116, 117], or using microscale/mesoscale wind evaluation models, according to global climatology data [117, 118].

Several studies have used global climatology data from a number of database centres, such as the National Aeronautics and Space Administration (NASA), NCEP/NCAR, Met office and ECMWF, to create a wind resource map [35, 117, 119]. In general, wind resources maps should provide average long term wind speed for different regions and supply the wind speed for several elevations after estimating the local effects of surface roughness and orography on wind speed. Long term data is required to obtain a deeper understanding for trend of wind flow in regions far away from the influence of climate phenomena, such el Niño or sunspot activity [23]. One of the most important benefits of using wind resource maps is that they give an initial visualization about regions which show promise with regard to obtaining wind power [120].

2.6.4 **Operational Forecast and Re-analysis Data.**

In order to assess wind resources anywhere in the world, the NWP models which produce operational forecasting and re-analysis data might be a part of the research tools used to create a map of wind resources, particularly in remote regions or places suffering from a lack of observation data. Recently, many studies have used re-analysis data from different database resource centres, such as NCEP/NCAR, MERRA data and others, to produce wind resources assessment [28]. The first function for NWP is the operational prediction for wind power, which branches into two groups:

- The operation of the first group depends on the analysis of historical wind data, using a statistical method to predict average hourly wind velocity.
- The second group depends on prediction data from another NWP technique as input data through driving mean hourly wind speed and direction from a wind dynamics meteorological technique [121].

In addition, NWP techniques have three key parts:

- The first part represents the adiabatic flow in the boundary layer.
- The second part consists of the physical equations which describe the variability of atmospheric processes, such as radiation and turbulence.
- The third part represents gathering and assimilating observational data [121].

NWP techniques utilize operational predicting and re-analysis data to improve the prediction of weather patterns. The procedure that has been used by NWP to develop a forecast weather pattern consists of analysing and assimilating observational data with multiple previous short term predictions to determine the forecast that has the best adequate with observation data. By using this procedure, NWP will produce various short-term predictions for weather maps in the future, and then the best short-term predictions will be used to create long term forecasts of weather patterns [122]. Although the prediction methodology is based on observation data, it does not mean that the NWP technique data is without errors [123]. Furthermore, NWP techniques create re-analysis data by describing the behaviour of weather variables such as wind speed, pressure, temperature and humidity through use of observation data, alongside historical forecasts using various operations [28, 124]. For instance, the retrospective forecasts, which are utilized to adjust and calibrate the real-time operational forecasts with historical forecasts [124] will increase the accuracy of re-analysis data by taking advantage of all previous re-analyses through finding out and correcting the last mistakes [28, 124]. To improve the results of operational forecasts, NWP should assimilate a great deal of observation data from different resources, such as

gathering data from radiosondes, ships, aircraft and surface weather stations to create a three-dimensional grid of weather variables [125].

Re-analysis data is a procedure of analyzing data a second time, which is produced by forecasting weather from the initial use of real-time data [125]. The re-analysis data helps to present observational data, which does not appear in the operation forecasting during real-time [28]. Additionally, there are several advantages from using the re-analysis data produced by the global NWP model [28]:

- Re-analysis data is considered the best solution for regions or countries that suffer from a lack of data or massive amounts of missing data.
- Recently, re-analysis data produced by NWP models in a number of data sets is now regarded as the cheapest data resource based on observation data.
- Re-analysis data which covers historical data for several decades might never be provided by weather stations for potential sites.
- Wind re-analysis data which is specifically based on observation data has been defined above displacement height at 2 m, 10 m and 50 m above the surface [126]. In addition, surface wind speed measures above sea surface such as observation data from offshore site or above airport surface for computational purposes [127].

Currently, there are several global climatology data sets which provide re-analysis data over many decades and for many regions, with a wide range of temporal and spatial resolutions [28]. The most famous global sets are NCEP/NCAR and MERRA [93].

2.6.5 **MERRA Re-analysis Data**

In the last decades, MERRA (Modern-Era Retrospective analysis for Research and Applications) [94] data set center has been considered as a reliable source of re-analysis data in comparison with observation data [28, 93]. Basically, MERRA outputs are produced using the Goddard Earth Observing System Data Assimilation System Version 5 the GEOS-5 DAS [128]. In addition, re-analysis data of MERRA database represent the retrospective-analyses of observation data by integrating wide range of observing systems with NWP, in order to produce "temporally and spatially consistent synthesis of observations and analyses of variables not easily observed" [129]. The MERRA was carried out by NASA's Global Modeling and Assimilation Office for two reasons:

- Firstly, it was used to employ monitoring data from NASA's Earth Observing System satellites within a climate situation.
- Secondly, it was used to develop the hydrologic cycle of previous reanalyses generations on a wide range of climates over spatial and temporal scales [94, 95].

Moreover, recent evidence suggests that the MERRA re-analysis data has shown higher temporal and spatial resolution data in comparison with the NCEP/NCAR in connection with the regional wind climate [93]. For instance, NCEP/NCAR has low spatial resolution of 2.5° latitude × 2.5° longitude, which represents 280 km × 170 km every 6 hours, while MERRA data has high spatial resolution data of 1/2° latitude × 2/3° longitude which represents 56 × 45 km with hourly temporal resolution [28, 94, 95]. In addition, Liléo [130] has asserted that MERRA and the Climate Forecast System Reanalysis (CFSR) data have better performance than NCEP/NCAR data and they also have shown high levels of accuracy with regard to power production.

Generally, the reanalysis technique of MERRA consists of incorporating the model fields with observation data for various climate elements, which have been distributed irregularly across place and time within a grid of a meteorological dataset, based on a historical data record using NWP as has been mentioned in section 2.6.4; this NWP model is called NASA GEOS-5 DAS data assimilation system [94]. Spatially, MERRA has a high grid resolution meteorological 1/2° latitude × 2/3° longitude with 72 columnar levels expanded through the stratosphere. In other words, it starts from ground level up to a height of 0.01 hPa [94, 95, 131]. Temporally, MERRA data has provided hourly reanalysis data for 24 hours per day since 1979, which will lead to a supply of data with a high temporal resolution in the long term [95, 131]. Basically, MERRA reanalysis data depends on different types of observation data and from different resource databases over the long term. For example, MERRA has benefitted from observation data produced by some important data archive centers, such as NCEP/NCAR reanalysis data, the CFSR and the ECMWF data. Figure 2-12 shows the amount of radiosonde data per year, for each main database center, for the period 1948 to 2000 [94].

The observation data that has been used by MERRA consists of measurements of standard climate variables, such as pressure, height, temperature and wind components, which have been gathered by various weather station instruments, such as balloons, ships, aircraft, buoys, and satellites. Most previous observation data covered the whole global map, measured since 1940 by NCEP/NCAR, which is represented in Figure 2-13 [94].

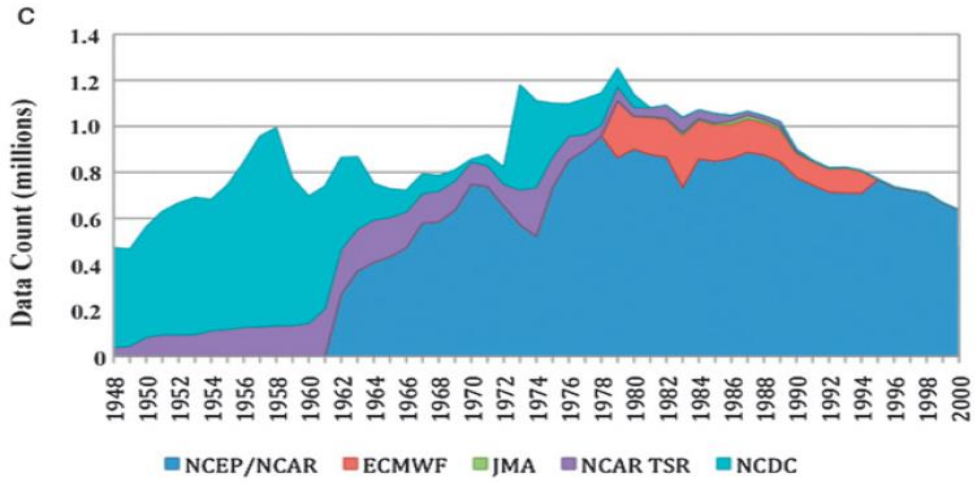

Figure 2-12. Counts of merged radiosonde data per year from each of the main archive database centres, 1948–2000 [94]. Japan Meteorological Agency (JMA). Time series raob (TSR). National Climatic Data Center (NCDC).

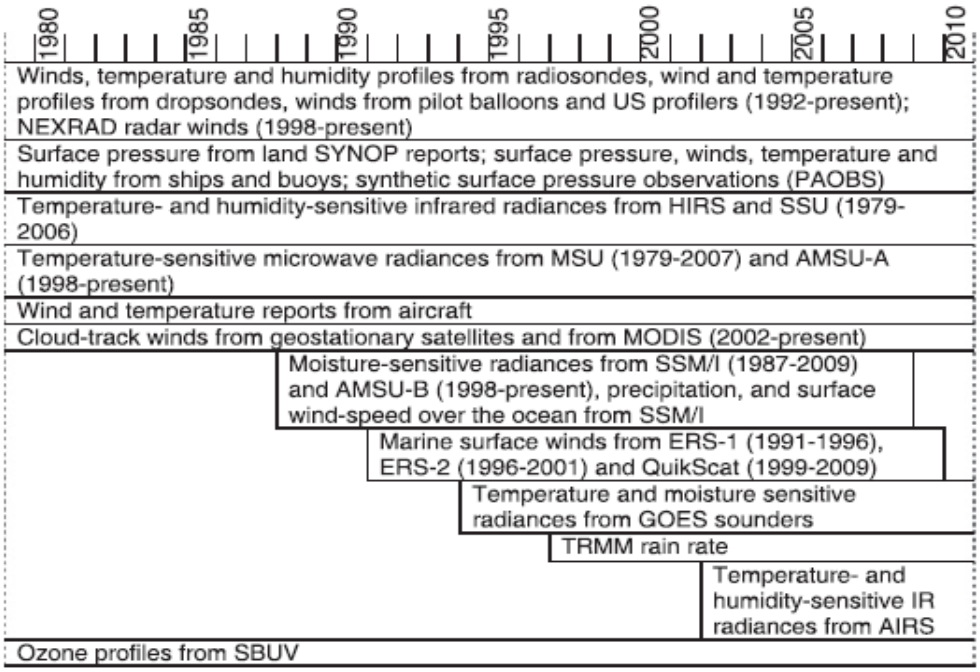

Figure 2-13. Outline of the observing regime used by MERRA, 1980–2010 [94]. NEXRAD or Next-Generation Radar is a network of 159 high resolution S-band Doppler weather radars. SYNOP (surface synoptic observations) is a numerical code created by WMO for reporting weather observation data. PAOBS is "data" used by the NCEP and ECMWF analyses/forecasts. High Resolution Infrared Radiation (HIRS) [132]. Stratospheric Sounding Unit (SSU) [133]. Microwave Sounding Unit (MSU) [134]. Advanced Microwave Sounding Unit-A (AMSU-A) [135]. Moderate Resolution Imaging Spectroradiometer (MODIS) [136]. The Special Sensor Microwave/Imager (SSM/I) [137]. European Remote Sensing Satellite, (ERS-1 and ERS-2)[138, 139]. Geostationary Operational Environmental Satellite (GOES) [140]

MERRA produces reanalysis data through a merged range of monitoring systems using numerical models to yield a temporally and spatially steady composition of monitoring and analyses of variables over a long time frame [131]. It is worth mentioning that the wind re-analysis data, which is specifically based on observation data, has been defined above displacement height at 2 m, 10 m and 50 m above the surface [126]. Furthermore, for

practical purposes, MERRA wind speed at 2m and 10m output are intended to compare with screen level weather stations [141].

Finally, the procedure of producing the reanalysis data from MERRA is explained in section 2.6.6. The wind speed of reanalysis data that is necessary to map the wind resources in Iraq was downloaded by Network Common Data Form (NetCDF) file format from Modeling Data and Information Services Center (MDISC) Subset — GES DISC Goddard Earth Sciences Data and Information Services Centre [142].

2.6.6 MERRA For Data Assimilation System

The MERRA is the source of reanalysis data for wind speed at 10 m and 50 m used by the DSM in this project [129]. MERRA produces the IAU 2-Dimensional atmospheric single-level diagnostics that includes east and north components of wind speed at 10 m and 50 m above the displacement height [128]. The reanalysis data from MERRA covers the period from 1979 to the present, with plans to expand the analysis in the future as resources allow [94].

The (GEOS-5 DAS) represents a substantial evolution of the system, depending on a joint analysis with the NCEP and NCAR [126]. The new GEOS-5 atmospheric general circulation model (AGCM) applied by MERRA uses finite-volume dynamics [126, 143].

In addition, MERRA utilizes three-dimensional variational data assimilation (3DVAR) analysis algorithm applied in the Grid-point Statistical Interpolation Scheme (GSI) to facilitate the application of anisotropic, heterogeneous differences [94, 144]. The 3DVAR has been used previously to resolve the problem of intermittent data that isolated sporadic forcing by applying a statistical interpolation system such as Optimum Interpolation (OI) and 3DVAR [94, 145].

For full understanding of the concept of the data assimilation system operation in MERRA which produces the components of wind speed above the displacement height [128], we should return to GEOS-1 DAS to understand how this system was working and the types of difficulty that it faced and the methods of solution that have been used so far.

The data assimilation system was performed by Data Assimilation Office at NASA / Goddard Space Flight Centre to produce multiyear assimilation, was running for the period from 1985 to 1993. This data assimilation system has been built on the procedure of combining the random distribution for meteorological observation data by using the General Circulation Model (GCM) to produce general four-dimensional information on the global atmosphere. This process includes the interaction between analysis measured data and proceeding of GCM integration within semi-operational constraints for the assimilation system [145].

The continued data assimilation required incorporation of the data into an ongoing model integration as the data was obtained. The main difficulty with this procedure is the instant data are often quite patchy and scattered data. That leads to the problem of operating GCM related to the right responses for isolated and separate data. To resolve this issue, some methods applied the technique of Repeated Insertion (RI) of data. This technique attempts to fill the gap between atmospheric data by carrying multiple uses for each observation of the data over a period [145]. This technique has reduced the accuracy of reanalysis data from the assimilation system. Subsequently, intermittent approaches were employed to increase the efficiency of the data assimilation system. These approaches usually start with a statistical interpolation system like OI and 3DVAR. These methods combine all measuring data in a time ''window'' (typically 6-hours) with a background field regularly taken from a 6-hours' GCM prediction, to form an analysis. This analysis is then utilized as initial data for the next 6-hours' prediction of the GCM process. Indeed, two related issues were increasing with the intermittent approach:

- Firstly, disturbance in the model work was caused by shocks and data rejection.
- Secondly, sudden local changes to the GCM fields can drive large nonphysical adjustment operations; in this way, the forecasting results from the model will not be useful due to the reduction of the impact of valid observation[145].

In order to minimize the fake periodic disturbances of the analysis from data assimilation, MERRA has used the Incremental Analysis Update (IAU) technique [126] that was improved by Bloom in 1996 [145].

2.6.6.1 **GEOS And IAU Process**

In 1996, Bloom developed the IAU technique by using GEOS-1 DAS [145]. The data assimilation system consists of two essential subsystems:

- The first one used analysis that incorporated observation data with the background field.
- The second one used the GCM forecast. Both of them supply the analysis background fields and transfer the analysis information forward in time.

The IAU process is the technique through which the analysis information is combined with the GEOS-1 DAS integration.

2.6.6.2 **GCM**

A General Circulation Model (GCM) is a kind of climate model, also known as a global climate model. It employs the self-same equations of motion as a NWP model [146]. In addition, it uses a mathematical model of the general circulation of an ocean or planetary

atmosphere. It employs the Navier–Stokes equations on a rotating sphere with thermodynamic and hydrodynamic terms for various power sources. These equations are the foundation for computer programs utilized to simulate the Earth's atmosphere or oceans [147]. The GEOS GCM employs the Aries/GEOS Dynamical Core presented in Suarez and Takacs [148]. This finite-difference dynamical model is based on the pattern of latitude and longitude in C-grid in NASA/ Goddard Space Flight Centre. In version 1, the GCM used the second-order energy stable scheme; the second-order scheme for advection in the momentum equation infinite difference and moisture equation [145, 148]. Besides, the dynamical core calculates the time tendencies of winds, surface pressure, temperatures and an arbitrary number of tracers in a complete set of subroutines [148]. Furthermore, the GCM employs Arakawa C grid with 2-degree latitude by 2.5 degrees for horizontal resolution with standard 20 sigma coordinate in the vertical [145].

The GEOS GCM has the maneuverability to use the Matsuno time-integration scheme or incorporation of an Asselin-Robert time filter with the leapfrog time-integration scheme. Moreover, it uses a few unique techniques for incorporating adjustments due to the fact of diabatic processes such as turbulence, radiation, and moisture convection — also, the analysis increments during an assimilation system [145]. At every time step in this model, all prognostication fields are updated because of both the sub-grid-scale diabatic process and dynamical. Equation 2-30employs the leapfrog time scheme for arbitrary prognostic field q as follows [145].

$$q^{n+1} = q^{n-1} + 2\Delta t\left(\frac{\partial q^n}{\partial t}\right)_{total} \qquad \text{Equation 2-30}$$

The time tendency expression is represented on the right-hand side in Equation 2-30. The total time tendency is separated into two main components, as expressed in Equation 2-31.

$$\left(\frac{\partial q^n}{\partial t}\right)_{total} = \left(\frac{\partial q^n}{\partial t}\right)_{dynamic} + \left(\frac{\partial q^n}{\partial t}\right)_{forcing} \qquad \text{Equation 2-31}$$

In this equation “dynamics’’ indicates that the adiabatic process is generated by the dynamic core (momentum and thermodynamic equations), besides any time tendency represented by the filtering process, which is computed at every time step. While the “forcing” tendency expression gives to GEOS-1 DAS a significant degree of flexibility as is expressed in Equation 2-32.

$$\left(\frac{\partial q^n}{\partial t}\right)_{forcing} = moist + turb + LR + SR + analysis \qquad \text{Equation 2-32}$$

The ''forcing'' expression consists of several main adiabatic time tendencies which are frequently updated at a time resolution related to each physical parameter. For this system, the adiabatic trends are updated as follow: the shortwave radiation SR is updated every 3 hours, longwave radiation LR is updated every 3 hours, the turbulence (turb) is updated every 30 minutes, while the moist convection (moist) is updated every 10 minutes. In the last part of Equation 2-32, the analysis represents the ability of GCM to incorporate the analysis increment straight into the prognostic equation [145].

2.6.6.3 **Analysis**

The GEOS-1 DAS used a multivariate analysis of the OI scheme. The OI system creates analysis increments of wind speed components, geopotential height and the mixing ratio length for 14 pressure levels above mean sea level that starts from 1000 to 20 hPa. Furthermore, the OI scheme produces analysis increments above sea level pressure and surface wind speed components over surface oceans only. The analyses of OI are employed at for synoptic times 0000, 0600, 1200, 1800 Coordinated Universal Time (UTC), which utilize an observation data in plus and minus 3-hours around time windows centered on the analysis times. Various observation data sources are used by GEOS-1 DAS: synoptic surface weather station, ships, radiosondes, buoys, TOVS (TIROS-N Operational Vertical Sounder); temperature, cloud-tracked wind speed and the upper-air analyses as reported by aircraft. The last step of the analysis process is represented by interpolating the analysis increments from the analysis pressure coordinate system to the GCM sigma-layer coordinate system [145].

2.6.6.4 **IAU Process**

The intermittent approach of the IO analyses in the GEOS-1 DAS requires some strategies to incorporate the analysis increments into the GCM integration. Various strategies have been used in different data assimilation systems to dampen any disfiguration or unwanted effects of intermittent assimilation. The improvement of the GEOS GCM has given the system an ability to update tendency expressions with forcing to have multiple time scales; this development provides an alternative method to assimilate intermittent analysis. In other words, the analysis increments are processed as extra forcing terms in the GEOS GCM time tendencies.

Figure 2-14 shows the scheme of how the IAU procedure advances through an assimilation cycle. Every six hours, at the beginning of the synoptic times (0000, 0600, 1200, 1800 UTC) an OI analysis is carried out using backgrounds of observations at that time, 3-hours before, and 3-hours after, which assimilates observations data throughout the six hours spanned by the three backgrounds. The results of this analysis are the outputs incorporated in the

two analysis collections. The analysis increments represent the difference between the analysis and the identical synoptic background, which are then divided by a time scale that uses 6 hours to produce an "analysis tendency" on the GCM grid to use as IAU forcing. The DAS model is then "backed-up", it recovers it from its initial state, which had been saved for this purpose three hours before the analysis time, and then the GCM run for 6 hours, adding in the fixed time "analysis tendency", in addition to its normal physical tendencies. At that stage, a restart is generated that will be used next time the model is backed-up, and the first background for the next OI analysis cycle is stored. This first six-hour period operates as the "corrector segment" of the IAU. The operation is then continued without an analysis tendency for the next 6 hours, stores the other two backgrounds required for the next analysis, the first one at the next synoptic time and the second one at the end of the six hours. We refer to this six-hour operation as the "predictor" segment of the IAU. The full cycle is then reiterated throughout the assimilation for subsequent synoptic times using GCM, with no IAU forcing. Note that throughout each of the four daily analysis cycles the model is run for 12 hours, a six-hour period as a "corrector" followed by six-hours as a "predictor"[126, 145].

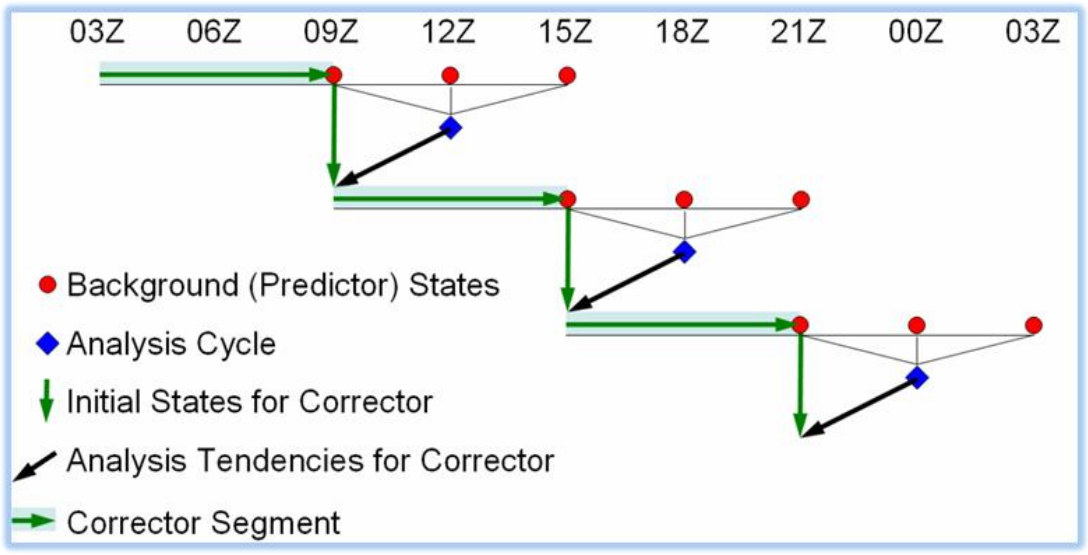

Figure 2-14. Schematic of the IAU application in GEOS-1 DAS [126].

To sum up, the application of IAU in GEOS-1 DAS illustrates a significant development over the previous data assimilation systems. In fact, the employment of IUA in GEOS-1 DAS remarkably reduces the adverse effect of the analysis increments on sensitive model field precipitation. However, some interpretations need to be considered when performing an IAU-based assimilation system as well as when comparing fields from it with those generated via other assimilation systems. The assimilation fields at the central synoptic times in the IAU system are fully and directly affected by the data in the preceding six-hour interval. However, in the other assimilation systems, the analyses at the synoptic time are

affected by data in the mid-time window on those analysis times [145]. Based on this reality of applying the IAU system, in cases where there is a shortage of observation data and side by side with weakness in data distribution within the horizontal resolution, this approach will increase the possibility of generating small errors and some deviations.

2.7 Conclusion

One of the main objectives of this project is to establish a wind resources map with high-resolution data for the whole of Iraq. The wind resources map will provide wind power developers with information about the mean wind speed in the long term. With respect to establishing a map of wind resources for Iraq, a great deal of high-resolution observation data is required from many climatology stations across Iraq. The IMOS database is suffering from severe data deficiency for numerous reasons. Firstly, few standard surface weather stations are available across Iraq (around 51 weather stations) [114], which does not meet the ambition of creating a wind resources assessment map with high resolution for Iraq. Secondly, a large number of weather stations are out of order. Thirdly a few weather stations that measure hourly wind speed are available, such as the weather station of Baghdad International Airport. Lastly, the type of weather station associated with departments in Iraqi universities and IAN do not apply the criteria of WMO for standard surface weather stations. In this case, the best solution is the use of reliable reanalysis databases as a long term alternative to observation.

Reanalysis data from MERRA represents a suitable alternative that provides an effective solution to overcome the problem. This research project requires gathering high-resolution data for each grid square within Iraq to produce a wind resource map with high-resolution. The re-analysis data from MERRA will be used as the primary source for the weather data to map and to assess the wind resources in Iraq. Moreover, the available observation data from Iraq will be used to validate the results of the wind resource assessment model that has been suggested in this project.

The DSM has been proposed to produce wind resource maps in this project, based on re-analysis from the MERRA database and land cover map (LCM) of Iraq as roughness length of the surface. The DSM has a broad range of advantages, as presented in Table ***2-2*** and Table 2-3. Finally, the power curve and the DSM using hourly wind speed from MERRA will be used to estimate the hourly energy production for candidate wind turbine at specific location. On the other hand, the power curve model and Weibull distribution function will be used, to estimate the Annual Energy Production (AEP) rather than hourly wind speed for whole of Iraq due to the computation over hourly data for whole of Iraq take very long time.

Chapter 3 **SOLAR ASSESSMENT**

3.1 **Introduction**

The classic style of generating electricity involves burning oil and other fossil fuels, which leads to an increase in pollution emission in the atmosphere and an increase in the greenhouse effect [149]. In addition, more than two billion people are suffering from a severe shortage of electricity supply, according to the United Nations Environment Programme (UNEP) report [150]. Solar power is clean power, abundant, quiet and it is a renewable energy source. It does not release pollutant emissions to the environment [149]. The solar power that arrives at the earth's surface is around 1.8×10^{11} MW. This quantity of power is several times larger than the current rate of power consumption.

This chapter aims to explain the importance of solar power and reveal the most important basic techniques that can be used to evaluate and calculate solar power production. In addition, the most important solar database to assess solar radiation and solar power production for the whole of Iraq will be discussed. This chapter is organized as commences with an overview of solar power application and solar power components in sections 3.2 and 3.3. In addition, an overview of the photovoltaic power output calculation is outlined in section 3.4. Finally, a survey of the most important solar data resources which are suitable to assess the solar power production in Iraq is presented in section 3.6.

3.2 **Solar Power**

The utilization of solar power has been done by several methods. One of these methods is photovoltaic technology (PV). PV is one of the best ways to take advantage of solar power [151], which converts solar radiation into electricity [149, 150]. There are two kinds of photovoltaic technology system: the first one is a stand-alone system which supplies the load without any connection to the national or local grid by relying on a set of batteries to cover the demand during solar power interruption (at night or when there is a cloudy sky). While the second one is called the grid-connected system which supports the utility grid by producing electricity to reduce the load on the grid [149]. There are many features of photovoltaic technology [149, 151]:

- Solar panels are robust and simple in design.
- A photovoltaic system requires very little care and maintenance.
- The stand-alone system can produce electricity from microwatts to megawatts.

- The stand-alone system is used to provide electrical to water pumping, off-grid building, the communication sector, satellites, solar home systems, and space vehicles.
- Recently the capacity of solar energy production systems has grown up exponentially throughout the world to excess totally 500 GW at the end of 2018 given an increase in the economic feasibility and reliability of solar systems to reach $ 69/MWh [152].

3.3 **Solar Power Component**

Solar power is the solar radiation (electromagnetic power) emitted by the sun from nuclear fusion that occurs in the sun [153]. The solar radiation that falls on the top of the Earth's atmosphere is called extra-terrestrial solar radiation, which represents 97% of spectral ranging between 290 and 3000 nm of the solar radiation (shortwave) [153]. The shortwave is classified as follows [154] and is shown in Figure 3-1. [155]:

- Ultraviolet radiation (UV): 290 nm to 400 nm
- Visible light (VIS): 400 nm to 770 nm
- Near-infrared radiation (NIR): 770 nm to 3000 nm.

While the overall amount of solar power falling on a horizontal Earth's surface is called Global Horizontal Irradiation (GHI) or global solar radiation ($\bar{G}$), the daily $\bar{G}$ represents the whole solar energy for a day, the typical amount for daily $\bar{G}$ ranges from 1 to 35 MJ/m^2 [156]. $\bar{G}$ includes two primary components; the first one is the solar radiation that comes from the sun directly toward the Earth's surface without any scattering through the atmosphere; this is called beam radiation or direct solar irradiance.

Whereas, the second component is the diffuse radiation that represents the rate of indirect solar radiation that comes from the atmosphere after scattering by different parts of the atmosphere towards the horizontal level at the Earth's surface. In other words, diffuse solar radiation is produced by the atmosphere scattering due to atmospheric dust, and water vapor, while some literature has called it either solar sky radiation or sky radiation [156, 157]. Equation 3-1 [156] is expressed to estimate $\bar{G}$ on a horizontal surface:

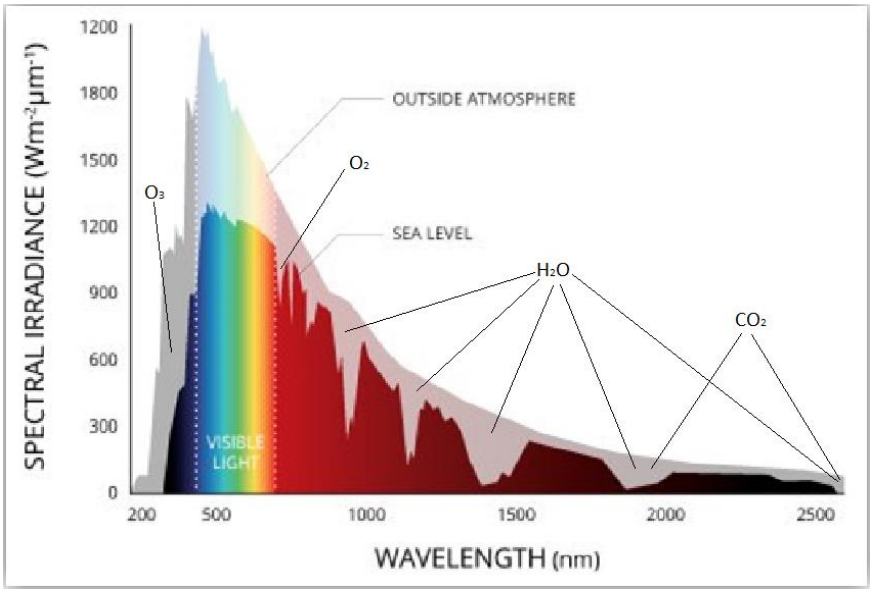

Figure 3-1. Solar radiation that reaches Earth consists of visible and infrared light, in which only a small amount of ultraviolet radiation reaches the surface or sea level [155].

$$\bar{G} = \bar{G}_d + \bar{G}_b \cos(z) \qquad \text{Equation 3-1}$$

- $\bar{G}$ represents Global Horizontal Irradiation on a horizontal surface,
- $\bar{G}_b$ symbolizes to direct beam radiation.
- $\bar{G}_d$ refers to diffuse radiation.
- z represents the sun's zenith angle.

Zenith angle (θ_z) is the angle between the beam radiation of the sun and the vertical axis on the Earth's surface as expressed in Equation 3-2 [158]. the elevation angle is similar to the zenith angle but it is measured from the horizontal rather than from the vertical.

$$\theta z = 90^{o} - \alpha \qquad \text{Equation 3-2}$$

Where α represents the elevation angle or altitude angle, which is defined as the angle between the beam radiation of the sun and the horizontal level of the Earth surface [158]. The elevation angle changes during the day. It is also built on the latitude of the location and the day of the year [158]. The elevation angle of the beam radiation is very important to the PV system. The maximum power is expected to produce by the PV system when the solar radiation falls vertically from a clear sky on the surface plane of the PV module [151]. For this reason, the estimation of elevation angle is considered very important. The elevation angle, α, can be estimated using the following Equation 3-3 [158] and as shown in Figure 3-2 [159].

$$\alpha = sin^{-1}[sin\delta\, sin\emptyset + cos\delta\, cos\emptyset\, cos\,(\omega)\,] \qquad \text{Equation 3-3}$$

- $\emptyset$ is the latitude of the location.
- δ is the declination angle.
- ω is the hour angle [158].

The declination angle is the angle that is located between the equator and a line of beam radiation that comes from the sun to the center of the earth. This angle varies based on the season as well as the Earth is inclined by 23.45° and the declination angle changes plus or minus this degree [158]. It can be estimated by Equation 3-4 [160].

$$\delta = 23.45^{o} \sin\left[\frac{360}{365}(d - 81)\right] \qquad \text{Equation 3-4}$$

Where d is the number of days since the start of a year. HRA converts the local solar time (LST) to the degrees based on the sun as it moves across the sky. HRA is estimated by Equation 3-5 [158].

$$\text{HRA} = 15^{o}\,(LST - 12) \qquad \text{Equation 3-5}$$

To produce high energy from a solar panel during the daytime, tracking the sun into skydome will be an useful technique. Tracking the sun should estimate the Azimuth angle. The Azimuth angle is the sunlight direction that is coming from the sun directly which is moving from east to west [158, 160]. The Azimuth angle is determined by Equation 3-6.

$$\text{Azimuth} = cos^{-1}\left[\frac{sin\delta\, cos\varphi - cos\delta\, sin\varphi \cos(\text{HRA})}{cos\alpha}\right] \qquad \text{Equation 3-6}$$

Furthermore, the other important factor related to daily $\bar{G}$ is the sunshine duration. This factor represents the sum of all the direct solar radiation periods during one day when the direct solar radiation equals 120 W/m^2 or more than that from the sunrise until sunset [156].

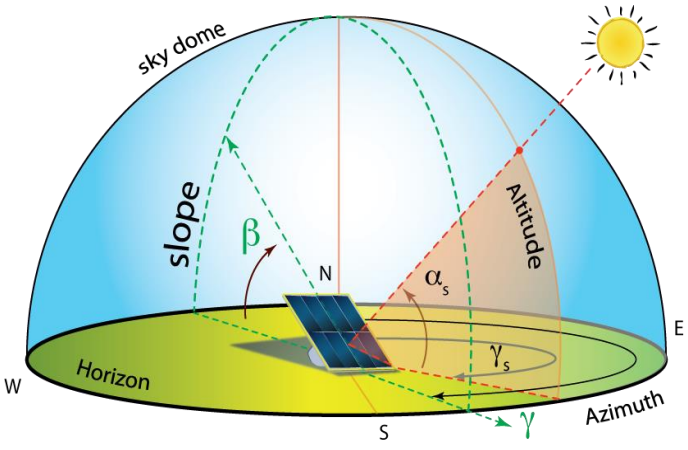

Figure 3-2. Skydome showing elevation angle α, the orientation angle of the solar panel (β) and the solar azimuth angle [159].

3.4 Photovoltaic Power Generation

A Photovoltaic system consists of a number of components such as a solar module which is regarded the main part of solar system, electrical and mechanical connections, wires, mountings, converters (solar inverter) that convert the Direct Current (DC) output of the solar panels into Alternating Current (AC) power and batteries for the stand-alone system and sometimes grid connected [149, 151]. The solar module consists of a number of PV cells connected in series or parallel. In fact, the arrangement of solar cells within one module plays an important role in producing power. The solar cells within a module or modules within a solar array can be arranged to form a specific configuration to generate a specific voltage [150]. In addition, the magnitude of power production from a solar array ranges from a few kilowatt-peak (kWp) for each unit housing to several gigawatt-peak (GWp) from a PV farm station [150]. The kilowatt-peak represents a larg magnitude of electrical energy that is expected to be produced by solar system when the solar radiation falls vertically from a clear sky [151]. The nominal peak power (P_{pk}) represents the ability of the photovoltaic array to produce the power production within Standard Test Condition (STC) that equals 1000 Watt of solar irradiance per 1 m^2 and 25 C^o for array temperature, the nominal peak power declared by the manufacturer. For example, 1 m^2 of PV cells will produce 1 kW with 100% efficiency, if their peak power is 1kWp under STC. Global solar radiation ($\bar{G}$), PV module efficiency (eff) and module temperature T_m, as expressed in Equation 3-7 [161].

$$P = \frac{\bar{G}}{1000}\ A\ \ eff(G, T_m) = \frac{\bar{G}}{1000}\ A\ eff_{nom}\ eff_{rel}(G, T_m) \qquad \text{Equation 3-7}$$

Where the actual efficiency represents the production of nominal efficiency (eff_{nom}) by relative efficiency $eff_{rel}(G, T_m)$. A: is the area of the model. Reformatting Equation 3-7 to yield Equation 3-8 [161].

$$P = \frac{\bar{G}}{1000}\ P_{pk}\ eff_{rel}(G, T_m) \qquad \text{Equation 3-8}$$

Furthermore, the efficiency of the first hand–made solar cell was 5%, where 2 cm^2 of the solar cell was generating just a few milliwatt, while the ability of modern laboratory solar cells has become more than 30% [157]. In fact, the solar system efficiency varies with G and T_m as expressed in Equation 3-9 [162]

$$\eta = \eta_{STC}\ (1\text{-}\beta_o\ .\ \Delta t + \gamma\ .\ log_{10}(G/G_{STC})) \qquad \text{Equation 3-9}$$
$$\Delta t = T_{cell} - T_{STC}$$

where η and η_{STC} are the calculated efficiency and the efficiency at STC. γ and β_o are the irradiance coefficients and temperature, respectively. The variables $T_{cell}\ and\ T_{STC}$ are the temperature cell and the temperature cell at STC, while $G\ and\ G_{STC}$ are the irradiance and the irradiance at STC [162]. Notton et al. [163] have determined the normal values are β_o = 0.0048 and γ = 0.12 for a silicon panel. Indeed, many factors affect the performance of the PV system:

- Electrical parameters such as short-circuit current I_{cc}, the open-circuit voltage V_{co} and the bandgap [164].
- Climate parameters, such as the ambient temperature T_a and insolation G.

Examining these parameters provides an understanding of how they influence the design and performance of a PV system. Also, there is onather factor play a significant role in improving the performance of a photovoltaic module:

- The crucial factor that has an effect mainly on the performance of PV module is the variation with respect to temperature, which influences the efficiency of a PV module. Usually, a high temperature reduces the efficiency of solar panels, which takes place with a non-tracking system. For example, if the PV module is fastened to the roof, there is no chance for the air to move around the PV module.
- In addition, the inclination angle represents a PV module angle with a horizontal plane for (non-tracking) module, which plays an essential role in reducing or increasing the output of a PV module [149, 161].

3.5 Types of PV Technology

The history of the PV can be divided into three distinct groups:

- The first group: crystalline silicon, single-junction
- The second group: Thin-film PV technologies, CdTe, a-Si, CIGS
- The third group: low-cost and high-efficiency thin films and multi-junction.

3.5.1 Crystalline Silicon

A crystalline silicon cell is made by silicon semiconductors that have a built-in electric field. There are two kinds of silicon wafer: monocrystalline and polycrystalline (multi-crystalline). Polycrystalline is cheaper and less material-intense to produce than multi-crystalline silicon but it has a lower efficiency [165].

PV of crystalline silicon still dominates the market with about a 90% share of the market in 2014 [166]. Polycrystalline technology with its lower cost and low efficiency makes up the most significant share with around 55% of total production in 2015 [167].

3.5.2 Thin Films

The thin-film PV has better light absorption characteristics, while the material requirement for thin-film PV is lower than crystalline cells by 100 times [16]. The first thin-film cell was made from amorphous silicon [168]. The issue with amorphous silicon is that it is inefficient and prone to light degeneration [169]. In spite of the capability of printing amorphous silicon onto elastic substrates, that could not mean it makes up a significant portion of the global PV market 2015 [167].

There are also thin-film cells constructed by using polycrystalline chalcogenides; cadmium indium gallium selenide (CIGS) and cadmium telluride (CdTe). Although crystalline, these materials have the best absorption characteristics compared to silicon and can be applied in much thinner layers [170]. CdTe and CIGS also have higher efficiency than amorphous silicon. One of the key advantages of thin-film PV cells over crystalline technologies is that they can be installed onto flexible substrates [167].

3.5.3 Multi-Junction

Multi-junction PV cells can overcome the restrictive Shockley limit by incorporating many p-n junctions into the same equipment; each one has different bandgap energies. Accordingly, multi-junction PV cells can absorb a greater ratio of the solar spectrum and thus produce more power per unit of irradiance [167].

Multi-junction PV cells are presently the most efficient PV cells with a record efficiency of 37.9% under STC [171]. The issue with multi-junction PV cells is that they are costly and therefore only suited to PV systems where high efficiency is needed, such as a power source for satellites [172].

3.6 Solar Radiation Data

In order to estimate solar power production and produce a map for solar power assessment for the whole Iraq, this requires monthly and daily solar observation data for a number of parameters of solar radiation across Iraq such as [149, 157]:

- Direct solar radiation (beam radiation) on a horizontal surface.
- Diffuse radiation (solar sky radiation) on a horizontal surface.
- Sunshine duration per day.
- The incident solar radiation angle.
- The ambient temperature.

The solar observation data is very scarce in Iraq for the same reason as the wind data, as illustrated in section 2.6.1. For this reason, the solar radiation database will be the best alternative source of solar data to evaluate solar resources assessment in Iraq. In the next

sections, several solar radiation databases and database developers are presented. These databases will be validated with observed data to determine the most accurate solar database for Iraq.

3.6.1 Photovoltaic Geographical Information System

The European solar radiation database has been developed by the Joint Research Centre of the European Commission (JRC) utilizing solar radiation techniques and climate datasets that have been integrated with the Photovoltaic Geographical Information System. (PVGIS) merges the long-term laboratory experience in the research field and observing and testing in the field of geographical knowledge. PVGIS is applied as a research tool to improve geographical evaluation of solar power and the performance of PV technology in Europe, Africa, and Asia [173, 174]. The website of PVGIS provides access to maps, databases such as PVGIS-HelioClim; CM-SAF, SARAH, and tools needed to estimate PV output in terms of off-grid and on-grid systems [174]. The solar radiation databases of PVGIS have been developed utilizing the solar radiation model called r.sun algorithms [174]. This model estimates the average values of solar radiation components for the period 1998-2005 and the second period, 2007-2016 [173]. The PVGIS provides several components of solar radiation such as [161, 173, 174]:

- Global radiation for the inclined and horizontal plane.
- Clear-sky and mean real-sky for daily radiation (terrain shadowing).
- The average beam, diffuse radiation and reflected of global radiation.
- The average power that is produced by fixed and tracking photovoltaic systems.
- The optimum orientation and inclination are fixed for photovoltaic modules to increase power production.
- Ambient temperature.

3.6.2 Helioclim1.

HelioClim-1 (PVGIS-HelioClim) is a group of surface solar radiation databases developed by Meteosat Second Generation satellite images. The method used to calculate surface solar radiation is called HelioSat-2, which was produced by the Centre for Energy and Processes, a joint research laboratory of the French school of engineers MINES Paris Tech [175]. This database consists of daily values of $\bar{G}$ and monthly and yearly average $\bar{G}$, systematically calculated over the period 1985- 2005. The spatial area of the HelioClim-1 database matches the field of view of the Meteosat Prime disc (the satellite is centered at latitude 0° and longitude 0°). The original spatial resolution of the HelioClim-1 database was around 15 arc minutes, which is the area of a grid cell close to the equator represents nearly 30x30 km^2. The accuracy of the HelioClim-1 was evaluated by comparisons with observed

data from WMO radiometric network in Africa (35 sites) and Europe (55 sites) for the period 1994-1997. The RMS error is 35 W/m^2 (17%) for daily mean irradiance, 25 W/m^2 (12%) for monthly mean irradiance, and bias is less than 1 W/m^2 for the whole data set [176, 177]. The original HelioClim-1 data (daily values and also monthly and yearly averages) can be obtained through the SoDa web system [178]. In addition, PVGIS is provided daily and monthly HelioClim-1 global irradiation data, in addition to a PV estimation, based on wide range of features [179].

3.6.3 **Helioclim3v5.**

HelioClim-3 version 5 is a group of surface solar radiation databases developed by Meteosat Second Generation satellite images MSG using HelioSat-2 method. In fact, HelioSat-2 method has been used to develop a series of HelioClim data such as HC1, HC3v4 and HC3v5 [180, 181]. The time series of the solar radiation over a horizontal, fix-tilted and normal plane for clear-sky conditions and the actual weather conditions were provided by the HC3v5 Archives Web service [181]. The HC3v5 is the most advanced and recommended of HC3 data. It uses ESRA clear-sky model [182] with observed data from a climatological database and the limitation of observed data has been sorted out by using McClear's model [183]. The geographical coverage of HC3v5 includes Africa, Europe, the Middle East, and Atlantic Ocean. While the spatial resolution is 3 km at (0°) and is rising as soon as moving away from this point [181]. HC3v5 provided data for different time series ranging from 15 min to 1 month. The free data only represents a limited period from 2004-02-01 up to Dec. 2006 [181], while the database for period from 2006 to the current two days is not free [180].

3.6.4 **CM-SAF.**

The Climate Monitoring Satellite Application Facility (CM-SAF) is a solar radiation database provided by The Photovoltaic Geographical Information System (PVGIS). CM-SAF is a part of the European Organization for the Exploitation of Meteorological Satellites (EUMETSAT) [184]. The CM-SAF solar radiation database consists of solar irradiance data derived from Meteosat Second Generation satellites (MSG), which provided data from June 2006 to December 2011. The CM-SAF database has in total of 12 years of data. The spatial resolution is 1.5 arc-minutes (3km under the satellite at 0° N, 0° W). The coverage spreads from 35° S to 58° N and from 18° W to 55° E [185, 186]. The CM-SAF dataset provides a list of services:

- Hourly solar radiation and PV energy with a wide range of features and for different types and sizes of solar technology for the period from 2007 to 2016.
- Daily solar radiation according to actual and clear sky conditions for 2D of tracking for the period from 2007 to 2016.
- Monthly solar radiation with a wide range of features ($\bar{G}$, $\bar{G}_d$, and $\bar{G}_b$ so on) for the period from 2007 to 2016.
- PV power estimation for off-grid and on-grid separately with a wide range of features.

3.6.5 **SARAH.**

The Surface Solar Radiation Data Set - Heliosat (SARAH) is climate data of the solar surface irradiance SSI, the surface direct normalized irradiance and the effective cloud albedo determined from satellite measurements of the visible channels of the MVIRI and SEVIRI instruments, which are installed on the geostationary Meteosat satellites. SARAH provides data from 2005 to 2016 and covers the region ±65° longitude and ±65° latitude. The data supply in terms of hourly, daily and monthly averages on latitude/longitude grid with a spatial resolution of 0.05° × 0.05° [184]. In addition, the SARAH-PVGIS dataset service provides the same data details that are provided by CM-SAF in section 3.6.4.

3.6.6 **MERRA and MERRA-2**

MERRA data is regarded as a second reanalysis project that has been created by National Aeronautics and Space Administration (NASA) which practices bring up to date new version of the Goddard Earth Observing System Data
Assimilation System. MERRA provides several variables including $\bar{G}$ which ranges from 1979 to the current. The MERRA's $\bar{G}$ data timescale resolution for 2D diagnostics dataset is 1 hourly and its spatial resolution is $0.5^{o} \times 0.667^{o}$ [94].
MERRA-2 dataset is version 2 of MERRA provides data beginning in 1980. It was created to replace the original MERA database because of the advances made in the assimilation system that enable assimilation of modern hyperspectral radiation and microwave measurements. The temporal resolution of MERRA-2 is 1 hour, while the spatial resolution equals 0.5o × 0.625o which is better than MERRA. MERRA-2 is the first long-term global re-analysis to assimilate space-based on measurements of aerosols and characterize their interactions with other physical procedures in the climate system [94]. The hourly data of $\bar{G}$ for both MERRA and MERRA-2 did not consider with other datasets in the validation process due to they have been detected later after the end of this project.

3.7 **Conclusion.**

This chapter aimed to explain the importance of solar power and to reveal the most important basic aspects and techniques need to evaluate and calculate solar power production. In addition, the most important solar databases to assess solar radiation and solar power production for the whole of Iraq were outlined. Regarding solar power, this thesis aims to evaluate the solar resources assessment for the whole of Iraq and provide a hybrid renewable energy system by hourly PV power output from any size of the PV system. This target requires a reliable database and suitable techniques to estimate the annual solar energy production and hourly solar energy production from different sizes of the solar power system.

The observed data of solar radiation is required and regarded as the most reliable source of data for solar power assessment. IMOS and IAN observed databases in Iraq suffer from severe data deficiency for the many reasons mentioned in sections 2.6.1 and 2.6.2. According to the apparent shortage in the observed data, an alternative reliable dataset is required for assessment purposes.

Different databases have been explored in this chapter. Most of the databases provide hourly, daily, and monthly solar radiation and some of the databases offer PV estimation techniques to calculate the annual PV power output. These datasets will be validated with observed data from IAN to determine the most accurate solar database for assessment purposes and calculation of solar power production within the hybrid system.

Chapter 4 **OPTIMIZATION METHODS OF HYBRID SYSTEM.**

4.1 Introduction.

Hybrid Renewable Energy Systems (HRES) have multiple renewable technologies that represent the most useful approach to satisfying energy demand in the residential sector. Also, the optimal sizing of HRES describes the optimization method to solve the problem of the uncertainty of wind speed and solar radiation characteristics [187]. Optimum system sizing includes determining the most economic-effective and reliable way to combine renewable energy technologies to provide an acceptable level of performance [188].

This chapter presents a general literature review of methods for determining the optimal sizes of HRES. Firstly, explain the assessment principles of HRES performance based on reliability and economic factors. Secondly, a review of different methods of optimization techniques to size HRES. Furthermore, the merits and demerits of software are extensively known and will be used for examining the optimal sizes of HRES and simulating the hybrid system. Finally, we present the challenges, which this work will face and suggest the best method and parameters for creating the optimization process.

4.2 The Concept of Reliability and Economic Assessment of HRES Performance.

According to the definition employed by the North American Electric Reliability Council (NERC), reliability represents to what extent the components of HRES can deliver electricity to all points of load demand in the quality and with the quantity required by the customer [189]. This concept will, therefore, provide a basis on which the performance of different types of power systems may be compared. On the other hand, the reliability factor is not the crucial factor to determine the most optimal HRES due to the cost of HRES and the cost of energy production. For this reason, the economic factor is significant when seeking to determine the optimal HRES, chosen according to the cheapest system in terms of the cost of the project or cost of energy. In the following sections, several common reliability standards and economic standards that have been used to evaluate different hybrid systems are discussed and explained.

4.2.1 Reliability Assessment

Many performance indicators have been mentioned in the literature to evalute the reliability of HRES. The most commonly used measures will be explained briefly.

4.2.1.1 Loss of Power Supply Probability

Loss of Power Supply Probability (LPSP) is defined as the probability of an insufficient power supply when the hybrid system is unable to meet the load demand [190]. If the LPSP equals 0, it means the load demand will always be satisfied, while if the LPSP equals 1, it means that the load will never be satisfied [191]. The loss of power supply probability is defined as the ratio of summation of all hourly losses of power supply values (LPS) when there is no interaction with the grid (off-grid) over the total required load [191-193], as expressed in Equation 4-1.

$$LPSP = \frac{\sum_{t=1}^{\mathrm{T}} LPS(t)}{\sum_{t=1}^{\mathrm{T}} E_{load}(t)} \qquad \text{Equation 4-1}$$

LPS (t) represents the loss of power supply at the time step (t), while $E_{load}(t)$ refers to the load demand at the time step. It is the most commonly used measure for reliability analysis in the HRES [194] and has been regarded both as a constraint to be satisfied in single objective design [195, 196] and an objective in multi-criteria design [197-199]. In this work, the LPSP has been chosen as reliability constraint to determine the reliability of the off-grid system in terms of outages from the national grid.

4.2.1.2 Grid Power Absorption Probability

HRES is always reliable for any size of system components as long as it is connected to the grid. However, the optimal sizing process of the grid-connected system aims to reduce the grid electricity purchases to satisfy load demand. A grid power absorption probability (GPAP) is defined as a performance indicator for grid-connected systems with apparent similarity to LPSP for stand-alone systems. The GPAP is the probability that the system needs to purchase electricity from the national grid when renewable energy is unable to meet the load demand [200]. It is defined as the ratio of purchased energy $E_{GP}(t)$ over the total load required during a given period [200, 201] as expressed in Equation 4-2. The GPAP technique is considered a technical performance criterion to size the grid-connected HRES employing a storage battery [200, 202]

$$GPAP = \frac{\sum_{t=1}^{8760} E_{GP}(t)}{\sum_{t=1}^{8760} E_{load}(t)} \qquad \text{Equation 4-2}$$

The GPAP is the most frequently used measure for reliability analysis for a grid-connected power system in terms of multi-objective design [202, 203]. It is considered as a technical performance criterion to size the grid-connected HRES employing a storage battery [200, 202]. In this work, the GPAP has been

selected as reliability constraint to determine the reliability of the on-grid system in terms of connecting to the national grid.

4.2.1.3 **Expected Energy Not Supplied**

The Expected Energy Not Supplied (EENS) is a gauge which estimates the amount of energy not provided by the power system when the load exceeds an available production level [194, 204]. In addition, the EENS (also known as the loss of energy expectation, LOEE [205] at any moment in time is given by the difference between the load demand and total energy production corresponding to that time instant [205], as expressed in Equation 4-3.

$$\mathrm{EENS}(t) = \begin{cases} E_{load}(t) - E_{\mathrm{supplied}}(t) \ \text{ when } \left(E_{load}(t) > E_{\mathrm{supplied}}(t)\right) \\ \quad 0 \qquad\qquad\qquad\qquad\qquad\qquad otherwise \end{cases} \qquad \text{Equation 4-3}$$

According to $\mathrm{EENS}(t)$, it is possible to estimate EENS over the entire period of operation, as expressed in Equation 4-4.

$$\mathrm{EENS} = \sum_{t=1}^{T} \mathrm{EENS}(t) \qquad \text{Equation 4-4}$$

EENS is an indicator of the extent of the failure of the energy system. The indicator has been used to evaluate the performance of hybrid PV-wind-diesel systems [205].

4.2.1.4 **Energy Index of Reliability**

The Energy Index of Reliability (EIR) is the fraction of the demand that has been covered by a power system that is directly linked to EENS [206], as expressed in Equation 4-5.

$$\mathrm{EIR} = 1 - \frac{\mathrm{EENS}}{\sum_{t=1}^{\mathrm{T}} E_{load}(t)} \qquad \text{Equation 4-5}$$

The EIR has been used in [206, 207] as an indicator to evaluate the performance of on-grid HRES.

4.2.1.5 **Renewable Energy Fraction**

The Renewable Energy Fraction (RF) is the fraction of the energy given to the load demand produced by renewable technologies. It is typically utilized for renewables-based systems that own diesel generators as a backup system to prevent power failure as is given mathematically in Equation

4-6 [195]. In addition, it represents the opposite of LPSP in case that is off-grid, or the inverse of GPAP in terms of on-grid, as used in Homer, which is expressed in Equation 4-6 [208].

$$\mathrm{RF} = 1 - \frac{\sum_{t=1}^{\mathrm{T}} E_{DG}(t)}{\sum_{t=1}^{\mathrm{T}} E_{load}(t)} \quad = \quad 1 - \mathrm{LPSP} \quad or \quad 1 - \mathrm{GPAP} \qquad \text{Equation 4-6}$$

Where $E_{DG}(t)$ represents the energy provided by diesel generators and $E_{load}(t)$ represents the load demand overtime period. The RF has been employed both as a constraint [209] and as an objective to be maximized [247] in power system sizing optimization [210].

4.2.2 **Economic Assessment.**

4.2.2.1 **Total Cost of Project**

The Total Cost of Project (TCOP) is one of the most important economic indicators to assess the feasibility of a HRES. However, it is evident that the total cost of the project is far from simplicity when compared to the total present value (TPV) of a project with a lifetime of a project. The TPV of a HRES represents the actual cost of all system components which includes the initial costs and variable costs over the lifespan of a project. In addition, another factor should be taken into considration when evaluating the total cost of a project. To estimate the time value of total project cost over the project lifespan, the Capital Recovery Factor (CRF) should be considered. In terms of understanding the future value of money, the value of money that is not gaining will erode over time, due to inflation that weakens the purchasing power of money. where the money available at the current time is worth more than a similar sum in the future [211]. The TCOP over the project lifetime can be estimated using Equation 4-7.

$$TCOP = (TPV \times CRF)\, T \qquad \text{Equation 4-7}$$

where the function of CRF transforms the TPV into a series of equal annual payments over a specified time, according to a specified interest rate [212], as expressed in Equation 4-8.

$$CRF = \frac{r\,(1+r)^T}{(1+r)^T - 1} \qquad \text{Equation 4-8}$$

r : the interest rate. T: the lifetime of the project.

4.2.2.2 **Levelized cost of energy (LCE)**

Several methods are used to assess the economic cost of renewable technologies; the Levelized Cost of Energy (LCE) is considered the most well-known and preferred indicator to estimate the price

of electricity that is generated from renewable energy technologies [3, 5, 11, 24]. In general, the LCE is defined as the ratio of total annualized project cost (Levelized annual cost), based on annual discounting financial flow to the annual energy production (AEP) from the project, as expressed in Equation 4-10 [212]. The Levelized annual costs (LAC) represent the yearly payment of the TPV of the project based on CRF , as shown in Equation 4-9[212].

$$LAC = TPV \times CRF \quad \text{Equation 4-9}$$

$$LCE = \frac{LAC}{AEP} \quad \text{Equation 4-10}$$

Where TPV is the total present value of a project. AEP is the annual energy production from different sizes of renewable technology. To estimate the time value of the total project cost over the project life span, the CRF should be used. The LCE has been used to minimize the cost of energy in a renewable energy system and also as an economic indicator for a HRES configuration in terms of multi-objective design [190, 213]. In this project, the LCE has been suggested as an economic constraint to minimize the cost of energy in a HRES and also as an economic indicator to evaluate a HRES configuration in terms of multi-objectives optimization technique.

4.2.2.3 **Payback period**

One of the most important economic indicators used to assess the viability of any project is the payback period (PBP) [214]. The PBP method will help the investor to evaluate how long a project needs to recover the total project cost within the lifespan of a project. For example, if the PBP was lower than the lifespan of a project, it means the project is feasible, but if the PBP was longer than the lifespan of a project, it means the project is not feasible. The PBP is the length of the period required to recover the total cost of a project's (TCOP), based on the annual cash inflow from the project itself [215]. The TCOP over the project's lifespan is taken into account when calculating the PBP.

$$PBP = \frac{TCOP}{Net\ Annual\ Cash\ inflow\ of\ AEP} \quad \text{Equation 4-11}$$

Net Annual Cash inflow of AEP: represents the revenue of annual energy production from a power system. In this project, the PBP has been chosen as an economic constraint to minimize the PBP of HRES and also as an economic indicator to assess the aptimal HRES configuration in terms of multi-objectives optimization technique.

4.2.2.4 Net Present Cost

The net present cost (NPC) is one of the economic constraints that has been used to evaluate and determine the optimal power system. The net present cost (life-cycle cost) of an element is the current value of all the expenditure of installing and operating the component over the project lifespan, minus the present value of all the incomes that it gains over the project lifespan. Homer uses the NPC as a constraint and calculates the NPC of each component in the power system and the power system as a whole. Costs may include initial expenditure, replacement expenditure, operating and maintenance costs, fuel prices, the cost of purchasing electricity from the grid. Revenues may consist of income from injecting power into the network, plus any salvage value that happens at the end of the project lifespan. The NPC is expressed in Equation 4-12 [216].

$$NPC = \sum_{t=0}^{T} \frac{R_t}{(1+f_d)^t} \qquad \text{Equation 4-12}$$

$$f_d = \frac{1}{(1+r)^N} \qquad \text{Equation 4-13}$$

Where R_t represents the net cash inflow-outflow during a single period, f_d : the discount factor is a ratio utilized to estimate the present value of a cash flow that happens in any year of the project lifespan. Homer estimates the discount factor using Equation 4-13 [216]. Where r refers to the interest rate , while N represents number of years.

4.3 Review of Optimization Techniques for Hybrid Systems.

A number of optimization methods have been developed for looking at the optimal sizes of HRESs. Luna-Rubio et al [217] summarize a number of optimization methodologies such: probabilistic methods, analytical methods, iterative methods and hybrid methods for both on-grid and off-grid HRESs. Banos et al [218] presented an overview of single and multi-objective optimization methods of renewable energy systems, specifically wind energy, solar energy, bioenergy, hydroenergy, geothermal energy, and hybrid energy systems. Nema et al [193] reviewed the present and future state of configuration design, performance and control requirements of off-grid hybrid PV-WT systems with backup systems such as a diesel generator, a battery or a grid-assisted mode system. Reviews of present simulation and optimization systems and software which consist of simulation modeling for grid-unconnected hybrid PV-WT-diesel systems with stored energy in batteries or hydrogen [219].

To obtain an optimal solution for real optimization problems, such as optimal configuration of the HRES that have fluctuating resources such as wind and solar power, the optimization problem requires a decent compromise between the precision of the optimization approach and the detail of the model of hybrid system in both mathematical models and meteorological data.

4.3.1 Iterative Technique

The iterative optimization procedure suggested to determining the optimal sizing of PV and WT stand-alone systems [220]. Yang et al [196, 221] have presented an iterative optimization technique to find the optimal size of PV system, wind turbine size and batteries for hybrid PV-WT-storage systems by considering Loss of Power Supply Probability (LPSP) and minimizing the cost of Hybrid system. Hocaoglu et al [222] used an iterative method to find the minimum size of PV system and wind turbine system and the maximum size of batteries that could be determined to satisfy demand. The optimum point represents the minimum cost of a power system that could be reached between minimum storage capacity and maximum storage system. Kaabeche et al [223] applied an iterative technique to follow the deficiency of power supply probability model and the Levelized Cost of Energy model to determine the optimal size of a HRES (PV-WT-battery). In this work, the iterative optimization technique has been suggested to determine the optimal HRES configuration due to the small probable numbers of wind turbine sizes, solar system sizes and storage system sizes.

4.3.2 Worst-Case Scenario Technique

Protogeropoulos et al [224] developed the sizing and techno-economical optimization technique for (solar-wind-battery), using the load fraction and bearing in mind the worst-load and the worst renewable period in a year. Habib et al [225] suggested an optimization process based on calculating the optimal percentage of power generated by the PV system and the wind turbine system at a constant load. These techniques were created using the worst case of a year to configure the systems. With monthly average data used, they might not give appropriate and accurate results because of the changeable nature of resources and loads. Furthermore, the worst-case technique will be expensive due to the price of data loggers, as suggested by [217, 226].

4.3.3 Probabilistic Approach

The probabilistic approach was compared with the independent time series and Markovian time series and then it was found that the serial correlation of surplus production should be used for assessing system reliability [226]. A general numerical probabilistic model of an autonomous system that included many wind turbines, many PV modules, and storage systems was presented by Karaki et

al [207]. Conti et al [227] developed a probabilistic model to compute the long-term performance of a HRES (wind-solar), in terms of the monthly average data, using Fuzzy logic according to the multi-objective optimization process. An analytical model of HRESs (wind-solar) using a probabilistic approach based on the convolution technique to assess long-term performance for both on-grid and off-grid applications was suggested by Tina et al [206]. This analytical model has been used to find the optimal sizing of an on-grid system with the Fuzzy logic based multi-objective optimization approach, which was presented by Terra et al [228].

Although the probabilistic approach is useful when evaluating long-term performance, it cannot be shown as the dynamic changing performance as the hybrid energy system [229].

4.3.4 **Multi-objective optimization technique**

Multi-objective optimization techniques have been utilized for complicated multi-objective problems, such as the HRESs with constraints, nonlinear and non-convex objectives. These techniques have confirmed that they are able to provide better results in comparison with other techniques, both the design of off-grid and on-grid hybrid renewable systems, for this reason, it has been applied in number of most important hybrid renewables softwares such as: Hybrid Optimization Model for Electric Renewables (Homer); Hybrid Optimization by Genetic Algorithms (HOGA); Multi-Objective Evolutionary Algorithms (MOEAs) and Strength Pareto Evolutionary Algorithm (SPEA) [218, 230-232]. Fadaee and Radzi [231] reviewed the multi-objective optimization of off-grid hybrid systems using Evolutionary Algorithms (EA). As a result, the Particle Swarm Optimization (PSO) and the Genetic Algorithm (GA) have been regarded as the most popular techniques. The GA was used with an elitist strategy to determine an optimal number of wind turbines, batteries, PV modules and a fixed slope of PV panels. Where elitist strategy represents a limited number of components with the best fitness values are determined to pass to the next generation. In addition, the objectives are the minimum total capital cost of a project according to a minimum LPSP [233]. The fast elitist Non-dominated Sorting Genetic Algorithm (NGAS-II) was used to minimize three objectives: the system autonomy level; the total system cost and the wasted energy rate [234]. Yang et al [235] applied the basic GA to optimize the size of a wind turbine, solar system, batteries and the fixed tilt angle of PV panels and a hub height of wind turbines by minimizing the LPSP and total annual cost. The suggested method has been used for a HRES that was producing power for a telecommunication relay station. [236] used the Breeder GA to minimize the total annual cost of a hybrid system and to optimize the size of a wind turbine, solar system, with batteries to support existing diesel generators for decreasing CO2 emission. [237] used a PSO algorithm to determine the optimal size of a wind turbine, solar system, and batteries with the minimum cost. [238] applied the Strength Pareto Evolutionary Algorithm (SPEA) for optimizing the size of an off-grid

hybrid PV-WT-battery-diesel system by minimizing the CO2 emission and the total system cost, for two different load profiles but without considering seasonal variations. [239] used SPEA to configure off-grid hybrid PV-WT-generator-battery-hydrogen systems by minimizing three objectives: the total cost, unmet load and CO2 emission. The multi-objective optimization techniques have been used more widely to provide valuable information about the connections between cost and the system's reliability [187]. The multi-objective optimization technique have been chosen in this work to determin the optimal HRES configuraqtion using LPSP and GPAP as reliably constrains and LCE and PBP as economic constrains due to the high flexibility which is provided by this techniques.

4.4 Optimization software of HRES.

Three optimization software applications are generally used for HRESs. The most important simulation and optimization software tools are Homer, HYBRID2, and HOGA, as these types of software provide many useful features.

4.4.1 Homer

Homer is one of software tools for simulation and optimizationwithin the field of HRESs [219, 240, 241]. It is a widely used, user-friendly software, and highly suitable to implement the optimization and feasibility and to assess uncertainty in the output in many possible system configurations [242]. Originally, Homer software has been developed by National Renewable Energy Laboratory (NREL), USA for both off-grid and on-grid configurations in 1993 [219, 243, 244]. Generally, Homer can optimize HRESs that include a wide range of renewable energy generators, such as wind turbine, solar panel, rechargeable batteries, hydraulic turbines, hydrogen tanks, fuel cells, AC generators, electrolysers hydrogen tanks, boilers and AC–DC bidirectional converters [219, 244, 245]. Homer is an multi-objective optimization software package that simulates a wide range of renewable energy sources; it can also suggest design for different systems depending on economic factors [240, 242, 243]. Homer works by assessing the performance of system configurations and estimates the NPC, which represents the total value of installing and operating a configuration during the lifespan of system; it can calculate the cost of capital, operation, replacement, fuel, maintenance and interest [242, 246]. In addition, it can provide minimum level of the LCE that accounts for the total cost of hybrid energy system divided by the power provided by the hybrid energy system [219, 240, 242]. Furthermore, Homer can assess the technical feasibility of the renewable energy sources system by evaluating whether this system is able to cover the electrical load needed to meet the demands of households, or a small community within different conditions [242]. In addition, Homer is able to optimize the energy supplied from system configuration according to the priority levels of each load and it can also reduce the excess energy to

achieve the lowest cost of generating [241, 243, 247]. Moreover, the optimization will provide an acceptable level of energy storage in the battery bank in order to meet peak load demand during the period of low wind speed and low or no solar radiation [247].

Furthermore, Homer simulates variable resources according to time series. For example, it applies a chronological simulation of solar and wind power according to a variable load to establish the best performance for the hybrid system [248]. Homer has the ability to simulate a wide range of parameters of load, input and output energy from the components of a hybrid system using 1-hour intervals per year [219]. Several studies stated that Homer could simulate a massive number of system configurations by applying energy balance calculations for each hour, 8760 h in a year, by comparing electric load with the energy that the system can be supplied with at the same hour [241]. In this regard, the hybrid system, which includes batteries, the simulation process for Homer will make a decision for each hour to operate the renewable generators with a view to charging or discharging the batteries [241]. Finally, Homer displays a list of simulation results for a number of tables and graphs, which are used to compare system configurations and to assess the lowest value of source to meet the load demand [241, 243].

4.4.2 **HYBRID 2**

HYBRID 2 is one of the well-known software between different types of simulation and optimization software for assessing the technical and economic performance of HRESs [219, 249]. Originally, Massachusetts University developed HYBRID 2 with support from the NREL. The Hybrid 1 was developed in 1994 and then HYBRID 2 in 1996 [219, 243]. Firstly, the HYBRID 2 software tool is a consistent platform used to assess the performance of HRESs over the long term, and it also has the ability to perform economic analysis on a wide range of hybrid energy systems [250]. Secondly, HYBRID 2 is a probabilistic/time series optimization technique, using chronology data for loads, solar radiation, temperature, wind speed, and the hybrid energy system, to forecast the performance of the hybrid energy system [243, 250]. In addition, this software allows the users to operate several strategies to optimize configuration of the system design [251]. Furthermore, HYBRID 2 takes into consideration the variations in wind, solar radiation and load demand within time series simulations for time steps, ranging from 10 minutes to 1 hour, in order to achieve the best performance predictions [219, 243, 250]. HYBRID 2 was invented to study a wide range of hybrid configurations systems that might include different types of photovoltaics, wind turbines, electrical loads, battery storage, diesel generators of different sizes and four types of power converter [219, 243]. Moreover, the HYBRID 2 modelled used many buses of power systems (AC and DC) at the same time [249]. A wide variety of control strategies might be implemented, which include interactions between diesel generators and battery storage [250]. Additionally, HYBRID 2 consist of economic analysis tools used to assess the costing economics life cycle

of hybrid energy systems such as the present value of system costs, Levelized annual costs and several economic and performance factors[251]. HYBRID2 is packed with a library of devices to help the user to establish many configurations of a hybrid energy system. Furthermore, the library incorporates sample power systems and projects that the user is able to use as a template [243, 250].

4.4.3 **HOGA**

HOGA is an optimization and simulation software developed by the Electric Engineering Department of the Zaragoza University in Spain [36]. The system modeling and process of the present version are demonstrated in [163]. Two GA techniques are used: The SPEA is applied for the main algorithm to find possible component combinations of the hybrid system to minimize the total costs of a system. SPEA2 is used for the second one to search for a suitable control strategy for each of the configurations, determined by the main algorithm. The new control strategy has been enhanced by two options of calculation of battery lifespan and two options of different mathematical models for battery operation [164]. The SPEA and SPEA2 of the HOGA is a suitable choice as it can optimize either a multi- or a single-objective optimization problem. Additionally, this method can look for the optimum sizing of component configurations, dissimilar from the Homer software, in which the user needs to fill the sizes to be considered. Nevertheless, HOGA software has not been organized for battery group management [187]. It is worth reviewing the popularly used sizing programs, highlighting their significant features, advantages, and disadvantages, as summarised in Table 4-1. According to the features of HOGA, HYBRID2 and Homer softwares, as a result of this specific issue, the decision has been taken to build a MATLAB model to deal with issues flexibly.

Table 4-1. Review of HRES sizing Software [252].

Software	Remarks	Advantages	Disadvantages
Homer	• Developed by NREL • Able to perform pre-feasibility studies, optimization and sensitivity analysis in many potential system configurations, for both on-grid and off-grid systems. • Able to perform a one-year of simulation, with hourly sampling rate. • Feasible configurations are fixed by net present cost (NPC).	• User-friendly Graphical User Interface (GUI) reduces the learning curve for new users. • Display simulation outcomes in a wide variety of graphs and tables which assist users in comparing and assessing each configuration according to economic and technical merits. • The software being updating and keeps supported.	• "Black box" code used. • Only allow a single objective function for minimizing NPC, hence incapable of solving multi-objective problems • Does not rank the hybrid system based on LCE • Does not take into account any degradation in batteries, regardless of its usage. For example, higher Depth Of Discharge (DOD) may decline the battery lifespan more than low an infrequent DOD. • Requires paid a license for the professional version, and the license pricing rises with additional libraries • Is not able to optimize a hybrid system suffering from unscheduled outage
HYBRID 2	• Developed by Renewable Energy Research Laboratory (RERL) at the University of Massachusetts, with support by NREL in the USA • Adopts probabilistic/time series method to perform in detail for long-term performance and economic analysis on a wide change of HRESs.	• A variety of different control strategies which includes the interactions between diesel generator dispatch and batteries. • Statistical methods to account inter-time step variations in the wind and load to improve the accuracy of forecasting for diesel generator dispatch.	• May not work with Windows system later than Windows XP • Software is not supported and not updated from developer • lack of flexibility and limited access to parameters • does not able to optimize a hybrid system suffering from unscheduled outage
HOGA	• Developed by the University of Zaragoza, Spain. • Single and multi-objective optimization can be implemented using a genetic algorithm (GA) • Can be used to analyse on-grid and off-grid system	• It was stated to be low in computation time • Allows probability analysis	• The professional version is valued and only limited features are given for education version • Needs internet connection to run professional Version • Not able to optimize a hybrid system suffering from unscheduled outage

4.5 Conclusion.

The main aim in this thesis is to estimate the potential power production from HRES which include wind, solar technologies, and rechargeable batteries to satisfy electricity demand of housing units, which is suffering from unscheduled outage from the national gr.

According to previous literature reviews related to the optimization techniques for HRESs, the iterative optimization procedure, and multi-objective optimization techniques have been suggested in this work. They have shown the capability to process a large number of HRES configurations, using several economic and reliability constraints as multi-objectives to determine the optimum configuration to satisfy housing units.

Concerning the objectives of reliability, LPSP and GPAP have been proposed as two constraints to determine the reliability of a hybrid system according to the off-grid and on-grid demand, respectively. Whereas, LCE and PBP were set as constraints to determine the feasibility of a hybrid system in terms of the cost of energy and payback period.

On the other hand, although Homer, HYBRID2, and HOGA are the most important optimization software applications, they are not able to optimize a hybrid system suffering from unscheduled outage from the national grid, which means using HRES to satisfy load demand in terms of on-grid and off-grid respectively. According to this specific issue, the decision has been taken to build a MATLAB model to deal with issues flexibly as is explained in Chapter 9.

Chapter 5 **BOUNDARY LAYER DOWNSCALING MODEL FOR WIND RESOURCE ASSESSMENT**

Wind resource assessment is essential in determining the potential power production of a wind turbine. A wind resource assessment ought to be sufficiently accurate to ensure that the calculated power output and fiscal revenues from a turbine represent reality as closely as possible. This chapter presents the methodology validation and resource prediction of the downscaling model (DSM) that was discussed in Chapter 2. The DSM has been designed based on similarity theory within the boundary layer according to neutral stability conditions as developed by the Met Office for wind resource assessment purposes [35, 36].

Several steps should be taken to realize the objective of using a DSM in Iraq. The first step includes a review the parameterization of the surface aerodynamics that will be developed based on a Land Cover Map (LCM) of Iraq. The second step describes the DSM using MERRA data as a source of reference wind data. The third step includes using sensitivity analysis to study the impact of proposed parameters when applying the DSM in Iraq. Finally, a validation proof using available observation data to appropriate parameter selection.

The methodology of the DSM will reveal the logical steps that use a number of semi-empirical equations in order to estimate the wind speed at hub height based on the aerodynamic roughness length (z_o) for the site and each upwind fetch. This methodology will be tested by validating the results with observational data previously obtained from several sites.

5.1 **Downscaling Methodology**

The downscaling methodology includes three steps of vertical scaling of the wind profile starting from a reference wind climatology, where wind speed changes logarithmically with height due to the influence of the aerodynamic characteristics of the surface such as vegetative cover or the built environment in urban areas which affect the momentum of the wind flow horizontally and vertically. The description of the logarithmic behavior of the wind profile in the boundary layer within neutral stability conditions has been illustrated in section 2.2.1 [26]. The downscaling technique consists of three main scaling steps as follows [35] and as shown in Figure 5-1. The details and calculations of necessary inputs in these main scaling steps will be discussed in section 5.2.

1. The first step is represented by scaling up vertically the wind climatology at 10 m to estimate wind speed at the reference height (Z_{ref}) which is usually located near to the

top of the boundary layer where the influences of terrain roughness are minimal [28] as performed in Equation 5-1.

2. The second step consists of downscaling the wind speed from the reference height to the blending height (Z_{bh}) to estimate the wind speed at the blending height [28] as expressed in Equation 5-2. Blending height is the height where the horizontal wind flow turns into homogeneous flow and is in equilibrium with the homogeneous effects to individual roughness elements at the surface [28]. There is also another definition which describes the blending height as the height where the flow perturbations of wind speed due to the surface tend to zero [36].
3. In the third step, the wind speed that is estimated at the blending height will be scaled down to determine the wind speed at the hub height based on the upwind fetch roughness for each target site. The equation format for this step will be designed based on the aerodynamic characteristics for each surface of the target site area. For instance, if the target site is located within a rural area, wind speed will be downscaled from the blending height directly to the hub height as expressed in Equation 5-3.

   If the target site is located within a suburban area, the displacement height (d) must be estimated and the surface roughness of the target site must be considered. In this case, the mathematical expression in Equation 5-4 will be most suitable to calculate wind speed at the hub height (u_{hh}) in the suburban area.

   Finally, if the hub height of a potential site is located in an urban canopy, the wind profile of wind speed will change from a logarithmic profile to an exponential profile as expressed in Equation 5-6 [36].

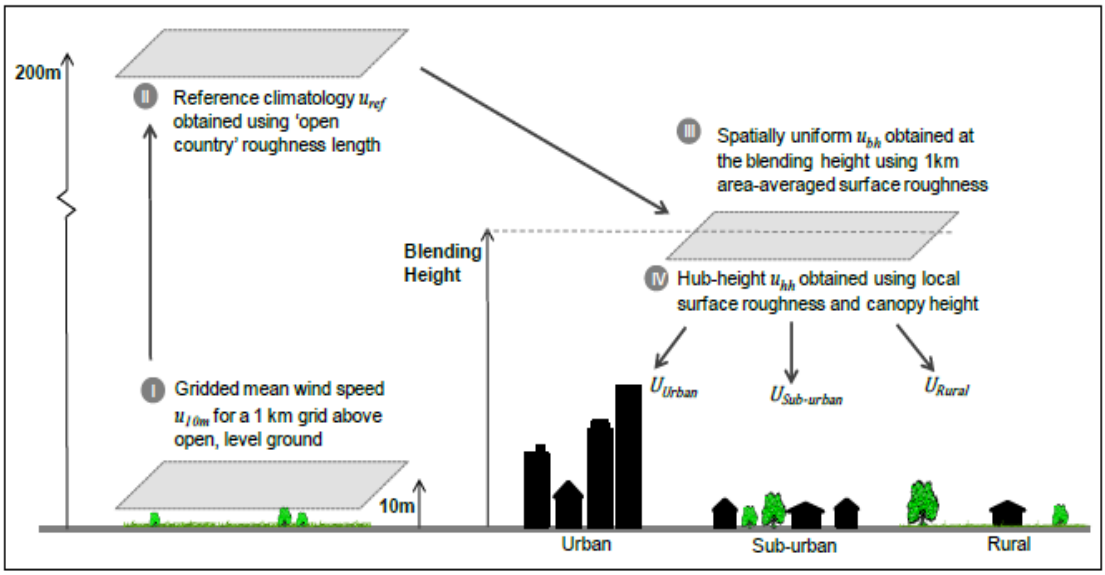

Figure 5-1. The three distinct steps outline of the downscaling methodology [35].

5.2 **Modeling Technique**

The reference wind climatology (u_{10}) at 10 m of hub height (Z_h) from MERRA data should be scaled up to the reference height(Z_{ref}) to estimate the reference wind speed u_{ref} at reference height (Z_{ref}) based on roughness length ($z_{o\,ref}$) at the reference site by applying Equation 5-1.

The reference height has been set at 200 m based on the technical report of the Met Office [36]. This value will be used in the first step in the DSM. In addition, a second proposed value of the reference height will be 600 m, which has been selected according to the wind speed profile above Baghdad's surface based on radiosonde data. The proposed heights (200m and 600m) will be examined and then the results of wind speed at a target site will be compared with observation data for the particular site in order to select the most appropriate height. More details about reference height are available in section 5.2.1. The $z_{o\,ref}$ has been set at 0.14 m according to the value of roughness length at open area based on the Met Office technical report [28, 36]. However, the first step in this work will examine another the value of $z_{o\,ref}$, the first value of $z_{0\,ref}$ = 0.103 m that represents the annual average of roughness length in open area based on observation data measured by the radiosonde in Baghdad International Airport (BIA) while the second value of roughness length at open area $z_{o\,ref}$ = 0.05 m, which represents one of monthly values of roughness length that has been estimated in BIA [32]. More details about surface roughness are available in section 5.2.2.

$$u_{ref} = u_{10}\,\frac{\log\left(Z_{ref}/z_{0\,ref}\right)}{\log(Z_h/z_{0\,ref})} \qquad \text{Equation 5-1}$$

The next step includes the process of downscaling the wind speed from the reference height to estimate wind speed at the Blending height (Z_{bh}) based on two parameters; the effective displacement height of the region (d_{eff}) and the effective local roughness of the upwind fetch around the target sit ($z_{o\,eff}$) [26, 36] as expressed in Equation 5-2.

(d_{eff}) is the effective displacement height of the upwind fetch. In general, displacement height is the height where the mean wind speed is equal to zero because of the presence of several roughness components rather than a single element. Displacement height is commonly used in suburban and urban areas where the surface roughness is higher than 0.4 m. The displacement height is estimated to be around two-thirds of canopy height [28]. The canopy height (C_h) represents the distance between the surface and a spatially averaged top of the roughness components where the wind speed in this layer is likely to be significantly reduced due to the wind flow being affected by site buildings [28].

$$u_{bh} = u_{ref} \frac{\log((Z_{bh} - d_{eff})/z_{o\,eff})}{\log((Z_{ref} - d_{eff})/z_{o\,eff})} \quad \text{Equation 5-2}$$

The third step in the downscaling process should be built based on the aerodynamic characteristics of the target site. If the wind speed is downscaled within a rural area, Equation 5-3 must be applied. where z_o of the target site is less than 0.4 m and the value of the displacement height equals zero [28].

$$u_{hh} = u_{bh} \frac{log\,(Z_{hh}/z_{o\,rural})}{log\,(Z_{bh}/z_{o\,rural})} \quad \text{Equation 5-3}$$

In other cases where the site is located in suburban areas, the value of the displacement height will not be zero. In this case the effective displacement height (d_{urban}) should be taken into consideration when downscaling the wind speed from the blending height to the hub height and also the model should consider the surface roughness of the target site $(z_{o\,urban})$ that must be higher than 0.4 m and lower than 1.1 m [28]. According to this condition of surface roughness, the mathematical expression in Equation 5-4 will be most suitable to calculate the wind speed at the hub height u_{hh} in a suburban area.

$$u_{hh} = u_{bh} \frac{\log((Z_{hh} - d_{urban})/z_{o\,urban})}{\log((Z_{bh} - d_{urban})/z_{o\,urban})} \quad \text{Equation 5-4}$$

In the case of an urban area, the surface roughness of a target site must be 1.1 m, and the wind speed should be downscaled from blending height to the hub height that located below the canopy height for desired hub height between high trees or high buildings. For this reason, the wind speed at canopy height should be calculated as expressed in Equation 5-5. The canopy height can be expressed as $C_h \approx 10\, z_o$ [28, 33]. In this case, the wind profile will change from a logarithmic profile to an exponential profile [28, 36] as expressed in Equation 5-6 to calculate the wind speed from canopy height to hub height u_{hh}.

$$u_{C_h} = u_{bh} \frac{\log((C_h - d_{urban})/z_{o\,urban})}{\log((Z_{bh} - d_{urban})/z_{o\,urban})} \quad \text{Equation 5-5}$$

$$u_{hh} = u_{ch} \exp\left(-9.6\, \lambda_f \frac{(C_h - Z_{hh})}{C_h}\right) \quad \text{Equation 5-6}$$

- u_{ch} represents the wind speed at the canopy height.
- λ_f represents the frontal surface area of an obstacle to the wind flow, which equals 0.3 [36] and as shown in Figure 5-2 [28].

- d_{urban} is the effective displacement height for the urban/suburban areas which is calculated by Equation 5-7 and Equation 5-8 [13]. The effective displacement height is shaped by the effect of the highest roughness length in each upwind fetch. To estimate the effective displacement height above an urban/suburban area for 12 wind direction sectors around a target site, should select the highest roughness length that equal to or higher than 0.4 m in each upwind fetch.

$$C_h = 10\, z_o \qquad \text{Equation 5-7}$$

$$d = \frac{2}{3} C_h \approx \frac{20}{3} z_o \qquad \text{Equation 5-8}$$

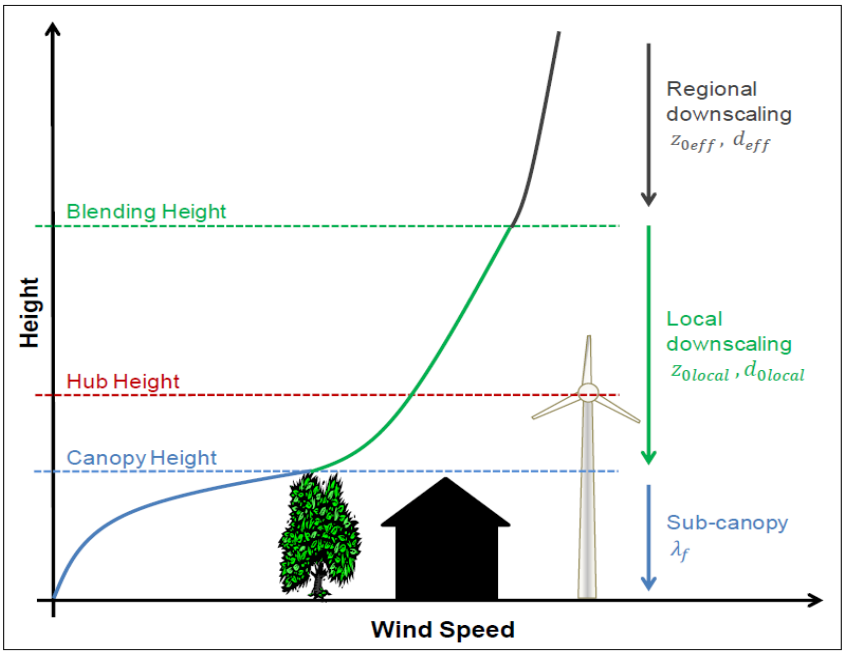

Figure 5-2. Schema shows the curve shape of the vertical wind profile within different layers and most important regions within the downscaling field [28].

5.2.1 Reference Height

The first step of the DSM, is scaling up the wind speed from hub height (data source) to suitable reference height. The idea behind scaling up a reference wind climatology to the reference height is to remove any surface effects on the reference wind climatology [36] as well as to be close to the geostrophic wind speed in both magnitude and direction [28]. In other words, the reference height shows a notable reduction in flow perturbations, which are generated by the effect of roughness at the surface on a reference wind speed above the reference site. In the same context, the reference height represents a sufficient depth which is located out of the influence range of terrain roughness [122]. The Met Office has selected 200 m as a reference height according to wind profiles and weather conditions in the UK.

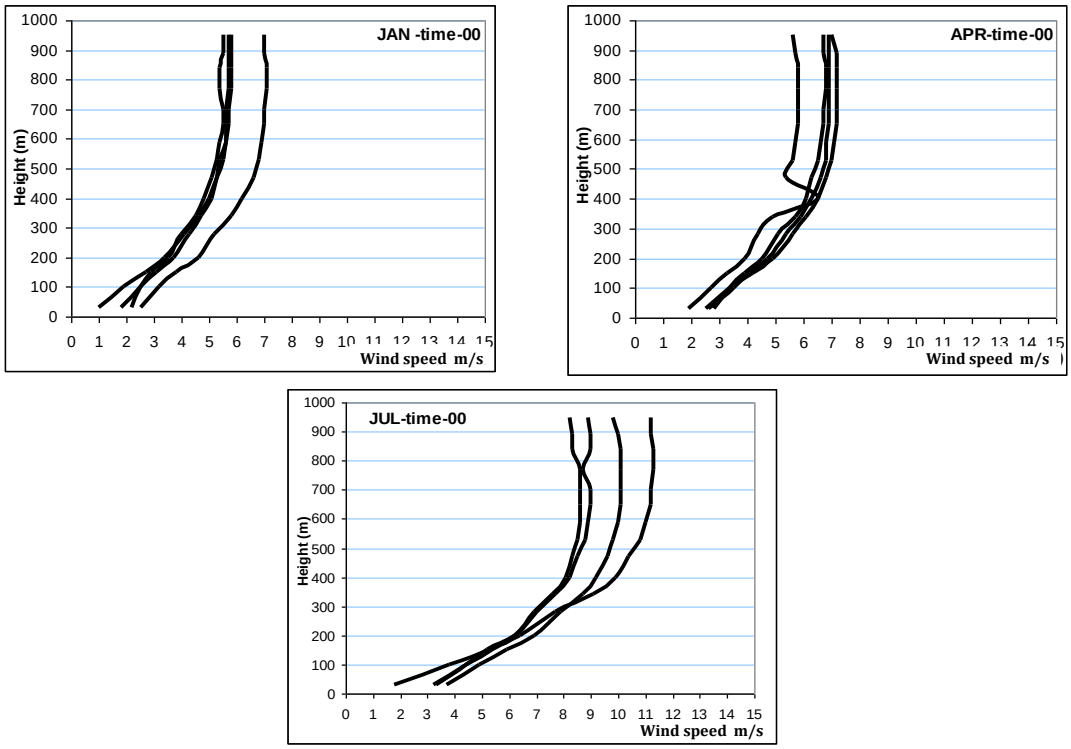

Figure 5-3. Shows merging the monthly wind profile rates of change to the wind speed above BIA with height for months: winter, spring, and summer, for four years 1985-1986 - 1987-1988 within stable conditions at 00 GMT [32].

On the other hand, wind profiles in Iraq should be taken into consideration to determine the appropriate reference height above a wind reference climatology site. For this reason, 600 m is suggested to be the reference height in the DSM. This elevation is selected based on observation data that had been measured by radiosonde above BIA for many years. This elevation has been chosen based on the definition of reference height from the literature with wind profiles based on neutral conditions at a height where wind speed does not change with height due to it is become out of surface roughness effect, as shown in Figure 5-3 [32].

5.2.2 **Surface Roughness**

The surface roughness of the reference site ($z_{o\,ref}$), the surface roughness of a target site z_o and the effective local roughness of the upwind fetch for a target site is required to apply the DSM in Iraq. Firstly, the surface roughness $z_{o\,ref} = 0.14$ m and the effective displacement height of the region $d_{ref} = 0$ have been suggested for an open area at the reference site. The $z_{o\,ref} = 0.14$ m value represents the surface roughness of uniform grass with few trees and hedges in open terrain based on the Met office's downscaling technique [28, 36]. This value has been estimated based on 1 km grid squares by the European Corine land cover database [122]. On the other hand, the average surface roughness for open terrain in Iraq $z_{o\,ref} = 0.103$ m as estimated based on observed data

measured using a radiosonde within the domain of the weather station of BIA by applying Equation 2-16 within neutral conditions. In addition, the average monthly value of $z_{o\,ref} = 0.05$ m has been chosen as one of the surface roughness values for BIA, which estimated by the same above process [32]. The reason behind the change in the roughness value stems from the change in the value of friction velocity affected by vertical wind speed and sensible heat flux as described in section 2.2.1.

Since the downscaling will be applied in Iraq to map wind resources assessment, the $z_{o\,ref} = 0.103$ m and $z_{o\,ref} = 0.05$ m will be examined as possible surface roughness value of reference sites in this project due to these values being representative of real measurements for open terrain in Iraq. This difference between z_o in Iraq and UK for open area stems from the lack of grass at the open terrain in Iraq such as at the surface of BIA.

Secondly, the value of surface roughness of a target site z_0 and the effective local roughness of the upwind fetch for a target site should be determined to apply the downscaling technique. Basically, the aerodynamic characteristic of the terrain is calculated based on the obstacles on the ground, such as the vegetative cover, buildings, the topography and morphology of the surface. All varieties of surface roughness should be taken into consideration. There are two methods to estimate z_o for each surface.

- The first method depends on estimating the frontal area density and plane area of obstacles in the terrain [28, 36].
- The second method determines the surface roughness value based on the characteristics of the land cover category for each surface.

The first method is difficult to apply because it requires estimating roughness length for a huge area equalling 438,320 km^2 (the area of Iraq) [253]. In addition, there is not enough information available about the frontal density and plan area for every building and obstacle in Iraq. For these reasons, the second method will be developed based on the LCM of Iraq.

The DSM has been developed by the Met Office, which estimated z_o across the UK based on geographical information from a 1990 LCM [36]. Concerning the work in this project, the strategy that has been used by the Met Office will be developed and applied using the LCM 2006 [254]. The LCM of Iraq has been produced by Department of Agro-Ecological Zoning (AEZ) Map Specialist Soil & Water GIS &Remote Sensing at Ministry of Agriculture in Iraq as shown in Figure 5-4 [254]. The LCM of Iraq will be used to calculate the aerodynamic properties for the whole of Iraq. The AEZ provides the map of Iraq land cover with cell size (x,y): 231.6 m × 231.6 m that equals 53638.56 m^2 = 0.0536 km^2 resolution and also the land cover map includes 19 detached categories as shown in Figure 5-4 [254]. The cell characteristics of the LCM in Figure 5-4 have been addressed to determine the surface roughness values for the whole of Iraq by matching each value of z_o with each category of land cover classification based on many literature reviews as revealed in Table 5-1.

The surface roughness length values in Table 5-1 have been determined for certain land cover categories [28, 255-260] based on the similar description of land covers between the land cover in the literature review and the land cover of Iraq. In addition, the LCM which was produced by AEZ in 2006 has included just vegetarian cover in Iraq without urban areas like towns and cities.

In order to cover this shortfall, urban areas have determined using 0.5 km MODIS-based Global Land Cover Climatology from the USGS Land Cover Institute (LCI) [261] that has covered all cities and towns in Iraq. The roughness surface cells 0.5 km from MODIS for all towns and cities in Iraq have been integrated with the LCM of Iraq using Raster Editor in the ArcGIS software. Figure 5-5 shows the LCM with urban areas for the whole of Iraq. The land cover classification of the urban area will be fitted with a value of z_o of urban areas a gathered from some literature review of surface roughness values as illustrated in section 20 in Table 5-1.

5.2.3 **Blending Height and Regional Averaged Surface Roughness**

In order to apply the second step in the DSM that relates to Equation 5-2, both of the average of blending height (Z_{bh}) and the effective local roughness ought to be identified for 12 directions of upwind fetches around the target site. A wide range of surface roughness values in Table 5-1 will be used for each patch within each upwind fetch to estimate the roughness drag that effects wind flow, as shown in part C in Figure 5-7. The blending height in this project will be estimated for 12 wind direction sectors using a variability scale (L_p) in Equation 5-9 to describe the nature of roughness drag and to understand the interactions among a series of patches that have different roughness values within each an upwind fetch. Tracking the evolution of a boundary layer within upwind fetch will provide a better physical description of the effects of surface roughness on the momentum of wind flow within upwind fetch [262]as shown in Figure 5-6.

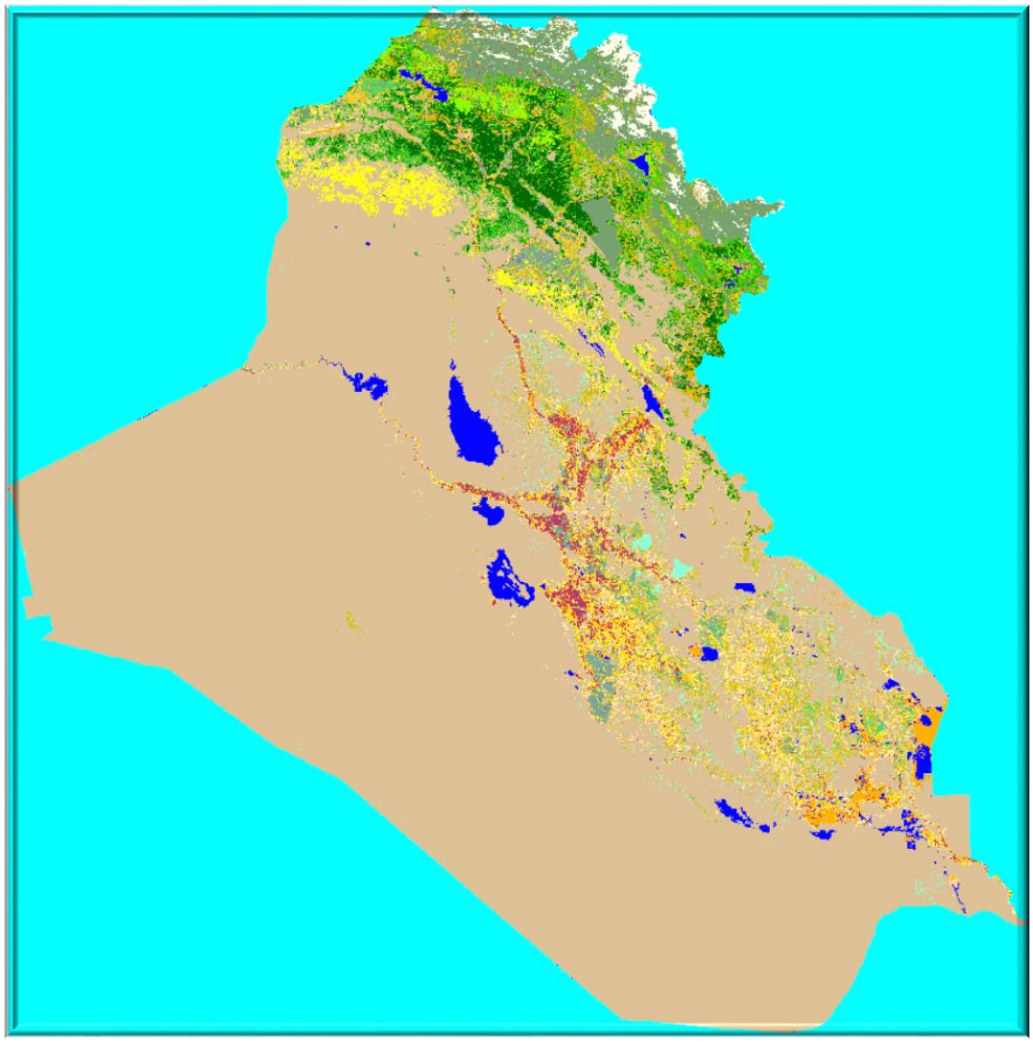

OID	Value	Count	Red	Green	Blue	Level_4_la	Area__ha_
0	0	0	0	0	0	No Data	0
1	1	125157	0	0	1	Water in Lakes, Canals, and Swamps	671651.28579
2	2	278053	0.44	0.59	0.41	Grasses and Shrubs; Mountains Slopes	1492163.08291
3	3	183800	1	0.84	0	Irrigated Summer crop	986357.186
4	4	67089	1	1	0.88	Snowy and Rocky Areas in the Mountains	360031.10583
5	5	598668	0.82	0.71	0.55	Barren, Desert, and Urban Areas	32127386.9178
6	6	93284	1	1	0	Rainfed Dry Lands	500605.78748
7	7	151509	1	0.91	0.7	Natural Vegetation	813068.50323
8	8	67567	1	0.65	0	Marshlands with Aquatic Vegetation	362596.27849
9	9	19434	0.53	0.61	0.39	Winter: Rainfed Wheat and Barley	104291.97798
10	10	242707	0.8	0.68	0	Rainfed Grass Pasture	1302479.83429
11	11	238330	0.2	0.73	0.07	Rainfed Wheat and Barley and Grass Pasture Mosaic	1278990.7951
12	12	206797	0	0.39	0	Rainfed Wheat	1109769.89659
13	13	42872	0.5	1	0	Winter: Rainfed Wheat and Barley	230071.30184
14	14	99145	0.69	0.19	0.38	Irrigated Orchards; Mostly Date Palms in the Plain	532058.66815
15	15	50822	0.5	1	0.83	Irrigated Fallwo land	272734.73834
16	16	110910	0.44	0.62	0.57	Winter: Irrigated Wheat and Barley; Summer: Rice and Vegeta	595195.1877
17	17	42537	0.65	0.68	0.38	Irrigated Wheat and Barley and Grass Pasture Mosaic	228273.53439
18	18	67603	0.94	0.76	0.12	Irrigated Wheat	362789.47141
19	19	31232	0.24	0.82	0.36	Winter: Irrigated Wheat and Barley	167605.59104

Figure 5-4. The land cover classification of Iraq in 2006 without urban and suburban areas [254].

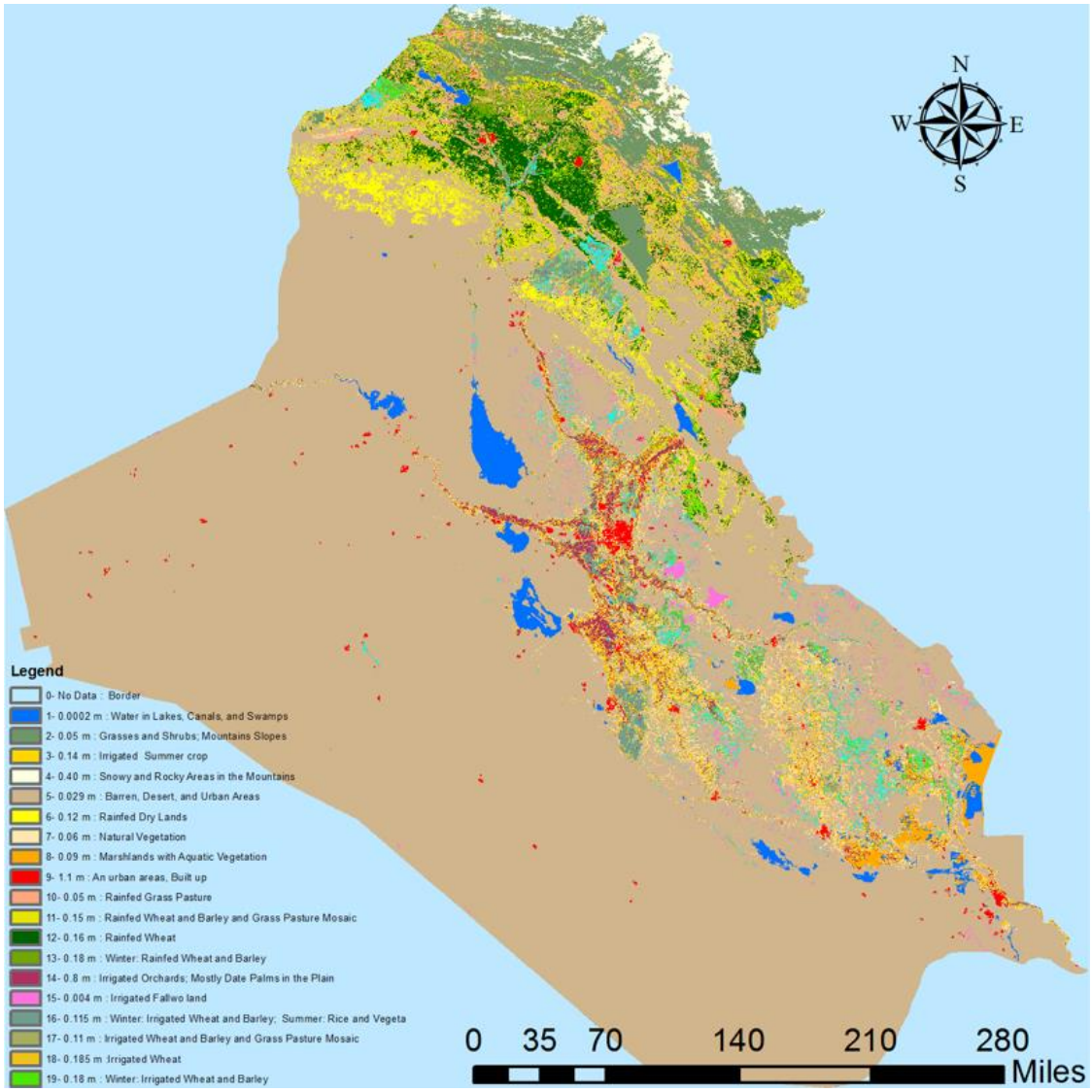

Figure 5-5. The land cover of Iraq including all the urban and suburban areas in Iraq from the 0.5 km MODIS-based Global Land Cover Climatology [261] that has been integrated with the land cover map of Iraq in Figure 5-4.

Equation 5-9 has two sides. The left-hand side (LHS) tracks the development of the boundary layer over the upwind fetch stream, while the right-hand side (RHS) represents the proportional force of the wind experiences for each patch of roughness in the upwind fetch.

$$\left(\frac{Z_{bh}}{1.7\ k_v\ L_p + \ Z_{bh}}\right)^2 = \sum_{i=1}^{N}\left(\frac{f_i}{\left(ln\frac{Z_{bh}}{z_{o,i}}\right)^2}\right) \qquad \text{Equation 5-9}$$

In order to get the value of the blending height (Z_{bh}), Equation 5-9 should be solved iteratively up to 30 iterations for each wind direction sector using roughness length of each patch $z_{o,i}$ in the upwind fetch. When the difference between the last two values of Z_{bh} equals 0.001, the iterative solution will be stopped and providing the result of Z_{bh} . The first value for Z_{bh} to be inserted in the RHS of Equation 5-9 before starting the iterative solution

is equal 10 m and then the procedure will estimate the second value of Z_{bh} in the LHS of Equation 5-9, after that, the iterative solution process will be started.

- $k_v = 0.41$ is the von Karman constant.
- f_i is the spatial fraction of each roughness length patch within the upwind fetch.
- L_p is the variability scale.
- N refers to the number of patches within the upwind fetch.

Table 5-1. Provides roughness length values according to the 20 land cover categories of the land cover map of Iraq that has been developed in this work based on many literature reviews.

Land cover map 2006 category	Surface roughness classification	Roughness length zo (m)			references		
		max	min	set	Max ref.	Min ref.	set
1. Water in lakes, canals, and swamps	Water	0.001	0.0001	0.0002	[257]	[256]	[255, 258]
2. Grasses and shrubs; mountains slopes	Grassland	0.1	0.01	0.05	[259]	[257]	[256]
3. Irrigated summer crop	Crops	0.18	0.1	0.14	[255, 260]	[258]	[36]
4. Snowy and rocky areas in the mountains	Roc& Coastal	0.75	0.28	0.40	[257]	[263]	[257]
5. barren, desert	Sand	0.06	0.0001	0.029	[256]	[259]	[263]
6. Rainfed drylands		0.3	0.09	0.12	[256]	[257]	[255, 260]
7. Natural vegetation		0.12	0.02	0.06	[257]	[260]	[255, 260]
8. Marshlands with aquatic vegetation	Wetland	0.17	0.03	0.09	[256]	[256]	[255]
9. Winter: rain fed wheat and barley	Grain	0.3	0.09	0.18	[256]	[257]	[255, 260]
10. Rain fed grass pasture	Pasture	0.1	0.01	0.05	[255]	[257]	[257]
11. Rainfed wheat and barley and grass pasture mosaic		0.3	0.01	0.15	[256]	[257]	averaged
12. Rain fed wheat	Grain	0.18	0.12	0.16	[260]	[260]	averaged
13. Winter: rain-fed wheat and barley.	Grain	0.3	0.09	0.18	[256]	[257]	[255, 260]
14. Irrigated orchards; mostly date palms in the plain.	Groves	1.6	0.5	0.8	[260]	[258]	[260]
15. Irrigated fallow land.		0.004	0.001	0.004	[255]	[255]	[255]
16. Winter: irrigated wheat and barley; summer: rice and vegetate.	Crops	0.17	0.03	0.115	[260]	[260]	averaged
17. Irrigated wheat and barley and grass pasture mosaic.	Pasture	0.14	0.04	0.11	[28]	[255]	averaged
18. Irrigated wheat.	Crops	0.25	0.12	0.185	[258]	[255]	averaged
19. Winter: irrigated wheat and barley.	Crops	0.3	0.09	0.18	[256]	[257]	[255, 260]
20. An urban areas, Built-Up	Urban	1.6	1	1.1	[256]	[261]	[257]

The L_p should be estimated before starting the iterative solution. To evaluate the variability scale L_p , the development of the boundary layer for each upwind fetch should be tracked using the structure-function in Equation 5-10 [64].

$$du(z_{o,t}) = \left(u\left(z_{o,i} + z_{o,t} \right) - u\left(z_{o,i} \right) \right)^2 \qquad \text{Equation 5-10}$$

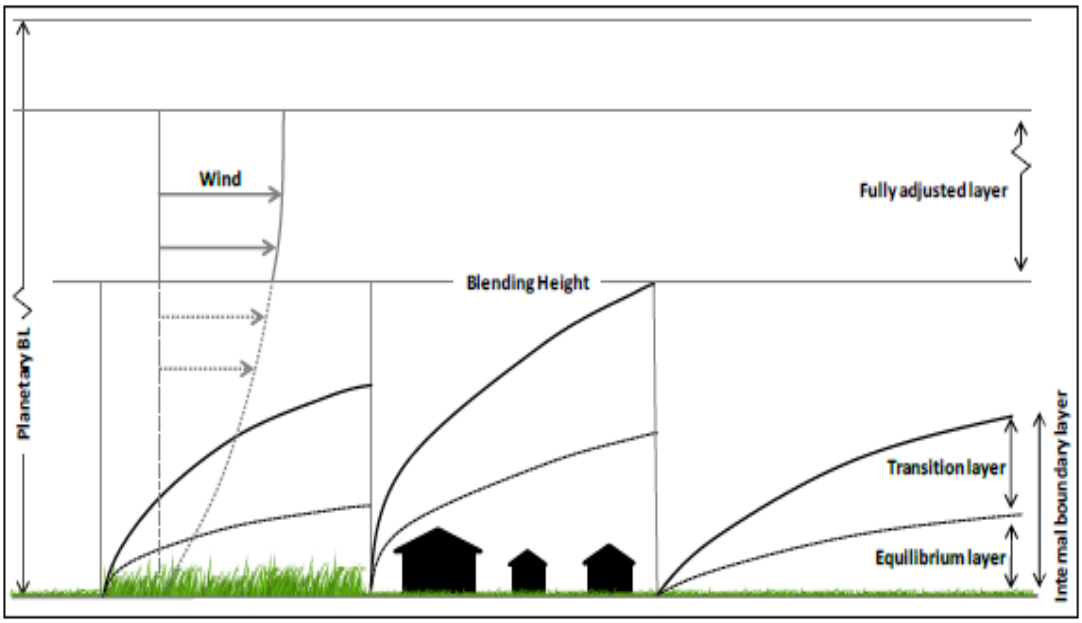

Figure 5-6. A schematic representation to describe the growth of the boundary layer over different patches of surface roughness [28].

The structure-function of this equation will examine the probable change in wind speed over the fetch. The variety of surface roughness from each patch ($z_{o,i}$) will produce turbulent wind flow. While $du(z_{o,t})$ represents the function of likely change in velocity due to turbulence from the preceding patches of surface roughness $z_{o,t}$ over the upwind fetch. The maximum likely speed change (max du) and the average likely speed change ($\overline{du(z_{o,t})}$) over the upwind fetch can be obtained from the structure-function utilized to describe the evolution of the surface roughness by integrating over the length scale (L_d). In other words, L_d "is the streamwise length of the domain" [262].

$$\boldsymbol{L_p = \int_0^{L_d} \left[1 - \frac{\overline{d\mathbf{u}(z_{o,t})}}{max\ d\mathbf{u}}\right] dz_{o,t}} \qquad \text{Equation 5-11}$$

The length of L_d in this project is set to 2.947 km, which represents the longest path through each direction sector. The value of L_d forms the hypotenuse of a right-angle triangle with sides of 2.084 km as shown in part c in Figure 5-7.

Now all the essential inputs are ready to estimate the blending height value from Equation 5-9. The value of Z_{bh} will be used to calculate the effective local roughness z_{oeff} in Equation 5-12 for each upwind fetch according to each wind direction sector.

$$\left[\ln\left(\frac{(Z_{bh} - d_{eff})}{z_{oeff}}\right)\right]^{-2} = \sum f_i \left(\frac{(Z_{bh} - d_i)}{z_{o,i}}\right)^{-2} \qquad \text{Equation 5-12}$$

- d_{eff} refers to the regional effective displacement height of the wind direction sector.
- z_{oeff} represents the effective local roughness of upwind fetch for each direction sector.
- $z_{o,i}$ refer to z_o of each patch.
- d_i represents the displacement height of each patch.

The effective displacement height d_{eff} is shaped by the effect of the highest roughness length in each upwind fetch. To estimate the effective displacement height for 12 wind direction sectors around a target site, we should select the highest roughness length that is equal to or higher than 0.4 m in each upwind fetch. To estimate d_i for each patch, z_o must be higher than 0.4 m. Both of d_{eff} and d_i can be estimated by Equation 5-8. The value of $z_{o\,eff}$ for each wind direction sector can then be estimated using Equation 5-12. To solve Equation 5-12 should calculate RHS of this equation firstly.

5.3 Wind Assessment By Downscaling Technique

This chapter aims to develop the DSM and improve the parameters of this technique to estimate the wind speed in Iraq accurately using MERRA data and the LCM of Iraq. There are two objectives which lie behind using the downscaling technique in Iraq:

- To evaluate the annual average wind speed for one year for the whole of Iraq.
- To estimate the hourly wind speed at selected locations in Iraq to feed into the HRES model.

This section will describe the techniques used to achieve each of their objectives.
First of all, Figure 5-7 shows an approximate description of the downscaling technique and the area and the resolution that MERRA data can cover. There are 151 grid points of MERRA data covering the whole LCM of Iraq. MERRA data represents the reference wind climatology at height of 10 m and 50 m, as symbolized by small orange points in part (A). Each orange grid point in part (B) represents the location of MERRA data in the center of the MERRA grid square that covers the reference wind climatology over the blue dotted grid that is surrounded by the green box. The blue dotted grid also represents the distribution of roughness patches that will be used as reference and target sites in the DSM. The green box covers spatial resolution 55.461 km × 61.589 km = 3415.7 km^2 which represents a MERRA grid square, that includes around 63727 cells, each cell size represents z_o patch (Cell size of LCM). Each roughness patch covers the spatial resolution 231.6 m × 231.6 m that equals 0.0536 km^2 according to the spatial resolution of the LCM of Iraq in Figure 5-4. The DSM will be applied to all roughness patches within each MERRA grid square. The DSM covers sites with an area equal to 16 km^{2,} which includes 324 cells of roughness patches surrounded by the purple square in part B of Figure 5-7. This area is called the downscaling square area (DS).

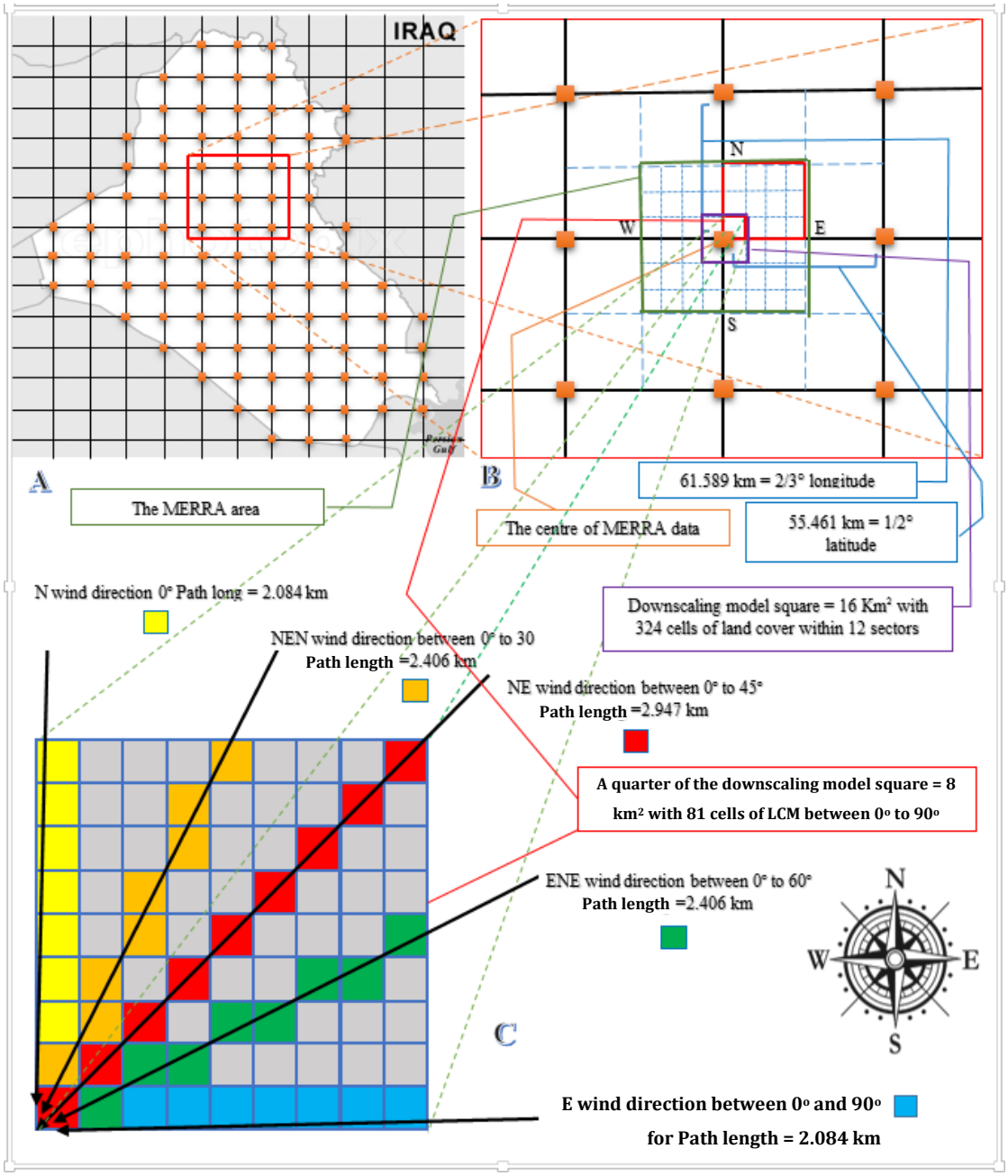

Figure 5-7. Schema A shows the approximate distribution of MERRA data across Iraq. Schema B shows the integration between MERRA data and land cover cells. Schema C shows wind direction sectors between 0o and 90o including the land cover patches that will be used in blending height estimation within the DSM.

In this project, there are 12 wind direction sectors of 30° degrees around each reference site in the roughness map. In terms of predicting the annual average wind speed within each wind direction sector that has been estimated based on hourly wind speed from MERRA for one year. The fraction of wind speed and direction, as well as the annual average wind speed to each wind direction sector, have been estimated based on the repetition of wind speed hours to each sector over one year as presented in Table 5-2.

Table 5-2. Distribution of annual average wind speed u_{10} and directions for reference wind climatology (MERRA data) at reference sit at 10 m according to 12 direction sectors at reference site.

sector	degree	Hours repetition	Annual average wind speed	The fraction of wind direction	Fraction of Wind speed	
1	0°-30°	597	3.252 m/s	0.068	0.221136	
2	30°-60°	347	2.797 m/s	0.04	0.11188	
3	60°-90°	262	2.905 m/s	0.03	0.08715	
4	90°-120°	359	3.454 m/s	0.041	0.141614	
5	120°-150°	743	4.906 m/s	0.085	0.41701	
6	150°-180°	491	4.028 m/s	0.056	0.225568	
7	180°-210°	323	3.317 m/s	0.037	0.122729	
8	210°-240°	236	2.562 m/s	0.027	0.069174	
9	240°-270°	344	2.701 m/s	0.039	0.105339	
10	270°-300°	818	3.661 m/s	0.093	0.340473	
11	300°-330°	2765	4.524 m/s	0.316	1.429584	
12	330°-360°	1475	4.017 m/s	0.168	0.674856	Annual Ave
sum		8760		1	3.9465 m/s	3.9468 m/s

To evaluate the annual average wind speed for one year for each target site over the whole of Iraq, the u_{10} in Equation 5-1 will represent the annual average wind speed of reference wind climatology (MERRA) at a reference site for a specific sector. For example:

- At the first step of the DSM, the first value of annual average wind speed in sector 1 is scaled up to Z_{ref} using Equation 5-1 to estimate u_{ref} based on the standard roughness parameter at the reference site.
- At the second step the value of u_{ref} in sector 1 is scaled down from Z_{ref} using Equation 5-2 to estimate the wind speed u_{bh} at blending height Z_{bh}. The effective displacement height d_{eff} and effective local roughness $z_{o\,eff}$ of the upwind fetch for sector 1 around the target site is estimated using Equation 5-8 and Equation 5-11, respectively.
- At the third step, the wind speed that is estimated at the Z_{bh} is scaled down to determine the wind speed at hub height u_{hh} according to the roughness characteristic of the target site and the upwind fetch in sector 1.

A frequency weighted average is then carried out for the 12 sectors to produce the annual average wind speed. This procedure is applied for all 63727 patches of roughness (target sites) within a MERRA grid square.

In order to predicting the hourly wind speed at a specific location for 8760 hours, u_{10} represents the value of hourly reference wind climatology from a MERRA in a specific sector at reference site based on the wind direction. For example:

- At the first step, of the DSM, the first hour of wind speed in sector 1 is scaled up to Z_{ref} using Equation 5-1 to estimate u_{ref} based on the standard roughness parameter at the reference site.
- At the second step, the value of u_{ref} for the first hour in sector 1 will be scaled down from Z_{ref} using Equation 5-2 to estimate the wind speed u_{bh} at Z_{bh}. The d_{eff} and $z_{o\,eff}$ of the upwind fetch in sector 1 around the target site is estimated using Equation 5-8 and Equation 5-11, respectively.
- At the third step, the first hour of wind speed u_{bh} that is estimated at the Z_{bh} is scaled down to determine the wind speed at hub height u_{hh} according to the roughness characteristic of a target site and the upwind fetch in sector 1.

The result of wind speed at hub height u_{hh} at the end of the third step is saved. After that, the second hour of wind speed at a reference site is processed by the DSM based on the roughness effect of the upwind fetch that located within the wind direction sector of the second hour.

This process is repeated for 8759 times based on the rest of 8760 hours of hourly reference wind climatology from MERRA. The process of the downscaling is vital to provide data for installation planning of small wind turbines at any height and location for one year in terms of wind farm or HRES development.

5.4 Sensitivity Analysis

In this project, the DSM has been applied using reanalysis wind speed data from MERRA at two levels 10 m and 50 m at the reference site to evaluate the wind speed in Iraq for long term from 2011 to 2015. In this section, sensitivity analysis has been applied to investigate the effect of different values for some parameters. In addition to the MERRA level data used, there are three other parameters in the DSM which play a crucial role in estimating wind speed accurately at a target site such as the reference height Z_{ref} at the reference site, the hub height Z_h at a reference site and the roughness length at a reference site $z_{o\,ref}$.

In addition, the sensitivity analysis was performed comparing the impacts of regular stripes of effective local roughness based on 9 patches in the upwind fetch and a full sector design for 32 patches within the upwind fetch. This comparison will show to what extent that this change can affect wind speed accuracy at the target site.

5.4.1 Regional Averaged Surface Roughness And Sensitivity Analysis

The second step of the DSM that has been applied using Equation 5-2 aims to downscale the wind speed from Z_{ref} to Z_{bh}, to achieve this estimation, the blending height

must be calculated for 12 wind direction sectors around a target site using Equation 5-9. This equation describes the impact of roughness drag on wind flow within each upwind fetch. To resolve Equation 5-9, the number of patches $z_{0,i}$ and the spatial fraction of each roughness patch within each upwind fetch f_i, must be determined.

Regular patterns of surface roughness (regular stripes) for each upwind fetch have been suggested by Bou-Zeid et al [262] to track the development of a boundary layer at different patches within upwind fetch. In the beginning, 9 patches of surface roughness were suggested for the regular stripes in the upwind fetch as shown in part C of Figure 5-7. the regular stripes of 9 patches wrer chosen based on the length scale L_d that was set at 2828 m and 2000 m in E, W, S and N directions according to David, 2017 [20]. Since, the size of the roughness length patch in this project equals 231.6 m × 231.6 m, the length scale L_d for the longest path has included 9 patches (9 red cells) covers 2947 m and 2084 m in E, W, S and N directions according to part C of Figure 5-7. While the upwind fetches which have orange cells and green cells equal 2406 m as shown in part C of Figure 5-7.

The regular stripes of the upwind fetch in Figure 5-7 have been used to calculate the effective local roughness z_{oeff} using Equation 5-12 for 12 wind direction sectors above Baghdad as a case study by depending on z_o map in Figure 5-8 which include Baghdad city and the area around it.

z_o map in Figure 5-8 is used to examine the effective local roughness for 2 wind direction sectors NE and SW above the Baghdad area as shown in Figure 5-9 and Figure 5-10 respectively. It is possible to note the stretch in the representation of effective local roughness.

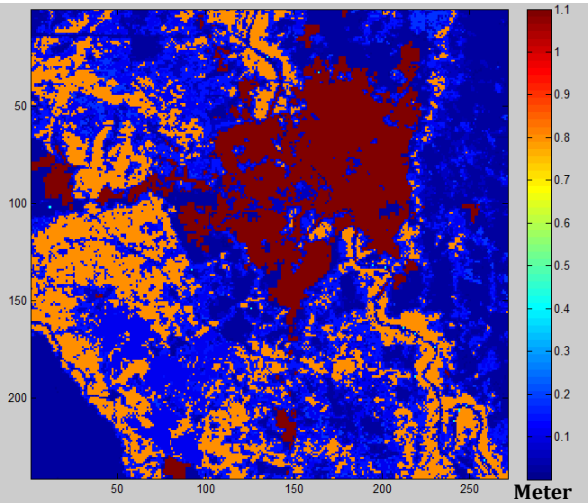

Figure 5-8. z_o map for Baghdad city and the area around it within MERRA area square.

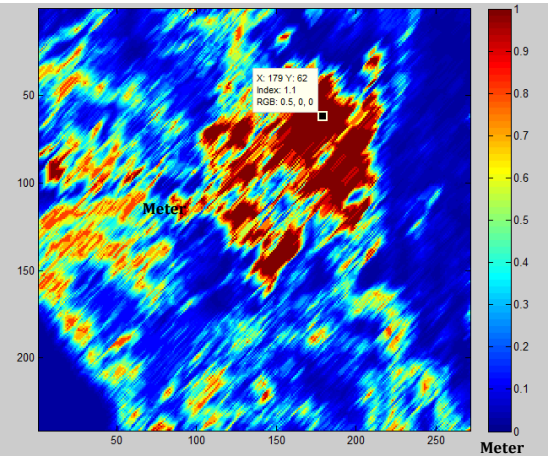

Figure 5-9. Represents the ($z_{o\,eff}$) map for the NE wind direction sector above the Baghdad area by applying the DSM within a MERRA area square.

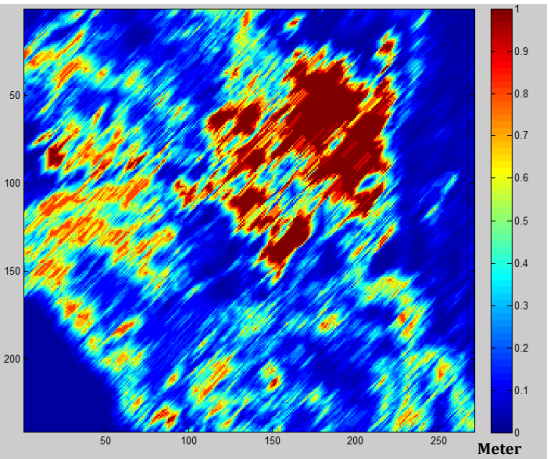

Figure 5-10. Represents the ($z_{o\,eff}$) map for the SW wind direction sector above the Baghdad area by applying the DSM within a MERRA area square.

In fact, the wind flow above various surface roughness lengths for an open area does not show laminar flow within a horizontal perspective. Usually, the different surface roughness lengths cause vertical and horizontal changes in wind speed and direction. The horizontal wind flow generates numerous rotating eddies above a coarse surface. For this reason, the stripe pattern for upwind fetch will not represent the full effect of the changes in roughness length across a wind direction sector. In order to improve the estimation of effective local roughness and increase the estimated wind speed accuracy, the full sector pattern with 30^{o} degrees sector has been suggested. According to this suggestion, 12 full wind direction sectors that include 32 roughness length patches around each target site have been designed in this project, as shown in Figure 5-11. According to this suggestion the effective local roughness will be estimated based on 32 roughness patches for each upwind fetch at each wind direction sector. Figure 5-12 shows the $Z_{o\,eff}$ for 4 directions as case study to show the difference of the roughness effect within each wind direction sector. At first glance, it is possible to note the difference between the effective local roughness maps that have been created based on 9 roughness patches in Figure 5-9 and Figure 5-10 with the effective local roughness maps that have been created based on 32 roughness patches in Figure 5-12. In addition, it is possible to note that the stretch effect of the effective local roughness that is caused by 9 patches in the upwind fetch has disappeared in Figure 5-12 when 32 patches have been used.

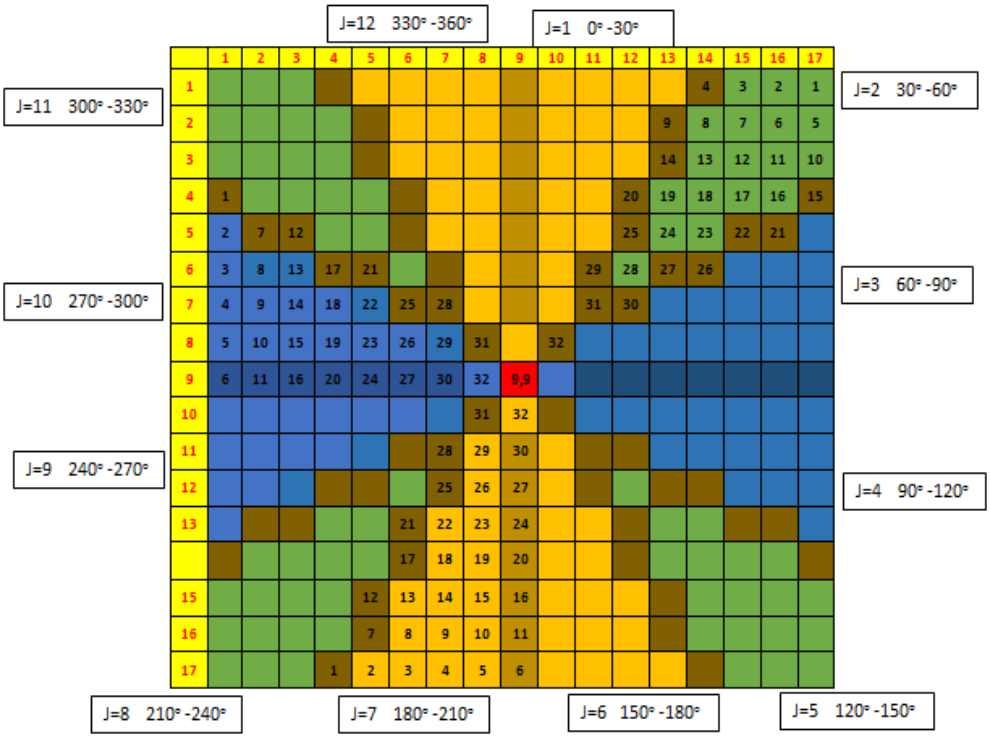

Figure 5-11. The number of cells within each wind direction sector. There are 12 direction sector which have been separated by dark cells as sheared area.

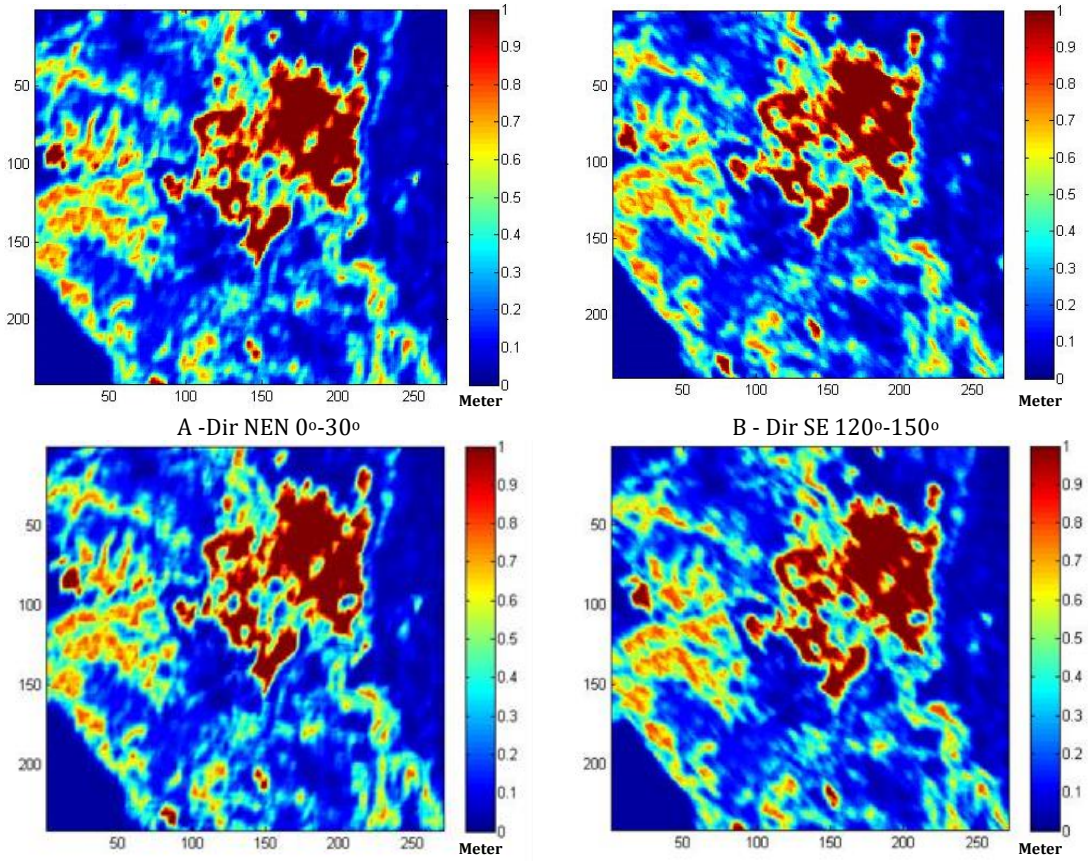

A -Dir NEN 0°-30°

B - Dir SE 120°-150°

C- Dir SWS 180°-210°

D - Dir WN 300°-330°

Figure 5-12. Represents the full sector test (32 patches in the upwind fetch) of effective local roughness for 4 direction sectors for Baghdad city and the area around it within a MERRA area square

According to the effective local roughness in Figure 5-12 that has been estimated based on the full sector pattern (32 roughness patches) in Figure 5-11, it becomes possible to estimate the blending height for 12 wind direction sectors around a target site using Equation 5-9.

The blending height estimation for two-direction NE and SW above Baghdad city according to full sector pattern is shown in Figure 5-13. The highest blending height that was recorded in Figure 5-13A equals 273.48 m and the lowest blending height equals 66.77 m. Furthermore, in Figure 5-13B the highest blending height is 273.91 m and the lowest height is 60.61 m. In order to compare with other literature the blending height was ranged from 50 m for low value to 280 m for a higher value [264]. In addition, it has been estimated that the blending height above an urban area ranged from 140 m to 230 m [265].

According to this classification, it is possible to see that the higher blending heights are located above the urban area which their roughness surface equals 1.1 and forest area which their roughness surface equals 0.8 in Figure 5-13A and Figure 5-13B.

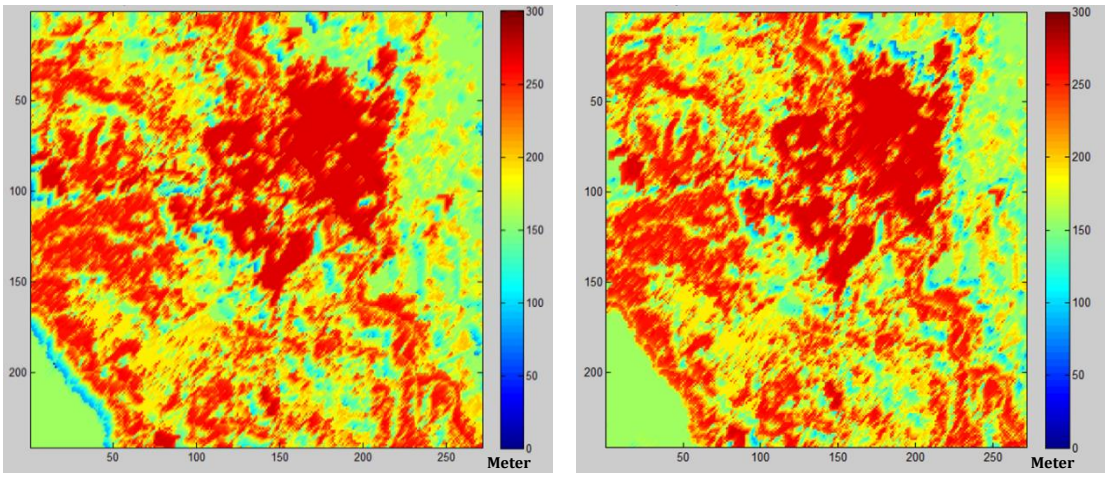

A - the (Z_{bh}) map for NE wind direction sector

B - the (Z_{bh}) map for SW wind direction sector

Figure 5-13. The blending height (Z_{bh}) results based on the full sector design (32 roughness patches in the upwind fetch) for Baghdad city and the area around it within MERRA area square.

5.4.2 Reference Height Sensitivity Analysis

In section 5.2 two values (200 m and 600 m) have been suggested to represent the reference height to apply the DSM in the boundary layer in Iraq. According to that, the comparison has been made between the annual average wind speed map in Figure 5-14 for 2015 that is modeled based on reference height Z_{ref} = 200 m at reference site using reanalysis data at hub height Z_h =10 m and roughness length $z_{0\,ref}$ =0.103 m at the reference site, with wind speed map in Figure 5-15 that applied the DSM at hub height Z_h =10 m based on reference height Z_{ref} = 600 m and $z_{0\,ref}$ =0.103 m at the reference site. The wind speed map difference in m/s in Figure 5-16 represents the absolute difference by subtracting the wind speed values in Figure 5-14 from the wind speed values in Figure 5-15. In addition, same

comparison has been made between wind speed maps in 2014 in Figure 5-17 and Figure 5-18. Figure 5-19 represents the absolute difference between Figure 5-17 and Figure 5-18. At first glance, it is possible to note that the wind speed in Figure 5-14 is consistently lower than the wind speed in Figure 5-15. The same feature is noted between Figure 5-17 and Figure 5-18. In addition, Figure 5-16 and Figure 5-19 show clear differences above the big lakes in Iraq that reach 0.33 m/s. This difference is linked with two important variables:

- Firstly, wind speed increases with the selected reference height. For example, the wind speed equals 6.53 m/s at Z_{ref} = 200 m while the wind speed equals 7.47 m/s at Z_{ref} = 600 m.
- Secondly, the significant reduction in roughness length above the lake surface.

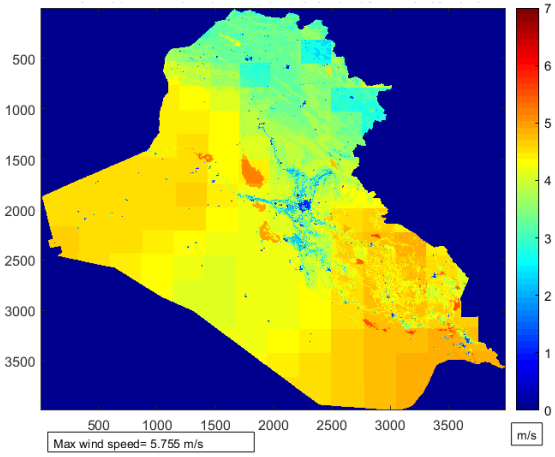

Figure 5-14. The annual average wind speed map at Z_{hh} = 10 m based on Z_h = 10 m, Z_{ref} = 200 m and $Z_{o\,ref}$ = 0.103 m at reference site in 2015

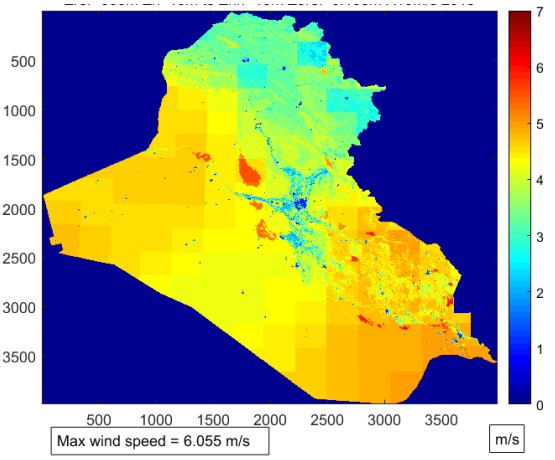

Figure 5-15. The annual average wind speed map at Z_{hh} = 10 m based on Z_h = 10 m, Z_{ref} = 600 m and $Z_{o\,ref}$ = 0.103 m at reference site in 2015

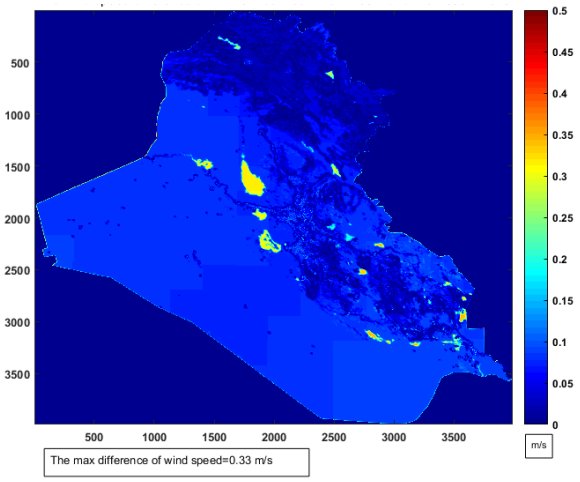

Figure 5-16. The absolute difference between Figure 5-14 and Figure 5-15.

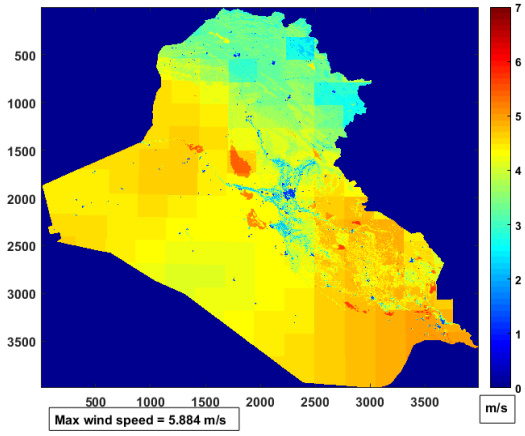

Figure 5-17. The annual average wind speed map at Z_{hh} = 10 m based on Z_h = 10 m, Z_{ref} = 200 m and $Z_{o\,ref}$ = 0.103 m at reference site in 2014

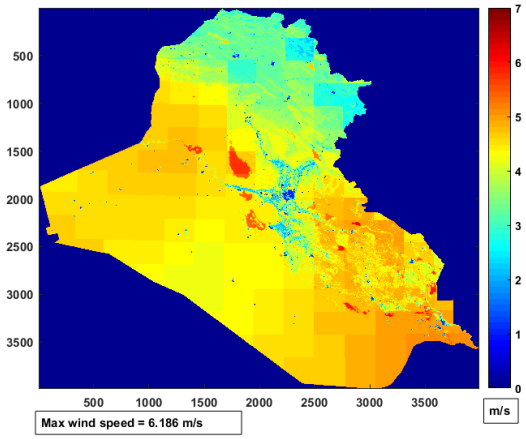

Figure 5-18. The annual average wind speed map at Z_{hh} = 10 m based on Z_h = 10 m, Z_{ref} = 600 m and $Z_{o\,ref}$ = 0.103 m at reference site in 2014

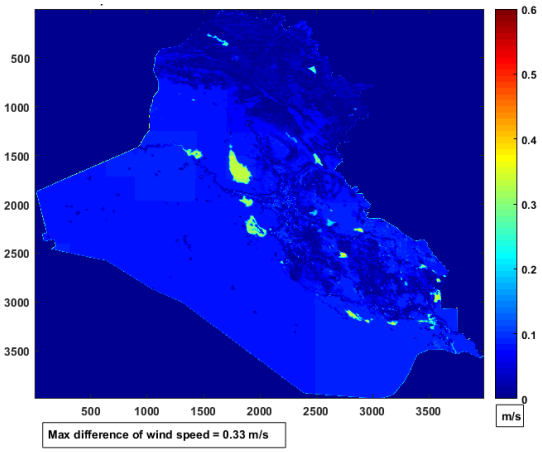

Figure 5-19. The absolute difference between Figure 5-17 and Figure 5-18.

5.4.3 Roughness Length Sensitivity Analysis

Further sensitivity analysis has been made by comparing the wind speed map in Figure 5-20 that uses $z_{0\,ref}$ = 0.103 m at the reference site with the wind speed map in Figure 5-21 that estimated wind speed based on $z_{0\,ref}$= 0.05 m. The DSM has been applied using MERRA data in 2014 at hub height Z_h= 10 m at the reference site and a reference height Z_{ref}= 200 m. The wind speed map difference in Figure 5-23 represents the absolute difference by subtracting the wind speed values in Figure 5-20 from the wind speed values in Figure 5-21. At first glance at Figure 5-20 and Figure 5-21, it is possible to note that in general, the wind speed in Figure 5-21 is lower than the wind speed in Figure 5-20. Also, the maximum difference of wind speed that is recorded in Figure 5-23 equals 0.317 m/s. The maximum differences concentrated above big lakes and some areas in the middle, west, and south-east of Iraq. The lowest differences are concentrated above urban areas and the north and northeast of Iraq. The reason behind the low difference above urban area returns to the general reduction of wind speed above cities and towns due to the presence of the displacement height above an urban area. The reason behind the low difference in the north

of Iraq is related to mountain nature in this area and reduction of the reference wind climatology from MERRA as shown in Figure 5-22. Whenever wind speed increases from the raw MERRA data the difference between wind speed maps in Figure 5-20 and Figure 5-21 at Z_h = 10 m will be increased due to the impact of roughness length at target site in the two Figures. Furthermore, the same comparison has been applied for the same factors based on wind speed from MERRA in 2013 between Figure 5-24 and Figure 5-25. It easy to note that the maximum wind speed in Figure 5-25 that used $z_{0\,ref}$ = 0.05 m is lower than the maximum wind speed in Figure 5-24 that used $z_{0\,ref}$ = 0.103 m. The maximum difference of wind speed that is estimated in Figure 5-26 is similar to the maximum difference of wind speed that is recorded in Figure 5-23. The distribution of wind speed difference in Figure 5-26 is quite similar to wind speed difference distribution in Figure 5-23. This similarity returns to the methodology of IAU in GEOS-5 DAS that has been applied in the data assimilation system of MERRA to re-analysis wind speed data as explained in section 2.6.6.4.

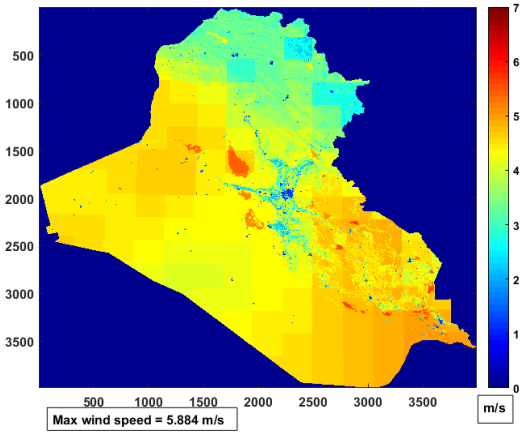

Figure 5-20. The annual average wind speed map at hub heightZ_h = 10 m based on MERRA data at Z_{hh} = 10 m, reference height Z_{ref} = 200 m and $Z_{o\,ref}$ = 0.103 m in the reference site using the DSM in 2014

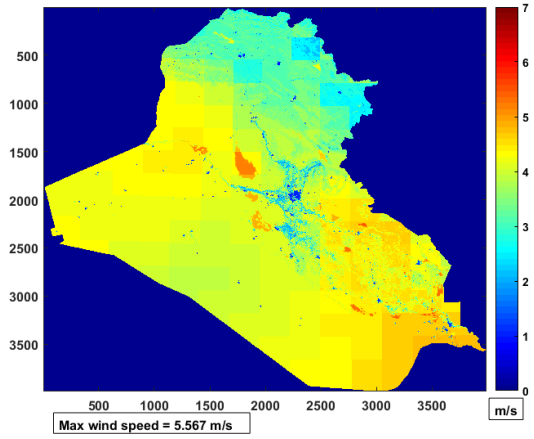

Figure 5-21. The annual average wind speed map at hub heightZ_h = 10 m based on MERRA data at Z_{hh} = 10 m, reference height Z_{ref} = 200 m and $Z_{o\,ref}$ = 0.05 m in the reference site using the DSM in 2014

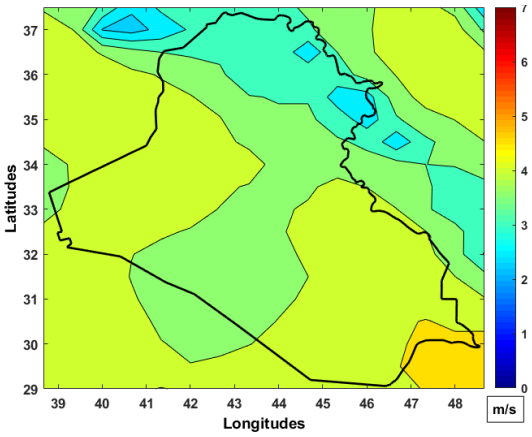

Figure 5-22. Color-scale map of annual average wind-speed which created based on the raw MERRA data at level of 10 m in 2014

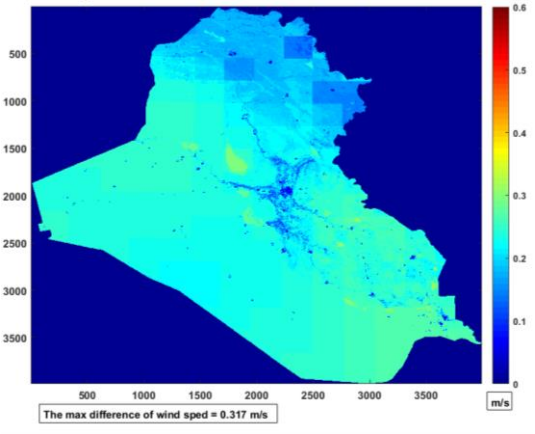

Figure 5-23. The wind speed difference at Z_{hh} =10 m between $Z_{o\,ref}$ = 0.103 m and $Z_{o\,ref}$ = 0.05 m site using the DSM in 2014

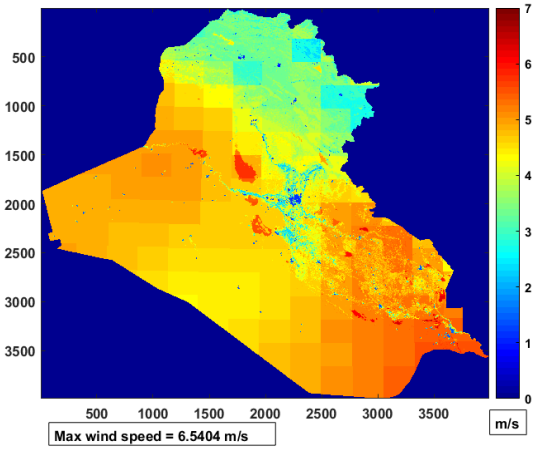

Figure 5-24. The annual average wind speed at hub height Z_{hh} = 10 m based on MERRA data at Z_h = 10 m, reference height Z_{ref} = 200 m and $Z_{o\,ref}$ = 0.103 m in the reference site using the DSM in 2013

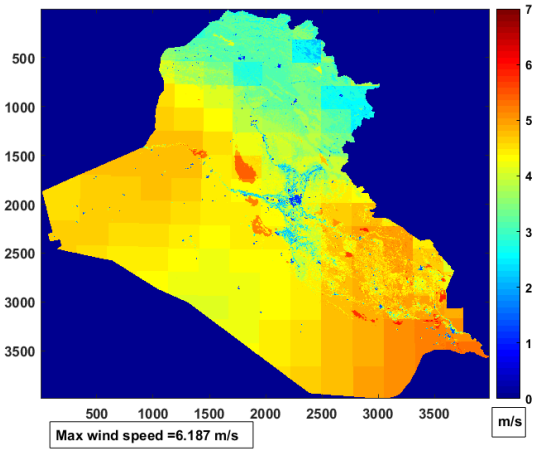

Figure 5-25. The annual average wind speed at hub height Z_{hh} = 10 m based on MERRA data at Z_h = 10 m, reference height Z_{ref} = 200 m and $Z_{o\,ref}$ = 0.05 m in the reference site using the DSM in 2013

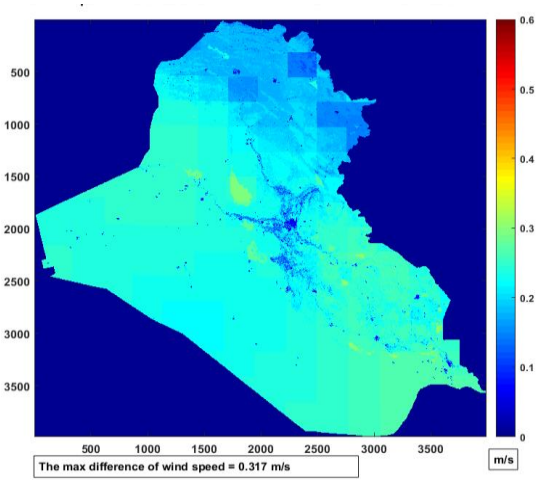

Figure 5-26. The wind speed difference at Z_{hh} = 10 m between $Z_{o\,ref}$ = 0.103 m and $Z_{o\,ref}$ = 0.05 m site using the DSM in 2013.

5.4.4 Sensitivity Analysis for The Hub Height of Wind Speed from MERRA

The most critical sensitivity analysis that has been implemented in this project, is the comparison between the wind speed maps in Figure 5-27 and Figure 5-28. The annual average wind speed in Figure 5-27 is estimated based on wind speed from MERRA at height Z_h=10 m while the wind speed map in Figure 5-28 is estimated based on wind speed from MERRA at height Z_h= 50 m. For both wind speed maps in Figure 5-27 and Figure 5-28, the DSM has been applied using reanalysis data from MERRA in 2012 with surface roughness length $z_{o\,ref}$= 0.103 m at the reference site and a reference height Z_{ref} = 200 m.

At first glance, it is possible to note that the wind speed in Figure 5-28 is generally lower than the wind speed in Figure 5-27. The wind speed map difference in Figure 5-29 represents the absolute difference between Figure 5-27 and Figure 5-28.

Figure 5-29 reflects a significant result from applying reanalysis data from different heights at the reference site. According to similarity theory, the result of the DSM should be similar

at the target site when applying two values of wind speed from two levels at the same vertical wind profile at a reference site. This feature is seen in many locations in Figure 5-29 that shows low differences signified by dark blue cells of wind speed differences between the two heights used.

The lowest differences in wind speed in Figure 5-29 are distributed across the middle, north, and southeast of Iraq which are recognized by blue and dark blue cells where the difference ranges between 0 and 0.2 m/s. The rest of the locations show differences ranging from 0.2 to 0.3 m/s and are distributed over the west and south-west of Iraq. The south of Iraq shows differences ranging from 0.3 to 0.4 m/s.

The most significant differences are located above Tharthar Lake in the middle of Iraq and Soran region in the north of Iraq. For both regions, the difference ranges from 0.5 to 0.6 m/s. The reason behind these bigger differences stems from the methodology of IAU in GEOS-1 DAS that has been applied by MERRA and the probability of getting errors during the reanalysis process as mentioned in section 2.6.6.4. There are several reasons behind this difference between results of the DSM that applied from Z_h = 50 m in Figure 5-28 and from Z_h = 10 m in Figure 5-27.

- The shortage of observation data, the accuracy of the data used as well as the poor distribution of observation data will affect the performance of the general circulation model (GCM) that employs C grid.
- In addition, the biggest discrepancies are seen in areas of sharp roughness change which stems from the insufficient data from observations to make the correction for the re-analysis data as well as this issue is related to the performance of the coarse GCM model that does not represent the new surface very well.

All these factors can create errors in some locations continue for long period as the same errors feature with the sensitivity analysis for four years from 2012 to 2015, as shown in Figure 5-29 and Figure 5-30.

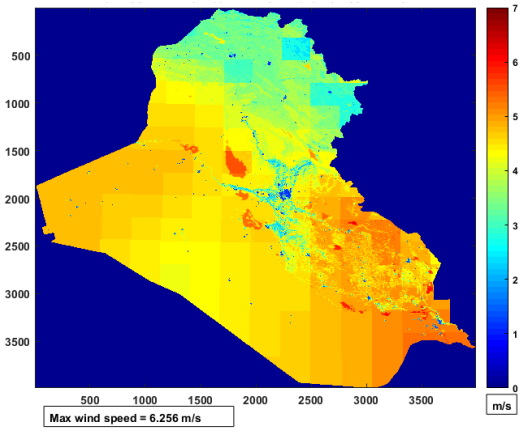

Figure 5-27.Wind speed map at hub height Z_{hh}=10m based on MERRA data at Z_h=10m, reference height Z_{ref}=200m and $z_{o\,ref}$=0.103m in the reference site using the DSM in 2012

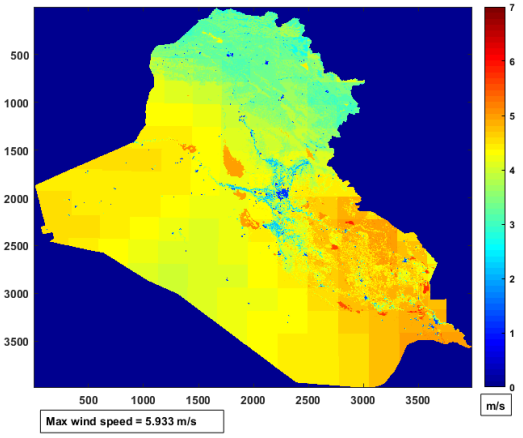

Figure 5-28. Wind speed map at hub height Z_{hh} =10m based on MERRA data at Z_h =50m, reference height Z_{ref}=200m and $z_{o\,ref}$=0.103m in the reference site using the DSM in 2012

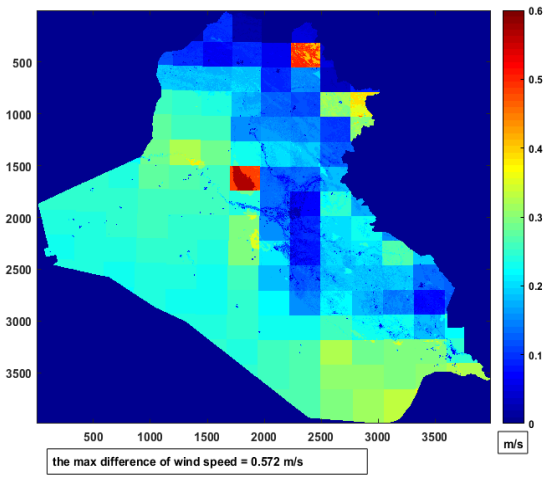

2012

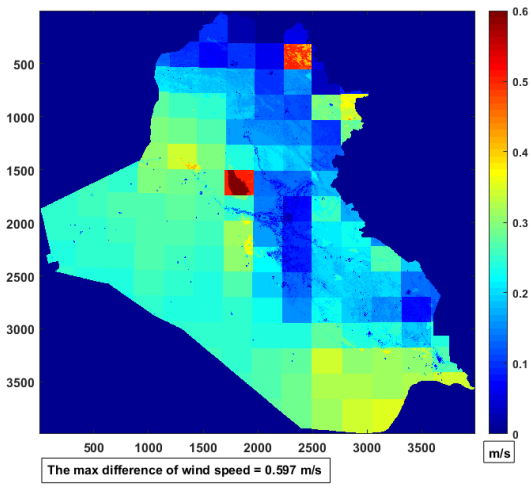

2013

Figure 5-29. The wind speed difference at Z_{hh}=10m between Z_h=10m and Z_h=50m site using the DSM in 2012 and 2013

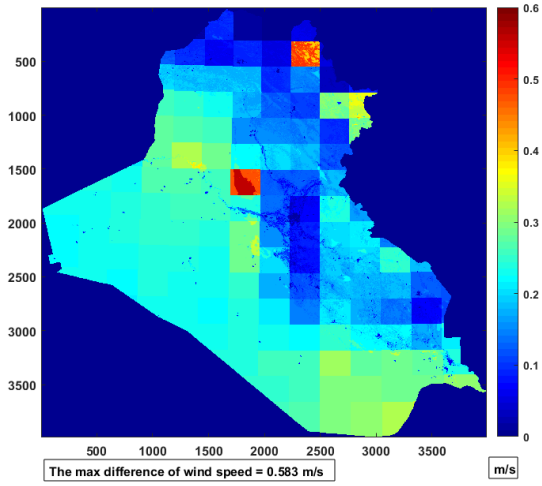

2014

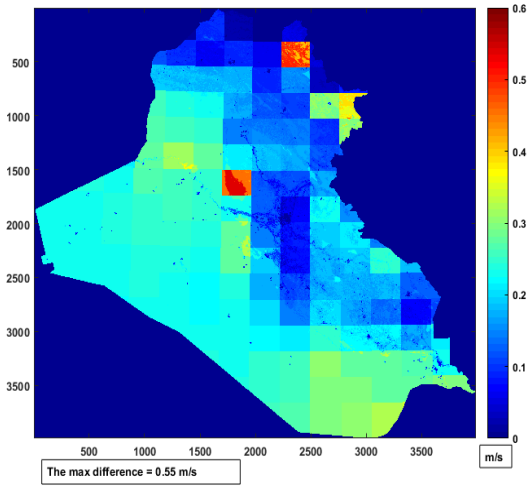

2015

Figure 5-30. The wind speed difference at Z_{hh}=10m between Z_h=10m and Z_h=50m site using the DSM in 2014 and 2015

5.5 Results Validation And Discussion

Validation is needed between observed and estimated data to check the accuracy of wind speed estimation by the DSM. A daily average of wind speeds calculated from estimated hourly data has been compared with equivalent data averaged from 3 hourly values from 16 weather stations throughout Iraq. The 16 sites represent the limited number of weather stations that have acceptable data of wind speeds over a year. The validations have been applied for one year for each weather station for the period between 2012 and 2015. The observation wind speed has been measured by an anemometer at 10 m height. These observation data have been gathered from the weather information service provided by the OGIMET website [266]. The locations of 16 weather stations as shown in Figure 5-31.

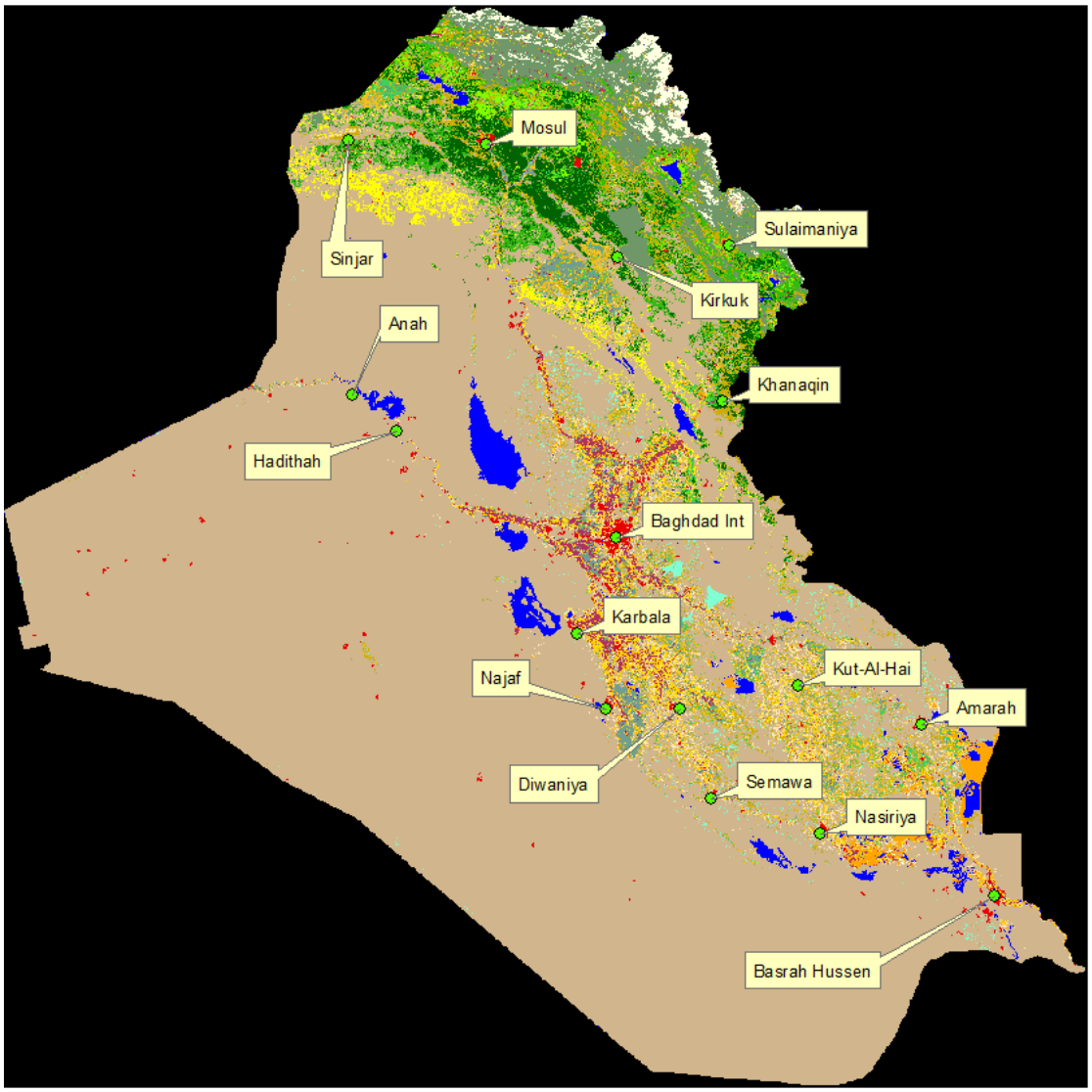

Figure 5-31. The locations of 16 weather stations distributed in different places in Iraq over the roughness map.

5.5.1 Different levels of MERRA data validation with observed data

Validation has been applied between the DSM results at hub height Z_{hh} = 10 m based on re-analysis data from MERRA at hub height of reference site Z_h = 10 m and Z_h= 50 m with observation data from the 16 weather stations. Different parameter values have also been applied in this validation, to check which contribution will give the best results by reducing the error between actual and forecasting wind speed.

This validation has been divided into two groups, as shown in Table 5-3. The first group includes applying the DSM using MERRA data at a reference site Z_h = 10 m to Z_{hh} = 10 m at target site with changing between reference height Z_{ref} = 200 m to Z_{ref}= 600 m and also changing between roughness length of reference site from $Z_{o\,ref}$= 0.103 m to $Z_{o\,ref}$= 0.05 m. In addition, the second group in Table 5-3, includes applying the DSM based on MERRA data from reference site at Z_h= 50 m to Z_{hh}= 10 m at the target site with the same values for reference height and roughness length in the first group. Table 5-3 has been created 9 combinations for each weather station based on 8 methods ranging from DM1 to DM8. It is worthy of mentioning that the DSM (from DM1 to DM8) has been applied based on full sector design (32 roughness patches) in terms of validation and also the maps in the previous Figures. The 9th combination has used to recognize the difference between the raw MERRA data at 10m and observation data at 10m for each single weather station for the same period in order to compare the error metric results with the other combinations as presented in Table 5-3

The re-analysis data from MERRA has been used for 2012, 2013, 2014 and 2015 for different weather stations depending on observed data availability. Furthermore, in this validation a number of error metrics have been applied to calculate the percentage of error between the estimated result and the observed data as follows:

1. MAPE: Mean Absolute Percentage Error in Equation 5-13 [267, 268]

$$MAPE = \left[\frac{1}{N}\sum_{i=1}^{N}\frac{|A-F|}{A}\right].100\ \% \qquad \text{Equation 5-13}$$

2. MBE: Mean Bias Error in Equation 5-14 [269].

$$MBE = \left[\frac{1}{N}\sum_{i=1}^{N}A-F\right].100\ \% \qquad \text{Equation 5-14}$$

3. RMSE: Root Mean Square Error in Equation 5-15 [35, 268, 269].

$$RMSE = \sqrt{\frac{\sum_{i=1}^{N}(A-F)^2}{N}} \quad \text{Equation 5-15}$$

4. MAE: the Mean Absolute Error in Equation 5-16 [35, 268].

$$MAE = \frac{1}{N}\sum_{i=1}^{N}|A-F| \quad \text{Equation 5-16}$$

5. R^2: R squared [270]

$$R^2 = \frac{N\,(\sum AF) - (\sum A)(\sum F)}{\sqrt{[N\sum A^2 - (\sum A)^2][N\sum F^2 - (\sum F)^2]}} \quad \text{Equation 5-17}$$

Where A represents the daily average of actual data (observation). F represents the daily average of forecasting data that estimated by the DSM. N represents the number of days per year. Table 5-3, shows that the MAPE for DM8 shows the lowest percentage error for 11 stations (green cells) among 16 weather stations through applying 8 proposals using DSM, when applied the DSM from Z_h= 50 m at reference site to the hub height Z_{hh}=10 m using $Z_{o\,ref}$ = 0.05 m for roughness length and Z_{ref} = 600 m for the reference height.

The MAPE in this validation calculates the size of the error in percentage between forecasting calculation and actual measurement [267]. According to the result of MAPE in proposal DM8, the factors that have used in DM8 show the most accurate wind speed in comparison with the other proposals. In addition, the RMSE shows the lowest difference for significant error in m/s between observation and estimation data for 8 weather stations (green cells) that applied the DSM based on factors that have been used in DM8. On the contrary, in the first group, the MAPE in the DM1 shows the highest percentage of error for 11 weather stations (red cells), while the RMSE shows the highest error between observation and estimation data for 7 weather stations (red cells) and the highest average of difference 1.15056 m/s in DM1.

5.5.2 The Reference Height Impact

The reference height Z_{ref} in this validation has been changed from 200 m to 600 m, where each value of this factor has interacted with other factors. The average MAPE and RMSE have reduced slightly from DM1 to DM3 in the first group in Table 5-3 when the value of Z_{ref} has been changed from 200 m to 600 m. In addition, in the second group, the average MAPE in DM5 and DM7 has reduced from 52.06% to 50.44% respectively, while the average

of RMSE has decreased slightly between DM5 and DM7. According to the betterment in error metrics, it is possible to note that the changing in reference height from 200 m to 600 m has improved the wind speed estimation. The reason behind the low error when using 600 m stems from that this value reflects the feature of the boundary layer in Iraq due to this height represents the level where wind speed does not change with height [32].

5.5.3 The Roughness Length Impact

The roughness length (z_o) at a reference site in this validation has been changed from 0.103 m to 0.05 m, where each value of this factor has interacted with other parameters. It is possible to note that the average MAPE and RMSE have reduced slightly from DM1 to DM2 in the first group in Table 5-3 when the value of roughness length has changed from 0.103 m to 0.05 m. In addition, in the second group, the average MAPE in DM5 and DM6 has reduced from 52.06 % to 51.02 % respectively. While the average of RMSE has reduced slightly from1.1396 m/s to 1.1343 between DM5 and DM6. According to the error reduction from DM1 to DM2 and DM5 to DM6, it is possible to note that the changing in roughness length from 0.103 m to 0.05 m will enhance the wind speed estimation. The result approves that the $Z_{o\ ref}$=0.05 m reflects the aerodynamic feature of roughness surface of open area in Iraq which has shortage grass and bushes.

5.5.4 The Roughness Length and Reference Height Impact

According to the effect of the reduction in error that has been achieved by changing reference height value and roughness length severally in the last two sections. The decision has been taken to integrate between applying the second value of roughness length $Z_{o\ ref}$=0.05 m with the second value of reference height 600m in DM4 and DM8.

The average value of MAPE in DM4 and DM8 shows a reduction in error in comparison with other MAPE values that have been calculated based on other combinations. The value of MAPE in DM4 has dropped down to 48.53%, while the value of MAPE in DM8 has dropped down to 48.91%. Also, the value of RMSE has reduced slightly in DM4 and DM8 in comparison with other proposals. Based on the improvement in MAPE and RMSE calculation in DM4 and DM8, we conclude it is quite useful to integrate between 600 m for reference height and $Z_{o\ ref}$ = 0.05 m for roughness length when applying the DSM in Iraq.

5.5.5 The Impact Of Applying The Downscaling Model From Z_h = 50 m to Z_{hh} = 10 m

The most applications of the DSM have been carried out from Z_h= 10 m to Z_{hh}= 10 m based on the availability of measuring wind speed just at 10 m in the surface weather stations [35, 36, 271]. However, re-analysis data from MERRA provide researchers wind

speed data at two levels 10 m and 50 m. Based on this opportunity, it is possible to apply DSM frm Z_h = 50 m to Z_{hh} = 10 m in this validation. ccording to Table 5-3, it is possible to note that the second group has shown a reduction in MAPE values in comparison with the first group particularly between DM1 and DM5 and also between DM3 and DM7. In fact, the change in values of MAPE is small. The small change in percentage between DM8 and DM4 reflects the accuracy of DSM performance. Despite the clear tendency of MAPE values reduction for 11 weather stations in DM8, but the average value for MAPE was higher than the average value for MAPE in DM4. This difference back to the unique MAPE value for Sulaimaniya weather station, which recorded 60.338% in DM4 and 70.3% in DM8 which leads to increase the average MAPE in DM8. In addition, the values of RMSE have boosted the general result for MAPE. It is possible to note that the error between the mean wind speed and estimation data in RMSE has reduced when applying DSM from Z_h= 50 m to Z_{hh}= 10 m in the second group. Finally, it is clear to note that applying the DSM from Z_h= 50 m to Z_{hh}= 10 m using 600m for reference height and Z_{oref}=0.05m for roughness length will contribute to improving the wind speed estimation and reduce the error between observation and modeling data.

5.5.6 **The Validation Before Applying The Downscaling Model**

At first glance between DM8 and obs-Vs-MERRA at 10 m in the second group, it is possible to see the weather stations that have a low error in MAPE between observation and raw MERRA data also have lower MAPE in DM8. For example, Karbala weather station has recorded low MAPE 29.65% in DM8 and 41.71% in Obs-Vs-MERRA. On the other hand, the weather stations that have recorded high MAPE in DM8. For instance, Mosul weather station has recorded 69.16% for MAPE in DM8, while the Obs-Vs-MERRA has recorded 383.12%. Also, Khanaqin weather station has recorded 69.99% for MAPE in DM8, while it has recorded 475.58% in Obs-Vs-MERRA. Through the above examples we conclude, that the weather stations which have low MAPE in Obs-Vs-MERRA have given a small error when applying the DSM for weather stations that are located within suburban area. While the weather stations that have high MAPE in Obs-Vs-MERRA, have given high MAPE after using the DSM for weather stations that are located within urban areas such as Khanaqin and Mosul weather stations. The stations that deviated from this trend are located within mountain environments such as Singar and Sulaimaniya weather stations that recorded 90.39% and 70.30% respectively. In general, the average MAPE in DM8 represents one third the error in Obs-Vs-MERRA. This difference reveals the efficiency of DSM in general. Moreover, the average RMSE in Obs-Vs-MERRA is about double that of DM8. Finally, the results of MBE in Obs-Vs-MERRA show high negative bias due to the vast difference between raw MERRA and observation data, where the raw MERRA data values that recorded were

higher than the observation data for the same weather station. This negative bias fluctuated from station to station.

Table 5-3. Reveals the validation results for 16 weather stations in different places in Iraq by calculating a number of error metrics: MAPE, RMSE, MBE and R2. The first group includes four proposals of Downscaling Model DM1, DM2, DM3and DM4 applied from Z_h= 10 m to Z_{hh}=10 m. The second group consists of four proposals of Downscaling Model DM5, DM6, DM7 and DM8 applied from Z_h= 50 m to Z_{hh}= 10 m. In addition, two values of reference height tested Z_{ref}=600m and 200m and also two values of $Z_{o\,ref}$ have tested 0.103 m and 0.05 m. The red colour represents the highest error has recorded, the green colour represent the lower error has recorded.

The first group	DM1: $Z_h = 10m$ *to* $Z_{hh} = 10m$ $Z_{ref} = 200m$, $Z_{oref} = 0.103m$				DM2: $Z_h = 10m$ *to* $Z_{hh} = 10m$ $Z_{ref} = 200m$, $Z_{oref} = 0.05m$				DM3: $Z_h = 10m$ *to* $Z_{hh} = 10m$ $Z_{ref} = 600m$, $Z_{oref} = 0.103m$				DM4: $Z_h = 10m$ *to* $Z_{hh} = 10m$ $Z_{ref} = 600m$, $Z_{oref} = 0.05m$				Obs-Vs-MERRA At 10m			
Weather Station	MAPE	RMSE m/s	MBE	R^2	MAPE	RMSE m/s	MBE	R2	MAPE	RMSE m/s	MBE	R^2	MAPE	RMSE m/s	MBE	R^2	MAPE	RMSE	MBE	R^2
1. Diwaniya 2015	45.13%	0.966	-52.98%	0.468	40.31%	0.872	-37.23%	0.468	42.46%	0.918	-44.49%	0.4659	37.50%	0.825	-26.26%	0.4659	85.75%	1.836	-154.18%	0.4067
2. Basrah Hussen 2015	38.51%	1.21	-37.61%	0.528	34.99%	1.146	-18.13%	0.528	35.54%	1.157	-21.78%	0.528	32.55%	1.121	0.46%	0.528	66.18%	1.874	-115.62%	0.406
3. Karbala 2014	34.19%	1.101	-21.78%	0.52	31.35%	1.071	-2.23%	0.52	32.33%	1.08	-9.01%	0.517	29.91%	1.079	13.50%	0.517	41.71%	1.246	-57.67%	0.52
4. Amarah 2014	28.00%	1.154	47.80%	0.512	34.61%	1.075	-29.31%	0.512	35.62%	1.094	-34.16%	0.511	31.65%	1.033	-12.97%	0.513	58.33%	1.653	-118.28%	0.51
5. Hadithah 2014	43.74%	1.447	63.95%	0.257	43.80%	1.494	73.23%	0.259	43.59%	1.448	64.62%	0.269	43.76%	1.504	75.65%	0.262	130.26%	2.292	-173.77%	0.261
6. Kut-Al-Hai 2014	40.64%	1.095	-36.43%	0.458	37.26%	1.025	-18.67%	0.458	38.56%	1.048	-23.92%	0.448	35.35%	0.997	-3.52%	0.448	73.13%	1.962	-149.77%	0.456
7. Nasiriya 2014	25.99%	1.029	-9.85%	0.468	24.36%	1.006	8.09%	0.468	24.73%	1.004	2.77%	0.471	23.77%	1.001	23.37%	0.471	50.71%	1.791	-86.98%	0.157
8. Semawa 2014	39.34%	1.391	23.02%	0.228	38.26%	1.411	40.07%	0.228	38.45%	1.401	35.10%	0.229	38.26%	1.445	54.67%	0.229	57.72%	1.769	-86.25%	0.229
9. Sulaimaniya 2014	69.13%	1.214	-9.63%	0.255	64.47%	1.213	1.48%	0.255	64.84%	1.208	0.57%	0.261	60.34%	1.22	13.17%	0.261	108.10%	1.449	-79.59%	0.256
10. Kirkuk 2013	47.71%	0.895	38.16%	0.084	47.27%	0.919	44.03%	0.084	47.34%	0.913	43.01%	0.088	47.10%	0.945	49.70%	0.088	217.32%	2.331	-201.20%	0.085
11. Mosul 2013	74.79%	0.815	21.73%	0.129	70.88%	0.83	26.90%	0.129	73.77%	0.821	23.46%	0.126	69.40%	0.839	29.52%	0.126	383.12%	2.526	-223.19%	0.127
12. Anah 2012	71.13%	1.638	52.08%	0.278	67.81%	1.675	61.04%	0.278	70.59%	1.632	52.08%	0.285	66.80%	1.677	62.64%	0.285	92.19%	2.378	-110.73%	0.046
13. Najaf 2012	55.89%	1.16	45.69%	0.252	53.94%	1.194	53.00%	0.252	54.19%	1.187	51.78%	0.254	52.77%	1.23	60.11%	0.254	253.59%	2.81	-244.93%	0.252
14. Baghdad Int 2012	52.23%	1.118	-40.22%	0.4014	48.11%	1.054	-23.57%	0.4014	51.24%	1.101	-36.29%	0.4	46.54%	1.035	-16.67%	0.4	84.59%	1.804	-134.93%	0.4003
15. Khanaqin 2014	80.38%	0.574	-12.73%	0.1447	75.26%	0.561	-7.32%	0.1447	76.25%	0.563	-8.49%	0.1461	70.80%	0.554	-2.30%	0.1461	475.58%	2.91	-268.38%	0.1452
16. Singar 2012	99.05%	1.602	-57.56%	0.2516	92.25%	1.54	-40.07%	0.2516	97.41%	1.579	-54.94%	0.2626	89.94%	1.511	-34.23%	0.2626	138.61%	2.11	-72.83%	0.1322
Average	52.87%	1.15056		0.32716	50.31%	1.130375		0.3272	51.68%	1.134625		0.3288	48.53%	1.126		0.3285	144.80%	2.0463		0.2743
The second group	DM5: $Z_h = 50m$ *to* $Z_{hh} = 10m$ $Z_{ref} = 200m$, $Z_{oref} = 0.103m$				DM6: $Z_h = 50m$ *to* $Z_{hh} = 10m$ $Z_{ref} = 200m$, $Z_{oref} = 0.05m$				DM7: $Z_h = 50m$ *to* $Z_{hh} = 10m$ $Z_{ref} = 600m$, $Z_{oref} = 0.103m$				DM8: $Z_h = 50m$ *to* $Z_{hh} = 10m$ $Z_{ref} = 600m$, $Z_{oref} = 0.103m$				Obs-Vs-MERRA At 10m			
Weather Station	MAPE	RMSE m/s	MBE	R^2	MAPE	RMSE m/s	MBE	R^2	MAPE	RMSE m/s	MBE	R^2	MAPE	RMSE m/s	MBE	R^2	MAPE	RMSE	MBE	R^2
1. Diwaniya 2015	42.45%	0.913	-44.62%	0.468	40.85%	0.882	-39.20%	0.468	40.07%	0.872	-36.38%	0.466	36.69%	0.806	-27.58%	0.487	85.75%	1.836	-154.18%	0.4067
2. Basrah Hussen 2015	35.07%	1.149	-20.09%	0.53	34.10%	1.134	-13.52%	0.53	32.96%	1.123	-5.03%	0.53	31.93%	1.117	4.81%	0.53	66.18%	1.874	-115.62%	0.406
3. Karbala 2014	31.75%	1.075	-5.08%	0.519	30.98%	1.0719	1.54%	0.519	30.52%	1.076	7.10%	0.516	29.65%	1.0716	16.27%	0.527	41.71%	1.246	-57.67%	0.52
4. Amarah 2014	36.48%	1.111	-38.41%	0.514	35.13%	1.085	-32.03%	0.513	33.80%	1.063	-25.13%	0.513	32.05%	1.038	-15.54%	0.513	58.33%	1.653	-118.28%	0.51
5. Hadithah 2014	43.79%	1.497	73.75%	0.259	43.90%	1.513	76.86%	0.259	43.79%	1.497	73.75%	0.259	43.92%	1.524	79.22%	0.262	130.26%	2.292	-173.77%	0.261
6. Kut-Al-Hai 2014	38.92%	1.041	-25.36%	0.4596	37.85%	1.02	-19.26%	0.4596	37.29%	1.029	-13.82%	0.4484	35.99%	0.995	-4.63%	0.4484	73.13%	1.962	-149.77%	0.456
7. Nasiriya 2014	24.51%	1.005	5.56%	0.47	24.15%	1.003	11.63%	0.47	23.89%	1.001	17.60%	0.474	23.69%	1.013	26.74%	0.474	50.71%	1.791	-86.98%	0.157
8. Semawa 2014	38.32%	1.404	37.28%	0.228	38.07%	1.415	43.06%	0.229	37.85%	1.427	48.80%	0.23	37.74%	1.452	57.50%	0.23	57.72%	1.769	-86.25%	0.229
9. Sulaimaniya 2014	79.30%	1.255	-31.18%	0.242	77.01%	1.245	-26.82%	0.242	73.45%	1.228	-19.89%	0.249	70.30%	1.22	-13.42%	0.249	108.10%	1.449	-79.59%	0.256
10. Kirkuk 2013	46.95%	0.905	41.59%	0.091	46.84%	0.914	43.61%	0.091	46.74%	0.925	46.30%	0.094	46.71%	0.94	49.31%	0.094	217.32%	2.331	-201.20%	0.085
11. Mosul 2013	72.00%	0.818	24.54%	0.135	70.70%	0.824	26.32%	0.135	71.10%	0.825	26.23%	0.138	69.16%	0.834	28.96%	0.138	383.12%	2.526	-223.19%	0.127
12. Anah 2012	67.01%	1.685	63.43%	0.278	66.14%	1.698	66.35%	0.278	66.56%	1.679	63.32%	0.286	65.27%	1.701	67.90%	0.285	92.19%	2.378	-110.73%	0.046
13. Najaf 2012	54.77%	1.178	49.54%	0.252	54.11%	1.19	52.06%	0.252	53.39%	1.206	55.46%	0.254	52.73%	1.225	58.85%	0.254	253.59%	2.81	-244.93%	0.252
14. Baghdad Int 2012	49.62%	1.078	-30.47%	0.4014	48.25%	1.058	-24.75%	0.4014	48.74%	1.065	-26.67%	0.3999	46.29%	1.025	-17.83%	0.4102	84.59%	1.804	-134.93%	0.4003
15. Khanaqin 2014	77.27%	0.564	-9.43%	0.1481	75.53%	0.56	-7.57%	0.1481	73.43%	0.556	-5.33%	0.1495	69.99%	0.546	-2.08%	0.1715	475.58%	2.91	-268.38%	0.1452
16. Singar 2012	94.81%	1.557	-48.54%	0.2624	92.71%	1.536	-42.50%	0.2624	93.54%	1.539	-46.03%	0.273	90.39%	1.507	-36.66%	0.273	138.61%	2.11	-72.83%	0.1322
Average	52.06%	1.1396		0.32878	51.02%	1.1343062		0.3287	50.44%	1.1319		0.3298	48.91%	1.1258		0.332	144.80%	2.0463		0.2743

5.5.7 Validation Between The Full Sector And Stripe Pattern For Upwind Fetch

In order to examine the improvement in resolution of effective local roughness for the full sector design and the effect of this development on wind speed accuracy using the DSM, validation has been suggested to calculate the error between estimated wind speed based on 32 roughness patches and observation data. The previous error will be compared with the error between estimated wind speed based on 9 roughness patches and observation data. In this validation, several error metrics have been applied to determine the difference between estimated wind speed and observation data such as MAPE, MBE, RMSE, and MAE. The calculated error metrics are shown in Table 5-4. The estimated wind speed in DM9 in Table 5-4 has been modeled based on the same factors in DM8 in Table 5-3 such as reference height Z_{ref} = 600 m in the reference site and roughness length Z_{oref}= 0.05 m. In addition, the DSM has been applied based on MERRA data from reference site at Z_h = 50 m to hub height at a target site Z_{hh} = 10 m. Moreover, the downscaling model in DM9 has been applied based on 9 roughness patches for each upwind fetch. Furthermore, the validation has been applied for the same 16 weather stations in Table 5-3 as shown in Figure 5-31.

At first glance in Table 5-4, the average of MAE in DM8 has shown lower error (difference) between estimated and measured wind speed 0.808 m/s while the average error between estimated and observed wind speed for MAE in DM9 has been 0.812 m/s. In addition, the average MAPE in DM8 has been 48.91% slightly lower than the average MAPE in DM9 49.090%. Furthermore, the average RMSE in DM8 was recorded 1.1258 m/s which represents significant weight for errors that have large absolute amount more than errors with small absolute amount [268]. While the average RMSE in DM9 was recorded 1.130 m/s which is slightly higher than the value of RMSE in DM8.

The approach of applying the DSM based on full sector design, which including 32 roughness patches shows better performance basd on four metrics in comparison with the stripe pattern for 9 roughness patches. It is very important to put in our consideration that the error metrics results represent the average error for 16 weather stations and also the average error for one year for each weather station.

In the case that weather station is located within a symmetrical surface roughness area such as large urban area or in the desert, small differences are seen between applying the full sector proposal for 32 patches and the stripe pattern proposal for 9 patches. However, in case of using 32 patches with various surface roughness area types around the target site, will improve the wind speed estimation. 13 out of 16 weather stations have shown low error for various metrics error in DM8 against the same metrics error in DM9 as revealed in Table 5-4.

The Kut-Al-Hai weather station in 2014 shows the same result for MAE in DM9 and DM8. This similarity in error values returns to the similarity of surface roughness areas in the direction sector of prevailing winds from the NW of Kut-Al-Hai weather station as shown in Figure 5-32. It is possible to note that the prevailing wind direction located at the NW within the urban area has played significant role to reduce the difference in MAE, but the effect of some different patches has appeared in RMSE between DM9 and DM8.

While in the case of Khanaqin weather station, the error metrics show different trends from others. The error values for MAE, MAPE, and RMSE in DM8 were higher than in DM9. In fact, this strange trend returns to the big difference in wind speed direction distribution between wind rose of observed data and wind rose of estimated data within various roughness areas as shown in Figure 5-33. It possible to note that the prevailing wind speed in Figure 5-33C is for the west of weather station and most observed data is concentrated in this wind direction sector. While the prevailing wind speed in Figure 5-33A concentrated between E to SE and between NW to W. That means the estimated wind speed will be concentrated in these directions, the various of roughness surface within these wind direction sectors will affect the error value when compared between observation and estimated wind speed.

Table 5-4. Reveals the comparison between the stripe pattern proposal in DM9 and the full sector pattern proposal in DM8. Validation has been applied for 16 weather station in different places in Iraq by calculating a number of error metrics: MAPE, RMSE, MBE and R2. The error metrics represent the difference between observation from and estimation data by DSM. Obs-Vs-MERRA represents the difference between raw MERRA data and observation data.

	DM9: $Z_h = 50m$ *to* $Z_{hh} = 10m$ $Z_{ref} = 600m$, $Z_{oref} = 0.05m$					DM8: $Z_h = 50m$ *to* $Z_{hh} = 10m$ $Z_{ref} = 600m$, $Z_{oref} = 0.05m$					Obs-Vs-MERRA At 10m				
	the stripe pattern for 9 roughness patches					the full sector pattern for 32 roughness patches									
Weather Station	MAE m/s	MAPE	RMSE m/s	MBE	R^2	MAE m/s	MAPE	RMSE m/s	MBE	R^2	MAE m/s	MAPE	RMSE	MBE	R^2
1. Diwaniya 2015	0.657	37.15%	0.818	-29.46%	0.485	0.648	36.69%	0.806	-27.58%	0.487	1.583	85.75%	1.836	-154.18%	0.4067
2. Basrah Hussen 2015	0.795	33.23%	1.135	-7.095	0.528	0.772	31.93%	1.117	4.81%	0.53	1.503	66.18%	1.874	-115.62%	0.406
3. Karbala 2014	0.732	29.90%	1.071	15.00%	0.524	0.73	29.65%	1.071	16.27%	0.527	0.942	41.71%	1.246	-57.67%	0.52
4. Amarah 2014	0.809	32.10%	1.038	-15.87%	0.513	0.801	32.05%	1.038	-15.54%	0.513	1.372	58.33%	1.653	-118.28%	0.51
5. Hadithah 2014	1.019	44.16%	1.53	79.86%	0.259	1.013	43.92%	1.524	79.22%	0.262	1.916	130.26%	2.292	-173.77%	0.261
6. Kut-Al-Hai 2014	0.791	35.97%	0.994	-4.43%	0.448	0.791	35.99%	0.995	-4.63%	0.448	1.635	73.13%	1.962	-149.77%	0.456
7. Nasiriya 2014	0.715	23.76%	1.012	25.464	0.473	0.716	23.69%	1.013	26.74%	0.474	1.397	50.71%	1.791	-86.98%	0.157
8. Semawa 2014	1.126	37.77%	1.455	58.106	0.229	1.124	37.74%	1.452	57.50%	0.23	1.391	57.72%	1.769	-86.25%	0.229
9. Sulaimaniya 2014	0.829	70.52%	1.219	-13.96	0.25	0.828	70.30%	1.22	-13.42%	0.249	1.147	108.10%	1.449	-79.59%	0.256
10. Kirkuk 2013	0.658	46.73%	0.944	49.66%	0.0957	0.655	46.71%	0.94	49.31%	0.094	2.076	217.32%	2.331	-201.20%	0.085
11. Mosul 2013	0.582	69.29%	0.835	29.237	0.135	0.58	69.16%	0.834	28.96%	0.135	2.243	383.12%	2.526	-223.19%	0.127
12. Anah 2012	1.1006	65.04%	1.715	69.95%	0.28	1.087	65.27%	1.701	67.90%	0.285	1.889	92.19%	2.378	-110.73%	0.046
13. Najaf 2012	0.855	52.83%	1.227	59.08%	0.255	0.852	52.73%	1.225	58.85%	0.254	2.52	253.59%	2.81	-244.93%	0.252
14. Baghdad Int 2012	0.838	46.33%	1.029	-17.73%	0.4062	0.836	46.29%	1.025	-17.83%	0.4102	1.513	84.59%	1.804	-134.93%	0.4003
15. Khanaqin 2014	0.405	69.69%	0.545	-1.87%	0.1715	0.406	69.99%	0.546	-2.08%	0.1715	2.684	475.58%	2.91	-268.38%	0.1452
16. Singar 2012	1.094	90.98%	1.514	-38.11%	0.27	1.09	90.39%	1.507	-36.66%	0.273	1.667	138.61%	2.11	-72.83%	0.1322
Average	0.812	49.09%	1.13		0.3326	0.808	48.91%	1.1258		0.3339	1.717	144.80%	2.0463		0.2743

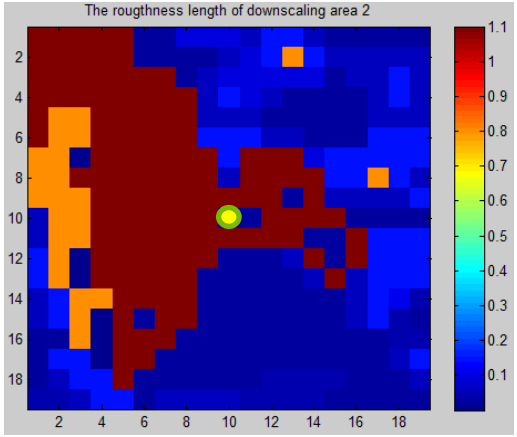

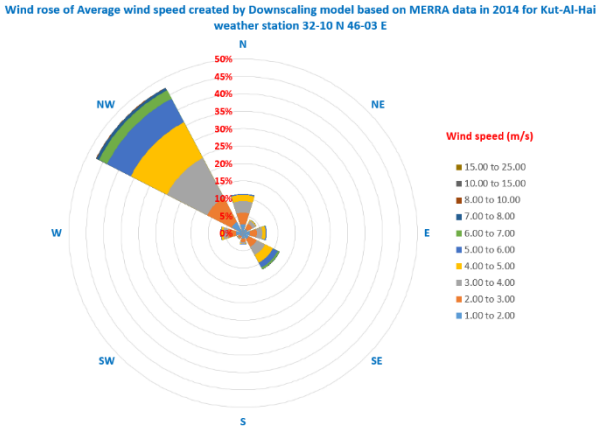

Figure 5-32. The location of Kut-Al-Hai weather station in z_o area which determined by yellow circle in the left side and the direction of prevailing wind speed in the NW of weather station location.

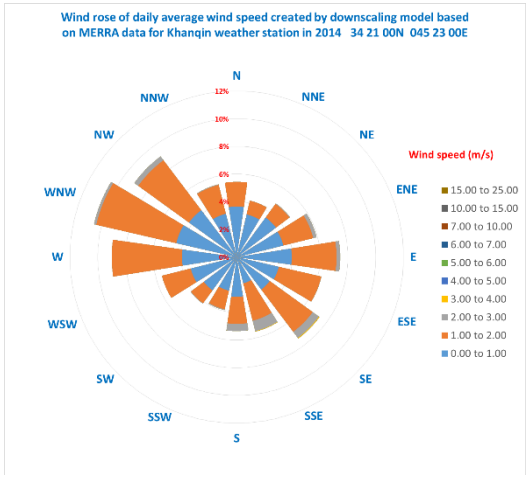

A-Wind rose created based on estimation data

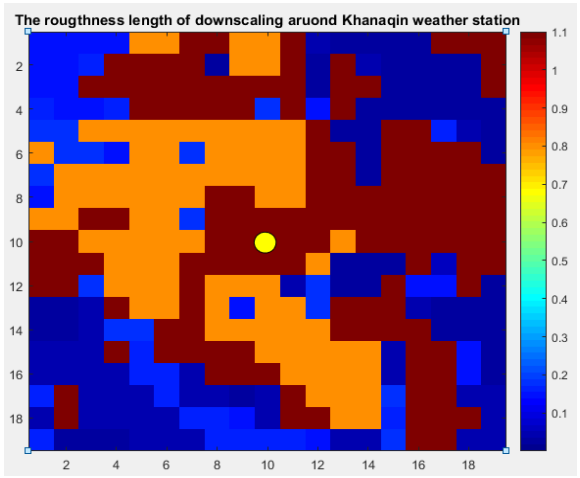

B- The yellow circle represents the location of the weather station

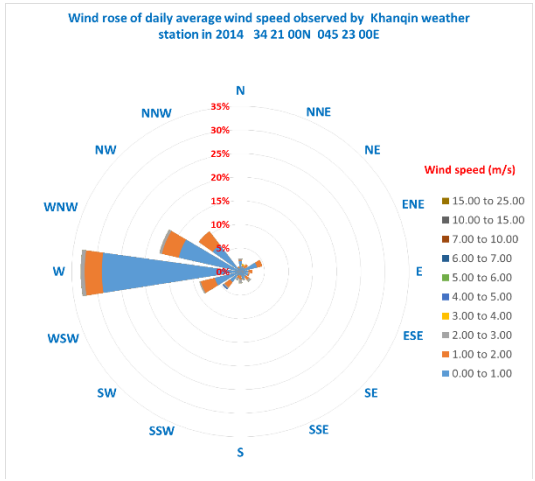

C- Wind rose created based on observation data

Figure 5-33. The location of Khanaqin weather station within various roughness area around the site in section B, while Figure A represents wind rose which created based on estimation data by DSM, whereas Figure C represent wind rose which created based on observation data from Khanaqin weather.

5.6 **Conclusions**

The main objective of this research is to evaluate wind resources in Iraq with high resolution using the DSM based on MERRA data as a reference wind climatology and LCM of Iraq to provide a roughness map. The DSM in this project has been developed to estimate accurately the annual average wind speed map for the whole of Iraq and to estimate the hourly wind speed at a hub height of wind turbines to feed the potential hybrid system calculation. The DSM in this work has been developed by creating the surface roughness values for each land cover category based on literature sources. In addition, the technique of evaluating the regionally averaged surface roughness has been developed according to the full sector design rather than the stripe pattern. Moreover, the performance of the DSM has been improved based on sensitivity analysis for a range of parameters that describe the boundary layer conditions in Iraq.

Sensitivity analysis, validations, and comparisons have been made to evaluate the difference between the DSM that has been applied using Z_{ref} = 200 m and Z_{ref} = 600 m. The results have shown a notable difference between them, where the Z_{ref} = 600 m have reduced the error between observed and estimated wind speed and confirmed that this reference height is less affected by surface roughness. In fact, Z_{ref} = 200 m represents the height when the wind speed does not change with height based on the neutral condition in the boundary layer in the UK. While the Z_{ref} = 600 m reflect the feature of vertical wind profile in Iraq where the laminar flow of wind speed is higher than the UK due to the convection of high heat transfer within the planetary boundary layer. In addition, sensitivity analysis and validation have been made between $Z_{o\,ref}$ = 0.103 m (the average of Z_o above BIA) and $Z_{o\,ref}$ = 0.05 m (selective average monthly value of Z_o above BIA) as surface roughness at a reference site. The results have shown the $Z_{o\,ref}$ = 0.05 m has reduced the error between observed and estimated wind speed. This value describes clearly the nature of the surface roughness at an open area in Iraq due to lack of grass and small shrubs. Both of reference height 600m and surface roughness 0.05 m at the reference site have contributed effectively in increasing the accuracy of wind speed assessment using the DSM. The results of this investigation show that the local boundary layer variables play a crucial role to reduce the error when applying the DSM.

Furthermore, another sensitivity analysis has been made between wind speed maps that are estimated by the DSM based on MERRA data at hub height Z_h = 10 m and Z_h = 50 m at a reference site. The results have shown good similarity based on the lowest difference of wind speed in many locations that distributed in the middle, north, and southeast of Iraq.

While the most significant variations are located above Tharthar Lake in the middle of Iraq and Soran in the north of Iraq. The reason behind increasing the difference above these regions returns mainly to the methodology of IAU in GEOS-1 DAS that has created MERRA and the probability of getting errors during the reanalysis process as mentioned in section 2.6.6 and section 2.6.6.4. In general, using the wind speed data from MERRA at hub height Z_h = 50 m has shown a slight improvement in wind resources assessment using the DSM. In order to improve evaluation of the blending height, the local reference effective $Z_{o\ eff}$ and wind speed over upwind fetches around the target site; a sensitivity analysis has been made between applying stripe pattern (9 roughness patches) and full sector (32 roughness patches) in the DSM. The results have shown, that the full sector design for upwind fetch can describe the wind flow over any wind direction sector better than stripe patterns for any area around a target site that has various roughness surfaces. Also, this technique has increased the accuracy of wind speed assessment. The full sector design (32 roughness patches)is regarded as new contrebution to improve evaluation of the blending height, the local reference effective $Z_{o\ eff}$ and wind speed over upwind fetches around the target site in the DSM. It is worthy of mentioning, that reference height 600m, surface roughness 0.05 m, reference wind climatology from MERRA at 50 m and applying full sector design for upwind fetch have played a significant role in improving wind resources assessment using the DSM in Iraq as revealed in DM8 in Table 5-3 and Table 5-4. This chapter tries to answer the main research questions in this project as follows:

- To what extent is the wind speed prediction using the developed the DSM accurate for Iraq?
- What are the advantages and disadvantages implementation of DSM using MERRA data?
- To what extent is the DSM useful in improving the wind resources assessment in Iraq using MERRA data?

According to the first question, the results of MAE that was calculated between estimated and observed data after applying the DSM, have shown that the DSM has succeeded in decreasing the MAE to 0.8 m/s which is around three times lower than the difference between MERRA data and observed data. In addition, the DSM has played a crucial role in terms of increasing the accuracy of estimated data when MERRA data has a low error with observed data. Also, the DSM has played a significant role in terms of reducing the error massively when the error between MERRA and observed data too high. In comparison with other researcher results that have used the same technique, [272] has reduced the MAE to 0.8 m/s using NOABL dataset and 0.49 m/s based on NCIC dataset in the UK.

According to the second question, on the other hand, the DSM has shown low performance within the mountain area, due to the DSM cannot deal with topographic diversity in the mountain area. In addition, MERRA data also has shown weakness in some areas due to the IAU system in GEOS-1 DAS method, in case of shortage in observation data and side by side with weakness in data distribution within the horizontal resolution that will increase the possibility of generating small errors and some deviations.

According to the third question, the difference in resolution between the two maps in Figure 5-34 shows how effective and useful using the DSM and MERRA data to assess the wind speed in Iraq. Firstly, MERRA has the highest spatial resolution as a source of a global dataset. Where the DSM has increased the resolution of MERRA data from 55.461 km × 61.589 km to 231.6 m × 231.6 m for the whole of Iraq. That means the resolution has increased by 64448 times. In fact, this is the highest resolution has been ever made to evaluate the wind speed in Iraq. Finally, according to DSM, it is become possible to evaluate the wind speed at any country or region in this world if we have the LCM for this area using DSM and MERRA data due to MERRA data cover all the world.

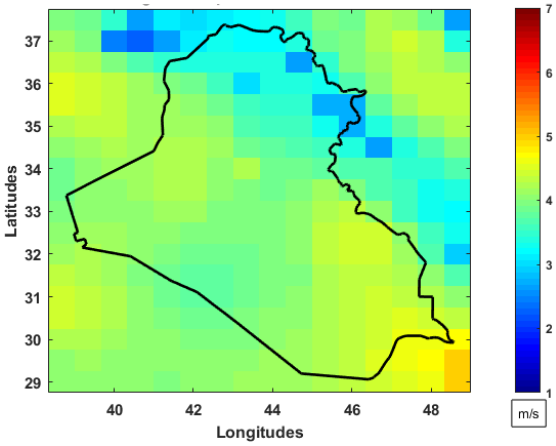

Figure A The annual average wind speed map from MERRA data at 10m

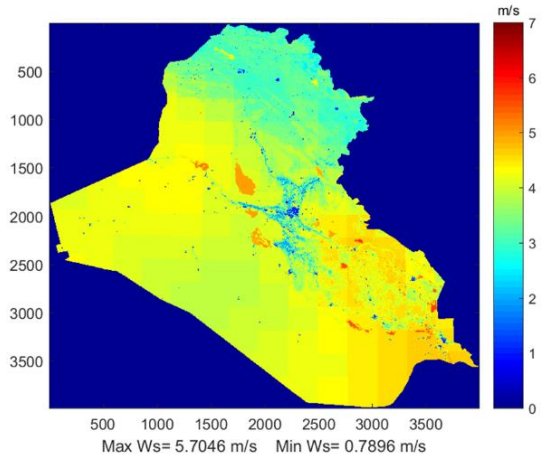

Figure B Wind speed map at Z_{hh}=10 m based on Z_h=50 m, Z_{ref} = 600 m and $Z_{o\,ref}$ = 0.05 m at a reference site

Figure 5-34. The difference in spatial resolution between MERRA data in Figure A and wind resources assessment map in Figure B that has been modeled by the DSM based on MERRA data in Figure A in 2014.

Chapter 6 **WIND TURBINE POWER PRODUCTION IN IRAQ**

6.1 Introduction

This chapter aims to evaluate the Annual Energy Production (AEP) for different sizes of a small wind turbine, to determine the location distribution of the highest and lowest AEP over the whole of Iraq, using a wind speed map that has been estimated by the downscaling model (DSM). The Weibull distribution is considered a key to carrying out the AEP calculation with reasonable accuracy and fast performance, which in turn depends on the shape and scale of the factors. This technique has been suggested to avoid the low capacity of PC to process a massive amount of data for long term: 8760 hours of wind speed across 8 millions pixels of the Iraq map. The K- profile has been proposed for use in this project to estimate correctly a shape factor with height. Besides that, the capacity factor (CF) and the percentage self-demand (PSD) has been suggested to present the ability of a specific wind turbine size to cover different levels of monthly electricity demand, based on monthly average energy production.

This chapter is organized as follows: several potential techniques to estimate the AEP for the whole of Iraq map have been discussed in section 6.2. How to determine the factors of Weibull distribution has been discussed in section 6.2.1. The analysis of the results and validation has been discussed in section 6.3. Finally, the most important finding has been summarized in section 6.4.

6.2 Potential techniques to calculate Annual Energy Production

Wind has kinetic energy, which is converted to electrical energy by rotating the blades of a wind turbine, which in turn produces electricity that comes from a rotating magnetic flux inside the wind turbine generator [28]. For the vast majority of researchers, there are two ways to calculate power production from a wind turbine. The first one was based on the blade sweep area of specific wind turbine and wind speed [103]. The second one was based on the power curve of wind turbine that described the relationship between power and wind speed [273].

In this project, power production from different wind turbine sizes is required to evaluate the potential AEP at different heights and for the whole of the Iraq map. In addition, the AEP calculation will be the substantial estimation for other requirements such as efficiency and economic calculation, which will be discussed in detail below in this chapter and in the

next chapter. There are three methods to calculate the annual energy of wind turbine, which will be described as follows:

6.2.1 Annual Energy Production based on hourly Energy Production

Hourly wind speeds that have been estimated by downscaling model (DSM) for each pixel in the Iraq map as shown in Figure 6-1A, it is useful to estimate power production from a wind turbine. MATLAB can be used to calculate hourly energy production using the power curve information from the specification of wind turbine as shown in Figure 6-1B. Finally, the sum of hourly energy production for one year represents the AEP by kWh that can be generated by potential wind turbine size. This procedure is regarded as an easy way to calculate the yearly energy of each size of the wind turbine. However, the disadvantage of this procedure is that it is not appropriate to apply it over 8 million pixels in the Iraq map, because a large memory is needed to achieve this technique. Otherwise this procedure is ideal for a small area.

6.2.2 Annual energy production based on wind speed distribution

There is another way to calculate AEP from different wind turbine size at various heights. First of all, in this procedure, the power curve information for each wind turbine size is required. Also, the hourly wind speed over one year that has been previously estimated by the downscaling model (DSM) is required for each pixel on the Iraq map, as shown in Figure 6-1A. On the other hand, wind speed distribution for one year should be estimated based on hourly wind data, by calculating the number of frequencies or percentage (fraction) of frequency for each wind speed bin, which ranged from 1 to 25 m/s as shown in Figure 6-2. Equation 6-1 has been expressed to estimate the AEP based on wind speed distribution for one year [274].

$$Annual\ Energy\ kWh = \frac{\sum_{v=1}^{n} p(v_i)\ .\ f(v_i).\ 8760}{\sum_{v=1}^{n} f(v_i)} \qquad \text{Equation 6-1}$$

- $p(v_i)$ represents the power production for each wind speed. This kind of estimation is processed based on information from the power curve information for the selected wind turbine.
- $f(v_i)$ refers to frequency for each wind speed that ranged from 1 to 25 m/s. The calculation of the AEP was based on wind speed distribution for one year, as expressed in Equation 6-1 [274].
- 8760 represents the number of hours per year.
- n represents the number of bins of wind speed.

The advantage in this process is that the wind speed distribution will show the weight of the highest frequency for potential wind speed in one year, and the result will be more accurate.

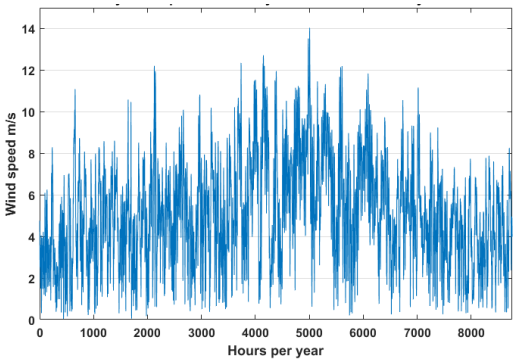

Figure A

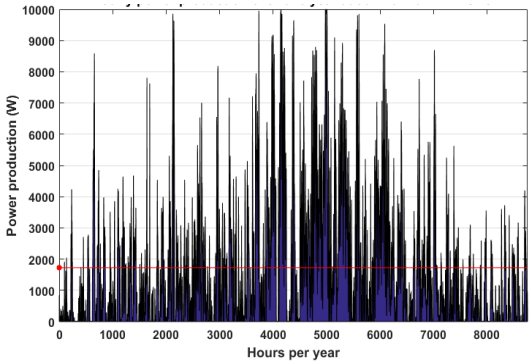

Figure B

Figure 6-1 The hourly wind speed which is estimated by the DSM for one year in the open area near Amarah city at 30m of hub height in 2014 in Figure A. Figure B shows the hourly energy production over one year for the same location and hourly wind speed in Figure A based on 10kW wind turbine size at 30m hub height; the red line represents the average power.

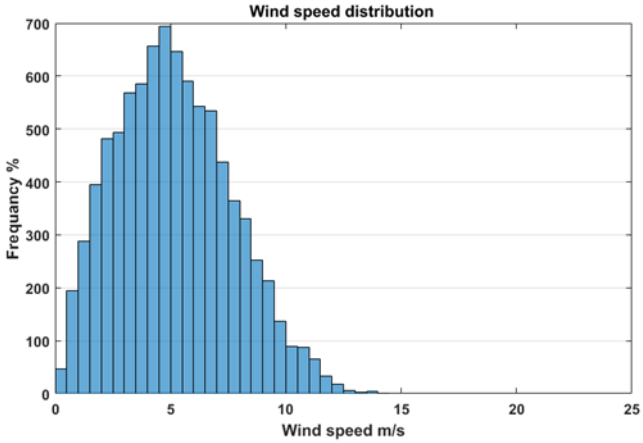

Figure 6-2 wind speed distribution for hourly wind speed that has been estimated by the DSM in Figure 6-1A.

6.2.3 Annual energy production based on Weibull Factors

It was challenging to apply the last two ways to calculate the annual energy production for 8 millions pixels for the whole of the Iraq map, due to the low capacity of a PC to process such a massive amount of data. However, to overcome this barrier, it is essential to find another method to provide enough accuracy and ability to achieve this calculation. The annual energy calculation based on Weibull distribution is considered as a key to carrying out these kinds of calculation process with reasonable accuracy and fast performance which in turn depends on the shape and scale of the factors [274].

Weibull distribution is considered to be the most common statistical distribution in wind energy analysis [28, 38, 48]. Weibull distribution is characterised by two factors: shape factor (k) and scale factor (c). The scale factor has a close relationship with the mean wind speed, while the shape factor measures the width of density distribution. In the case where

only annual and monthly average wind speeds are available, the factors of Weibull distribution are capable of presenting the hourly change of wind speed in any region [48]. The Weibull distribution function $f(v)$ is expressed in Equation 6-2 [39, 40, 42, 44-50, 52, 53, 55, 57].

$$f(v) = \left(\frac{k}{c}\right)\left(\frac{v}{c}\right)^{k-1} \exp^{-\left(\frac{v}{c}\right)^{k}} \qquad \text{Equation 6-2}$$

(v) is the particular wind speed. It is worth noting that the scale factor has units m/s, while the shape factor of Weibull distribution unitless factor .

Equation 6-2 gives the probability of wind distribution for each wind speed bin in the format of relative (fractional or percentage). Fractional probability for values of wind speed that exceed zero or present it as an absolute value (number of data points), such as the number of hours per year for wind speed that exceed zero ranging between 1 to 25 m/s [48]. Also, the zero value should be removed because the distribution will give a null probability for zero wind speeds [275]. In order to apply Weibull distribution, the values of shape and scale factors must be calculated. Several methods have been developed to estimate Weibull distribution factors using wind speed data [53, 57], which are described in section 2.3.

The Maximum Likelihood method has been considered to be one of the most significant ways to estimate the Weibull distribution factors [48]. This method requires several iterations and time-series of wind velocity data such as 8760 hours of data for one year, taking into consideration nonzero wind speeds. Where the wind speed is $(\boldsymbol{v_i})$ in time step (i) for several nonzero data (n), the two Weibull factors (k) and (c) can be estimated as follows in Figure 6-4 and Equation 6-4, respectively [48, 49, 59].

$$k = \left(\frac{\sum_{i=1}^{n} v_i^k \ln(v_i)}{\sum_{i=1}^{n} v_i^k} - \frac{\sum_{i=1}^{n} \ln(v_i)}{n}\right)^{-1} \qquad \text{Equation 6-3}$$

Figure 6-4 must be applied by utilizing an iterative procedure. Also, $k = 2$ will be the value of the shape factor for the first beginning [48]. The iterative process will stop when the difference between the last two k will equal ≥ 0.0001.

$$c = \left(\frac{\sum_{i=1}^{n} (v_i)^k}{n}\right)^{1/k} \qquad \text{Equation 6-4}$$

The value of the scale factor $(\boldsymbol{c})$ is usually influenced by the variance in wind velocity [23]. It is possible to represent the variance of wind speed using a standard deviation or mean wind speed [42, 48]. Finally, one of the common methods to estimate scale factors of Weibull

distribution involves using the mean wind speed as follows in Equation 6-5 [41, 42, 46, 49, 51, 52, 59]. $\bar{v}$ is the average of wind speed, Γ is a gamma function.

$$c = \frac{\bar{v}}{\Gamma\left(1+\frac{1}{k}\right)} \qquad \text{Equation 6-5}$$

In this project, Equation 6-3 was used to calculate the value of shape factor by using the hourly wind speed for one year from MERRA data for each MERRA grid point, rather than using hourly wind speeds for each pixel that has been estimated by the DSM. There are different reasons for this decision.

- Firstly, the comparison has been carried out between the values of shape factor which were calculated based on estimated wind speed by DSM for each pixel on the wind speed map and the values of shape factor that were calculated based on MERRA data for a specific grid point. The results have shown insignificant difference between them, as presented in Table 6-1. The reason behind the lack of change in the value of shape factor for MERRA data after applying the DSM is due to the absence of the stability correction factors in the DSM.
- Also, the technique of using MERRA data rather than estimated wind speed at each pixel will be useful, avoiding the need for a huge RAM to run the model long term.

Furthermore, there is another feature that attracts the attention in Table 6-1: the similarity between the values of shape factor at 10m and 50m for both MERRA data and modelled data. This issue will be discussed and resolved in the next section.

6.2.3.1 **Shape factor profile**

At initial inspection of Table 6-1 reveals that the value of shape factor (k) does not change significantly with height according to MERRA data. otherwise, the shape factor does not change at all with height after applying the DSM. Furthermore, the values of shape factor from MERRA at 10 m in Table 6-1 have shown high values in various sites in comparison with a normal range of shape factor values that expected to get it at this height as shown in Figure 6-4. In the same context, it is universally acknowledged that the value of shape factor at 10 m must be lower than the value of shape factor at 50 m, because the value of shape factor is increasing with height; it reaches the maximum value at a well-known height called the reversal height. It represents the average height of diurnal cycle for different sites. The value of shape factor changes from a minimum value near the surface at night time, to the maximum value at the reversal height at the next night in the boundary layer. Meanwhile the reversal height ranges between 50 m at coasts, to 90 m inland [272, 276].

Table 6-1. Comparison between the value of shape factor (k) of MERRA data for specific grid points at different height and the values of shape factor, after using the DSM, based on hourly wind speed for each pixel at different heights and for different land cover category.

MERRA grid point location	The height of MERRA	the shape factor of MERRA	Location in LCM	land cover category	The height of location	Shape factor after modeling
Lon:47.333 Lat: 32	10m	**2.1849**	m=2641	**Amarah**	10m	**2.1887**
	50m	**2.1693**	n=3400	**Desert**	50m	**2.1887**
			m=2646	**Amarah**	10m	**2.1596**
			n= 3400	**Urban**	50m	**2.1596**
			m=2642	**Amarah**	10m	**2.1688**
			n=3409	**Water**	50m	**2.1688**
lon:45.3333 Lat:35.5	10m	**2.2685**	m= 886	**Sulaimaniya**	10m	**2.2649**
	50m	**2.2290**	n= 2678	**Desert**	50m	**2.2649**
			m= 886	**Sulaimaniya**	10m	**2.2673**
			n= 2669	**Urban**	50m	**2.2673**
lon:44 Lat:32.5	10m	**2.3539**	m=2314	**Karbala**	10m	**2.35**
	50m	**2.3514**	n=2111	**Desert**	50m	**2.35**
			m=2310	**Karbala**	10m	**2.33**
			n=2100	**Urban**	50m	**2.33**
			m=2304	**Karbala**	10m	**2.34**
			n=2114	**Palms**	50m	**2.34**
lon: 45.3333 Lat: 34.5	10m	**2.1536**	m=1467	**Khanaqin**	10m	**2.12**
	50m	**2.1470**	n=2660	**Desert**	50m	**2.12**
			m=1465	**Khanaqin**	10m	**2.149**
			n =2647	**Urban**	50m	**2.149**
			m=1462	**Khanaqin**	10m	**2.148**
			n =2648	**Palms**	50m	**2.148**

Figure 6-4 shows how shape factor values change with altitude and the potential levels of reversal heights phenomena for two inland sites in the US [276]. In order to calculate AEP from different wind turbine size using Weibull distribution function, the shape factor value must be estimated correctly from MERRA to represent a realistic wind speed distribution at different heights. The K- profile in Equation 6-6 has been suggested for use in this project to estimate correctly a shape factor with height [272, 276].

$$k_z - k_s = \Delta k_z = c_k(z - z_s)exp^{\left[-\frac{z-z_s}{z_r-z_s}\right]} \quad \text{Equation 6-6}$$

k_s is the initial shape factor value at surface level z_s = 10m, while k_z refers to the shape factor at a target height that should be estimated. z_r represents the reversal height, which ranged between 60m and 80m. $c_k = 0.22$ is the experimental coefficient determined to represent the gradient of a linear regression of shape factors that was estimated based on observed data at different heights [272, 276]. K-profile is commonly applied to scale up shape factor from surface layer to reversal height. However, in this project, the K-profile equation has been suggested for use from 50m to 10m to downscale the value of shape factor from up to down. There are different reasons for this technique:

- Firstly, the annual average wind speed in this project has been estimated by downscaling a model that depended on hourly MERRA data at 50 m, rather than 10 m for each grid point.

- Secondly, the difference between the values of shape factor for MERRA data at 10 m and 50 m is too small and illogical; sometimes the value of shape factor at 10 m is higher than 50 m as can be seen in Table 6-1.
- Also, the value of shape factor at 50 m is consistent with the general context of shape factor value, as shown in Figure 6-4.
- Furthermore, if the K-profile equation is applied (based on shape factor values at 10 m as is shown in Figure 6-3), the result of shape factor at 20 m and 30 m will be very high and will not reflect realistic values of shape factor at those heights.

The formula of Equation 6-6 will be expressed as follows, applying the equation of K-profile from 50 m to 10 m:

$$k_z = k_{50} - c_k(z_s - z)\, exp^{\left[-\frac{(z_s - z)}{(z_r - z_s)}\right]} \qquad \text{Equation 6-7}$$

k_{50}: is the initial shape factor value which is calculated by using maximum likelihood method based on MERRA data at 50 m. $c_k = 0.022$ is the experimental coefficient. $z_{50} =$ 50 m. $z_r = 90\ m$ represents the reversal height above inland place. The results of Equation 6-7 need to be validated with the observed shape factor values for the same locations, heights and periods. The implementation this kind of verification needs a number of towers with different heights and in various places in Iraq. Unfortunately just one tower has been found in Iraq that provides such a type of data; this tower is called Shihabi.

Observed wind speed every 10 minutes has been recorded from Shihabi tower for one year in 2014 at different heights: 10 m, 30 m and 50 m. This tower is located in the south-east of Iraq, close to the Iraqi-Iranian border (46°42'0"E, 32°46'12"N). The observed data from the Shihabi tower will be beneficial for comparison and validation purposes, for shape factor values which are estimated from MERRA data for the same location and at the same heights. In addition, it is worth mentioning that the hourly wind speed for one year from 151 MERRA grid points and at the height of 50 m have been used to calculate the shape factor for each MERRA grid point on the Iraq map. Also, the annual average wind speed maps in 2014 at Z_{hh}=10 m, 15 m, 20 m, 25 m and 30 m were estimated by DSM based on MERRA data at hub height Z_h= 50 m, roughness length at the reference site Z_o=0.05 m and reference height Z_{ref} = 600m.

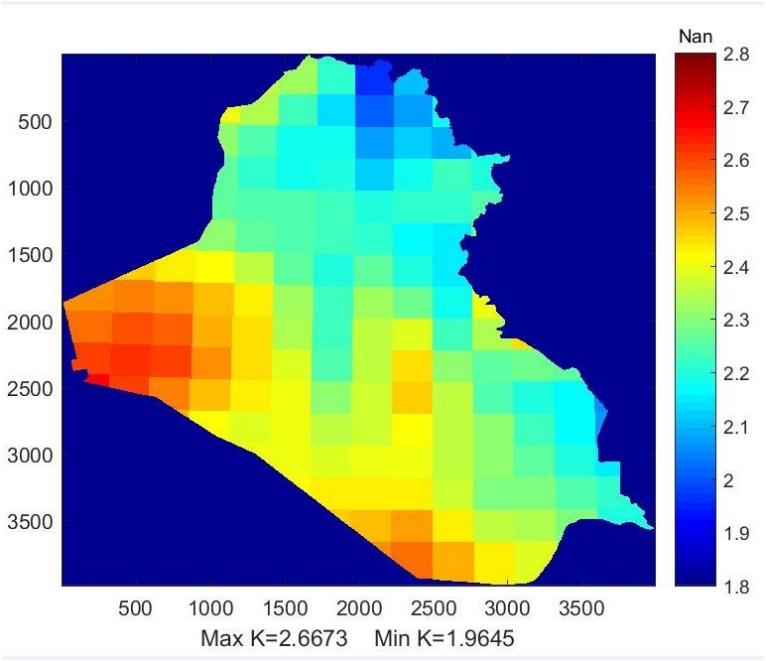

Figure 6-3. The values of shape factor, which were calculated based on hourly wind speed for 151 MERRA grid points at 10m in 2014 for whole of Iraq, using the maximum likelihood method.

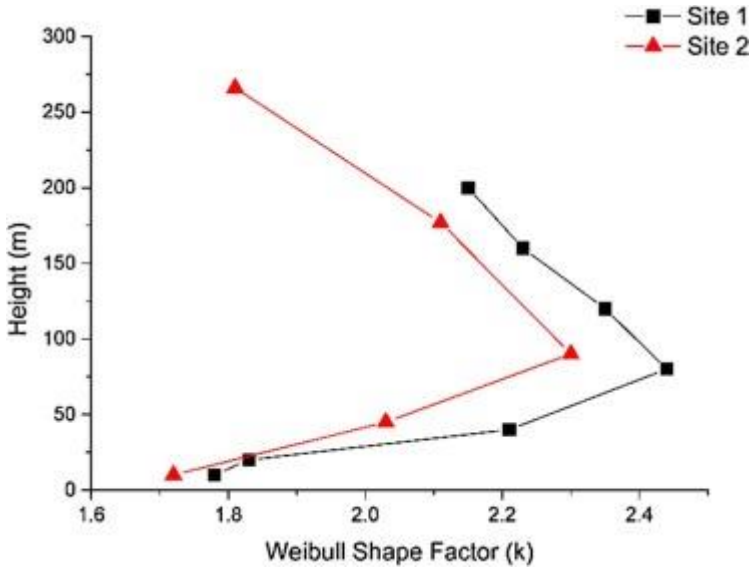

Figure 6-4. Natural changes in the Weibull shape factor (k) value with height for two sites in the U.S. [272].

In this study, the result of Equation 6-7 has been compared with the values of shape factor based on observed data from the Shihabi tower, which were calculated using the maximum likelihood method, based on hourly average wind speed at different heights and for the same location, as presented in Table 6-2. Unfortunately, it is easy to note that the values of shape factor after applying Equation 6-7 based on MERRA data did not match the values of shape factor based on observed data from the Shihabe tower at different heights. Nonetheless, the amount of shape factor from MERRA data has increased with height, but there is still a significant gap between the observed shape factor at 10 m and 30 m from the Shihabi tower and the estimated shape factor from MERRA data at the same heights.

Table 6-2. Comparison between the shape factor (k) values for both observed data from the Shihabi tower and MERRA data for the same location (based on the original K-profile)

location		shape factor Before using K-profile Function	shape factor After using K-profile Function
		Shape factor	Shape factor
Shihabi	10m	1.52	
	30m	1.83	
	50m	2	
MERRA	10m	2.36	2.13
	30m	2.36	2.14
	50m	2.36	2.36

$c_k = 0.22$ is the experimental coefficient that represents a linear regression of observed shape factors at different heights. In order to achieve an acceptable fit between the observed and the estimated shape factors at 10m and 30m, the coefficient regression c_k should be calculated again, based on the value of shape factor from MERRA at 50m and the values of shape factor from the Shihabi tower at 30m and 10m. In this case, the new calculation of c_k aims to reduce the error between the estimated shape factor and the observed shape factor from the Shihabi tower at 10 m and 30 m. The MATLAB curve fitting app has been used to calculate a new value of regression coefficient c_k based on Equation 6-7 and by regarding the reversal height $z_r = 120m$.

Figure 6-5 shows the new value of the regression coefficient c_k = 0.03705, which represents the gradient between the value of the shape factor from MERRA at 50m and the values of the shape factor from the Shihabi tower at 30m and 10m. The new value of c_k = 0.03705 and $z_r = 120m$ have been used in Equation 6-7 to estimate shape factor values at 10 m and 30 m. Table 6-3 reveals the comparison between the observed shape factor from Shihabi tower and the estimated shape factor from MERRA. The results of the shape factor from MERRA data after applying modified K-profile at 10 m and 30 m have shown a satisfactory agreement with values of the shape factor from the Shihabi tower.

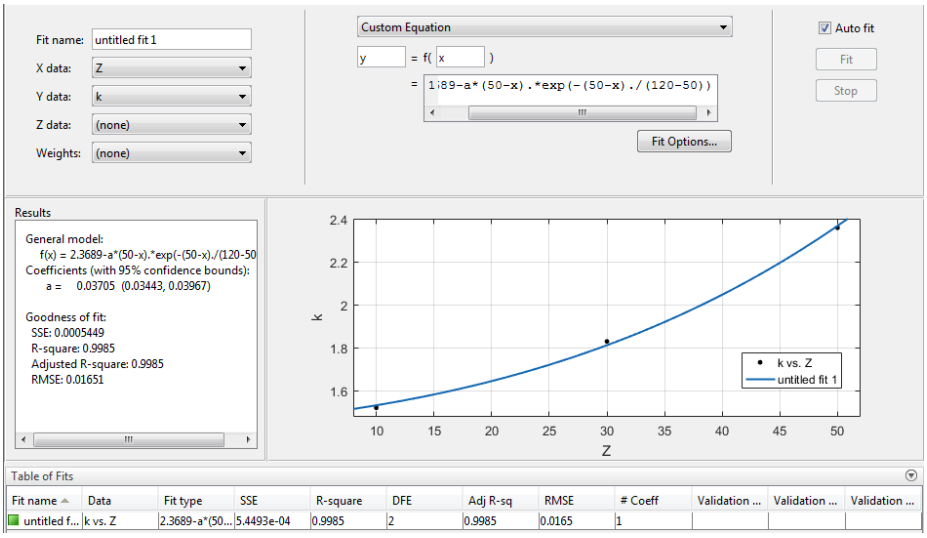

Figure 6-5.The fitting curve app in MATLAB has been used to calculate the new coefficient regression c_k, based on K-profile equation in Equation 6-7.

Table 6-3. Comparison between observed shape factor from the Shihabi location and the estimated shape factor from MERRA data using (modified K-profile) for the same location.

location		Shape factor Before using K-profile	Shape factor After using the modified K-profile function
		Shape factor	Shape factor
Shihabi	10m	1.52	
	30m	1.83	
	50m	2	
MERRA	10m	2.36	1.53
	30m	2.36	1.81
	50m	2.36	2.36

According to the last results of the shape factor after applying the modified K-profile function in Equation 6-7, this equation will be applied based on the new value of c_k = 0.03705 and $z_r = 120m$ to calculate the shape factor value for the 151 MERRA grid point for the whole of Iraq and at different heights (10m, 15m, 20m, 25m and 30m), as shown in Figure 6-6A.

According to Figure 6-6B, the values of the shape factor ranged from 1.12 (minimum) to the 1.83 (maximum) at 10m. Figure 6-6B show low values of shape factor in comparison with the shape factors in Figure 6-3 at 10 m. Furthermore, Figure 6-6B, C and D show that the high value of the shape factor was concentrated in the west and south-west of Iraq and the lower values were focused on the north of Iraq. The difference in the distribution of the shape factor values returns to the topography of these areas and wind speed distributions in these areas. The shape factor values have increased in the desert and plateau in the west of Iraq, while the values of shape factor have reduced in the mountainous area in the north of Iraq.

6.2.3.2 **Gamma function calculation**

With regard to the calculation of scale factor, Equation 6-4 is deemed suitable to calculate scale factor, based on time series for wind speed for the long term, such as hourly wind speed for one year for each pixel on the Iraq map. In fact, this method requires a vast memory, when it is resolved by MATLAB. This method is regarded as a hard procedure because Equation 6-4 will process 8760 hours of wind speed for more than 8 millions pixels on Iraq map. However, Equation 6-5 has been considered as a suitable alternative to calculating the scale factor for each pixel on the Iraq wind speed map. In this section of the project, Equation 6-5 is applied by using the annual average wind speed ($\bar{v}$) that has been estimated by DSM for each pixel as well as with the value of the shape factor that was been determined by using the modified K-profile function for each MERRA grid point.

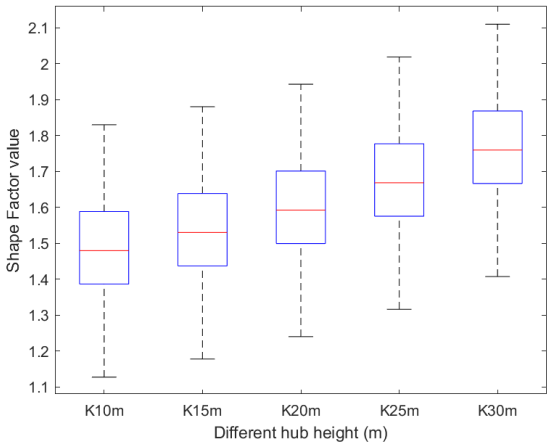

Figure A

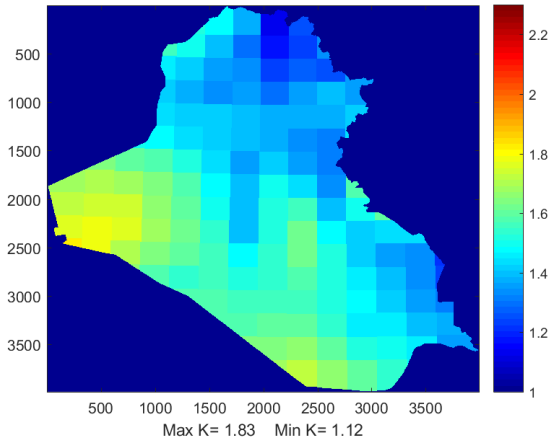

Figure B

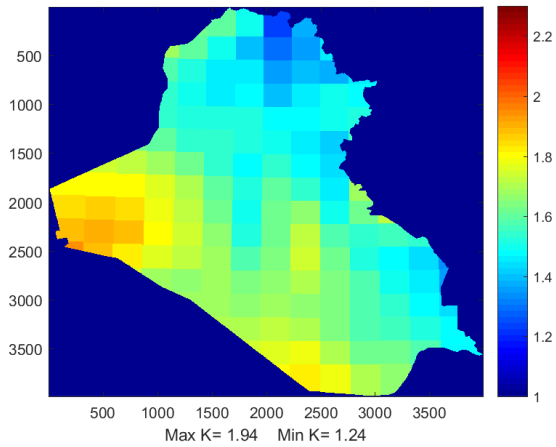

Figure C

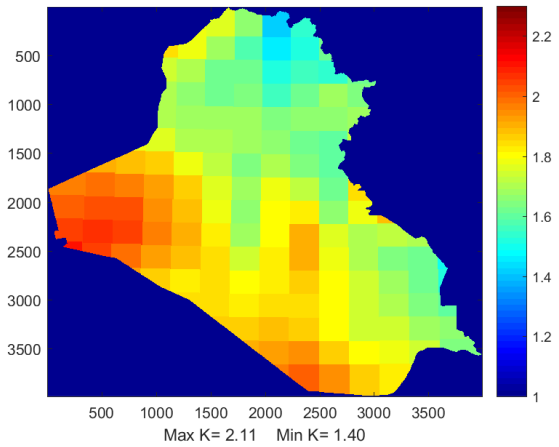

Figure D

Figure 6-6. The shape factor map for 151 MERRA grid point, which was estimated by using the modified k-profile function at 10 m in Figure B, 20 m in Figure C and 30 in Figure D. Figure A shows the boxplot of shape factor maps at different height 10m, 15m, 20m, 25m and 30m which was applied using the modified k-profile function.

Table 6-4. Evaluating the Gamma function based on the value of shape factor [277].

$$\Gamma\left(1+\frac{1}{k}\right)$$

	0.0	0.1	0.2	0.3	0.4	0.5	0.6	0.7	0.8	0.9
0	∞	362880.	120.000	9.26053	3.32335	2.00000	1.50458	1.26582	1.13300	1.05218
1	1.00000	0.96491	0.94066	0.92358	0.91142	0.90275	0.89657	0.89224	0.88929	0.88736
2	0.88623	0.88569	0.88562	0.88591	0.88648	0.88726	0.88821	0.88928	0.89045	0.89169
3	0.89298	0.89431	0.89565	0.89702	0.89838	0.89975	0.90111	0.90245	0.90379	0.90510
4	0.90640	0.90768	0.90894	0.91017	0.91138	0.91257	0.91374	0.91488	0.91600	0.91710
5	0.91817	0.91922	0.92025	0.92125	0.92224	0.92320	0.92414	0.92507	0.92597	0.92685
6	0.92772	0.92857	0.92940	0.93021	0.93100	0.93178	0.93254	0.93329	0.93402	0.93474
7	0.93544	0.93613	0.93680	0.93746	0.93811	0.93874	0.93937	0.93998	0.94058	0.94117
8	0.94174	0.94231	0.94286	0.94341	0.94395	0.94447	0.94499	0.94550	0.94599	0.94648
9	0.94697	0.94744	0.94790	0.94836	0.94881	0.94925	0.94968	0.95011	0.95053	0.95094

For example, when k=2.5, we can read (3rd row, 6th column),

$$\Gamma\left(1+\frac{1}{2.5}\right)=\Gamma(1.4)=0.88726 \;=\Gamma=0.63375$$

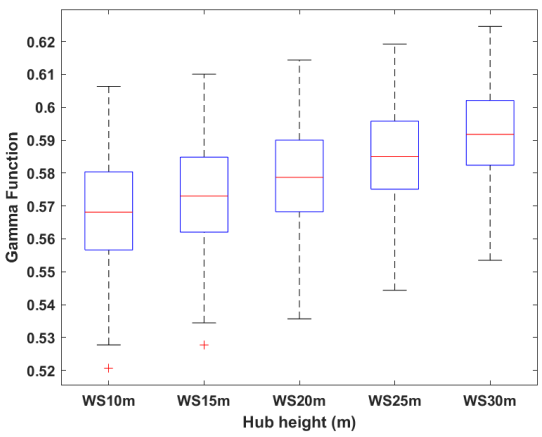

Figure A

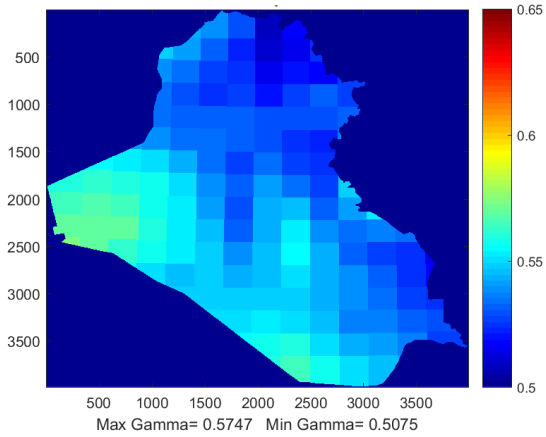

Figure B

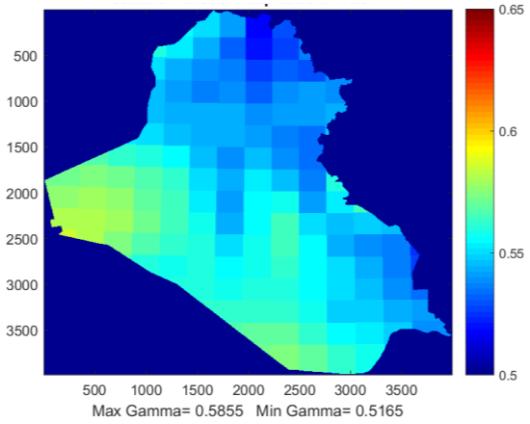

Figure C

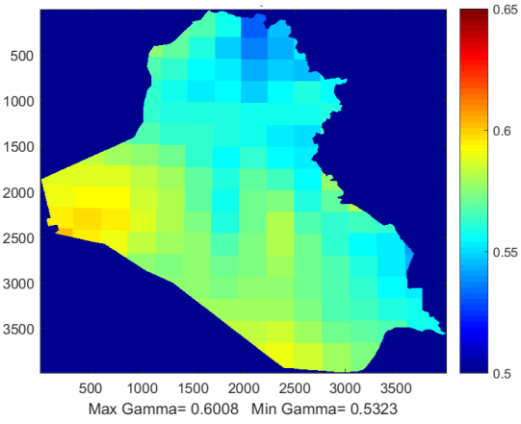

Figure D

Figure 6-7. Gamma function (Γ) maps in Figure B, C and D have been estimated based on the values of the shape factor maps at 10 m, 20 m and 30 m in Figure 6-6 respectively and based on Table 6-4 according to 151 grid points of MERRA data. Figure A shows a boxplot of Gamma function maps at different heights: 10m, 15m, 20m, 25m and 30m.

In addition, Equation 6-5 needs a value of gamma function that is related to the value of the shape factor at each height. Gamma function values in this project have been estimated, based on Table 6-4 [277]. Furthermore, the values of Gamma function in this table have been validated with the values of ($1/\Gamma\ (1+1/k)$) in the Met Office Technical Report [36].

Figure 6-7 show how values of gamma function change with height, similarly with shape factor values change.

6.2.3.3 Scale Factor Calculation

As mentioned in the last section, the scale factor is calculated by Equation 6-5 for each pixel on the Iraq map, at different heights (10 m, 15 m, 20 m, 25 m and 30 m) based on:

- Annual average wind speed which was estimated by the DSM for each pixel and at the specific height (10 m, 15 m, 20 m, 25 m and 30 m).
- Shape factor values which were estimated by modified K-profile function for each MERRA grid point that covers the local pixels of average wind speed at the same heights.
- Gamma function values, which were estimated for each MERRA grid point at different heights based on Table 6-4 and the value of the shape factor at the same MERRA grid point location and elevation.

Figure 6-8 shows scale factor maps at different heights and a boxplot that shows the scale factor distribution for each map at 10 m, 15m, 20 m, 25 m and 30 m.

6.2.3.4 Annual energy and Capacity factor Calculation based on Weibull distribution

According to the previous calculations for shape factor and scale factor for the whole of Iraq, it would be possible to perform Weibull distribution for each pixel on the Iraq wind speed map by applying Equation 6-2 to calculate the density distribution for each wind speed bin from 1 to 25 m/s. Nonetheless, the power production for each wind speed will be estimated using power curve information for each specific wind turbine size, based on a polynomial function based on a curve fitting tool in MATLAB.

According to the previous information and calculations (such as the Weibull distribution and power production based on power curve information for each wind turbine size), it becomes possible to estimate an AEP for any wind turbine size at different heights by using Equation 6-1. The $f(v_i)$ in Equation 6-1 is represented by the probability density of Weibull distribution for each wind speed v_i . While $p(v_i)$ represents the power production for each wind speed v_i . The summation is estimated for v_i from 1 to 25 m/s with intervals of 1 m/s [274].

Concerning the CF of the wind turbine, it is represented as a ratio of actual energy produced from the wind turbine during a period to maximum possible output power that the specific wind turbine can generate based on the rated power of this wind turbine during the same period [278]. The CF in this project has been estimated, based on average power production for specific wind turbine size, using $P\ mean$ in Equation 6-8 to the rated power for the wind

turbine. CF has been estimated for different wind turbine sizes, for different heights and each pixel on the Iraq wind speed map.

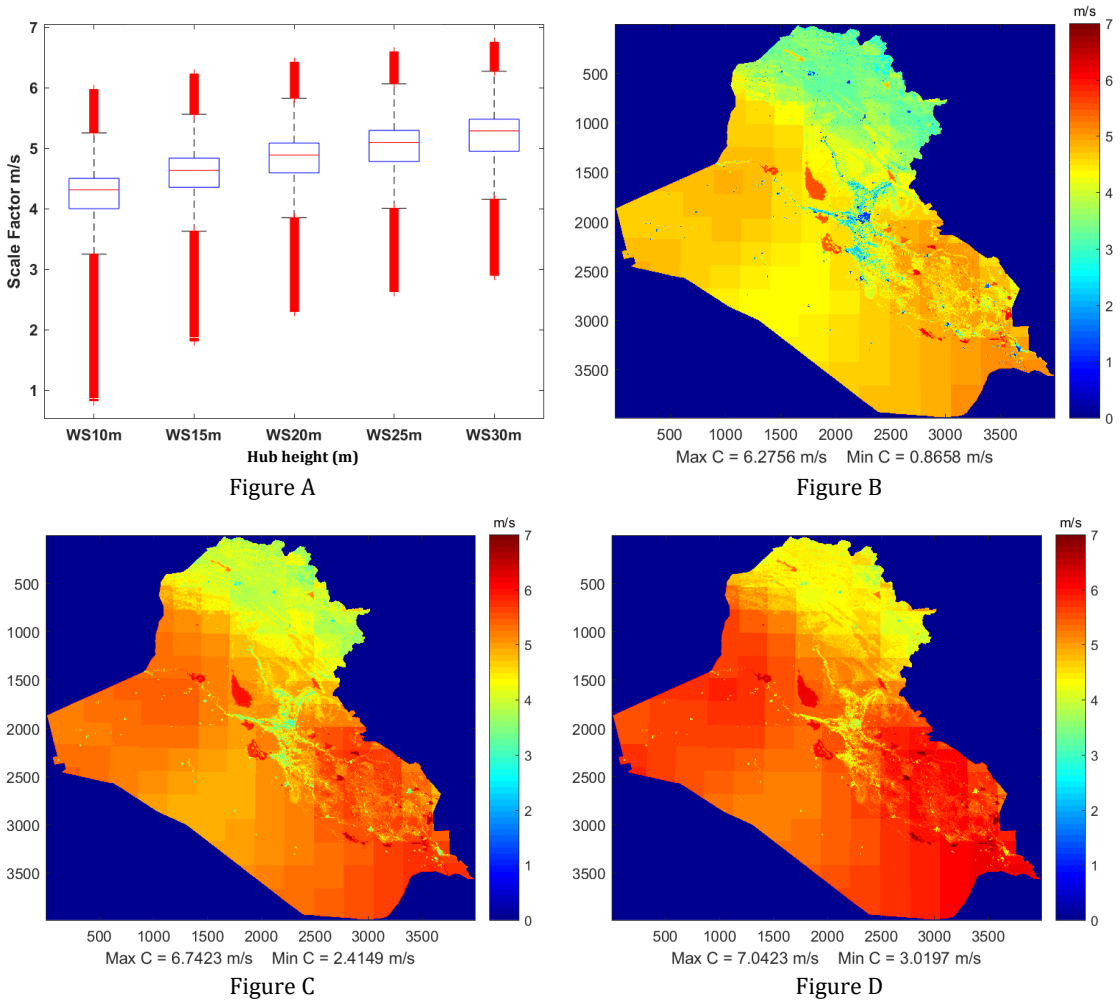

Figure 6-8. The scale factor maps calculated using Equation 6-5 were based on the mean wind speed, the shape factor and Gamma function at the same height Figure B represents the scale factor at 10 m, Figure C at 20 m and Figure D at 30m. Figure A shows a boxplot of scale factor maps at different heights: 10m, 15m, 20m, 25m and 30m.

In this project, different sizes of a small wind turbine have been suggested to supply energy for housing units with varying scenarios of electricity demand in order to check the wind turbine sizes that can meaningfully satisfy the various need of housing unites in Iraq. Senwei Energy Technology Inc has produced economic and reliable fixed pitch wind turbines at different sizes; a number of them have been selected to provide energy in this study, as presented in Table 6-5 [279]. Table 6-5 reveals four sizes of wind turbine alongside information about the price of each one and annual average energy production at specific average wind speed, based on experimental tests.

Different scenarios of electricity demand have been suggested: 1000, 2000, 3000, 4000, 5000 kWh/month. The different scenarios of electricity demand represent the change in electricity demand throughout the four seasons in a year, according to Iraqi weather

conditions and also based on different sizes of household unit. It is worth mentioning that the electricity demand for house units increases dramatically during summer, due to use of air conditioners as well as little bit during the winter due to the use of heaters and water boilers. Whereas electricity demand usually decreases during the spring and autumn due to the temperate climate [14]. In the following section, the results of AEP and CF will be analyzed and discussed.

Table 6-5. Different wind turbine sizes have been suggested in this study, as well as some important details, such as the price of the wind turbine itself and annual average power production for each wind turbine size based on average wind speed [41]. Free On Board (FOB).

Wind turbine size	Rated power	wind speed		Rotor diameter	Annual average energy production	Total FOB price
		Cut-in	Rated			
SW-2 kW	2 kW	2.5m/s	8.0m/s	3.5m	4672 kWh (in rate 5m/s)	£ 1390
SW-5kW	5 kW	2.5m/s	9.0m/s	5.0m	11315kWh (in rate 5m/s)	£ 3420
SW-10kW	10 kW	3.0m/s	10.0m/s	7.0m	20MWh (in rate 5m/s)	£ 8266
SW-20kW	20 kW	3.0m/s	10.0m/s	10.0m	98MWh (in rate 8m/s)	£ 14103

6.3 Discussion and analysis of the results

In this section a number of calculations have been carried out:

- The AEP has been calculated for four wind turbine sizes, as presented in Table 6-5 at 10 m, 15 m, 20 m, 25 m and 30 m, based on Equation 6-1.
- The CF has been estimated for four wind turbine sizes and at different heights as in the previous point. The estimation of the CF in this chapter has been applied using the following equation [280].

$$Capacity\ Factor\ CF = \frac{P\ mean = \int_{v_{ci}}^{v_{co}} p(v_i)\ .f(v_i).dv}{P_r} * 100 \qquad \text{Equation 6-8}$$

$P\ mean$: is the average of power production, while P_r: represents the rated power for any wind turbine sizes, it means the maximum power production could be generated by a specific wind turbine.

- PSD at different levels of monthly electricity demand (1000, 2000, 3000, 4000, and 5000 kWh/month) has been carried out to examine the percentage of supplying from each wind turbine size for each level of electricity demand. The calculation of PSD has been applied using the following expression:

$$Percentage\ self-demand\ PSD = \frac{MEP}{PMED} * 100 \qquad \text{Equation 6-9}$$

MEP: Monthly Energy Production represents the AEP/12. While the PMED: represents the Potential Monthly Electricity Demand which ranges from 1000 to 5000 kWh/month. In the following sections the result of each wind turbine size will be discussed and analysed.

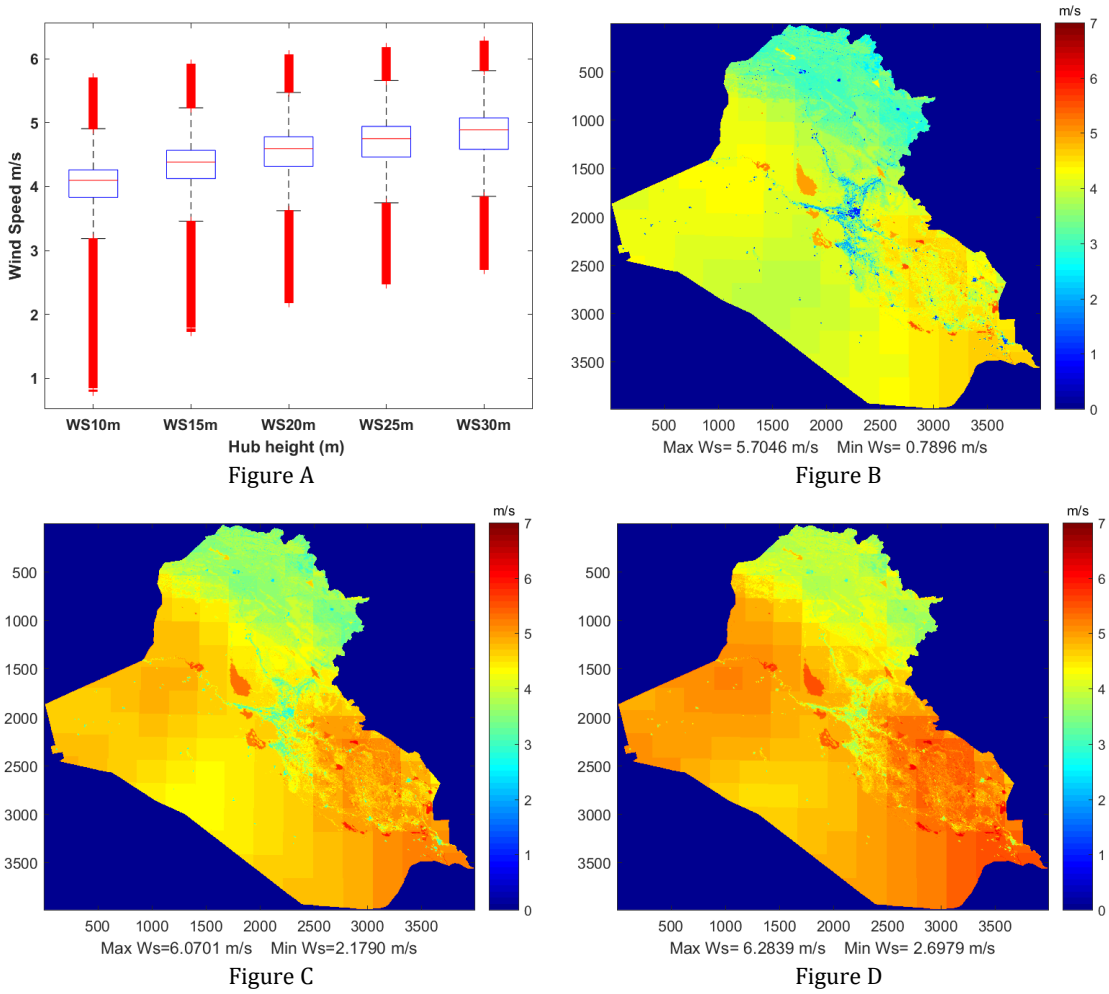

Figure 6-9. Annual average wind speed maps that have been estimated by DSM based on hourly MERRA data in 2014 at hub height of reference site Z_h= 50m, $Z_{o\,ref}$= 0.05m and reference height Z_{ref}= 600m and at hub height in the target site (Z_{hh}=10m in Figure B, Z_{hh}=20m in Figure C and Z_{hh}=30m in Figure D). Figure A shows annual average wind speed distribution at different heights from 10m to 30m. Large boxes are the interquartile range show the 25th, 50th and 75th percentile values, whiskers are the 5th and 95th percentile values and crosses are the 1st and 99th percentile values of each sample.

6.3.1 **SW-2kW**

6.3.1.1 **Annual energy production for SW-2kW**

SW-2kW is the smallest wind turbine size that has been suggested to supply the housing units with electricity. The AEP calculation from 2kW wind turbine size was performed according to the whole of Iraq wind speed map, as presented in Figure 6-9. The aim of this calculation was to determine the location distribution of the highest and lowest AEP in Iraq.

Figure 6-10A shows the boxplot of the AEP distribution for each AEP map at each height, from 10 m to 30 m, as shown in Figure 6-10B, C and D. The large box represents the interquartile range showing the 25th, 50th and 75th percentile values, whiskers are the 5th and 95th percentile values and the crosses are the 1st and 99th percentile values of each sample.

According to Figure 6-10A, it is possible to note that the average of AEP is increased around 1000 kWh/year with the height from 10 m to 30 m, whereas red crosses represent a minimal number of places around 1% that showed the lowest and highest AEP in Iraq at each height.

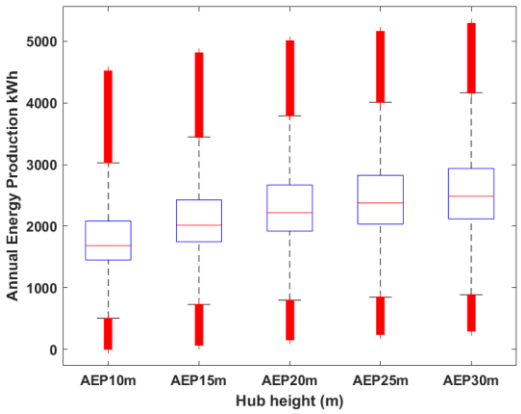

Figure A

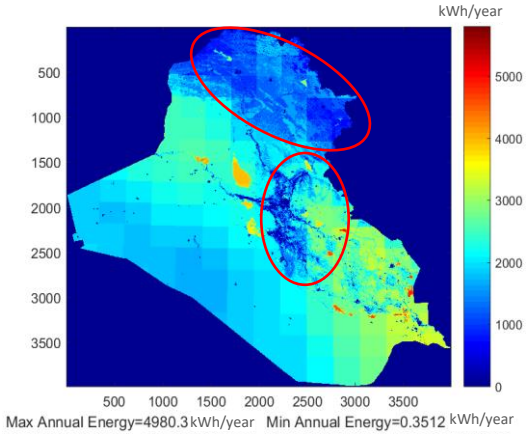

Figure B

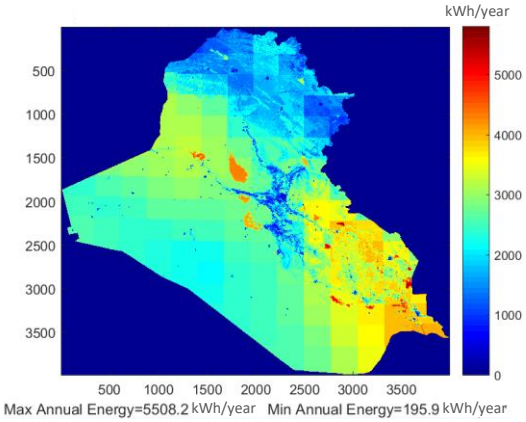

Figure C

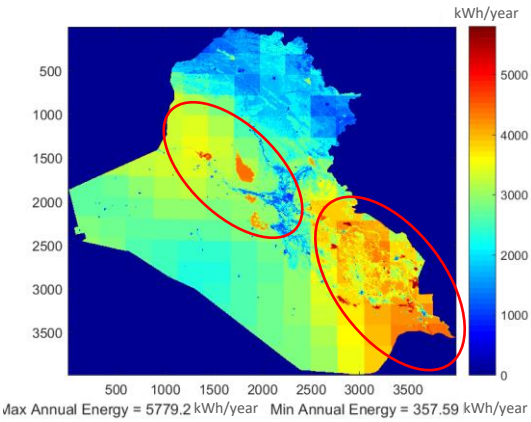

Figure D

Figure 6-10. AEP maps for 2kW wind turbine size, based on annual average wind speed in 2014 at 10m in Figure B, 20m in Figure C and at 30m in Figure D. Figure A shows the boxplots of AEP distribution for 2kW wind turbine size at different heights.

Figure 6-10D shows that high AEP, which is higher than 4500 kWh/year is concentrated above water bodies such as marshes and lakes on the Iraq map. While the AEP for 50% of locations in Iraq at 30 m ranges between 2400 and 3400 kWh/year, it is spread out across the deserts and Mesopotamia in the central and southern Iraq. In general, the most abundant area of power in Iraq is concentrated in Mesopotamia, northwest and southeast of Iraq, which is surrounded by the two red circles in Figure 6-10D. Furthermore, the lowest AEP is concentrated in the cities and towns (urban area) as well as in the north of Iraq, due to reduction in wind speed over towns, urban areas and also the limited performance of the DSM above mountain area. These areas have been surrounded by red circles in Figure 6-10B. As indicated, when the hub height of a wind turbine is increased the AEP will increase. Also, the most productive areas in Iraq are located above lakes and marshes which are highlighted with red and dark red areas in Figure 6-10D.

6.3.1.2 **The capacity factor for SW-2kW**

The CF contributes to determining the most efficient area of power production in Iraq. Figure 6-11 shows boxplot and maps of the CF for the 2kW wind turbine for the whole of Iraq at different heights. The boxplot in Figure 6-11A shows the CF distribution for each CF map at each height from 10 m to 30 m. Firstly, it is possible to note that 25% of CF ranges from 14% to 20% at 10 m, concentrated in Mesopotamia from central to southeast Iraq, which is represented with light green colour in Figure 6-11B.

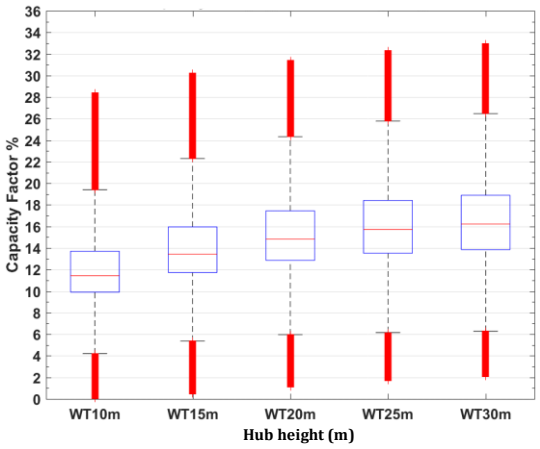

Figure A

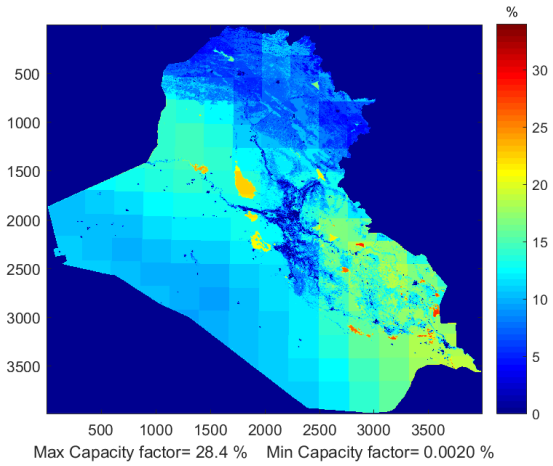

Figure B

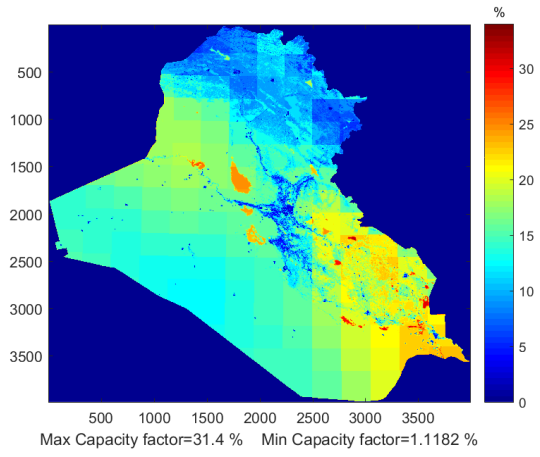

Figure C

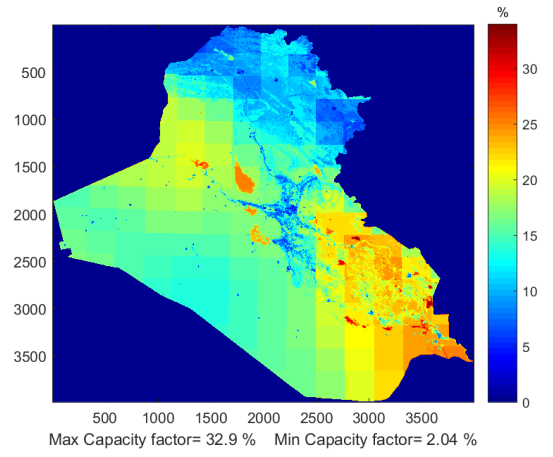

Figure D

Figure 6-11. CF maps for 2kW wind turbine size, based on average power production to the rated power of the wind turbine in 2014 at 10m in Figure B, at 20 m in Figure C and at 30 m in Figure D. Figure A shows the boxplot, the CF distribution for 2kW wind turbine size at different heights.

The highest values of CF which are represented by red crosses ranging from 20% to 28% at 10m in Figure 6-11A have been distinguished by orange and red spots that represent marshes and lakes in Iraq. Also, it is clear that the values of CF increase with increasing hub height of the wind turbine, as shown in Figure 6-11A.

On the other hand, the lowest CF is located in the mountainous areas in the north of Iraq and above towns and urban areas over the country. It is possible to distinguish these areas by blue and dark blue spots in Figure 6-11B, C and D.

6.3.1.3 The percentage self-demand for 2kW

The percentage of self-demand aims to present the ability of a specific wind turbine size to cover different levels of monthly electricity demand, based on monthly average energy production. Different levels of monthly electricity demand have been suggested, starting from 1000 to 5000 kWh/month. In this case, the PSD calculation for 2kW wind turbine size has been applied for the whole of Iraq and different heights, as shown in Figure 6-12.

At first glance, it is easy to note that the PSD increases with height as D1=1000 kWh/month. In addition, the PSD at D2=2000 kWh/month has dropped dramatically in comparison with D1.

50% of locations in Iraq based on D2.30 have recorded an ability to cover from 10% to 14% of 2000 kWh/month electricity demand at 30m. While all locations in Iraq based on D5=5000 kWh/month electricity demand at different heights did not show a PSD higher than 10%.

According to the percentage, with self-demand for 2kW it was found that generally, the trend of PSD increased with height at different levels of electricity demand and recorded a high percentage of covering with a low level of demand. However, the 2kW wind turbine size in the best-case scenario did not show a PSD higher than 48% for less than 1% of locations in Iraq. In general, 50% of areas in Iraq in the best case scenario showed almost 20% to 27% of electricity demand was covered by 2kW wind turbine size. While the 2kW wind turbine size showed a low ability to cover a respectable percentage of electricity demand within 5000 kWh/month.

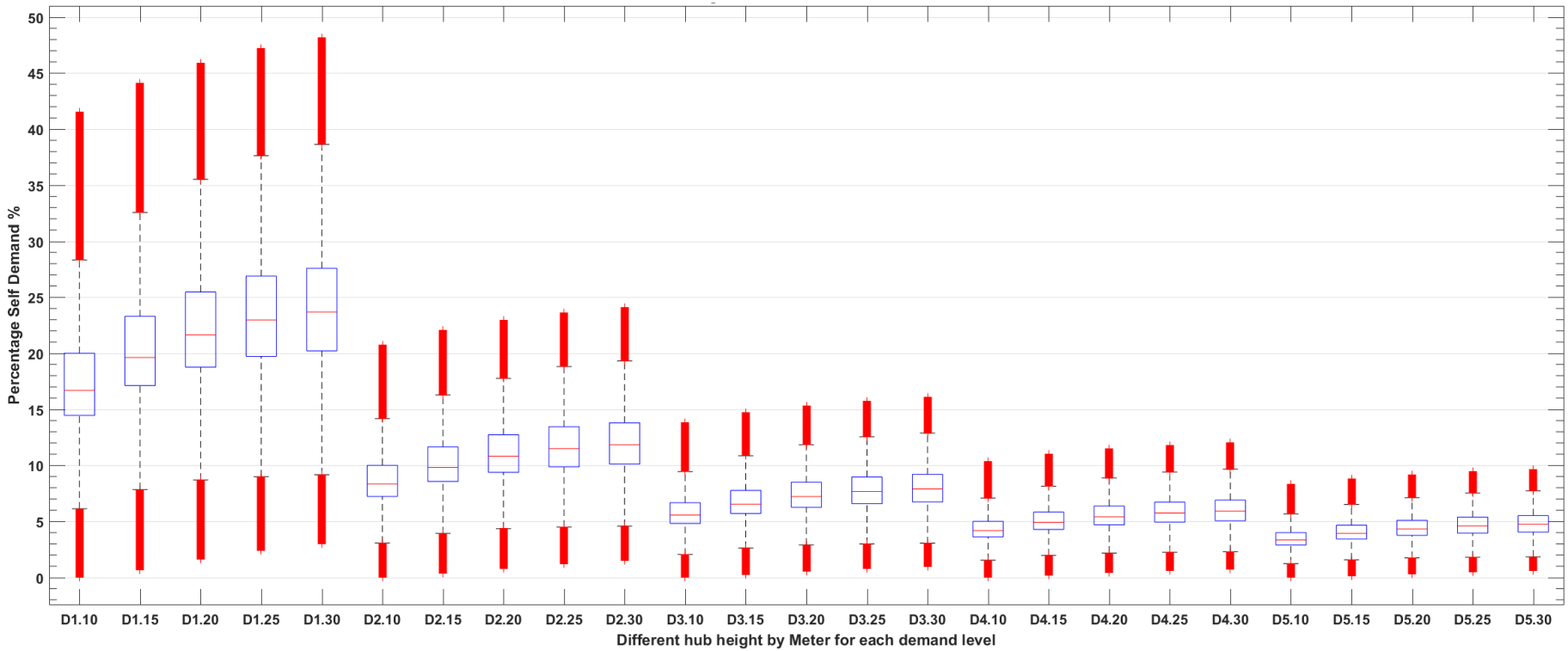

Figure 6-12. The change of PSD from height to height and from level of demand to others based on 2kW wind turbine size. For example, D1.10 refers to 1000kWh/month level of electricity demand at 10m, while D5.30 represents 5000kWh/month level of electricity demand at 30m. In Figure 5 the level of electricity demand has been applied at D1=1000, D2=2000, D3=3000, D4=4000 and D5=5000 kWh/month and the experiment has been applied at 5 hub heights levels: 10m, 15m, 20m, 25m and 30m.

6.3.2 **SW-5kW**

6.3.2.1 **Annual energy production for SW-5kW**

SW-5kW is the second small wind turbine size that has been suggested to supply the housing units with electricity. The AEP calculation for SW-5kW wind turbine has been estimated based on the whole of Iraq wind speed map at different heights as presented in Figure 6-9. Also, the estimation of AEP from 5kW gives a perception of how much energy this turbine can generate in different locations for one year. Figure 6-13A shows the boxplot of the AEP for more than 8 millions pixels on the Iraq map, according to different heights from 10m to 30m, as shown in Figure 6-13B, C, and D.

The blue box in Figure 6-13A at AEP30= 30 m shows that the 50% of locations in Iraq map produce AEP ranging between 9000 and 11000 kWh/year. These locations that appear in the green areas represent desert on the Iraq map in Figure 6-13D. While 25% of locations at 30m generate annual energy ranging from 11000 to 16000 kWh/year (distinguished by yellow and orange areas), this output represents the most productive areas such as the desert in northwest of Iraq and Mesopotamia from central to southeast of Iraq. Also, around 1% of locations in Iraq generated the highest annual energy at 30m, ranging from 16000 to 20000 kWh/year (distinguished by red and dark red spots), which represent marshes and lakes in Iraq, as shown in Figure 6-13D.

In addition, the blue areas in Figure 6-13B represent the most locations in Iraq that generate lower energy in comparison with others. The most important finding that can be summarized from Figure 6-13 is that the highest power production is concentrated above marshes and lakes in Iraq, especially in middle and southeast of Iraq, while the lowest power production was consecrated above cities and urban areas in Iraq and the mountainous area in the north and northeast of Iraq. In addition, the area that appears in orange spots from central to southeast of Iraq in Figure 6-13D produced the most high energy (5kW wind turbine) in Iraq and this area is regarded as the most promising in Iraq.

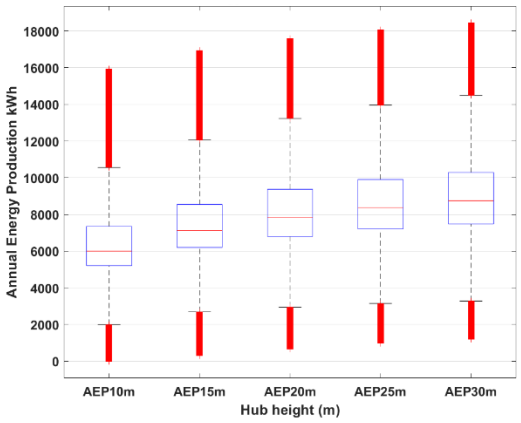

Figure A

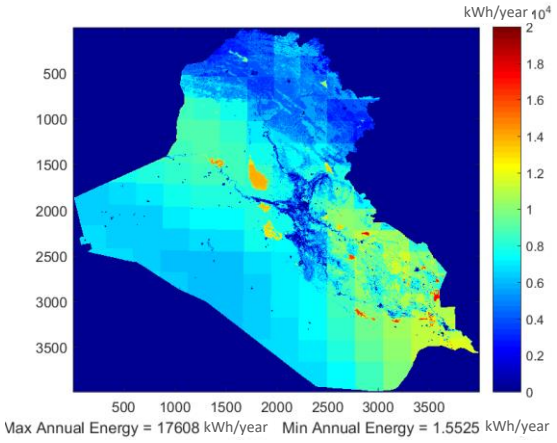

Figure B

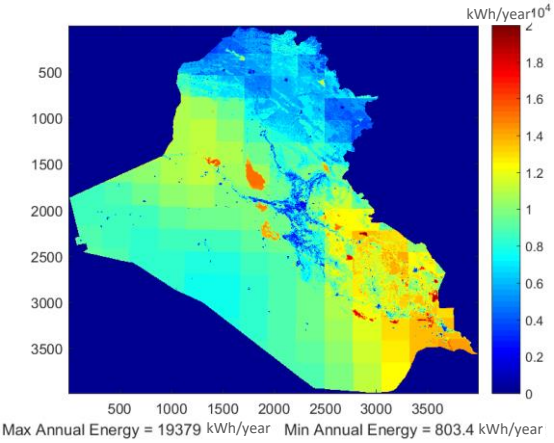

Figure C

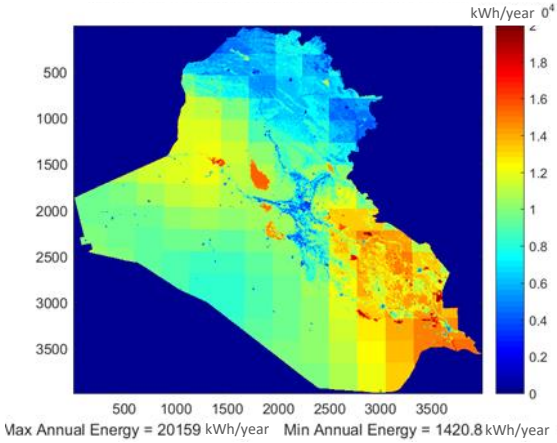

Figure D

Figure 6-13. AEP maps for 5kW wind turbine size, based on annual average wind speed in 2014 at 10m in Figure B, at 20m in Figure C and 30m in Figure D. Figure A shows the boxplots of AEP distribution for 5kW wind turbine size at different heights.

6.3.2.2 **The capacity factor for SW-5kW**

Figure 6-14 shows box-and-whisker plot and maps of the CF of 5kW wind turbine for the whole of Iraq and at different heights. The boxplot in Figure 6-14A shows the CF distribution for each CF map to varying heights from 10m to 30m.

In general, the CF value increases with height: the median of boxplot at 10m increases 3% from 16% to 19% at 15m and 2% from 19% to 21% at 20m, while the CF increases step by step from 20m to 25m to 30m around 1% respectively at each height, reaching 23%. There is a logical similarity between increasing the CF in Figure 6-14A and increasing the AEP in Figure 6-13A, because the calculation of the CF mainly depends on the average annual power production.

The maximum CF was recorded at 30 m by 2kW wind turbine 32.9%, whereas the minimum CF at the same height was 2.04%, as shown in Figure 6-11D. On the other hand, the

maximum CF at 30 m for 5kW wind turbine size was 46%, while the minimum value was 3.24%, as shown in Figure 6-14D.

It is worth mentioning that the CF dramatically increases with height for locations that have high wind speed and annual energy, as shown in Figure 6-14A. Where the change between the maximum CF for the last quarter at 10 m and 30 m is 10%, the locations that had low wind speed and AEP have shown an increase with height, where the change between the minimum CF at the first quarter from 10 m to 30 m was 3%.

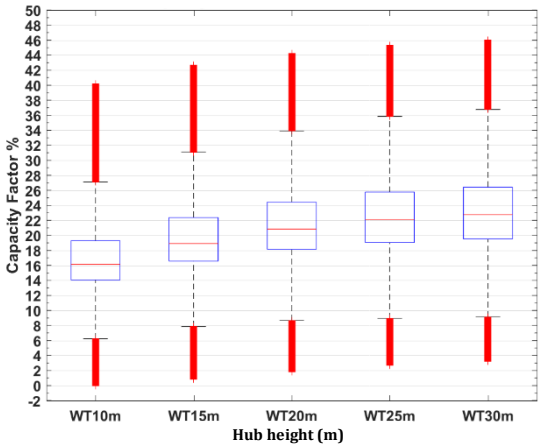

Figure A

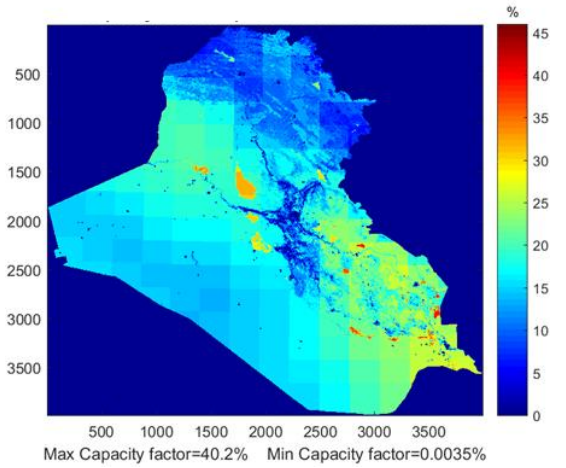

Figure B

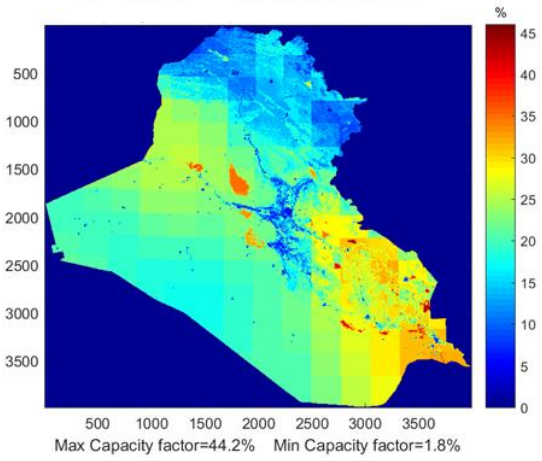

Figure C

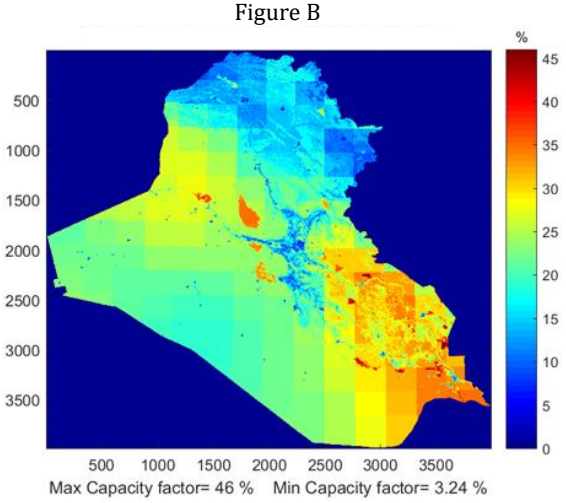

Figure D

Figure 6-14. CF maps for 5kW wind turbine size, based on average power production to the rated power of the wind turbine in 2014 at 10m in Figure B, at 20 m in Figure C and at 30 m in Figure D. Figure A shows the boxplot for the CF distribution for 5kW wind turbine size at different heights.

The most important finding that can be summarized from Figure 6-14. Firstly, the CF increases dramatically with a decreaseing the value of the rated speed according to Table **6-5** and with increased wind speed. In addition, the CF changed significantly with height between 10m to 20m and slightly between 20m to 30m.

6.3.2.3 **The percentage self-demand for 5kW**

The PSD estimation for 5kW wind turbine size has been performed for the whole of Iraq at different heights, as shown in Figure 6-15. At first glance, it is possible to note 50% of locations in Iraq at D1.30 show that the 5kW wind turbine were able to cover from 71% to 96% of 1000 kWh/month electricity demand per month at 30 m, while the same wind turbine could cover from 51% to 70% of 1000 kWh/month electricity demand per month at 10m for 50% of locations in Iraq. That result means the ability of wind turbine to cover high percentage of electricity demand will increase when there is increased turbine hub height. Furthermore, interestingly, the locations that have high AEP which are represented by upper whiskers for D1 groups (D1=1000 kWh/month electricity demand per a month) showed a dramatic increase with height from 10m to 30m with difference approximating 35%.

It is worth mentioning that there were significant changes amongst group D1 and another groups in Figure 6-15, where the ability of wind turbine was decreased with increased in the monthly electricity demand from 1000 to 5000 kWh/month, where the median of D5 group ranged from 12% at 10m, to 18% at 30m.

Summary. The PSD calculation in this section has generally shown that the PSD increased dramatically with height and with low electricity demand for locations that had high annual energy, while they increased slightly with height and with high electricity demand. Finally, the 5kW turbine showed good ability to cover the electricity demand within 1000 kWh/month

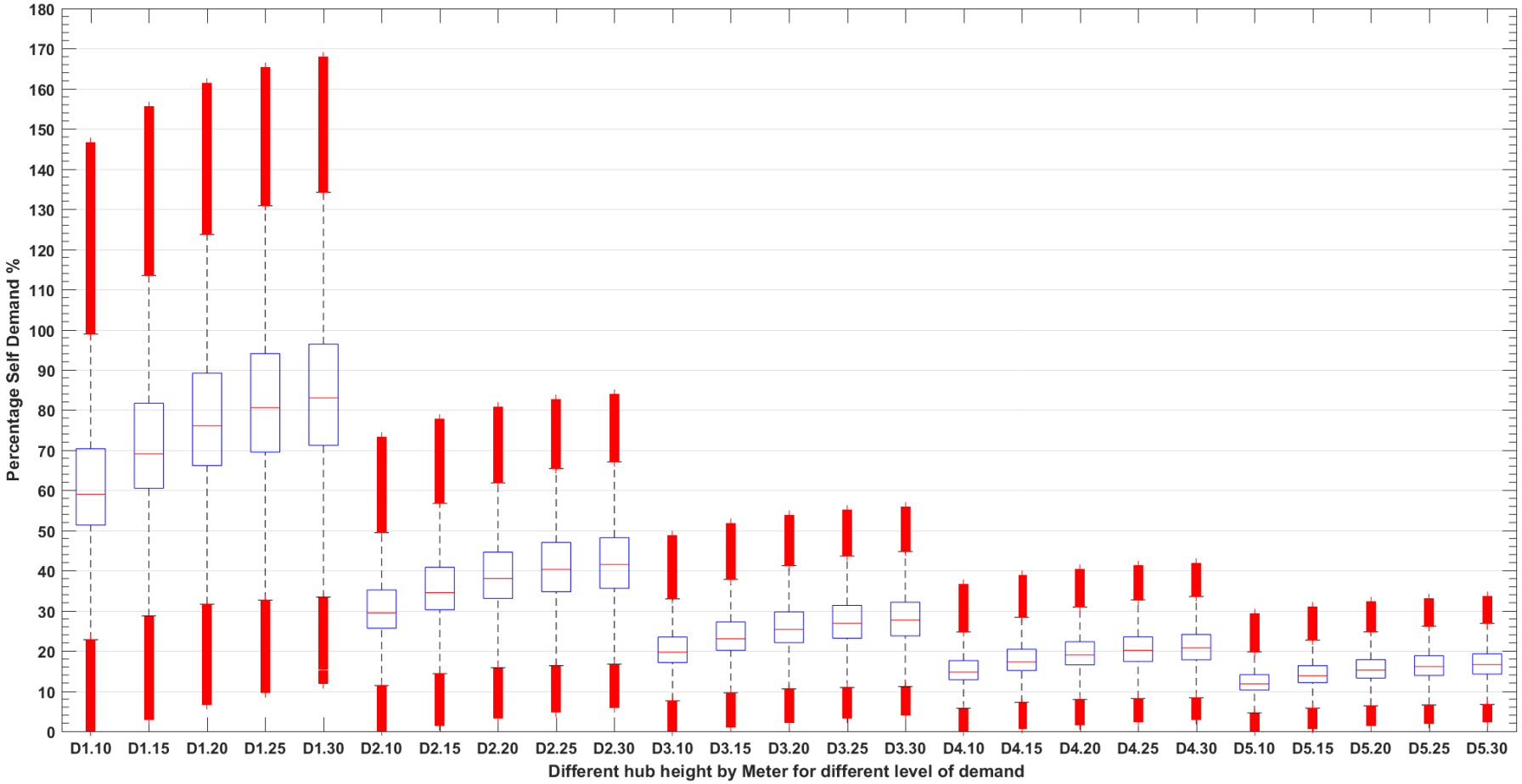

Figure 6-15. The change of PSD from height to height and from level of demand to other for 5kW wind turbine size. For example, D1.10 refers to 1000kWh/month level of electricity demand at 10m, while D5.30 represents 5000kWh/month level of electricity demand at 30m. In this Figure 5 levels of electricity demand were applied: D1=1000, D2=2000, D3=3000, D4=4000 and D5=5000 kWh/month and the experiment has applied at 5 hub height levels: 10m, 15m, 20m, 25m and 30m.

6.3.3 SW-10kW

6.3.3.1 Annual energy production for SW-10kW

SW-10kW is the third small wind turbine size that was suggested to supply housing with electricity. The AEP calculation for 10kW wind turbine was performed based on the whole of Iraq wind speed map, as presented in Figure 6-9. Figure 6-16A shows the boxplots of the annual energy distribution for more than 8 millions pixels on Iraq map for five different heights from 10 m to 30 m.

In general, the SW-10kW AEP showed the same trend of power production distribution as well as the same slope of power production of SW-5kW.the power production of SW-10kW was growing from 10 m to 30 m in Figure 6-16A. Also, 25% of locations in Iraq that distributed between the upper quartile and the upper whisker into AEP30m group at 30 m in Figure 6-16A have shown significant AEP. These locations are represented in yellow and orange in the north-west, east and south-east of Iraq. In general, these locations are considered a promising area to produce power in Iraq.

6.3.3.2 The capacity factor for SW-10kW

Figure 6-17 shows CF distribution for 10kW wind turbine size for the whole of Iraq at different heights. The boxplot in Figure 6-17A shows the CF distribution for five heights from 10 m to 30 m. It is possible to note that the highest CF that has been recorded at 30 m by 10kW turbine was 35.2%, whereas the minimum CF that has been recorded at the same height was 3.8%, as shown in Figure 6-17B. On the other hand, the maximum CF at 30m for 5kW wind turbine size was 46%, while the minimum value was 3.24%, as shown in Figure 6-14D.

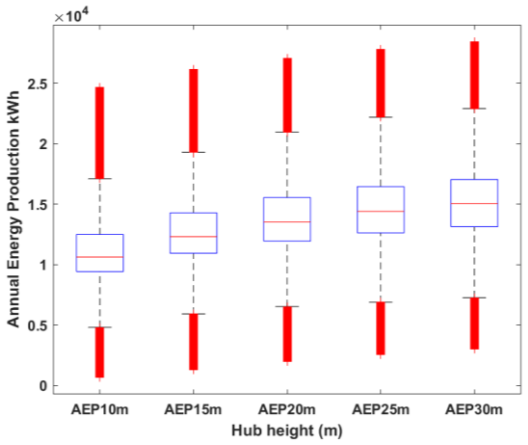

Figure A

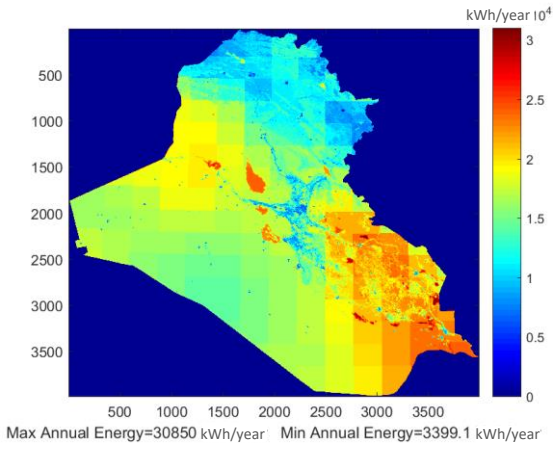

Figure B

Figure 6-16. AEP maps for 10kW wind turbine size, based on annual average wind speed in 2014 at 30m in Figure B. Figure A shows the boxplots of AEP distribution for 10kW wind turbine size at different heights.

In addition, the fourth quartile in group WT30m which represents 25% of locations in Iraq, shows that their CF ranged from 21% to 29%. These locations are represented in yellow and orange and are concentrated in the northwest of Iraq and extend from central to southeast of Iraq between and around the two rivers.

The main finding can be summarized: the CF of 10kW turbine is lower than the 5kW turbine but higher than 2kW turbine, as mentioned above. In addition, the area which is located between and around the two rivers has been approved as the most promised area to generate high power, based on the high CF and annual energy that has been estimated in this area.

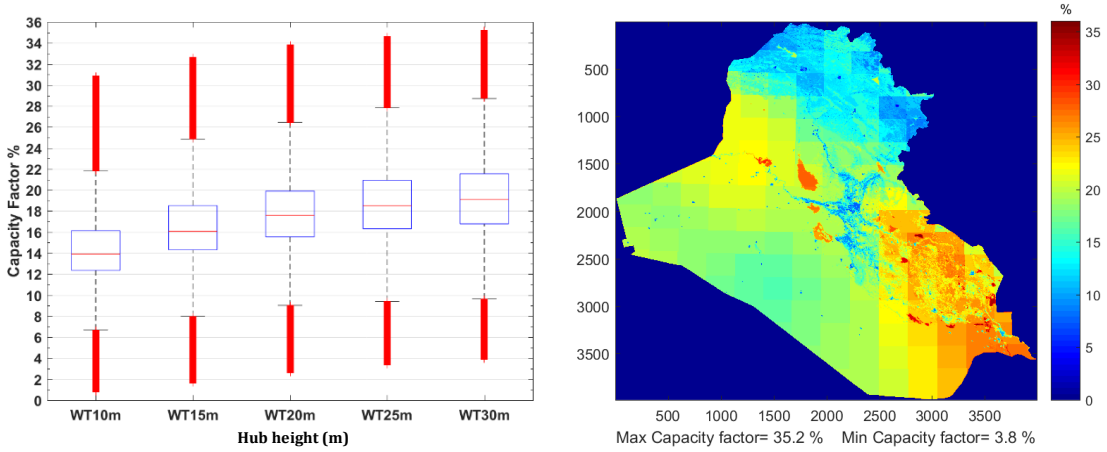

Figure A Figure B

Figure 6-17. CF maps for 10kW wind turbine size, based on average power production to the rated power of the wind turbine in 2014 at 30m in Figure B. Figure A shows the boxplot of the CF distribution for 10kW wind turbine size at different heights.

6.3.3.3 The percentage self-demand for 10kW

In this section, the PSD estimation for 10kW wind turbine size has been performed for the whole of Iraq and for different heights, as is shown in Figure 6-18. At first glance, it is possible to note the similarity of trend amongst the Figure 6-18, for the PSD for 10kW turbine and the PSD for 5kW and for the 2kW turbine in Figure 6-15 and Figure 6-12, respectively.

The PSD for D1 groups shows that power production from 10kW was more than enough to cover 1000 kWh/month of electricity demand at different heights. The interquartile within D1 groups ranged between 90% and 158%. It is worth mentioning that the 10kW turbine was able to cover most electricity demand when the monthly electricity demand equals 2000 kWh/month, as shown with D2 groups.

The D2-25 and D2-30 groups show that 10kW for 50% of locations in Iraq were able to cover from 60% to 80% of 2000 kWh/month of demand at 25m and 30m respectively. The

fourth quartile in groups D2-20, D2-25 and D2-30 show that 25% of locations in Iraq can cover 100% of 2000kWh/month of demand.

The most important finding to emerge from PSD estimation for 10kW wind turbine is that this turbine was able to cover from 50% to 100% of monthly electricity demand from approximately 75% of locations in Iraq.

6.3.4 **SW-20kW**

6.3.4.1 **Annual energy production for SW-20kW**

SW-20kW is the fourth small wind turbine size that has been suggested to supply the small housing units by electricity. The AEP calculation for 20kW wind turbine has been performed for the whole of the Iraq wind speed map, as presented in Figure 6-19 from 10 m to 30 m.

Figure 6-19 shows that the highest annual energy was generated by 20kW wind turbine equal to 74168 kWh/year, which was recorded in Figure 6-19B. Also, it is possible to note the similarity of a trend in Figure 6-19 with AEP for 20kW turbines and AEP for 10kW, 5kW and 2kW turbines in Figure 6-16, Figure 6-13 and Figure 6-10, respectively.

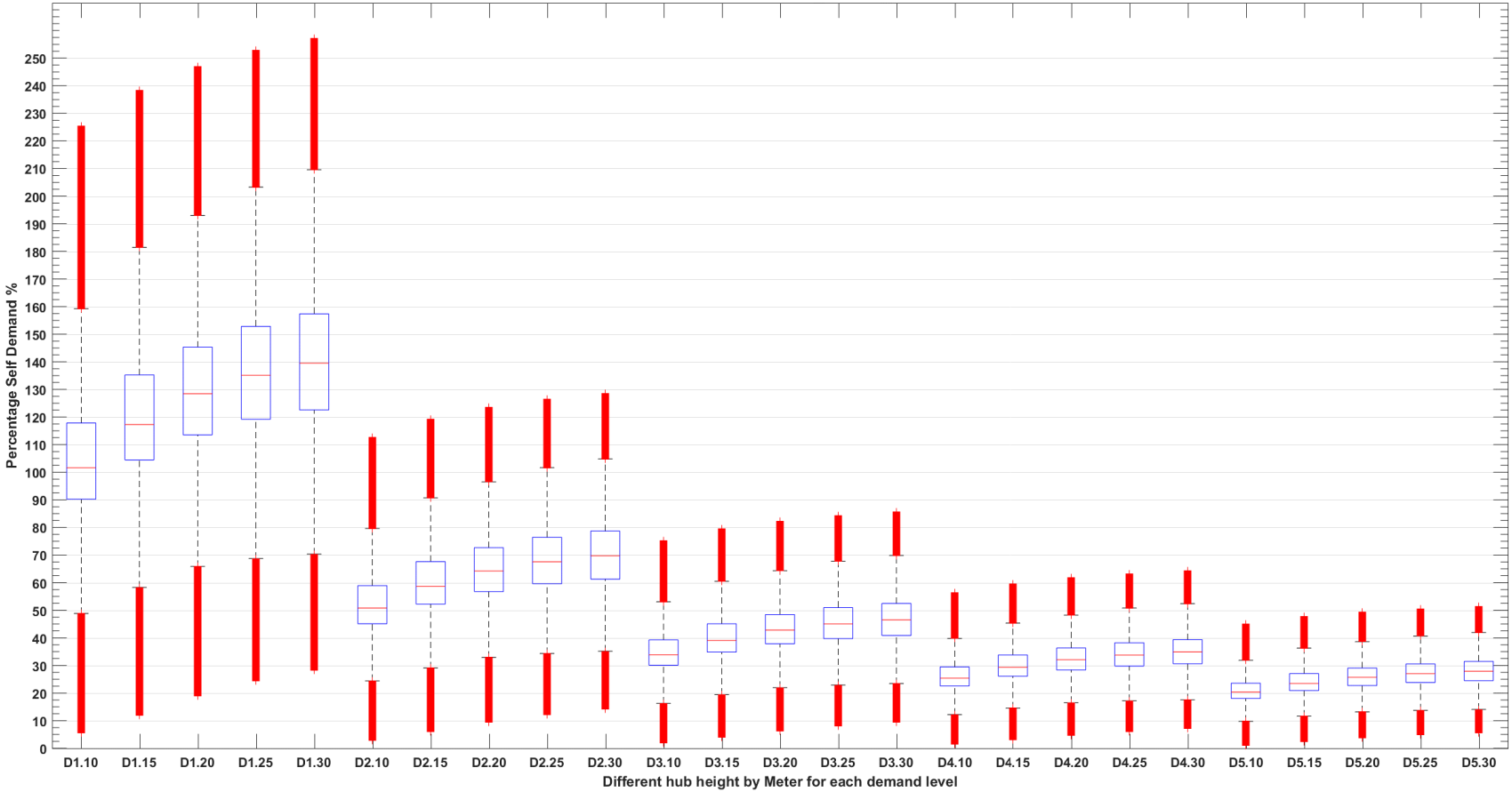

Figure 6-18. The change of PSD from height to height and from level of demand to other for 10kW wind turbine size. For example, D1.10 refers to 1000kWh/month level of electricity demand at 10m, while D5.30 represents 5000kWh/month level of electricity demand at 30m. In this Figure 5 levels of electricity demand were applied: D1=1000, D2=2000, D3=3000, D4=4000 and D5=5000 kWh/month and the experiment was applied at 5 hub height levels: 10m, 15m, 20m, 25m and 30m.

In addition, it is possible to note the similarity of trends in Figure 6-19: for AEP for 20kW turbine and AEP for 10kW, 5kW and 2kW turbines in Figure 6-16, Figure 6-13 and Figure 6-10, respectively. According to the last calculation of AEP for 2kW, 5kW, 10kW and 20kW turbine, the high AEP changed dramatically from 10 m to 30 m for high wind speed, while the change of low AEP with heights was slight. The dramatic change with high annual energy and slight change with low annual energy is due to the power production, which represents threefold of wind speed at this specific site; for this reason the locations that have high wind speed show dramatic change with height, whereas the locations that have low wind speed showed slight change with height, as shown in Figure 6-19. For example, the difference between upper whisker for AEP10m and upper whisker for AEP30m is around 10000kWh/year, while the difference between lower whisker for AEP10m and lower whisker for AEP30m is around 7000kWh/year.

One more time, the fourth quartile in AEP30m group which represent 25% of locations in Iraq showed high AEP ranging between 47000 and 61000 kWh/year.

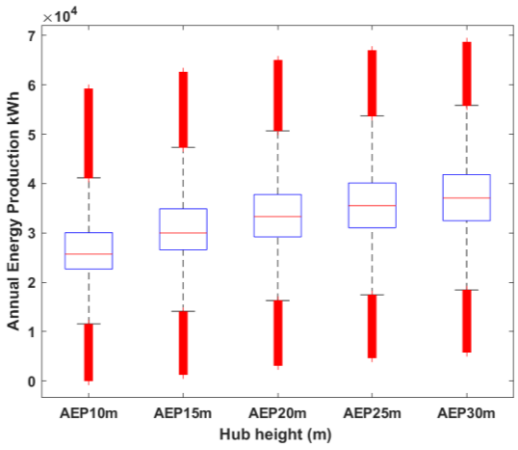

Figure A

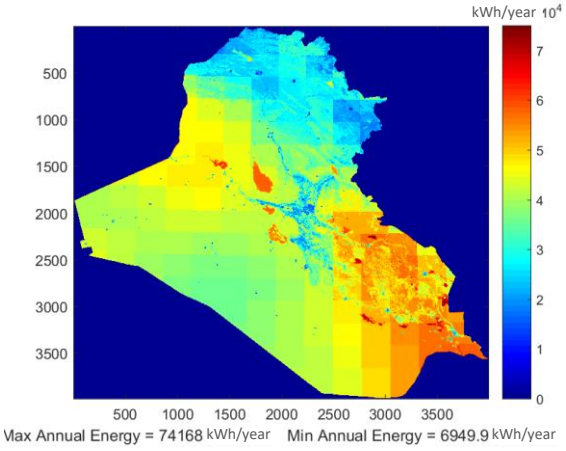

Figure B

Figure 6-19. AEP maps for 20kW wind turbine size based on annual average wind speed in 2014 at 30m in Figure B. While Figure A shows the boxplots of AEP distribution for 20kW wind turbine size at different heights.

6.3.4.2 The capacity factor for SW-20kW

The boxplot in Figure 6-20 shows the CF distribution for each CF map at each height from 10 m to 30 m. At first glance, it is possible to note that the highest CF that was recorded at 30 m by 20 kW turbine was 42.3%, whereas the highest CF at 10 m was 37%, as shown in Figure 6-20B.

The most important finding to emerge from the CF distribution and map in Figure 6-20, is that the CF for 20kW turbine for high wind speed are higher than 10kW and 2kW at the same locations and circumstances, while the 5kW turbine showed the highest CF based on the same locations and conditions. In addition, the area which is located between and

around the two rivers has been approved as the most promising area to generate high power, based on the high CF and annual energy that have been estimated in this area. Furthermore, the CF distribution in Figure 6-20 has shown a similar trend with CF for 2kW, 5kW and 10kW turbines, as shown in Figure 6-11A, Figure 6-14A and Figure 6-17A.

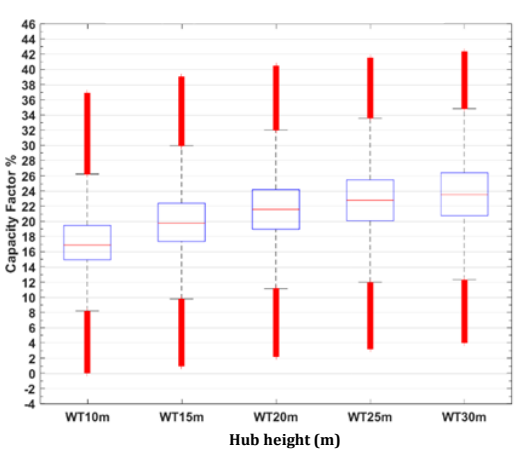

Figure A

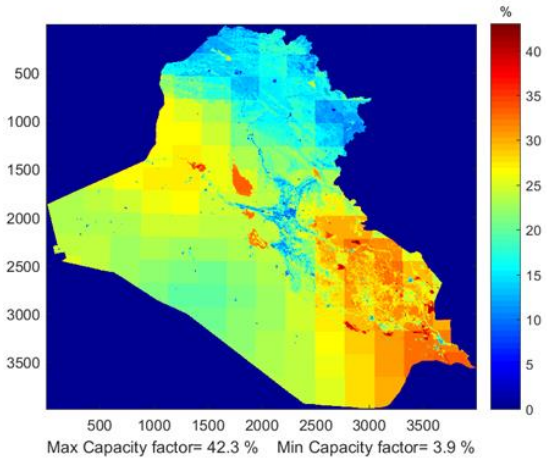

Figure B

Figure 6-20. CF maps for 20kW wind turbine size based on average power production to the rated power of the wind turbine in 2014 at 30m in Figure B. Figure A shows the boxplot for the CF distribution for 20kW wind turbine size at different heights.

6.3.4.3 **The percentage self-demand for 20kW**

There was a similarity of trend in Figure 6-21 for the PSD for 20kW turbine and the PSD for 10kW, 5kW and 2kW turbines in Figure 6-18, Figure 6-15 and Figure 6-12, respectively. In addition, it is noted that the highest PSD was recorded by the D1.30 group: 620% based on 1000 kWh/month electricity demand at 30 m.

Significantly, the result in Figure 6-21 shows that the 20kW turbine was able to cover from 50% to 100% of 4000 kWh/month of monthly electricity demand from 50% of locations in Iraq (interquartile range) from 10 m to 30 m, as shown in Figure 6-21 by D4 groups. At the same time, 25% of areas in Iraq (located between upper quartile and upper whisker into D5 groups) were able to cover from 60% to 100% of 5000 kWh/month of monthly electricity demand from 10 m to 30 m, as shown in Figure 6-21.

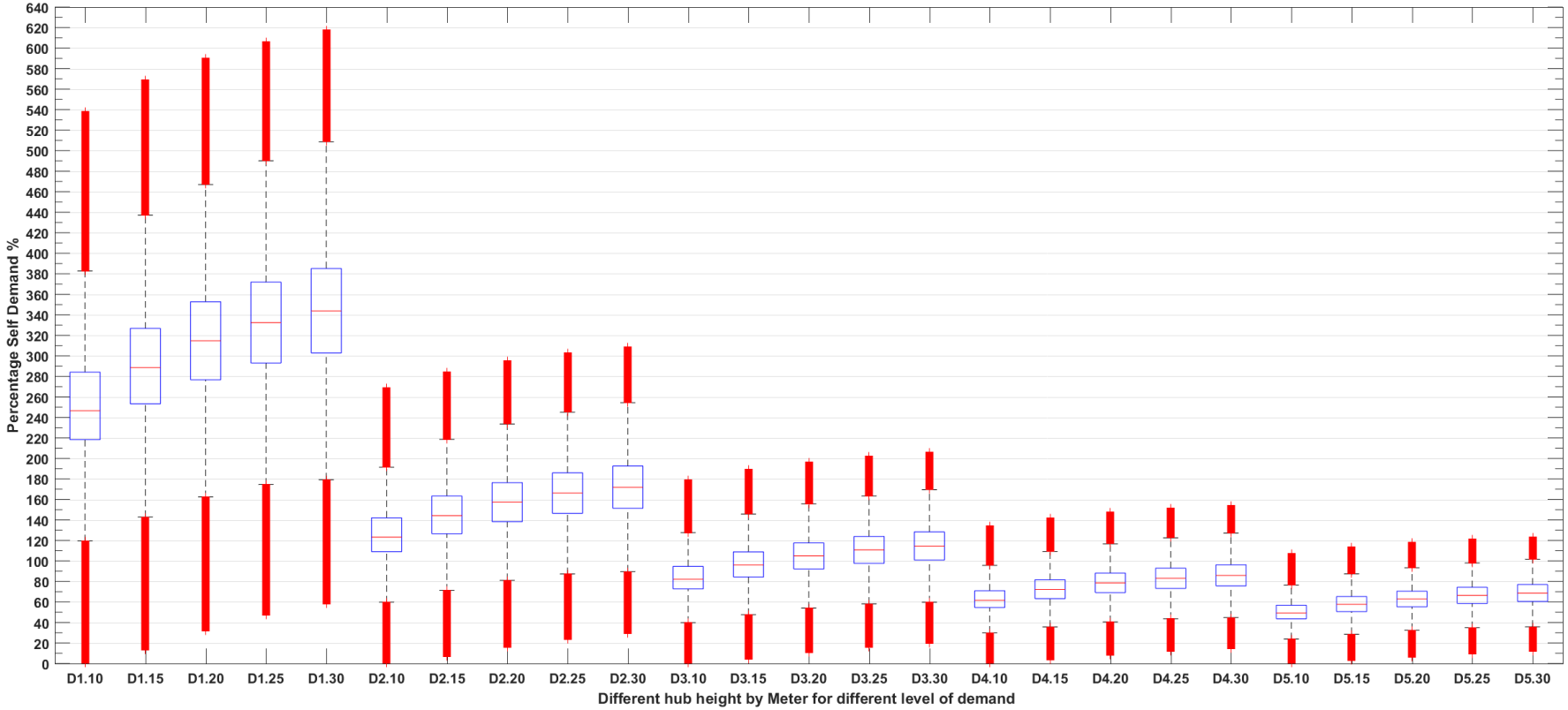

Figure 6-21. The change of PSD from height to height and from level of demand to other as for 20kW wind turbine size. For example, D1.10 refers to 1000kWh/month level of electricity demand at 10m, while D5.30 represents 5000kWh/month level of electricity demand at 30m. In this Figure 5 levels of electricity demand were applied: D1=1000, D2=2000, D3=3000, D4=4000 and D5=5000 kWh/month and the experiment was applied at 5 hub height levels: 10m, 15m, 20m, 25m and 30m.

6.3.5 **Annual Energy Production Validation**

In order to validate the accuracy of AEP calculations for different wind turbine sizes in this study, a comparison was carried out between AEP estimation by MATLAB model based on wind speed from DSM and AEP by Homer calculations based on wind speed from the DSM too. The reason behind comparing MATLAB model results with Homer results back that the energy production data isn't available from a real wind turbine in Iraq due to is the wind turbine uses still is not common in Iraq which is regarded as one of the limitations in this work. The validation in terms of the MATLAB and Homer has been applied based on several scenarios:

- Two sizes of a wind turbine have been used in this validation: 2kW and 10kW.
- The validation has been applied in different land cover category (urban, desert and water areas) which are located in various places: Amara; Anah; Mosul and Basrah.
- The validation has been applied at two heights 10 m and 30 m.

The validation has been applied by using the Absolute Percentage Error (APE), which is mean absolute percentage size of the error between actual and forecasting data divided by actual data, as expressed in Equation 6-10 [267].

$$APE = \sum \left| \frac{Actual - Forecast}{Actual} \right| * 100 \qquad \text{Equation 6-10}$$

$Actual$ refers to Homer results as standerd, while $Forecast$ represents the MATLAB model results. At first glance in Figure 6-22, two things will bring attention: firstly, the high APE for four cities in Figure 6-22 A in Urban 10m. The low wind speed above the urban area at 10 m leads to the generation of low energy and any small difference results in a significant error according to APE calculation. For example, the energy production from 2 kW turbine size at 10m based on MATLAB estimation in Figure 6-22 A in Urban 10m in Anah equals 2.74 kWh/year, while AEP based on Homer equals 8.04 kWh/year. As a result of this calculation the APE equals 65.92%, as shown in Figure 6-22A. Whilst On the other hand, at the same high above water surface where wind speed is higher than the urban area, the AEP based on MATLAB equals 2955.9 kWh/year, while, the AEP based on Homer equals 3007 kWh/year. As a result, the APE equals 1.7%, as shown in Figure 6-22A. The second striking result was for Mosul in Figure 6-22A and B, which showed a high APE across all heights and land cover categories, due to the low wind speed above this area, which is located at the north of Iraq. Finally, the small APE between Homer and MATLAB model confirms the accuracy of the MATLAB model calculation for AEP for different turbines.

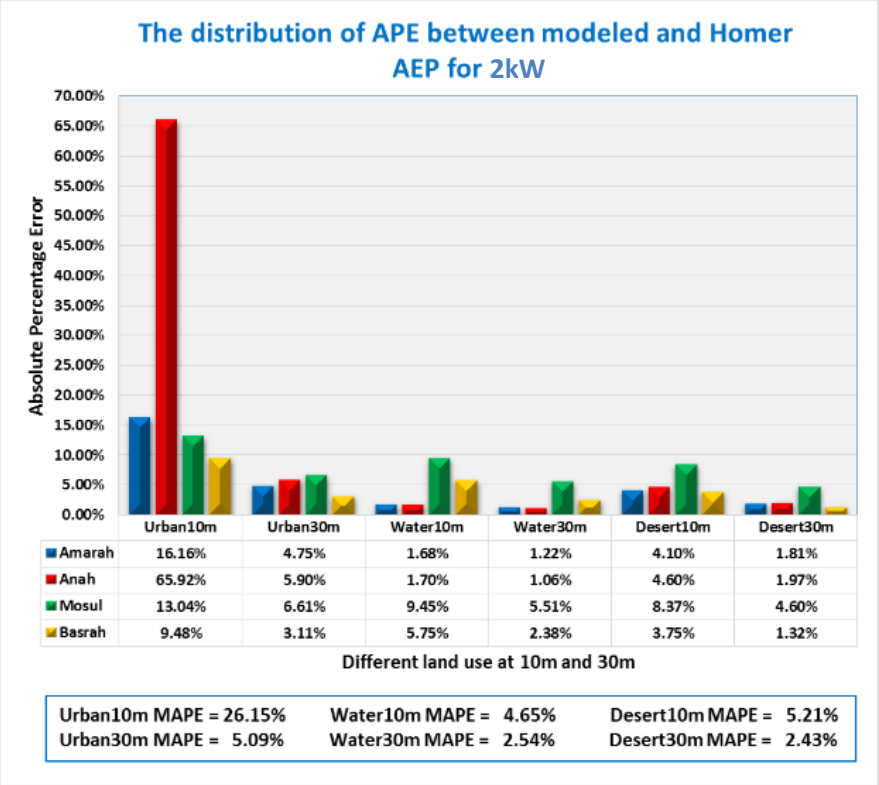

Figure A

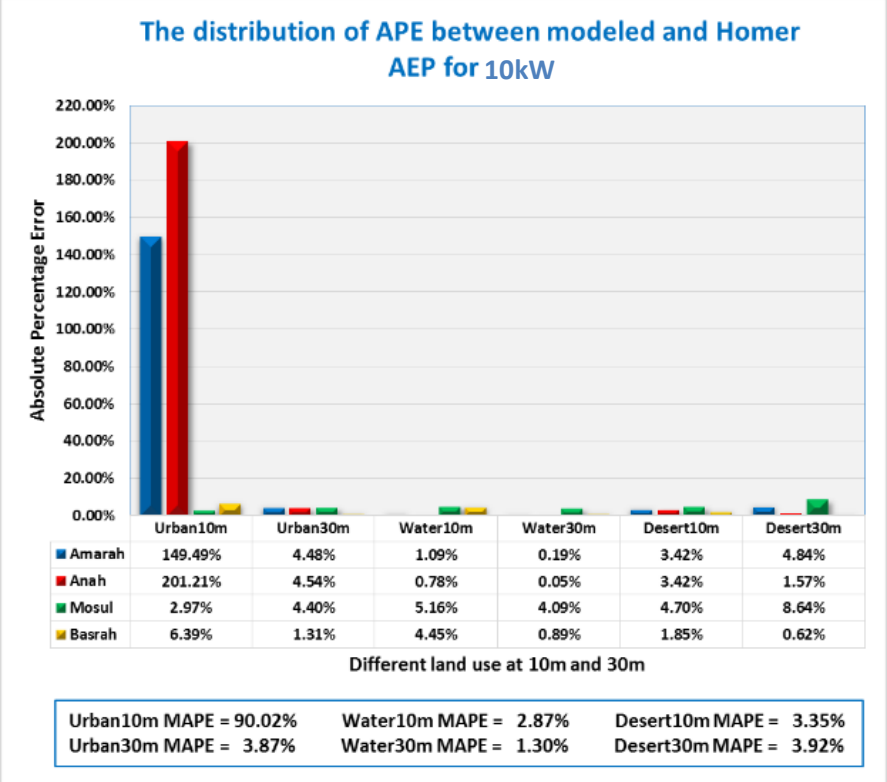

Figure B

Figure 6-22. The Absolute Percentage Error (APE) between AEP which is estimated by Homer and AEP. which is determined by the MATLAB model, based on the wind speed that was evaluated by the DSM at 10 m and 30 m above different land cover category (urban, water and desert areas) at four cities (Amarah, Anah, Mosul and Basrah). The validation was applied by using the 2kW wind turbine size in Figure A and 10kW turbine size in Figure B

6.4 Conclusion

The first part of this chapter aimed to calculate the AEP for the whole of Iraq, based on different sizes of wind turbines at varying heights, in order to evaluate the potential energy production at different regions and to identify locations that have high and low AEP in Iraq. In addition, the AEP provides information for another kind of calculation such as CF, PSD and some economical calculation which will be discussed in the next chapter. Moreover, the calculation of AEP for different sizes of turbine will give us a perception of how much energy each turbine size can generate in different locations and at various heights for one year.

Weibull distribution is based on shape factor and scale factor; it has been suggested to estimate AEP to avoid running 8760 hours of data over more than 8 million pixel on Iraq map. The results show that the shape factor does not change significantly with height as for MERRA data. In addition, the shape factor does not change completely with height after applying the DSM for different pixels in Iraq. Furthermore, the values of shape factor for MERRA have shown a strange trend when decreasing with height at some sites in comparison with a normal trend of shape factor profile and observed shape factor profile from Shihabe tower at different heights.

K- profile has been suggested as a method to estimate shape factor with height correctly

In order to get acceptable fit between observed and estimated shape factors at 10 m and 30 m, the coefficient regression c_k has been calculated again based on the value of the shape factor from MERRA at 50 m, with the values of shape factor from Shihabi tower at 30 m and 10 m by using a curve fitting app in MATLAB. The new value of c_k = 0.03705 and $z_r = 120m$ have been used to estimate shape factor values at 10 m and 30 m. The results of shape factor from MERRA data after applying the modified K-profile at 10 m and 30 m have shown good agreement with values of shape factor from Shihabi tower.

The difference in distribution of the shape factor values return to topography of these area and wind speed distribution in these area. In fact, shape factor values have increased in the desert and plateau in the west of Iraq, while the value of shape factor has reduced in the mountainous area in the north of Iraq.

The AEP evaluation based on different sizes of wind turbines at different heights and for the whole of Iraq map have shown some important features. The first important regions form around 1% of locations in Iraq that have generated the highest annual energy at 30 m. These locations are regarded as the most productive areas; the marshes and lakes extend from central to southeast of Iraq. In addition, the CF for different sizes of wind turbine at these locations have recorded the highest value.

The second important regions in Iraq form around 25% of locations and are distributed between northwest, east and southeast of Iraq. In general, these locations are considered a promising area to produce AEP from different sizes of wind turbine in Iraq.

The third important regions in Iraq is represented by 50% of locations. These locations represent deserts that extend from north-west, west to southwest in Iraq.

The fourth important regions form 25% of locations in Iraq that show the lowest AEP and are concentrated in the cities and towns and in the north of Iraq, due to reduction in wind speed over urban areas and the limitated performance of DSM within a mountainous area.

In addition, the CF increases with increasing the size of a wind turbine and with increasing the wind speed and hubheight. In addition, the low rated speed of wind turbine will increase the CF of a wind turbine. The CF for 20kW turbine within high wind speed is higher than 10kW and 2kW at the same locations and circumstances, while the 5kW turbine showed the highest efficiency, based on the same locations and conditions.

The results of PSD change according to different heights, at different levels of electricity demand and different wind turbine size. It is possible to note that the PSD increases dramatically with height and with low electricity demand for locations that have high AEP, while they increase slightly with height and with high electricity demand for locations that have low AEP.

Chapter 7 **ECONOMICS OF WIND ENERGY INVESTIGATION IN IRAQ**

7.1 **Introduction**

This chapter aims to calculate the Payback Period (PBP) and Levelized Cost of Energy (LCE) based on AEP from four sizes of wind turbine (2kW, 5kW, 10kWand 20kW) that have been estimated at different heights in chapter 6. In addition, the PBP and LCE is calculated based on varying levels of monthly energy demand (1000 to 5000 kWh/month) for the whole of Iraq. The aim of LCE calculation is as follows:

- To determine the lower electricity cost for each wind turbine size at different heights.
- To identify the spatial distribution for the low values of LCE throughout the whole of Iraq based on different turbine sizes, different heights and different levels of demand.
- To determine the most feasible turbines that could produce energy at a lower cost.

The PBP calculations will be performed for each specific wind turbine size based on a saving strategy under the Increasing Block Tariffs (IBT) prices in 2017 and the IBT prices in 2015 according to the Iraqi Electricity Ministry. The PBP calculations aim:

- To recognise the best pricing model that can be applied to attain the shortest PBP within a turbine's lifetime.
- To determine the most reliable and productive locations that are able to achieve a short PBP within a wind turbine's lifespan.
- To determine which are the most feasible turbines that can achieve the shortest PBP.

To carry out the LCE and PBP calculations, information about the total cost of different wind turbine sizes over the lifespan of the turbine project should be available. In fact, the absence of accurate sources of information or a database in Iraq has complicated the process of estimating the capital cost and variable cost of wind turbines throughout the project period. According to these requirements, the main cost categories of wind turbine project have been sized using a new method that has integrated the relative weight for capital and variable expenditure. This technique works on extraction of the relative weight of some costs from the literature, with several equations to estimate variable costs affected by time value over the project's life span.

In this chapter, the capital cost of a wind turbine project has been estimated. It is based on some reliable sources of information in section 7.2.1. After that, the variable cost has been determined by integrating the relative weight of some variable costs with evaluations of the value of Operation and Maintenance (OMC) and Replacement and Spare part Cost (RSC) over the turbine's lifetime, taking the inflation rate and the net interest rate into

consideration, as discussed in section 7.2.2. Evaluating the Total Cost of Project (TCOP) over the project lifetime has been designed based on the Total Present Value (TPV) of a wind turbine, the Present Value of Scrap (PVS) and Capital Recovery Factor (CRF), as outlined in section 7.2.3. The electricity pricing systems in Iraq IBT has been described in section 7.3. The LCE used to estimate the cost of energy production based on different levels of demand has been analysed in section 7.4. In section 7.5 the PBP calculations employed to assess the viability of any project has been suggested, based on saving strategy and different levels of energy demand. Analysis of the results and discussion of LCE and PBP for different sizes of wind turbine have been carried out in section 7.6. The most important results have been summarized in conclusion in section 7.7.

7.2 Economic Methodology

In the beginning, this study attempts to evaluate the main cost categories of wind turbine investment and determine the relative weight for different expenditures. The most important renewable energy studies have broken down the cost of wind power project into capital cost and variable cost [190, 281-283]. Based on the consultation with European Wind Energy Association members (EWEA), the wind turbine investment has been broken down into 80% for the capital cost (Initial cost) and 20% for variable cost (OMC and others) [281].

7.2.1 Capital Cost

The capital cost represents the dominant cost in the total wind turbine project expenditure [282]. Also, the capital cost according to EWEA includes the wind turbine itself, road construction, foundations and grid connection, which can be as much as 80% of the total project cost over its entire lifetime [281]. However, in this study the capital cost will be built based on the price of wind turbine itself (WTC) from manufactory with total Free On Board (FOB) by dollar as well as the sea and land transport plus customs based on customs clearance companies in Iraq. Other costs have been evaluated based on small turbine requirement from different literature. In this project four sizes of small wind turbine have been proposed to supply energy for houses. Senwei Energy Technology Inc has produced economic and reliable fixed pitch wind turbines at different sizes; a number of them have been selected to produce energy in this study, as presented in Table 7-1[279].

First, the capital cost in this project forms 80% of the total cost over the lifespan of the project, which equals 20 years [2]. In addition, the SW-5kW will use such an example in this methodology to follow the calculation steps.

Table 7-1. Presents different wind turbine sizes that have been suggested in this study as well as some important details such as the price of wind turbines in dollars and pounds. **[279]**.

Wind turbine size	Rated power	wind speed		Rotor diameter	Total FOB price in $	Total FOB price in £	TCOP over 20 years
		Cut-in	Rated				
SW-2kW	2kW	2.5m/s	8.0m/s	3.5m	$ 1.968	£ 1476	£ 4733.3
SW-5kW	5kW	2.5m/s	10.0m/s	5.0m	$ 4.842	£ 3631	£ 12799.8
SW-10kW	10kW	3.0m/s	10.0m/s	7.0m	$ 11.702	£ 8776.5	£ 29531.9
SW-20kW	20kW	3.0m/s	10.0m/s	10.0m	$ 19.964	£ 14973	£ 47854.09

The WTC forms 65% of the capital cost based on [282]. According to SW-5kW the price of the WTC with FOB equals £ 3631 from the manufacturer in China. The content of WTC includes [279] :

- Wind turbine body: £ 1732.5.
- Wind turbine controller: £ 547.5.
- Guyed tower: £ 407.2.
- The grid on/off connected inverter: £ 944.25.

Based on the wind turbine price itself and the percentage cost of the wind turbine to the capital cost, it becomes possible to estimate it. Also, other capital expenditures should be considered. The cost of the sea and land transport plus customs cost (SLTC) from China to the installation location in Iraq . The SLTC per one cubic meter of shipment (SLTCm) equals £97/m^3 based on most customs clearance companies in Iraq.

In this study, the sea and land transport plus customs cost SLTC will be calculated for each wind turbine size based on the length of wind turbine blades multiply £97 regardless of the number of blades. For instance, the SLTC for SW-5kW equals £242.5, which form around 5% of capital cost in this study, as expressed in Equation 7-1.

$$SLTC = (RD/2) * SLTCm \qquad \text{Equation 7-1}$$

RD : the rotor diameter of the wind turbine. There are other expenditures that represent 30% of the capital cost that cannot be ignored. Taxes constitute 20% of the price of electrical equipment that is imported to Iraq, which equals £ 1117.4 based on SW-5kW, as expressed in Equation 7-1 [284].

$$Taxes = WTC * 0.2 \qquad \text{Equation 7-1}$$

Moreover, the Installation cost, civil work and foundation (ICF) form 10% of the capital cost [281, 285], which equals £ 558.6, based on SW-5kW, as is expressed in Equation 7-2.

$$ICF = (WTC/0.65) * 0.1 \qquad \text{Equation 7-2}$$

Finally, the capital expenditure will equal £ 5792, based on Equation 7-3.

$$Capex = WTC + SLTC + Taxes + ICF \quad \text{Equation 7-3}$$

This technique has been applied to all four wind turbine sizes in Table 7-1 to calculate the capital cost for each turbine in this project.

7.2.2 **Variable cost**

The second important part of the total cost of a wind turbine over the lifespan of the project is the variable cost. The variable cost is not as well-known as capital cost due to the categories varying from size to size, site to site and country to country. In addition, a small number of turbines have reached the end of their project's lifespan [281]. However, in this study the variable cost forms 20% of the total cost over the lifetime of the project [281]. Furthermore, the variable cost categories in this study have been determined based on numbers of requirements and evident in the literature:

- Firstly, in this project small wind turbine sizes have been suggested for supplying energy to houses or a small community that includes several houses without selling electricity to the national grid.
- Secondly, the default lifetime is 20 years for these turbines.

The variable cost in this study has been broken down into several categories with different percentages of variable cost. These percentages were selected from the literature to calculate a primitive cost for some of the following categories [281]:

- Operation and Maintenance cost (OMC) forms 12% of the variable cost to calculate a primitive value (2 - 3% of capital cost [103]).
- Replacement and spare part cost (RSC) form 26% of variable cost.
- Insurance cost forms 13% of variable cost.
- Land cost or land rent form 18% of the variable cost.
- Other costs form 31% of variable cost.

With respect to the OMC , there are two choices: first, to sign a contract with a company to manage maintenance over project lifespan; second, to estimate the cost of OMC over the turbine's lifetime, taking the inflation rate and the net interest rate into consideration and using the percentage of 12% of the variable cost as primitive value. Furthermore, the RSC is also rather complicated as it is difficult to determine the number and size of replacement, even with a warranty. In fact, the percentage of replacement, which equals 26% of variable cost, is still acceptable concerning the cheap and secondary spare parts in wind turbine. However, here is a possibility of generator failure even after the warranty period expires. In this case, the RSC percentage which equals 26% of variable cost cannot cover the cost of generator failure replacement. In addition, there is another opinion regarding the cost of

replacement as equal to the turbine cost [103]. For these reasons, the OMC and RSC costs will be estimated over the lifespan of the project to make the evaluation process of total project cost related to time value [281, 285-287]. In order to estimate the OMC over 20 years, Equation 7-4 has been applied [286, 287]:

$$OMC = OMC_0 \left(\frac{1+i}{r-i}\right)\left(1-\left(\frac{1+i}{1+r}\right)^T\right) \qquad r \neq i$$
$$OMC = OMC_0 * T \qquad r = i \qquad \text{Equation 7-4}$$

- OMC: Operation and Maintenance Cost for 20 years.
- OMC_0: represents the initial cost of operation and maintenance for the first year of project equal 12% of variable cost.
- T: represents the lifetime of project = 20 years.
- $r = 4\%$ is the net interest rate for investment and residential loans in Iraq in 2018 [288].
- $i = 4\%$ is the inflation rate in Iraq in 2018 [289].

On the other hand, replacement of the wind turbine generator for one time over 20 years is regarded as the worst scenario that has been taken into consideration to estimate the RSC over 20 years in this study. This part represents the most expensive part of the wind turbine that is possible to be damaged over the lifespan (turbine generator). The RSC can be estimated by the following equation [286, 287].

$$RSC = \sum_{j=1}^{N_{rep}} \left(C_{nom} * C_{unit} * \left(\frac{1+i}{1+r}\right)^{T*j/N_{rep}+1} \right) \qquad \text{Equation 7-5}$$

- C_{nom}: is the nominal capacity of a replacement unit in watt.
- While C_{unit}: represents the price of replacement unit £/Watt.
- N_{rep}: refers to the number of replacement over the lifespan of a turbine which assumed only one replacement (turbine generator).

Finally, in order to estimate the variable cost VC over the project lifetime, Equation 7-6 should be applied.

$$VC = OMC + RSC + Land\ cost + Insurance\ cost + Other\ cost \qquad \text{Equation 7-6}$$

7.2.3 **The Total Cost of Project**

It is vital for governments and investors to evaluate the total cost of the project. It looks obvious that the total cost of the project is far from simple when compared to the Total Present value (TPV) of a project with a lifetime of a project. In addition, another factor should be taken into account when evaluating the total cost of a project. In fact, the present value of a wind turbine scrapped at the end of project could not be ignored when calculating the TPV of wind turbine project. PVS is the present value of scrap, which is expressed in terms of the value of scrap SV = 5% of the wind turbine itself at the end of wind turbine lifespan, as expressed in Equation 7-7 [287].

$$PVS = \sum_{j=1}^{N_{rep}} SV * \left(\frac{1+i}{1+r}\right)^{T*j/N_{rep}+1} \quad \text{Equation 7-7}$$

N_{rep}: refers to the number of scrap components at the end the lifespan of a project, which represents the wind turbine itself. According to this additional factor, the TPV of the project can be expressed in Equation 7-8 as follows:

$$TPV = Capex + VC - PVS \quad \text{Equation 7-8}$$

When we discuss the total cost of the project over the turbine's lifespan, it is imperative to distinguish between the total present value and the lifetime value of the project. In order to estimate the time value of total project cost over the project lifespan, the CRF should be used. CRF transforms a present value into series of equal annual payments over a specified time, according to specified interest rate [212], as expressed in Equation 7-9.

$$CRF = \frac{r\,(1+r)^T}{(1+r)^T - 1} \quad \text{Equation 7-9}$$

r : the interest rate. T: the lifetime of project. In order to calculate the Levelized annual costs LAC, which represents the annual payment of TPV of project based on CRF look at the following expression in Equation 7-10[212].

$$LAC = TPV * CRF \quad \text{Equation 7-10}$$

According to the Levelized annual costs in Equation 7-10, it becomes possible to calculate the TCOP over the project lifetime, as expressed in Equation 7-11.

$$TCOP = (TPV * CRF) * T \qquad \text{Equation 7-11}$$

The TCOP value is instrumental in estimating PBP for several wind turbines in this study. Also, it is essential to calculate the cost of electricity production from several wind turbines by applying LCE. Finally, the TCOP for the four turbines in this study have generally reached approximately three times the original prices for each one, as is revealed in Table 7-1 depending on the above methodology.

7.3 The cost of energy in Iraq

In the last ten years, the Iraqi government has applied the Increasing Block Tariffs (IBT) prices as a pricing policy. The electricity price was reduced twice in 2015 and 2017 as is presented in Figure 7-1, due to the political crises and widespread protests against poor services.

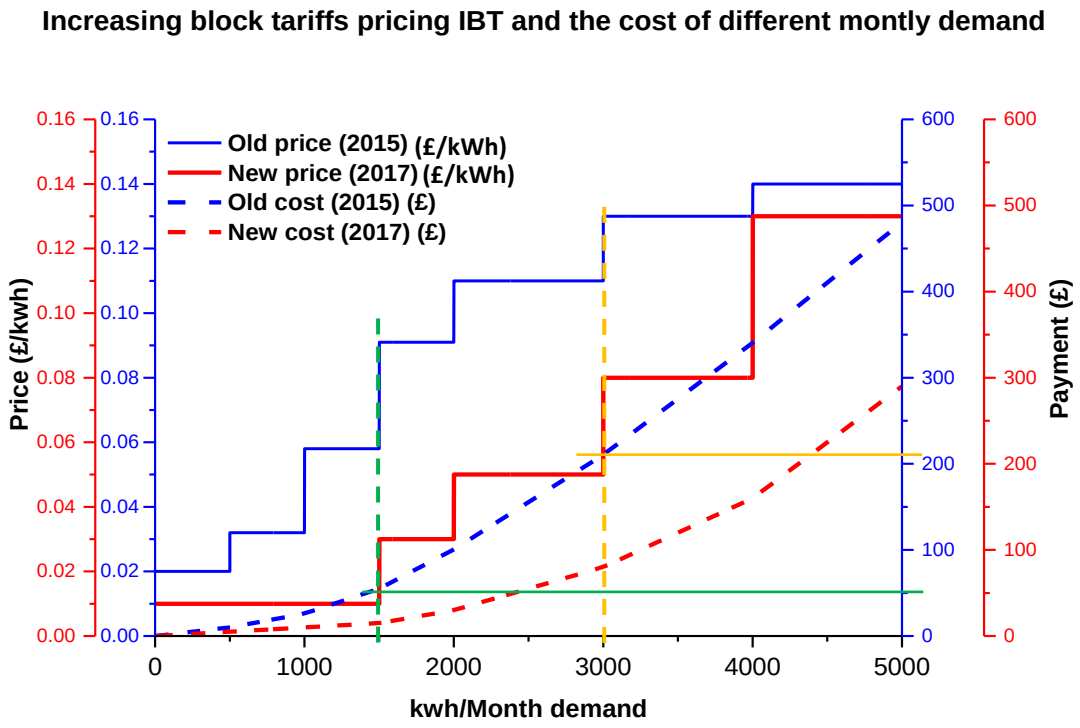

Figure 7-1. Presents two curves of marginal price; the solid blue line represents IBT in 2015, and the solid red line represents IBT in 2017. This Figure also shows the cost of various levels of demand: the blue dashed line represents the cost of consumption in 2015 and the red dashed line represents the cost of consumption in 2017

Figure 7-1 was created to figure out the levels of marginal prices reported bills which were scheduled in 2015 and 2017 respectively, as well as the calculation of possible costs for different levels of monthly electricity consumption. In fact, the IBT in 2017 was lower than

the IBT in 2015, as shown in Figure 7-1, where this represents a discouraging indicator of energy investment in Iraq.

Figure 7-1 provides an excellent view to assessing the cost of consumption based on any level of demand for both the marginal prices in 2015 and 2017. In addition, the cost of consumption increases dramatically with increasing the level of demand. Alternatively, the marginal price might be useful when covering the high cost of high consumption with power production from a wind turbine.

For example, if a level of monthly demand is 3000 kWh/month (orange dashed line), the householder will pay just £ 210 (solid orange line) for national grid, according to the marginal price in 2015 (solid blue line). If the wind turbine generates 1500 kWh/month (green dashed line), according to marginal price in 2015 (solid blue line), the householder will pay just £ 55 (green s line) for national grid, based on the remaining energy demand (that do not cover by power production from wind turbine), which is equal 1500 kWh/month. In this case, the householder will save £ 155 per this month. According to this example, the saving strategy that depends on IBT and different levels of demand considered is more realistic and has shown a good trend because it is not possible to consume all power production from wind turbines when the energy produced exceeds the limits of need. According to the last reasons, a saving strategy will be applied by covering different levels of energy demand (that ranges from 1000 to 5000 kWh/month) by producing power from different sizes of wind turbine when estimating the PBP and the LCE for all of Iraq.

7.4 **Levelized Cost of Electricity .**

The Levelized Cost of Electricity (LCE) of renewables technologies varies according to the different variables such as the renewables resources availability, capital and variable costs, and the efficiency/ performance of renewables technologies [282]. In general, the LCE is defined as the ratio of total annualized project cost (Levelized annual costs) based on annual discounting financial flow to the AEP from the project as is expressed in Equation 7-12[290].

$$LCE = \frac{TPV * CRF}{AEP} \qquad \text{Equation 7-12}$$

TPV: Total present value of project. CRF: Capital Recovery Factor which recovers the time value of money. AEP : The annual energy production from different sizes of wind turbines. Equation 7-12 calculates the electricity price based on the principle of consuming all electricity that is generated from different wind turbine sizes without taking into consideration the capacity of demand if it is higher or lower than power production.

Indeed, it is not reasonable to account for the amount of generated electricity from wind turbine that might exceed the potential energy demand and which will never be used again. For this reason, the saving strategy that was proposed in the last section will be applied in the LCE calculation, based on different scenarios of energy demand against different amounts of AEP from different sizes of wind turbine. The energy demand which was suggested in this study ranges from 1000 to 5000 kWh/month, while, the AEP that have been estimated according to the 2kW, 5kW, 10kW and 20kW at different heights in Chapter 6 will be used in LCE calculations. Equation 7-12 has been modified as is expressed in Equation 7-13 to meet the requirement of different monthly demand.

$$LCE = \frac{TPV * CRF}{(MEP \leq MD_i) * 12} \qquad \text{Equation 7-13}$$

MEP: represents the monthly energy production = AEP/12. While, MD_i: represents monthly demand at different levels: MD_1= 1000 kWh/month, MD_2= 2000 kWh/month, MD_3= 3000 kWh/month, MD_4= 4000 kWh/month and MD_5= 5000 kWh/month. In addition, 12 refers to the number of months per year to calculate the AEP. The LCE calculations aim to determine the lower cost of energy production and the location distribution of lower cost that have been generated by different sizes of wind turbine at different heights.

7.5 Payback Period

The payback period (PBP) is the length of period that is required to recover the cost of a project based on the net annual cash inflow from the project itself [26]. In this work, the total cost of project (TCOP) over the project's lifespan will be taken into account when we calculate the PBP as is expressed in Equation 7-14.

$$PBP = \frac{TCOP}{Net\ Annual\ Cash\ inflow\ of\ AEP} \qquad \text{Equation 7-14}$$

In addition, the saving strategy that has been suggested in section 7.3 will be used, rather than the net annual cash inflow. In other words, the PBP in this study is an estimate based on TCOP divided by saving money, based on different levels of demand and IBT in Iraq. Furthermore, the PBP in this study is calculated based on IBT in 2015 and IBT in 2017 as mentioned in section 7.3, in order to examine which price is more feasible. The payback period equation that used in this study is expressed in Equation 7-15.

$$PBP = \frac{(TPV * CRF) * T}{AnnSavCost} \qquad \text{Equation 7-15}$$

$AnnSavCost$: represents Annual Saving Cost, which in this study that has been estimated based on Equation 7-16.

$$AnnSavCost = \left(CostMD_i - Cost\left(MD_i - (MEP \leq MD_i)\right)\right) * 12 \qquad \text{Equation 7-16}$$

$MEP \leq MD_i$: represents the monthly energy production = AEP/12 that does not exceed MD_i : the monthly level of energy demand which ranges from 1000 to 5000 kWh/month. $CostMD_i$: represents the cost of monthly demand based on IBT in 2015 or 2017 in Iraq as presented in section 7.3. $Cost\left(MD_i - (MEP \leq MD_i)\right)$: refers to the cost of rest monthly demand after covering the MD_i by MEP from specific wind turbine. The cost of rest monthly demand has been estimated based on the same IBT that was used with $CostMD_i$. The AnnSavCos has been estimated based on summation of 12 months of saving cost $\left(CostMD_i - Cost\left(MD_i - (MPE \leq MD_i)\right)\right)$. Finally, it is worth mentioning that the PBP based on saving cost will be calculate for the whole of Iraq, based on the IBT in 2015 and 2017 and for four sizes of wind turbine as is outlined in Figure 7-1and at five heights: 10m, 15m, 20m, 25m and 30m. The PBP calculation aims to determine which wind turbine size can provide lower PBP throughout the lifetime of turbine project, with 8 years as the best scenario according to reviews studies [291, 292]. Also, to determine the locations that can show short PBP throughout the lifetime of the turbine and within 8 years. In fact, there are several considerations behind selecting 8 years as the maximum PBP for turbines that have been chosen in this study:

- The turbine that can achieve 8 years of PBP or lower than that, which is considered a reliable turbine in this location and eligible for nomination to the optimal hybrid system in the next work.
- The condition of determining 8 years of PBP is useful to replace the old turbine with new technology, to keep the high performance of the wind turbine away from deterioration.
- The area that is able to achieve PBP of less than 8 years or lower is considered a promising and feasible area to invest or install the wind turbine.

7.6 Result analysis and discussion

In this section, the results of LCE calculations will be analysed based on different sizes of wind turbine in Table 7-1 and at different heights (10 m, 15 m, 20 m, 25 m and 30 m), based on varying levels of energy demand (from 1000 to 5000 kWh/month). Also, the results of PBP calculations are analysed based on the same sizes of wind turbine and at the same heights and also based on the saving strategy and the same levels of energy demand that were suggested in section 1.5.

7.6.1 **SW-2kW**

7.6.1.1 **LCE calculation for SW-2kW**

SW-2kW is the smallest wind turbine size that has been suggested to supply housing units with electricity. The LCE has been estimated for the whole of Iraq, based on AEP from SW-2kW at 10 m, 15 m, 20 m, 25 m and 30 m hub heights (as represented in Figure 6-10 in Chapter 6), based on a different level of demand from 1000 to 5000 kWh/month. Figure 7-2A, C and D show the boxplots of the LCE distribution for varying levels of demand, different heights and for more than 8 millions pixels in Iraq map (Figure 7-2B).

Figure 7-2 reveals three points of significance. First, the LCE is decreased from 10 m to 30 m at hub height due to increasing the AEP with height. The second interesting point is that all LCE boxplots in Figure 7-2 have shown the same distribution for all levels of demand at different heights because the maximum and minimum monthly energy production MEP from 10 m to 30 m is lower than 1000 kWh/month according to Figure 6-10D in Chapter 6. The third exciting observation is that in Figure 7-2, around 25% of locations in Iraq distribute between 0.1 £/kWh (lower quartile) and 0.0475 £/kWh (lower whisker) for all levels of demand. The sites that have shown lower prices distribute among the blue areas that represent lakes in Iraq, light blue areas that spread over southeast of Iraq and the green area that extends from northwest to south of Iraq as is shown in Figure 7-2B. The minimum and maximum LCE values have been inserted in Table 7-2 to show to what extent the amount of LCE changes with height as well as to present the LCE value for the most productive area in Iraq that forms around 25% of Iraq locations.

Table 7-2. The minimum and maximum LCE from WS-2kW at different heights and the lower LCE quartile that represents the most productive area in Iraq, which forms 25% of locations in Iraq.

LCE level	Min LCE	Max LCE	The lower LCE quartile
LCE at 10m	0.0475 £/kWh	673.8 £/kWh	Ranges from 0.095 to 0.05 £/kWh
LCE at 15m	0.0447 £/kWh	2.879 £/kWh	Ranges from 0.082 to 0.043 £/kWh
LCE at 20m	0.0430 £/kWh	1.208 £/kWh	Ranges from 0.079 to 0.0415 £/kWh
LCE at 25m	0.0418 £/kWh	0.814 £/kWh	Ranges from 0.075 to 0.041 £/kWh
LCE at 30m	0.0410 £/kWh	0.661 £/kWh	Ranges from 0.071 to 0.0405 £/kWh

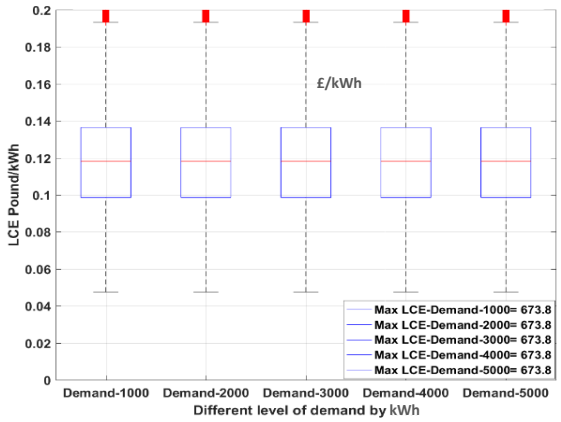

Figure A

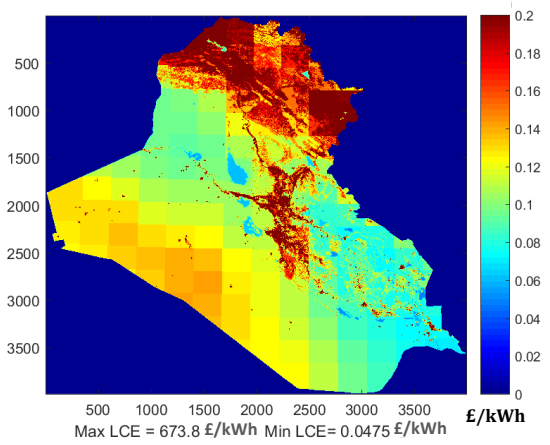

Figure B

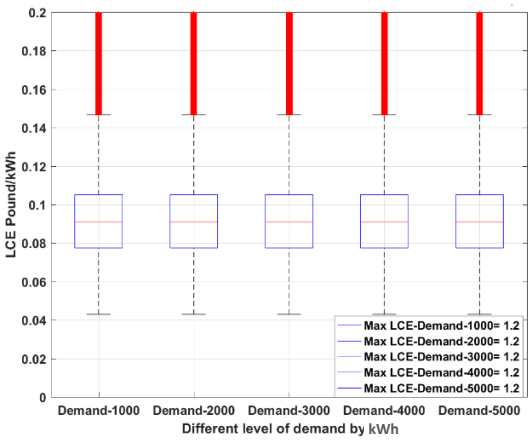

Figure C

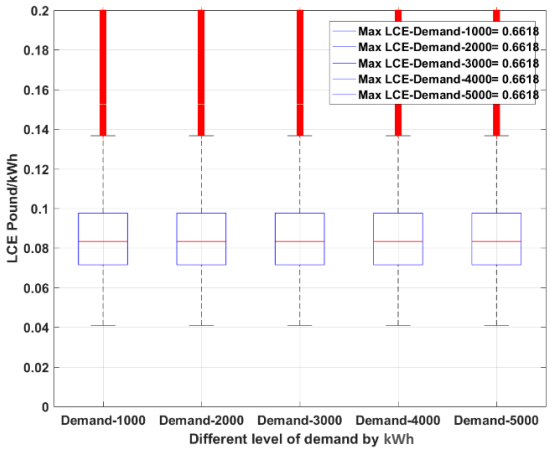

Figure D

Figure 7-2. LCE boxplot distribution for 2kW wind turbine size at 10m in Figure A, 20m in Figure C and 30m in Figure D for different levels of demand from 1000 to 5000 kWh/month. Large boxes are the interquartile range showing the 25th, 50th and 75th percentile values, whiskers are the 5th, and 95th percentile values and crosses are the 1st and 99th percentile values of each sample. Figure B Shows LCE map for 2kW wind turbine size at 10m based on AEP of 2kW in 2014 and 5000 kWh/month demand

7.6.1.2 **PBP calculation for SW-2kW**

The PBP for SW-2kW turbine has been calculated at different heights (10 m, 15 m, 20 m, 25 m and 30 m) and for varying levels of demand from 1000 to 5000 kWh/month based on IBT prices in 2017 and IBT prices in 2015. Figure 7-3A and B show the PBP for 2kW turbine sizes from 10 m to 30 m respectively, based on IBT prices in 2017 and for different levels of demand. At first glance over the two figures, it possible to summarize the most important findings from PBP calculation based on IBT in 2017 that SW-2kW was able to achieve PBP < 20 years:

- The 3000 kWh/month of energy demand has only achieved PBP for tiny areas that are concentrated over lakes in Iraq.
- The 2000 and 1000 kWh/month demands have failed to make any PBP of less than 20 years, as shown in Figure 7-3A and B and also Table **7-3**.
- In general, the PBP for all levels of demand has been reduced with the height increasing.

- Although the 2017 prices are too low, the SW-2kW turbine has shown acceptable PBP of less than 20 years, due to the reduction of the TCOP in comparison with size of saving.

Table 7-3. Reveals the minimum PBP that achieved by SW-2kW by using IBT prices in 2017 and based on different heights at the left column and different levels of monthly demand at the first row.

Hub height	1000 kWh/month demand	2000 kWh/month demand	3000 kWh/month demand	4000 kWh/month demand	5000 kWh/month demand
10m	39.4 years	31.6 years	19 years	11.88 years	7.3 years
15m	39.4 years	29.8 years	17.8 years	11.17 years	6.87 years
20m	39.4 years	28.6 years	17.1 years	10.74 years	6.61 years
25m	39.4 years	27.8 years	16.7 years	10.4 years	6.4 years
30m	39.4 years	27.3 years	16.3 years	10.2 years	6.3 years

With respect to the PBP calculation based on IBT prices in 2015, Figure 7-4A and B show the PBP for 2kW turbine size from 10 m to 30 m based on IBT in 2015 and for different levels of demand. We now come to the most important findings that can be summarized from PBP calculation based on IBT in 2015:

- The 5000, 4000, 3000 and 2000 kWh/month of energy demand have achieved PBP of less than 20 years with different percentage of areas that cover Iraq across the five heights from 10 m to 30 m.
- In addition, when comparing the results of PBP between 2015 IBT and 2017 IBT, many locations achieved PBP of less than 20 years according to 3000 kWh/month of demand, based on 2015 IBT against the same level of demand based on 2017 IBT.
- The 2kW turbine has achieved PBP of less than 20 years for quarter of locations in Iraq, based on 2000 kWh/month of energy demand, based on the 2015 IBT in Figure 7-4A and B. While the same level of demand based on 2017 IBT failed to achieve any PBP of less than 20 years, as shown in Figure 7-3A and B.
- Furthermore, it is clear that the PBP for all levels of demand was creeping gradually towards 20 years when the height was increasing from 10m to 30m.
- According to Table 7-4 and Figure 7-4A and B, the 1000 and 2000 kWh/month of energy demand failed to attain PBP of less than 20 years across all the heights.
- In addition, the PBP decreased with increasing the level of demand and also with increasing the level of height, as shown in Figure 7-4A and B and also Table 7-4.

For more analysis to raise reliability on wind turbine performance and also to determine the most reliable and productive locations in Iraq, the calculation of PBP within 8 years has been applied based on the 2017 and 2015 IBT. The results show the SW-2kW can achieve PBP within 8 years that ranges from 7.3 years for 5000 kWh/month demand at 10m to 6.3 years at 30 m for the same level of demand as is revealed in Table 7-3.

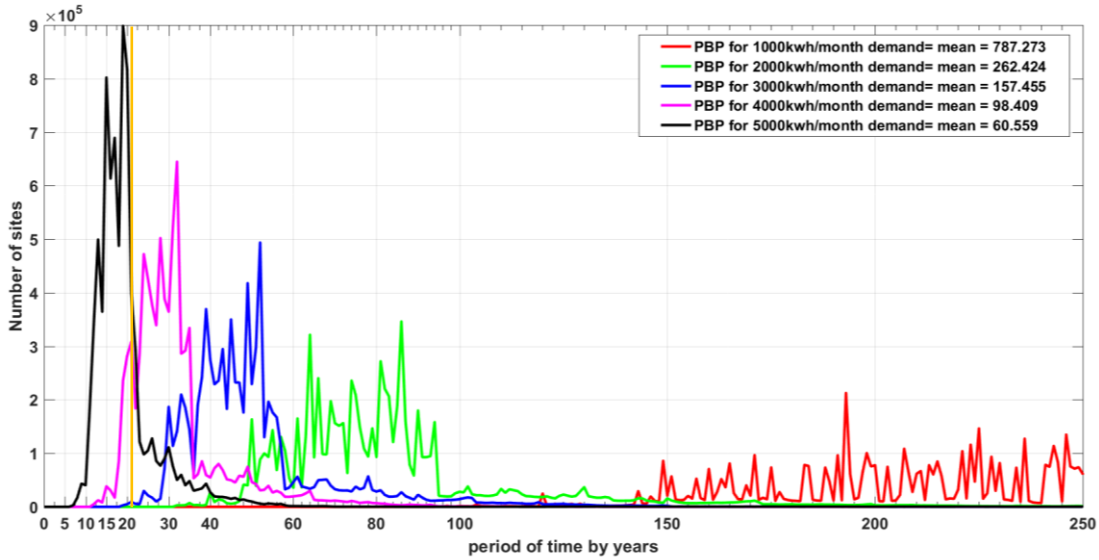

Figure A

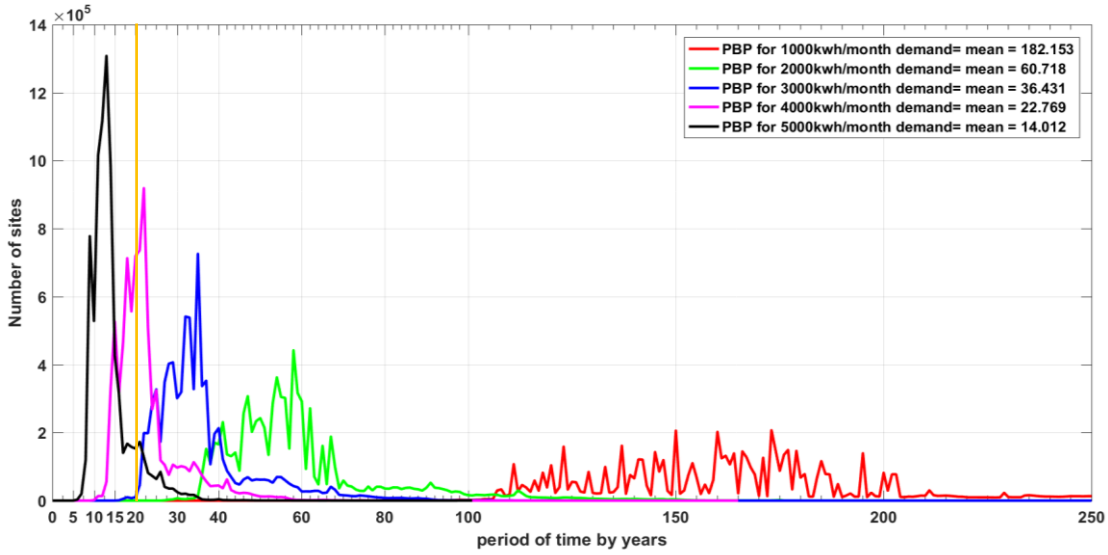

Figure B

Figure 7-3. The PBP for SW-2kW based on IBT prices in 2017 for different levels of demand at 10m in Figure A and at 30m in Figure B.

Table 7-4. Reveals the minimum PBP achieved by SW-2kW using IBT prices in 2015 and based on different heights at the left column and different levels of monthly demand at the first row

Hub height	1000 kWh/month demand	2000 kWh/month demand	3000 kWh/month demand	4000 kWh/month demand	5000 kWh/month demand
10m	29.7 years	8.3 years	8.6 years	7.31 years	6.78 years
15m	27.9 years	9.8 years	8.12 years	6.87 years	6.38 years
20m	26.8 years	9.44 years	7.8 years	6.61 years	6.13 years
25m	26.1 years	9.1 years	7.5 years	6.4 years	5.9 years
30m	25.5 years	9 years	7.4 years	6.3 years	5.85 years

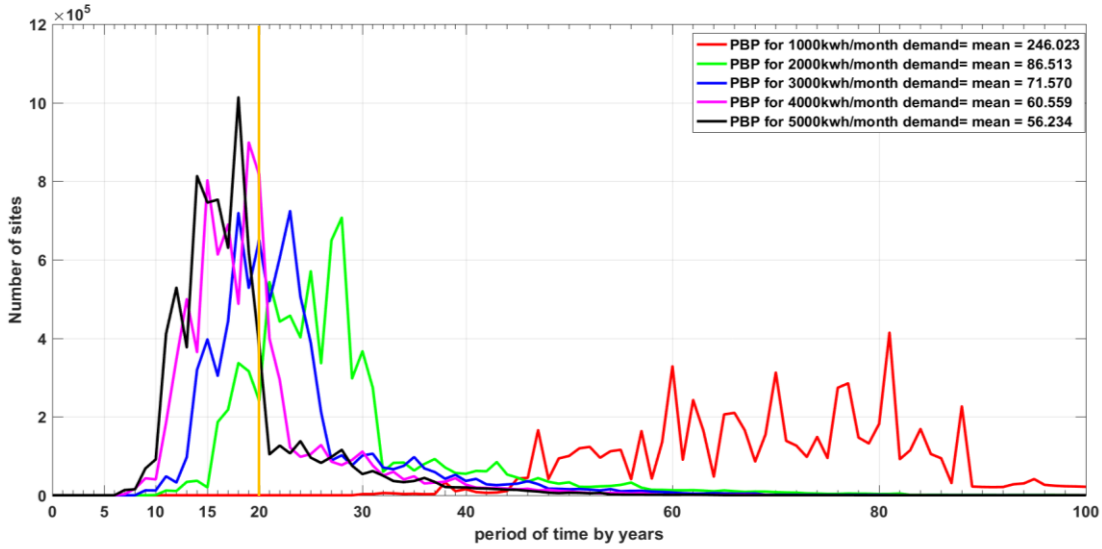

Figure A

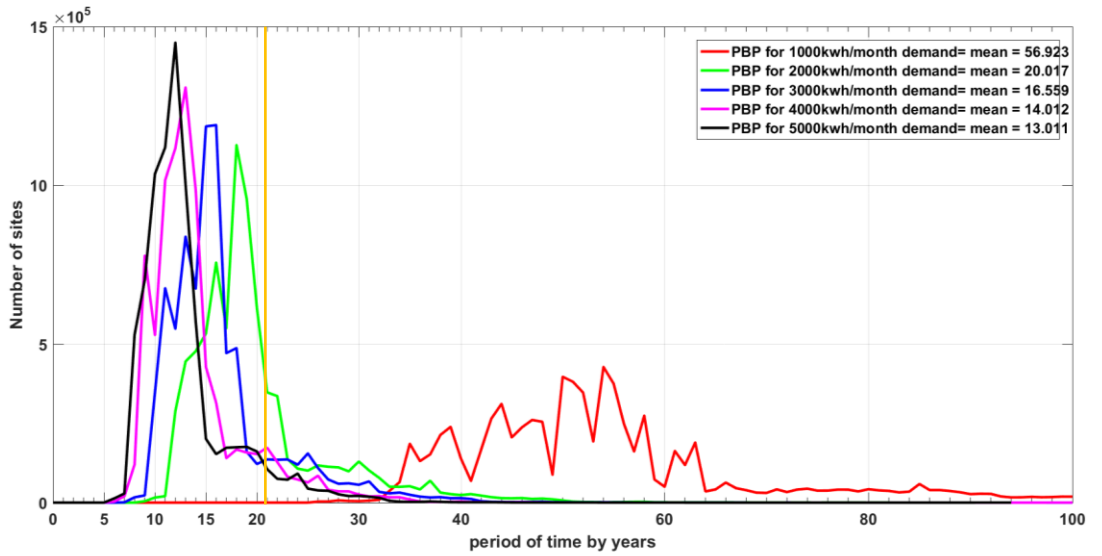

Figure B

Figure 7-4. The PBP for SW-2kW based on IBT prices in 2015 for different levels of demand at 10m in Figure A and at 30m in Figure B.

While according to Figure 7-5 and Figure 7-6 it is possible to note that the areas that have achieved PBP lower than 8 years focusing above lakes and marshlands in the southeast of Iraq and these areas expand with raising the height from 10 m to 30 m.

Concerning PBP of less than 8 years based on the 2015 IBT, the results show that the SW-2kW can achieve PBP of less than 8 years in terms of 5000, 4000 and 3000 kWh/month of energy demand at different heights (Table 7-4). Figure 7-6 shows how the areas of PBP of less than 8 years for 5000 kWh/month of energy demand have extended from water bodies in the south-eastern of Iraq to the land that is located around lakes and marshlands as well as some lakes in the north western of Iraq after applying the 2015 IBT.

There are three important finding that can be summarized from PBP calculation based on 2017 and 2015 IBT, that the SW-2kW able to achieve PBP lower 8 years:

- Firstly, the SW-2kW has achieved PBP lower than 8 years based on 2017 IBT prices that are regarded as very low prices in comparison with 2015 IBT prices. However, the PBP of less than 8 years - based on 2017 IBT prices - is fruitful just with 5000 kWh/month demand.
- Secondly, the PBP of less than 8 years based on 2015 IBT prices has shown better results in comparison with 2017 IBT and achieved PBP with 3000, 4000, 5000 kWh/month demand.
- Thirdly, the most important finding from these results that the areas that achieved PBP of less than 8 years according to 2017 IBT prices are regarded as the most significant area for wind power technology (as shown Figure 7-5A) because these areas have achieved PBP of less than 8 years, despite the low prices of electricity and the low altitude for hub height. According to these results, the SW-2kW is considered the most suitable turbine to supply housing units with electricity for locations that have appeared in Figure 7-5 and Figure 7-6 and also this turbine is considered as one of best candidate turbines to work with optimal design for renewable hybrid system in the next work.

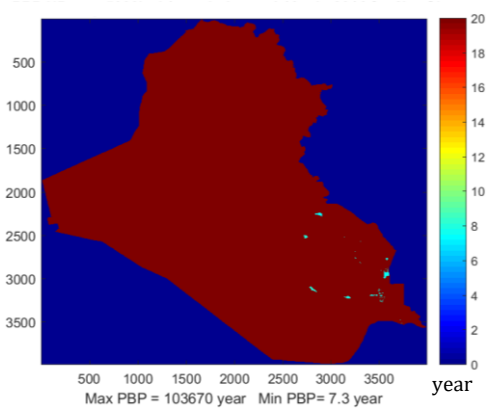

Figure A

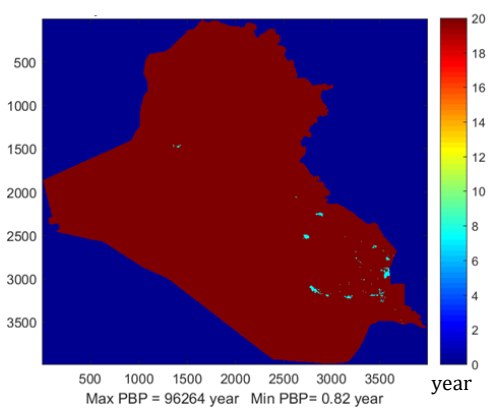

Figure A

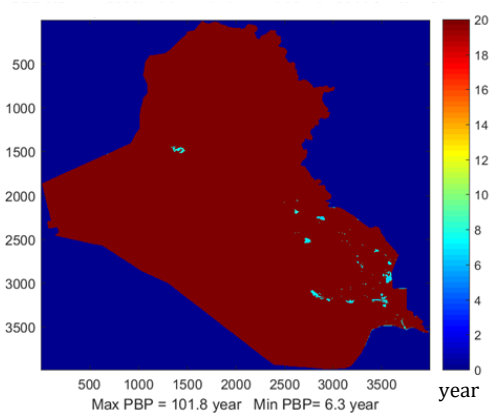

Figure B

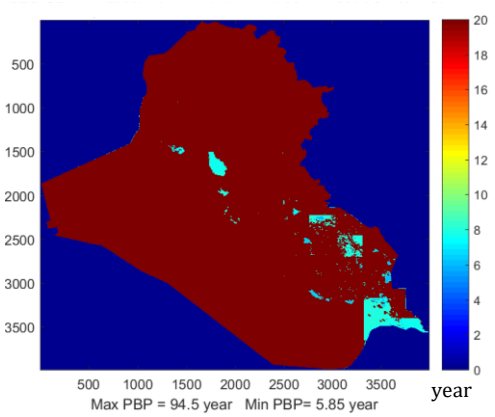

Figure B

Figure 7-5. The distribution of PBP of less than 8 years, based on the IBT in 2017 at 10m in Figure A and at 30m in Figure B for 5000 kWh/month demand

Figure 7-6. The distribution of PBP of less than 8 years, based on the IBT in 2015 at 10m in Figure A and at 30m in Figure B for 5000 kWh/month demand

7.6.2 **SW-5kW**

7.6.2.1 **LCE calculation for SW-5kW**

SW-5kW is the second small wind turbine size that has been suggested in this work. The LCE in this section has been calculated based on AEP from 5kW wind turbine size at different heights as represented in Figure 6-13B and D in the previous chapter and based on the different levels of energy demand. Figure 7-7A, C and D show the boxplots of the LCE distribution for varying levels of energy demand at different heights for more than 8 millions pixels in Iraq (as shown in Figure 7-7B).

At first glance Figure 7-7 shows two things that are striking. First, the difference between the lowest LCE that has been recorded at 10m for 1000 kWh/month (0.0533 £/kWh) and the lowest LCE that has been recorded at 10m, based on energy demand from 2000 to 5000 kWh/month (0.0363 £/kWh). This difference in returns to the LCE has been estimated based on 1000 kWh/month of monthly energy demand as limitation, rather than 1467.3 kWh/month, which is the highest MEP that has been generated by 5kW turbine size at 10m according to Figure 6-13B in Chapter 6.

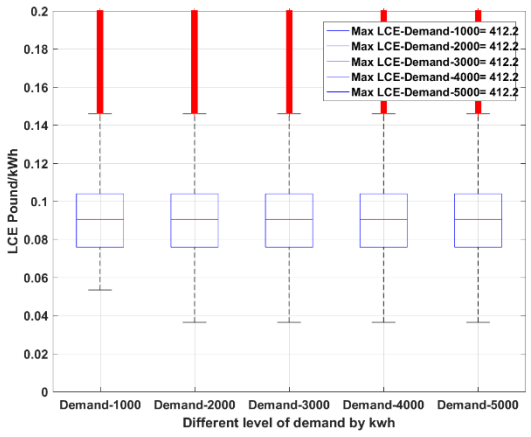

Figure A

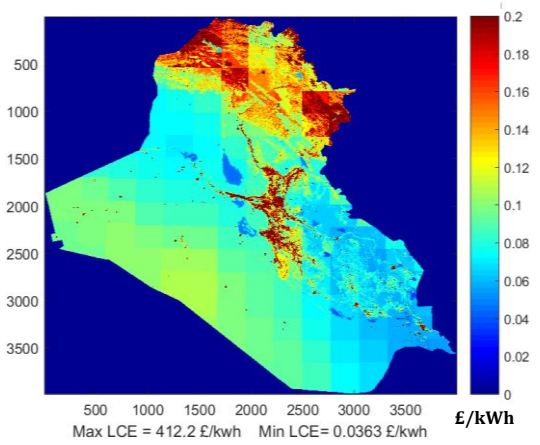

Figure B

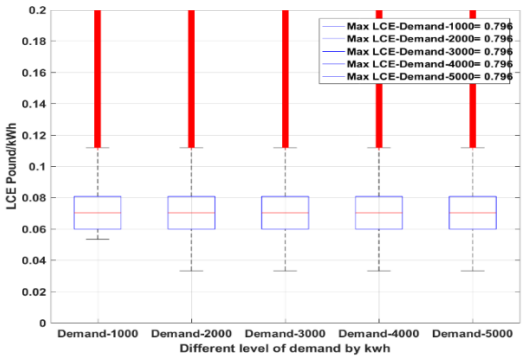

Figure C

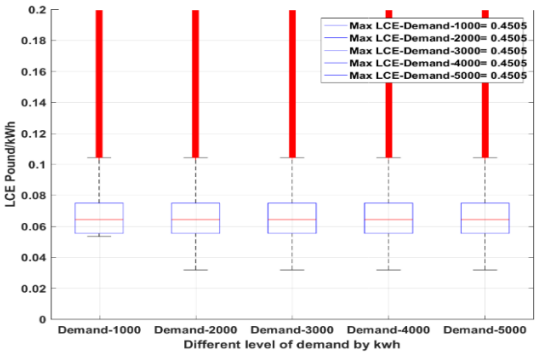

Figure D

Figure 7-7. LCE boxplot distribution for 5kW wind turbine size at 10m in Figure A, 20m in Figure C and 30m in Figure D for different levels of demands from 1000 to 5000 kWh/month. Figure B Shows LCE map for 5kW wind turbine size at 10m based on AEP of 5kW in 2014 and 5000 kWh/month demand

The second exciting observation is the similarity among the Lowest LCE values for 2000 to 5000 kWh/month. The reason for this similarity of returns is that the maximum MEP from 5kW turbine (1467.3 kWh/month) is lower than the monthly demand from 2000 to 5000 kWh/month. According to Figure 7-7A, C and D around 25% of locations in Iraq between lower quartile and lower whisker from 2000 to 5000 kWh/month of demand have lower prices that distribute among the blue areas (represent lakes), light blue regions spread over the south-east of Iraq and the green area which extended from northwest to south of Iraq as is shown in Figure 7-7B.

In addition, it is noted that the LCE from 2000 to 5000 kWh/month demand gradually decreased from 10 m to 30 m because of increasing the AEP with height. The most important finding that can be summarized from this section, is that the SW-5kW has shown LCE values lower than the LCE of SW-2kW in section 7.6.1.1, when comparing the values of LCE in Table 7-5 with those in Table 7-2.

Table 7-5. The minimum and maximum LCE from WS-5kW at different heights and for 1000 and 2000-5000 kWh/month demand and also the lower LCE quartile that represents the most productive area in Iraq which forms 25% of locations in Iraq for 2000-5000 kWh/month demand

	LCE for 1000 kWh/month demand			LCE for 2000 – 5000 kWh/month demand		
LCE level of height	Min LCE £/kWh	Max LCE £/kWh	The lower LCE quartile	Min LCE £/kWh	Max LCE £/kWh	The lower LCE quartile
LCE at 10m	0.0533	412.2	From 0.076 to 0.0533	0.0363	412.2	From 0.076 to 0.0363
LCE at 15m	0.0533	1.802	From 0.067 to 0.0533	0.0343	1.802	From 0.067 to 0.0343
LCE at 20m	0.0533	0.7966	From 0.06 to 0.0533	0.0330	0.7966	From 0.06 to 0.0330
LCE at 25m	0.0533	0.5501	From 0.056 to 0.0533	0.0322	0.5501	From 0.056 to 0.0322
LCE at 30m	0.0533	0.4505	From 0.055 to 0.0533	0.0317	0.4505	From 0.055 to 0.0317

7.6.2.2 **PBP calculation for SW-5kW**

The PBP for SW-5kW turbine has been calculated at different heights (10 m, 15 m, 20 m, 25 m and 30 m) and for varying levels of demand (1000 to 5000 kWh/month) based on 2017 IBT prices and 2015 IBT prices. Figure 7-8A and B show the results of PBP for 5kW turbine size from 10m to 30m, respectively based on IBT in 2017 and for different levels of demand. At first glance over the two Figures, it is possible to note that 5000, 4000 and 3000 kWh/month of electricity demand achieved PBP of less than 20 years across the five heights from 10 m to 30 m.

In comparison between PBP for SW-2kW and SW-5kW based on 2017 IBT prices, it is possible to note that the SW-5kW turbine has achieved PBP shorter than the SW-2kW. Whereas the PBP based on 3000 kWh/month of energy demand showed that approximately 25% of locations in Iraq at 30 m achieved a PBP of less than 20 years. Moreover, the minimum PBP results for SW-5kW at different heights and for different levels of demands in Table 7-6 show values lower than the minimum PBP results of SW-2kW in Table 7-3. There are different reasons behind shrinking the PBP for SW-5kW:

- Firstly, the AEP for SW-5kW is higher than SW-2kW.
- Secondly, the CF of SW-5kW is higher than SW-2kW as is presented in Chapter 6.

Notably, the PBP at 106.6 years was based on 1000 kWh/month demand and 35.5 years based on 2000 kWh/month demand over five heights in Table 7-6. The reason for these returns to the monthly demand limitation itself according to the saving strategy and IBT price for this demand.

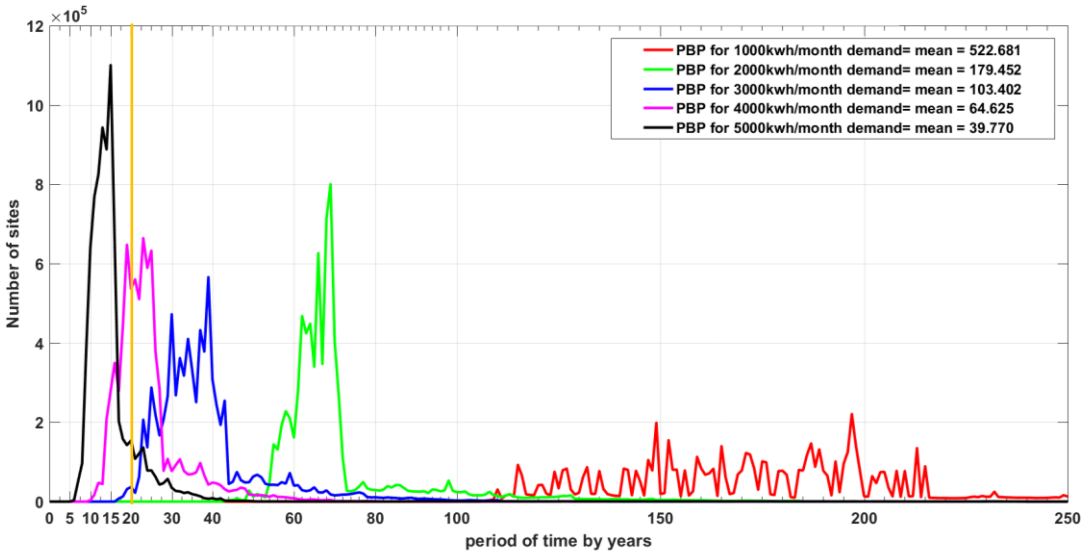

Figure A

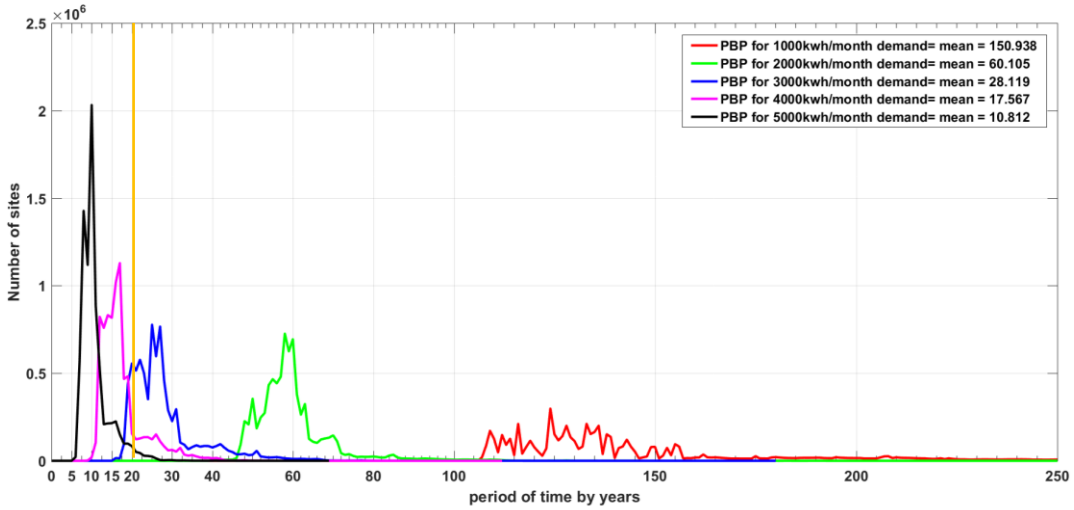

Figure B

Figure 7-8. The PBP for SW-5kW based on IBT prices in 2017 for different levels of demand at 10m in Figure A and at 30m in Figure B.

Table 7-6- The minimum PBP achieved by SW-5kW using 2017 IBT prices, based on different heights at the left column and different levels of monthly demand at the first row

Hub height	1000 kWh/month demand	2000 kWh/month demand	3000 kWh/month demand	4000 kWh/month demand	5000 kWh/month demand
10m	106.6 years	35.5 years	16.6 years	10.3 years	6.3 years
15m	106.6 years	35.5 years	16.2 years	9.8 years	6.1 years
20m	106.6 years	35.5 years	16.1 years	9.6 years	5.9 years
25m	106.6 years	35.5 years	16 years	9.4 years	5.8 years
30m	106.6 years	35.5 years	15.9 years	9.3 years	5.7 years

In addition, it is noted that the PBP for 1000, 2000 and 3000 kWh/month of electricity demand was concentrated gradually close to lower PBP for each level of demand when the height was increasing from 10 m to 30 m according to Figure 7-8A and B. And that, in turn, will lead to an increase in the areas that have achieved PBP of less than 20 years for SW-5kW more than what SW-2kW can be achieve at the same level of demand and height (see Figure 7-9A and B).

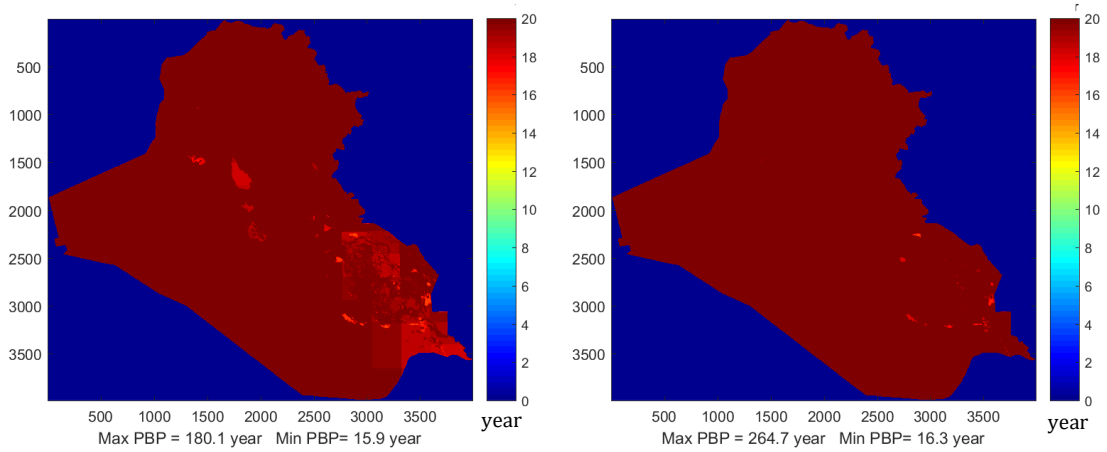

Figure A Figure B

Figure 7-9. The areas that have achieved PBP lower than 20 years for whole of Iraq at 30m for 3000 kWh/month demand for WS-5kW in Figure A and WS-2kW in Figure B.

Concerning the PBP calculation based on 2015 IBT prices, Figure 7-10A and B show the number of locations that have achieved PBP for SW-5kW from 10m to 30m, based on IBT prices in 2015 and for different levels of demand. At first glance over the two Figures, it possible to note that just 5000, 4000, 3000 and 2000 kWh/month demand achieved PBP of less than 20 years.

However, when comparing the PBP between 2015 IBT and 2017 IBT, the SW-5kW has succeeded to get PBP of less than 20 years for 2000 kWh/month of demand, based on the 2015 IBT in Figure 7-10A and B; yet it does not achieve PBP of less than 20 years, based on the 2017 IBT in Figure 7-8A and B.

Furthermore, the PBP for 5000, 4000 and 3000 kWh/month demand, based on 2015 IBT was concentrated gradually close to 10 years when the height was increasing from 10m to 30m. Moreover, the PBP based on 1000 kWh/month demand has remained constant for 41

years at all heights, without changing in Table **7-7**, due to the MEP exceeding the monthly demand limitation at all heights. While with respect to similarity among results of minimum PBP for 2000, 3000 and 4000 kWh/month demand at 25 m and 30 m in Table **7-7**, it returned to rapprochement between maximum MEP from WS-5kW at 25m and 30m heights, which was equal to 1654 and 1679 kWh/month respectively.

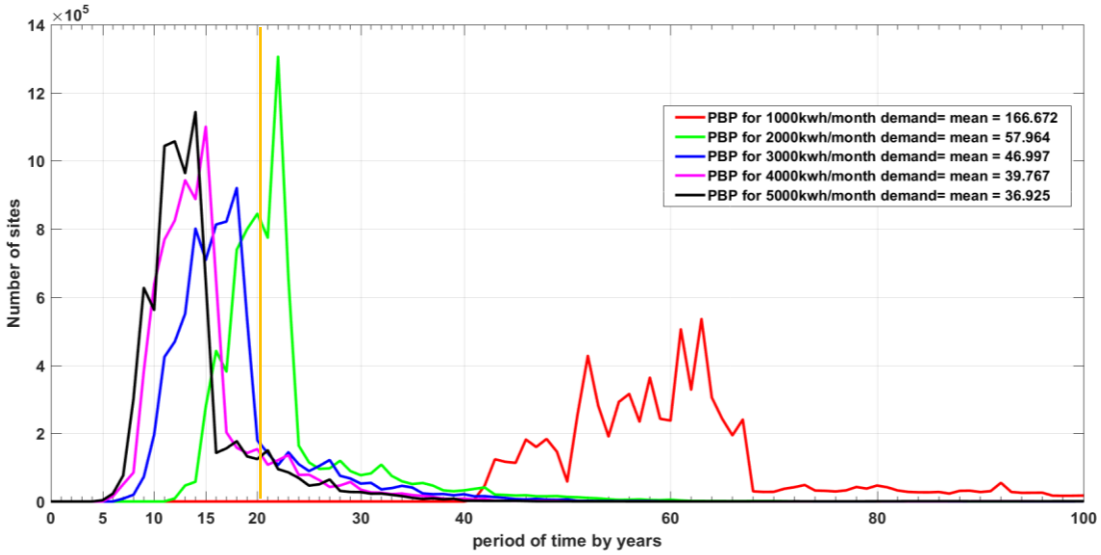

Figure A

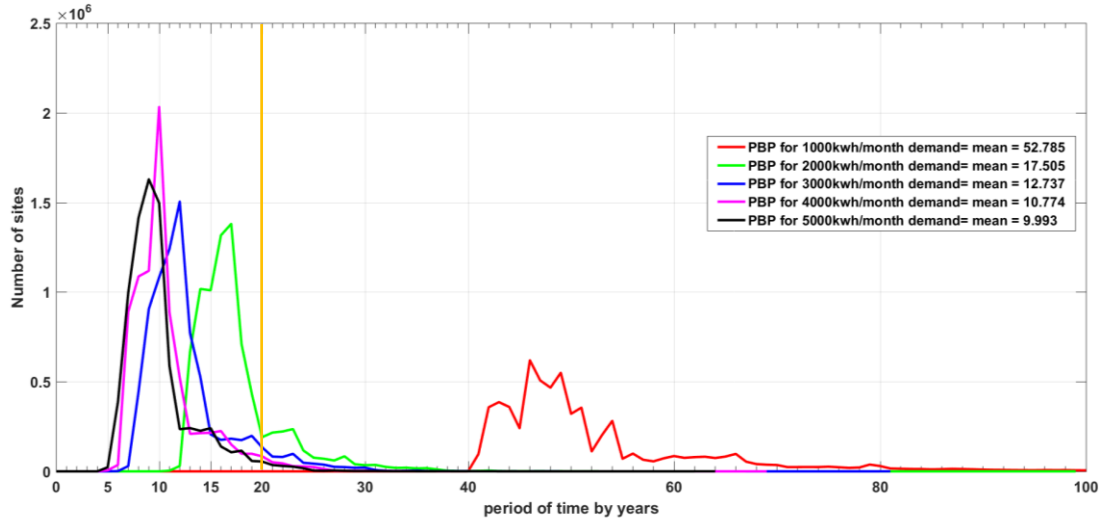

Figure B

Figure 7-10. The PBP for SW-5kW based on IBT prices in 2015 for different levels of demand at 10m in Figure A and at 30m in Figure B.

Table 7-7. Reveals the minimum PBP achieved by SW-5kW, using 2015 IBT prices and based on different heights at the left column and different levels of monthly demand at the first row.

Hub height	1000 kWh/month demand	2000 kWh/month demand	3000 kWh/month demand	4000 kWh/month demand	5000 kWh/month demand
10m	41 years	11.9 years	6.9 years	5.8 years	5.3 years
15m	41 years	11.6 years	6.7 years	5.5 years	5.0 years
20m	41 years	11.4 years	6.5 years	5.3 years	4.8 years
25m	41 years	11.3 years	6.4 years	5.2 years	4.7 years
30m	41 years	11.3 years	6.4 years	5.2 years	4.6 years

The most important finding that can be summarized from the PBP calculation, based on IBT in 2015, is that SW-5kW is able to achieve PBP of less than 20 years for several levels of demand (2000, 3000, 4000 and 5000 kWh/month) lower than what SW-2kW can make according to the same conditions when comparing Table 7-7 and Table 7-4.

For more analysis to determine the most reliable and productive locations in Iraq, the calculation of PBP of less than 8 years has been applied, based on the 2017 and 2015 IBT. According to the PBP calculations within 8 years, based on the 2017 IBT, the WS-5kW has achieved PBP for broad areas at 10m based on 5000 kWh/month of energy demand. The areas that have made PBP of less than 8 years based on WS-5kW are larger than the areas achieved by WS-2kW, as shown in Figure 7-11A and B. While the areas that have made PBP of less than 8 years have extended towards the nearby lands of the lakes in south-eastern Iraq and also include a number of lakes in the northwest of Iraq as is shown in Figure 7-11A.

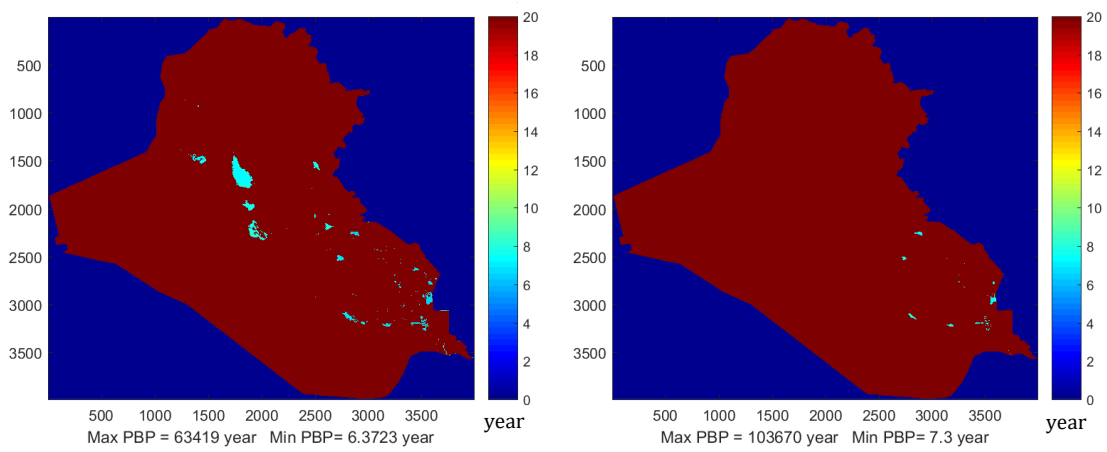

Figure A Figure B

Figure 7-11. The comparison between WS-5kW in Figure A and WS-2kW in Figure B according to the distribution of PBP of less than 8 years, based on the IBT in 2017 at 10m for 5000 kWh/month demand.

It is worth mentioning that the areas that were able to achieve PBP of less than 8 years have increased when the height was increased from 10 m to 30 m and also the value of PBP has decreased gradually with increasing height as illustrated in Table 7-7. In fact, SW-5kW based on 2015 IBT and 5000 kWh/month of energy demand at 30m has succeeded to expand areas of PBP of less than 8 years massively in comparison with SW-2kW at the same height and with the same level of energy demand, as shown in Figure 7-12A and B. The most important findings that can be summarized from PBP calculation within 8 years based on 2017 and 2015 IBP:

- The SW-5kW can reduce the PBP and increase the areas of PBP of less than 8 years, particularly when increasing the height and increasing a level of demand. Also, the WS-5kW has succeeded in meeting PBP of less than 8 years, based on 2015 IBT prices and particularly in 3000 kWh/month of energy demand at 10m and 15m.

- The results have shown that the areas where that they achieved PBP of less than 8 years according to the 2017 IBT prices are considered the most appropriate areas for wind energy investments. Despite the low hub heights of wind turbine and the low IBT prices, it achieved this lower PBP.
- Therefore, the results deem the SW-5kW a very suitable turbine for supplying housing units with electricity and this turbine could be involved in being a part of the optimal design for the renewable hybrid system in the next work.

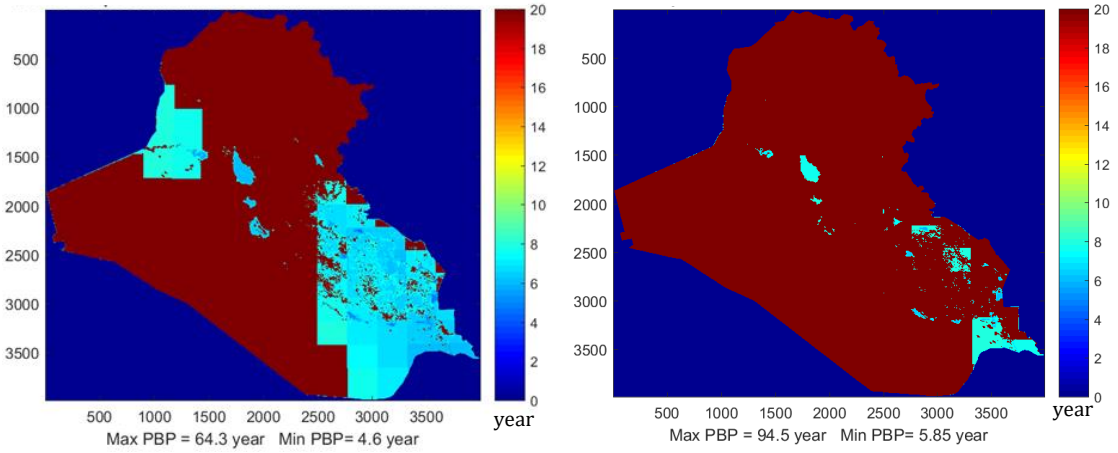

Figure A Figure B

Figure 7-12. The comparison between WS-5kW in Figure A and WS-2kW in Figure B according to the distribution of PBP of less than 8 years, based on the IBT in 2015at 30m for 5000 kWh/month of energy demand.

7.6.3 **SW-10kW**

7.6.3.1 **LCE calculation for SW-10kW**

SW-10kW is the third small wind turbine size that has been considered to supply housing units with electricity in this study. The LCE has been calculated for the whole of the Iraq map, based on AEP from SW-10kW at different heights as is shown in Figure 6-16 in Chapter 6 and based on different levels of energy demand. Figure 7-13A, C and D show the boxplots of LCE distribution, based on varying levels of energy demand, different heights and for more than 8 millions pixels on the Iraq map. At first glance, two things will likely attract attention in Figure 7-13A. One of the most striking things, is the difference between the lowest LCE that recorded at 10m for 1000 kWh/month which equal 0.123 £/kWh (the median) and the minimum LCE value, which was recorded at 10m based on energy demand for 3000, 4000 and 5000 kWh/month which equal 0.0546 £/kWh (lower quartile). The reason behind forming the minimum LCE value as the median in Demand-1000 group in Figure 7-13A is due to the fact that 50% of locations in Iraq generate MEP higher than 1000 kWh/month as is shown in AEP10m in Figure 6-16 in Chapter 6. Therefore, the results of

LCE which are restricted by 1000 kWh/month of energy demand will equal 0.123 £/kWh for 50% of locations in Iraq.

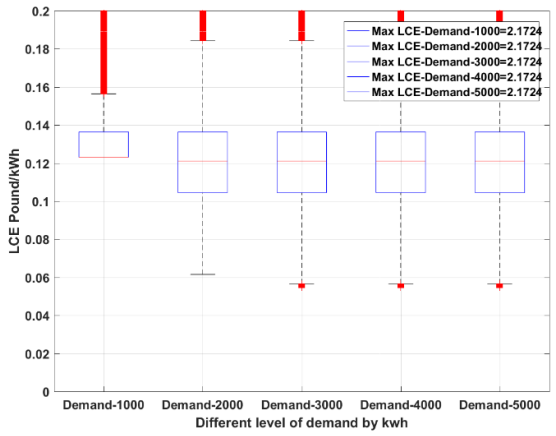

Figure A

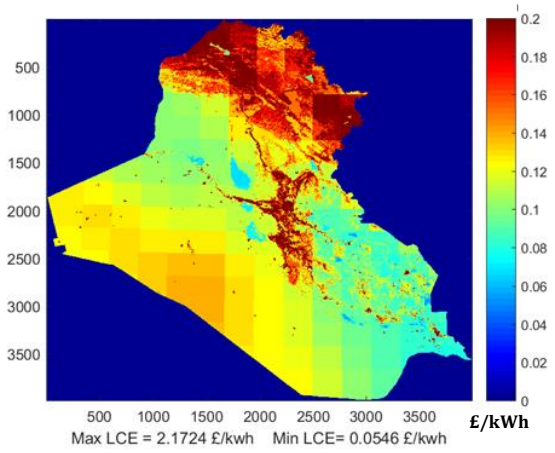

Figure B

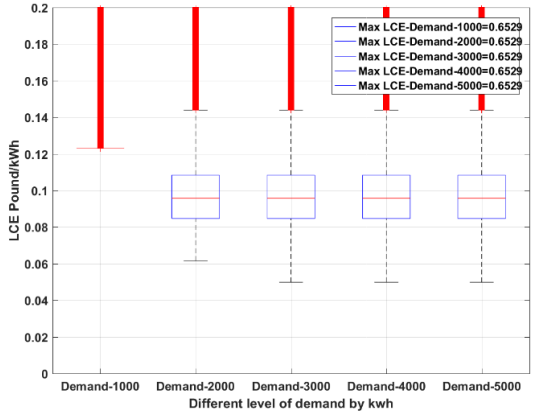

Figure C

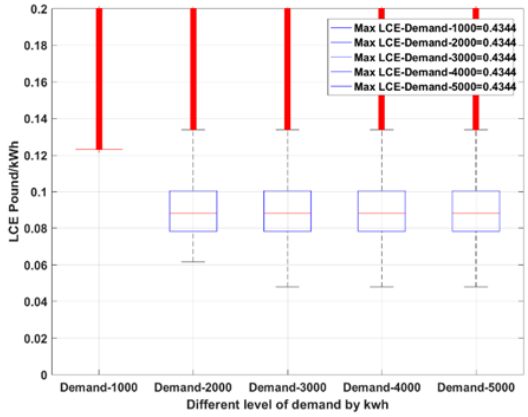

Figure D

Figure 7-13. LCE boxplot distribution for 10kW wind turbine size at 10m in Figure A, 20m in Figure C and 30m in Figure D for different levels of demand from 1000 to 5000 kWh/month. Figure B shows the LCE map for 10kW wind turbine size at 10m based on AEP of 10kW in 2014 and 5000 kWh/month demand

In the same context, a small number of locations in Iraq have generated MEP higher than 2000 kWh/month as was shown in Figure 6-16A in the previous chapter. For this reason the lowest value of LCE based on 2000 kWh/month of energy demand for all locations in Iraq did not exceed 0.0615 £/kWh.

On the other hand, the reason behind the similarity among the Lowest LCE values of 3000, 4000 and 5000 kWh/month returns to the maximum MEP from SW-10kW equals 2254.8 kWh/month, which is lower than the monthly energy demand in terms of 3000 to 5000 kWh/month. In addition, the lowest LCE = 0.0546 £/kWh that was calculated was based on AEP from SW-10kW for 3000 kWh/month of energy demand, which is lower than 0.13 £/kWh the price of electricity for 3000 kWh/month, based on 2015 IBT in level six in Figure 7-1. And also it is lower than 0.08 £/kWh, the price of electricity for 3000 kWh/month, based on 2017 IBT in the level six in Figure 7-1. 25% of locations in Iraq have low prices that are distributed among the blue areas that represent lakes, light blue areas which spread

over the southeast of Iraq and the green area which extends from northwest to south of Iraq as is shown Figure 7-13B.

In general, it is possible to observe that the lower quartile of LCE for 2000, 3000, 4000 and 5000 kWh/month of energy demand gradually decreased from 10m to 30m (except the lower quartile in Demand-2000) due to the AEP increase with height as shown Figure 6-16 in Chapter 6.

The minimum and maximum LCE values have been inserted in Table 7-8 to show to what extent the value of LCE changes with height and to represent the LCE value for the most productive areas in Iraq that form around 25% of Iraqi locations that are distributed between lower quartile and lower whisker for each boxplot in Figure 7-13A, C and D.

Table 7-8. The minimum and maximum LCE from WS-10kW at different heights and for 2000 and 3000-5000 kWh/month demand and the lower LCE quartile that represents the most productive area in Iraq which forms 25% of locations in Iraq for 3000-5000 kWh/month demand

	LCE for 1000 kWh/month demand	LCE for 2000 kWh/month demand			LCE for 3000 – 5000 kWh/month demand		
level of height	Median LCE £/kWh	Min LCE £/kWh	Max LCE £/kWh	The lower LCE quartile	Min LCE £/kWh	Max LCE £/kWh	The lower LCE quartile
LCE at 10m	0.123	0.0615	2.172	0.105 -0.0615	0.0546	2.172	0.105 - 0.0546
LCE at 15m	0.123	0.0615	1.032	0.092 - 0.0615	0.0516	1.032	0.092 - 0.0516
LCE at 20m	0.123	0.0615	0. 652	0.085 - 0.0615	0.0498	0. 652	0.085 - 0.0498
LCE at 25m	0.123	0.0615	0.505	0.08 - 0.0615	0.0487	0.505	0.08 - 0.0487
LCE at 30m	0.123	0.0615	0.434	0.079 - 0.0615	0.0479	0.434	0.079 - 0.0479

7.6.3.2 PBP calculation for SW-10kW

The PBP will be helpful in determining the most reliable and productive locations that can achieve a short PBP within wind turbine lifespan.

Figure 7-14A and B show the PBP for SW-10kW from 10m to 30m based on IBT in 2017 and for different levels of demand. At first glance over the two Figures, it is possible to note that 5000 and 4000 kWh/month of energy demand have succeeded to achieve PBP of less than 20 years over the two heights from 10m to 30m. Furthermore, it is also possible to observe the areas that achieved PBP of less than 20 years, which tend to increase when increasing the height, as shown in Figure 7-14A and B. In comparison, between SW-10kW and SW-5kW based on PBP and according to the 2017 IBT prices, it is possible to note that SW-10kW had a lower capability than SW-5kW to reduce the PBP and increase the areas of PBP, as shown in Figure 7-14 and Figure 7-8.

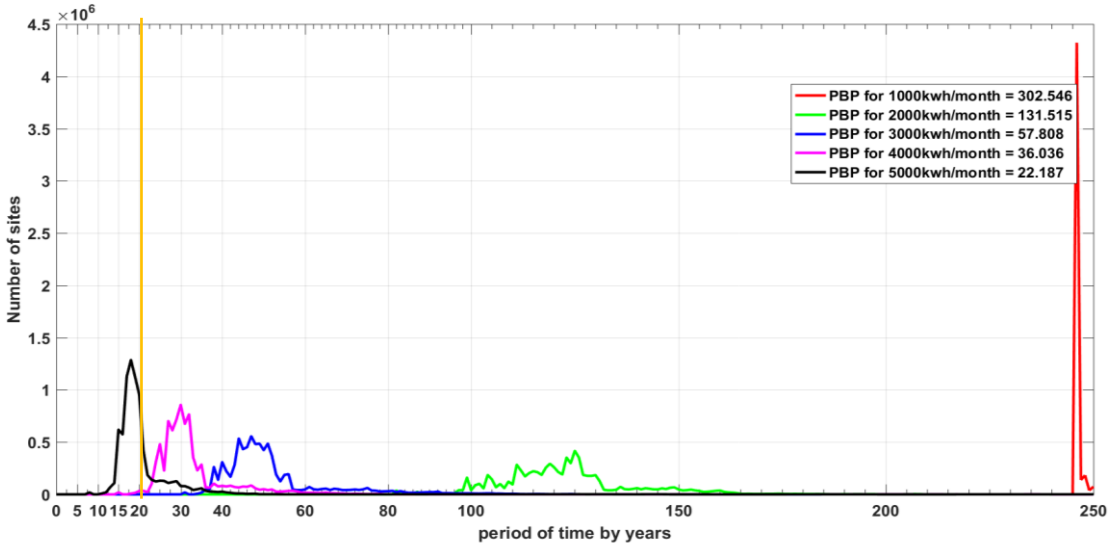

Figure A

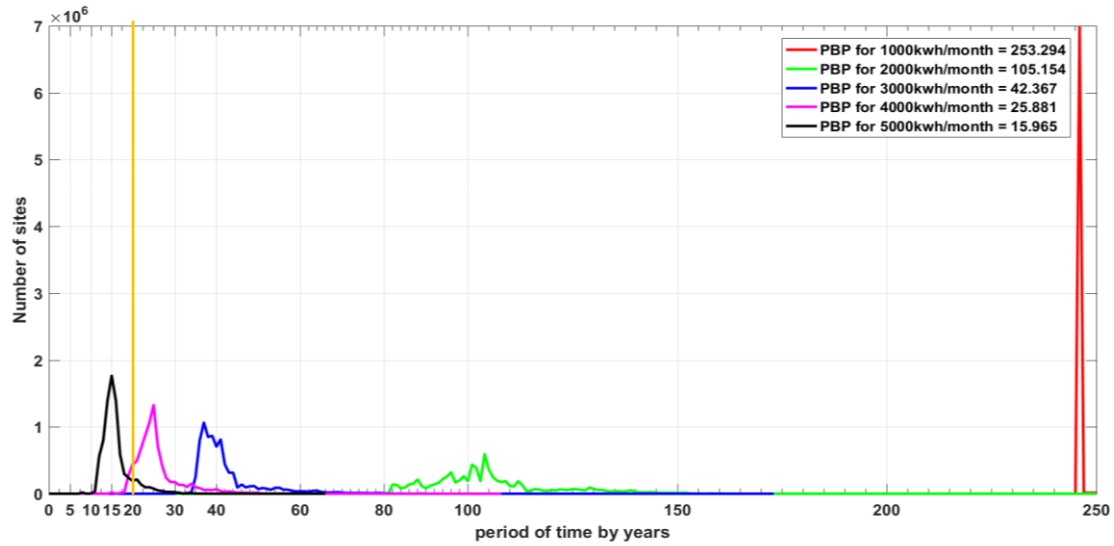

Figure B

Figure 7-14. The PBP for SW-10kW based on IBT prices in 2017 for different levels of demand at 10m in Figure A and at 30m in Figure B.

Moreover, the minimum PBP results from SW-10kW at different heights and for varying levels of demand in Table 7-9 reveal values higher than the minimum PBP results of SW-5kW in Table 7-6. In the same context, the areas that achieved PBP of less than 20 years based on SW-10kW have reduced in comparison with the areas that achieved PBP based on SW-5KW, as shown in Figure 7-15A and B. There are different reasons behind increasing the PBP with SW-10kW in comparison with SW-5kW:

- The main reason is that the cost of SW-10kW is higher than the price of SW-5kW by more than two times, as is revealed in Table 7-1.
- Secondly, the maximum AEP from SW-5kW equals two-thirds of the maximum AEP from SW-10kW and also the CF of SW-5kW is higher than SW-10kW.

Table 7-9. Minimum PBP values of SW-10kW by using 2017 IBT prices and based on different heights at the left column and different levels of monthly demand at the first row

Hub height	1000 kWh/month demand	2000 kWh/month demand	3000 kWh/month demand	4000 kWh/month demand	5000 kWh/month demand
10m	246 years	82 years	30.7 years	17.8 years	11 years
15m	246 years	82 years	30.7 years	17.3 years	10.7 years
20m	246 years	82 years	30.7 years	17 years	10.5 years
25m	246 years	82 years	30.7 years	16.9 years	10.4 years
30m	246 years	82 years	30.7 years	16.8 years	10.3 years

It is noteworthy that the min PBP for 1000, 2000 and 3000 kWh/month of energy demand did not change over different heights as revealed in Table 7-9, due to the monthly demand limitation which was lower than MEP for SW-10kW at different heights. The most important finding that can be summarised from the results of PBP based on 2017 IBT prices is that it confirms that the performance of SW-10kW is lower than SW-5kW.

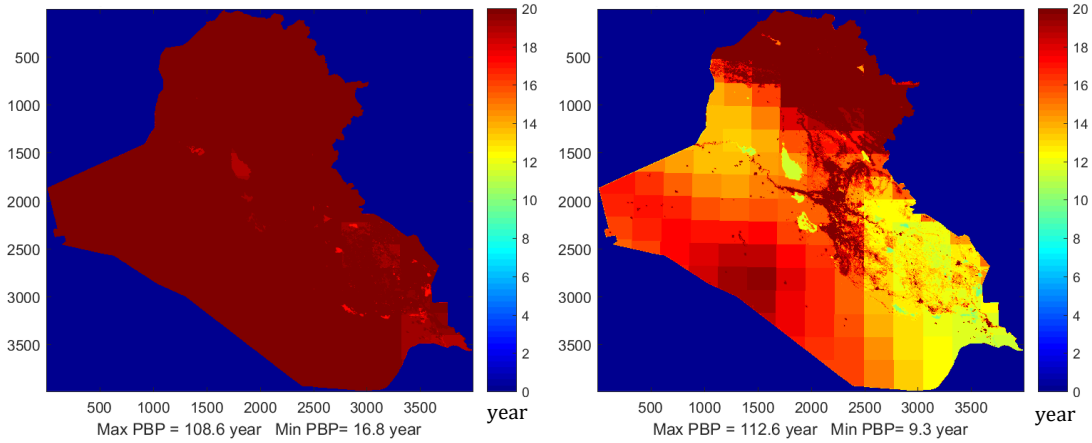

Figure A Figure B

Figure 7-15. The areas that achieved PBP of less than 20 years for the whole of Iraq, based on WS-10kW in Figure A and WS-5kW in Figure B at 30m for 4000 kWh/month of energy demand.

Concerning the PBP calculation based on 2015 IBT prices, Figure 7-16A and B show the size of areas that have achieved PBP of less than 20 years based on SW-10kW from 10m to 30m based on 2015 IBT prices and for different levels of demand.

At first glance over the two Figures, it is possible to note that just 5000, 4000 and 3000 kWh/month of energy demand achieved PBP of less than 20 years. Again, when comparing the calculation of PBP between 2015 IBT and 2017 IBT, the 2015 price has played a vital role to achieve PBP of less than 20 years for low-level of demand such as 3000 kWh/ month of energy demand, as is shown in Figure 7-16. Furthermore, it is clear that the PBP for 5000, 4000 and 3000 kWh/month demand based on 2015 IBT creeping gradually towards 15 years when the height increasing from 10m to 30m as are shown in Figure 7-16A and B. Table 7-10 reveals the minimum PBP that was achieved by SW-10kW using IBT prices in 2015 and based on several levels of energy demand across five heights from 10m to 30m. The results show that only the 1000 and 2000 kWh/month of energy demand failed to attain PBP of less than 20 years at all heights, as shown in Figure 7-16. The most important finding that can be summarized from PBP calculation based on IBT in 2015, is that SW-10kW can

achieve PBP of less than 20 years, based on three levels of demand: 3000, 4000 and 5000 kWh/month of energy demand. In comparison, the SW-10kW was able to achieve PBP of less than 20 years, based on the 2017 IBT just in 4000 and 5000 kWh/month of energy demand, as revealed in Table 7-10 and Table 7-9. Also, the SW-10kW had the capability lower than SW-2kW and SW-5kW due to the results of minimum PBP shown in Table 7-10, Table 7-7 and Table 7-4, where the min PBP of SW-10kW > the min PBP of SW-2kW > the min PBP of SW-5kW.

Table 7-10. Reveals the minimum PBP values achieved by SW-10kW by using 2015 IBT prices, based on different heights at the left column and different levels of monthly demand at the first row

Hub height	1000 kWh/month demand	2000 kWh/month demand	3000 kWh/month demand	4000 kWh/month demand	5000 kWh/month demand
10m	94.6 years	24.4 years	12.7 years	9.3 years	8.2 years
15m	94.6 years	24.4 years	12.5 years	8.9 years	7.8 years
20m	94.6 years	24.4 years	12.3 years	8.7 years	7.6 years
25m	94.6 years	24.4 years	12.2 years	8.5 years	7.4 years
30m	94.6 years	24.4 years	12.1 years	8.4 years	7.3 years

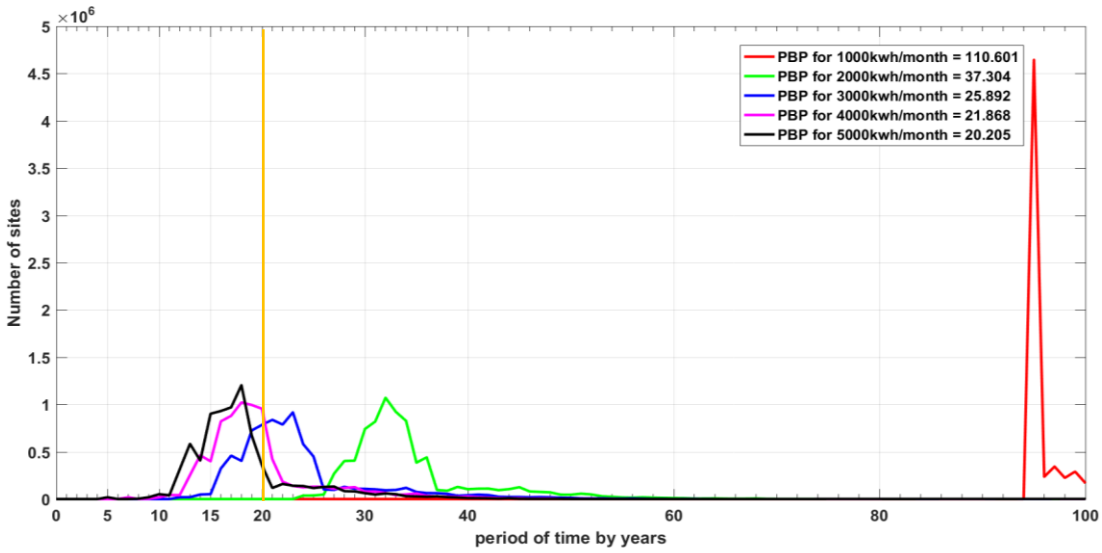

Figure A

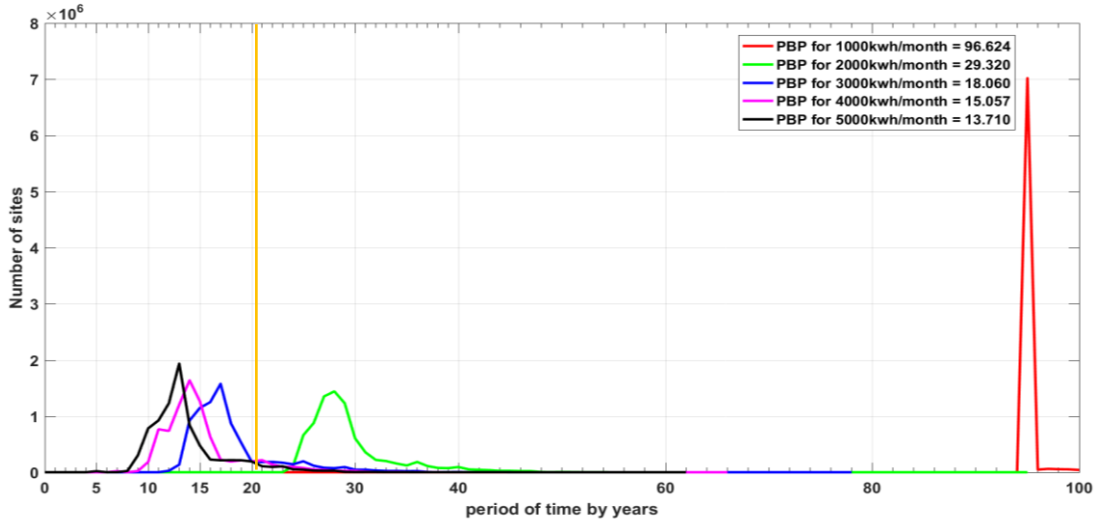

Figure B

Figure 7-16. The PBP for SW-10kW based on IBT prices in 2015 for different levels of demand at 10m in Figure A and at 30m in Figure B.

For more analysis to determine the most reliable and productive locations in Iraq, the calculation of PBP within 8 years has been applied based on the 2017 IBT. According to this calculation, the WS-10kW has wholly failed to achieve PBP of less than 8 years across all heights and based on all levels of monthly energy demand as revealed in Table 7-9.

Concerning the calculation of PBP of less than 8 years based on the 2015 IBT, the results show that the SW-10kW can achieve PBP of less than 8 years for just a small area, based on 5000 kWh/month of energy demand from 15m of hub height and above. In addition, these regions have expanded with height increasing from 15 m to 30 m as shown in Figure 7-17A and Figure 7-17B.

In fact, the performance of SW-5kW based on 2015 IBT prices, 5000 kWh/month of energy demand and at 30 m has successfully increased the areas of PBP of less than 8 years, which is highly significant in comparison with SW-2kW and SW-10kW at the same height and same level of energy demand (see Figure 7-18B, Figure 7-18A and Figure 7-17B respectively).

The most important findings that can be summarized from PBP calculation according to 2017 and 2015 IBT, the SW-10kW shows lower ability than WS-2kW and WS-5kW to reduce the PBP of less than 8 years. Finally, according to the results of PBP of less than 8 years for the three turbines WS-10kW, WS-5kW and WS-2kW, it is possible to classify the WS-10kW as a third turbine after WS-2kW and WS-5kW.

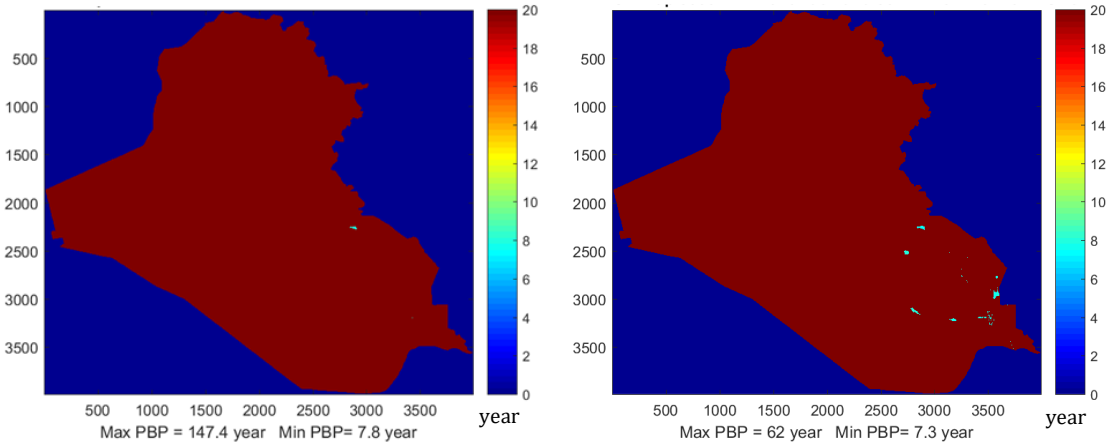

Figure A Figure B

Figure 7-17. The distribution of the regions that have succeeded to achieve PBP of less than 8 years by WS-10kW based on the 2015 IBT according to 5000 kWh/month of energy demand at 15 m in Figure A and at 30m in Figure B.

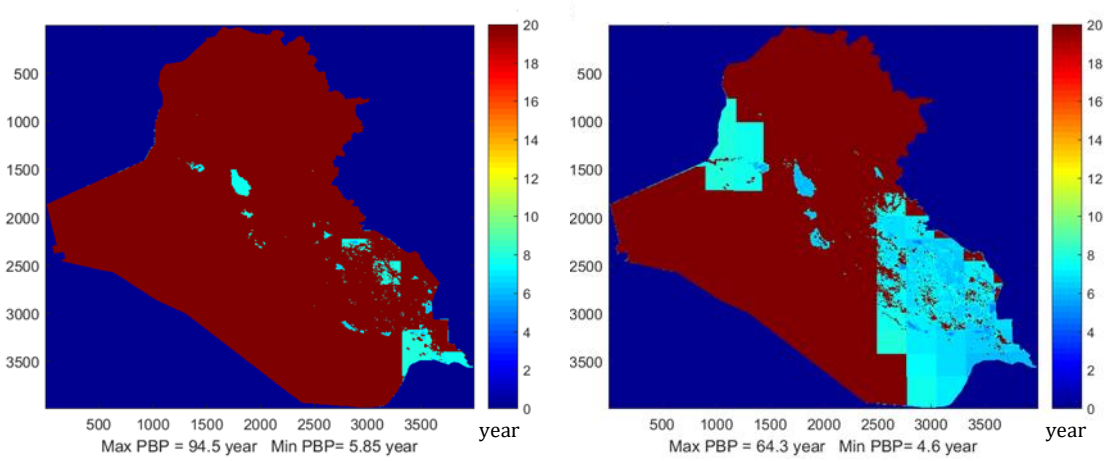

Figure A Figure B

Figure 7-18. The distribution of the regions that achieved PBP of less than 8 years, based on the 2015 IBT at 30m, according to 5000 kWh/month of energy demand by WS-2kW in Figure A and by WS-5kW in Figure B

7.6.4 **SW-20kW**

7.6.4.1 **LCE calculation for SW-20kW**

SW-20kW is the fourth small wind turbine size that has been considered for supplying housing units with electricity in this study. The LCE has been calculated for the whole of the Iraq map, based on AEP from SW-20kW at different heights and for the different levels of energy demand (see Figure 7-19).

At first glance, there are several findings attract attention in Figure 7-19. One of the striking things is that the median of LCE distribution that has formed the minimum value of LCE based on 1000 and 2000 kWh/month of demand at 10 m and 1000, 2000 and 3000 kWh/month of demand for each 20m and 30m respectively. This is due to the fact that the majority of locations in Iraq have shown one value of LCE inasmuch the level of demand.

With regard to the comparison between the LCE based on 3000 kWh/month of energy demand at 10 m and the price of electricity for the same level of demand based on 2015 and 2017 IBT in Figure 7-1, it is noted that the most productive locations in Iraq which form 25% show LCE ranging between 0.07 to 0.08 £/kWh which is lower than 0.13 £/kWh the price of electricity for 3000 kWh/month based on 2015 IBT in the level six in Figure 7-1. Also, approaching 0.08 £/kWh, the price of electricity for 3000 kWh/month of demand is based on 2017 IBT in level four in Figure 7-1.

The minimum and maximum LCE values have been inserted in Table 7-11 to show to what extent the value of LCE changes with height as well as representing the LCE value for the most productive area in Iraq that forms around 25% of locations in Iraq that distributed between lower quartile and lower whisker for each boxplot in Figure 7-19.

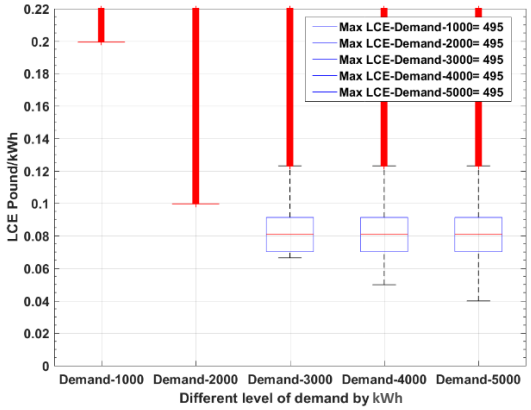

Figure A

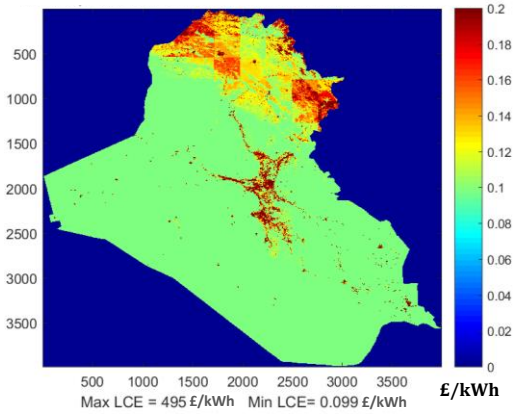

Figure B

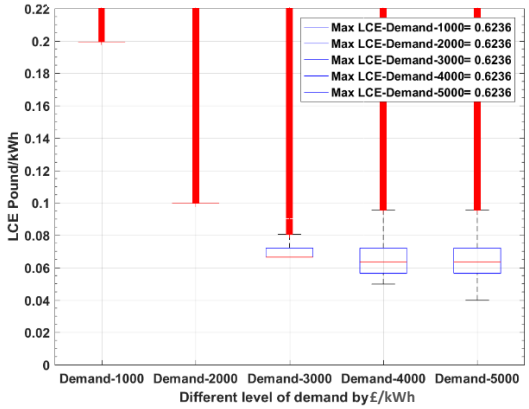

Figure C

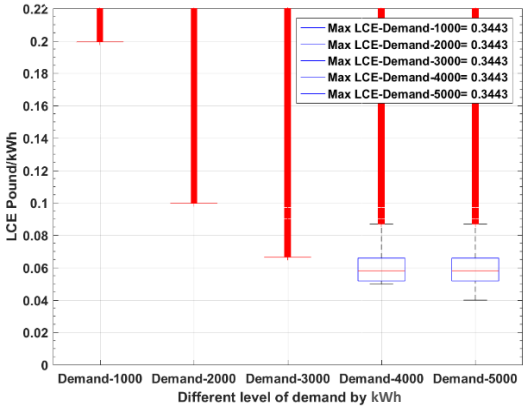

Figure D

Figure 7-19. LCE boxplot distribution for 20kW wind turbine size at 10m in Figure A, 20m in Figure C and 30m in Figure D for different levels of demands from 1000 to 5000 kWh/month. Figure B Shows LCE map for 20kW wind turbine size at 10m based on AEP of 20kW in 2014 and 2000 kWh/month demand

Table 7-11. The minimum and maximum LCE from WS-20kW at different heights and from 1000 -5000 kWh/month demand.

LCE for 1000 kWh/month			LCE for 2000 kWh/month		LCE for 3000 kWh/month		LCE for 4000 kWh/month		LCE for 5000 kWh/month	
LCE level of height	Median LCE £/kWh	Max LCE £/kWh	Median LCE £/kWh	Max LCE £/kWh	Min LCE £/kWh	Max LCE £/kWh	Min LCE £/kWh	Max LCE £/kWh	Min LCE £/kWh	Max LCE £/kWh
LCE at 10m	0.199	495	0.099	495	0.066	495	0.049	495	0.039	495
LCE at 15m	0.199	1.496	0.099	1.496	0.066	1.496	0.049	1.496	0.039	1.496
LCE at 20m	0.199	0.623	0.099	0.623	0.066	0.623	0.049	0.623	0.039	0.623
LCE at 25m	0.199	0.424	0.099	0.424	0.066	0.424	0.049	0.424	0.039	0.424
LCE at 30m	0.199	0.344	0.099	0.344	0.066	0.344	0.049	0.344	0.039	0.344

In summary, the most important finding from LCE calculation based on WS-20kW in this section is that the majority of locations in Iraq except the mountains, and urban areas have generated low LCE, based on 3000 kWh/month of demand from 15 m to 30 m in comparison with 2015 IBT in level five in Figure 7-1. In comparison, the majority of locations in Iraq generated low-cost of energy based on 3000, 4000 and 5000 kWh/month from 15 m to 30 m. Nonetheless, the result of LCE as for WS-10kW was generally lower than the result of LCE for WS-20kW when comparing the results of Table 7-11 and Table 7-8. According to WS-20 kW, the results of LCE for more than 50% of locations in Iraq matched the 2017 IBT

prices, particularly from 3000 to 5000 kWh/month of energy demand (see the comparison of results in Figure 7-19 and Figure 7-1).

7.6.4.2 **PBP calculation for SW-20kW**

The PBP calculations for SW-20kW are calculated based on the 2017 IBT prices and 2015 IBT prices. Figure 7-20 shows the PBP for SW-20kW from 10 m to 30 m based on IBT in 2017 and for different levels of demand. At first glance over the two Figures, it is possible to note that just 5000 kWh/month of energy demand achieved PBP of less than 20 years over the five heights from 10 m to 30 m.

Figure 7-20 and Table 7-12 show that the minimum PBP remained steady for all levels of demand over all heights due to the highest value of MEP, which exceeded all levels of energy demand at all altitudes.

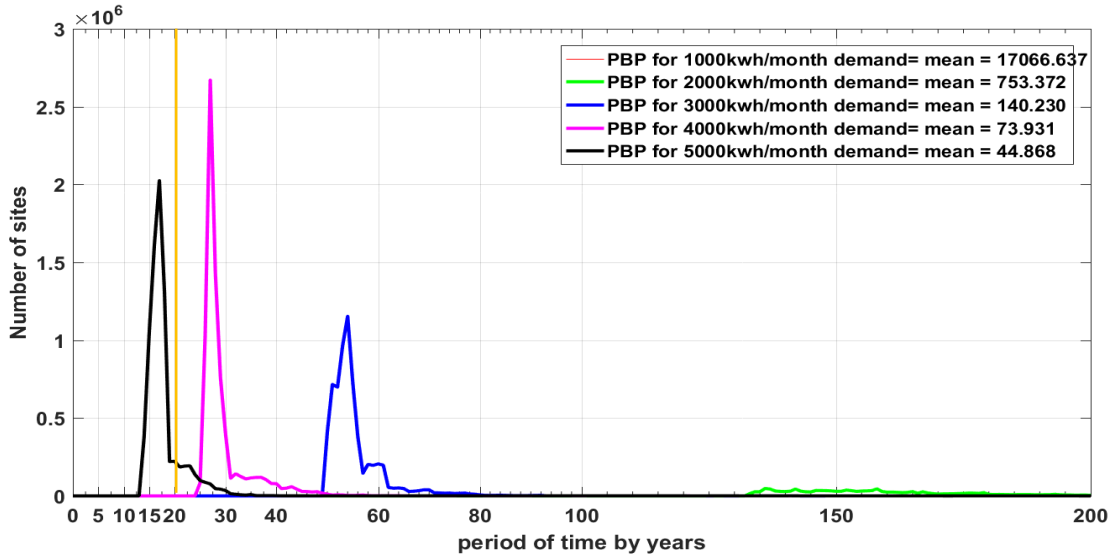

Figure A

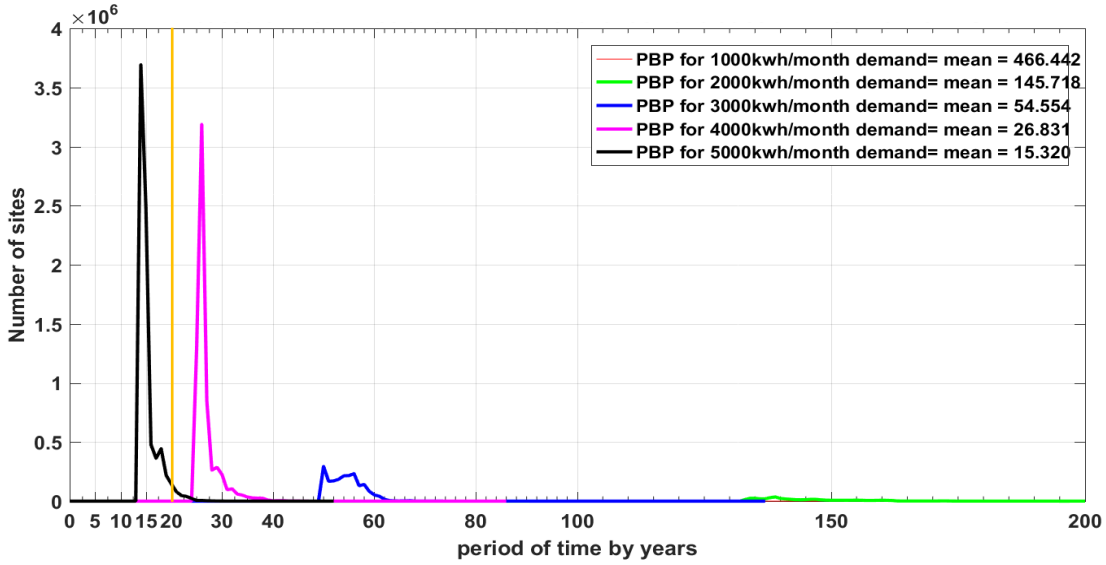

Figure B

Figure 7-20. The PBP for SW-20kW based on 2017 IBT prices for different levels of demand at 10m in Figure A and at 30m in Figure B.

In a comparison between SW-20kW, SW-10kW, SW-5kW and SW-2kW based on PBP and according to the 2017 IBT prices, it is possible to note that SW-20KW shows capability lower than SW-10kW, SW-2kW and SW-5kW respectively in terms of reducing the PBP and increasing the areas of PBP. The main reason behind increasing the PBP for SW-20kW in comparison with others return to the price of SW-20kW, which is almost double the price of SW-10kW (see Table 7-1).

Table 7-12. Reveals the minimum PBP achieved by SW-20kW, using 2017 IBT prices, based on different heights at the left column and different levels of monthly demand at the first row

Hub height	1000 kWh/month demand	2000 kWh/month demand	3000 kWh/month demand	4000 kWh/month demand	5000 kWh/month demand
10m	398.7 years	132.9 years	49.8 years	24.9 years	13.7 years
15m	398.7 years	132.9 years	49.8 years	24.9 years	13.7 years
20m	398.7 years	132.9 years	49.8 years	24.9 years	13.7 years
25m	398.7 years	132.9 years	49.8 years	24.9 years	13.7 years
30m	398.7 years	132.9 years	49.8 years	24.9 years	13.7 years

Concerning the PBP calculation based on 2015 IBT prices, Figure 7-21 shows number of locations that achieved PBP of less than 20 years by SW-20kW from 10 m to 30 m based on 2015 IBT prices and for different levels of demand. Closer inspection of the results shows that 5000, 4000 and 3000 kWh/month of energy demand achieved PBP of less than 20 years, with different sizes of area for each time scale at the five heights from 10m to 30m. Furthermore, there are two things will likely attract attention in Figure 7-21:

- First , the minimum PBP remained steady for all levels of demand and over all heights, based on 2015 IBT as is shown in Figure 7-21 and Table 7-13, due to the highest value of MEP, which exceeded all levels of energy demand at all heights, as shown in Figure 6-19 in Chapter 6.
- The second striking thing, is the increase in locations that were able to achieve low PBP with height increasing according to 3000, 4000 and 5000 kWh/month of energy demand, which is shown in Figure 7-21.

Table 7-13 reveals the minimum PBP that achieved by SW-20kW using IBT prices in 2015 and based on several levels of energy demand across five heights from 10m to 30m. The results show that only the 1000 and 2000 kWh/month of energy demand failed to attain PBP of less than 20 years at all heights.

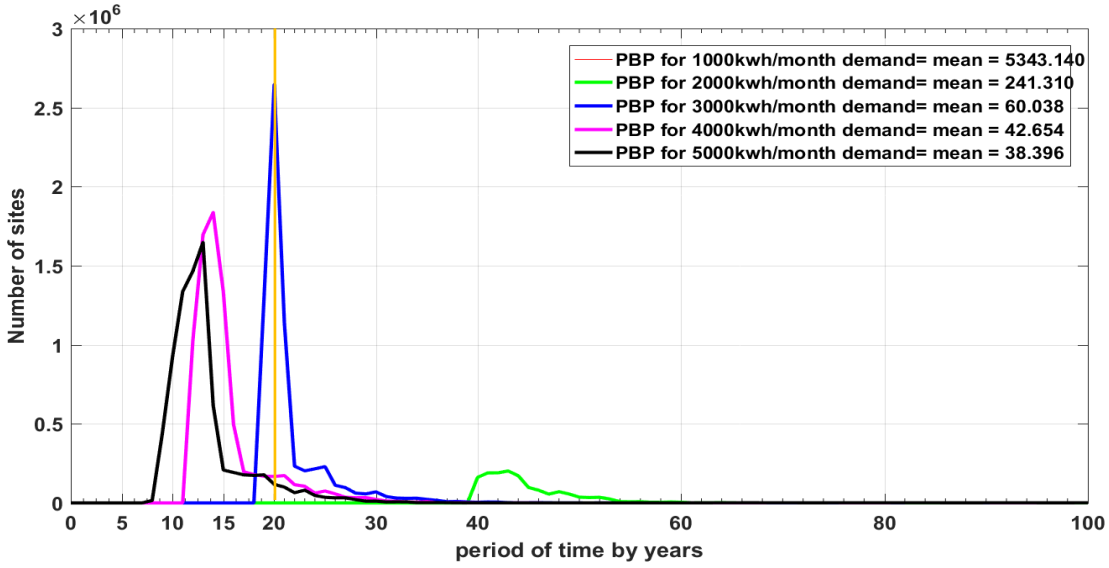

Figure A

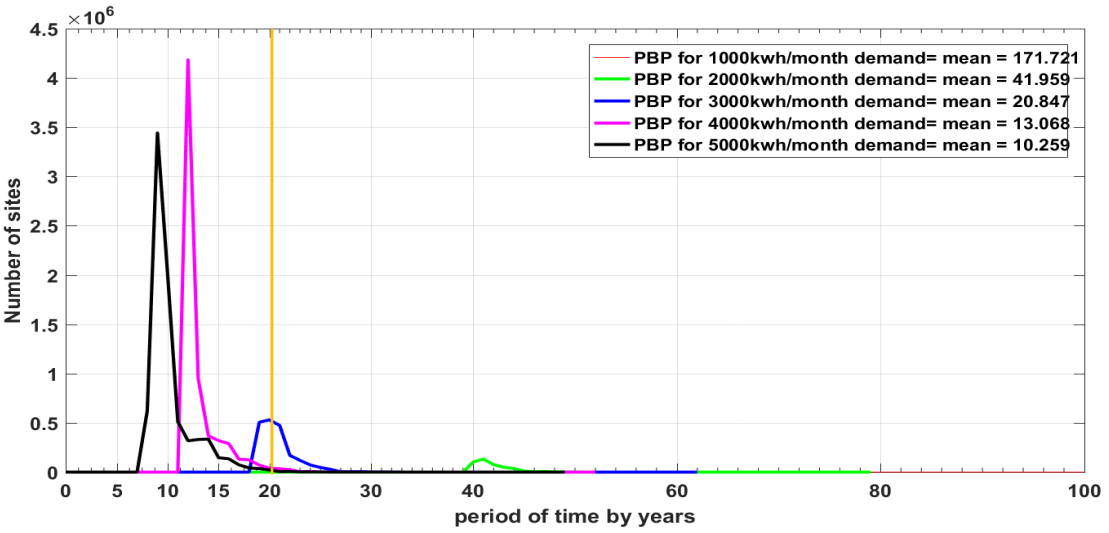

Figure B

Figure 7-21. The PBP for SW-20kW based on 2015 IBT prices for different levels of demands at 10m in Figure A and at 30m in Figure B.

The most important finding that can be summarized from PBP calculation based on IBT in 2015, is that the SW-20kW demonstrated an ability to achieve PBP of less than 20 years based on three levels of demand: 3000, 4000 and 5000 kWh/month of energy demand. While, the SW-20kW has shown ability to achieve PBP of less than 20 years based on the 2017 IBT particularly, according to 5000 kWh/month of energy demand, as are revealed in Table 7-13 and Table 7-12.

In addition, the SW-20kW has shown capability lower than SW-10kW, SW-2kW and SW-5kW due to the results of minimum PBP (see Table 7-13, Table 7-10, Table 7-7 and Table 7-4 respectively), where the min PBP of SW-20kW > the min PBP of SW-10kW > the min PBP of SW-2kW > the min PBP of SW-5kW. Finally, the SW-20kW has completely failed to achieve any PBP of less than 8 years according, for both the 2017 and 2015 IBT.

Table 7-13. Reveals the minimum PBP achieved by SW-20kW, using 2015 IBT prices, based on different heights at the left column and different levels of monthly demand at the first row

Hub height	1000 kWh/month demand	2000 kWh/month demand	3000 kWh/month demand	4000 kWh/month demand	5000 kWh/month demand
10m	153.3 years	39.6 years	18.9 years	11.7 years	8.3 years
15m	153.3 years	39.6 years	18.9 years	11.7 years	8.3 years
20m	153.3 years	39.6 years	18.9 years	11.7 years	8.2 years
25m	153.3 years	39.6 years	18.9 years	11.7 years	8.2 years
30m	153.3 years	39.6 years	18.9 years	11.7 years	8.2 years

7.7 Conclusion

This chapter aimed to calculate the PBP and LCE based on AEP for four sizes of wind turbine (2kW, 5kW, 10kW and20kW) and for different levels of monthly demand and for all of Iraq. The aim of LCE calculation is to determine the low electricity costs and the spatial distribution of the low LCE throughout whole of Iraq map. Moreover, the PBP was calculated based on saving strategy, under the 2017 and the 2015 IBT prices, in order to identify the best pricing model that could be applied to attain the shortest PBP within the lifetime of a turbine. In addition, the PBP calculations aimed to determine the most reliable and productive locations that were able to achieve a short PBP within the wind turbine's lifespan. According to these requirements, the main cost categories of a wind turbine project have been sized /estimated by a new method, which has integrated the relative weight for capital and variable expenditure. This was derived from literature review and equations designed to estimate variable costs that were affected by time value over the project's life span.

The WS-5kW had the lowest LCE over all heights, particularly based on monthly demand between 2000 to 5000 kWh/month in comparison with others. In addition, the most productive area that generated the lowest cost of energy based on different wind turbine sizes was located in the southeast of Iraq and formed 25% of locations in Iraq. In the same contest, the lakes and marshland had the lowest LCE in the southeast of Iraq. In general , the LCE based on different level of demand decreased with height. Consequently, the WS-5kW based on 2000-5000 kWh/month has shown the lowest LCE result, ranging between 0.055 and 0.0317 particularly in the southeast of Iraq. Moreover, the wind turbines 2kW, 5kW, 10kW have succeeded in reducing the LCE at different levels of demand and have succeeded in meeting the 2017 IBT prices from 2000 to 5000 kWh/month of demand and the 2015 IBT prices from 1000 to 5000 kWh/month of demand.

Concerning the PBP calculations that were calculated based on the 2017 IBT prices and the 2015 IBT prices, the aim was to recognise the best pricing model that could be applied to attain the shortest PBP within the lifetime of the turbine. In addition, the PBP

also helps in determining the most reliable and productive locations that are able to achieve a short PBP within a wind turbine's lifespan.

In a comparison between the PBP result based on the 2017 and 2015 IBT prices in accordance with four sizes of wind turbines, the PBP calculation based on 2015 IBT prices have shown the shortest PBP in different places in Iraq, despite the absence of a feed-in tariff policy in Iraq. The main reason returns to the saving mechanism used by applying different levels of monthly energy demand and the relatively high prices in 2015 IBT prices. The results of PBP based on 2015 IBT prices according to the saving strategy will contribute to encouraging householders to use small wind turbines within an grid system in order to reduce the monthly payments for national grid and decrease PBP for small wind turbines. In fact, the WS-5kW has shown the best performance and has achieved the shortest PBP 4.6 years at 30 m, based on the 2015 IBT prices and 5000 kWh/month of monthly energy demand.

The calculation of PBP of less than 8 years has been applied, based on the 2017 and 2015 IBP, as sensitive analysis to determine the most reliable and productive locations in Iraq. The WS-5kW and WS-2kW achieved wide areas of PBP of less than 8 years generally at different heights and for 3000, 4000, 5000 kWh/month of energy demand. The areas and the turbines that achieved the most significant results of PBP of less than 8 years, based on 3000 kWh/month and of energy demand at 20m heights will be used to apply the optimal hybrid system in the next work

Chapter 8 **ASSESSMENT OF SOLAR POWER PRODUCTION IN IRAQ**

8.1 **Introduction**

The main objective of this chapter is to evaluate solar radiation and solar power production derived from various solar system sizes throughout Iraq. Accurate data sources must be validated by using observed data from several weather stations. In addition, it is crucial to evaluate the cost of energy production and the payback period (PBP) of capital cost, according to different sizes of solar system and to determine the spatial distribution for high power production, lowest price of energy and the shortest payback period. The annual solar energy production was estimated by PVGIS, based on HelioClim1, and validated with Homer estimation for different locations in Iraq.

In addition, it is essential to improve the performance of the hourly solar energy production model (HSEP-WT model) by involving the impact of hourly ambient temperature and hourly wind speed at 2m. The hourly solar energy production which is estimated by HSEP-WT model will be used in the optimal hybrid system in the next chapter based on different sizes of the solar systems at any location in Iraq. Furthermore, the AEP of HSEP-WT model based on HelioClim3v5 has been validated with Homer estimation based on NASA data.

This chapter is organised as follows: the importance of solar sources is demonstrated in section 8.2. The source of observed data and the validation process is presented in section 8.2.1. Section 8.2.2 explains the methodology for evaluating the annual energy production from different sizes of solar system for all of Iraq. In addition, describes the economic methodology that was used to estimate the cost of a solar project, the cost of energy and the payback period. Moreover, section 8.3 outlines the method of developing the HSEP-WT model to calculate the hourly solar energy production from different sizes of solar system at any location in Iraq. Furthermore, the analysis and discussion of the results will be presented in section 8.4. The conclusions will be delivered in section 8.5.

8.2 **Solar Data Resources Assessment.**

One of the objectives of this project is to carry out solar resources assessment for the whole of Iraq. A precise solar data resource which is able to show good agreement with observed data is required, to achieve the above objective. This research used satellite data -rather than observed data - because observed data in Iraq is measured by a limited number of the weather stations and also there is a considerable amount of missing data in the

records of some of those stations. For these reasons, it becomes common to use satellite data to calculate the solar radiation at the earth's surface instead of observed data. Most of the databases of solar radiation use data from geostationary meteorological satellites. However, various solar data resources have been suggested for this work. According to this suggestion, the solar radiation data which is generated by the satellite images must be checked against observed data from ground level to get an idea of how much uncertainty there is in the satellite's solar radiation data. Furthermore, it must be recognized that this is the most accurate solar data resource to use as the primary source of solar radiation data for solar resources assessment in this project. The features of each suggested database are explained in section 3.6.

8.2.1 The Validation of Dataset with Observation Data

Solar power assessment in Iraq requires a global dataset that has high spatial and temporal resolution due to the limitation of weather stations in Iraq. Following this requirement, verification should be carried out between observed data for a number of weather stations in Iraq and estimated data from different solar radiation datasets. For this purpose, the average of daily global solar radiation ($\bar{G}$) data from 10 weather stations that are distributed over all parts of Iraq has been validated with HelioClim1, Helioclim3v5, CM-SAF and SARAH. Information about observed data from different weather stations in Iraq has been inserted in Table 8-1

Table 8-1. The name, locations and periods of records for a number of weather station that have used their data in validation in this project [115].

Weather station	Longitude	Latitude	Time Period
Basra station - Albrjsuh	47°3'36" East	30°17'23" North	7 years from 2008 to 2014
Baghdad station-Abu Ghraib	44°13'47" East	33°19'12" North	3 years from 2012 to 2014
Nineveh station - Ba'shiqah	43°19'47" East	36°27'0" North	4 years from 2011 to 2014
KIRKUK station - DAQUQ	44°25'12" East	35°9'35" North	4 years from 2011 to 2014
Anbar station - Aldour	43°1'48" East	33°27'36" North	7 years from 2008 to 2014
Qadisiya station - Diwaniyah	44°53'24" East	32°0'35" North	4 years from 2011 to 2014
Maysan station - Alekhala	47°11'23" East	31°48'0" North	7 years from 2008 to 2014
Karbala station - Razzazah	43°58'11" East	32°32'59" North	7 years from 2008 to 2014
Muthanna station - Al-khidhir	45°37'48" East	31°7'47" North	6 years from 2009 to 2014
Diyala stations -Baqubah	44°37'11" East	33°45'0" North	4 years from 2011 to 2014

The weather stations in Table 8-1 are controlled by the Iraqi Agrometeorological Network (IAN) which is a specialised department that gathers weather data for agricultural purposes and is related to the Ministry of Agriculture in Iraq [115]. These weather stations have a wide range of weather instruments and sensors. The instruments and the sensors were used in the solar radiation measurement system are presented as follows [115]:

- Solar panel 16.8V / 20 W
- Type: LI200X Pyranometer
- Light Spectrum Waveband: 400 to 1100 nm
- Accuracy: ± 3% typical

Some common error metrics have been used in the validation process to measure the error of forecasting data against observed data like Mean Absolute Percentage Error (MAPE). It is testing the forecast accuracy statistically, by measuring the percentage size of the error between actual and forecasting data as is expressed in Equation 5-13 [267]. In addition, Mean Bias Error (MBE) is the difference between the average of the forecasted and actual data. It indicates the degree to which the forecasted data are over or under actual data, as expressed in Equation 5-14 [269].

Furthermore, the Absolute Percentage Error (APE), which is the mean the absolute percentage size of the error between actual and forecasting data, divided by actual data as is expressed in Equation 6-10 [267].

8.2.2 Annual Solar Energy Production and Economic Evaluation

The main objective of this chapter is to identify areas with high solar radiation and their importance in the construction of feasible solar systems. Later in this project, the maps of the yearly average of daily global irradiation, annual solar energy production and economic assessment will play a significant role in determining the most feasible locations for the hybrid system in Iraq. To achieve this objective, reliable solar data sources and reliable software to estimate solar power production are required.

According to these requirements, HelioClim1 and HelioClim3v5 data sources have shown good agreement with observed data for 9 out of 10 weather stations in Iraq, as presented in the results in section 8.4. In accordance with this outcome, the HelioClim1 data source was integrated into PVGIS and processed to provide improved data such as monthly and daily radiation. This data has been used to create a yearly average of daily global irradiation for the whole of Iraq. In addition, PVGIS offers some useful calculation services such as solar power production estimation [179] that have been used to estimate the AEP for different sizes of solar systems for the whole of Iraq in this chapter. This section is organised as follows to achieve solar resource assessment for the whole of Iraq:

- First of all, the yearly average of daily global irradiation and AEP for specific solar systems for the whole of Iraq were carried out based on HelioClim1 from PVGIS.
- In addition, the Capacity Factor (CF) and percentage self-demand (PSD) assessment was carried out for three sizes of the solar system.
- On the other hand, the economic methodology used to estimate the total capital cost of solar system project TCOP is outlined.
- Furthermore, the economic evaluation for LCE and PBP is presented.

8.2.3 PVGIS and Annual Solar Energy Production Methodology.

The PVGIS provides average daily and monthly solar irradiance data based on PVGIS-HelioClim, SARAH and CM-SAF data sources [293]. The average daily solar irradiance data is represented by a typical day (data every 15 mins) for each month at different inclinations [0; 90] and orientations [-180; 180]. In addition, it provides various types of solar radiation, such as average global irradiance, clear-sky global irradiance and direct normal irradiance. On the other hand, PVGIS offer some services such as solar power production estimation for grid-connected and stand-alone PV power production estimation. The PV power production estimation services in PVGIS is backed by the same data that were mentioned above, with different types of solar panels such as Crystalline silicon; CIS; CdTe for different sizes. Furthermore, there are several fixed mounting options: Slope [0; 90], Optimize slope, Azimuth [-180; 180] and optimize azimuth. Also, there is an option of estimating the other system losses [0; 100], while the default percentage of combined PV system losses: 26.8% [293].

In this project, the yearly average of daily global irradiation (kWh/m^2/year) for the whole of Iraq is carried out based on the average daily solar irradiance on a horizontal surface based on HelioClim1. Equation 8-1 is expressed to estimate the yearly sum of global solar radiation.

$$Yearly\ sum\ of\ global\ solar\ radiation = \sum_{i=1}^{n} \frac{Hh_i * ND_i}{1000} \qquad \text{Equation 8-1}$$

- Hh : the typical average of daily global solar radiation on a horizontal surface for each month in a year Wh/m^2/day from PVGIS dataset.
- : number of days for each month in a year (28 days to 31 days).
- : the particular month per year from January until December.
- n: represents number of months per one year.

This estimation is applied for each coordinate on the Iraq map with spatial resolution $1/2^o$ latitude × $2/3^o$ longitude. Figure 8-1 shows the yearly sum of global solar radiation on the horizontal surface.

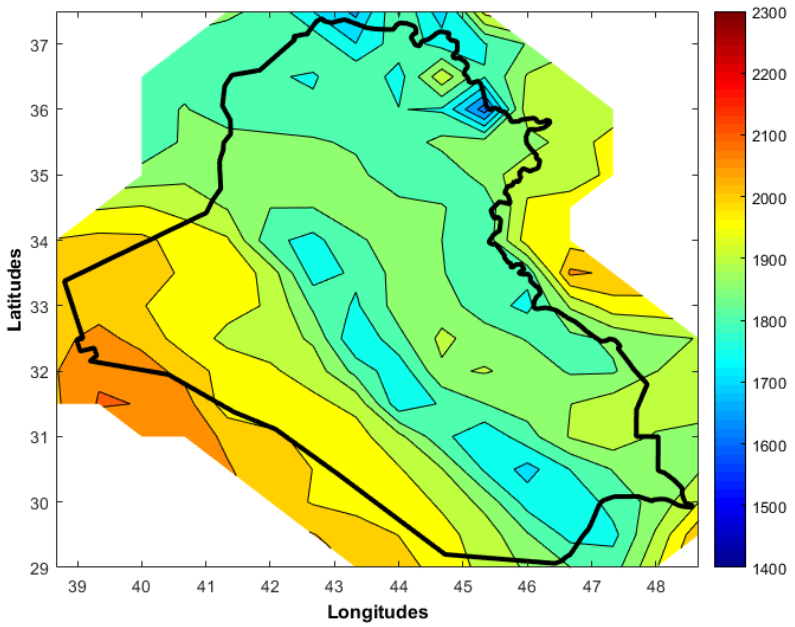

Figure 8-1. Contour colour map for yearly sum of global solar radiation on the horizontal surface (kWh/m^2/year) from the PVGIS- HelioClim dataset.

Three sizes of solar system 3.1 kW, 5.2 and 10.4 kW have been proposed to estimate the annual solar energy production, to recognise the cost of electricity that can be generated by different sizes of solar system. In order to estimate solar power production for three sizes of solar systems, some key information is involved:

- The maps of solar power production are mapped based on spatial resolution 1/2° latitude × 2/3° longitude.
- PV module of Polycrystalline silicon has been used due to the low cost, high efficiency and its wide use in Iraq.
- The free-standing mounting option has been proposed due to the flat roofs of all buildings in Iraq with 0° azimuth as optimal orientation, while, the annual optimal slope distribution for all of Iraq have been determined by using annual optimal slope feature in PVGIS according to spatial resolution 1/2° latitude × 2/3° longitude. [293], as shown in Figure 8-2.
- 12.5 % represents the losses of the system due to temperature and low irradiance, where 2.8 % represents the loss due to angular reflectance effects and 14 % as other losses (cables, inverter, etc.). The percentages of losses are estimated by PVGIS as default values [293].

The power production from any solar system according to PVGIS is estimated based on the expression in Equation 3-7.

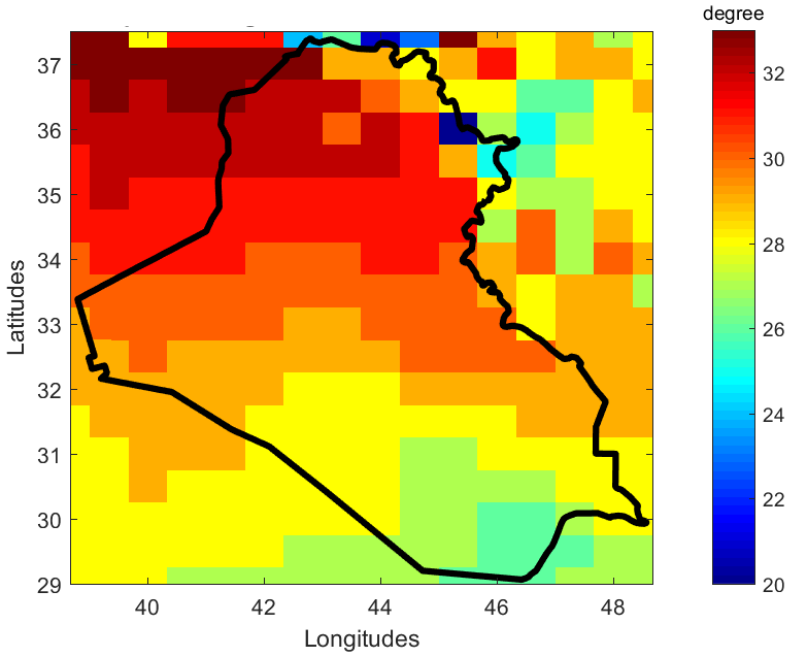

Figure 8-2. The annual optimum angle of solar module for the whole of Iraq based on PVGIS [293].

8.2.4 Capacity factor and the percentage self-demand

In order to evaluate the AEP from different sizes of solar system and to evaluate their performance, CF and the PSD assessment have been carried out for the whole of Iraq.

First of all, with regard to the CF of the solar system, it is represented as a ratio of actual energy produced from solar system during a period of time to maximum possible output power that the specific solar system can generate, based on the rated power of this solar system during the same period of time [278]. Equation 8-2 and Equation 8-3 are expressed to estimate the CF .

$$Capacity\ Factor\ CF = \frac{P\ mean}{P_r} * 100 \qquad \text{Equation 8-2}$$

$$P\ mean = \frac{ASEP}{8760} \qquad \text{Equation 8-3}$$

- $P\ mean$: is the average of hourly energy production that has been estimated by Equation 8-3 based on Annual Solar Energy Production (ASEP) from PVGIS.
- While P_r: represents the rated power of a solar system, which means the maximum power production that could be generated from the specific size of solar system.

Different scenarios of electricity demand that are suggested in this chapter represent the change of electricity demand throughout the four seasons according to Iraqi weather conditions and also based on different sizes of housing units.

It is worth mentioning that the electricity demand in housing units increases dramatically during the summer due to people using air conditioners slightly more during winter, due to

the use of heaters and water boilers. For this reason, the PSD are suggested at different levels of monthly electricity demand 1000, 2000, 3000, 4000, and 5000 kWh/month. The calculation of PSD is expressed in Equation 6-9.

8.2.5 Economic Methodology

In the beginning, this study attempts to estimate the main cost categories of solar system investment and determine the relative weight for different expenditures. The most important renewable energy studies have broken down the cost of solar system project into capital cost and variable cost [294]. In the next sections, the total capital cost of solar system project is determined by estimating the initial cost and variable cost. Also, the methodology of the levelized cost of electricity and the PBP are presented.

8.2.6 The Total Cost of Project

The total capital cost of solar system project (TCOP) consists of the capital cost at the first year of installation and the variable cost to the end of the project's lifespan .First of all, there are different definitions of capital cost; one of them is the dominant cost in the total PV system expenditure which can be broken down as follows [282]:

- The PV modules, cables, inverter cost and their taxes;
- Civil works, which include construction costs for site preparation and installation;
- Sea and land transport plus customs based on customs clearance companies in Iraq.

The Polycrystalline 60 cells 260 watts (99cm × 165cm) solar module [295] has been used to estimate solar energy in this chapter which costs £96 and includes cables in 2018. According to the price of one Polycrystalline module, the value of one watt of the PV system is £0.37. Furthermore, the cost of a DC-AC inverter depends on the rated power of the solar system. Also, taxes constitute 5% of the amount of electrical equipment (PV module, cables and inverter) imported to Iraq [284]. Moreover, the civil works cost of construction and installation equals £37 per one module. Furthermore, the another capital expenditure is the cost of sea and inland transport plus customs which equal £97.4 per one cubic meter of shipment of imported PV module. This cost determined based on most customs clearance companies in Iraq in 2018. Equation 8-4 is expressed to estimate the capital cost or capital expenditure (Capex) for solar system.

$$Capex = PVC + InverterC + Taxes + ICF \qquad \text{Equation 8-4}$$

- PVC: PV cost.
- Whereas, InverterC: inverter cost which is determined based on solar system size.
- Taxes: which represents 5% of electrical equipment.

- While, ICF refers to the Installation, Civil work and Foundation cost of the solar system.

The Variable Cost (VC) represents the second important part of total cost of a solar system over the lifespan of project. In general, the variable cost of solar system consists of [286]:

- Operation and Maintenance cost OMC .
- Replacement cost

The OMC and replacement costs should be estimated over the lifespan of the project to make the evaluation process for a total project cost more realistic [281, 285-287]. To determine the operation and maintenance cost over 20 years, Equation 7-4 has been applied [286, 287]. OMC: Operation and Maintenance Cost over 20 years. While OMC_0: represents the primary cost of operation and maintenance for the first year of the project equals 1% of (Capex / 20 years) [287]. T: represents the lifetime of project = 20 years. In addition, the replacement part costs should be estimated over the lifespan of project. In this study, the inverter only has been assumed to be replaced once , due to the lifespan of an inverter being ten years [287]. The expression in Equation 7-5 is used to estimate the replacement and spare part cost (RSC). N_{rep}: refers to the number of replacement over the Solar lifespan system, which is assumed to be only one replacement (Inverter). Finally, to estimate the variable cost (VC) over the project lifetime, Equation 8-5 should be applied.

$$VC = OMC + RSC \qquad \text{Equation 8-5}$$

Furthermore, there another factor should be taken into account when evaluating the total cost of the project. In fact, the present value of solar system scrap at the end of project could not be ignored when calculating the TPV of solar system project. PVS : is the present value of scrap (PVS) which is expressed in terms of the value of scrap SV = 20 % of the capital cost [296], as expressed in Equation 7-7 [287].

The TCOP is far from simple in terms of a project's lifetime. For this reason, the TPV must be estimated and then the lifetime value of the project should be taken into consideration when calculating the total cost of the project over the PV's system lifespan. The TPV of project is expressed in Equation 8-6.

$$TPV = Capex + VC - PVS \qquad \text{Equation 8-6}$$

In order to estimate the time value of total project cost over the project's life span the Capital Recovery Factor (CRF) should be used [212] as is expressed in Equation 7-9. Now it becomes possible to calculate the TCOP over the project lifetime as is expressed in Equation 8-7.

$$TCOP = (TPV * CRF) * T$$ Equation 8-7

The TCOP is required to estimate PBP for different sizes of the solar system in this study. In addition, it is essential to calculate the cost of electricity production from several solar system sizes by applying Levelized Cost of Electricity (LCE).

8.2.7 **Levelized Cost of Electricity LCE.**

LCE is one of the most important economic indicators employed to evaluate the cost of energy for any renewable technology. It has been used to calculate the cost of potential energy that has been estimated by different size of wind turbines in Chapter 7. In general, the LCE is defined as the ratio of total annualised project cost (levelized annual costs) based on discounting the yearly financial flow to the AEP from the project, as expressed in Equation 7-12 [290]. While the Levelized annual costs LAC represent the annual payment of TPV of project based on CRF, look at the following expression in Equation 8-8 [212].

$$LAC = TPV * CRF$$ Equation 8-8

$$LCE = \frac{LAC}{AEP}$$ Equation 8-9

AEP : The AEP from different sizes of a solar system. Equation 8-9 calculates the electricity price based on the principle of consuming all electricity generated by the PV system, without taking into consideration the capacity of demand if it is higher or lower than the energy production. For this reason, a saving strategy that was suggested in Chapter 7 was applied in LCE calculation, based on different scenarios of energy demand against varying amounts of AEP from different sizes of solar system. The energy demand which was suggested in this study ranged from 1000 to 5000 kWh/month. In addition, the annual energy productions that were estimated by 3.1 kW, 5.2 kW and 10.4 kW in the LCE calculations. Equation 8-9 has been modified to meet the requirement of different monthly demand, as expressed in Equation 7-13 in Chapter 7.

The LCE in this study was estimated for the whole of Iraq based on AEP of different solar system size and the spatial resolution $1/2^{o}$ Latitude × $2/3^{o}$ Longitude. The LCE calculations aim to determine the distribution of the locations of the lower cost of energy that have been generated by different sizes of solar systems.

8.2.8 **Payback Period PBP**

The PBP is the length of period required to recover the TCOP based on the net annual cash inflow from AEP the project [214] as is expressed in Equation 7-14.

In this chapter, the TCOP has been estimated over the project's lifespan of 20 years. In addition, the Annual saving cost strategy AnnSavCost that was suggested in section 7.3 is applied rather than the (Net Annual Cash inflow of AEP) in the original equation. In other words, the PBP in this study provides an estimate based on total cost of the project divided by saving money, based on different levels of demand and different IBT in Iraq as outlined in section 7.3. The PBP equation that used in this study is expressed as Equation 7-15 and Equation 7-16.

The PBP calculation aims to determine which solar system size can give the lower PBP throughout the lifetime of a project. While eight years is chosen as the best scenario for short PBP for a renewable project [291, 292], it will play a vital role to determine the locations that can show short PBP throughout the lifetime of the solar system.

8.3 **Hourly Solar energy Production.**

The annual energy production from a PV array is necessary to evaluate the spatial distribution of solar energy availability and the economic feasibility of using solar system in Iraq. Otherwise, it is not useful in case of assessing the performance of hybrid systems optimization. The optimization of hybrid system needs data of hourly solar energy production over one year for any solar system size with different tilt and azimuth angles of solar panel surface at any location in Iraq.

According to that, this section aims to calculate the hourly energy production from different sizes of a solar system that are able to track the sun in two directions and at various locations in Iraq. Also, this calculates the effect of wind speed and ambient temperature on solar panels productivity.

Firstly, the solar power production calculation in this section has been developed based on Homer calculation for PV array power output [33]. In addition, the Polycrystalline 60 cells 260 watts (99cm × 165cm) solar module [19] was used to produce solar power in this project. Furthermore, all necessary technical information for solar power calculation is provided by the manufacture specification sheet of Polycrystalline solar module as illustrated in Table 8-2 [295]. Homer utilises Equation 8-10 to estimate the output of the PV [297].

$$P_{PV} = Y_{PV} f_{PV} \left(\frac{\bar{G}_T}{\bar{G}_{T,STC}} \right) \left[1 + \alpha_P \left(T_c - T_{c,STC} \right) \right] \qquad \text{Equation 8-10}$$

- P_{PV} : represents the PV power production in the current time step (t =1 hour).
- Y_{PV} : refers to the rated capacity of the solar system [kW].
- f_{PV}: refers to the PV derating factor that equals 80% after 25 years and (1-0.00888) in the first year.

- $\bar{G}_T$: represents the solar radiation incident on the solar module in the current time step [kW/m2] which is provided by Equation 8-11.
- $\bar{G}_{T,STC}$: refers to the incident radiation at standard test conditions STC which equals 1 kW/m^2 as is presented in Table 8-2.
- α_P : represents the temperature coefficient of power -0.41 %/°C as presented in Table 8-2. A negative number shows how strongly the solar module power production depends on the surface temperature of the PV array [297].
- T_c : denotes the PV cell temperature [°C] in the current time step, which is provided by Equation 8-25.
- $T_{c,STC}$: refers to the PV cell temperature under STC, which equals 25°C as presented in Table 8-2.

Firstly, we will progress through several arithmetic processes to get $\bar{G}_T$ and secondly, will go through T_c calculation. To calculate the solar radiation incident $\bar{G}_T$ on the PV array, Homer has used Equation 8-11 [297].

$$\bar{G}_T = (\bar{G}_b + \bar{G}_d A_i) R_b + \bar{G}_d (1 - A_i) \left(\frac{1 + \cos\beta}{2}\right) \left[1 + f\, sin^3\left(\frac{\beta}{2}\right)\right] + \bar{G}\, \rho_g \left(\frac{1 + \cos\beta}{2}\right) \quad \text{Equation 8-11}$$

- $\bar{G}_b$: refers to the beam radiation kW/m^2.
- $\bar{G}_d$: is the diffuse radiation kW/m^2.
- $\bar{G}$: is called global solar radiation kW/m^2 and sometimes calls Global Horizontal Irradiation (GHI).

Global solar radiation includes beam solar radiation that travels directly from the sun to the earth's surface to form shadow and diffuse radiation, which comes from all parts of the atmosphere and does not create a shadow. For this reason, both of them form global solar radiation as expressed in Equation 8-12 [297].

$$\bar{G} = \bar{G}_b + \bar{G}_d \quad \text{Equation 8-12}$$

Moreover, β represents the slope of the surface [°]. The value of this angle has been determined by the annual optimum slope between (0-90^o) according to PVGIS-HelioClim1 [293], as shown in Figure 8-2.

Table 8-2. Presents the most important technical information for Polycrystalline 60 cells 260 watts (99cm × 165cm) solar module, derived from the manufacturer's specification sheet of Polycrystalline solar module [19].

Working Conditions

Maximum system voltage	DC1000V
Operating Temperature	-40 ~+85
Maximum series fuse rating	15A
load, frontside load backside	5400Pa 2400Pa
(NOCT)	45 ±2
Application level Class	A

- 25 years liner power output warranty

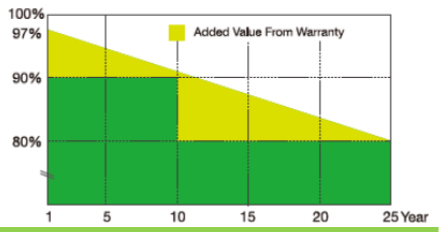

Electrical Parameters

Module	BSM260P-60	BSM265P-60	BSM270P-60	BSM275P-60
Maximum Power(Pmax)	260W	265W	270W	275W
Open-circuit Voltage (Voc)	38.1V	38.3V	37.9V	38.5V
Maximum Power Voltage (Vmp)	30.6V	30.8V	30.9V	31.1V
Short-circuit Current (Isc)	9.01A	9.10A	9.22A	9.25A
Maximum Power Current(Imp)	8.50A	8.61A	8.73A	8.84A
Module Efficiency (%)	15.90%	16.21%	16.51%	16.82%
Power Tolerance	0 ~ +5W			
Temperature Coefficient of Isc	0.05%/°C			
Temperature Coefficient of Voc	-0.32%/°C			
Temperature Coefficient of Pmax	-0.41%/°C			
STC	Irradiance 1000w/m², Cell temperature 25 °C, Spectrum AM1.5			

- ρ_g : refers to the ground reflectance, which is also called the albedo [%]; it is possible to get the value of ground reflectance from PVGIS-HelioClim1, ranking between 2.8 % and 2.7 % for whole Iraq [293].
- f : represents horizon brightening, which means the diffuse radiation that comes from the horizon more than the rest of the atmosphere. This is related directly to the cloudiness as expressed in Equation 8-13 [297].

$$f = \sqrt{\frac{\bar{G}_b}{\bar{G}}} \qquad \text{Equation 8-13}$$

- A_i represents the anisotropy index, which is a measure of the atmospheric transmittance of direct radiation. This parameter is used to calculate the amount of circumsolar diffuse radiation. The anisotropy index is expressed in Equation 8-14 [297]:

$$A_i = \frac{\bar{G}_b}{\bar{G}_o} \qquad \text{Equation 8-14}$$

- $\bar{G}_o$: refers to the extra-terrestrial horizontal radiation averaged over the time step kW/m2.

In fact, we need to calculate a list of variables as follows to be able to estimate $\overline{G}_o$:

- δ : the solar declination [°] Equation 8-15.
- ω : the hour angle [°] Equation 8-16.
- E : the equation of time [hour] Equation 8-18.
- θ : the angle of incidence [°] Equation 8-19.

- θ_z: the zenith angle [°]Equation 8-2.
- G_{on}: the extra-terrestrial normal radiation [kW/m2] Equation 8-21.
- R_b: is the ratio of direct radiation on the sloped surface to direct radiation on the horizontal surface Equation 8-24.

The declination angle, which is denoted by δ, varies daily across four seasons due to the slope of the Earth on its axis of rotation and the rotation of the Earth around the sun. The declination angle is given in Equation 8-15 [297, 298]:

$$\delta = 23.45^o sin\left(360^o \frac{284+n}{365}\right) \quad \text{Equation 8-15}$$

n refers to the day of the year (a number 1 through 365). The placement of the sun in the sky is influenced by the time of day, which can be described by a hour angle. The hour angle equals zero at solar noon, which is negative before noon 12:00 pm, and positive in the afternoon. For example: 1:00 am=-165°, 10:00 am=-30°, 12:00=0, 14:00=30° and 24:00=180°. The hour angle expressed by Equation 8-16 has been modified based on [297]:

$$\omega = (t_s - 720)/4 \quad \text{Equation 8-16}$$

t_s : refers to the solar time [hour]. The value of t_s at solar noon = 720 min = 12 hr, while t_s = 810 min , = 13:30 hr. Equation 8-16 is based on the fact that the sun moves across the sky every 15 degrees per hour = 60 min. The t_s is ranges from 0 to 23 hr, where 0 equivalent to 12: 00 am and equals 1440 min according to GMT. The solar time is given by Equation 8-17[299]:

$$t_s = t_c + 4(L_{st} + L_{loc}) + E \quad \text{Equation 8-17}$$

- t_c : is the civil time or local time zone in hours for any country that is ranging from 1 to 24.
- L_{st} : is the standard meridian for local time zone.
- L_{loc}: represents the location longitude in degrees $0^o < L < 360^o$ [299].
- E : refers to the equation of time which represents the difference between solar time and mean solar time. The equation of time is expressed by Equation 8-18 [297]:

$$\mathrm{E} = 3.82(0.000075 + 0.001868\,.\,cosB - 0.032077\,.\,\sin B - 0.014615.\cos 2B - 0.04089.\sin 2B)$$
$$B = 360^o \frac{(n-1)}{365} \quad \text{Equation 8-18}$$

In order to estimate the solar radiation incident, for a PV surface with any orientation, the angle of incidence should be defined, which is represented by the angle between the beam

radiation and the normal to the surface, as shown in Figure 8-3. The incidence angle can be estimated by using Equation 8-19 [297]:

$$\cos\theta = \sin\emptyset \sin\delta \cos\beta - \cos\emptyset \sin\delta \sin\beta \cos Z_s + \cos\emptyset \cos\delta \cos\beta \cos\omega + \sin\emptyset \cos\delta \sin\beta \cos\omega \cos Z_s + \cos\delta \sin\beta \sin\omega \sin Z_s \quad \text{Equation 8-19}$$

- θ : refers to the angle of incidence.
- Z_s : represents the azimuth of the surface, as shown in Figure 8-3.
- $\emptyset$ is the latitude of a location.

On the other hand, there is another important angle is called the zenith angle, which is located between a normal vertical line and the beam solar radiation. The zenith angle equals zero when the sun is in a perpendicular position, and 90° when the sun is at the horizon. The zenith angle can be calculated when setting β = 0° in Equation 8-19 to get the value of zenith angle θ_z in Equation 8-20 [297]:

$$cos\,\theta_z = cos\,\emptyset\, cos\,\delta\, cos\,\omega + sin\,\emptyset\, sin\,\delta \quad \text{Equation 8-20}$$

The amount of solar radiation striking the top of the atmosphere varies over the year, due to the distance between the sun and the earth, which changes over the year because of the eccentricity of the earth's orbit.

To estimate the extra-terrestrial normal radiation G_{on} kW/m^2 , which is defined as the amount of sunlight striking a surface normal (perpendicular) to the solar radiation at the top of the earth's atmosphere, Homer uses the following equation [297]:

$$G_{on} = G_{sc}\left(1 + 0.033.cos\frac{360\,n}{365}\right) \quad \text{Equation 8-21}$$

G_{sc} is the solar constant [1.367 kW/m2]. While Equation 8-22 has been applied to calculate the average extra-terrestrial horizontal radiation $\overline{G_o}$ over one day [297]:

$$\overline{G_o} = \frac{12}{\pi} G_{on}\left[cos\,\emptyset\, cos\,\delta\ (sin\,\omega_2 - sin\,\omega_1) + \frac{\pi(\omega_2-\omega_1)}{180^o} sin\,\emptyset\, sin\,\delta\right] \quad \text{Equation 8-22}$$

$\omega_1\ and\ \omega_2$ represent the hour angles at the beginning (sunrise) and the end (sunset) of the time step respectively, as expressed in Equation 8-23 [298].

$$\omega_1 = -(cos^{-1}[-tan(\emptyset-\beta)\,tan\,\delta])$$
$$\omega_2 = cos^{-1}[-tan(\emptyset)\,tan\,\delta] \quad \text{Equation 8-23}$$

While R_b represents the ratio of direct radiation on the sloped surface to direct radiation on the horizontal surface as expressed in Equation 8-24 [297].

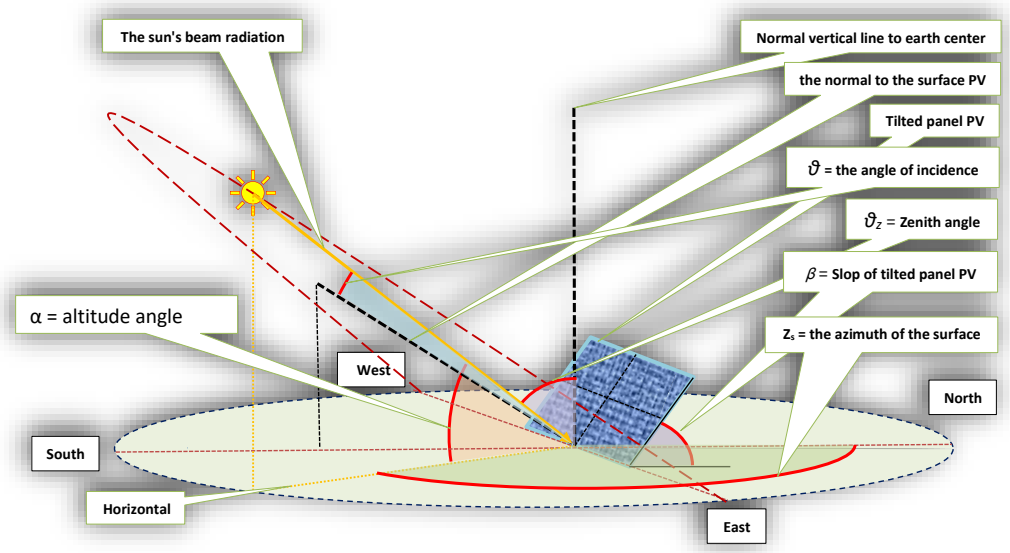

Figure 8-3. Geometrical description of the Sun's movement within the framework of the planetarium to Figure out the angle of incidence, the tilted panel PV, Zenith angle, the azimuth angle of the surface, altitude angle, the sun's beam radiation and other information related to the tilted PV module.

$$R_b = \frac{\cos\theta}{cos\ \theta_z} \qquad \text{Equation 8-24}$$

Now, the all-important variables to apply Equation 8-11 have been prepared to get the value of $\bar{G}_T$ every hour across 8760 hours. In this calculation, the PV surface has been oriented toward the south Z_s = zero (azimuth angle). The slope of tilted PV surface β has been chosen based on annual optimum slope for each location according to PVGIS-HelioClim1 [293] as is shown in Figure 8-2. The first important variable $\bar{G}_T$ in Equation 8-10 is calculated. The second important variable is T_c in Equation 8-10 is estimated in different way from Homer's calculation method. Homer calculated the T_c based on the coefficient of heat transfer to the surroundings (U_L) [kW/m2°C] [297], according to the ambient temperature and the radiation striking the array rather than using the effect of wind speed at solar module.

The photovoltaic cell temperature T_c represents the temperature of the surface of the solar panel. Throughout the night, T_c is the same as the ambient temperature, whereas, during a day with full sun, the cell temperature can exceed the ambient temperature by 30°C or more. However, the wind speed at the level of PV can significantly reduce cell temperature. To calculate the cell temperature at each time step Equation 8-25 is used, applying the effect of wind speed, ambient temperature and the radiation striking on the PV array according to Skoplaki's method in [201].

$$T_c = T_a + \frac{\bar{G}_T}{I_{NOCT}} . \left(T_{NOCT} - T_{a,NOCT}\right) . \frac{h_{w,NOCT}}{h_w(v)} . \left[1 - \frac{\eta_{STC}}{\tau . \alpha}(1 - \beta_{STC} . T_{C,STC})\right] \quad \text{Equation 8-25}$$

- T_a : is the ambient temperature [°C] according to the time step.
- v : is hourly wind speed m/s.
- η_{STC} : refers to module efficiency [201] 15.9% under standard conditions according to Table 8-2 [1] in this project.
- β_{STC} : represents temperature coefficient of maximal power [201] - 0.41 %/°C according to Table 8-2 [1].
- $T_{C,STC}$: refers to the cell temperature under standard test conditions 25°C [201].
- τ : is the solar transmittance of any cover over the PV array 0.9%.
- $h_w(v)$: is the wind convection coefficient which was estimated according to Equation 8-26.
- I_{NOCT} equals 800W/m2 the Irradiance at normal operating cell temperature [201].
- $T_{NOCT} = 45$ °C while $T_{a,NOCT} = 25$°C is ambient temperature at nominal operating cell temperature [201].
- $h_{w,NOCT}$ refers to the wind convection coefficient for wind speed according to NOCT conditions, i.e. v_w= 1 m/s [201].

$$h_w = 5.7 + 2.8\, v_w \quad \text{Equation 8-26}$$

v_w: is the local wind speed close to the module at 2.5 m or 2 m height. This wind speed can be calculated using the downscaling model at 2 m. Finally, Equation 8-10 can be applied to get hourly P_{PV}.

8.3.1 Data Resources for Hourly energy Production

The hourly energy production from several sizes of solar systems have been estimated based on three components of solar radiation from HelioClim3v5 [181] as follows:

- Global Solar Radiation $\bar{G}$ kWh/m² for 8760 hours, as shown in Figure 8-4.
- Beam radiation (called direct radiation) Gb kWh/m² for 8760 hours per year.
- Diffuse radiation Gd kWh/m² for 8760 hours per year.
- Ambiant temperature T (C°) for 8760 hour.

The simulation code of hourly energy production for a solar system requires input of site coordination, tilt angle of solar module and some technical data related to the module manufacturer. In fact, the typical hourly solar radiation data over one year for periods (2004, 2005 and 2006) have been used to estimate hourly energy production everywhere in Iraq by selecting a typical day of solar radiation data for 2004, 2005 and 2006.

However, validation has been performed between observed data against a wide range of datasets (HelioClim1, HelioClim3v5, CMSAF and SARAH). The results have confirmed that 9 out of 10 weather stations in Iraq for the period between 2004 and 2006 have shown a reliable agreement between HelioClim1, HelioClim3v5 and the observed data.

The data provided by HelioClim3v5 for the period between 2006 and 2018 is very expensive. In addition, the simulation model that was developed in section 8.3 to calculate hourly energy production from different size of solar system required hourly wind speed at 2 m and ambient temperature to calculate the photovoltaic cell temperature [300]. The hourly wind speed at 2 m has been estimated by the DSM based on MERRA data [131]. The hourly ambient temperature has been provided by MERRA-2 RE-ANALYSIS in 2006 [301]. The wind speed at 2 m is gathered for the same period of data used to calculate the energy production from wind turbines in 2014. Figure 8-5 shows typical solar radiation, ambient temperature and wind speed at 2 m.

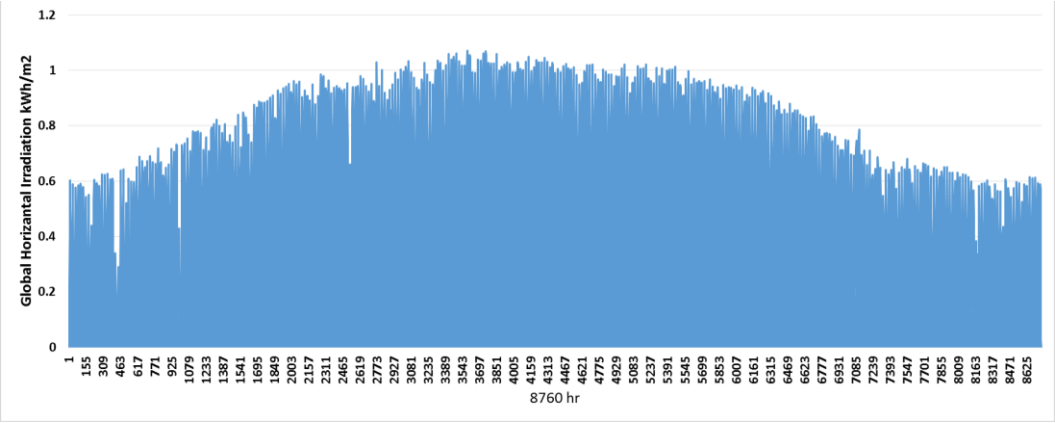

Figure 8-4. The global solar radiation $\bar{G}$ kWh/m² for one year (8760 hours) from HelioClim3v5 based on typical daily data for 2004, 2005 and 2006 in Amara location in Iraq.

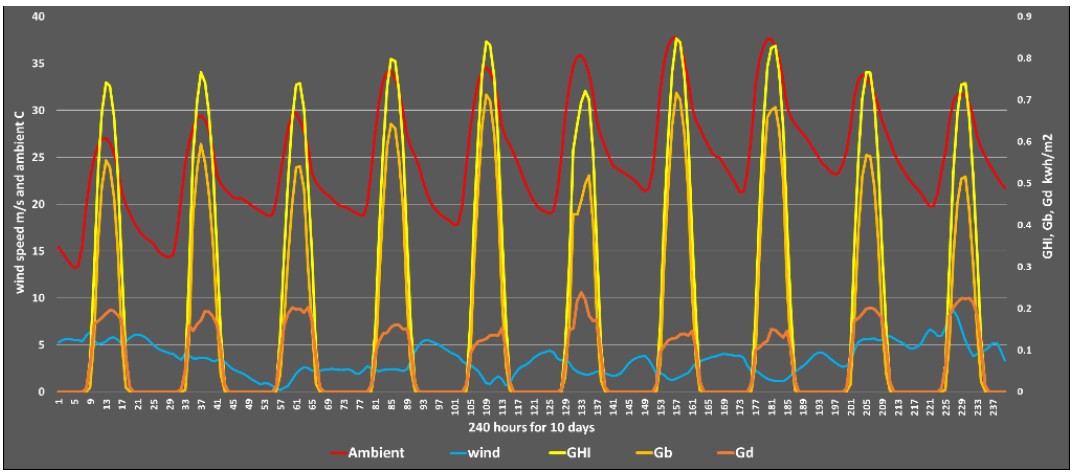

Figure 8-5. Hourly input data of $\bar{G}$, $\bar{G}_b$, $\bar{G}_d$, Ambient temperature and wind speed at 2m for the first 10 days of March. These data were used in the hourly power production simulation.

8.4 Analysis of results and discussion.

8.4.1 The validation of several datasets with observation data.

In order to determine the most accurate solar data resources for solar power production assessment in Iraq, validation has been carried out between observed data of Solar Surface Irradiation SSI (which has been gathered from 10 weather stations in Iraq as is maintained in Table 8-1) and SSI of database provided by HelioClim1, HelioClim3v5, CMSAF and SARAH. First of all, APE was estimated between monthly average observed data and monthly average estimated data from different databases for each weather station. Furthermore, MAPE was calculated based on annual SSI, as shown in Figure 8-6, which represents a sample of the validation process that has been achieved in this study for each weather station in Table 8-1.

Figure 8-6 shows a sample of the validation process that has been applied for 10 weather stations located in different places in Iraq, as shown in Figure 8-7. The most significant finding in Figure 8-7 was that 9 out of 10 weather stations showed the lowest MAPE for HelioClim1 and HelioClim3v5 against CMSAF and SARAH in this validation. Just one weather station has shown that MAPE for CMSAF was lower than HelioClim3v5.

In order to understand the reason behind this results, the distribution of annual SSI for observed data and other data resources for the 10 weather stations can give reasonable justification for the low MAPE for HelioClim1 and HelioClim3v5 against CMSAF and SARAH, as shown in Figure 8-8. According to the annual $\bar{G}$ distribution of CMSAF and SARAH, the median and the large box of the boxplot are out of the range of majority distribution for observed data, as shown in Figure 8-8, while both HelioClim1 and HelioClim3v5 have shown data distribution close the median of observed data.

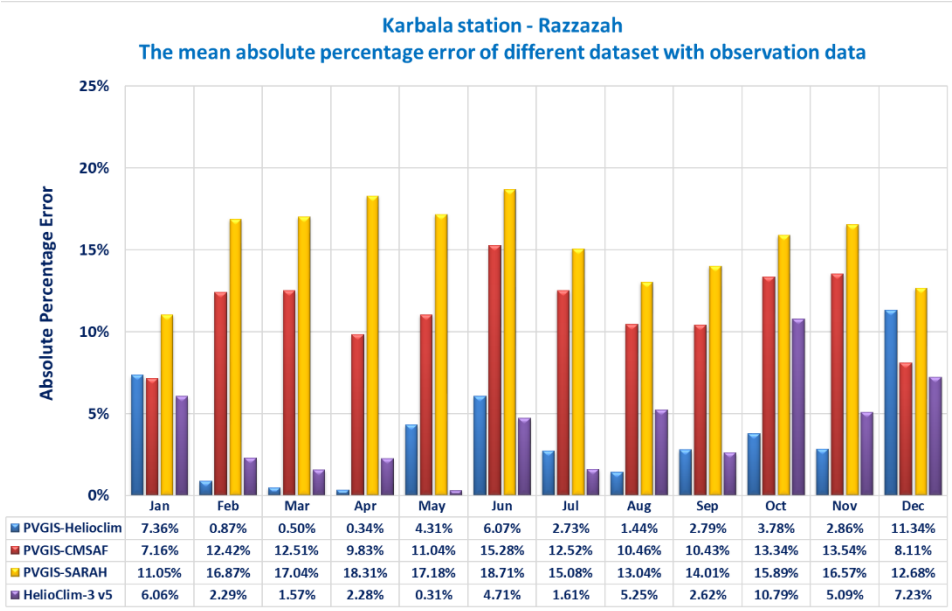

	Jan	Feb	Mar	Apr	May	Jun	Jul	Aug	Sep	Oct	Nov	Dec
PVGIS-Helioclim	7.36%	0.87%	0.50%	0.34%	4.31%	6.07%	2.73%	1.44%	2.79%	3.78%	2.86%	11.34%
PVGIS-CMSAF	7.16%	12.42%	12.51%	9.83%	11.04%	15.28%	12.52%	10.46%	10.43%	13.34%	13.54%	8.11%
PVGIS-SARAH	11.05%	16.87%	17.04%	18.31%	17.18%	18.71%	15.08%	13.04%	14.01%	15.89%	16.57%	12.68%
HelioClim-3 v5	6.06%	2.29%	1.57%	2.28%	0.31%	4.71%	1.61%	5.25%	2.62%	10.79%	5.09%	7.23%

Figure A

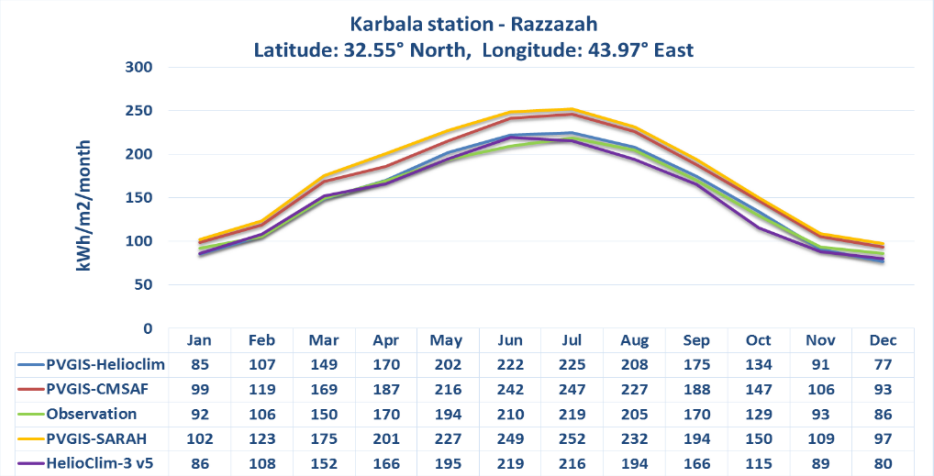

	Jan	Feb	Mar	Apr	May	Jun	Jul	Aug	Sep	Oct	Nov	Dec
PVGIS-Helioclim	85	107	149	170	202	222	225	208	175	134	91	77
PVGIS-CMSAF	99	119	169	187	216	242	247	227	188	147	106	93
Observation	92	106	150	170	194	210	219	205	170	129	93	86
PVGIS-SARAH	102	123	175	201	227	249	252	232	194	150	109	97
HelioClim-3 v5	86	108	152	166	195	219	216	194	166	115	89	80

Figure B

Figure 8-6. Figure A shows APE for monthly average data of SSI and MAPE for annual SSI data between observed data from the Karbala weather station and the SSI database, which was provided by HelioClim1, HelioClim3v5, CMSAF and SARAH. Figure B shows several curves of monthly SSI of observed data and a different database for the Karbala weather station in Iraq.

The approximation distribution of HelioClim1 and HelioClim3v5 from observed data and spacing distribution of CMSAF and SARAH from observed data distribution interpret the reason for the low error between both HelioClim1 and HelioClim3v5 with observed data. For more sensitive analysis, MBE distribution was carried out, based on annual $\bar{G}$ for the data of HelioClim1, HelioClim3v5, CMSAF and SARAH with observed data for the 10 weather stations, aiming to recognize which of the HelioClim1 and HelioClim3v5 databases was more accurate and had a lower error with observed data.

Figure 8-9 shows to what extent that HelioClim3v5 data is close to observed data, the median of error of HelioClim3v5 was close to zero. This finding means that HelioClim3v5 data has the best fit with observed data and also both of HelioClim1, HelioClim3v5 dataset are regarded as a useful data for solar power assessment in Iraq.

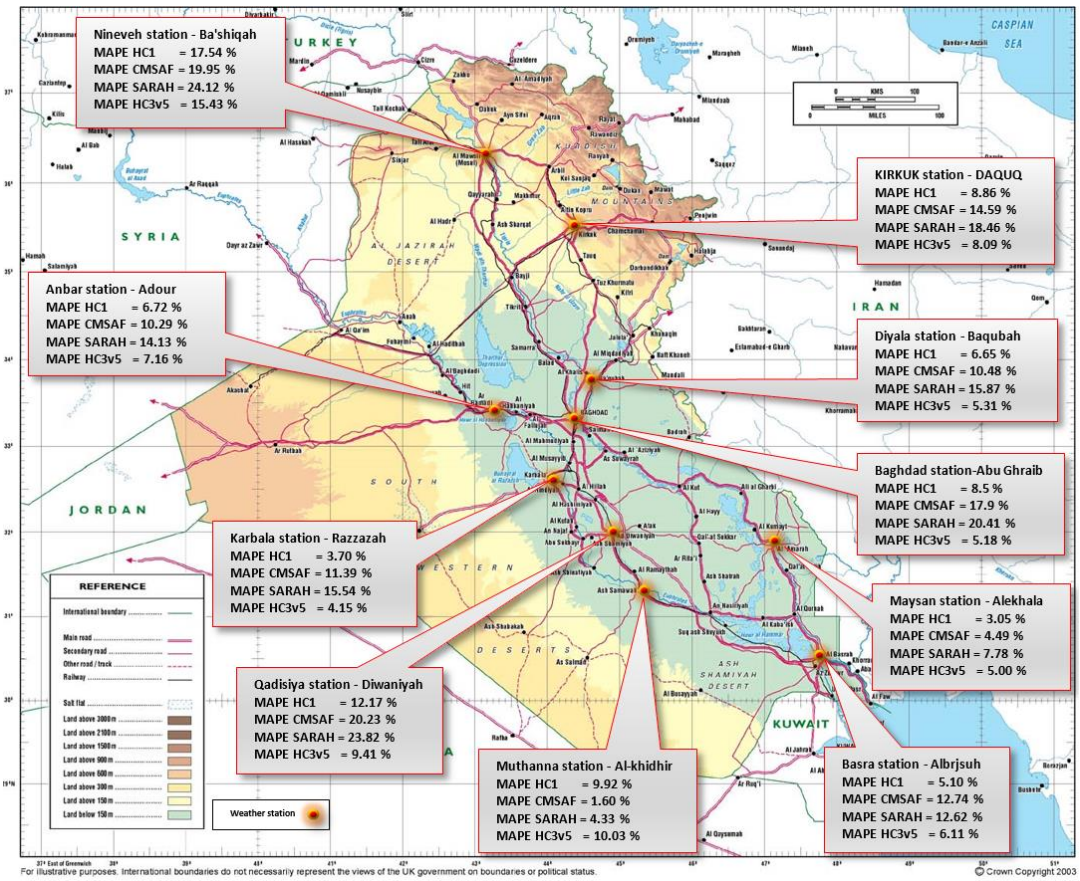

Figure 8-7. Distribution of the 10 weather stations across Iraq that have their measured data used for validation purposes with HelioClim1, HelioClim3v5, CMSAF and SARAH based on MAPE for annual SSI.

In order to interpret the difference between the low accuracy of the CMSAF and SARAH datasets and high accuracy for HelioClim1 and HelioClim3v5 dataset against observed data for 10 weather stations in Iraq, two explanations are offered:

- Basically, the solar radiation of CMSAF and SARAH dataset was estimated based on the satellite images to determine the influence of clouds on the solar radiation by evaluating effective cloud albedo from the image with the regular comparison with ground images, taking into consideration the absorbed radiation by aerosols, water vapour and ozone [302, 303].
- While the solar radiation of HelioClim1 (HC1) used the same procedure as the CMSAF and SARAH dataset, the accuracy has been developed by comparison with observed data from the WMO radiometric network in Africa (35 sites) and Europe (55 sites) for the period 1994-1997 [176]. On the other hand, the accuracy of HelioClim3v5 (HC3v5) dataset has been supported by observed data from climatological database [183]; for this reason, the HC3v5 has shown results higher than HC1 against observed data in Iraq.

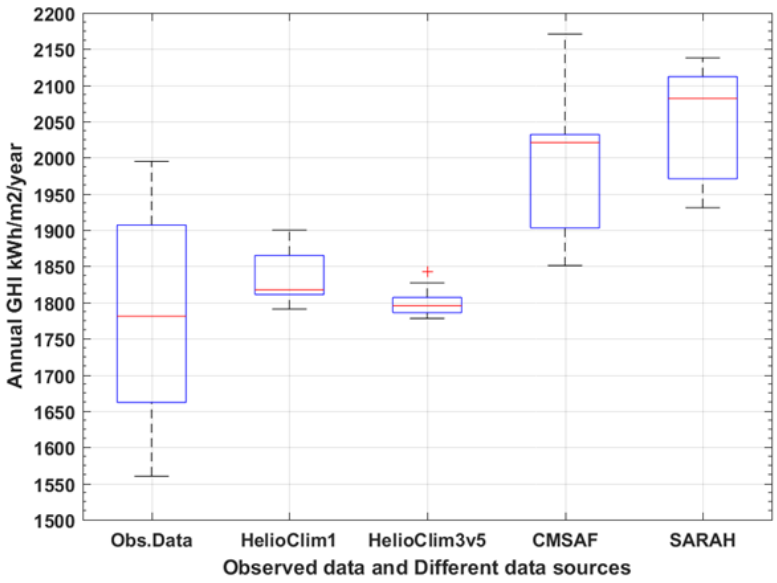

Figure 8-8. Annual $\bar{G}$ distribution for observed data and another data resources for the 10 weather stations in Iraq. Large boxes are the interquartile range showing the 25th, 50th and 75th percentile values, whiskers are the 5th and 95th percentile values and crosses are the 1st and 99th percentile values of each sample.

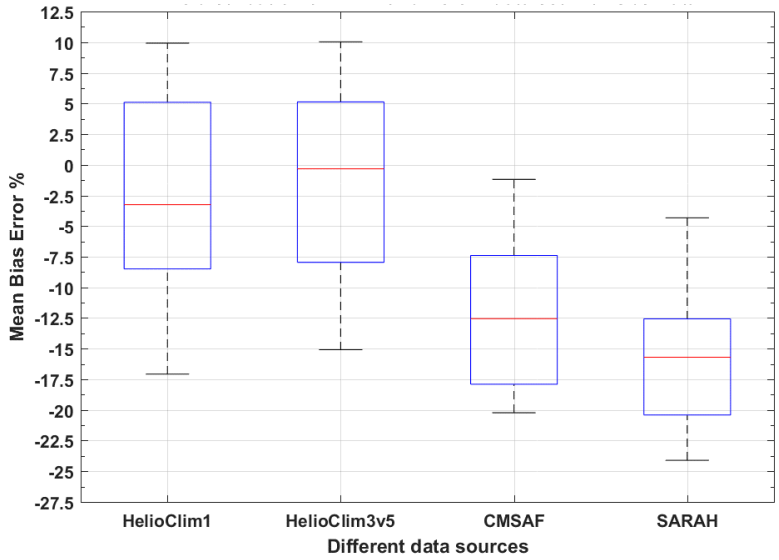

Figure 8-9. The distribution of MBE based on annual $\bar{G}$ distribution for different data resources (HelioClim1, HelioClim3v5, CMSAF and SARAH) with observed data according to the 10 weather stations in Iraq.

8.4.2 Annual energy Production and Capacity Factor Assessment for 3.1 kW, 5.2 kW and 10.4 kW.

Three sizes of solar systems (3.1 kW, 5.2 and 10.4 kW) have been suggested to estimate the annual solar energy production in this chapter for the whole of Iraq based on HelioClim1. Various inputs and information have been listed in section 8.2.3. Figure 8-10 shows that the AEP of 3.1 kW, 5.2 and 10.4 kW PV system had the same spatial distribution and indicated that the high solar power production from different size of PV systems was

concentrated in the west of Iraq. According to 10.4 kW PV system Figure 8-10A, the boxplot of AEP shows wide distribution due to the relatively large size of the system in comparison with 3.1 and 5.2 kW. In fact, the AEP of PV system does not reflect the efficiency and feasibility of the PV system in Iraq; for this reason, CF calculation for each size of PV system is required.

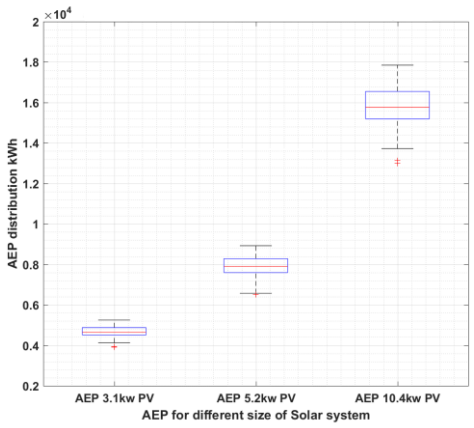

Figure A

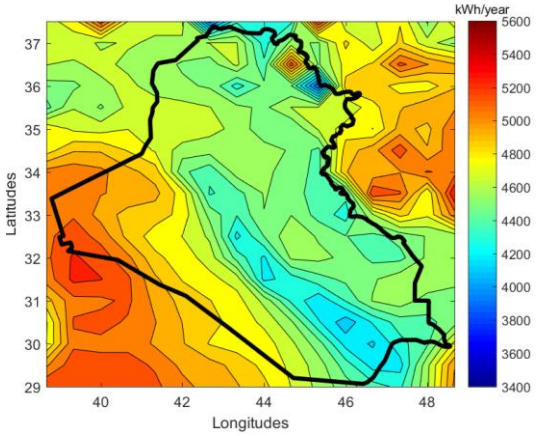

Figure B

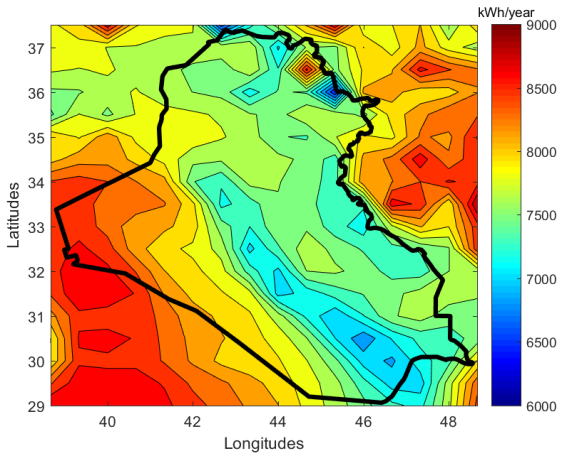

Figure C

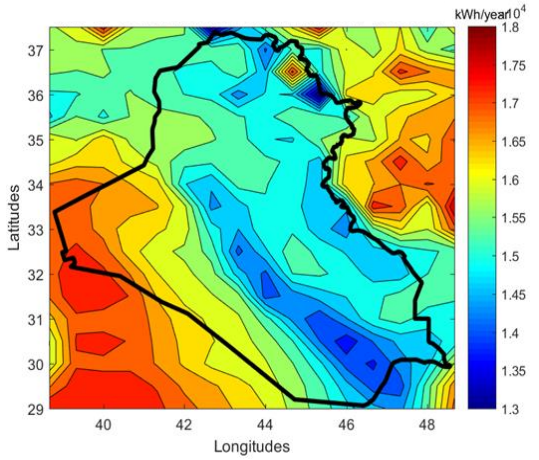

Figure D

Figure 8-10. Spatial distribution of AEP, based on HC1 1985-2005 for Iraq for 3.1 kW in Figure B, for 5.2 kW in Figure C and 10.4 kW in Figure D. Figure A shows the boxplot distribution of AEP for three sizes of solar system (3.1 kW, 5.2 and 10.4 kW).

According to Figure 8-12, the CF calculation for the three sizes of PV system has shown approximately the same distribution for the whole of Iraq. In addition, this result has demonstrated that the west of Iraq had the highest CF , while the Euphrates river valley and lakes attached to it (extending from middle even southeast of Iraq in Figure 8-11) showed a low CF and low AEP for the three PV systems, as shown in Figure 8-10. The lowest values of AEP and CF are located above the large lakes such as Mosul Dam Lake and Dokan Dam Lake in the north of Iraq and the Al-Thar Thar, Al-Habbaniyah and Al-Razzaza lakes, which are located close to Baghdad and Karbala cities, as shown in Figure 8-7. In addition, there

are a lot of forests and palms groves located on both sides of Euphrates and Tigris and between them. The reason for the lowest values of solar radiation above these areas back to the high percentage of water vapour that is emitted from lakes and rivers and the palm groves areas. If the level of water vapour has increased in the atmosphere, the absorption of water vapour will increase for solar radiation. Furthermore, the increasing solar radiation absorption reduces the output power of solar system for different kinds of solar panel, as shown in Figure 8-13 [304].

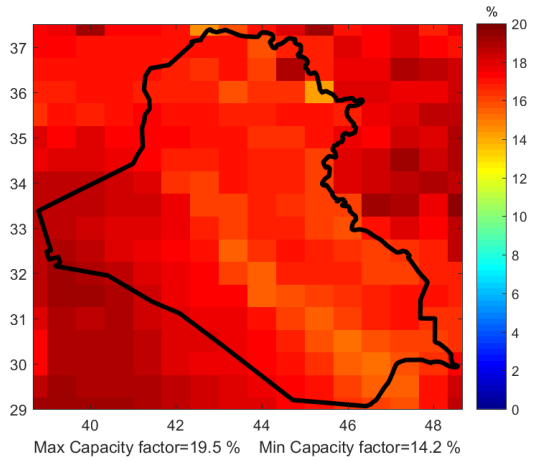

Figure 8-11. Spatial distribution of CF for 5.2 kW for Whole of Iraq.

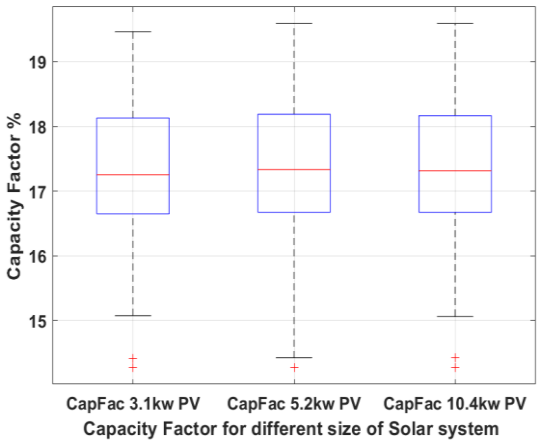

Figure 8-12. The boxplot distribution of CF for 3.1, 5.2 and 10.4 kW

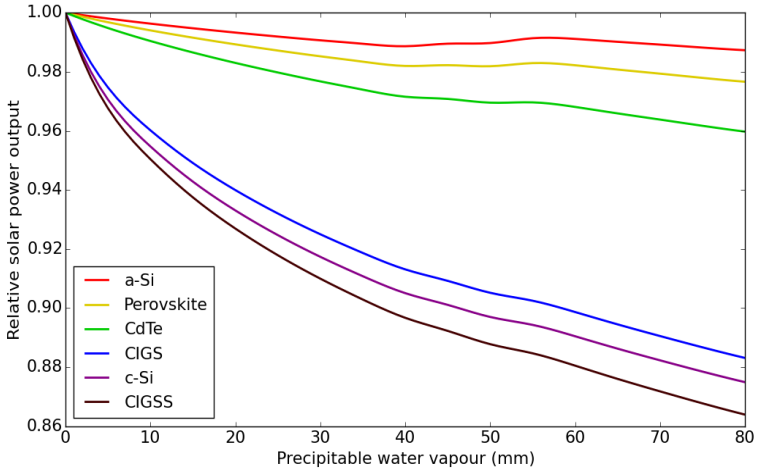

Figure 8-13. The effect of perceptible water vapour level on relative solar power output from different kinds of PV semiconductors [304].

8.4.3 The PSD for 3.1 kW, 5.2 kW and 10.4 kW.

The PSD aims to present the ability of a specific PV system size to cover different levels of monthly electricity demand, based on monthly average energy production from the PV system. Different levels of monthly demand have been suggested that start from 1000 to

5000 kWh/month in order to simulate the electricity demand for different sizes of house and the possibility of a change in the electricity demand from season to season based on climate conditions. In this case, the PSD calculation for 3.1 kW, 5.2 kW and 10.4 kW solar system size has been applied for the whole of Iraq, as shown in Figure 8-15. The 5.2 kW and 10.4 kW solar system have shown a good ability to cover 1000 and 2000 kWh/month of monthly electricity demand in terms 5.2 kW PV system and covers 2000, 3000 and 4000 kWh/month of demand in terms 10.4 kW. The 5.2 kW and 10.4 kW of solar system can play a significant role to reduce dependence on electricity supply from grid. Although that 5.2 kW and 10.4 kW solar systems show an acceptable ability to cover electricity for most places in Iraq, the LCE and PBP will contribute to evaluate the feasibility of these solar systems

8.4.4 The LCE Evaluation for 3.1 kW, 5.2 kW and 10.4 kW.

According to AEP from 3.1 kW, 5.2 kW and 10.4 kW, the LCE has been calculated for the whole of Iraq based on the different levels of demand from 1000 to 5000 kWh/month. The aim of LCE calculation determines the lower cost of electricity from each PV system and determines the spatial distribution of the low cost of energy throughout Iraq.

According to Figure 8-14A, B and C, the lowest LCE was located in the west of Iraq and a small spot in the north of Iraq due to the high solar irradiation in these areas. Also, the 10.4 kW PV system has shown the lowest LCE distribution for the whole of Iraq in comparison with 3.1 kW, 5.2 kW, as shown in Figure 8-16A, B and C due to the high relative cost of the inverter, with 24% to the total present value (TPV) of 3.1 kW solar system and the low relative cost of inverter 22% to the TPV for 10.4 kW PV.

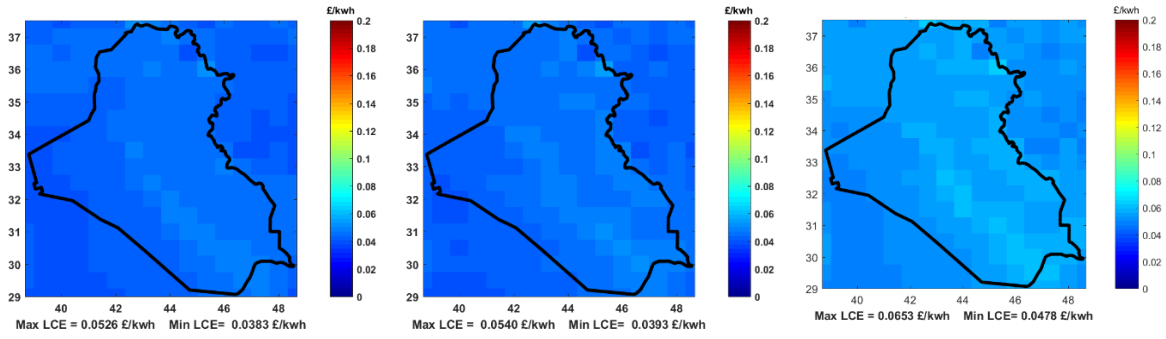

Figure 8-14. The spatial distribution of LCE for the whole of Iraq based on AEP for different size of solar system, according just 5000 kWh/month level of demand. Sub Figure A shows the LCE distribution for 10.4 kW, Sub Figure B for 5.2 kW and Sub Figure C for 3.1 kW. The AEP of these PV systems estimated is based on HelioClim1 data for 1985-2005.

.

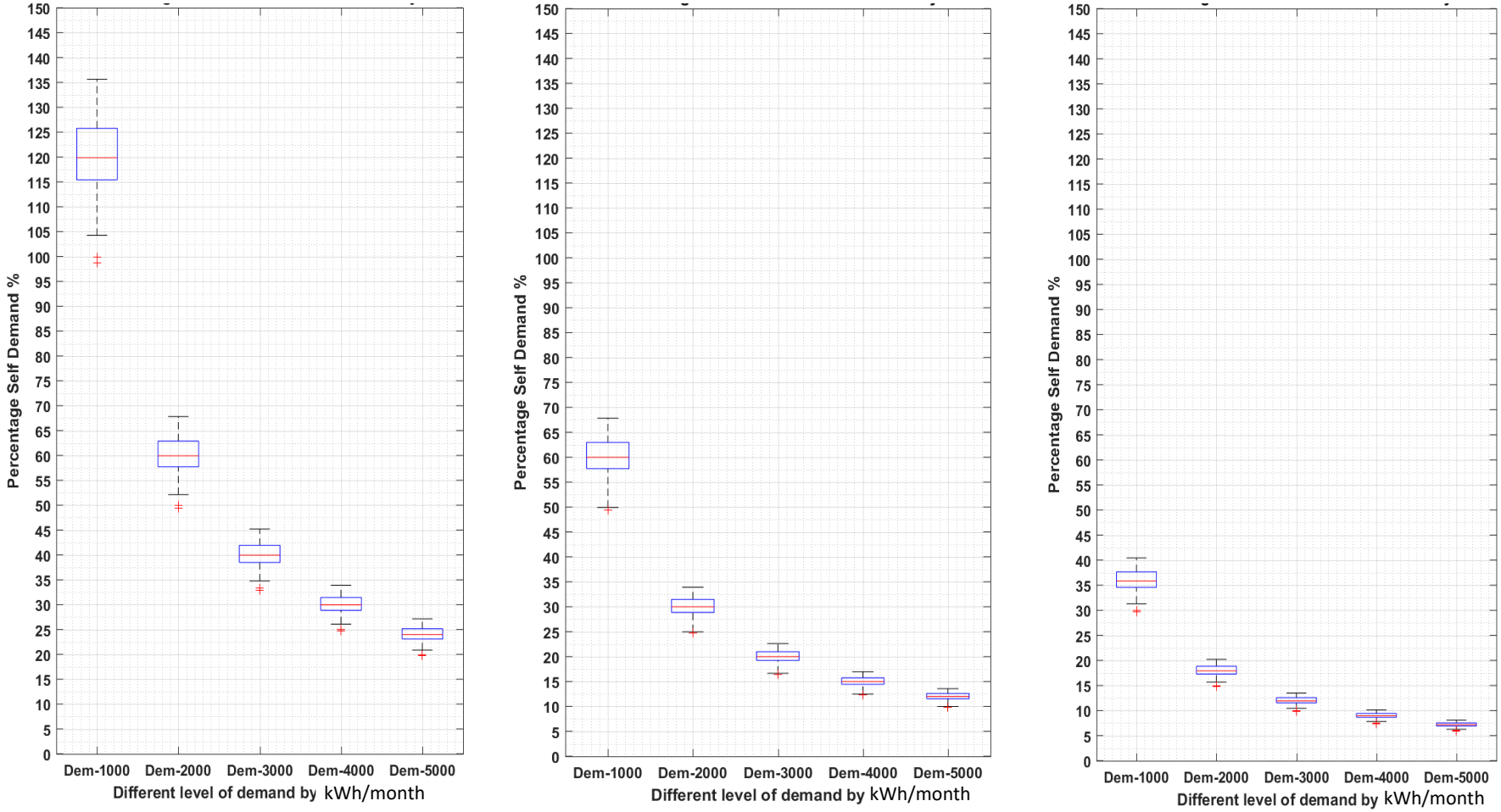

Figure 8-15. The distribution of the PSD by using boxplot for three sizes of PV system 10.4 kW, 5.2 kW and 3.1 kW, based on five levels of monthly electricity demand. Figure A represents PSD for 10.4 kW, Figure B represents PSD for 5.2 kW and Figure C represents PSD for 3.1 kW. Dem: Demand.

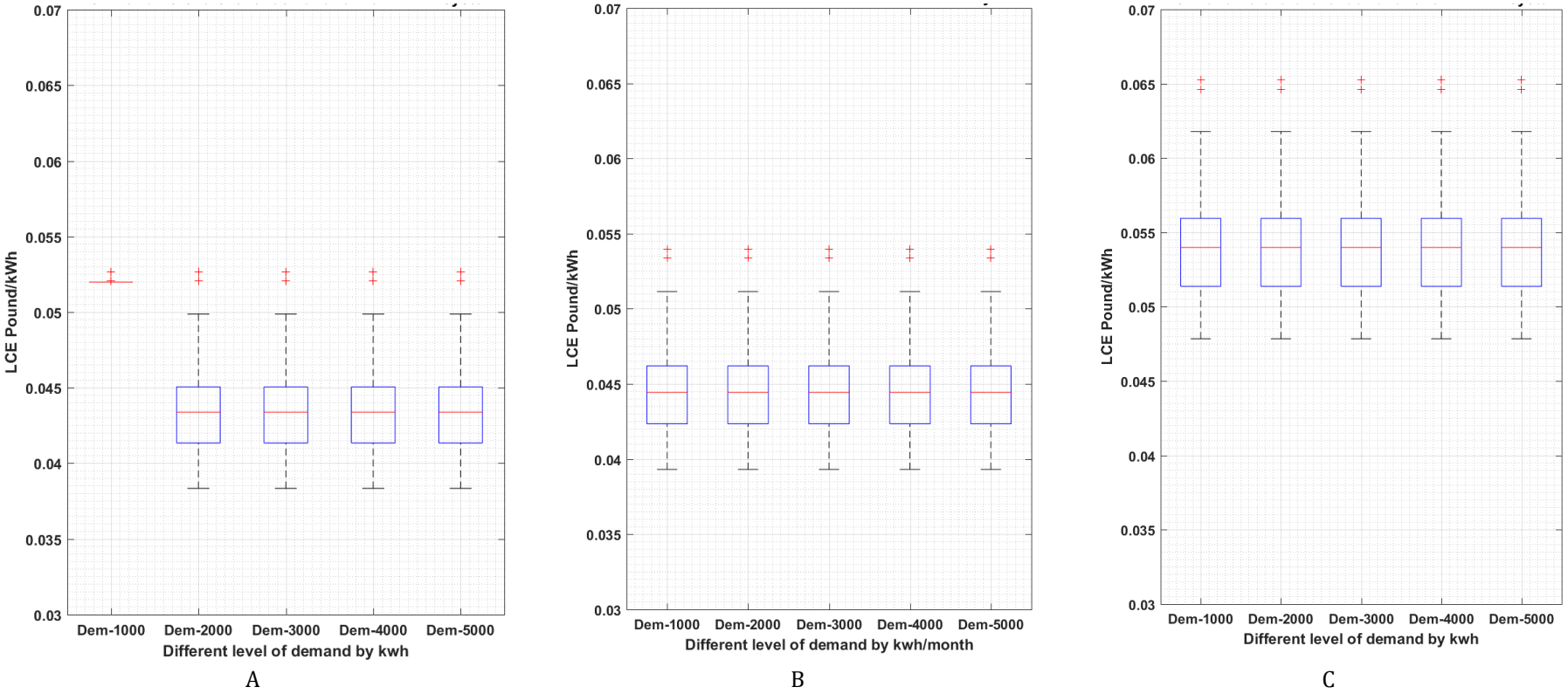

Figure 8-16. The boxplot distribution of LCE for whole of Iraq and for different size of solar system according to different levels of demand from 1000 to 5000 kWh/month. Sub Figure A shows the LCE distribution for 10.4 kW, Sub Figure B for 5.2 kW and Sub Figure C for 3.1 kW. Dem refers to level of demand.

The similarity between the LCE distribution for all levels of monthly demand for each PV system size returns that the highest monthly energy production is lower than 2000 kWh/month, as shown in Figure 8-10A. Otherwise, just 1000 level of demand for 10.4 kW has shown an odd result when the LCE distribution was just £0.052 £/ kWh for the whole of Iraq due to the fact that the MEP was higher than 1000 kWh/month

8.4.5 **The PBP Evaluation for 3.1 kW, 5.2 kW and 10.4 kW.**

The PBP for 3.1 kW, 5.2 kW and 10.4 kW PV systems was calculated based on IBT prices in 2017 and IBT prices in 2015. The PBP calculation in this section has three target aims:

- To recognize the best IBT pricing model can provide the shortest PBP.
- To determine best location in Iraq that can achieve shortest PBP in terms of 2015 and 2017 IBT.
- To find out to what extent a different level of monthly demand could achieve the shortest PBP, based on different sizes of solar system.

Firstly, the 3.1 kW PV system was examined to understand to what extent different IBT prices and different levels of monthly demand have an effect on PBP. Figure 8-17 shows clearly that the 2015 IBT price has played a significant role to reduce PBP. In addition, the level of monthly demand shows a reverse relationship with PBP; for example, if the monthly demand has increased, the PBP is decreased, as shown in Figure 8-17.

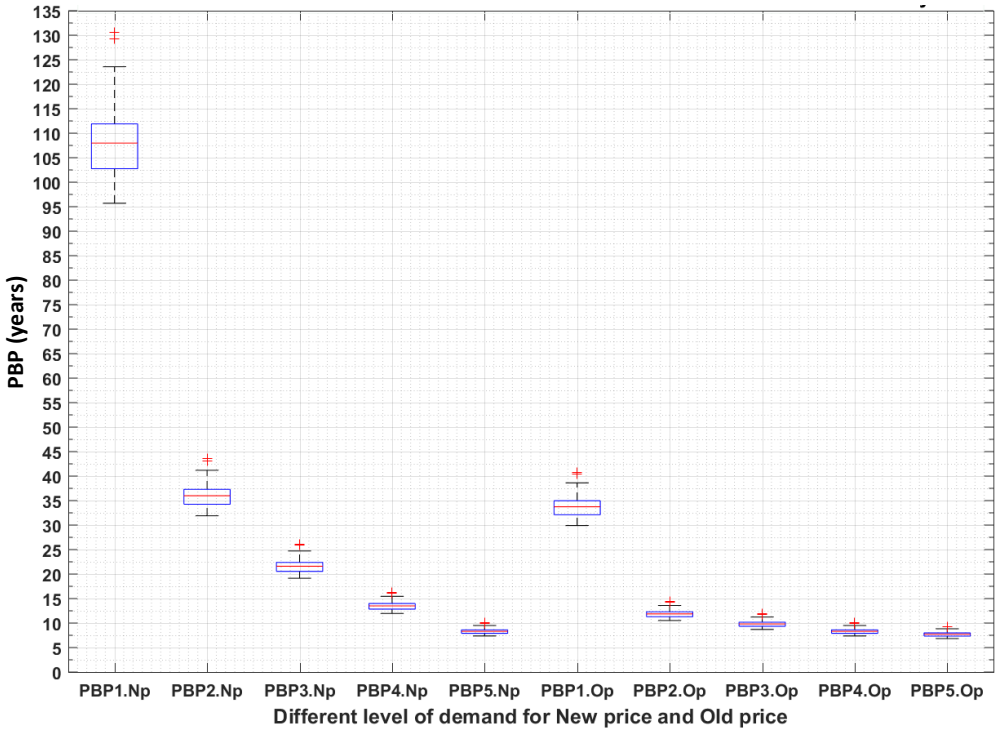

Figure 8-17. The boxplot distribution of PBP for 3.1 kW and for different level of monthly demand from 1000 to 5000 kWh/month and based on the 2015 and 2017 IBT prices from national grid. For example the PBP1. NP refers to PBP for 1000 kWh/month of monthly demand based on Np (2017 IBT price). While PBP3.Op refers to PBP for 3000 kWh/month of monthly demand, based on Op (2015 IBT price).

For more analysis to raise the reliability on PV system performance and also to determine the most reliable and productive locations in Iraq, the calculation of PBP of less than 8 years has been applied, based on the 2017 and 2015 IBT. With regard to the calculation of PBP within eight years based on the 2017 IBT, the results show that the 3.1 kW can achieve PBP

within eight years just based on 5000 kWh/month demand in the west of Iraq, as shown in Figure 8-18A. While the PBP within eight years was based on the 2015 IBT showed up in many areas in the west, south-west, middle and north of Iraq, based on 5000 kWh/month demand, as shown in Figure 8-18C.

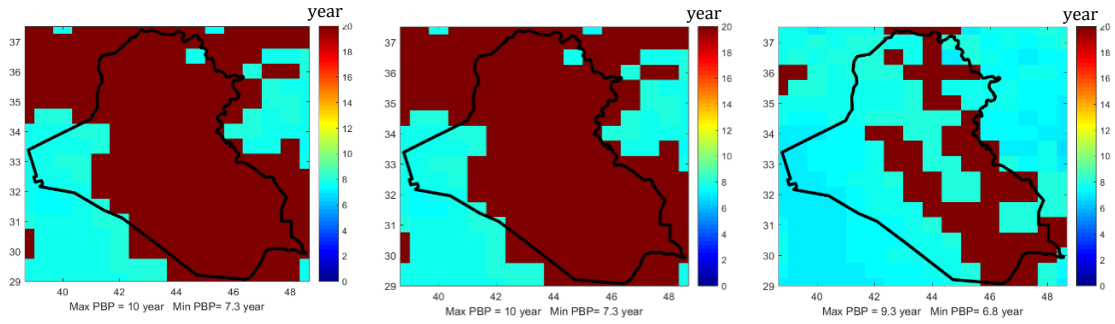

Figure A Figure B Figure C

Figure 8-18. The distribution of PBP of less than 8 years, based on the 2017 and 2015 IBT for 3.1 kW PV system. NP refers to the 2017 Price and OP refers to the 2015 Price. Figure A shows PBP, based on NP and 5000 kWh/month of demand, Figure B shows PBP, based on OP and 4000 kWh/month and Figure C shows PBP, based on OP and 5000 kWh/month.

Regarding the PBP calculation for 5.2 kW, the results of 2015 and 2017 IBT have shown the same trend impact for 3.1 kW PV system and also the same trend of decreasing PBP with increasing monthly demand. However, the 5.2 kW PV system showed that 2000 to 5000 kWh/month demand achieved PBP lower than 20 based on the 2015 IBT price. While 5000 to 3000 kWh/month demand achieved PBP shorter than 20, based on the 2017 IBT price, as shown in Figure 8-19.

For more analysis, the calculation of PBP of less than 8 years shows that 5.2 kW succeeded to cover a wide area in Iraq in terms of 5000 kWh/month, based on 2017 IBT price that ranged between 6 to 8 years, as shown in Figure 8-20A. While the 2015 IBT price to achieved PBP of less than 8 years for 3000 kWh/month demand by covering the west of Iraq, as shown in Figure 8-20B.

Regarding the calculation of PBP for 10.4 kW, the results have shown also the same trend of 5.2kW and 3.1kW in terms of 2015 and 2017 IBT and also in terms of decreasing PBP when increasing the level of demand. In addition, the calculation of PBP for 10.4 kW has shown almost the same results of 5.2kW in terms of the boxplot of PBP distribution and spatial distribution across Iraq. According the results of PBP for 3.1kW, 5.2kW and 10.4 kW PV systems and the difference between 3.1kW and 5.2kW return also to relative cost of inverter to the TPV of PV system project as is mentioned in section 8.4.4.

In addition, the result confirms that the solar system is feasible for houses with a high level of demand and that the 2015 price has played a significant role to reduce PBP, due to the high saving in terms of a high level of demand that leads to a short PBP. Also, the spatial

distribution has confirmed that the west of Iraq is the most feasible area for solar system investment.

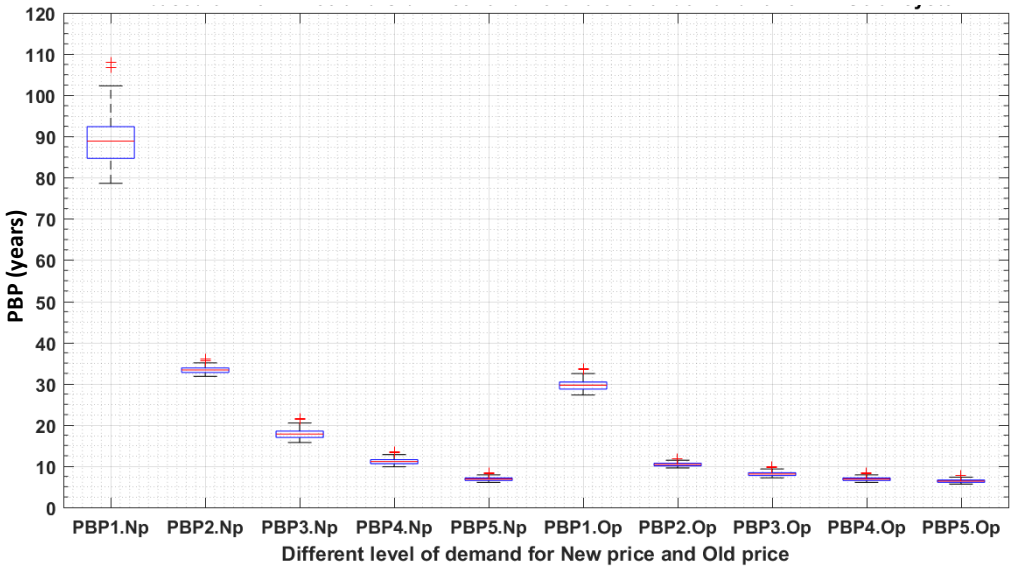

Figure 8-19. The boxplot distribution of PBP for 5.2kW for different levels of monthly demand from 1000 to 5000 kWh/month, based on the 2015 and 2017 IBT prices from the national grid. For example, the PBP2.NP refers to PBP for 2000 kWh/month of monthly demand based on Np (2017 IBT price), while PBP4.Op refers to PBP for 4000 kWh/month of monthly demand based on Op (2015 IBT price).

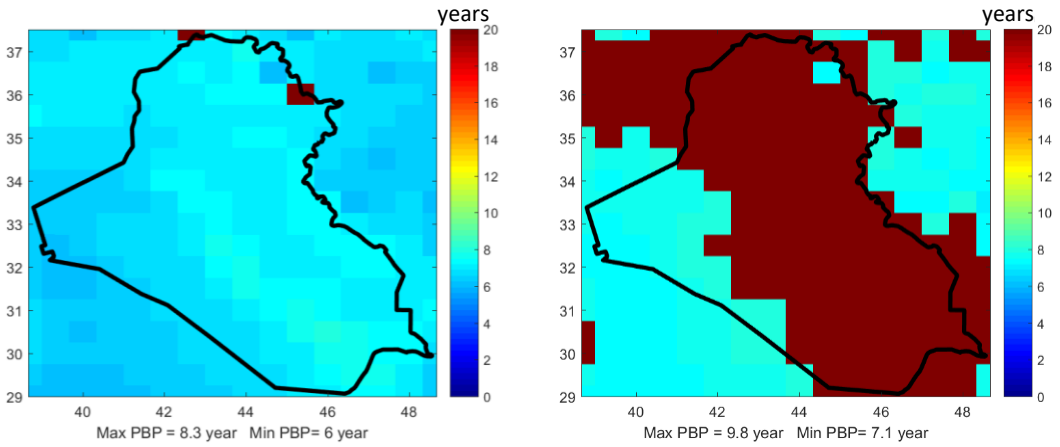

Figure A Figure B

Figure 8-20. The distribution of PBP of less than 8 years for 5.2kW, based on the 2017 IBT in Figure A and based on the 2015 IBT in Figure B. NP refers to the 2017 Price and OP refers to the 2015 Price.

8.4.6 Validation of Solar Power Production With Homer

In order to validate the accuracy of AEP for PV systems, a comparison has been carried out between PVGIS PV estimation based on HC1 data and Homer calculations based on HC1 and based on NASA data (NASA Surface meteorology and Solar Energy Database) [43] as the default sources of data for Homer. The validation has been carried out using 5kW solar system for 8 locations in different places in Iraq, as listed in Table 8-3.

The AEP distribution for 5 kW based on PVGIS-HC1, Homer-HC1 and Homer-NASA shows a significant difference between PVGIS-HC1 and Homer-HC1, while there is a remarkable difference between PVGIS-HC1 and Homer-NASA, as shown in Figure 8-21

Table 8-3. List of locations chosen for validation purposes, to estimate the AEP for a 5kW solar system, based on HC1 by PV estimation from PVGIS, HC1 by Homer calculation, based on NASA data by Homer calculation.

	Location	PVGIS-HC1-AEP 5 kW KWh/year	Homer-HC1-AEP 5 kW KWh/year	Homer-NASA 5 kW KWh/year
PV1	32°30'0''N 39°19'59'' E	8310	9282	7524
PV2	30°30'0''N 42°40'0'' E	7230	9312	6827
PV3	30°30'0''N 46°0'0'' E	6600	9055	6874
PV4	30°30'0''N 45°19'59'' E	7070	9153	7088
PV5	32°0'0''N 42°00'0'' E	7690	9189	7130
PV6	33°30'0''N 44°00'0'' E	7320	9137	6851
PV7	35°0'0''N 42°00'0'' E	7600	9238	7039
PV8	30°30'0''N 44°00'6'' E	7580	9122	7231

For more sensitive analysis, an absolute percentage error APE was carried out between PVGIS-HC1 and Homer-HC1 on one side and between PVGIS-HC1 and Homer-NASA on the other side, to show the difference between the PVGIS calculation based on HC1 and the Homer calculation based on HC1 and NASA, as shown in Figure 8-22. The result shows a significant MAPE (24.17%) between PVGIS-HC1 and Homer-HC1, while the result of MAPE between PVGIS-HC1 and Homer-NASA was lower (5.64%). The reason for the large difference between PVGIS-HC1 and Homer-HC1 we must return to the PV system losses in Homer calculation, which is lower than in PVGIS PV system losses and the difference between NASA data and HC1 that leads to reduce the difference between AEP results based on PVGIS and Homer calculation.

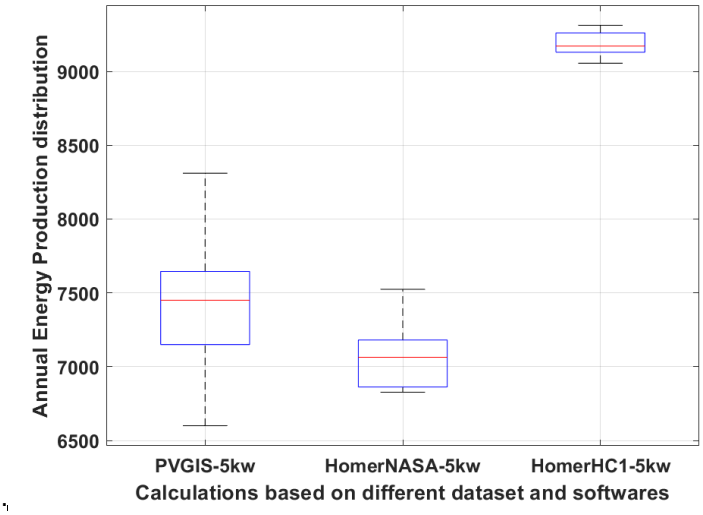

Figure 8-21. The AEP distribution for 8 locations based on PVGIS-HC1 (PVGIS5kW), Homer-NASA data resources (HomerR5kW) and Homer-HC1 (HomerPVGIS5kW).

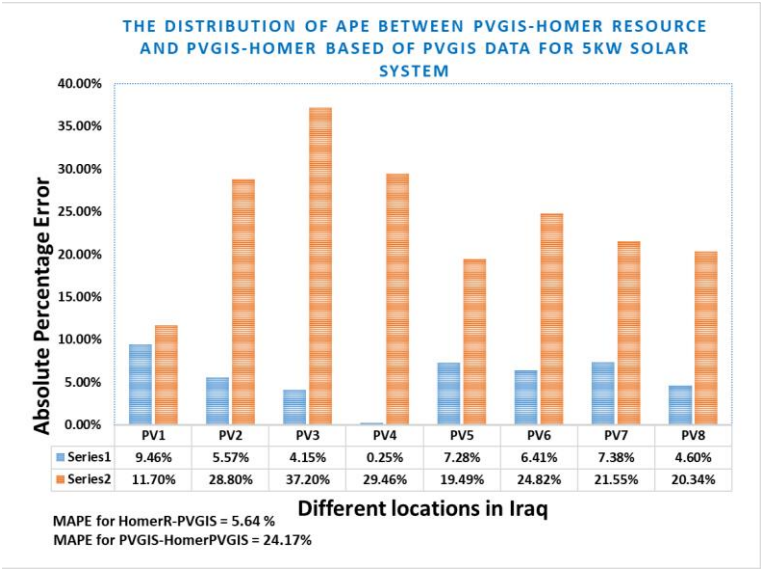

Figure 8-22. Absolute percentage error APE for 8 locations between Homer-Nasa and PVGIS-HC1 data (HomerR-PVGIS), which is represented by blue columns as well as between PVGIS-HC1 and Homer-HC1 (PVGIS-HomerPVGIS) which are represented by orange columns.

8.4.7 Result Analysis of Hourly Solar Energy Production and Validation

In order to validate the result of hourly solar energy production from the HSEP-WT model that has been presented in section 8.3, a comparison has been carried out among the AEP results of the HSEP-WT model based on typical HC3v5 data, AEP of PVGIS based on HC1 data and the AEP of Homer based on NASA data, using the Polycrystalline 10kW PV system for four locations in Iraq, as presented in Table 8-4. To recognize the difference between the AEP of HSEP-WT model and the other software results, comparison has been carried out between AEP distributions of the HSEP-WT model and the others, as shown in Figure 8-23.

The AEP distribution of the HSEP-WT model shows results higher than PVGIS and Homer distribution.

Table 8-4. Results of AEP from the 10kW PV system, based on the HSEP-WT model for hourly solar energy production, based on typical HC3v5 data, PVGIS estimation based on HC1 data and Homer estimation based on NASA data for four locations in Iraq. The AEP calculation of HSEP-WT model has been applied at different land covers

location	AEP of hourly solar energy production HC3v5 kWh/year			AEP of PVGIS estimation HC1 kWh/year	AEP of Homer estimation NASA kWh/year	Annual Optimal angle
	Urban	Desert	Water			
Basrah 47.678, 30.55	18716	19435	no result	16500	16612	28
Haditha 42.31, 34.13	17065	19090	19501	17200	17963	30
Musal 43.05, 36.456	18484	20040	20029	17600	18145	30
Baghdad 44.27, 33.31	18782	20079	20338	17500	17165	29

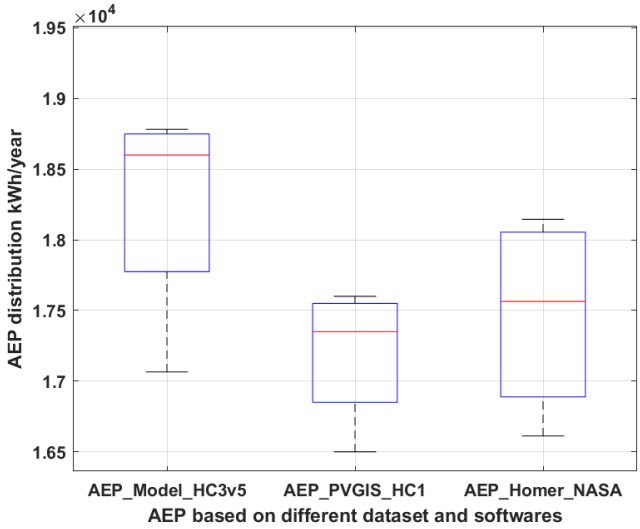

Figure 8-23. AEP distribution for 10kW PV system for four locations in Iraq, using different software and datasets: HSEP-WT model based on HC3v5 data, Homer based on NASA data and PVGIS estimation based on HC1 data.

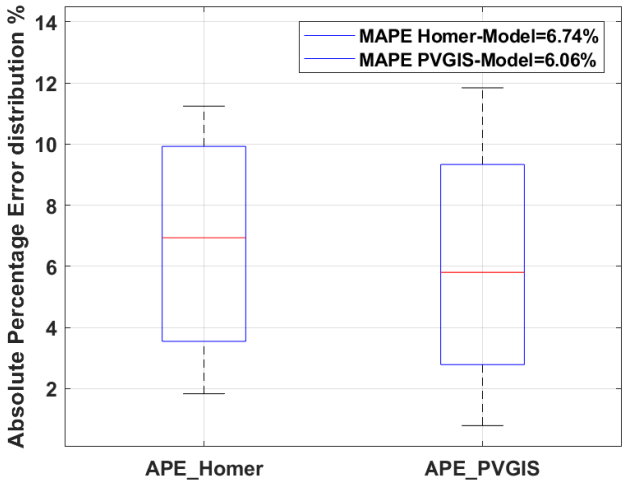

Figure 8-24. MAPE and APE distribution between Homer- HSEP-WT model and between PVGIS- HSEP-WT model for four locations in Iraq.

For sensitivity analysis, comparison between the (HSEP-WT model – Homer) and (HSEP-WT model – PVGIS) was carried out using APE and MAPE, as shown in Figure 8-24. The APE distribution for Homer and PVGIS ranged between 1% and 12%, while the MAPE for (HSEP-WT model – Homer) was 6.74%, while the (HSEP-WT model – PVGIS) = 6.06 %. The result of PVGIS, based on HC1 was closer to the results of the HSEP-WT model. The reason for the difference between the HSEP-WT model and other software relates to the cooling calculation based on wind speed effect at 2 m, even in urban areas.

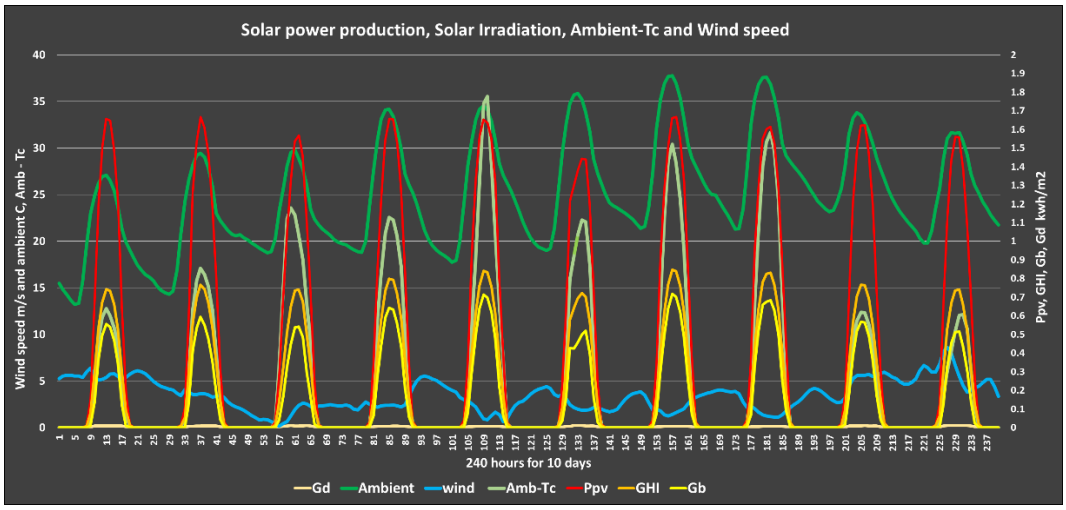

Figure 8-25. A sample of hourly input data of $\bar{G}$, Gb, Gd, ambient and wind speed at 2m for the first 10 days of March. These data have been used in hourly energy production simulation for 2kW solar system sizes. In addition, this Figure shows the Ppv: the output hourly solar energy production from 2kW PV system and also Amb-Tc: the difference between the ambient and cell temperature (Tc).

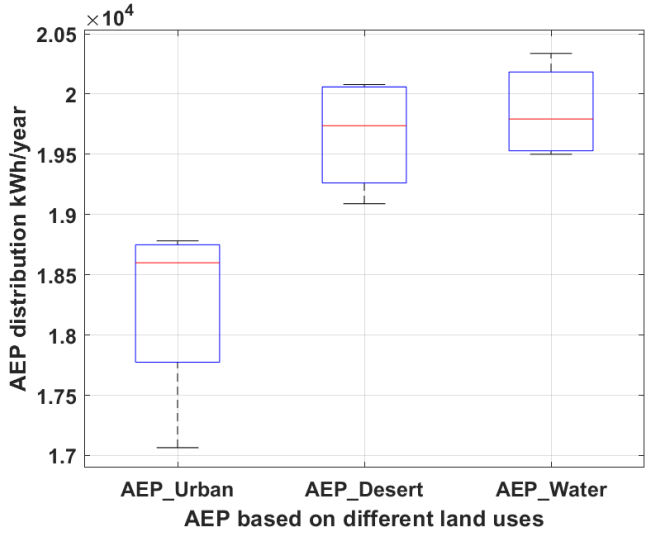

Figure 8-26. AEP distribution for 10kW PV system for four locations in Iraq, using the HSEP-WT model to estimate the hourly output power from solar system, using HC3v5 data at different land covers: desert, water surfaces and urban areas.

In fact, the wind speed has played vital role in terms of reducing cell temperature and increasing the efficiency of solar system, resulting in increased production capacity, as

shown in Figure 8-25. It is well known that cell temperature has the same ambient temperature during the night, while the cell temperature increased dramatically (around 30°) during the day, while the high wind speed usually reduces the cell temperature. In it is possible to see the harmony relation among the wind speed, ambient-Tc and Power PV production (Ppv). Accordingly, the effect of high wind speed on increasing the output power of PV system in Figure 8-26 shows the development in PV output in an open area (such as desert and water surfaces). The impact of wind speed can give a realistic interpretation to the difference between the results of HSEP-WT model, Homer and PVGIS estimation.

8.5 Conclusion

The most validated dataset for solar resources assessment has been determined among several data resources according to the observed data from 10 weather stations in Iraq. According to the validated dataset, annual solar energy production and some economic aspects that include the cost of energy and PBP have been evaluated for all of Iraq. This has involved developing the HSEP-WT model of estimating the hourly solar system output by combining the effects of wind speed that were modeled in earlier chapters and the effect of ambient temperature on cell temperature in the solar system. The HSEP-WT model aims to provide the optimization process of a hybrid system in the next chapter by means of realistic and reliable solar power data for different sizes of solar system in any location in Iraq.

Firstly, according to the validation among several datasets: HC3v5, HC1, CM-SAF, SARAH with observed data in Iraq, the HC3v5 and then HC1 have shown the lowest error against observed data respectively. These results led to the use of HC1 data resources for annual solar resources assessment in Iraq, while HC3v5 was used to estimate hourly solar energy production, which will be used for the optimization processin the hybrid system in the next chapter.

Secondly, the annual solar resources assessment for the whole of Iraq confirmed that the highest solar availability is located in the west of Iraq and to a lesser extent in the centre and southeast of Iraq. The lowest solar irradiation and PV power output are concentrated above lakes and forest along the Euphrates River, due to the high absorption of water vapour for solar radiation. In terms of percentage self-demand, the 5.2 kW PV system is able to meet the low levels of monthly demand, while the 10.4 kW PV system is more efficient to meet 2000 and 3000 kWh/month levels of demand. In addition, the cost of energy ranged from 0.0375 and 0.05 £/kWh for 3.1 and 5.2kW PV system. While the LCE for 10.4 kW PV system ranged from 0.045 to 0.062 £/kWh. There is a difference between the LCE of 10.4 kW and 5.2kW return to the high relative cost of the inverter to the TPV for 5.2 kW PV system. Furthermore, the PBP assessment shows that the high level of demand and the 2015

IBT prices have played an essential role to reduce the PBP to lower than 8 years in the west of Iraq, in terms of the low level of demand and for whole of Iraq in terms of the high level of demand. Besides, the validation between AEP of PVGIS calculations based on HC1 and Homer based on NASA data shows a low degree of error, while the validation between AEP of PVGIS calculations and Homer based on HC1 shows a high degree of error due to the PV system losses in Homer calculation, which were lower than in PVGIS estimation based on HC1.

Thirdly, according to the HSEP-WT model, the hourly wind speed has played a significant role to reduce the cell temperature of PV system, which leads to an increase in the efficiency of the solar system and an increase in the capacity of power production. On the other hand, the validation between PV output power for HSEP-WT model on one side, Homer and PVGIS on other side shows that the MAPE was approximately 6%. According to the effect of wind speed on PV output power, the variety of land cover has also played an important role in terms of increasing the AEP from PV system in open areas such as lakes and deserts and reduced AEP in the urban area.

Chapter 9 **OPTIMAL HYBRID RENEWABLE ENERGY SYSTEM FOR HOUSE UNITS**

9.1 **Introduction**

The main objective of this chapter is to improve a mathematical model and develop a unique computational code to size and optimize a Hybrid Renewable Energy System (HRES) to satisfy an electricity demand which is suffering from unscheduled outage from the national grid. In other words, developing a computational tool for a hybrid system that can control energy flow to cover house electricity demand when it is connected or unconnected with the national grid. This methodology should help to design power system that can resolve the problem of unscheduled outage from the national network to the residential sector in Iraq. The HRES in this project consists of a wind turbine, an array of solar panels, rechargeable batteries and an inverter. The process of optimization will examine some energy flow strategies and economic solutions to enhance the hybrid system performance in terms of decreasing the total cost of a project, payback period (PBP) and cost of energy supply as well as increasing the reliability (section 4.2) of covering energy demand from optimal HRES in the case of on-grid and off-grid. The process of sizing and optimizing involved different weather conditions of wind speed and solar radiation for various land covers to understand to what extent the optimal HRES configuration can change under different climatological circumstances. Three styles of optimization process including several logical constraints are suggested to satisfy customer willingness in terms of reliability, cost of energy and PBP based on three examples of energy demand profiles which were recorded from three houses in Iraq as part of this project.

This chapter is organized as follows: an overview of the optimization methodology and energy management of the HRES is introduced in section 4.29.2 which includes the demonstration of the component of the HRES configuration in this project in section 9.2.1. Description of the necessary input data such as wind speed, wind power production, solar radiation, solar power production and details about electricity demand recorded from several house units at different places in Iraq are given in section 9.2.2. Section 9.2.3 explains the modeling of system components (wind turbine and solar system) and the sources of data that are used in this project. The mathematical model, features of the storage system and energy flow management for different scenarios have been demonstrated in section 9.2.4. Modeling of system reliability and system economics are demonstrated in sections 9.2.5 and 9.2.6, respectively. Validation and results analysis of optimization for

different locations in Iraq are revealed in section 9.3. Finally, the conclusions are presented in section 9.4.

9.2 System Description

A novel approach of combining on-grid and off-grid systems (On-off-grid Op-HRES) is developed in an unique design using MATLAB to determine an optimal HRES configuration to resolve the problem of frequent and unscheduled outage for some hours per day from the national grid as shown in Figure 9-2. The non-scheduled electricity outages in Iraq result from the low total energy production from the national network in comparison with the total of energy consumption for the whole of Iraq [2]. It has been a common problem facing Iraqi people almost every day per year since 1991. For this reason, they are using a private generator or buying electricity from a neighbourhood generator with expensive prices [2] to meet their domestic needs for 24 hours across a year. This approach is examined according to different scenarios of grid Increasing Block Tariffs (IBT) prices, strategies of energy flow management and based on different land covers and various weather conditions (wind speed and solar radiation). The HRES is composed of different sizes of components to form 10136 potential configurations. The proposed system includes a wind turbine, solar system, controllers, lithium-ion storage with an energy storage charger and a DC-AC inverter. The dump load is used to get rid of excess energy when the energy production from the HRES exceeds the load demand $E_{load}(t)$ and maximum power charge of storage in off-grid case. A diesel generator is used as an optional component to cover the electricity demand when the HRES power production and the maximum power which can be discharged from the storage system are lower than demand.

All three HRES components (wind turbine, solar system, storage system) are connected in parallel to the DC bus through three individual non-isolated DC/DC boost controller that are employed for maximum power point tracking (MPPT) to reduce power fluctuation and improve the stability of the DC bus voltage [305-307]. The DC/DC boost controller divides the DC bus voltage into two parts, variable voltage at the output terminal of the energy system V_i and fixed DC voltage at the DC bus V_{dc}. The fixed DC bus voltage has been set for 48V according to the nominal battery voltage [308]. In general, the DC/DC boost controller is considered advantageous due to the low cost and high efficiency [306, 307]. In addition, the hybrid inverter is used to integrate the load demand and grid in an AC bus with the HRES in the DC bus. The outputs from the three power systems are integrated on the DC bus line and combined in parallel to provide the desired power to the AC bus load even if only one source is available, and the others are diminished [306, 307].

Figure 9-1 shows the schematic diagram of HRES design that is suggested in this project. A package of hourly weather data, energy production and electricity demand data have been gathered, estimated and logged for one year to feed the optimization process using necessary data.

The optimization process in this work has determined the optimal HRES configuration according to the iterative technique using multi-objective for several scenarios. The Loss of Power Supply Probability (LPSP) is used as a constraint to focus on the reliability of optimum size for the HRES configuration according to the off-grid case. At the same context, the Grid Power Absorption Probability (GPAP) is used as a constraint of reliability for the on-grid system. On the other hand, the Levelized Cost of Energy (LCE) is used as a constraint to minimize the cost of the HRES as an economic indicator for the HRES configuration [190, 213]. Furthermore, the PBP is regarded as one of the important financial constraints that is helpful to determine the optimal configuration that is able to get back the Total Cost of Project (TCOP) during the lifetime of a project. In addition, the LPSP, GPAP, LCE, PBP and TCOP, some of them or all of them have been used as multi-objective according to several scenarios to determine the optimal HRES which fitting the consumer desire.

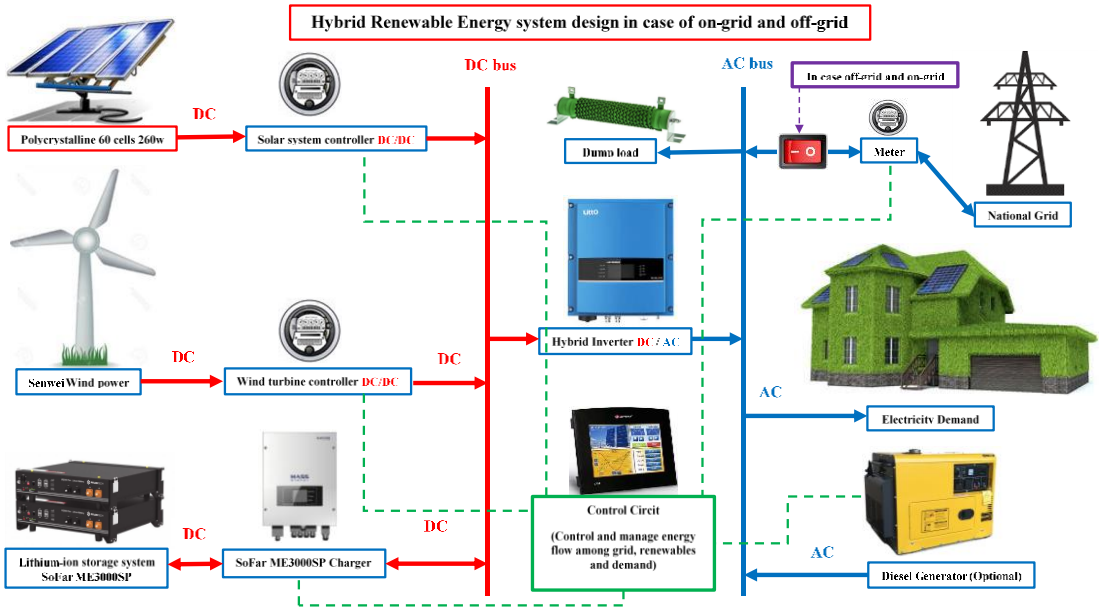

Figure 9-1. Schematic diagram of on-grid and off-grid for the HRES design and components: wind turbine; solar system; storage system; inverter and diesel generator (optional).

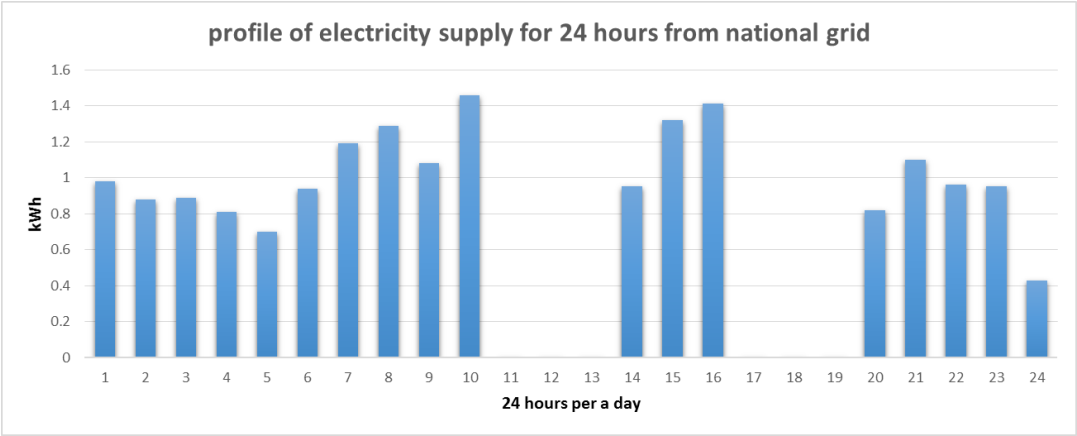

Figure 9-2. The energy consumption by kWh for one day (1st of January 2018) from BG (Baghdad house) and unscheduled outage for several hours from the national grid.

9.2.1 The HRES Configuration

In this section, the underlying reasons behind each chosen component according to the economic and technical evaluation are mentioned as follows:

- small wind turbines SW-2kW, SW-5kW, SW-10kW and SW-20kW, are used from Senwei Energy Technology Inc [279]. These wind turbines have achieved short PBP and low LCE in areas that have high availability of wind speed, especially SW-2kW, SW-5kW and SW-10kW as was revealed in Chapter 7.
- Polycrystalline 60 cells 260 watts (99cm × 165cm) solar modules [295] have been used to estimate solar energy in Chapter 8. This type of photovoltaic panel is chosen due to the low cost.
- A Lithium-ion storage unit of 2.4 kWh (SoFar ME3000SP) is proposed with different sizes of energy storage inverters (charger) [308], due to their long lifetime, high technical features and competitive price against the traditional kind of storage system like lead-acid [309]. Table 9-2 illustrates the main characteristics of a Lithium-ion battery and breakdown the cost of different battery sizes with battery charger [308].
- A DC-AC inverter (SUNTREE) [310] is used to convert power from a DC bus to AC bus and also to dump load to consume the waste energy in the case of off-grid when the power production from the HRES exceeds the demand and maximum power charging for a battery.

Equation 9-1 formulated to determine the typical size of inverter that is able to convert the maximum power flow from a configuration of the HRES at the DC bus to demand at the AC bus.

$$Inverter\ size = PV\ size + WT\ size + Max.Pdischarg \quad \text{Equation 9-1}$$

$Max.Pdischarg$: represent the maximum power that can be discharged from a storage system based on battery features. Equation 9-2 calculates $Max.Pdischarg$ as follows:

$$Max.Pdischarg = 0.52084 * C_{bat\,n} \quad \text{Equation 9-2}$$

$C_{bat\,n}$: represents the nominal storage capacity while, $0.52084 = 2C$ represents the max. C-rate of the 2.4 kWh battery unit in this project [308]. On the other hand, various sizes of each component are suggested, and many possible combinations are taken into consideration to install a flexible, reliable and economic HRES configuration. Firstly, 25 wind turbine combinations, are recommended, as presented in Table 9-1. Besides this, 29 solar system configurations are proposed by using Polycrystalline 60 cells 260 W solar module as shown in Table 9-3. Also, 14 configurations of storage system designed by using the Lithium-ion storage unit of 2.4 kWh, are shown in Table 9-3. Several configurations of HRES have been suggested to determine the optimal HRES configuration that able to meet the electricity demand at various scenarios and conditions. The majority of configurations consists of a wind turbine, solar system and battery for reliability reason, while some of these configurations do not include one or two of the main components.

Table 9-1. Wind turbine size and the possible wind turbine configurations that can be integrated to create the wind turbine system.

Wind turbine size	Wind turbine size	Wind turbine size
2 kW = SW-2kW	12 kW = SW-10kW + SW-2kW	22 kW = SW-20kW + SW-2kW
4 kW = SW-2kW * 2	14 kW =SW-10kW + (SW-2kW * 2)	24 kW = SW-20kW + (SW-2kW* 2)
5 kW = SW-5kW	15 kW = SW-10kW+SW-5kW	25 kW = SW-20kW + SW-5kW
6 kW = WS-2kW * 3	16 kW =SW-10kW + (SW-2kW * 3)	26 kW =SW-20kW + (SW-2kW* 3)
7 kW = SW-5kW + WS-2kW	17 kW = SW-10kW + SW-5kW + SW-2kW	27 kW = SW-20kW + SW-5kW + SW-2kW
8kW = SW-2kW * 4	18 kW = SW-10kW + (SW-2kW * 4)	28 kW = SW-20kW + (SW-2kW * 4)
9 kW =SW-5kW + (SW-2kW*2)	19 kW = SW-10kW + SW-5kW + (SW-2kW*2)	29 kW = SW-20kW + SW-5kW + (SW-2kW*2)
10 kW = SW-10kW	20 kW = SW-20kW	30 kW = SW-20kW + SW-10kW
		0 kW

However, the configurations which included just batteries in their system have been excluded from this project because the aim of this project is to determin a HRES configuration that is able to meet demand by using renewable energy. To determine the number of HRES configurations that are suggested in this study, 25 WT * 29 PV * 14 Batteries =10150 - 14 configurations that have only batteries. According to the above calculation, the total number of configurations in this study equals to 10136.

Table 9-2. Characteristics of the Lithium-ion battery storage system and the cost of the charger and different sizes of batteries [308].

Lithium-ion Battery storage system SoFar ME3000SP			
Total of energy for 1 unit	2.4 kWh	SoFar ME 3000SP energy storage inverter	£ 1000
Nominal battery voltage	48 V	Pylontech 2.4kWh lithium battery = 1 unit	£ 995
Battery voltage range	Discharge 40 V- Charge 60 V	inverter + 4.8kWh lithium battery	£ 2990
battery capacity	50A h	inverter + 7.2kWh lithium battery	£ 3985
Max. Charging Current	26 A	inverter + 9.6kWh lithium battery	£ 4980
Max. Discharging Current	26 A	inverter + 12 kWh lithium battery	£ 5975
Depth of discharge: DOD	0 – 90 %	inverter + 14.4 kWh lithium battery	£ 6970
Max. Charge-discharge power	1.25 kW	inverter + 16.8 kWh lithium battery	£ 7965
Max. C-rate	2C = 0.5 * $C_{bat\,n}(i)$	inverter + 19.2 kWh lithium battery	£ 8960
Life cycle	4500	inverter + 21.6 kWh lithium battery	£ 9955
Max. charging efficiency	94.5 %	inverter + 24 kWh lithium battery	£10950
Max. discharging efficiency	94 %	inverter + 26.4 kWh lithium battery	£11945
		inverter + 28.8 kWh lithium battery	£12940
		inverter + 31.2 kWh lithium battery	£13935

Table 9-3. 29 sizes of solar system configuration that have been configured by using Polycrystalline 60 cells 260 W of solar module, and 14 sizes of storage system configuration that are formatted by using the Lithium-ion storage unit of 2.4 kWh.

PV size	PV size	PV size	PV size	PV size	Battery size	Battery size
1.56 kW	9.36 kW	16.6 kW	23.92 kW	0 kW	2.4 kWh	19.2 kWh
3.12 kW	10.4 kW	17.6 kW	24.96 kW		4.8 kWh	21.6 kWh
4.16 kW	11.44 kW	18.7 kW	26 kW		7.2 kWh	24 kWh
5.2 kW	12.48 kW	19.7 kW	27.04 kW		9.6 kWh	26.4 kWh
6.24 kW	13.52 kW	20.8 kW	28.08 kW		12 kWh	28.8 kWh
7.28 kW	14.56 kW	21.84 kW	29.12 kW		14.4 kWh	31.2 kWh
8.32 kW	15.6 kW	22.88 kW	30.16 kW		16.8 kWh	0 kWh

9.2.2 **Input Data**

The optimization process requires reliable hourly meteorology data to ensure the accuracy of the optimal configuration results as follows: wind speed; solar radiation and temperature as well as reliable load data that should be gathered from trustworthy sources. Also, the optimization process requires a wide range of technical and economic information related to the solar system, wind turbine, storage system, the prices of electricity from national grid IBT and local diesel generator.

9.2.2.1 **Wind Speed And Turbine Power Production**

The hourly energy production from four wind turbine sizes (2 kW, 5 kW, 10 kW and 20 kW) are calculated in this project based on power curve information and typical hub heights according to the specification sheet of each turbine. Hourly wind speed data for one year (2014) has been estimated by the developed downscaling model (DSM) using MERRA data [131] and land cover map (LCM) [254] at the hub height for each specific wind turbine to estimate the potential power production at any location in Iraq as described in Chapter 5.

9.2.2.2 **Solar Radiation Data And Solar Power Production**

The hourly energy production from several sizes of solar systems is estimated based on three components global solar radiation ($\bar{G}$), direct beam radiation ($\bar{G}_b$) and diffuse radiation ($\bar{G}_d$) of solar radiation from HelioClim3v5 [181] and some technical inputs that are related to the module manufacturer and a location. Typical hourly solar radiation data over one year for periods 2004, 2005 and 2006 have been used to estimate hourly energy production everywhere in Iraq. The HelioClim3v5 data from 2004 to 2006 show good agreement with observed data for 9 out of 10 weather stations in Iraq in comparison with some datasets (PVGIS-HelioClim1, CMSAF and SARAH) as discussed in Chapter 8. However, the data which is provided by HelioClim3v5 for the period between 2006 and 2018 is costly. However, the Total Solar Irradiance (TSI) has increased around 3.2932 W/m^2 between 1610 and 2008 and also around 1.02 W/m^2 between 1975 and 1998 based on the 11 years cycle of sunspots [311, 312]. According to the slight increase in surface solar radiation (SSR) for many decades or in the case of a short term such as the 11 years cycle, it is possible to use solar radiation data gathered between 2004 and 2006 and apply in optimization process with load data collected in 2018.

9.2.2.3 **Load Profile**

It is well known that 8760 hours of demand data is essential input data for any optimization process [190, 200, 213]. For this reason, it was vital to gather hourly data of electricity demand from some housing units in Iraq. Unfortunately, it was complicated to find such data in Iraq and as a result of this lack the decision was taken to travel to Iraq to install several data loggers to record and monitor energy consumption online [313].

In fact, there are numbers of factors play a significant role to control the electricity consumption for different houses such as:

- Climate conditions in Iraq, which changes according to temperature, wind speed and solar radiation that effect on consumption and power production.
- The lifestyle and income of the householders Which in turn affects the number of devices in the house and an amount of consumption.
- The type of the secondary electricity supplier in case of off-grid like privet diesel generator or local generator and the capacity of supplying play a role in determining the amount of deferrable secondary loads.
- The number of a householder, their ages, the nature of their daily activities and house size plays an essential role in determining the amount of electricity consumption for each house.

All of these factors have been taken into consideration, but a host of obstacles have prevented this such as:

- The interruptions in internet connection during the outage periods in some houses that have low income due to the data logger need connection with platform every 10 minutes.
- The nature of logging data for one year that needs patient volunteers like friends and some relatives to take care of data loggers and changes the batteries regularly.
- The security condition in Iraq and the nature of political conflicts that prevented installing two of the data loggers in the west and north of the country.

Accordingly, the data loggers were installed on the 15th of October 2017 in three houses at three cities to cover some essential territories in Iraq. The equipment that has been used to record and monitor hourly energy consumption is called Efergy Engage hub kit online wireless home electricity monitor 3-phase kit [314] as shown in Figure 9-3.

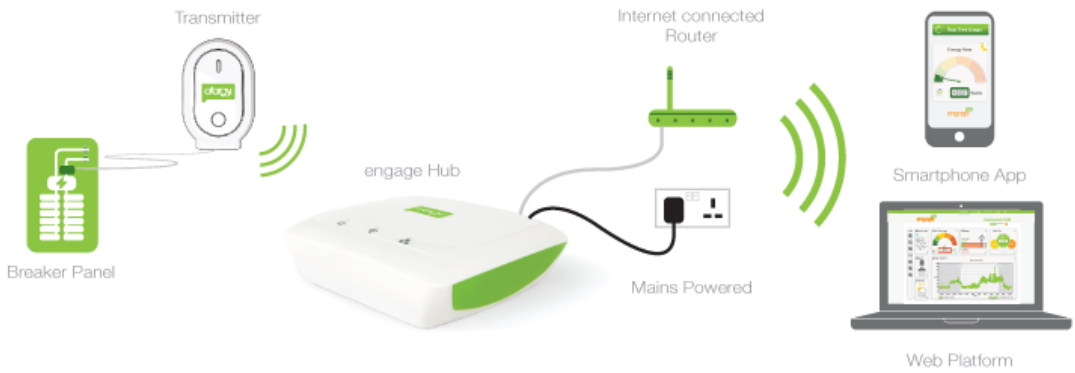

Figure 9-3. Energy engage hub kit online wireless home electricity monitor 3 phase that have been installed in three houses in Iraq to monitor and record the hourly energy consumption [20].

The plan of measuring data demand aimed to record hourly electricity consumption from three housing units that had different numbers of residents, various life quality, different behaviours of electricity consumption and different location for each house as follows:

1. Baghdad house BG: located in the middle of Iraq (Almansor, Baghdad, Iraq the grid reference 33.322535, 44.339421). There are four residents in this house. The life quality of this family is high with good income. The energy consumption basically from the national grid during the period of supplying from the network (on-grid) is 14909.45 kWh/year, while the energy supplied during outage periods which is provided by a local diesel generator in the case of unconnected to the grid (off-grid) equals 6997.12 kWh/year. The cost of energy from the local diesel generator £325 for 25 Amp/month, which equals £13 for 1 Amp. In fact, to supply any house in Iraq by power at any time during 24 hours for any period of outage, there are two choices: the first option, using private generator and the second option is called Golden line which costs a customer £13 for one Amp/month whether this amount of energy has been fully used or not. According to this price of energy, a customer should determine the necessary amount

of current to meet their demand based on 220 V. For this reason, most customers try to reduce their consumption as they can to avoid any extra payment by deferring unnecessary load to the period of on-grid supply. This behaviour of load deferring leads to an increase in the demand dramatically during on-grid supply as it is cheaper than the price of diesel generator during off-grid. Figure 9-4 shows the trend of consumption for BG in cases of on-grid and off-grid (diesel generator). Also, the main reason behind the high consumption within the summer season is the use of a number of air-conditions for cooling purposes.

2. Karbala house KR: is located south-west of Baghdad (Maytham al-Tamar St, Karbala, Iraq with grid reference 32.613561, 44.042958). There are three residents in this house. The life quality of this family is high with good income. The energy consumption basically from the national grid during the period of supply from the national network (on-grid) is 26561.9 kWh/year, while the energy supply during the outage period is provided by a private diesel generator that is able to cover regular demand for this house of 4914.94 kWh/year as shown in Figure 9-5. The residents in this house consume energy from the diesel generator as much as the hourly energy consumption from the national grid, for this reason, there is low difference between energy consumption in the case of on-grid and off-grid.

3. Basra house BS: is located south of Iraq (Altwesa, Basra, Iraq, at grid reference 30.515271, 47.818658). There are seven residents in this house. The life quality of this family is high with good income. The energy consumption was wholly supplied by the national grid (on-grid) at 36696.22 kWh/year. Also, the supplement from the grid was covering the energy demand for 24 hours over one year, as shown in Figure 9-6.

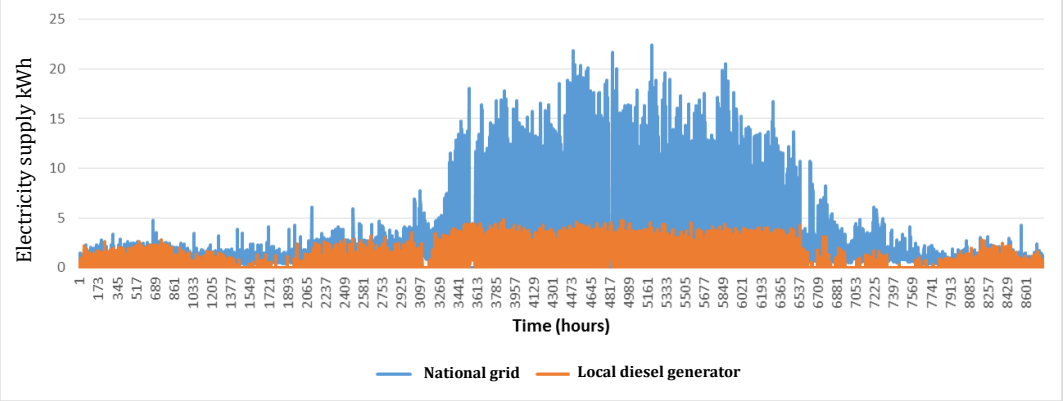

Figure 9-4. Energy consumption of BG for one year in 2018, according to the two of consecutive cases of demand. The first case is on-grid when demand was being supplied by electricity from the grid (blue line) and the second case represents the energy consumption during outage hours (off-grid) which was being covered by limited supplements from local diesel generator (Orange line)

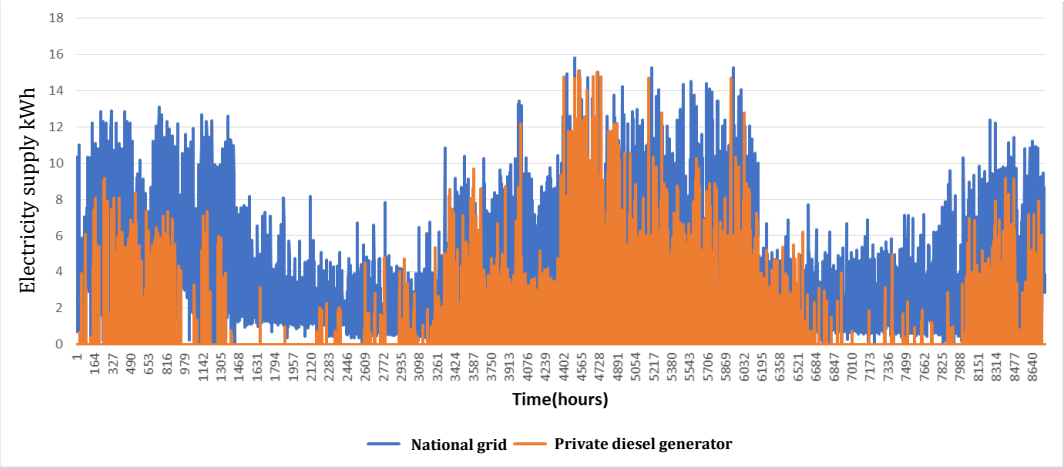

Figure 9-5. Energy consumption of KR for one year in 2018, according to the two consecutive cases of demand. The first case is on-grid when demand was being supplied by electricity from the national grid (blue line) and the second case represents the energy consumption during outage hours (off-grid) which was being covered by private diesel generator (Orange line)

9.2.3 Modeling of PV/Wind System Components

Modeling is a necessary stage before any process of optimization, where several modeling techniques have been developed to model HRES in this study. This section briefly describes the mathematical models of the HRES which relate to the solar system and wind turbine while the mathematical model of the storage system has been described in detail.

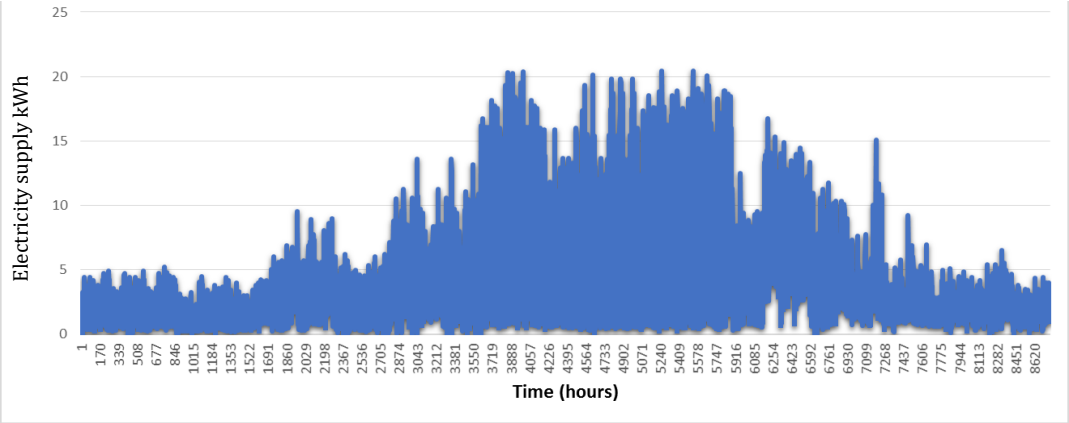

Figure 9-6. Energy consumption of BS for one year in 2018. The blue line is on-grid when demand was being entirely supplied by electricity from the national grid

9.2.3.1 Wind Turbine Mathematical Model

The power production of the wind turbine is estimated based on three key factors:

- The hourly wind speed over one year at any location and height that was estimated by the DSM that has been developed in Chapter 5 based on re-analysis data of wind speed from MERRA and roughness length based on land cover data.

- Also, the typical hub height of each wind turbine has been selected from the specification sheet of manufacture as follows: 12 m for SW-2kW, 15 m for SW-5kW, 18 m for SW-10kW and 20 m for SW-20kW [279].

Furthermore, the power production was estimated by using power curve information based on the power curve approach that has been described in section 2.5

9.2.3.2 PV Mathematical Model

The HSEP-WT model has been developed based on Homer PV power output calculation [297] to estimate the hourly energy production from a solar system as presented in Chapter 8. The technical details are provided by the panel manufacturer of Polycrystalline 60 cells 260 W in Chapter 8**,** which is used as an unit of producing energy from different sizes of the solar system. The hourly energy production from PV needs the annual optimum fixed tilted plane (tilt angle) which is provided by PVGIS [293] and hourly solar radiation data ($\bar{G}, \bar{G}_b$ and $\bar{G}_d$) from HelioClim-3 version 5 from SoDa [181]. The azimuth angle of the solar panel usually fixed toward the south, which equals 0°. In addition, the HSEP-WT model required hourly wind speed at 2 m has been estimated by the DSM based on MERRA data [131]. Furthermore, hourly ambient temperature has been provided by MERRA-2 RE-ANALYSIS in 2006 [301].

9.2.4 Mathematical Model of Storage System and Energy Flow Management.

9.2.4.1 Battery Bank Model and Features

A storage system is the most important part of a hybrid system that supports the stability of energy flow from the DC to AC bus against the intermittency of renewables due to the absence of solar radiation during the cloudy period or night time and also during low wind speed periods. The storage system plays a significant role in terms of feasibility according to the reliability and cost of a HRES. The essential feature in any storage system is the battery capacity at the time step (t) which depends on several factors such as maximum depth of discharge (DOD), maximum and minimum allowable storage capacity ($C_{bat\ max}$) and ($C_{bat\ min}$) , self-discharge rate (σ), battery charge and discharge efficiency, and so on [190, 213, 315]. The size and effectiveness of each factor depends on the battery type. In this project, the lithium-ion battery has been suggested to be the storage system in the HRES, due to the high performance and a marked decline in cost recently [316]. The maximum power charge and discharge of a battery (C-rate) represents the cornerstone in the battery modeling system to determine the amount of energy flow among the renewables, battery and demand in terms of charging and discharging a storage system as

shown in Figure 9-7. At the beginning, the total renewable energy generated by the HRES at the time step (t) is estimated by Equation 9-3 [200].

$$E_{RE}(t) = E_{pv}(t) + E_w(t) \quad \text{Equation 9-3}$$

$E_{pv}(t)$ and $E_w(t)$ represent the energies produced by the PV and wind turbine, respectively. The energy flow from the DC bus to the load $E_{load}(t)$ in the AC bus is limited by the inverter efficiency (η_{inv}), whereas $D(t)$ represents equivalent DC load demand corresponding to the inverter input as expressed in Equation 9-4. Equation 9-5 expresses the energy flow when the energy production from the HRES is higher than the demand $D(t)$ [200].

$$D(t) = \frac{E_{load}(t)}{\eta_{inv}} \quad \text{Equation 9-4}$$

$$E_{Ex}(t) = E_{RE}(t) - D(t) \quad \text{Equation 9-5}$$

Equation 9-6 expresses the energy flow when energy production from the HRES is lower than the load $E_{load}(t)$).

$$E_{need}(t) = max\left(0, \left(D(t) - E_{RE}(t)\right)\right) \quad \text{Equation 9-6}$$

The energy flow ($P_{charg}(t)$) between renewables and battery in the time step (t) when $E_{Ex}(t) > 0$, is determined by Equation 9-5. The state of storage capacity should be estimated, which depends on the previous state of capacity at a previous time step ($C_{bat}(t-1)$), the self-discharge rate ($1-\sigma$) and the maximum storage capacity ($C_{bat\,max}$) and battery charge efficiency (η_{bc}). Also, the maximum power charge ($Max.P_{charg}$) which controls the maximum amount of energy that can be injected to the battery according to the times step (Δt) based on the C-rate as expressed in Equation 9-7.

$$P_{charg}(t) = min\left[\left(E_{RE}(t) - \frac{E_{load}(t)}{\eta_{inv}}\right), \left(\frac{C_{bat\,max} - C_{bat}(t-1).(1-\sigma)}{\eta_{bc}.\,\Delta t}\right), Max.P_{charg}\right] \quad \text{Equation 9-7}$$

According to the amount of power charging from Equation 9-7 it is possible to calculate the battery capacity at the time step (t) based on the previous state of battery capacity ($C_{bat}(t-1)$) and self-discharge rate ($1-\sigma$) as expressed in Equation 9-8.

$$C_{bat}(t) = C_{bat}(t-1).(1-\sigma) + P_{charg}(t).\eta_{bc}\,.\,\Delta t \qquad \text{Equation 9-8}$$

On the other hand, if $(E_{need}(t) > 0)$ in Equation 9-6 the storage system will cover the energy demand, and the energy flow between battery and demand will be determined by other parameters like the previous state of capacity at time step $(C_{bat}(t-1))$, self-discharge rate $(1-\sigma)$ minimum storage capacity $(C_{bat\,min})$ and battery discharge efficiency (η_{bd}). Furthermore, the maximum power discharge $(Max.P_{discharg})$ which determine the maximum amount of power that can be discharged from the battery as expressed in Equation 9-9.

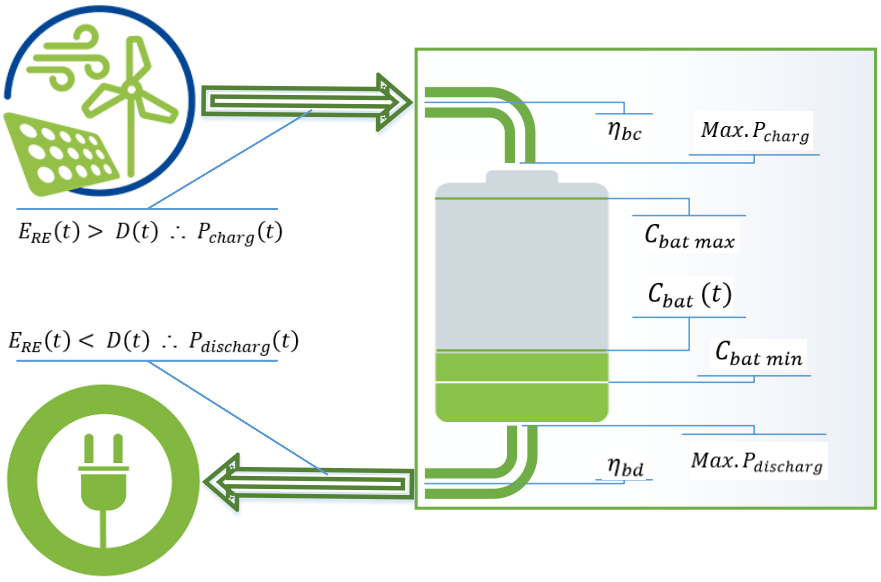

Figure 9-7. The parameters like battery charge and discharge efficiency $(\eta_{bc})$and (η_{bd}) respectively and the maximum power charge and discharge of a battery (C-rate) $(Max.P_{charg})$ and $(Max.P_{discharg})$ respectively which determine the energy flow in the HRES.

$$P_{discharg}(t) = min\left[\left(\frac{E_{load}(t)}{\eta_{inv}} - E_{RE}(t)\right), \left(max\left(0, \left(\frac{(C_{bat}(t-1).(1-\sigma) - C_{bat\,min}).\eta_{bd}}{\Delta t}\right)\right), Max.P_{discharg}\right]\right. \qquad \text{Equation 9-9}$$

According to the amount of power discharging $(P_{discharg}(t))$ from Equation 9-9, it is possible to calculate the battery capacity at time step (t) based on the previous state of battery capacity $(C_{bat}(t-1))$ and self-discharge rate $(1-\sigma)$ as expressed in Equation 9-10.

$$C_{bat}(t) = C_{bat}(t-1).(1-\sigma) - \frac{P_{discharg}(t)}{\eta_{bd}}.\,\Delta t \qquad \text{Equation 9-10}$$

There is a point when the load demand is equal to the available energy generated by a hybrid system and $E_{Ex}(t) = 0$ in Equation 9-5, then the battery bank will be in the state of self-discharge, as expressed in Equation 9-11.

$$C_{bat}(t) = C_{bat}(t-1).(1-\sigma) \qquad \text{Equation 9-11}$$

$P_{charg}(t)$ and $P_{discharg}(t)$ represent the energy flow into/from the battery, while the $(P_{charg}(t).\eta_{bc})$ represents the required amount of energy to charge battery. $(\frac{\boldsymbol{P_{discharg}(t)}}{\boldsymbol{\eta_{bd}}})$ represents the amount of energy to discharge from inside the battery. The above methodology of energy flow between renewable, battery and demand is developed according to [190, 213, 287, 317, 318]. Since the lithium-ion battery (SoFar ME3000SP) has been suggested to be the storage system in this project, the values of parameters that related to battery type should be presented as follows:

- In general, the self-discharge rate of the lithium-ion battery ranks between 2% to 5% per month [319-321]. In this study $\boldsymbol{\sigma}$ = 0.0013 per a day and σ = 5.5*10^{-5} per hour based on 4% per month [319].
- η_{inv}: is the inverter efficiency that converts the current from the DC to the AC = 98% [310].
- η_{bc} : is the battery charge efficiency which equals 94.5% for lithium-ion battery according to ME3000SP [308].
- η_{bd}: is the battery discharge efficiency which equals 94% for the Lithium-ion battery, according to ME3000SP [308].
- The calculation of maximum power charge and discharge of lithium-ion battery depends on the (Max. C-rate), which is equal to 0.52084 according to ME3000SP in this project [308] and the storage nominal capacity $C_{bat\,n}$.

  $Max.P_{charg} = Max.P_{discharg} = 0.52084 * C_{bat\,n} = 1.2$ kW for one unit of 2.4 kWh for ME3000SP.

At any time step, the storage capacity ($C_{bat}(t)$) should be located between the two following constraints:

$$C_{bat\,min} \leq C_{bat}(t) \leq C_{bat\,max}$$

$C_{bat\,max}$ and $C_{bat\,min}$ represent the maximum and minimum allowable storage capacity, respectively. The $C_{bat\,max}$ for the lithium-ion battery represents 98% of the storage nominal capacity $C_{bat\,n}$ [319] as expressed in Equation 9-12.

$$C_{bat\,max} = 0.98 * C_{bat\,n} \qquad \text{Equation 9-12}$$

While the minimum storage capacity $C_{bat\ min}$ of the lithium-ion battery is determined based on DOD and $C_{bat\ n}$ of the battery as expressed Equation 9-13 [213].

$$C_{bat\ min} = (1 - DOD) * C_{bat\ n} \qquad \text{Equation 9-13}$$

DOD (%) represents the maximum depth of battery discharge. For the lithium batteries According to ME3000SP DOD = 90 % [308].

9.2.4.2 Energy Flow Management Strategies

Five scenarios of energy management simulation can be examined to determine which one of them is the most reliable and economical:

- **Scenario A off-grid**

  The power management strategy for off-grid is described by the three following cases:

  - Case 1. The total renewable energy generated by the HRES $E_{RE}(t)$ at the time step [t= 1 hour] should satisfy the load. The excess electricity is stored in the battery. If the excess electricity $E_{Ex}(t)$ exceeds $P_{charg}(t)$, the surplus electricity will go to the dump load as wasted energy.
  - Case 2. If renewable energy is less than the demand, the energy deficit will be covered by discharging the stored energy in the battery.
  - Case 3. If the battery is empty $C_{bat\ min}$ and renewable energy production is zero and $E_{need}(t) > P_{discharg}(t)$, the necessary electricity to satisfy the demand will be supplied by an optional diesel generator.

- **Scenario A on-grid with discharge**

  The power management strategy for on-grid can be described by the two following cases:

  - Case 1. Firstly, the total renewable energy generated by the HRES $E_{RE}(t)$ should satisfy the load. The excess electricity will be stored in the battery. If the battery capacity $C_{bat}\ (t)$ exceeds $(C_{bat\ max})$, the surplus electricity will be exported to the grid.
  - Case 2. When renewable energy is less than the demand, the energy deficit is satisfied by discharging the stored energy in the battery.
  - Case 3. If renewable energy is less than the load demand and the battery capacity $C_{bat}\ (t) = C_{bat\ min}$, the demand will be satisfied by purchasing electricity from the grid based on 2017 IBT prices to satisfy the load demand.

- **Scenario B off-grid**

  The power management strategy in the case of off-grid has the same description of Scenario A off-grid according to the three cases.

- **Scenario B on-grid without discharge**

The power management strategy for on-grid is described by the two following cases:

- Case 1. The total renewable energy generated by the HRES $E_{RE}(t)$ should satisfy the load. The excess electricity is saved in the battery. If the battery capacity $C_{bat}\ (t)$ exceeds $C_{bat\ max}$, the surplus electricity is exported to the grid.
- Case 2. When renewable energy is less than the demand and the battery capacity ($C_{bat}\ (t) \neq\ C_{bat\ min}$) or ($C_{bat}\ (t) =\ C_{bat\ min}$), the energy deficit will not be satisfied by discharging the stored energy in the battery. The stored energy in the battery will be kept to the next job in the off-grid mode, instead of that, the demand will be satisfied by purchasing electricity from grid based on the 2017 or 2015 IBT prices.

- **Scenario C off-grid** and **Scenario C on-grid with discharge** show the same power management strategies of Scenario A but relying on the 2015 IBT prices from the grid.

- **Scenario D off-grid** and **Scenario D on-grid without discharge** show the same power management strategies of Scenario B but relying on the 2015 IBT prices from the grid. All these scenarios are applied by using the data demand from BG and KR in different locations in Iraq.
- **Scenario E on-grid with discharge**
  This scenario is designed for energy management strategy of on-grid for Basra house BS, which can be described by the same Scenario A on-grid with discharge. Firstly according to the 2017 IBT prices and secondly according to the 2015 IBT prices.
- **Scenario E on-grid without discharge**
  This scenario is designed for power management strategy of on-grid for Basra house BS, which can be described according to Scenario B on-grid without discharge. Firstly according to the 2017 IBT prices and secondly according to the 2015 IBT prices.

9.2.4.3 On-grid and off-grid system with discharge the storage system

The approach of combining between on-grid and off-grid (On-off-grid Op-HRES) systems is developed by using a MATLAB script based on Scenario A off-grid and Scenario A on-grid with discharge as illustrated by the flow chart in Figure 9-8 and without discharge in B in Figure 9-9.

- Firstly, prepare hourly demand for off-grid and on-grid, wind speed at 2 m, 12 m, 15 m, 18 m and 20 m, hourly ambient temperature and solar radiation ($\bar{G}, \bar{G}_b$and $\bar{G}_d$) based on-site coordination.
- Secondly, prepare the solar power production for one module of Polycrystalline 60 cells 260 W to be able to calculate the power production for different sizes of the solar system at any configuration. Calculate the power production from an essential size of wind turbines according to the typical height as presented in section (9.2.3.1).
- Then, insert the necessary technical information which is related to the storage system, financial information such as cost of renewables components (wind turbine, solar panel, batteries and inverters) and bracket price of 2015 and 2017 IBT.
- After that, the optimization process will start from the first configuration and continue until the last configuration no 10136. The simulation will start from t=1 by calculating

the total energy generated by wind turbine and PV system from the first configuration by Equation 9-3.

- The most important step in the optimization process is the decision that will be taken by the MATLAB code according to the on-grid demand condition. If it is zero at time step (t), the code will run the HRES configuration through the off-grid process based on the Scenario A off-grid. While, if the on-grid demand is not zero, the code will run the HRES through the on-grid state according to Scenario A on-grid with discharge as shown in Equation 9-8 and Equation 9-9.
- In terms of Scenario A off-grid and according to Case1, $E_{RE}(t)$ in Equation 9-3 should satisfy the off-grid demand $D_{off-grid}(t)$ as shown in Figure 9-8. If $E_{Ex}(t) = 0$ in Equation 9-5, the battery capacity $C_{bat}(t)$ should be estimated according to Equation 9-11. On the first hand, if $E_{Ex}(t) > 0$ in Equation 9-5, the storage system should be charged by applying Equation 9-7 and Equation 9-8. On the other hand, if, $E_{Ex}(t)$ exceeds $P_{charg}(t)$, the control system will stop the charging process and then the surplus electricity will be sent to the dump load such wasted energy as expressed in Equation 9-14.

$$E_{WE}(t) = E_{Ex}(t).\Delta t - P_{charg}(t) \qquad \text{Equation 9-14}$$

According to, Case 2 when there is no interaction with the grid, $E_{Ex}(t) < 0$ in Equation 9-5 the load demand should be satisfied by discharging the battery according to Equation 9-9. Then, the state of storage capacity is calculated based on Equation 9-10. According to Case 3, when renewable energy is less than the load demand and $E_{need}(t) > P_{discharg}(t)$. The required electricity to cover the demand will be supplied by optional diesel generator according to Equation 9-15.

$$E_{DG}(t) = E_{need}(t).\Delta t - P_{discharg}(t) \qquad \text{Equation 9-15}$$

$E_{DG}(t)$ refers to the energy from the diesel generator DG purchased for the period (Δt). When the battery capacity decreases to the minimum level $C_{bat\,min}$, the energy deficit will be determined as loss of power supply (LPS) at time step (t) that is equal to the (DG) purchased at time step $E_{DG}(t) = \text{LPS}(t)$. $\text{LPS}(t) = 0$ when $E_{Ex}(t) \geq 0$ and when charging and sometimes discharging the storage system.

- At this point, the system will pass to the next step (t+1) and check if the on-grid demand is zero or there is supply from the national grid. If there is supply from the national grid, the MATLAB script will run the HRES configuration through the on-grid process according to Scenario A on-grid with discharge.
- In terms of Scenario A on-grid with discharge and according to Case1 and $E_{RE}(t)$ in Equation 9-3, the on-grid demand $D_{on-grid}(t)$ should be satisfied as shown in Figure 9-8. If $E_{Ex}(t) = 0$ in Equation 9-5, the battery capacity $C_{bat}(t)$ should be estimated according to Equation 9-11. If $E_{Ex}(t) > 0$ in Equation 9-5, the storage system should be

charged by applying Equation 9-7 and Equation 9-8. If $E_{Ex}(t)$ exceeds $P_{charg}(t)$, the control system will send the surplus electricity to the national grid as expressed in Equation 9-16.

$$E_{SP}(t) = E_{Ex}(t).\Delta t - P_{charg}(t) \quad \text{Equation 9-16}$$

- According to, Case 2 when, $E_{Ex}(t) < 0$ in Equation 9-5, the load demand is satisfied locally by discharging the battery according to Equation 9-9. Then, the state of storage capacity will be calculated according to Equation 9-10.
- According to Case 3, when $E_{need}(t) > P_{discharg}(t)$. The required electricity to cover the demand will be purchased from the grid as expressed in Equation 9-17.

$$E_{GP}(t) = E_{need}(t).\Delta t - P_{discharg}(t) \quad \text{Equation 9-17}$$

$E_{GP}(t)$ is equivalent to the $LPS(t)$ in the off-grid case. In this case, the purchased electricity from the national grid will be estimated based on 2017 IBT prices or based on 2015 IBT prices according to Scenario C on-grid with discharge.

- At this point, the system will pass to the next step (t+1), and the simulation will continue to finish one year (8760 h) of operating.

The performance of any configuration over 8760 hours of running should be evaluated whether there is interaction with the grid or not. The optimization process should minimise the LPSP. LPSP is defined as the ratio of summation of all hourly loss of power supply values (LPS) when there is no interaction with the grid over the total required load [191-193] as expressed in Equation 9-18.

$$LPSP = \frac{\sum_{t=1}^{8760} LPS(t)}{\sum_{t=1}^{8760} E_{load}(t)\Delta t} \quad \text{Equation 9-18}$$

On the other hand, the optimization process should minimise the GPAP for a considered period t = 8760. GPAP is defined as the ratio of purchased electricity $E_{GP}(t)$ over the total load required during that period of 8760 hours [200, 201] as expressed in Equation 9-19.

$$GPAP = \frac{\sum_{t=1}^{8760} E_{GP}(t)}{\sum_{t=1}^{8760} E_{load}(t)} \quad \text{Equation 9-19}$$

In addition, the performance of any configuration over 8760 hours should be evaluated based on economic constraints such as LCE and PBP that will be described in details in section (9.2.5).

9.2.4.4 **On-grid and off-grid system without discharge the storage system**

According to this energy flow management strategy, the optimization process is combing between on-grid and off-grid systems as explained in section (9.2.4.3), but without discharging the storage system when $(E_{Ex}(t) > 0)$ even when the battery capacity $C_{bat}\ (t) \neq\ C_{bat\ min}$ or $C_{bat\ max}$ The energy deficit will not be satisfied by discharge the stored energy in the battery in order to keep the stored energy to the next job in the off-grid mode. Rather than that, on-grid demand will be covered by purchasing electricity from national grid in order to increase the lifetime of a battery according to Scenario B on-grid without discharge as illustrated by the flowchart in Figure 9-9B that can be substituted by discharge process in the red dots box in Figure 9-8 and also based on 2015 and 2017 IBT prices. The performance of any configuration will be evaluated by LPSP in the case of off-grid and GPAP in the case of on-grid as well as based on LCE and PBP in terms of economic assessment.

9.2.4.5 **On-Grid System With and Without Discharge a Storage System**

The energy flow management in this section has been designed only for grid-connected demand purposes, which have been represented by Basra house BS that has been fed fully from the national grid as shown in Figure 9-6. The first suggestion of energy flow management is designed based on Scenario E on-grid with discharge, which is similar to Scenario A on-grid with discharge that has been described in details in section (9.2.4.3). Scenario E on-grid with discharge for BS is presented in Figure 9-9A. On the other hand, the second suggestion of energy flow management is designed according to Scenario E on-grid without discharge which is similar to Scenario A on-grid without discharge that has been explained in section (9.2.4.3). The flow chart of the second suggestion of energy flow management is presented by replacing the flowchart of discharging the battery in the red doted box in Figure 9-9A with the non-discharging process in Figure 9-9B.

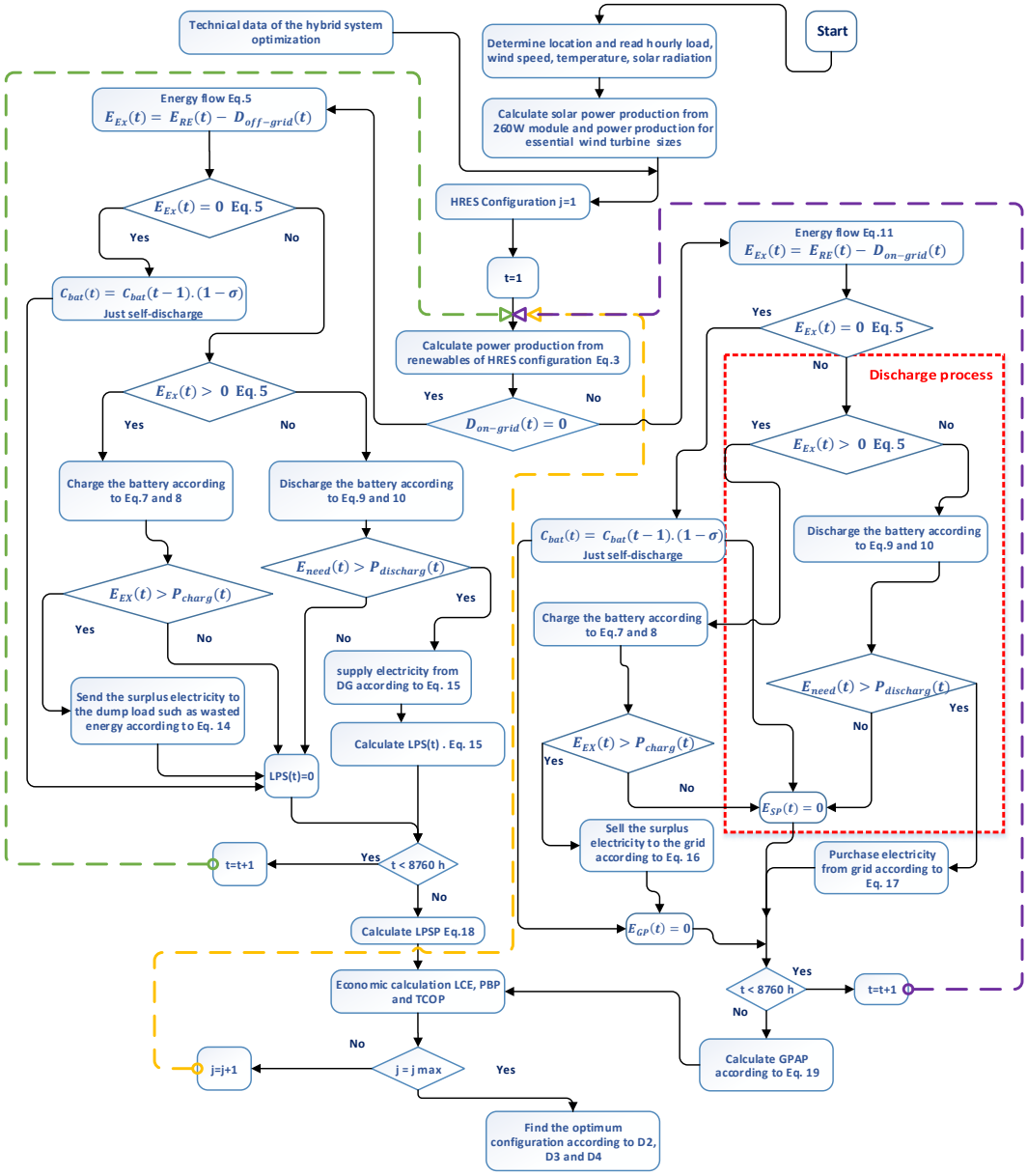

Figure 9-8. Flowchart for the optimization process of off-grid and on-grid for the HRES (On-off-grid Op-HRES) with discharge of the storage system in the case of on-grid that is determined by dotted red box. This flowchart represents the optimization process of off-grid and on-grid for the HRES without discharge of the storage system in the case of on-grid according to the dotted red box when replaced by the non-discharge process flowchart in Figure 9-9B.

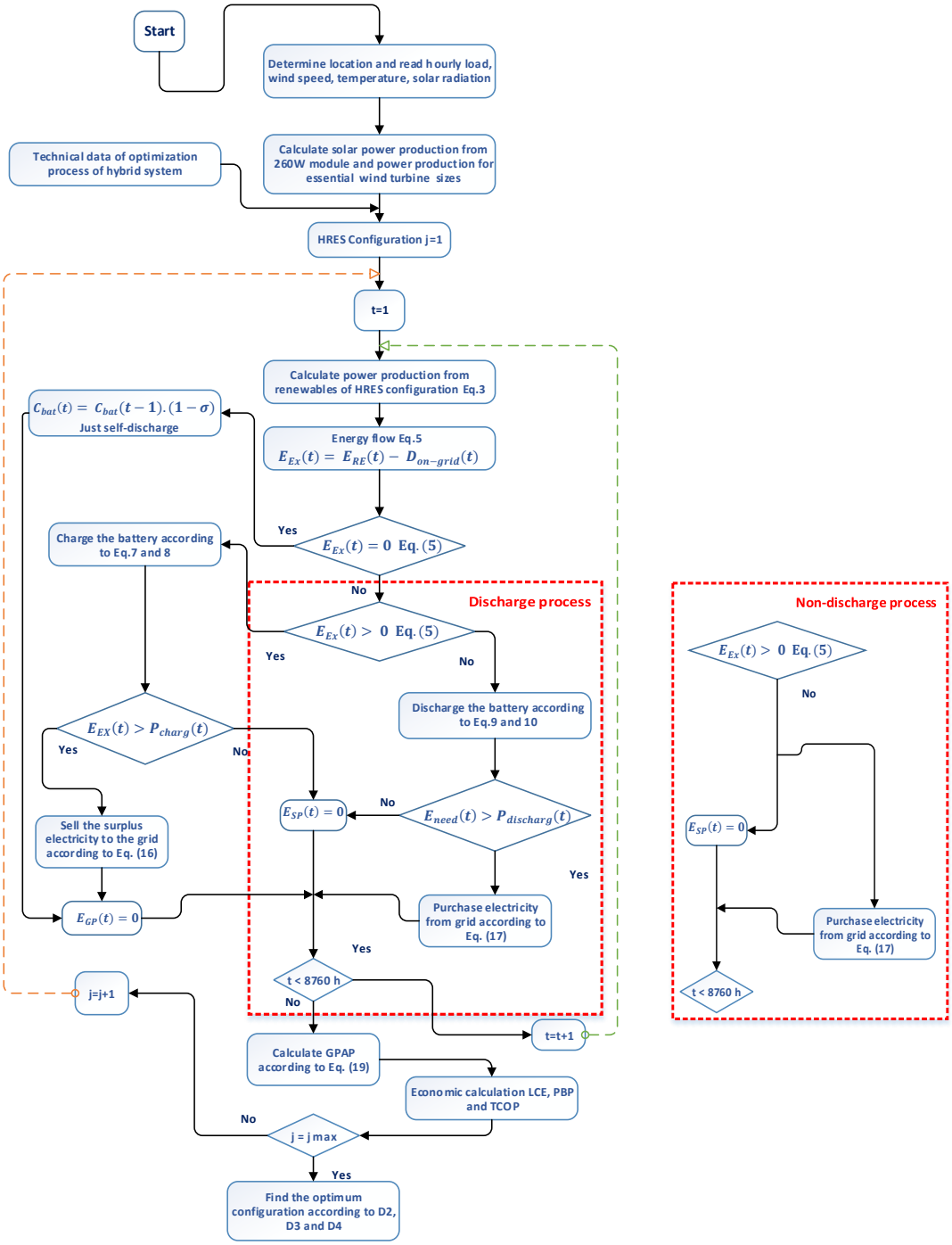

A- B- without discharge process

Figure 9-9. Flowchart for the optimization process on-grid for the HRES with discharge of the storage system in the case of on-grid according to flowchart A and the flowchart of the without discharge process in flowchart B

9.2.5 Modeling of System Economic And Reliability

The economic and reliability constraints should be considered to determine the optimal HRES configuration. The constraints of reliability (LPSP and GPAP) are explained in section (9.2.4.3). Whereas, the mathematical model to calculate the economic constraints (LCE and PBP) are described in the next sections. The LCE and PBP calculation in this project

should be supported by a technical and financial estimate for each component in the HRES, as presented in sections (9.2.5.1) and (9.2.5.2).

9.2.5.1 **Levelized Cost of Energy**

In general, the definition LCE and Capital Recovery Factor (CRF) have been described in section 4.2.2.2. The annual energy production (AEP) in LCE calculation from the HRES is represented by the energy production that has covered Annual Electricity load (AE_{load}) (off-grid and on-grid demand over 8760 hours) including the Annual Energy of surplus electricity (AE_{SP}) that was injected to the grid, and excluding what has been covered by grid supply (Annual Energy grid purchase (AE_{GP})) and the diesel generator (Annual Energy diesel generator supply (AE_{DG})). The Levelized annual cost (LAC) represents the annual values of total present value (TPV) for each component based on (CRF) as expressed in Equation 9-20 [212].

$$LAC = TPV * CRF \qquad \text{Equation 9-20}$$

According to the above description, the LCE of the HRES is expressed in Equation 9-21.

$$LCE = \frac{LAC_{battery} + LAC_{WT} + LAC_{PV} + LAC_{inv}}{(AEload - (AE_{GP} + AE_{DG})) + AE_{SP}} \qquad \text{Equation 9-21}$$

$LAC_{battery}, LAC_{WT}, LAC_{PV}$ and LAC_{inv} represent the LAC of battery, wind turbine, solar system and inverter respectively. The Annual Energy Load ($AEload$) is expressed in Equation 9-22.

$$AEload = \sum_{t=1}^{8760} D_{on-grid}(t) + D_{off-grid}(t) \qquad \text{Equation 9-22}$$

Whereas, AE_{GP} , AE_{DG} and AE_{SP} are expressed in Equation 9-23,Equation 9-24 and Equation 9-25 respectively.

$$AE_{GP} = \sum_{t=1}^{8760} E_{GP}(t) \qquad \text{Equation 9-23}$$

$$AE_{DG} = \sum_{t=1}^{8760} E_{DG}(t) \qquad \text{Equation 9-24}$$

$$AE_{SP} = \sum_{t=1}^{8760} E_{SP}(t) \qquad \text{Equation 9-25}$$

9.2.5.2 **Payback Period PBP**

In general, the definition and the mathematical model of PBP has been described in section 4.2.2.3. TCOP is estimated over the project lifespan which is assumed to be 20 years. The Annual saving cost strategy ($AnnSavCost$) that was suggested in section 7.3 has been applied instead of the ($Net\ Annual\ Cash\ inflow\ of\ AEP$) in the original definition. The ($AnnSavCost$) represents the annual amount that can be saved when using the HRES against the annual cost of total demand if it was covered by the national grid or diesel generator as expressed in Equation 9-26:

$$AnnSavCost = \sum_{i=1}^{12} \Big(CostMD_i - Cost\big(MD_i - (MEP_i \leq MD_i)\big)\Big) \qquad \text{Equation 9-26}$$

MD_i: refers to monthly demand, while $i =$ month. (MEP_i) represents the monthly energy production. ($CostMD_i$) represents the cost of monthly demand based on provider prices. In this chapter, the cost of monthly on-grid demand ($CostMD_i\ on\ grid$), has been calculated based on IBT price from the national grid according to Figure 7-1. While the cost of monthly off-grid demand ($CostMD_i\ off\ grid$), has been estimated based on the price of a local diesel generator as mentioned in section (9.2.2.3). The cost of the rest monthly demand that could not be satisfied by the HRES, and has been covered by the national grid or local diesel generator is calculated as discussed below:

The equivalent of the rest monthly demand ($Cost\big(MD_i - (MEP \leq MD_i)\big)$) in Equation 9-26 is represented by the cost of monthly net grid trade ($Cost\ MNetgrid_i$) between the surplus electricity $E_{sp}(t)$ and grid purchases $E_{GP}(t)$ from the national grid, in the case of on-grid as expressed in Equation 9-27.

$$Cost\ MNetgrid = Cost \sum_{t=1}^{720} E_{GP}(t) - E_{sp}(t) \qquad \text{Equation 9-27}$$

$t = 720$ represents the number of hours per month. There is no interest or income from the surplus electricity $E_{sp}(t)$ that is injected to the national grid in Iraq, for this reason, the ($Cost\ MNetgrid = 0$) if ($E_{sp}(t) > E_{GP}(t)$). The cost of monthly net grid trade has been estimated based on IBT price from the grid. While the equivalent of ($Cost\big(MD_i -$

$(MEP_i \leq MD_i))$) in Equation 9-26 in the case of off-grid is represented by the cost of rest monthly demand that has been covered by diesel generator as expressed in Equation 9-28.

$$Cost\ RMD\ offgrid = Cost \sum_{t=1}^{720} E_{DG}(t) \qquad \text{Equation 9-28}$$

The price of electricity from the diesel generator is calculated based on the maximum energy consumption from the diesel generator per month that is equivalent to the Amp price according to the Iraqi energy market price, 1Amp= £13. According to the monthly cost saving in the case of on-grid and off-grid demand, Equation 9-29 is expressed to estimate the annual cost saving in this project.

$$AnnSavCost = \sum_{i=1}^{12}(CostMDon\ grid\ (i) - \ Cost\ MNetgrid(i)) + (CostMD\ offgrid(i) - \ Cost\ RMD\ offgrid(i)\ ) \qquad \text{Equation 9-29}$$

According to the above calculation, the PBP of the HRES in this chapter is expressed in Equation 9-30:

$$PBP = \frac{TCOP_{WT} + TCOP_{pv} + \ TCOP_{Batt} + TCOP_{inv}}{AnnSavCost} \qquad \text{Equation 9-30}$$

$TCOP_{WT}$, $TCOP_{pv}$, $TCOP_{Batt}$ and $TCOP_{inv}$ refer to the total cost of the project for a wind turbine, solar system, battery and inverter respectively. The $TCOP_{WT}$ and $TCOP_{pv}$ calculation have been explained in Chapter 7 and Chapter 8 respectively, but both of them have been applied in this chapter without including the inverter cost in the HRES calculation. On the other hand, the estimation of $TCOP_{Batt}$ and $TCOP_{inv}$ are explained in section (9.2.5.3) and (9.2.5.4), respectively.

9.2.5.3 Technical and Economic Calculation for The Storage System

In this section, the methodology which is used to calculate the TCOP of the storage system is revealed according to several logical steps as follows:

- Battery Life cycle per year.
- Number of storage replacements during the project lifespan.
- The battery capital cost.
- Replacement and spare part cost (RSC) of the battery over the project lifespan.
- The TCOP of storage system.

The battery cycle capacity and annual energy charging should be calculated to estimate the battery life cycle per year for each storage size. The battery cycle capacity represents the

necessary amount of power to charge the battery fully to complete one cycle of the life battery cycle. The annual energy charging represents the total amount of energy that has been used to charge a storage system over one year. Equation 9-31 expresses the (Annual Battery life cycle) as follows.

$$Annual\ Battery\ life\ cycle\ = \frac{Annual\ P_{charg}}{Battery\ cycle\ capacity} = \frac{\sum_{t=1}^{8760} P_{charg}(t).\eta_{bc}}{C_{bat\ max} - C_{bat\ min}} \quad \text{Equation 9-31}$$

To calculate the number of storage replacements over the project lifespan ($Nrep$) for each battery configuration, which is expressed in Equation 9-32, the life cycle of battery = 4500 cycle according to ME3000SP is required.

$$Nrep = \frac{Annual\ life\ Battery\ cycle\ *\ T}{Life\ cycle} \quad \text{Equation 9-32}$$

T is the lifespan of project of 20 years. Determination of the realistic number of battery replacements requires some necessary conditions: if the ($Nrep \leq 1$), the ($Nrep = 0$), while if ($Nrep > 1$), the ($Nrep = 1$). According to these conditions, if the number of storage replacements was more than 1 e.g. 1.1, the number of replacement will be 1, which means the HRES will keep the first battery and then it will be replaced by another one during the lifespan of a project. While if the $Nrep < 1$ that means keeping the first one during the lifespan of a project. The TPV must be estimated as expressed in Equation 9-33 [287], to calculate the total cost of storage system TCOP for the HRES.

$$TPV\ =\ Capex\ +\ VC\ -\ PVS \quad \text{Equation 9-33}$$

($Capex$) represents the initial capital cost of a storage system, as presented in Equation 9-34.

$$Storage\ Capex\ = Inverter\ cost + ((\frac{C_{bat\ n}}{2.4}) * Battery\ cost) \quad \text{Equation 9-34}$$

$Inverter\ cost$: represents the cost of the energy storage inverter or charger, which is shown in Table 9-2. The battery number is determined by the storage nominal capacity ($C_{bat\ n}$) that has been chosen as a part of the HRES configuration and divided by the size of storage unit of 2.4 kWh (SoFar ME3000SP). The cost of each battery unit is shown in Table 9-2. (VC): refers to the Variable Costs, which includes mainly Operation and Maintenance Cost (OMC)

and Replacement and Spare part Costs (RSC). The OMC has been assumed to be zero in the case of the storage system because there are no real payments related to the storage system in the case of operation and maintenance. Concerning the RSC calculation, there are two conditions to control this calculation as expressed in Equation 9-35.

$$\text{If Nrep} = 0$$
$$\text{RSC} = 0$$
$$\text{If Nrep} = 1$$
$$\text{RSC} = \sum_{j=1}^{N_{rep}} \left(C_{nom} * C_{unit} * \left(\frac{1+i}{1+r}\right)^{T*j/N_{rep}+1} \right) \quad \text{Equation 9-35}$$
$$C_{nom} = C_{bat\,n} * 1000$$
$$C_{unit} = \text{Storage Capex} / C_{nom}$$

$r = 4\%$ is the net interest rate for investment and residential loans in Iraq in 2018 [288]. $i = 4\%$ is the inflation rate in Iraq in 2018 [289]. (C_{nom}): is the nominal capacity of the replacement unit in Wh. (C_{unit}): represents the price of the replacement unit. T: represents the life time of project 20 years.

The present value of battery scrap, whether at the end of battery life cycle or at the end of the project, could not be ignored when calculating the TPV of storage system project. PVS is the present value of scrap, which is expressed in Equation 9-38 depending on the value of scrap SV of the batteries themselves, as shown in Equation 9-36 [322].

$$SV = Battery\ cost * \left(\frac{1}{Lifespan\ Battery}\right) \quad \text{Equation 9-36}$$

$$Lifespan\ Battery = * \left(\frac{Lifecycle}{Annual\ life\ Battery\ cycle}\right) \quad \text{Equation 9-37}$$

$$PVS = \sum_{j=1}^{N_{rep}} SV * \left(\frac{1+i}{1+r}\right)^{T*j/N_{rep}+1} \quad \text{Equation 9-38}$$

Finally, it is possible to calculate the TCOP of the storage system in the HRES configuration as expressed in Equation 9-39.

$$TCOP = (TPV * CRF) * T \quad \text{Equation 9-39}$$

9.2.5.4 Technical and Economic Calculation For The Inverter

The Total Present value (TPV) is a significant variable for all the HRES components to calculate the TCOP according to Equation 9-39, while the LAC should be calculated based on Equation 9-20. To calculate the TPV of the DC-AC inverter (SUNTREE) [310] in this project, just RSC should be considered. The other variables like OMC is not required, because there is no real payment to repair or operate the inverter. In this case $TPV_{inv} = RSC$. The potential size of the inverter and the cost of it should be determined. The size of the inverter is determined by Equation 9-1. The Suntree Electric Group Co. [310] produces various inverter sizes with changes of 5kW, 10kW, 15kW and 20kW until 80kW. The suitable size of the inverter could be determined based on the standard sizes of inverters from the manufacturer. For example, if 5kW < inverter size ≤ 10kW, the potential size will be 10kW. Also, the lifespan of inverter is ten years, for this reason, $Nrep = 1$. According to Equation 9-35, it is possible to calculate RSC of different sizes of an inverter. ($C_{nom} = \text{Inverter size} * 1000\ W$). The cost of one watt was determined by ($C_{unit} = \text{Inverter cost} / C_{nom}$).

9.2.6 Optimization Process And Constrains

This section will illustrate the modeling and optimization process which has been used to determine the most optimum the HRES configuration. As mentioned earlier in this chapter, three strategy plans have been suggested to determine the optimum configuration to meet consumer requirement in terms of cost and reliability or one of them based on economic and reliability constraints as follows:

1. The first plan for an optimum the HRES configuration is called (2D). The 2D system is designed to be always reliable and give priority to satisfy the demand in the case of off-grid. This means this configuration should be able to meet energy demand reliably according to the minimum LPSP result based on the lowest cost of energy that can be obtained from the most reliable systems. It represents the most common optimization process which has been used by several studies [190, 193]. The process of reliability has been applied based on 10136 configurations in which just 50 configurations are selected that have shown the highest reliability when LPSP ≥ 0 (equal or close to zero). And then, the configuration that has shown the lowest LCE, has been chosen as the most optimal configuration. This strategy should meet customers requirement in terms of high reliability.
2. The second strategy of optimization is (3D). The 3D plan satisfy both reliability (LPSP and GPAP) and economic LCE constraints at, the same level of importance to determine the optimal configuration. According to this conception, the configuration that can show the lowest sum of minimum normalisation for each LPSP, GPAP and LCE, that is chosen as the optimal configuration.
3. The third plan of optimum the HRES configuration is named (4D). The 4D is created based on min LPSP, min GPAP, min LCE and min PBP equally for all of these constraints. This plan should meet consumers requirements in terms of cost and short PBP.

Normalisation deals with parameters which have different units and scales. Therefore, all data should have the same scale for a fair comparison between them where normalisation scales all numeric variables in the range of [0,1] as expressed in Equation 9-40 [323].

$$X_{nor}(j) = \frac{X(j) - X_{min}}{X_{max} - X_{min}} \quad \text{Equation 9-40}$$

The process of 3D optimization includes several steps, as follows:

- Calculate the results of LPSP, GPAP and LCE for 10136 configurations (j).
- Calculate the normalised equation for each of LPSP, GPAP and LCE using Equation 9-40 for each (j)..
- Finally, the min value of the sum for a specific configuration will be regarded as the most optimal configuration ($Opti_{conf}$) of the HRES as expressed in Equation 9-41.

$$Opti_{conf} = min\left[\sum_{j=1}^{10136} LPSP_{nor}(j) + GPAP_{nor}(j) + LCE_{nor}(j)\right] \quad \text{Equation 9-41}$$

$LPSP_{nor}$, $GPAP_{nor}$ and LCE_{nor} represent the normalisation of LPSP, GPAP and LCE, respectively based on Equation 9-40. The 4D optimization has given both reliability and economic constraints the same weight. The same process of optimization that has been used to determine the optimal configuration in the 3D optimization plan has been applied in this strategy as expressed in Equation 9-42.

$$Opti_{conf} = min\left[\sum_{j=1}^{10136} LPSP_{nor}(j) + GPAP_{nor}(j) + LCE_{nor}(j) + PBP_{nor}(j)\right] \quad \text{Equation 9-42}$$

The 4D optimization should meet customer requirements in terms of cost and short PBP as well as for reliability.

9.3 Results And Discussion

Verification has been carried out between Homer, and On-off-grid Op-HRES results in section (9.3.1), to support the accuracy of the optimization approach in this study. The optimization results have been created based on different scenarios of economic and environmental analysis. Also, different strategies of energy flow management have been discussed in section (9.3.2). The optimization approach in this study has been examined by using:

- Data demand of BG, KR and BS, which is described in section (9.2.2.3).
- Six locations in different places in Iraq has been chosen according to three categories of land cover and different classification of wind speed as presented in Figure 9-10 in order

to assess the impact of climatological and land cover difference on optimal system design.

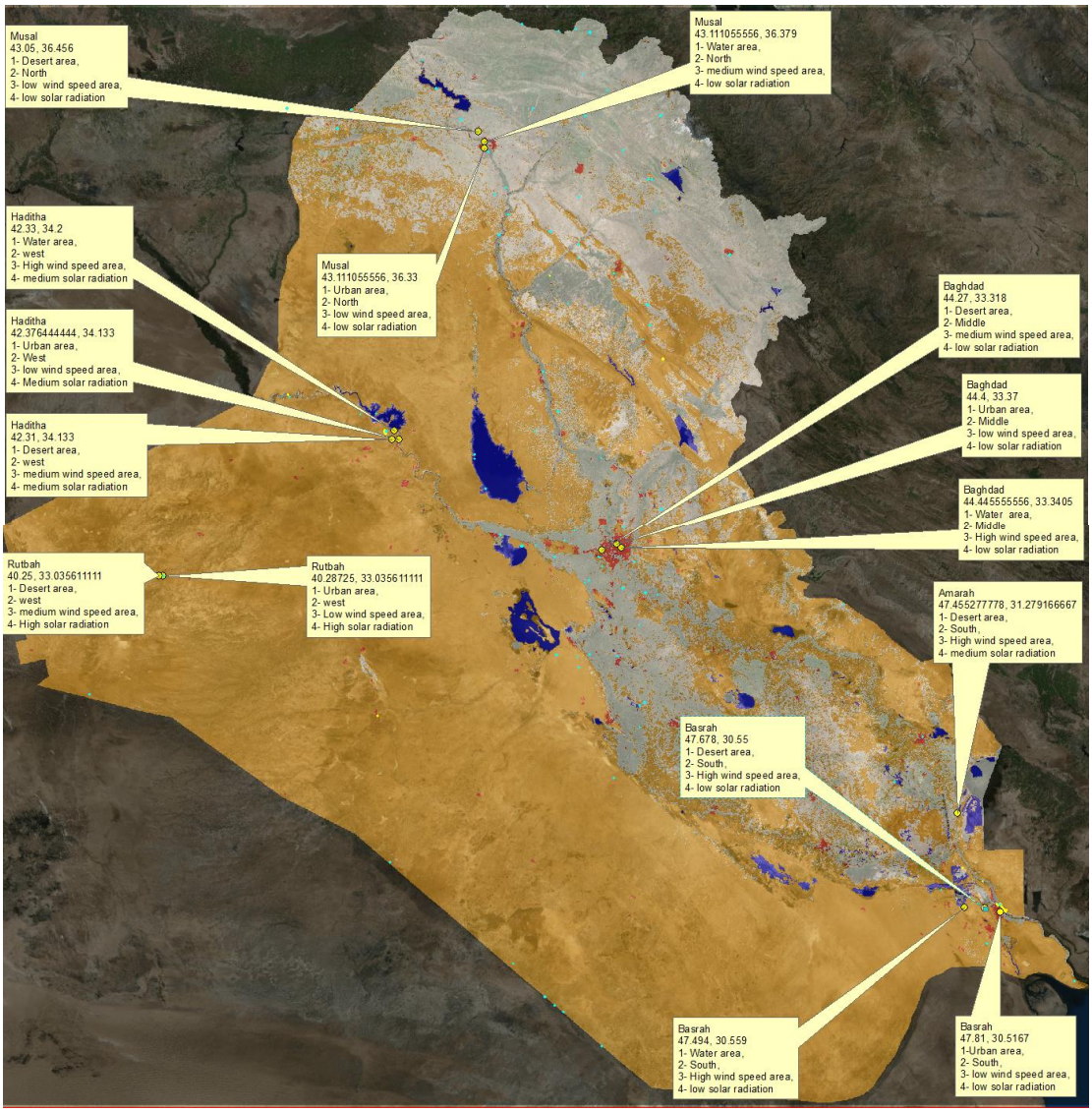

Figure 9-10. Land cover Iraq map that shows the main land cover categories: red spots for urban areas, blue spots for water surfaces and amber areas for desert. In addition, this map includes the six main locations that have been chosen according to wind speed and solar radiation availability. For Four locations, each one of them has three sites that have been distributed based on water, desert and urban areas.

9.3.1 Validation against Homer Software

At the beginning of this project, Homer software was proposed to be used to determine the optimal configuration of the HRES rather than rewrite unnecessary MATLAB code. Unfortunately, this suggestion has been defeated by a set of gaps in Homer, which prevent the software from meeting the requirements of the optimization process for HRES design in Iraq as follows:

- The optimization process in Homer has not been designed to satisfy off-grid and on-grid demand respectively and in an unscheduled way by using same HRES configuration and within the same period. Homer software can choose an optimal configuration and optimize a HRES performance in the case of on-grid or off-grid separately. This process does not meet Iraqi residential requirements in terms of electricity outage from the national grid.
- Homer could not deal with Increasing Block Tariffs prices IBT (nonlinear tariff) [324] that was described in section 7.3.
- Homer does not have enough flexibility to deal with different features of the storage system except system which are embedded in the software. For example, it is not possible to set the technical features of another storage system that was not included previously in Homer's library.

According to these specific issues, Homer has been used just for verification purposes and a new MATLAB code (On-off-grid Op-HRES) has been created. The On-off-grid Op-HRES that has been developed in this project and has been validated with Homer based on BG on-grid demand and based on Homer constraints: Renewable Fraction (RF) and Total Net Present Cost (NPC) using different sizes of the components as presented in Table 9-4.

At first, the validation was performed between On-off-grid Op-HRES (using GPAP and LCE) and Homer (using RF and NPC), but the results of On-off-grid Op-HRES did not match the results of Homer. For this reason, the Homer's constraints (RF and NPC) have been applied in the On-off-grid Op-HRES rather than (using GPAP and LCE), which leads to get close results as presented in Table 9-4. The difference between Homer and On-off-grid Op-HRES results at the first try is a return to the difference between TPV calculation in this study and NPC calculation in Homer as explained in Chapter 4 section 4.2.2.4.

Table 9-4. Homer optimization results for 2, 4, 6, 8, 10 kW of wind turbine size and 3.12, 5.2 and 10.4 kW of PV size and also 11.7 and 23.4 kWh of Li-ion battery size with 25 kW size of inverter based on BG on-grid demand.

The optimal configuration that has been determined by On-off-grid Op-HRES Homer based on RF and NPC		The optimal configuration that has been determined by Homer based on RF and NPC	
PV size	3.12 kW	PV size	3.12 kW
WT size	4 * 2kW	WT size	4 * 2 kW
Battery size	2 * 11.7 kWh	Battery size	2 * 11.7 kWh
Inverter size	25 kW	Inverter size	25 kW
LCE	0.034 $	LCE	0.0334 $
NPC of system	29.89 $	NPC of system	31.477 $
Initial Capital of system	21.590 $	Initial Capital of system	21.590 $
RF %	49.6	RF %	50.3
PV production	6193 kWh/year	PV production	4322 kWh/year
WT production	11519 kWh/year	WT production	11519 kWh/year

9.3.2 **Result Analysis**

9.3.2.1 **Evaluation of Energy Flow Management And IBT Prices**

The priority of covering off-grid demand is crucial in terms of reliability. On the other hand, the energy flow management and IBT prices of grid supply are also significant to optimize the HRES performance and in choosing the most economical configuration. Scenario A on-grid with discharge (D) and Scenario B on-grid without discharge (W) have been applied based on BG, KR and BS demand at different land cover categories and locations in Iraq, to determine which energy flow management shows good results. LPSP, GPAP, LCE, PBP, TCOP and configuration size have been used as parameters to evaluate the optimal configuration and some of them as logical constraints in several optimization plans (2D, 3D and 4D).

In this section, the results of (LPSP, GPAP, LCE, PBP, TCOP and configuration size) have been used to evaluate the performance of the optimal configuration based on BG using the 2D optimization plan for 12 locations as are presented in Figure 9-11. The results of LPSP have shown high reliability without discharging the storage system in the case of on-grid based on both 2015 and 2017 IBT price (Without discharging a storag system based on New IBT prices in 2017 (W.N) and Without discharging a storag system based on Old IBT prices in 2015 (W.O)) for all locations in Iraq and over the three land-use categories (water, desert and urban areas) as shown in LPSP in Figure 9-11. The reason behind this result is that the fully charged battery is saved to the next job in the case of off-grid demand and is discharged when needed. In this way the opportunity of losing power supply (LPS) from the HRES against demand is reduced.

The energy flow management of (W.N and W.O) has achieved a significant discount in terms of TCOP as shown in Figure 9-11 due to the reduction in the configuration size for some cases. In this case, the decrease in the size of the HRES is directly related to extending the lifespan of the battery by reducing the annual battery life cycle according to Equation 9-31. According to TCOP reduction, the W.N and W.O have also shown a significant discount in terms of LCE over all locations in comparison with (Discharg a storag system based on New IBT prices in 2017 (D.N) and Discharg a storag system based on Old IBT prices in 2015 (D.O)) .

On the other hand, the PBP has shown gradual decline due to the change in the energy flow management from discharg ing to without discharging and also the change in IBT prices from 2017 price (low price) to 2015 price (high prices). The annual cost saving strategy that has been used to estimate PBP depends on the price of electricity from the national grid and also the reliability of the HRES, as expressed in Equation 9-29.

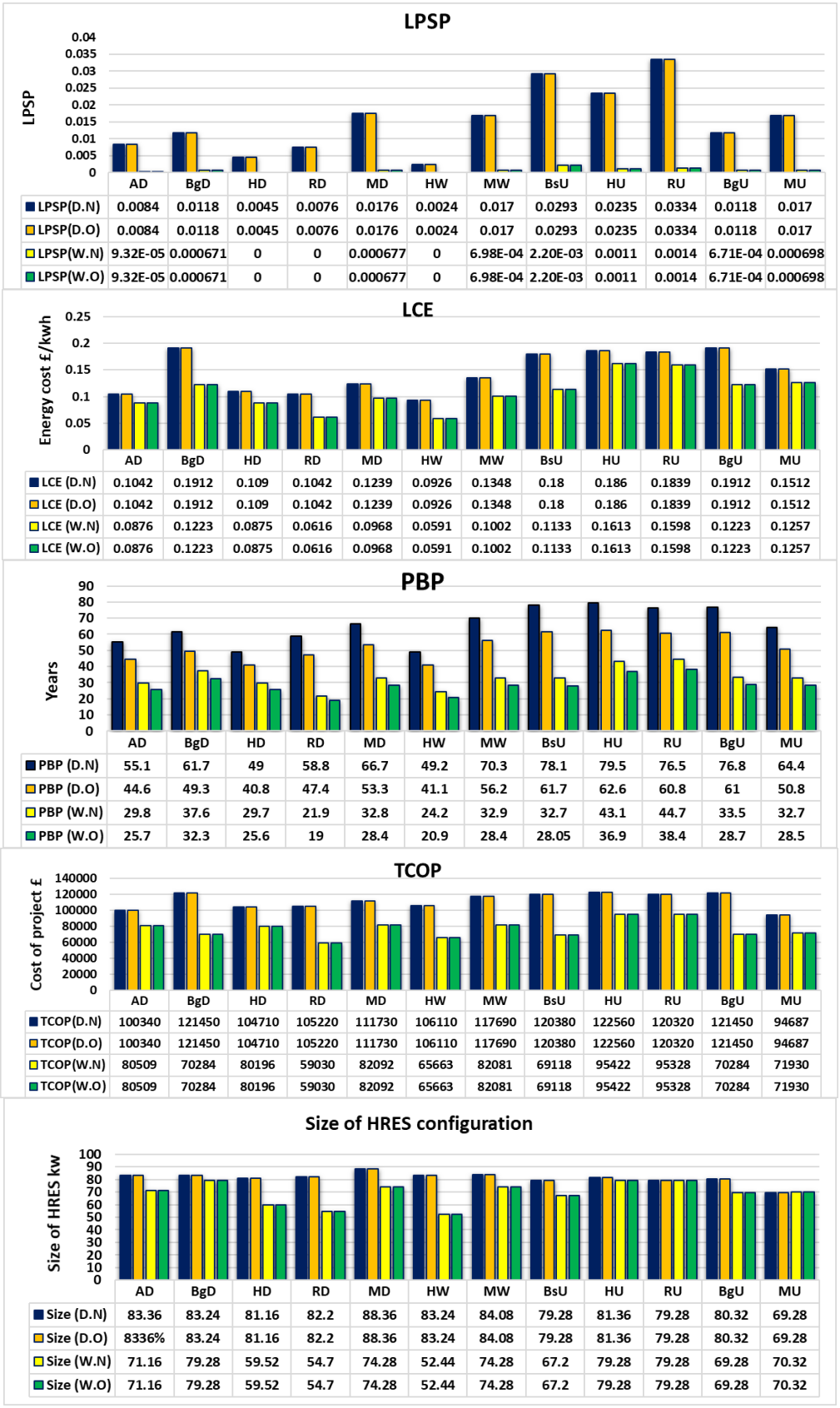

Figure 9-11. Result of LPSP, LCE, PBP, TCOP and Size of the HRES configuration to evaluate the performance of different optimal configurations that have been determined in 12 locations in Iraq by using just BG demand and by applying the 2D strategy. D.N: Discharge battery and 2017 IBT price, D.O: Discharge battery and 2015 IBT price, W.N: without discharge battery and 2017 IBT price, W.O: without discharge battery and 2015 IBT price. While AD: Amara location. Desert land cover, BsU: Basra. Urban, RU: Rutbah. Urban, MU: Musal. Urban, HD: Haditha. Desert, BgU: Baghdad. Urban, MW: Musal. Water, MD: Musal. Desert, HW: Haditha. Water, HU: Haditha. Urban, BgD: Baghdad. Desert, RD: Rutbah. Desert.

The change in the IBT prices has the same impact on LCE, LPSP and TCOP in terms (W.N and W.O) or (D.N and D.O), because LCE depends on TCOP and the amount of energy production that has covered the Annual Energy Load (AE_{load}). The TCOP depends on the configuration size and market prices. It is possible to note that some urban locations have shown almost same configuration size in the case of W.N, W.O, D.N and D.O, due to the low wind speed in the urban area which leads to keeping the HRES approximately at the same size in order to meet the energy demand. The 3D and 4D optimization plans for 12 locations, have shown the same trend in terms of energy flow management for 2015 and 2017 IBT prices regarding LPSP, LCE, TCOP and PBP for BG and KR demand. Overall, these results indicate that the W.O shows the best HRES performers in terms of PBP and (W.N and W.O) to gather shows the best HRES performance in terms of LPSP, LCE, TCOP and the HRES size.

9.3.2.2 Effect of Different Land Covers on Optimal HRES Configuration

Several variables play a pivotal role to determine the size of the HRES and the size of each component approximately. One of these variables is wind speed, which is changed by the effect of roughness length of land cover and the geographical distribution of wind availability. In this section, the influence of land cover on the HRES size, LPSP, LCE and PBP is discussed according to D.O and W.O system choices. The D.O and D.N have shown the same trend in terms of LPSP, LCE and TCOP as shown in Figure 9-11, as well as W.O and W.N, have shown the same similarity between them based on the above parameters. Besides, the evaluation in this section is carried out using KR demand based on the 2D scenario, as shown in Figure 9-12.

According to LPSP in Figure 9-12 there is a gradual decrease in reliability (reliability definition in section 4.2) of the HRES from water surfaces to desert to urban area as follows: Baghdad, Basra, Haditha and approximately in Mosul locations, due to the high wind speed above lakes and weak wind speed above an urban area. In the same context, the LCE results have shown increases in the cost of energy when changing land cover from beaches to deserts to urban areas as shown in LCE for Baghdad, Basra and Hadith locations in Figure 9-12. Through the gradually decrease in the PBP from (D.N) to (W.O) as shown in Figure 9-11 and Figure 9-12, there is another inclination for PBP could be noted according to the variation of land cover category. The PBP for the HRES decreases at the desert or close to lakes and marshes against clear increasing in PBP at urban areas. The rise in annual cost-saving results in a reduction in PBP due to the increase in power production from a wind turbine as expressed in Equation 9-29. Increasing PBP in urban areas is due to low wind speeds that leads to reduce the annual saving cost. Each of Baghdad, Basra and Haditha have shown the same tendency in PBP in Figure 9-12, while Mosul locations have shown another trend for PBP that is decreased from lakes to deserts to urban areas.

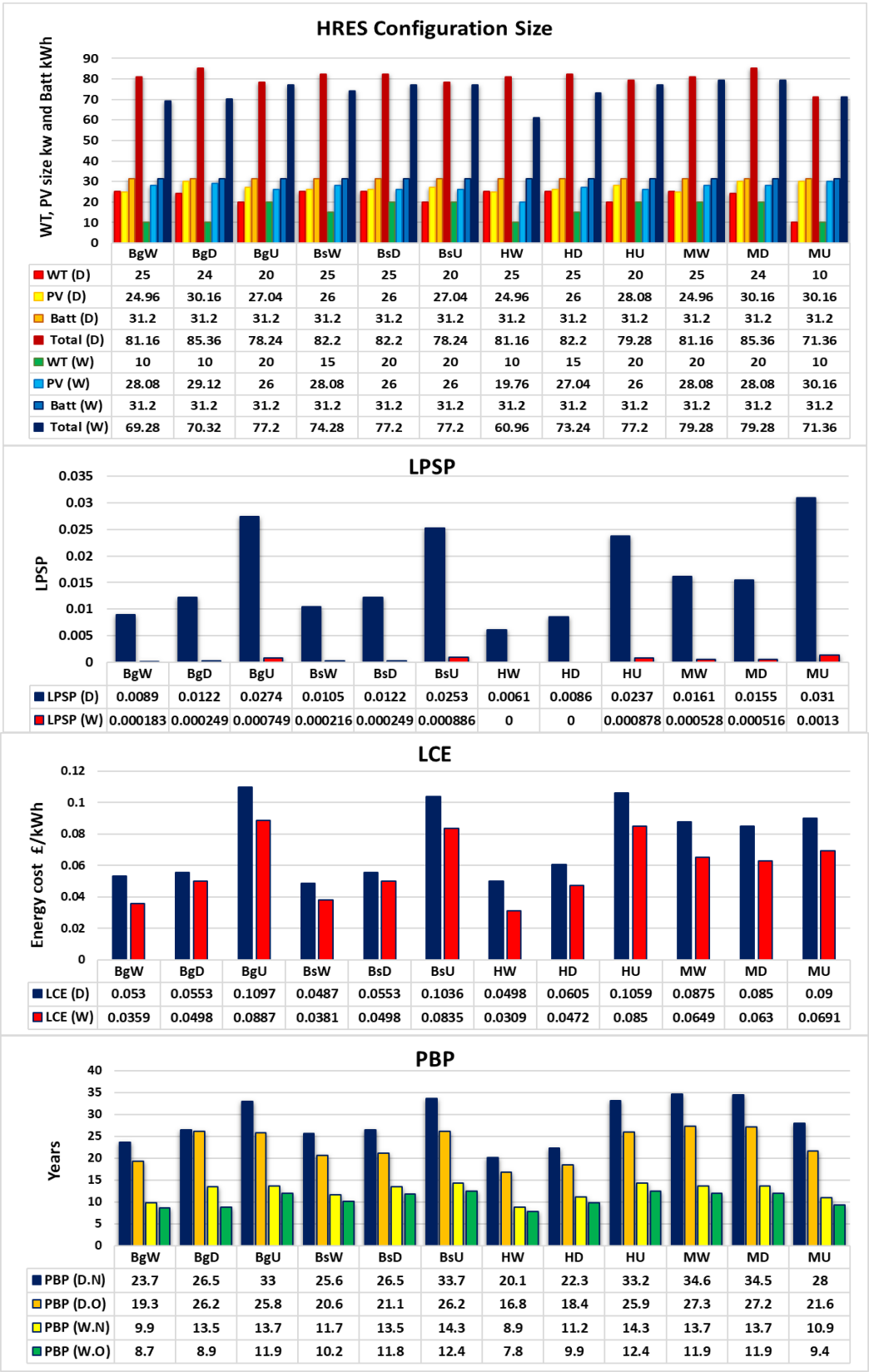

	BgW	BgD	BgU	BsW	BsD	BsU	HW	HD	HU	MW	MD	MU
WT (D)	25	24	20	25	25	20	25	25	20	25	24	10
PV (D)	24.96	30.16	27.04	26	26	27.04	24.96	26	28.08	24.96	30.16	30.16
Batt (D)	31.2	31.2	31.2	31.2	31.2	31.2	31.2	31.2	31.2	31.2	31.2	31.2
Total (D)	81.16	85.36	78.24	82.2	82.2	78.24	81.16	82.2	79.28	81.16	85.36	71.36
WT (W)	10	10	20	15	20	20	10	15	20	20	20	10
PV (W)	28.08	29.12	26	28.08	26	26	19.76	27.04	26	28.08	28.08	30.16
Batt (W)	31.2	31.2	31.2	31.2	31.2	31.2	31.2	31.2	31.2	31.2	31.2	31.2
Total (W)	69.28	70.32	77.2	74.28	77.2	77.2	60.96	73.24	77.2	79.28	79.28	71.36

	BgW	BgD	BgU	BsW	BsD	BsU	HW	HD	HU	MW	MD	MU
LPSP (D)	0.0089	0.0122	0.0274	0.0105	0.0122	0.0253	0.0061	0.0086	0.0237	0.0161	0.0155	0.031
LPSP (W)	0.000183	0.000249	0.000749	0.000216	0.000249	0.000886	0	0	0.000878	0.000528	0.000516	0.0013

	BgW	BgD	BgU	BsW	BsD	BsU	HW	HD	HU	MW	MD	MU
LCE (D)	0.053	0.0553	0.1097	0.0487	0.0553	0.1036	0.0498	0.0605	0.1059	0.0875	0.085	0.09
LCE (W)	0.0359	0.0498	0.0887	0.0381	0.0498	0.0835	0.0309	0.0472	0.085	0.0649	0.063	0.0691

	BgW	BgD	BgU	BsW	BsD	BsU	HW	HD	HU	MW	MD	MU
PBP (D.N)	23.7	26.5	33	25.6	26.5	33.7	20.1	22.3	33.2	34.6	34.5	28
PBP (D.O)	19.3	26.2	25.8	20.6	21.1	26.2	16.8	18.4	25.9	27.3	27.2	21.6
PBP (W.N)	9.9	13.5	13.7	11.7	13.5	14.3	8.9	11.2	14.3	13.7	13.7	10.9
PBP (W.O)	8.7	8.9	11.9	10.2	11.8	12.4	7.8	9.9	12.4	11.9	11.9	9.4

Figure 9-12. Result of LPSP, LCE, PBP and the HRES configuration Size to evaluate the performance of different optimal configurations that have been determined in different land covers (water, desert and urban) for four locations in Iraq (Baghdad, Basra, Haditha and Mosul) by using just KR demand and by applying the 2D strategy plan. D.N: Discharge battery and 2017 IBT price, D.O: Discharge battery and 2015 IBT price, W.N: without discharge battery and 2017 IBT price, W.O: without discharge battery and 2015 IBT price. While BgW: Baghdad location. Water land cover, BgD: Baghdad location. Desert land cover, BgU: Baghdad location. Urban land cover, BsW, BsD and BsU: Basra location at the water, desert and urban land cover. HW: Hadiata. Water, HD: Haditha. Desert, HU: Haditha. Urban, MW: Mosul. Water, MD: Mosul. Desert, MU: Mosul. Urban.

To understand this strange tendency for PBP in the case of Mosul locations, we need to take a closer look at the the HRES configuration size in Figure 9-12. The size of the HRES in Mosul city (urban area) is lower than the size of the HRES in the desert area and close to the water surfaces. It returns to the low wind speed and solar radiation generally in the north of Iraq that results in the absence of increasing effect for the HRES size on the level of production according to the constraints of efficiency and cost.

Concerning the discharge process, the wind turbine size (in the HRES Configuration size) decreases from lakes to desert to urban areas overall sites (Baghdad, Basra, Haditha and Mosul) to reduce the cost of the project. In other words, the discharge process leads to replacing the storage system once within the lifetime of the project, but this, in turn, raises the cost of energy production LCE.

For this reason, the size of the wind turbine is reduced to reduce the cost of configuration in the case of an urban area. In addition, the low wind speed in the urban area leads to a decrease in the feasibility of a wind turbine. It represents a suitable justification for getting the same size for the HRES in the case of discharge and without discharge process in urban areas, as shown in Figure 9-12. The same consideration has been used to justify the reason behind shrinking the size of the wind turbine in terms of discharge and without discharge process in the case of Mosul locations.

9.3.2.3 Effect of Wind Speed and Solar Radiation Variety on Optimal HRES Configuration Performance For Several Locations In Iraq

The process of evaluating the impact of wind speed and solar radiation on the performance and feasibility of the HRES seems to be rather complex, due to the integration between the effect of wind speed, hub height of wind turbine and solar radiation. To achieve this assessment, desert areas have been chosen for this process, because wind speed assessments show wide variety above open areas compared to urban area. BG and KR demand are used to support the assessment process with different household consumption habits. The 2D scenario to determine the optimal design is applied. Six desert locations (AD, RD, BsD, BgD, HD and MD) are used and arranged in descending order from max to min sum of annual wind and solar energy normalisation according to Equation 9-40 as shown in Figure 9-13 I and J in Part B.

In general, the trend of decreasing wind and solar energy from AD to MD has reflected on the results of LPSP and LCE for optimal configuration according to the six locations, where LPSP increased (reliability decreased) from AD to MD as represented by the linear gradient of LPSP (D) for both BG and KR demands in Figure 9-13 C and D in Part A.

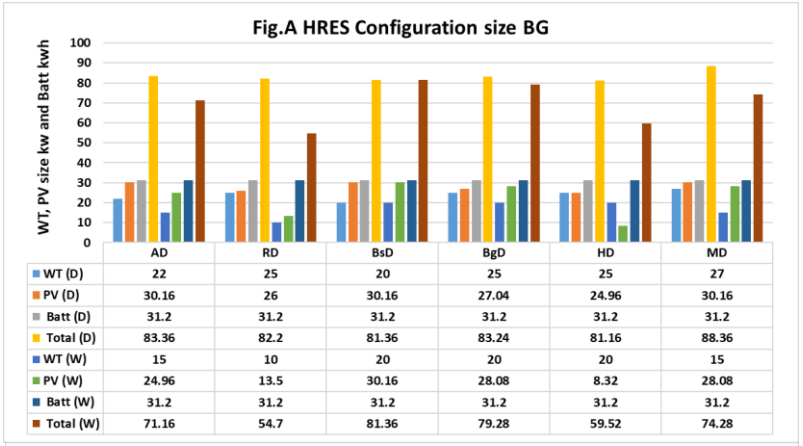

	AD	RD	BsD	BgD	HD	MD
WT (D)	22	25	20	25	25	27
PV (D)	30.16	26	30.16	27.04	24.96	30.16
Batt (D)	31.2	31.2	31.2	31.2	31.2	31.2
Total (D)	83.36	82.2	81.36	83.24	81.16	88.36
WT (W)	15	10	20	20	20	15
PV (W)	24.96	13.5	30.16	28.08	8.32	28.08
Batt (W)	31.2	31.2	31.2	31.2	31.2	31.2
Total (W)	71.16	54.7	81.36	79.28	59.52	74.28

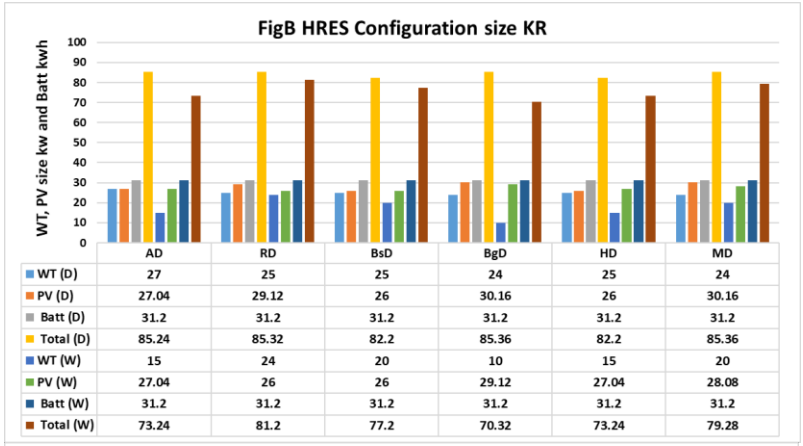

	AD	RD	BsD	BgD	HD	MD
WT (D)	27	25	25	24	25	24
PV (D)	27.04	29.12	26	30.16	26	30.16
Batt (D)	31.2	31.2	31.2	31.2	31.2	31.2
Total (D)	85.24	85.32	82.2	85.36	82.2	85.36
WT (W)	15	24	20	10	15	20
PV (W)	27.04	26	26	29.12	27.04	28.08
Batt (W)	31.2	31.2	31.2	31.2	31.2	31.2
Total (W)	73.24	81.2	77.2	70.32	73.24	79.28

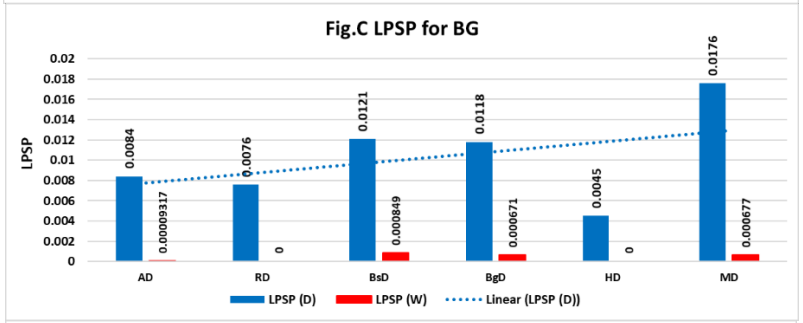

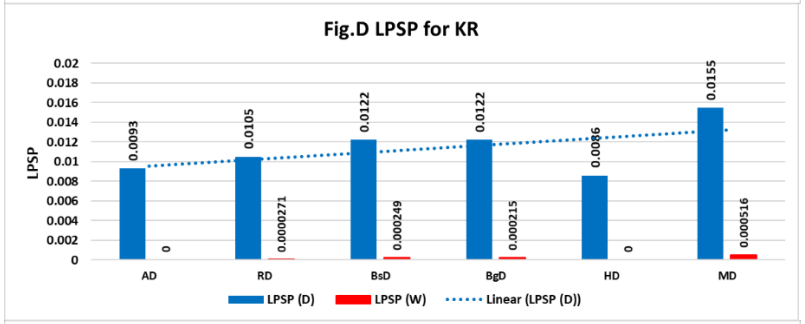

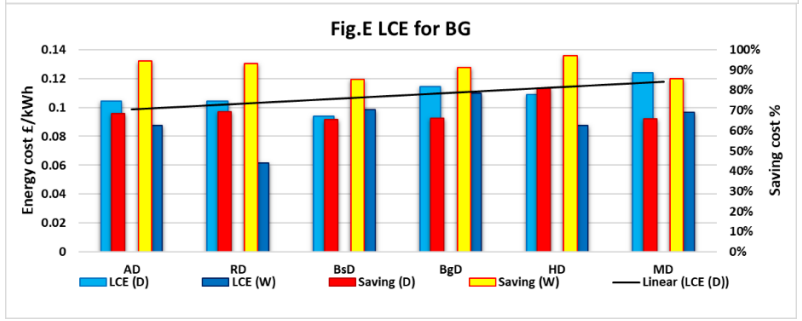

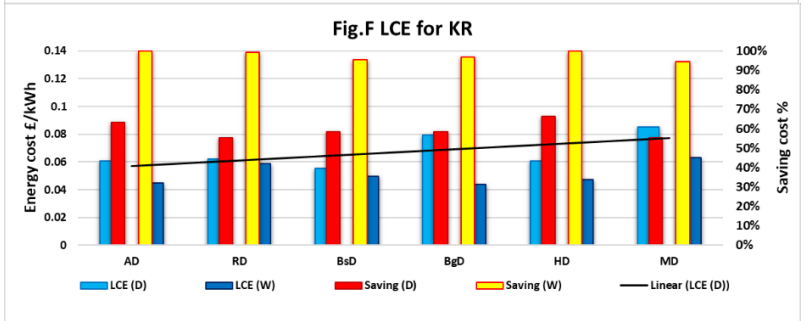

Part A

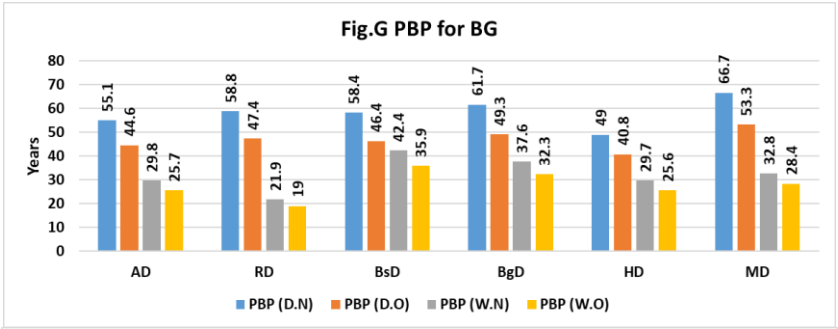

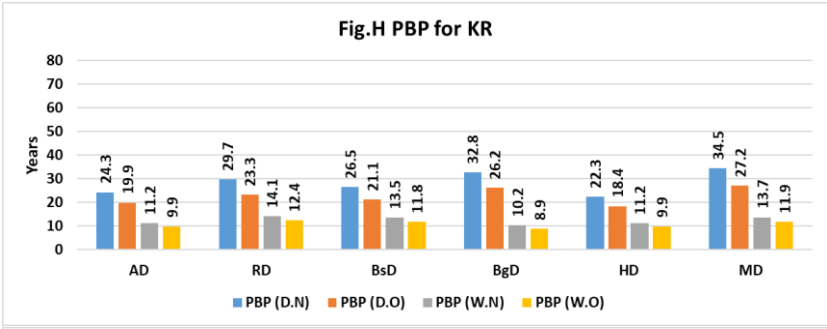

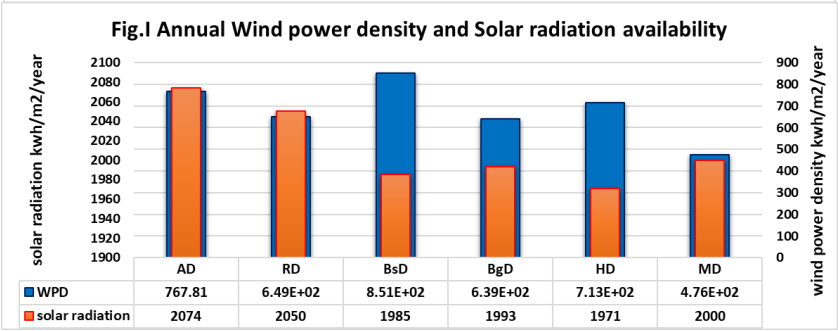

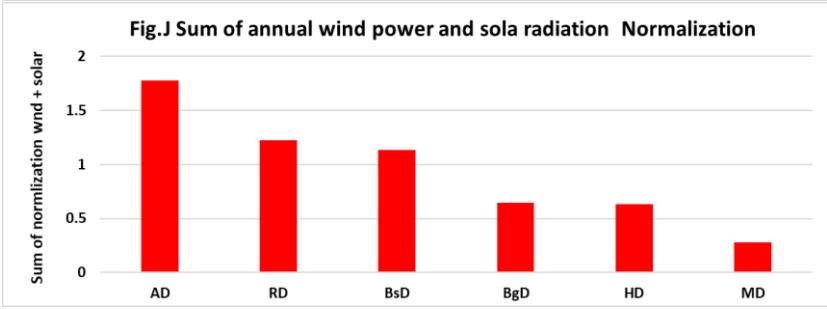

Part B

Figure 9-13. Results of LPSP, LCE, Saving and the HRES configuration Size in Part A and PBP in Part B, to evaluate the performance of different optimal configurations that have been determined based on desert land cover at different locations in Iraq (Haditha HD, Amara AD, Basra BsD, Baghdad BgD and Mosul MD) by using KR and BG demand and by applying 2D strategy. D.N: Discharge battery based on 2017 IBT price, D.O: Discharge battery based on 2015 IBT price, W.N: without discharge battery based on 2017 IBT price, W.O: without discharge battery based on 2015 IBT price. (Annual Wind energy density and Solar radiation availability) and (Sum of annual wind energy and solar radiation normalization) in Part B show the availability of solar and wind resource at each location.

In the same context, LCE results have shown the same tendency, according to LCE (D) for BG, and KR demands in Figure 9-13 E and F in Part A. The results generally indicate that the high availability of wind and solar power leads to high reliability and low cost of energy, which leads to short PBPs.

On the other hand, the optimal configuration in the Haditha desert location (HD) has shown strange results. In spite of, the low solar radiation in Figure 9-13I in Part B and the low sum of annual solar and wind energy normalisation in Figure 9-13F Part B, the HD location has shown high reliability according to BG and KR demands. The reason again goes back to the high wind speed at HD in Figure 9-13I in Part B and the size of wind turbine 20 kW at 20m height which supplies lots of energy during 24 hours. There is another interesting result, KR demand has shown low LCE and PBP in comparison with the outcomes of LCE and PBP for BG demand. It results from the low wastage of energy that is not consumed but is sent freely to the grid, reducing the battery replacement cost resulting in the high percentage of cost saving as shown in Figure 9-13F in Part A.

9.3.2.4 2D, 3D and 4D Strategies To Determine The Optimal The HRES

The 2D strategy has been regarded as the most common strategy in the case of off-grid demand [190, 193]. This approach was used in this project to determine the most reliable configuration that able to meet the energy demand for BG and KR, as shown in Figure 9-13, Figure 9-12, Figure 9-11 and Table 9-5. The 2D, 3D and 4D strategies of optimization processes, as explained in section 9.2.6, are applied in different scenarios of energy flow managements and IBT prices for BG, KR and BS demands over 15 locations.

In order to review the results of 2D, 3D and 4D performance and avoid repetition, BG demand is used based on the 2015 IBT price and without discharging storage system for four sites: Baghdad, Basra, Haditha and Mosul over water, desert and urban land cover as shown in Figure 9-14. The reason behind choosing the above analysis goes back to some common results in the optimization process as shown in Table 9-5. Table 9-5 shows the performance of 2D, 3D and 4D systems across two types of energy flow management and two IBT prices N.D, O.D, N.W and O.W.

At first glance, it is easy to note in Table 9-5 the similarity among the results of 2D, 3D and 4D between N.D and O.D as well as between N.W and O.W in terms of the HRES size, LPSP, GPAP and LCE. The similarity between the results of N.W and O.W is due to that both using the same energy flow management (Without discharge the storage system) in terms of on-grid as explained in section 9.3.2.1. In the same context, there is similarity between the results of N.D and O.D which results from discharging the storage system in terms of on-

grid too. In addition, the 2D, 3D and 4D approaches have shown notable gradually improvements in terms of LCE, and PBP but also a gradual decline in terms of reliability measuring LPSP, GPAP and cost saving for both discharge and without discharge techniques. The change in these results is due to the balance among LPSP, GPAP and LCE in terms of 3D optimization and the balance among LPSP, GPAP, LCE and PBP in terms the 4D approach as highlighted in green in Table 9-5. Also, both discharge and without discharge methods have shown a significant difference in terms of LPSP and GPAP results across 2D, 3D and 4D, where, LPSP decreases when the change from discharge to without discharge while, the GPAP increases due to without discharge the battery and increase purchase from the grid.

In general, O.W has shown the best result in terms of PBP as well as LPSP and LCE for 2D, 3D and 4D. For this reason, O.W method has been used to show the performance of 2D, 3D and 4D over four locations and based on BG and KR demands as shown in Figure 9-14.

Table 9-5. Results of optimization process to determine the optimal design according to 2D, 3D and 4D strategies for Haditha desert location based on different scenarios of energy flow management (N.D, O.D, N.W and O.W). The green cells represent constraints that have been used in each strategy to determine the optimal design. Saving% represents the percentage of the annual cost saving of energy when using the HRES to the annual cost when purchas electricity from diesel generator in the case of off-grid and cost of electricity from grid based on 2015 and 2017 IBT prices. LCE, PBP and Saving are considered as an economic indicator, while LPSP and GPAP are regarded as reliability indicators.

	Baghdad House BG1-8760								
	New Price with discharge N.D								
	WT size kW	PV size kW	Batt size kWh	System size kW	LPSP	GPAP	Min LCE £/kWh	PBP year	Saving %
2D	25	24.96	31.2	81.16	0.0045	0.0465	0.109	49	78%
3D	15	19.76	31.2	65.96	0.0089	0.0852	0.0785	35.2	64%
4D	7	6.24	28.8	42.04	0.0511	0.2801	0.0407	18.3	38%
	Old Price with discharge O.D								
2D	25	24.96	31.2	81.16	0.0045	0.0465	0.109	40.8	81%
3D	15	19.76	31.2	65.96	0.0089	0.0852	0.0785	29.3	69%
4D	7	6.24	28.8	42.04	0.0511	0.2801	0.0407	15.2	43%
	New Price without discharge N.W								
2D	20	8.32	31.2	59.52	0	0.2881	0.0875	29.7	99%
3D	20	16.64	4.8	41.44	0.0117	0.2508	0.074	25.1	47%
4D	5	14.56	9.6	29.16	0.0282	0.4304	0.0318	10.7	39%
	Old Price without discharge O.W								
2D	20	8.32	31.2	59.52	0	0.2881	0.0875	25.6	97%
3D	20	16.64	4.8	41.44	0.0117	0.2508	0.074	21.6	53%
4D	5	14.56	9.6	29.16	0.0282	0.4304	0.0318	9.3	42%

According to Figure 9-14 A1 and A2, there is a notable decline in the size of the HRES from 2D to 3D to 4D due to the change in priority of the optimization process from reliability in the performance of 2D to the economic side in the 4D performance to satisfy the customer requirements in terms of cost savings. One of the significant changes in the size of the HRES is the disappearance of the wind turbine from the optimal configuration for urban areas due to the low wind speed and the high cost of a wind turbine according to the 3D and 4D strategies.

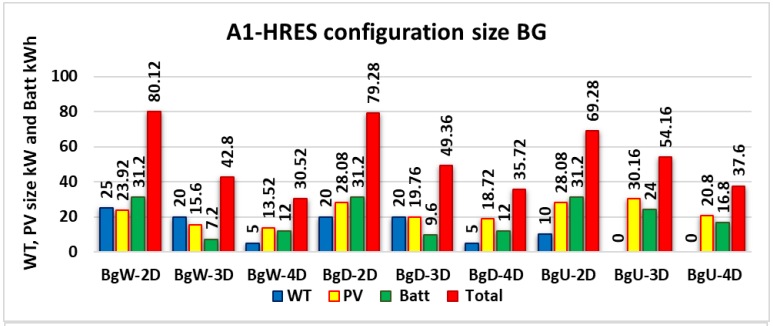
A1-HRES configuration size BG
WT, PV size kW and Batt kWh
BgW-2D BgW-3D BgW-4D BgD-2D BgD-3D BgD-4D BgU-2D BgU-3D BgU-4D
WT PV Batt Total

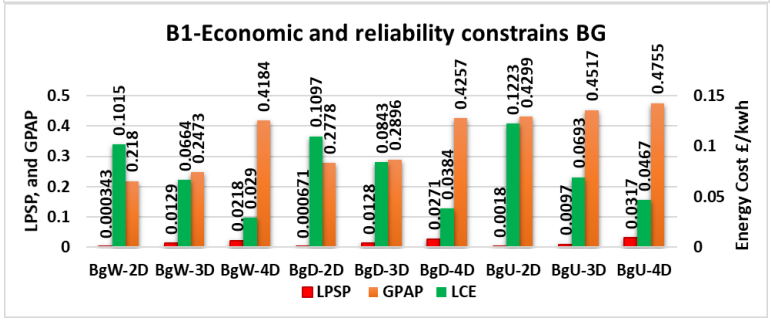
B1-Economic and reliability constrains BG
LPSP, and GPAP
Energy Cost £/kwh
BgW-2D BgW-3D BgW-4D BgD-2D BgD-3D BgD-4D BgU-2D BgU-3D BgU-4D
LPSP GPAP LCE

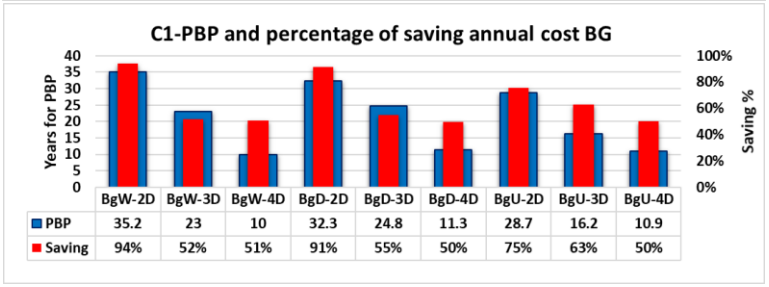
C1-PBP and percentage of saving annual cost BG
Years for PBP
Saving %
BgW-2D BgW-3D BgW-4D BgD-2D BgD-3D BgD-4D BgU-2D BgU-3D BgU-4D
PBP 35.2 23 10 32.3 24.8 11.3 28.7 16.2 10.9
Saving 94% 52% 51% 91% 55% 50% 75% 63% 50%

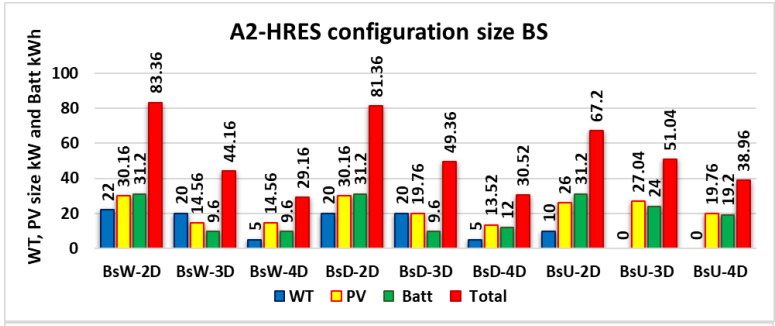
A2-HRES configuration size BS
WT, PV size kW and Batt kWh
BsW-2D BsW-3D BsW-4D BsD-2D BsD-3D BsD-4D BsU-2D BsU-3D BsU-4D
WT PV Batt Total

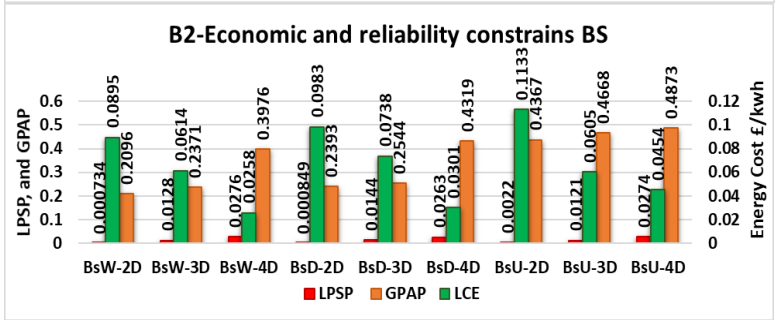
B2-Economic and reliability constrains BS
LPSP, and GPAP
Energy Cost £/kwh
BsW-2D BsW-3D BsW-4D BsD-2D BsD-3D BsD-4D BsU-2D BsU-3D BsU-4D
LPSP GPAP LCE

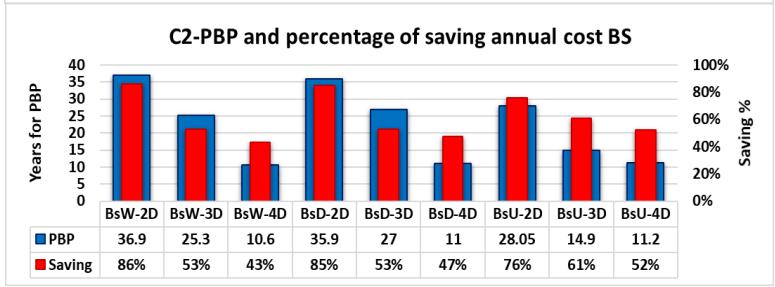
C2-PBP and percentage of saving annual cost BS
Years for PBP
Saving %
BsW-2D BsW-3D BsW-4D BsD-2D BsD-3D BsD-4D BsU-2D BsU-3D BsU-4D
PBP 36.9 25.3 10.6 35.9 27 11 28.05 14.9 11.2
Saving 86% 53% 43% 85% 53% 47% 76% 61% 52%

Part A

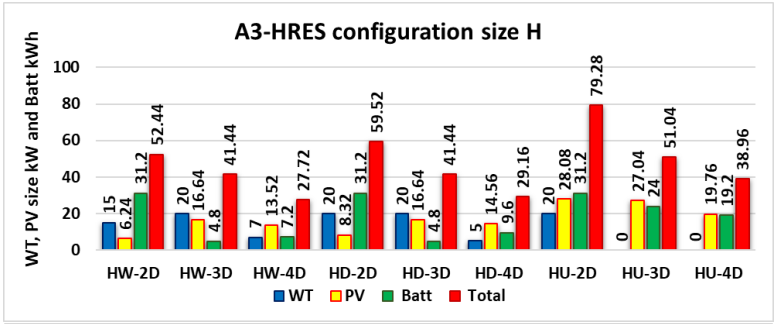

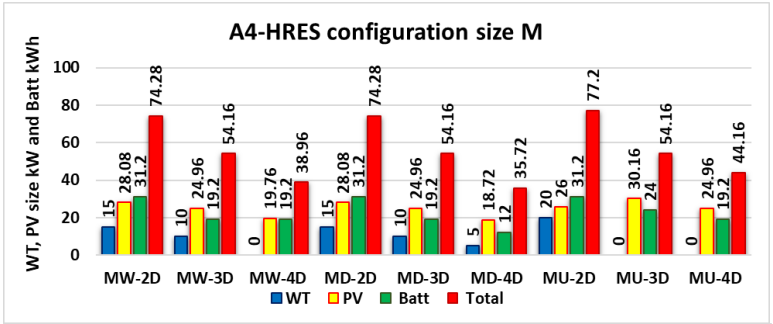

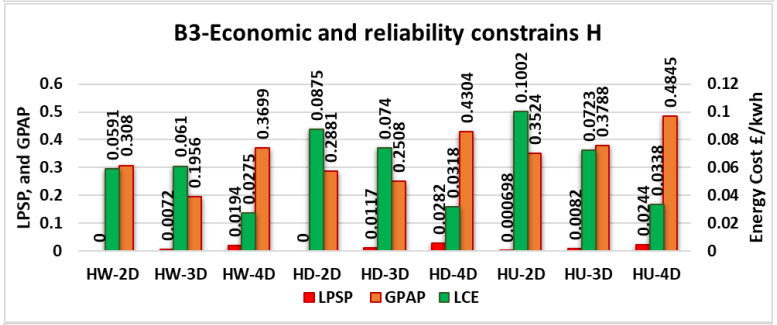

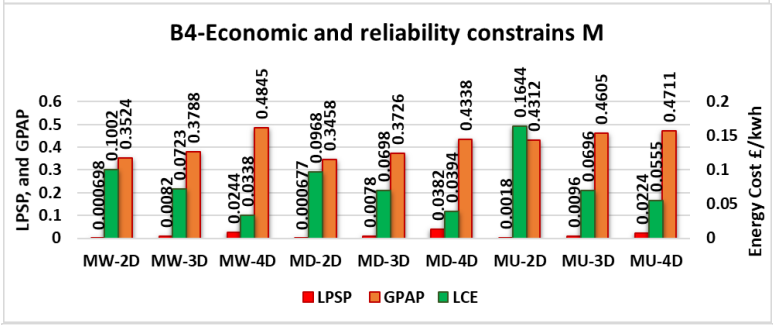

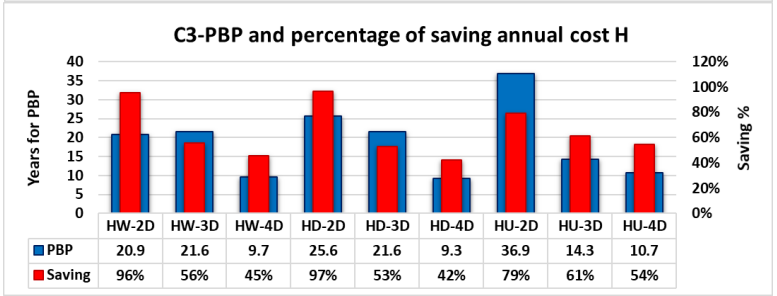

	HW-2D	HW-3D	HW-4D	HD-2D	HD-3D	HD-4D	HU-2D	HU-3D	HU-4D
PBP	20.9	21.6	9.7	25.6	21.6	9.3	36.9	14.3	10.7
Saving	96%	56%	45%	97%	53%	42%	79%	61%	54%

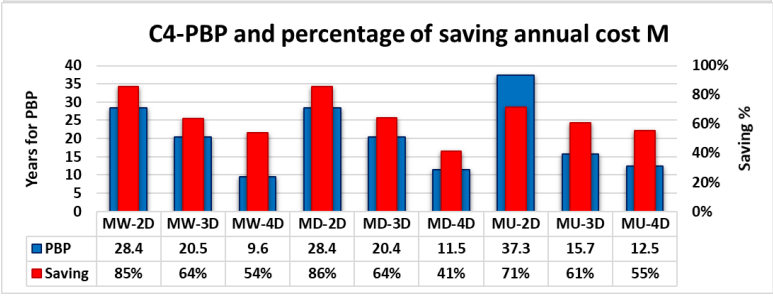

	MW-2D	MW-3D	MW-4D	MD-2D	MD-3D	MD-4D	MU-2D	MU-3D	MU-4D
PBP	28.4	20.5	9.6	28.4	20.4	11.5	37.3	15.7	12.5
Saving	85%	64%	54%	86%	64%	41%	71%	61%	55%

Part B

Figure 9-14. Result of 2D, 3D and 4D strategies of the optimization process to determine the optimal HRES based on 2015 IBT price and without discharge O.W according to BG and KR demands at four locations in Iraq: Baghdad BG, Basra BS, Haditha Ha and Mosul M across the water, desert and urban land covers. In this Figure have been used many parameters like the HRES configuration size in sub-Figures A1, 2, 3 and 4, which shows the size of WT, PV, Batt and total system size. Also, Economic and reliability constraints like LCE, LPSP and GPAP across sub-Figures B1, 2, 3 and 4 for above locations. Beside, PBP and percentage of saving annual cost across sub-Figures C1, 2, 3 and 4. Furthermore, In order to define some abbreviations BgW: Baghdad water area, BgD: Baghdad desert area, BgU: Baghdad urban area, BsW: Basra water area, BsD: Basra desert area, BsU: Basra urban area, HW, HD and HU: Haditha water, desert and urban areas respectively, MW, MD and MU: Mosul water, desert and urban areas respectively.

Concerning the reliability and cost of energy, again the LCE indicator shows an apparent reduction in the cost of produced energy. In spite of, the LCE has stayed high in the urban areas due to low wind speeds and dependence on the solar system. Once again, O.W proves to be effective in reducing LPSP, notably. Otherwise, LPSP increases slightly from 2D to 3D to 4D, as shown across all locations in Figure 9-14B1, B2, B3 and B4. In the same context, GPAP increases significantly from 2D to 3D to 4D and increases dramatically within urban areas as well as at locations that have low wind speeds like Mosul. Finally, PBP and cost savings have shown clear decreasing trends due to the reduction in the size of the HRES from 2D to 3D to 4D and more dramatically in urban areas.

9.3.2.5 **Basra house on-grid demand.**

There are some housing units supplied by electricity during 8760 hours per year, such as on-grid demand. The on-grid demand of BS in Figure 9-6 is examined using GPAP, LCE and PBP as constraints to determine the optimal configuration, while the HRES size and cost saving are used as parameters to evaluate an optimal HRES design. The optimization process for the on-grid system has been applied over all locations, land covers, and the energy flow management system to determine the optimal design. The strategy plans that have been used to recognize the optimal design are defined as follows:

- Dx: is a strategy to determine the optimal design of the HRES based on the lowest LCE for the lowest GPAP at any configuration, while PBP and cost saving have been used as a parameter to evaluate the feasibility of each optimum design.
- 2D: is a strategy to determine the optimal design of the HRES by calculating the min-sum of GPAP and LCE normalization, which means taking in consideration the weight of GPAP and LCE equally to determine the optimal design.
- 3D: is a strategy that takes into account a configuration that can show the lowest value of sum for GPAP, LCE and PBP normalization as an optimal configuration.

To understand the on-grid performance across all locations and to avoid repetition with GPAP, LCE, configuration size values between discharge and without discharge process, the energy flow management of O.D and O.W have been used according to Dx, 2D and 3D at four locations in Iraq as shown in Figure 9-15 and Figure 9-16. Table 9-6 has been included to show the change of PBP and cost saving over N.D, O.D, N.W and O.W.

The energy flow managements of discharging and non-discharging the storage system within on-grid demand have shown a significant change in the battery size, as shown in Table 9-6, according to the Dx strategy. The Dx strategy focuses on reliability, which leads to the use of the largest battery size to meet the demand. On the other hand, the storage

system disappears from the optimal configuration according to the Dx strategy in the case of N.W and O.W due to the system, in this case, not allowing to the use and discharge of the battery. In spite of the size of the HRES changing between discharge and without discharge strategy according to the Dx, the cost saving has remained steady at 100% due to the net trading between grid purchas and surplus energy to grid that equal zero in both cases as expressed in Equation 9-27. The process of discharging and non-discharging the storage system leads to an increase in GPAP and an decrease in LCE according to O.D against O.W for the Dx due to the decrease in the size of the HRES from O.D to O.W and the absence of a storage system in O.W as presented in Table 9-6, and A1, A2, A3 and A4 in Figure 9-15 and Figure 9-16, respectively. One of the significant notes, is that the PBP is increased within the O.D process against decreased PBP in O.W according to the Dx technique as illustrated in Table 9-6, where the high PBP is mainly returned to the 2017 IBT price which is lower than the 2015 IBT price and also due to the large size of storage system within the N.D process. The low difference between PBP in O.D and O.W results from the cost of the 31.2 kWh battery and the 100% saving cost.

Various land covers always play a significant role to determine the size of the WT into the HRES. The WT size usually reduces within an urban area due to the high cost of WT and the low wind speeds, resulting in non-economical use of wind turbines. However, it is possible to obtain 20 kW WT in the urban area according to the Dx technique, as the WT has a 20 m hub height that was able to access higher wind speeds. According to this analysis, the WT size reduces from water to urban areas as shown in A1, A2, A3 and A4 in Figure 9-15 and Figure 9-16, respectively. Otherwise, the WT size does not show any sensitivity against the change in the land cover within without discharge storage system due to the disappearance of the battery from the HRES. There is a gradual increase in GPAP and LCE for the Dx, 2D and 3D from the water surface to desert area to urban area which occurs due to the decreased wind speed at urban area as shown in B1, B2, B3 and B4 in Figure 9-15 and Figure 9-16 respectively. The absence of WT in the HRES at desert and urban areas for 3D and sometimes for 2D go back to the tend of 3D and 2D strategy to reduce the cost which leads us to the conclusion that the solar system in terms of on-grid is feasible and economic more than the wind turbine. In the same context, the PBP is extending slightly from water to urban area as shown in C1, C2, C3 and C4 in Figure 9-15 and Figure 9-16 respectively. The reason behind that is the high TCOP due to the large size of the HRES, which leads to increase the PBP. On the other hand, 2D strategy has shown good results in terms of the cost savings and PBP, which is often lower than 10 years for both discharge and without discharge techniques. In addition, the 2D optimization system has shown low LCE and low HRES size against low reliability. In fact, reliability is not a crucial parameter in terms of on-grid demand due to the fact that shortage of energy supply from the HRES can be covered

by the grid.It is worth mentioning, the HRES configuration without a storage system in the case of the 2D and 3D system and according to discharge and without discharge technique is not required due to the influence of economic constraints that aims to reduce the TCOP. In addition, the 2D has shown small size of WT 5 kW and 7 kW in terms of water areas and sometimes in desert areas due the high wind speed in these areas as shown in C1, C2, C3 and C4 in Figure 9-15 and Figure 9-16, respectively. The HRES has missed both battery and WT in terms of 3D strategy responding to the influence of economic constraints. In spite of 3D shows low LCE and PBP, it also has shown low cost saving and low reliability. Dx, 2D and 3D optimization strategies have shown significant results in terms of reliability and economic effect. The Dx strategy has shown impractical performance in terms of PBP that ranked between 30 to 40 years even when it has shown 100% of cost saving and high reliability.

Table 9-6 Results of optimization to determine the optimal design according to Basra demand for Baghdad desert location based on different scenarios of energy flow management (N.D, O.D, N.W and O.W). The green cells represent constraints that have been used in each strategy to determine the optimal design GPAP, LCE and PBP. Saving% represents the percentage of the annual cost saving of energy when using the HRES to the annual cost when purchas electricity from national grid based on 2015 and 2017 IBT prices.

	BS-BgD							
	Basra House BS-8760							
	New Price with discharge N.D							
	WT size kW	PV size kW	Batt size kWh	System size kW	GPAP	Min LCE £/kWh	PBP year	S
Dx	29	29.12	31.2	89.32	0.1058	0.0604	68.9	
2D	0	24.96	0	24.96	0.5125	0.0092	10.5	
3D	0	19.76	0	19.76	0.5397	0.0075	8.6	
	Old Price with discharge O.D							
Dx	29	29.12	31.2	89.32	0.1058	0.0604	38.7	
2D	0	24.96	0	24.96	0.5125	0.0092	5.9	
3D	0	19.76	0	19.76	0.5397	0.0075	4.8	
	New Price without discharge N.W							
Dx	30	27.04	0	57.04	0.2432	0.0518	59.5	
2D	0	24.96	0	24.96	0.5125	0.0091	10.5	
3D	0	19.76	0	19.76	0.5397	0.0075	8.6	
	Old Price without discharge O.W							
Dx	30	27.04	0	57.04	0.2432	0.0518	33.4	
2D	0	24.96	0	24.96	0.5125	0.0091	5.9	
3D	0	19.76	0	19.76	0.5397	0.0075	4.8	

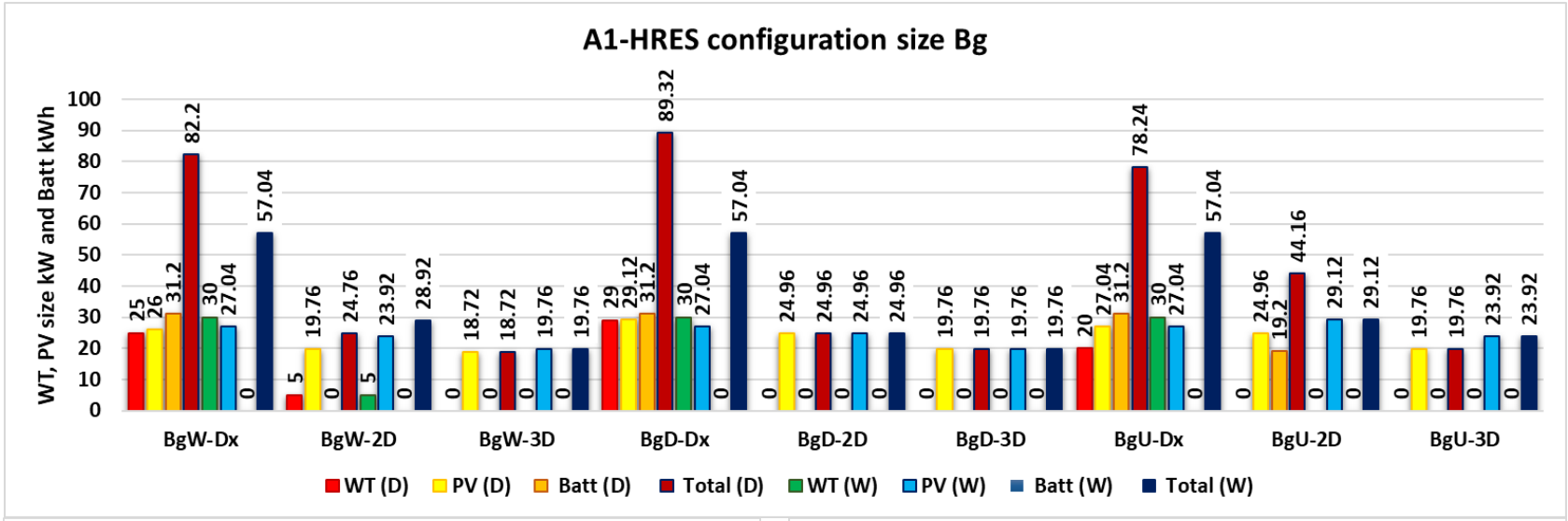
A1-HRES configuration size Bg
WT, PV size kW and Batt kWh
BgW-Dx BgW-2D BgW-3D BgD-Dx BgD-2D BgD-3D BgU-Dx BgU-2D BgU-3D
WT (D) PV (D) Batt (D) Total (D) WT (W) PV (W) Batt (W) Total (W)

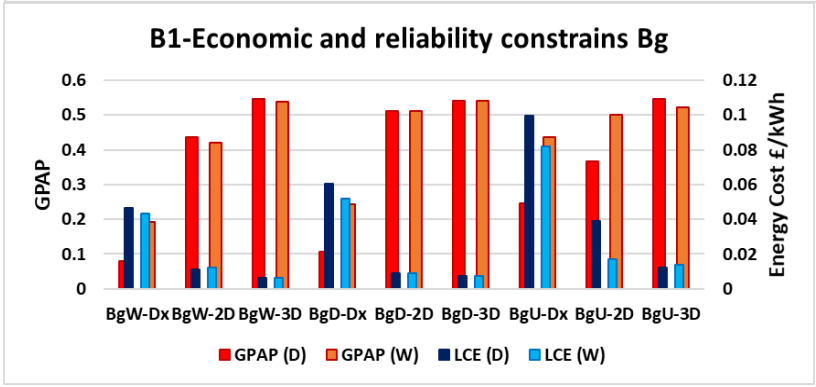
B1-Economic and reliability constrains Bg
GPAP
Energy Cost £/kWh
BgW-Dx BgW-2D BgW-3D BgD-Dx BgD-2D BgD-3D BgU-Dx BgU-2D BgU-3D
GPAP (D) GPAP (W) LCE (D) LCE (W)

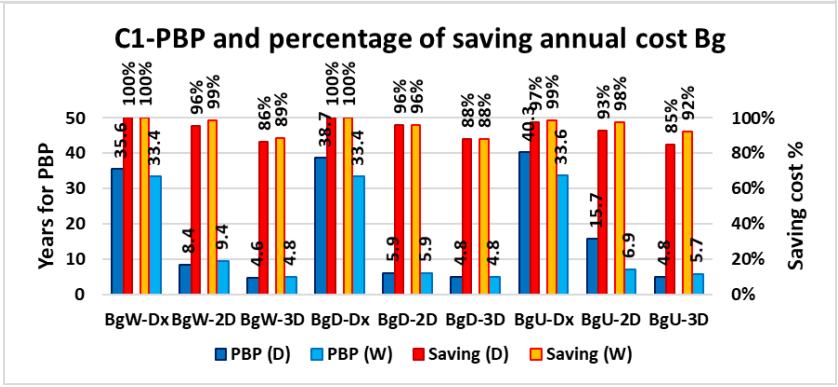
C1-PBP and percentage of saving annual cost Bg
Years for PBP
Saving cost %
BgW-Dx BgW-2D BgW-3D BgD-Dx BgD-2D BgD-3D BgU-Dx BgU-2D BgU-3D
PBP (D) PBP (W) Saving (D) Saving (W)

Part A

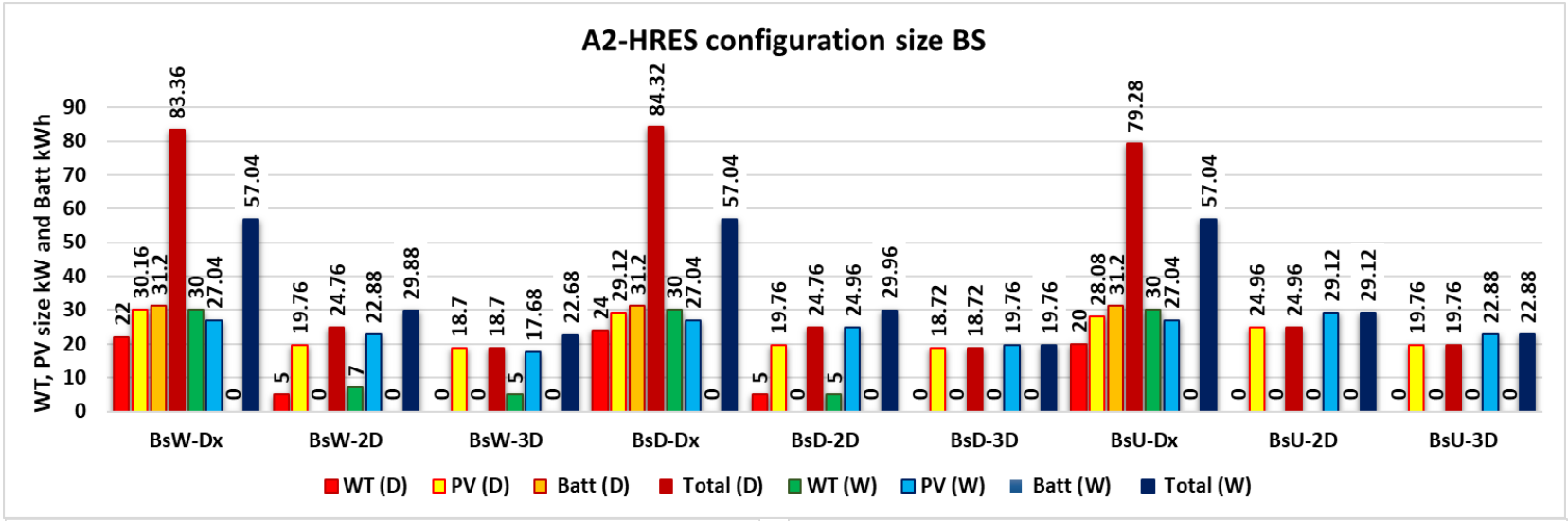

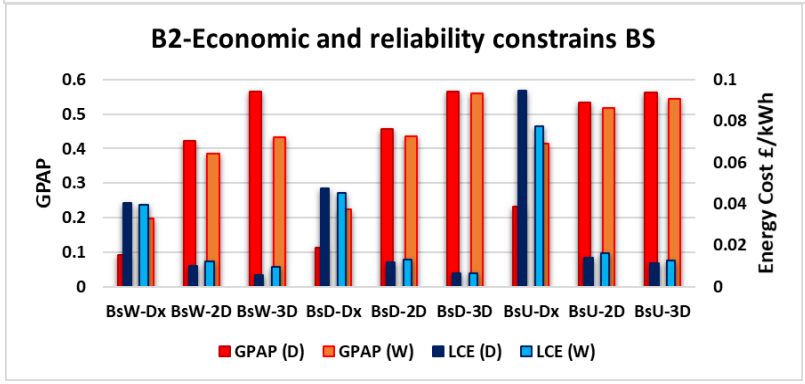

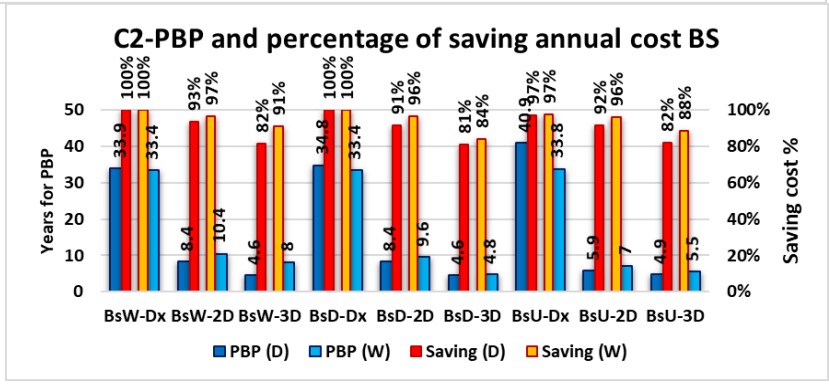

Part B

Figure 9-15. Results of optimization based on Basra house demand to determine the optimal HRES design using 2015 IBT price with discharge O.D and 2017 IBT price without discharge O.W for four locations in Iraq: Baghdad Bg and Basra BS across the water, desert and urban land covers. In this Figure have been used many parameters like the HRES configuration size in sub-Figures A1 and 2, which shows the size of WT, PV, Batt and total system size. Also, Economic and reliability constraints like LCE and GPAP across sub-Figures B1 and 2 for the above locations. Beside, PBP and percentage of saving annual cost across sub-Figures C1and 2. Furthermore, In order to define some abbreviations BgW: Baghdad water area, BgD: Baghdad desert area, BgU: Baghdad urban area, BsW: Basra water area, BsD: Basra desert area, BsU: Basra urban area, HW, HD and HU: Haditha water, desert and urban areas respectively, MW, MD and MU: Mosul water, desert and urban areas respectively.

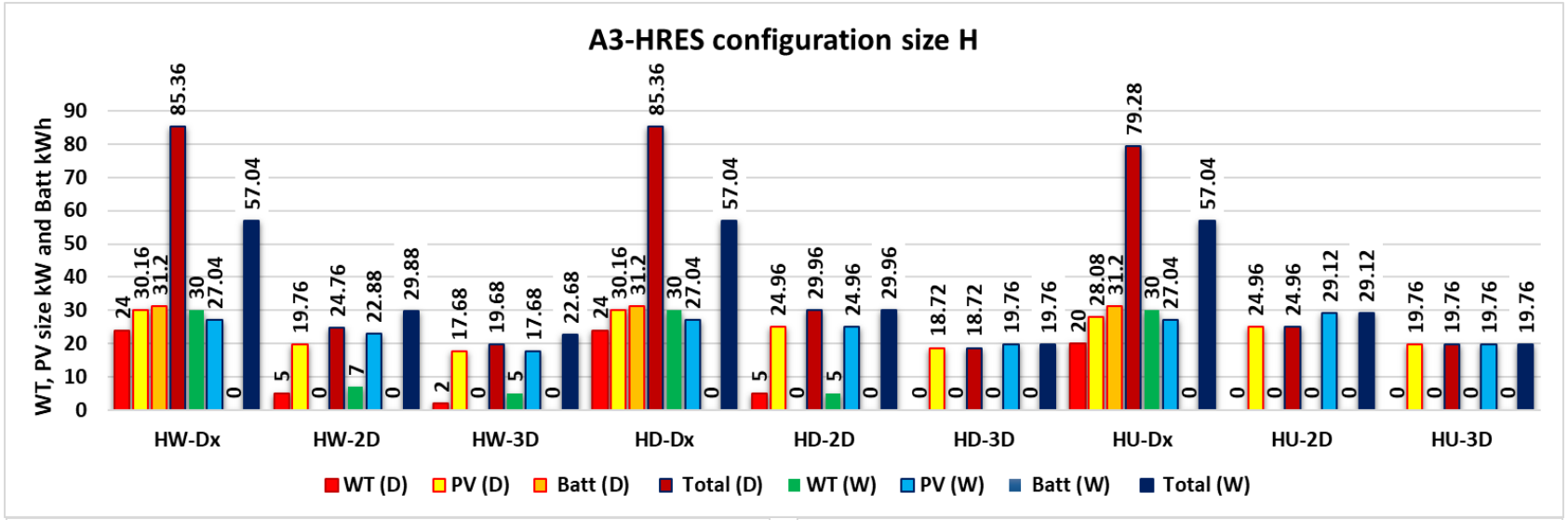
A3-HRES configuration size H
WT, PV size kW and Batt kWh
HW-Dx HW-2D HW-3D HD-Dx HD-2D HD-3D HU-Dx HU-2D HU-3D
WT (D) PV (D) Batt (D) Total (D) WT (W) PV (W) Batt (W) Total (W)

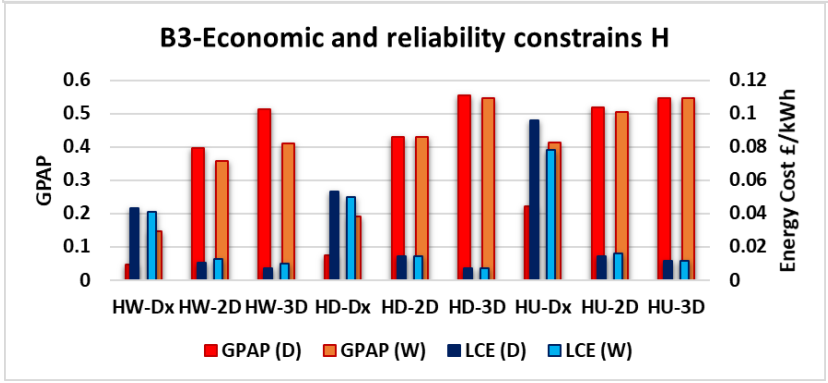
B3-Economic and reliability constrains H
GPAP
Energy Cost £/kWh
HW-Dx HW-2D HW-3D HD-Dx HD-2D HD-3D HU-Dx HU-2D HU-3D
GPAP (D) GPAP (W) LCE (D) LCE (W)

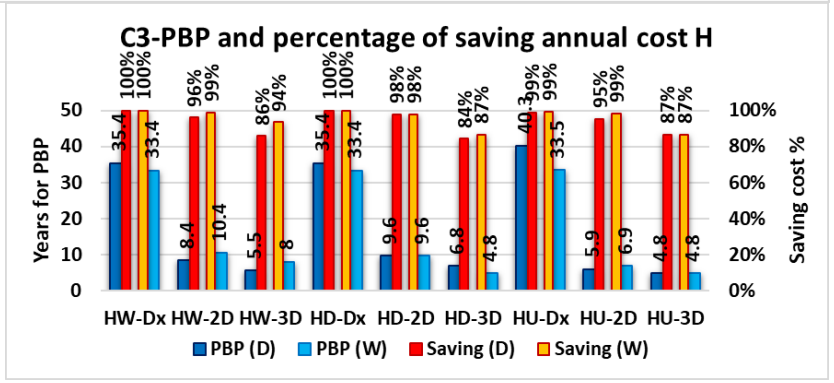
C3-PBP and percentage of saving annual cost H
Years for PBP
Saving cost %
HW-Dx HW-2D HW-3D HD-Dx HD-2D HD-3D HU-Dx HU-2D HU-3D
PBP (D) PBP (W) Saving (D) Saving (W)

Part A

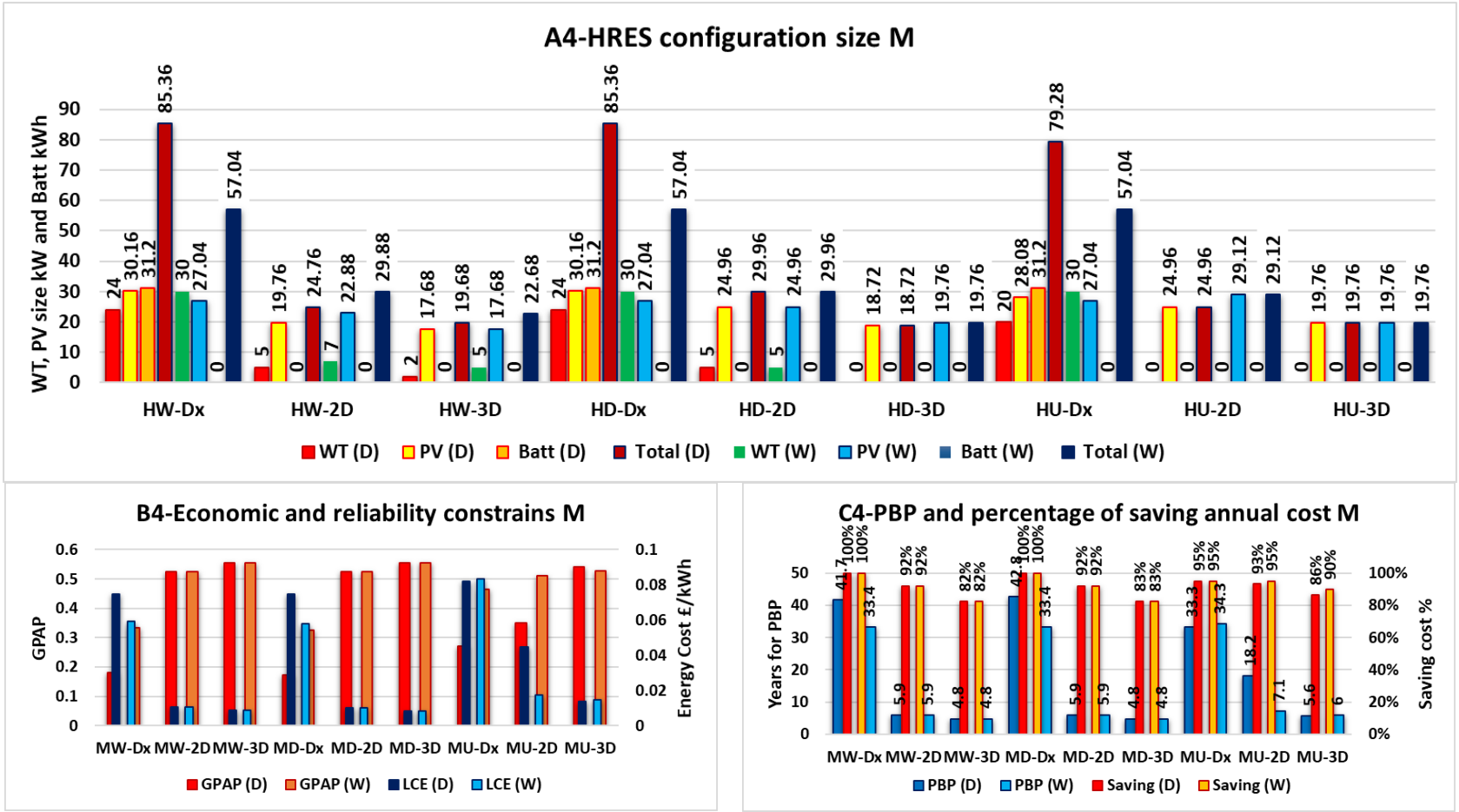

Part B

Figure 9-16. Result of optimization in Basra house demand to determine the optimal HRES design based on 2015 IBT price and with discharge O.D and 2015 IBT price and without Typical O.W for four locations in Iraq: Baghdad Bg and Basra BS across the water, desert and urban land covers. In this Figure have been used many parameters like the HRES configuration size in sub-Figures A3 and 4, which shows the size of WT, PV, Batt and total system size. Also, Economic and reliability constraints like LCE and GPAP across sub-Figures B3 and 4 for the above locations. Beside, PBP and percentage of saving annual cost across sub-Figures C 3 and 4. Furthermore, the abbreviations BgW, BgD, BgU, BsW, BsD, BsU, HW, HD, HU, MW, MD and MU have been defined in Figure 15.

9.4 CONCLUSION

A technique for identifying optimal combinations of wind, solar and battery technologies for domestic scale renewable energy provision has been developed and demonstrated. A key innovation in the approach is the way in which it has been designed with the unique features of the electricity grid in Iraq, predominantly the unreliable supply meaning that resultant system must have the flexibility to cover the frequent interruptions in grid supply. The technique has been implemented in MATLAB drawing extensively on the resource modeling work described in earlier chapters of this thesis, and on detailed electricity demand data logged from three houses specifically for this project.

The technique has been applied to a range of scenarios that have been structured around different cost and reliability targets, as well as different energy flow management strategies. An extensive set of calculations have been carried out for 6 locations in Iraq, demonstrating that the optimal system configuration varies significantly with location and according to cost/reliability trade-off. Examination of the results has produced a number of important conclusions.

Firstly, the local wind resource has a major impact on the viability of small scale the HRES systems for application in Iraq. In high wind speed areas, the HRES is readily able to improve supply reliability at a reasonable cost. However, in low wind speed areas, typically within cities, much larger, more expensive systems are required to overcome grid unreliability. This is likely to limit the feasibility of the HRES systems in Iraq's urban areas.

Also, the high availability of wind speed and solar radiation in the southeast of Iraq (Amara) and west of Iraq (Rutbah) has shown marked efficiency in the performance of the HRES in terms of improving supply reliability at reduced cost with short payback period. Otherwise, the reduction of wind speed and solar radiation resources have led to reduce the feasibility of the HRES dramatically in the north of Iraq, Mosul is a case in point.

Secondly, the technique of non-discharging of the storage system at the 2015 grid price has shown the most significant impact on the HRES performance for a series of optimization strategies (2D, 3D and 4D). According to this energy flow management, the HRES has a great ability to improve supply reliability at a reduced cost of energy with a reasonable total capital cost of the project as well as has played a significant role to achieve short payback period. According to this conclusion, it is hugely recommended to return to the 2015 IBT price to support the renewable energy sector in Iraq.

Furthermore, various optimization strategies that have been suggested to determine the optimal HRES design based on parameters of reliability and economic feasibility have

shown different results which are consistent with the diversity of consumers' desires. The 2D strategy has shown a high capacity to meet the reliability requirement but with an expensive cost. The 3D strategy has demonstrated commercial viability with a short payback period and reasonable saving cost. The 3D strategy has the ability to meet the willingness of the consumer who aspires to a system aims to make a balance between reliable and economic at the same time.

In the same context, the 2D strategy which is built based on the same weight for GPAP and LCE according to the demand data logged from Basra has shown reliable supply, low cost of energy, short payback period, low TCOP and a small size of the HRES configuration.

Finally, the results of optimization according to the demand data logged from KR showed that the cheap supplies of renewable energy to meet off-grid demand will reduce the deferred loads in the case of on-grid demand and therefore will also reduce the purchase probability from a national grid.

Chapter 10 **FINAL DISCUSSION AND CONCLUSIONS**

10.1 **Research Summary**

The main aim of this thesis is to develop an unique method of optimizing a HRES to control energy flow to meet house electricity demand which is suffering from unscheduled outage from the national grid. HRES will generate energy using small wind turbines, solar panels and rechargeable batteries based on the power availability in Iraq and energy demand that recorded from several housing units in different places in Iraq. in order to achieve this goal,, this project aims to assess the wind and solar power availability in Iraq to estimate the potential power production from renewables.

In order to evaluate the wind resources precisely, a downscaling model (DSM) was developed in Chapter 5 to estimate the annual average and hourly wind speed everywhere in Iraq using MERRA data. The potential power production was calculated for different sizes of wind turbine, using Weibull distribution then shape factor at different heights evaluated using the K- profile equation. Furthermore, to assess the feasibility of different wind turbine sizes, economic assessment was achieved by estimating the payback period and the levelized cost of energy.

The annual solar energy production was evaluated for the whole of Iraq using different sizes of the PV system, to determine the spatial distribution of high and low power production. HSEP-WT model was then developed to estimate the hourly solar energy production by combining the effects of wind speed and ambient temperature on cell performance.

Finally, an unique computational code to size and optimize HRES was developed. The process of sizing and optimizing involved different weather conditions, various land covers to identifying the optimal HRES configuration in each circumstances. Conclusions have been drawn with respect to the most appropriate hybrid system in each circumstances.

10.2 **Results and Implications**

10.2.1 **Wind Resources Assessment by the Downscaling Model**

In chapter 5, one main objective was to evaluate wind resources in Iraq with high resolution by improving a DSM. MERRA data was used as a reference wind climatology with an Iraq land cover map (LCM) to create a roughness map. The DSM was developed to estimate accurately the annual average wind speed across the whole of Iraq, and to estimate the hourly wind speed at the hub height of wind turbine. Moreover, the performance of the DSM

has been improved by sensitivity analysis for a range of parameters that describe the boundary layer conditions in Iraq. Sensitivity analysis, validations and comparisons were made to evaluate the difference between the DSM that was applied using different parameters:

- The reference height Z_{ref} = 200 m and Z_{ref} = 600 m.
- The surface roughness at a reference site, $Z_{o\,ref}$ = 0.103 m and $Z_{o\,ref}$ = 0.05 m.
- The reference wind climatology from MERRA data at hub height Z_h = 10 m and Z_h = 50 m at a reference site.
- To improve evaluations of the Z_{bh}, local reference effective $Z_{o\,eff}$ and wind speed over upwind fetches (wind direction sector) around the target site, sensitivity analysis was made between stripe pattern (9 roughness patches) and full sector (32 roughness patches) in the DSM.

The results have shown that the reference height 600m, surface roughness 0.05 m, reference wind climatology from MERRA at 50 m and applying full sector design for upwind fetch have played a significant impact in improving wind resources assessment using the DSM in Iraq. Chapter 5 answers some of the main research questions in this project:

- To what extent does the DSM predict the wind speed accurately in Iraq?
- What are the disadvantages of implementation of a DSM using MERRA data?
- To what extent is the DSM useful in improving the wind resources assessment in Iraq using MERRA data?

According to the first question, the Mean Absolute Error (MAE) that was calculated between estimated and observed data after applying the DSM, the results have shown that the DSM succeeded in decreasing the error to 0.8 m/s, which is approximately three times lower than the difference between MERRA data and observed data. In addition, the DSM has played a crucial role in terms of increasing the accuracy of estimated data when MERRA data has a low error with observed data. Also, the DSM has played a significant role in terms of reducing the error massively when the error between MERRA and observed data is too high. The DSM has succeeded in increasing the accuracy and the resolution of coarse wind speed data from MERRA.

According to the second question, on the other hand, the DSM has shown low performance within the mountain area, because the DSM could not deal with topographic diversity in the mountain area. In addition, MERRA data also has shown weakness in some areas due to the IAU system in GEOS-1 DAS method, in cases where there is a shortage of observation data,alongside weakness in data distribution within the horizontal resolution. This led to an increase in the possibility of generating small errors and some deviations.

Whith respect to the third question, the difference in resolution between the two maps in Figure 10-1 shows how effective and useful using the DSM and MERRA data is to assess the wind speed in Iraq. Firstly, MERRA has the highest spatial resolution as a source of global dataset in Iraq. The DSM has increased the resolution of MERRA data from 55.461 km × 61.589 km to 231.6 m × 231.6 m for the whole of Iraq. That means the resolution has increased by 64448 times. In fact, this is the highest resolution that ever been used to evaluate the wind speed in Iraq. Finally, according to the DSM it is has possible to evaluate the wind speed in any country or region if the LCM for this area uses the DSM and MERRA data, as MERRA data cover all the world.

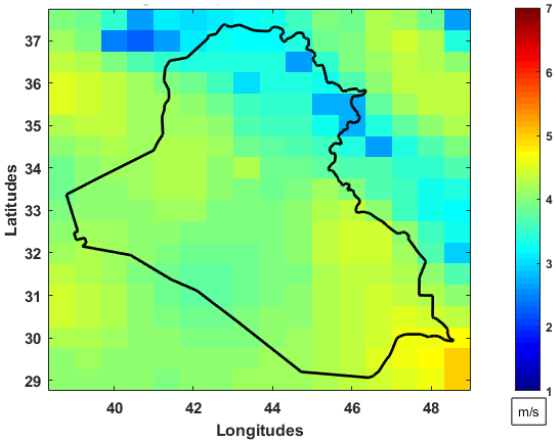

Figure A The annual average wind speed map from MERRA data at 10m

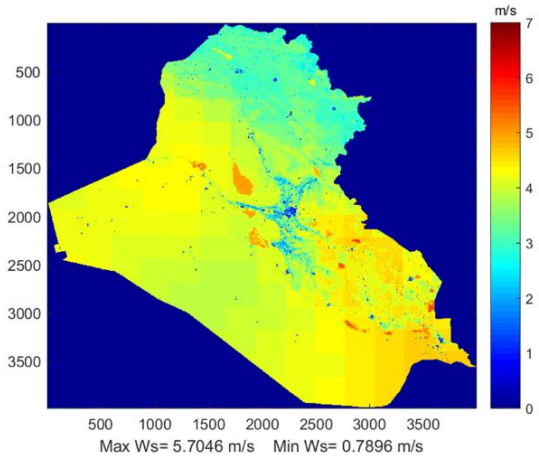

Figure B Wind speed map at Z_{hh}=10 m based on Z_h=50 m, Z_{ref}= 600 m and $Z_{o\,ref}$= 0.05 m at a reference site

Figure 10-1 The difference in spatial resolution between MERRA data in Figure A and wind recourses assessment map in Figure B, which has been modelled by the DSM, based on MERRA data in Figure A in 2014.

10.2.2 Wind Power Production Evaluation

The first part of chapter 6 aimed to calculate the annual energy production (AEP) for the whole of Iraq, based on four sizes of wind turbine (2 kW, 5 kW, 10 kW and 20 kW) at different heights, to evaluate the potential power production at different regions and to find the locations that have high and low AEP in Iraq. In addition, the AEP calculation will provide information for further computations, such as the capacity factor (CF), percentage self-demand (PSD) and some economic estimation, as outlined in Chapter 7.

Weibull distribution based on shape factor and scale factor has been used to estimate AEP to avoid running 8760 hours of data over more than 9 million pixels on the Iraq map. The results show that the shape factor does not change significantly with height as for MERRA data. Also, the shape factor does not change entirely with height after applying the DSM for the whole of Iraq, which is regarded as an unusual alteration in the shape factor values with the altitude.

According to the above problem, the K-profile equation was proposed to estimate the shape factor with height correctly, the new value of c_k = 0.03705 and $z_r = 120m$ was used to estimate shape factor values at 10 m and 30 m. The results of the shape factor from MERRA data after applying the modified K-profile at 10 m and 30 m have shown good agreement with the values of the shape factor from the Shihabi tower. The results showed a difference in the distribution of shape factor values over the Iraq map, which returns to the topographic nature for these areas and wind speed distribution at these areas.

According to the results of PSD which is at different heights, different levels of electricity demand and different wind turbine sizes, the PSD increased dramatically with height and with low electricity demand at locations that have high AEP. However, it is slightly increasing with height and with high electricity demand for areas that have low AEP. This finding leads to the critical conclusion that increasing the hub height of the wind turbine will increase the power production exponentially and cover the low level of electricity demand without extra cost, especially in the locations that have high power production. Chapter 6 tried to answer some of the main research questions in this project :

- To what extent is the wind resources assessment in Iraq helpful to determine the spatial distribution of power production?
- Which areas of Iraq best suited to wind power production?

According to the first question, wind resources assessment has played an essential role in terms of determining the spatial distribution of AEP, based on different sizes and heights of a wind turbine, due to the accuracy of the DSM and the high resolution of roughness map.

With respect to the second question, Firstly, the most productive regions are marshes and lakes that form about 1 % of locations in Iraq at the hub height of 30 m, which extends from central to the southeast of the country. Also, the CF for different sizes of a wind turbine at these locations recorded the highest values. Secondly, the second most productive regions are distributed between northwest, east and southeast of the country that form approximately 25 % of locations which are considered as a promising area in Iraq.

10.2.3 **Economic Evaluation of Wind Turbine Investments**

Chapter 7 aimed to calculate the payback period (PBP) and levelized cost of energy (LCE), based on AEP for four sizes of wind turbine and for different levels of monthly demand for the whole of Iraq. The LCE calculation aims to determine the low electricity costs and the spatial distribution of the low LCE throughout the whole of the Iraq map. Also, the payback period has been calculated based on a saving strategy under the 2017 IBT and the 2015 IBT prices (the increasing block tariffs prices), aiming to recognise the best pricing model that could be applied to attain the shortest PBP within the lifetime of a turbine. Also, the PBP

calculations aimed to determine the most reliable and productive locations that could be achieved with a short PBP within a wind turbine's lifespan. According to these requirements, the main costs of a wind turbine project have been sized by a new method. The new approach has integrated the relative weight for capital and variable expenditure that depend on the literature and equations to estimate variable costs that are affected by time value over the project's life span.

According to the results, the WS-5 kW showed the lowest LCE at all heights, mainly based on monthly demand between 2000 to 5000 kWh/month in comparison with others. In general, the LCE based on spacific level of demand decrease with height and as well as the LCE at specific height decrease with an increasing level of demand from 1000 to 5000 kWh/month. Consequently, the WS-5 kW, based on 5000 kWh/month has shown the lowest LCE result, ranging between 0.055 and 0.0317 £/kWh, particularly in the southeast of Iraq.

The PBP calculation based on 2015 IBT prices showed the shortest PBP in different places in Iraq, despite the absence of feed-in tariff policy in Iraq. The results of PBP based on 2015 IBT prices according to the saving strategy will contribute to encouraging the householders to use small wind turbine within the on-grid systems. The WS-5 kW has shown the best performance and achieved the shortest PBP 4.6 years.

The identification of locations achieving PBP within 8 years has been applied, based on the 2017 and 2015 IBT as a sensitivity analysis to determine the most reliable and productive locations in Iraq. The WS-5 kW and WS-2 kW achieved wide areas of PBP of less than 8 years, generally at different heights and for 3000, 4000, 5000 kWh/month of energy demand.

Chapter 7 tried to answer some of the main research questions in this project as follows:

- To what extent is investment in wind turbine is feasible in Iraq?
- Which locations and circumstances are the most economically for wind turbine investment?

According to this question, two factors determine the feasibility of wind turbine investment: the ICE and PBP. According to these indicators, the water surfaces, desert, and the areas that are distributed between northwest, east and southeast of Iraq at 30 m height with the high level of energy demand have shown high feasibility in terms LCE and short PBP, based on 2015 IBT prices. Also, the investment in the renewable energy sector needs reconsideration in IBT prices and the possibility of buying electricity from houses that generate electricity.

With respect to answer the second question, the most productive area that generated the lowest cost of energy was based on different wind turbine sizes located in the southeast of Iraq which forms 25 % of locations in Iraq. In the same context, the lakes and marshland

showed the lowest LCE in the southeast of Iraq. The regions and the turbines that achieved the most significant results of PBP within eight years based on 3000 kWh/month of energy demand at 20 m heights are for WS-5 kW and WS-2 kW considered the best locations, in terms of wind speed to invest in the hybrid renewable energy system (HRES).

10.2.4 **Assessment of Solar Resources**

The main objective in chapter 8 was to evaluate the solar radiation and solar power production from different size of solar systems throughout the whole of Iraq, depending on accurate data sources that are validated by observed data from several weather stations. According to the validated dataset, annual solar energy production and some economic aspects that include the cost of energy and payback period have been evaluated for the whole of Iraq. In addition, the HSEP-WT model was developed to estimate the hourly solar energy production by combining the effects of wind speed and ambient temperature on cell performance in the solar system. The HSEP-WT model aims to provide the optimization process of the hybrid system in chapter 9, by realistic and reliable hourly solar energy data for different sizes of solar system in any location in Iraq.

Also, the cost of energy ranged from 0.0375 to 0.05 £/kWh for 3.1 and 5.2kW PV system, while the LCE for 10.4 kW PV system ranged from 0.045 to 0.062 £/kWh. Furthermore, the PBP assessment shows that the high level of demand and the 2015 IBT prices played an essential role in reducing the PBP to lower than eight years in the west of Iraq. Also, the validation between AEP of PVGIS calculations, based on HC1 and Homer based on NASA data showed a low error, while the validation between AEP of PVGIS calculations and Homer based on HC1 showed a high error due to the calculation PV system losses in Homer, which were lower than in PVGIS estimation based on HC1.

According to the HSEP-WT model, the hourly wind speed played a significant role to reduce the cell temperature of a PV system, which leads to an increase in the efficiency of the solar system and increases the capacity of power production. On the other hand, the validation between PV output power from HSEP-WT model on one side, and Homer and PVGIS on other side shows that the MAPE ranged around 6%. According to the effect of wind speed on PV output power, the type of land cover also has played an essential role, in terms of increasing the output of a PV system in the open areas like lakes and deserts and reduces the output on the urban area. Chapter 8 aimed to answer several of the research questions:

- Where are the best locations for PV in Iraq?
- To what extent is the investment in solar systems feasible in Iraq?
- To what extent does the wind speed and temperature have an effect on the performance and efficiency of the solar system?

- What are the best solar dataset?

According to the first question, the annual solar resources assessment for the whole of Iraq demonstrated that high solar availability is located in the west of Iraq and to a lesser extent in the centre and southeast of Iraq. Nonetheless, the lowest solar irradiation and PV power output are concentrated above lakes and forest along the Euphrates river due to the high absorption of water vapour for solar radiation.

According to the second question, for both wind turbine and solar system, the ICE and PBP evaluation have shown that investment in both of these technologies is feasible and worthwhile in Iraq, but the solar system could be invested in, almost everywhere in Iraq, with little contrast in terms of LCE or PBP results.

With respect to the third question, the influence of high temperature on a solar panel's efficiency during the summer season could not be ignored. However, involving the effects of both wind speed and temperature will make the possibility of assessing the production of electrical energy from solar panels more realistic; accurate calculations will play a key role in improving the estimated performance of a solar system. The effects of both wind speed and temperature were notable when comparing the AEP between open areas like water surfaces and deserts with urban areas.

According to the fourth question, the validation among several datasets: HC3v5, HC1, CM-SAF, SARAH with observed data in Iraq, showed that the HC3v5 and then HC1 have the lowest error against observed data respectively. These results have led to the use of HC1 data resources for annual solar resources assessment in Iraq, while HC3v5 was used to estimate hourly solar energy production.

10.2.5 **Optimize HRES**

In Chapter 9, a technique for identifying optimal combinations of wind, solar and battery technologies for domestic scale renewable energy provision was developed and demonstrated. A key innovation in the approach was the way in which it was designed for the unique features of the electricity grid in Iraq, predominantly the unreliable supply, meaning that the resultant system must have the flexibility to cover the frequent interruptions in grid supply. The technique implemented in MATLAB drew extensively on the resource modeling work described in earlier chapters of this thesis, and on detailed electricity demand data logged from three houses specifically for this project.

The technique was applied to a range of scenarios that were structured around different cost and reliability targets, as well as various energy flow management strategies. An extensive set of calculations were carried out for 6 locations in Iraq, demonstrating that the

optimal system configuration varied significantly with location and according to cost/reliability trade-off. Examination of the results has produced several important conclusions.

Firstly, the local wind resource has a significant impact on the viability of small scale HRES systems for application in Iraq. In high wind speed areas, HRES is readily able to improve supply reliability as measured by On-off-grid Op-HRES at a reasonable cost. However, in low wind speed areas, typically within cities, much larger, more expensive systems are required to overcome grid unreliability. This is likely to limit the feasibility of the HRES system in Iraq's urban areas.

Also, the high availability of wind speed and solar radiation in the southeast of Iraq (Amara) and west of Iraq (Rutbah) has shown marked improvement in the performance of HRES, in terms of improving supply reliability at reduced cost with a short payback period. The low wind speed and solar radiation lead to much reduced feasibility of HRES in the north of Iraq, e.g. Mosul.

Secondly, the technique of non-discharging the storage system based on the 2015 IBT price has shown the most significant impact on the HRES systems performance for a series of optimization strategies (2D, 3D and 4D). According to this energy flow management, HRES has a remarkable ability to improve supply reliability at a reduced cost of energy with a reasonable total capital cost of the project; it has also played a significant role to achieve a short payback period. According to this conclusion, it is highly recommended to return to the 2015 IBT price to support the renewable energy sector in Iraq.

The various optimization strategies have been used to determine the optimal HRES designs, based on reliability and economic feasibility; they have shown different results. The 2D strategy has demonstrated a high capacity to meet the reliability requirement but at an expensive cost. The 3D strategy has proved commercial viability with a short payback period and reasonable costs. The 3D strategy has the ability to meet the needs of the consumer who aspires to a system that is reliable and economic at the same time.

In the same context, the 2D strategy which is built based on the same weight for GPAP and LCE according to the demand data logged from Basra has shown reliable supply, low cost of energy, short payback period, low TCOP and small size of HRES configuration.

Finally, the results of optimization according to the demand data logged from KR showed that the cheap supplies of renewable energy to meet off-grid demand will reduce the deferred loads in case of on-grid demand and therefore reduce the purchase probability from a national grid. Chapter 9 aimed to answer several research questions in this project:

- To what extent will an optimization HRES successfully cover the energy demand?

- To what extent will the optimized HRES be feasible and economical for households in Iraq in terms of on-grid and off-grid scenarios?
- How does the feasibility vary with different land cover?

According to the first question, the optimized HRES has succeeded in satisfying an electricity demand which is suffering from unscheduled outage from the national grid, where housing units have high availability of wind speed and solar radiation (such as Rutbah and Amara), with low cost in comparison with others.

To answer the second question, in spite of the availability of wind speed and solar radiation which play a significant role in increasing the feasibility and reducing the cost, non-discharging the battery on-grid and applying the 2015 IBT prices, are crucial in making HRES more feasible and economical, even in areas that have poor sources of wind speed and solar power.

According to the third question, the land cover categories have played a vital role in terms of raising or reducing the feasibility of HRES. For example, in open areas like water surface or desert, the wind speed increases and increase the wind power production and increase the solar system output, while in the urban area wind power production and the solar system output have been reduced significantly.

10.3 Improvement of Futures of This Work

Many futures work could be developed to improve the wind and solar resources assessment and HRES in Iraq:

Firstly, the DSM has been applied within a neutral boundary layer condition and also based on unequal lengths of upwind fetch for the 12 wind directions within the downscaling square area. In order to improve the performance of the DSM, a stability correction in terms of stable, neutral and unstable condition should be applied, equal lengths of upwind fetch within the downscaling square area could be used to estimate the effect of effective local roughness equally for the 12 wind direction and using different data resources.

In addition, MERRA dataset provides wind speed and direction for different altitudes according to pressure units by millibar that is matching different heights in the troposphere. According to the reference height $Z_{ref} = 600m$ in the DSM in this work which is matching 943.19 millibar, might be possible to apply the DSM from reference height using wind speed and direction at 943.19 millibar from MERRA data to estimate the wind speed at blending height Z_{bh} as a first step in the downscaling technique rather than starting from 10 m at hub height at the reference site. This technique could be checked in the future and then validated to examine to what extent this suggestion is possible to apply.

Secondly, in order to validate accurately the AEP that has been estimated by Weibull distribution for each pixel in the Iraq map in Chapter 3, these results could be compared with AEP for 8760 hours of wind speed at a few sample data points according to the different sizes of wind turbine and at different heights rather than comparing the AEP with results of another software like Homer

Thirdly , the hourly data of GHI for both MERRA and MERRA-2 would be to compare with other datasets such as HC1, HC3v5, CM-SAF and SARAH against observed GHI data from several weather station in Iraq.

Fourthly , the optimization of the HRES in this study has covered the energy demand for housing units without studying the most appropriate pricing policy to encourage renewable energy investments in Iraq. According to this limitation, future research could be applied, based on a small community to avoid wasting energy in terms of satisfying the housing units demand and also testing different scenarios of pricing policies, such as feed-in-tariff, and buying electricity from householders who are using renewable technologies

Fifthly , if the energy flow management of without discharging the storage system in case of on-grid was so useful, the re-charge the storage system using grid electricity through a two-way hybrid inverter (DC-AC and AC-DC) will increase the reliability of HRES. Accordingly, using a two-way hybrid inverter (DC-AC and AC-DC) in the future will support HRES reliability by charging the storage by electricity from grid and renewables.

Sixthly, consideration could be given to studying the possibility of using another source of power (such as heating by using heating storages system), in terms of getting advantages from high temperatures during the summer and integrating this technology with wind and solar power in terms of large power plants.

REFERENCES

[1] U. Nations. (2012). *United Nations General Assembly Declares 2014-2024 Decade of Sustainable Energy for All*.

[2] J. R. C. o. T. E. Commission. (2009). *Renewable energy*. Available: https://ec.europa.eu/jrc/en/research-topic/renewable-energy

[3] A. R. Prasad and E. Natarajan, "Optimization of integrated photovoltaic–wind power generation systems with battery storage," *Energy,* vol. 31, no. 12, pp. 1943-1954, 2006.

[4] J.-D. P. Reina Maeda, Peter Zhang,, "Small Wind World Report 2013," New Energy Husum, Bonn, GermanyApril 2013 2013, Available: http://www.wwindea.org/webimages/SWWR_summary.pdf.

[5] M. Z. Jacobson, "Review of solutions to global warming, air pollution, and energy security," *Energy & Environmental Science,* vol. 2, no. 2, pp. 148-173, 2009.

[6] I. Dincer, "Renewable energy and sustainable development: a crucial review," *Renewable and Sustainable Energy Reviews,* vol. 4, no. 2, pp. 157-175, 2000.

[7] IPCC, "Climate Change 2014 Synthesis Report Summary for Policymakers," World Meteorological Organization, CH- 1211 Geneva 2, Switzerland2014, Available: http://www.ipcc.ch/pdf/assessment-report/ar5/syr/AR5_SYR_FINAL_SPM.pdf.

[8] T. F. Stocker, *Climate change 2013: the physical science basis: Working Group I contribution to the Fifth assessment report of the Intergovernmental Panel on Climate Change*. Cambridge University Press, 2014.

[9] R. K. Pachauri and A. Reisinger, *Climate change 2007 synthesis report: Summary for policymakers*. IPCC Secretariat, 2007.

[10] B. Kruyt, D. P. van Vuuren, H. De Vries, and H. Groenenberg, "Indicators for energy security," *Energy Policy,* vol. 37, no. 6, pp. 2166-2181, 2009.

[11] H. A. Kazem and M. T. Chaichan, "Status and future prospects of renewable energy in Iraq," *Renewable and Sustainable Energy Reviews,* vol. 16, no. 8, pp. 6007-6012, 2012.

[12] T. T. T. Bulletin. *Historical Energy Data about Iraq*. Available: https://www.tititudorancea.com/z/ies_iraq_population_millions.htm

[13] M. Reda, N. Saied, A. Khaldi, M. Abdul-Hussain, and A. Ekwue, "Iraq Electrical Power Infrastructure-Past, Present and Future Developments and Expectations," in *Power Systems Conference and Exposition, 2006. PSCE'06. 2006 IEEE PES*, 2006, pp. 1792-1795: IEEE.

[14] D. F. Birol, "Iraq's Energy Sector A Roadmap to a Brighter Future," 2019, Available: https://www.iea.org/publications/iraqenergyoutlook/.

[15] A. Darwish and A. Sayigh, "Wind energy potential in Iraq," *Solar & wind technology,* vol. 5, no. 3, pp. 215-222, 1988.

[16] A. J. N. Khalifa, "Evaluation of different hybrid power scenarios to Reverse Osmosis (RO) desalination units in isolated areas in Iraq," *Energy for Sustainable Development,* vol. 15, no. 1, pp. 49-54, 2011.

[17] S. Ahmed, "A review of solar energy and alternative energies applications in Iraq," in *The First Conference between Iraqi and Germany Universities DAAD, Arbil, Iraq*, 2010.

[18] R. Borja, C. Austin, and J. Phillips, "Operation solar eagle: a study examining photovoltaic (pv) solar power as an alternative for the rebuilding of the iraqi electrical power generation infrastructure," 2005.

[19] S. S. Dihrab and K. Sopian, "Electricity generation of hybrid PV/wind systems in Iraq," *Renewable Energy,* vol. 35, no. 6, pp. 1303-1307, 2010.

[20] D. J. Allen, "Analysis of the uptake of small and medium scale wind turbines under the Feed-in Tariff in Great Britain," University of Leeds, 2017.
[21] S. Weekes, A. Tomlin, S. Vosper, A. Skea, M. Gallani, and J. Standen, "Long-term wind resource assessment for small and medium-scale turbines using operational forecast data and measure–correlate–predict," *Renewable Energy,* vol. 81, pp. 760-769, 2015.
[22] H. B. Azad, S. Mekhilef, and V. G. J. I. T. o. S. E. Ganapathy, "Long-term wind speed forecasting and general pattern recognition using neural networks," vol. 5, no. 2, pp. 546-553, 2014.
[23] T. Burton, D. Sharpe, N. Jenkins, and E. Bossanyi, *Wind energy handbook*. John Wiley & Sons, 2001.
[24] G. Boyle, *Renewable energy*. OXFORD university press, 2004.
[25] T. R. Oke, *Boundary layer climates*. Routledge, 2002.
[26] R. B. Stull, *An introduction to boundary layer meteorology*. Springer Science & Business Media, 1988.
[27] J. R. Garratt, "Review: the atmospheric boundary layer," *Earth-Science Reviews,* vol. 37, no. 1-2, pp. 89-134, 1994.
[28] S. M. Weekes, "Small-scale wind energy: methods for wind resource assessment," University of Leeds, 2014.
[29] A. Monin and A. Obukhov, "Basic laws of turbulent mixing in the surface layer of the atmosphere," *Contrib. Geophys. Inst. Acad. Sci. USSR,* vol. 151, pp. 163-187, 1954.
[30] U. Schumann, "Minimum friction velocity and heat transfer in the rough surface layer of a convective boundary layer," *Boundary-Layer Meteorology,* vol. 44, no. 4, pp. 311-326, 1988.
[31] D. H. Mclntosh and A. S. Thom, "Essentials of meteorology," *Essentials of meteorology,* 1969.
[32] A. Hussain, "Characteristics of the boundary layer above the surface of Baghdad city and estimating the mixing length.," Msc degree, Atmospheric science Almustansiriya University, Baghdad 2006.
[33] C. Grimmond and T. R. Oke, "Aerodynamic properties of urban areas derived from analysis of surface form," *Journal of applied meteorology,* vol. 38, no. 9, pp. 1262-1292, 1999.
[34] D. Drew, J. Barlow, and T. Cockerill, "Estimating the potential yield of small wind turbines in urban areas: A case study for Greater London, UK," *Journal of Wind Engineering and Industrial Aerodynamics,* vol. 115, pp. 104-111, 2013.
[35] S. Weekes and A. Tomlin, "Evaluation of a semi-empirical model for predicting the wind energy resource relevant to small-scale wind turbines," *Renewable Energy,* vol. 50, pp. 280-288, 2013.
[36] M. B. A. B. P. C. D. H. D. M. G. R. D. T. C. Wilson, "Small-scale wind energy -Technical Report," August 2008 2008.
[37] S. L. Walker, "Building mounted wind turbines and their suitability for the urban scale—A review of methods of estimating urban wind resource," *Energy and Buildings,* vol. 43, no. 8, pp. 1852-1862, 2011.
[38] A. Ucar and F. Balo, "Evaluation of wind energy potential and electricity generation at six locations in Turkey," *Applied Energy,* vol. 86, no. 10, pp. 1864-1872, 2009.
[39] R. Bansal, T. Bhatti, and D. Kothari, "On some of the design aspects of wind energy conversion systems," *Energy conversion and management,* vol. 43, no. 16, pp. 2175-2187, 2002.
[40] S. Persaud, D. Flynn, and B. Fox, "Potential for wind generation on the Guyana coastlands," *Renewable Energy,* vol. 18, no. 2, pp. 175-189, 1999.
[41] P. Bhattacharya and R. Bhattacharjee, "A study on Weibull distribution for estimating the parameters," *Journal of Applied Quantitative Methods,* vol. 5, no. 2, pp. 234-241, 2010.

[42] A. Keyhani, M. Ghasemi-Varnamkhasti, M. Khanali, and R. Abbaszadeh, "An assessment of wind energy potential as a power generation source in the capital of Iran, Tehran," *Energy,* vol. 35, no. 1, pp. 188-201, 2010.
[43] J. A. Carta, P. Ramirez, and S. Velazquez, "A review of wind speed probability distributions used in wind energy analysis: Case studies in the Canary Islands," *Renewable and Sustainable Energy Reviews,* vol. 13, no. 5, pp. 933-955, 2009.
[44] F. A. Jowder, "Wind power analysis and site matching of wind turbine generators in Kingdom of Bahrain," *Applied Energy,* vol. 86, no. 4, pp. 538-545, 2009.
[45] I. Y. Lun and J. C. Lam, "A study of Weibull parameters using long-term wind observations," *Renewable Energy,* vol. 20, no. 2, pp. 145-153, 2000.
[46] A. S. Dorvlo, "Estimating wind speed distribution," *Energy Conversion and Management,* vol. 43, no. 17, pp. 2311-2318, 2002.
[47] A. Garcia, J. Torres, E. Prieto, and A. De Francisco, "Fitting wind speed distributions: a case study," *Solar Energy,* vol. 62, no. 2, pp. 139-144, 1998.
[48] J. Seguro and T. Lambert, "Modern estimation of the parameters of the Weibull wind speed distribution for wind energy analysis," *Journal of Wind Engineering and Industrial Aerodynamics,* vol. 85, no. 1, pp. 75-84, 2000.
[49] S. A. Akdağ and A. Dinler, "A new method to estimate Weibull parameters for wind energy applications," *Energy conversion and management,* vol. 50, no. 7, pp. 1761-1766, 2009.
[50] S. Rehman, T. Halawani, and T. Husain, "Weibull parameters for wind speed distribution in Saudi Arabia," *Solar Energy,* vol. 53, no. 6, pp. 473-479, 1994.
[51] M. Islam, R. Saidur, and N. Rahim, "Assessment of wind energy potentiality at Kudat and Labuan, Malaysia using Weibull distribution function," *Energy,* vol. 36, no. 2, pp. 985-992, 2011.
[52] E. K. Akpinar and S. Akpinar, "An assessment on seasonal analysis of wind energy characteristics and wind turbine characteristics," *Energy Conversion and Management,* vol. 46, no. 11, pp. 1848-1867, 2005.
[53] J. Hetzer, D. C. Yu, and K. Bhattarai, "An economic dispatch model incorporating wind power," *Energy Conversion, IEEE Transactions on,* vol. 23, no. 2, pp. 603-611, 2008.
[54] C. Justus, W. Hargraves, and A. Yalcin, "Nationwide assessment of potential output from wind-powered generators," *Journal of applied meteorology,* vol. 15, no. 7, pp. 673-678, 1976.
[55] S. L. Hawkins, "High resolution reanalysis of wind speeds over the British Isles for wind energy integration," 2012.
[56] D. R. Drew, J. F. Barlow, T. T. Cockerill, and M. M. Vahdati, "The importance of accurate wind resource assessment for evaluating the economic viability of small wind turbines," *Renewable Energy,* vol. 77, pp. 493-500, 2015.
[57] B. Safari and J. Gasore, "A statistical investigation of wind characteristics and wind energy potential based on the Weibull and Rayleigh models in Rwanda," *Renewable Energy,* vol. 35, no. 12, pp. 2874-2880, 2010.
[58] A. N. Celik, "A statistical analysis of wind power density based on the Weibull and Rayleigh models at the southern region of Turkey," *Renewable energy,* vol. 29, no. 4, pp. 593-604, 2004.
[59] T. P. Chang, "Performance comparison of six numerical methods in estimating Weibull parameters for wind energy application," *Applied Energy,* vol. 88, no. 1, pp. 272-282, 2011.
[60] R. D. Prasad, R. C. Bansal, and M. Sauturaga, "Some of the design and methodology considerations in wind resource assessment," *IET Renewable Power Generation,* vol. 3, no. 1, pp. 53-64, 2009.
[61] F. Fiedler and H. A. Panofsky, "Atmospheric scales and spectral gaps," *Bulletin of the American Meteorological Society,* vol. 51, no. 12, pp. 1114-1120, 1970.

[62] J. Badger, "Introduction to mesoscale and microscale wind resource mapping," presented at the ESMAP 2012 Knowledge Exchange Forum Washington, DC, USA, 9th May, 2012.
[63] M. Beaudin, H. Zareipour, A. Schellenberglabe, and W. Rosehart, "Energy storage for mitigating the variability of renewable electricity sources: An updated review," *Energy for Sustainable Development,* vol. 14, no. 4, pp. 302-314, 2010.
[64] D. T. Bailey, *Meteorological monitoring guidance for regulatory modeling applications*. DIANE Publishing, 2000.
[65] E. L. Petersen, N. G. Mortensen, L. Landberg, J. Højstrup, and H. P. Frank, "Wind power meteorology," *Risø National Laboratory, Roskilde, Denmark, Technical Document No. Risø-I-1206 (EN),* 1997.
[66] A. HANDBOOK, "WIND RESOURCE ASSESSMENT HANDBOOK," 1997.
[67] T. R. Oke, *Initial guidance to obtain representative meteorological observations at urban sites*. World Meteorological Organization Geneva, 2004.
[68] J. Woods and S. Watson, "A new matrix method of predicting long-term wind roses with MCP," *Journal of wind engineering and industrial aerodynamics,* vol. 66, no. 2, pp. 85-94, 1997.
[69] S. M. Weekes and A. S. Tomlin, "Low-cost wind resource assessment for small-scale turbine installations using site pre-screening and short-term wind measurements," *Renewable Power Generation, IET,* vol. 8, no. 4, pp. 348-358, 2014.
[70] A. L. Rogers, J. W. Rogers, and J. F. Manwell, "Comparison of the performance of four measure–correlate–predict algorithms," *Journal of wind engineering and industrial aerodynamics,* vol. 93, no. 3, pp. 243-264, 2005.
[71] L. Landberg *et al.*, "Wind resource estimation—an overview," *Wind Energy,* vol. 6, no. 3, pp. 261-271, 2003.
[72] A. M. Sempreviva, R. J. Barthelmie, and S. Pryor, "Review of methodologies for offshore wind resource assessment in European seas," *Surveys in Geophysics,* vol. 29, no. 6, pp. 471-497, 2008.
[73] S.-D. Kwon, "Uncertainty analysis of wind energy potential assessment," *Applied Energy,* vol. 87, no. 3, pp. 856-865, 2010.
[74] N. Dixon, J. Boddy, R. Smalley, and A. Tomlin, "Evaluation of a turbulent flow and dispersion model in a typical street canyon in York, UK," *Atmospheric Environment,* vol. 40, no. 5, pp. 958-972, 2006.
[75] R. Cattin, B. Schaffner, and S. Kunz, "Validation of CFD wind resource modeling in highly complex terrain," in *Proceedings of the 2006 European Wind Energy Conference and Exhibition*, 2006.
[76] J. Manning *et al.*, "Validation and challenges of CFD in complex terrain for real world wind farms," ed: EWEA, 2011.
[77] A. Kalmikov, G. Dupont, K. Dykes, and C. Chan, "Wind power resource assessment in complex urban environments: MIT campus case-study using CFD Analysis," in *AWEA 2010 WINDPOWER Conference. Dallas, USA*, 2010.
[78] J. Sumner, C. S. Watters, and C. Masson, "CFD in wind energy: the virtual, multiscale wind tunnel," *Energies,* vol. 3, no. 5, pp. 989-1013, 2010.
[79] B. Blocken, W. Janssen, and T. van Hooff, "CFD simulation for pedestrian wind comfort and wind safety in urban areas: General decision framework and case study for the Eindhoven University campus," *Environmental Modelling & Software,* vol. 30, pp. 15-34, 2012.
[80] S. Belcher and O. Coceal, "Scaling the urban boundary layer," in *COST Action*, 2002, vol. 715, pp. 7-16.
[81] A. Bayón Barrachina, "Mapeo de recursos eólicos por reducción de escala de NCEP/NCAR Reanalysis Data 1 mediante el modelo de microescala WAsP," 2012.
[82] M. GARCÍA-DÍEZ, J. FERNÁNDEZ, L. FITA, M. MENÉNDEZ, F. J. MÉNDEZ, and J. M. GUTIÉRREZ, "Using WRF to generate high resolution offshore wind climatologies," in *Poster, 8 Congreso Internacional AEC, Salamanca*, 2012.

[83] Detlev Heinemann, "wind speed variation with height in the surface layer for different static stabilities , semi-log graph ", ed. OLDENBURG UNIVERSITY: For wind - center of wind energy research, Jul 02, 2011.
[84] B. Jimenez, F. Durante, B. Lange, T. Kreutzer, and J. Tambke, "Offshore wind resource assessment with WAsP and MM5: comparative study for the German Bight," *Wind Energy,* vol. 10, no. 2, pp. 121-134, 2007.
[85] F. Chen and J. Dudhia, "Coupling an advanced land surface-hydrology model with the Penn State-NCAR MM5 modeling system. Part I: Model implementation and sensitivity," *Monthly Weather Review,* vol. 129, no. 4, pp. 569-585, 2001.
[86] S. Al-Yahyai, Y. Charabi, and A. Gastli, "Review of the use of Numerical Weather Prediction (NWP) Models for wind energy assessment," *Renewable and Sustainable Energy Reviews,* vol. 14, no. 9, pp. 3192-3198, 2010.
[87] S. S. Soman, H. Zareipour, O. Malik, and P. Mandal, "A review of wind power and wind speed forecasting methods with different time horizons," in *North American Power Symposium (NAPS), 2010*, 2010, pp. 1-8: IEEE.
[88] D. H. Bromwich *et al.*, "Mesoscale Modeling of Katabatic Winds over Greenland with the Polar MM5*," *Monthly Weather Review,* vol. 129, no. 9, pp. 2290-2309, 2001.
[89] G. J. Haltiner, *Numerical weather prediction*. Wiley New York, 1971.
[90] UCAR., " NWP model fundamentals. ," in *Meteorological Education.*, ed: University Corporation for Atmospheric Research.
[91] D. Bhaskar Rao, D. Hari Prasad, and D. Srinivas, "Impact of horizontal resolution and the advantages of the nested domains approach in the prediction of tropical cyclone intensification and movement," *Journal of Geophysical Research: Atmospheres (1984–2012),* vol. 114, no. D11, 2009.
[92] S. Salcedo-Sanz, Á. M. Pérez-Bellido, E. G. Ortiz-García, A. Portilla-Figueras, L. Prieto, and D. Paredes, "Hybridizing the fifth generation mesoscale model with artificial neural networks for short-term wind speed prediction," *Renewable Energy,* vol. 34, no. 6, pp. 1451-1457, 2009.
[93] B. Jimenez, K. Monnich, and F. Durante, "Comparison between NCEP/NCAR and MERRA reanalysis data for long term correction in wind energy assessment," *Proceedings of the EWEA Annual Event 2012, Copenhagen, Denmark,* 2012.
[94] M. M. Rienecker *et al.*, "MERRA: NASA's modern-era retrospective analysis for research and applications," *Journal of Climate,* vol. 24, no. 14, pp. 3624-3648, 2011.
[95] R. Reichle, "The MERRA-land data product," *GMAO Of,* 2012.
[96] K. M. Hines and D. H. Bromwich, "Development and testing of polar weather research and forecasting (WRF) model. Part I: Greenland ice sheet meteorology*," *Monthly Weather Review,* vol. 136, no. 6, pp. 1971-1989, 2008.
[97] W. C. Skamarock *et al.*, "A description of the advanced research WRF version 2," DTIC Document2005.
[98] W. C. Skamarock, J. B. Klemp, and J. Dudhia, "Prototypes for the WRF (Weather Research and Forecasting) model," in *Preprints, Ninth Conf. Mesoscale Processes, J11–J15, Amer. Meteorol. Soc., Fort Lauderdale, FL*, 2001.
[99] (27/12/2015). *The Weather Research & Forecasting Model*. Available: http://www.wrf-model.org/index.php
[100] J. Done, C. A. Davis, and M. Weisman, "The next generation of NWP: Explicit forecasts of convection using the Weather Research and Forecasting (WRF) model," *Atmospheric Science Letters,* vol. 5, no. 6, pp. 110-117, 2004.
[101] A. K. DuVivier and J. J. Cassano, "Evaluation of WRF model resolution on simulated mesoscale winds and surface fluxes near Greenland," *Monthly Weather Review,* vol. 141, no. 3, pp. 941-963, 2013.
[102] X.-M. Hu, J. W. Nielsen-Gammon, and F. Zhang, "Evaluation of three planetary boundary layer schemes in the WRF model," *Journal of Applied Meteorology and Climatology,* vol. 49, no. 9, pp. 1831-1844, 2010.

[103] K. M. Sunderland, M. Narayana, G. Putrus, M. F. Conlon, and S. McDonald, "The cost of energy associated with micro wind generation: International case studies of rural and urban installations," *Energy,* vol. 109, pp. 818-829, 2016/08/15/ 2016.
[104] Y.-K. Wu and J.-S. Hong, "A literature review of wind forecasting technology in the world," in *Power Tech, 2007 IEEE Lausanne*, 2007, pp. 504-509: IEEE.
[105] S. Shokrzadeh, M. J. Jozani, and E. Bibeau, "Wind Turbine Power Curve Modeling Using Advanced Parametric and Nonparametric Methods," *Sustainable Energy, IEEE Transactions on,* vol. 5, no. 4, pp. 1262-1269, 2014.
[106] L. Campos-Arriaga, "Wind energy in the built environment: a design analysis using CFD and wind tunnel modelling approach," University of Nottingham, 2009.
[107] C. Carrillo, A. O. Montaño, J. Cidrás, and E. Díaz-Dorado, "Review of power curve modelling for wind turbines," *Renewable and Sustainable Energy Reviews,* vol. 21, pp. 572-581, 2013.
[108] D. Drew, "Analysis tools for urban wind turbines," University of Reading, 2011.
[109] N. G. Mortensen, L. Landberg, I. Troen, E. Lundtang Petersen, O. Rathmann, and M. Nielsen, "Wind Atlas Analysis and Application program (WAsP): Vol. 3: Utility programs," Risø National Laboratory1999.
[110] Z. Guo and X. Xiao, "Wind Power Assessment Based on a WRF Wind Simulation with Developed Power Curve Modeling Methods," in *Abstract and Applied Analysis*, 2014, vol. 2014: Hindawi Publishing Corporation.
[111] (2015). *The WindPower and UK Wind Speed Database programs.* Available: http://www.wind-power-program.com/turbine_characteristics.htm
[112] B. P. Hayes, I. Ilie, A. Porpodas, S. Z. Djokic, and G. Chicco, "Equivalent power curve model of a wind farm based on field measurement data," in *PowerTech, 2011 IEEE Trondheim*, 2011, pp. 1-7: IEEE.
[113] R. Karki, P. Hu, and R. Billinton, "A simplified wind power generation model for reliability evaluation," *Energy conversion, IEEE Transactions on,* vol. 21, no. 2, pp. 533-540, 2006.
[114] m. o. transportation. (2012, 01-01-2016). *the Iraqi Meteorological Organization and Seismology (IMOS)*. Available: http://meteoseism.gov.iq/index.php?name=Pages&op=page&pid=30
[115] M. o. Agriculture. (2016, 2/1/2016). *Iraqi Agrometeorological Network*. Available: http://agromet.gov.iq/index.php
[116] M. Perry and D. Hollis, "The generation of monthly gridded datasets for a range of climatic variables over the UK," *International Journal of Climatology,* vol. 25, no. 8, pp. 1041-1054, 2005.
[117] M. Khan and M. Iqbal, "Wind energy resource map of Newfoundland," *Renewable energy,* vol. 29, no. 8, pp. 1211-1221, 2004.
[118] M. Perry and D. Hollis, "The development of a new set of long‐term climate averages for the UK," *International Journal of Climatology,* vol. 25, no. 8, pp. 1023-1039, 2005.
[119] D. Dee *et al.*, "The ERA‐Interim reanalysis: Configuration and performance of the data assimilation system," *Quarterly Journal of the Royal Meteorological Society,* vol. 137, no. 656, pp. 553-597, 2011.
[120] S. M. Weekes and A. S. Tomlin, "Low-cost wind resource assessment for small-scale turbine installations using site pre-screening and short-term wind measurements," *IET Renewable Power Generation,* vol. 8, no. 4, pp. 349-358, 2014.
[121] A. M. Foley, P. G. Leahy, A. Marvuglia, and E. J. McKeogh, "Current methods and advances in forecasting of wind power generation," *Renewable Energy,* vol. 37, no. 1, pp. 1-8, 2012.
[122] K. S. Walter, A. Wilson, C, "Virtual Met Mast (TM) verification report," UK Met Office 2014.
[123] J. Sack, L. von Bremen, A. Kyriazis, and R. Donelly, "From NWP Ensembles to Probabilistic Wind Energy Production Forecasts."

[124] S. Saha *et al.*, "The NCEP climate forecast system reanalysis," *Bulletin of the American Meteorological Society,* vol. 91, no. 8, pp. 1015-1057, 2010.
[125] M. C. Brower, "The use of NCEP/NCAR reanalysis data in MCP," in *Proceedings of the EWEC*, 2006.
[126] M. Rienecker, "File Specification for GEOS-5 MERRA Reanalysis Gridded Output."
[127] U. B. Gunturu and C. A. Schlosser, "Characterization of wind power resource in the United States," *Atmospheric Chemistry and Physics,* vol. 12, no. 20, pp. 9687-9702, 2012.
[128] G. M. a. A. O. (GMAO). (2011, 08/09/2015). *tavg1_2d_slv_Nx: MERRA 2D IAU Diagnostic, Single Level Meteorology, Time Average 1-hourly (2/3x1/2L1),version 5.2.0*.
[129] G. M. a. A. O. (GMAO). (2012). *MERRA: MODERN ERA-RETROSPECTIVE ANALYSIS FOR RESEARCH AND APPLICATIONS*. Available: http://gmao.gsfc.nasa.gov/research/merra/intro.php
[130] S. Liléo and O. Petrik, "Investigation on the use of NCEP/NCAR, MERRA and NCEP/CFSR reanalysis data in wind resource analysis," *sigma,* vol. 1, no. 2, 2000.
[131] National Aeronautics and Space Administration. (2012). *GMAO MERRA_ Modern Era Retrospective-Analysis for Research and Applications*. Available: http://gmao.gsfc.nasa.gov/research/merra/intro.php
[132] C. Cao *et al.*, "Intersatellite radiance biases for the High-Resolution Infrared Radiation Sounders (HIRS) on board NOAA-15,-16, and-17 from simultaneous nadir observations," vol. 22, no. 4, pp. 381-395, 2005.
[133] K. P. Shine, J. J. Barnett, and W. J. J. G. r. l. Randel, "Temperature trends derived from Stratospheric Sounding Unit radiances: The effect of increasing CO2 on the weighting function," vol. 35, no. 2, 2008.
[134] N. C. Grody, K. Y. Vinnikov, M. D. Goldberg, J. T. Sullivan, and J. D. J. J. o. G. R. A. Tarpley, "Calibration of multisatellite observations for climatic studies: Microwave Sounding Unit (MSU)," vol. 109, no. D24, 2004.
[135] T. J. I. T. o. M. T. Mo and Techniques, "Prelaunch calibration of the advanced microwave sounding unit-A for NOAA-K," vol. 44, no. 8, pp. 1460-1469, 1996.
[136] C. Hu, Z. Lee, R. Ma, K. Yu, D. Li, and S. J. J. o. G. R. O. Shang, "Moderate resolution imaging spectroradiometer (MODIS) observations of cyanobacteria blooms in Taihu Lake, China," vol. 115, no. C4, 2010.
[137] F. Weng and N. C. J. J. o. G. R. A. Grody, "Retrieval of cloud liquid water using the special sensor microwave imager (SSM/I)," vol. 99, no. D12, pp. 25535-25551, 1994.
[138] E. J. Rignot, J. J. J. I. T. o. G. Van Zyl, and R. sensing, "Change detection techniques for ERS-1 SAR data," vol. 31, no. 4, pp. 896-906, 1993.
[139] M. Eisinger and J. P. J. G. R. L. Burrows, "Tropospheric sulfur dioxide observed by the ERS‐2 GOME instrument," vol. 25, no. 22, pp. 4177-4180, 1998.
[140] T. J. Schmit *et al.*, "Validation and use of GOES sounder moisture information," vol. 17, no. 1, pp. 139-154, 2002.
[141] S. Kempler. (2015). *Goddard Earth Sciences Data and Information Services Center*. Available: http://disc.sci.gsfc.nasa.gov/mdisc/additional/faq/faq#ques0
[142] National Aeronautics and Space Administration-Goddard Earth Sciences Data and Information Services Center. (2010, 07-September). *IAU 2d atmospheric singlelevel diagnostics (tavg1_2d_slv_Nx)*. Available: http://disc.sci.gsfc.nasa.gov/daac-bin/FTPSubset.pl
[143] S.-J. Lin, "A "vertically Lagrangian" finite-volume dynamical core for global models," *Monthly Weather Review,* vol. 132, no. 10, pp. 2293-2307, 2004.
[144] W.-S. Wu, R. J. Purser, and D. F. Parrish, "Three-dimensional variational analysis with spatially inhomogeneous covariances," *Monthly Weather Review,* vol. 130, no. 12, pp. 2905-2916, 2002.

[145] S. Bloom, L. Takacs, A. Da Silva, and D. Ledvina, "Data assimilation using incremental analysis updates," *Monthly Weather Review,* vol. 124, no. 6, pp. 1256-1271, 1996.
[146] K. McGuffie and A. Henderson-Sellers, *A climate modelling primer*. John Wiley & Sons, 2005.
[147] B. Bolin, "Studies of the general circulation of the atmosphere," *Advances in geophysics,* vol. 1, pp. 87-118, 1952.
[148] M. J. Suarez and L. L. Takacs, *Documentation of the Aries/GEOS dynamical core, version 2*. National Aeronautics and Space Administration, Goddard Space Flight Center, 1995.
[149] A. Al-Hasan, A. Ghoneim, and A. Abdullah, "Optimizing electrical load pattern in Kuwait using grid connected photovoltaic systems," *Energy conversion and management,* vol. 45, no. 4, pp. 483-494, 2004.
[150] S. Rehman, M. A. Bader, and S. A. Al-Moallem, "Cost of solar energy generated using PV panels," *Renewable and Sustainable Energy Reviews,* vol. 11, no. 8, pp. 1843-1857, 2007.
[151] B. Parida, S. Iniyan, and R. Goic, "A review of solar photovoltaic technologies," *Renewable and sustainable energy reviews,* vol. 15, no. 3, pp. 1625-1636, 2011.
[152] A. J. E. Jäger-Waldau, "Snapshot of photovoltaics—February 2019," vol. 12, no. 5, p. 769, 2019.
[153] W. M. Organization, *Guide to meteorological instruments and methods of observation*. Secretariat of the World Meteorological Organization, 1983.
[154] R. S. Agarwal, *Emerging Technologies in Airconditioning and Refrigeration*. Allied Publishers, 2001.
[155] F. E. INC. (2015). *Solar Radiation & Photosynthetically Active Radiation*. Available: http://www.fondriest.com/environmental-measurements/
[156] A. G. B. o. Meteorology. (2012). *Solar Radiation Definitions*. Available: http://www.bom.gov.au/climate/austmaps/solar-radiation-glossary.shtml
[157] J. A. Duffie and W. A. Beckman, *Solar engineering of thermal processes*. Wiley New York etc., 1980.
[158] C. H. a. S. Bowden. (2016). *Properties of sunlight*. Available: http://pveducation.org/pvcdrom/properties-of-sunlight/elevation-angle
[159] J. Brownson. (2014, 11 April 2016). *Collector Orientation*. Available: https://www.e-education.psu.edu/eme810/node/576
[160] P. Cooper, "The absorption of radiation in solar stills," *Solar energy,* vol. 12, no. 3, pp. 333-346, 1969.
[161] P. G. I. S. (PVGIS). (2016). *Performance of Grid-connected PV*. Available: http://re.jrc.ec.europa.eu/pvgis/apps4/PVcalchelp_en.html
[162] L. D. Murillo-Soto and C. Meza, "A simple temperature and irradiance-dependent expression for the efficiency of photovoltaic cells and modules," in *2018 IEEE 38th Central America and Panama Convention (CONCAPAN XXXVIII)*, 2018, pp. 1-6: IEEE.
[163] G. Notton, C. Cristofari, M. Mattei, and P. J. A. t. e. Poggi, "Modelling of a double-glass photovoltaic module using finite differences," vol. 25, no. 17-18, pp. 2854-2877, 2005.
[164] H. Zondag, "Flat-plate PV-Thermal collectors and systems: A review," *Renewable and Sustainable Energy Reviews,* vol. 12, no. 4, pp. 891-959, 2008.
[165] A. Goetzberger, C. Hebling, and H.-W. Schock, "Photovoltaic materials, history, status and outlook," *Materials Science and Engineering: R: Reports,* vol. 40, no. 1, pp. 1-46, 2003.
[166] F. Ise, "Photovoltaics report," *Fraunhofer ISE,* 2014.
[167] J. Allan, "The development and characterisation of enhanced hybrid solar photovoltaic thermal systems," Brunel University London., 2015.
[168] D. E. Carlson and C. R. Wronski, "Amorphous silicon solar cell," *Applied Physics Letters,* vol. 28, no. 11, pp. 671-673, 1976.

[169] D. Staebler and C. Wronski, "Reversible conductivity changes in discharge - produced amorphous Si," *Applied physics letters,* vol. 31, no. 4, pp. 292-294, 1977.
[170] A. Luque and S. Hegedus, *Handbook of photovoltaic science and engineering*. John Wiley & Sons, 2011.
[171] M. A. Green, K. Emery, Y. Hishikawa, W. Warta, and E. D. Dunlop, "Solar cell efficiency tables (Version 45)," *Progress in photovoltaics: research and applications,* vol. 23, no. 1, pp. 1-9, 2015.
[172] N. S. Fatemi, "Satellite market trends and the enabling role of multi-junction space solar cells," in *2008 33rd IEEE Photovoltaic Specialists Conference*, 2008, pp. 1-4: IEEE.
[173] J. R. Centre, "Photovoltaic Geographical Information System (PVGIS)," 2012.
[174] M. Šúri, T. A. Huld, E. D. Dunlop, and H. A. Ossenbrink, "Potential of solar electricity generation in the European Union member states and candidate countries," *Solar energy,* vol. 81, no. 10, pp. 1295-1305, 2007.
[175] SODA. (2015). *HelioClim, overview*. Available: http://www.soda-is.com/eng/helioclim/index.html
[176] T. Huld, M. Suri, E. Dunlop, M. Albuisson, and L. Wald, "Integration of Helioclim-1 database into PV-GIS to estimate solar electricity potential in Africa," in *Proceedings, 20th European Photovoltaic Solar Energy Conference*, 2005.
[177] M. Suri, T. Huld, E. Dunlop, M. Albuisson, and L. Wald, "Online data and tools for estimation of solar electricity in Africa: the PVGIS approach," in *21st European photovoltaic solar energy conference and exhibition*, 2006.
[178] M. P. Transvalor. (2014-2019). *The HelioClim-1 Database*. Available: http://www.soda-pro.com/web-services/radiation/helioclim-1
[179] J. R. C. JRC. (2013). *Solar radiation data*. Available: http://re.jrc.ec.europa.eu/pvgis/download/download.htm
[180] C. Thomas, E. Wey, P. Blanc, L. Wald, and M. Lefèvre, "Validation of HelioClim-3 version 4, HelioClim-3 version 5 and MACC-RAD using 14 BSRN stations," *Energy Procedia,* vol. 91, pp. 1059-1069, 2016.
[181] M. P. Transvalor. (2014-2019, 2018). *HelioClim-3 Version5* Available: www.soda-pro.com/web-services/radiation/helioclim-3-archives-for-free
[182] C. Rigollier, O. Bauer, and L. Wald, "On the clear sky model of the ESRA—European Solar Radiation Atlas—with respect to the Heliosat method," *Solar energy,* vol. 68, no. 1, pp. 33-48, 2000.
[183] Z. Qu, B. Gschwind, M. Lefèvre, and L. Wald, "Improving HelioClim-3 estimates of surface solar irradiance using the McClear clear-sky model and recent advances in atmosphere composition," *Atmospheric Measurement Techniques,* vol. 7, no. 11, pp. 3927-3933, 2014.
[184] K. Cieslak and P. Dragan, "Comparison of the existing photovoltaic power plant performance simulation in terms of different sources of meteorological data," in *E3S Web of Conferences*, 2018, vol. 49, p. 00015: EDP Sciences.
[185] T. Huld, R. Müller, and A. Gambardella, "A new solar radiation database for estimating PV performance in Europe and Africa," *Solar Energy,* vol. 86, no. 6, pp. 1803-1815, 2012.
[186] J. Schulz *et al.*, "Operational climate monitoring from space: the EUMETSAT Satellite Application Facility on Climate Monitoring (CM-SAF)," *Atmospheric Chemistry and Physics,* vol. 9, no. 5, pp. 1687-1709, 2009.
[187] U. Sangpanich, "Optimization of wind-solar energy systems using low wind speed turbines to improve rural electrification," University of Strathclyde, 2013.
[188] O. O. Amusat, "Design and optimization of hybrid renewable energy systems for off-grid continuous operations," UCL (University College London), 2017.
[189] J. Osborn and C. Kawann, "Reliability of the US Electricity System: Recent Trends and Current Issues," 2001.

[190] S. Diaf, D. Diaf, M. Belhamel, M. Haddadi, and A. Louche, "A methodology for optimal sizing of autonomous hybrid PV/wind system," *Energy policy,* vol. 35, no. 11, pp. 5708-5718, 2007.
[191] C. E. C. Nogueira *et al.*, "Sizing and simulation of a photovoltaic-wind energy system using batteries, applied for a small rural property located in the south of Brazil," *Renewable and Sustainable Energy Reviews,* vol. 29, pp. 151-157, 2014.
[192] L. Xu, X. Ruan, C. Mao, B. Zhang, and Y. Luo, "An improved optimal sizing method for wind-solar-battery hybrid power system," *IEEE transactions on sustainable energy,* vol. 4, no. 3, pp. 774-785, 2013.
[193] P. Nema, R. Nema, and S. Rangnekar, "A current and future state of art development of hybrid energy system using wind and PV-solar: A review," *Renewable and Sustainable Energy Reviews,* vol. 13, no. 8, pp. 2096-2103, 2009.
[194] A. Mahesh and K. S. Sandhu, "Hybrid wind/photovoltaic energy system developments: Critical review and findings," *Renewable and Sustainable Energy Reviews,* vol. 52, pp. 1135-1147, 2015.
[195] A. A. Al‐Shamma'a and K. E. Addoweesh, "Techno‐economic optimization of hybrid power system using genetic algorithm," *International journal of energy research,* vol. 38, no. 12, pp. 1608-1623, 2014.
[196] H. Yang, L. Lu, and W. Zhou, "A novel optimization sizing model for hybrid solar-wind power generation system," *Solar energy,* vol. 81, no. 1, pp. 76-84, 2007.
[197] D. Abbes, A. Martinez, and G. Champenois, "Life cycle cost, embodied energy and loss of power supply probability for the optimal design of hybrid power systems," *Mathematics and Computers in Simulation,* vol. 98, pp. 46-62, 2014.
[198] S. Diaf, M. Belhamel, M. Haddadi, and A. Louche, "Technical and economic assessment of hybrid photovoltaic/wind system with battery storage in Corsica island," *Energy policy,* vol. 36, no. 2, pp. 743-754, 2008.
[199] B. O. Bilal, V. Sambou, P. Ndiaye, C. Kébé, and M. Ndongo, "Optimal design of a hybrid solar–wind-battery system using the minimization of the annualized cost system and the minimization of the loss of power supply probability (LPSP)," *Renewable Energy,* vol. 35, no. 10, pp. 2388-2390, 2010.
[200] O. Nadjemi, T. Nacer, A. Hamidat, and H. Salhi, "Optimal hybrid PV/wind energy system sizing: Application of cuckoo search algorithm for Algerian dairy farms," *Renewable and Sustainable Energy Reviews,* vol. 70, pp. 1352-1365, 2017.
[201] C. Schwingshackl *et al.*, "Wind effect on PV module temperature: Analysis of different techniques for an accurate estimation," *Energy Procedia,* vol. 40, pp. 77-86, 2013.
[202] T. Nacer, O. Nadjemi, and A. Hamidat, "Optimal sizing method for grid connected renewable energy system under Algerian climate," in *IREC2015 The Sixth International Renewable Energy Congress*, 2015, pp. 1-5: IEEE.
[203] R. Dufo-Lopez, I. R. Cristobal-Monreal, and J. M. Yusta, "Stochastic-heuristic methodology for the optimisation of components and control variables of PV-wind-diesel-battery stand-alone systems," *Renewable Energy,* vol. 99, pp. 919-935, 2016.
[204] H. Chen, T. N. Cong, W. Yang, C. Tan, Y. Li, and Y. Ding, "Progress in electrical energy storage system: A critical review," *Progress in natural science,* vol. 19, no. 3, pp. 291-312, 2009.
[205] D. K. Khatod, V. Pant, and J. Sharma, "Analytical approach for well-being assessment of small autonomous power systems with solar and wind energy sources," *IEEE Transactions on Energy Conversion,* vol. 25, no. 2, pp. 535-545, 2009.
[206] G. Tina, S. Gagliano, and S. Raiti, "Hybrid solar/wind power system probabilistic modelling for long-term performance assessment," *Solar energy,* vol. 80, no. 5, pp. 578-588, 2006.
[207] S. Karaki, R. Chedid, and R. Ramadan, "Probabilistic performance assessment of autonomous solar-wind energy conversion systems," *IEEE Transactions on Energy Conversion,* vol. 14, no. 3, pp. 766-772, 1999.

[208] H. p. 3.12. (2019). *The Renewable Fraction*. Available: https://www.homerenergy.com/products/pro/docs/3.12/_renewable_fraction.html
[209] R. Hosseinalizadeh, H. Shakouri G, Mohsen S. Amalnick, and P. Taghipour, "Economic sizing of a hybrid (PV–WT–FC) renewable energy system (HRES) for stand-alone usages by an optimization-simulation model: Case study of Iran," *Renewable and Sustainable Energy Reviews,* vol. 54, pp. 139-150, 2016/02/01/ 2016.
[210] B. Zhao, X. Zhang, P. Li, K. Wang, M. Xue, and C. Wang, "Optimal sizing, operating strategy and operational experience of a stand-alone microgrid on Dongfushan Island," *Applied Energy,* vol. 113, pp. 1656-1666, 2014.
[211] T. Datta and A. J. E. J. o. O. R. Pal, "Effects of inflation and time-value of money on an inventory model with linear time-dependent demand rate and shortages," vol. 52, no. 3, pp. 326-333, 1991.
[212] H. Khatib, *Economic evaluation of projects in the electricity supply industry* (no. 44). IET, 2003.
[213] E. M. Mokheimer, A. Al-Sharafi, M. A. Habib, and I. Alzaharnah, "A new study for hybrid PV/wind off-grid power generation systems with the comparison of results from homer," *International Journal of Green Energy,* vol. 12, no. 5, pp. 526-542, 2015.
[214] L. M. Surhone, M. T. Tennoe, and S. F. Henssonow, *Payback Period*. Betascript Publishing, 2011.
[215] Investopedia. (2018). *Payback Period*. Available: https://www.investopedia.com/terms/p/paybackperiod.asp
[216] H. p. 3.12. (2019). *The net present cost* Available: https://www.homerenergy.com/products/pro/docs/3.11/net_present_cost.html
[217] R. Luna-Rubio, M. Trejo-Perea, D. Vargas-Vázquez, and G. Ríos-Moreno, "Optimal sizing of renewable hybrids energy systems: A review of methodologies," *Solar Energy,* vol. 86, no. 4, pp. 1077-1088, 2012.
[218] R. Banos, F. Manzano-Agugliaro, F. Montoya, C. Gil, A. Alcayde, and J. Gómez, "Optimization methods applied to renewable and sustainable energy: A review," *Renewable and sustainable energy reviews,* vol. 15, no. 4, pp. 1753-1766, 2011.
[219] J. L. Bernal-Agustín and R. Dufo-Lopez, "Simulation and optimization of stand-alone hybrid renewable energy systems," *Renewable and Sustainable Energy Reviews,* vol. 13, no. 8, pp. 2111-2118, 2009.
[220] W. Kellogg, M. Nehrir, G. Venkataramanan, and V. Gerez, "Generation unit sizing and cost analysis for stand-alone wind, photovoltaic, and hybrid wind/PV systems," *IEEE Transactions on energy conversion,* vol. 13, no. 1, pp. 70-75, 1998.
[221] H. Yang, L. Lu, and J. Burnett, "Weather data and probability analysis of hybrid photovoltaic–wind power generation systems in Hong Kong," *Renewable Energy,* vol. 28, no. 11, pp. 1813-1824, 2003.
[222] F. O. Hocaoğlu, Ö. N. Gerek, and M. Kurban, "A novel hybrid (wind–photovoltaic) system sizing procedure," *Solar Energy,* vol. 83, no. 11, pp. 2019-2028, 2009.
[223] J. Manwell, "Hybrid energy systems," *Encyclopedia of Energy,* vol. 3, pp. 215-229, 2004.
[224] C. Protogeropoulos, B. Brinkworth, and R. Marshall, "Sizing and techno - economical optimization for hybrid solar photovoltaic/wind power systems with battery storage," *International Journal of Energy Research,* vol. 21, no. 6, pp. 465-479, 1997.
[225] M. Habib, S. Said, M. El-Hadidy, and I. Al-Zaharna, "Optimization procedure of a hybrid photovoltaic wind energy system," *Energy,* vol. 24, no. 11, pp. 919-929, 1999.
[226] A. N. Celik, "Techno-economic analysis of autonomous PV-wind hybrid energy systems using different sizing methods," *Energy Conversion and Management,* vol. 44, no. 12, pp. 1951-1968, 2003.

[227] S. Conti, G. Tina, and U. Vagliasindi, "A new method for estimating the long-term average performance of hybrid Wind/PV systems," *Proceedings of Eurosun, Copenhagen, Denmark, June,* pp. 19-22, 2000.
[228] G. La Terra, G. Salvina, and G. Tina, "Optimal sizing procedure for hybrid solar wind power systems by fuzzy logic," in *MELECON 2006-2006 IEEE Mediterranean Electrotechnical Conference*, 2006, pp. 865-868: IEEE.
[229] M. Bolinger, "Understanding trends in wind turbine prices over the past decade," 2011.
[230] W. Zhou, C. Lou, Z. Li, L. Lu, and H. Yang, "Current status of research on optimum sizing of stand-alone hybrid solar–wind power generation systems," *Applied energy,* vol. 87, no. 2, pp. 380-389, 2010.
[231] M. Fadaee and M. Radzi, "Multi-objective optimization of a stand-alone hybrid renewable energy system by using evolutionary algorithms: A review," *Renewable and sustainable energy reviews,* vol. 16, no. 5, pp. 3364-3369, 2012.
[232] A. Alarcon-Rodriguez, G. Ault, and S. Galloway, "Multi-objective planning of distributed energy resources: A review of the state-of-the-art," *Renewable and Sustainable Energy Reviews,* vol. 14, no. 5, pp. 1353-1366, 2010.
[233] D. Xu, L. Kang, L. Chang, and B. Cao, "Optimal sizing of standalone hybrid wind/PV power systems using genetic algorithms," in *Canadian Conference on Electrical and Computer Engineering, 2005.*, 2005, pp. 1722-1725: IEEE.
[234] J. H. Shi, X. J. Zhu, and G. Y. Cao, "Design and techno‐economical optimization for stand‐alone hybrid power systems with multi‐objective evolutionary algorithms," *International Journal of Energy Research,* vol. 31, no. 3, pp. 315-328, 2007.
[235] H. Yang, W. Zhou, L. Lu, and Z. Fang, "Optimal sizing method for stand-alone hybrid solar–wind system with LPSP technology by using genetic algorithm," *Solar energy,* vol. 82, no. 4, pp. 354-367, 2008.
[236] H. Suryoatmojo, T. Hiyama, A. A. Elbaset, and M. Ashari, "Optimal design of wind-PV-diesel-battery system using genetic algorithm," *IEEJ Transactions on Power and Energy,* vol. 129, no. 3, pp. 413-420, 2009.
[237] A. K. Kaviani, H. R. Baghaee, and G. H. Riahy, "Optimal sizing of a stand-alone wind/photovoltaic generation unit using particle swarm optimization," *Simulation,* vol. 85, no. 2, pp. 89-99, 2009.
[238] J. L. Bernal-Agustín, R. Dufo-López, and D. M. Rivas-Ascaso, "Design of isolated hybrid systems minimizing costs and pollutant emissions," *Renewable Energy,* vol. 31, no. 14, pp. 2227-2244, 2006.
[239] R. Dufo-López and J. L. Bernal-Agustín, "Multi-objective design of PV–wind–diesel–hydrogen–battery systems," *Renewable energy,* vol. 33, no. 12, pp. 2559-2572, 2008.
[240] M. S. Ngan and C. W. Tan, "Assessment of economic viability for PV/wind/diesel hybrid energy system in southern Peninsular Malaysia," *Renewable and Sustainable Energy Reviews,* vol. 16, no. 1, pp. 634-647, 2012.
[241] S. K. Nandi and H. R. Ghosh, "Prospect of wind–PV-battery hybrid power system as an alternative to grid extension in Bangladesh," *Energy,* vol. 35, no. 7, pp. 3040-3047, 2010.
[242] S. Rehman and L. M. Al-Hadhrami, "Study of a solar PV–diesel–battery hybrid power system for a remotely located population near Rafha, Saudi Arabia," *Energy,* vol. 35, no. 12, pp. 4986-4995, 2010.
[243] S. Sinha and S. Chandel, "Review of software tools for hybrid renewable energy systems," *Renewable and Sustainable Energy Reviews,* vol. 32, pp. 192-205, 2014.
[244] M. S. Alam and D. W. Gao, "Modeling and analysis of a wind/PV/fuel cell hybrid power system in HOMER," in *Industrial Electronics and Applications, 2007. ICIEA 2007. 2nd IEEE Conference on*, 2007, pp. 1594-1599: IEEE.

[245] A. Singh, P. Baredar, and B. Gupta, "Computational Simulation & Optimization of a Solar, Fuel Cell and Biomass Hybrid Energy System Using HOMER Pro Software," *Procedia Engineering,* vol. 127, pp. 743-750, 2015.
[246] B. U. Kansara and B. Parekh, "Modelling and simulation of distributed generation system using HOMER software," in *Recent Advancements in Electrical, Electronics and Control Engineering (ICONRAEeCE), 2011 International Conference on*, 2011, pp. 328-332: IEEE.
[247] P. Balamurugan, S. Ashok, and T. Jose, "Optimal operation of biomass/wind/PV hybrid energy system for rural areas," *International Journal of Green Energy,* vol. 6, no. 1, pp. 104-116, 2009.
[248] N. R. E. Lab. (2009). *Hybrid Optimization of Mutiple Energy Resources (HOMER) model*. Available: http://www.homerenergy.com/index.html
[249] J. McGowan, J. Manwell, C. Avelar, and C. Warner, "Hybrid wind/PV/diesel hybrid power systems modeling and South American applications," *Renewable Energy,* vol. 9, no. 1, pp. 836-847, 1996.
[250] R. E. R. L. (RERL). (1996). *HYBRID 2*. Available: http://www.umass.edu/windenergy/research/topics/tools/software/hybrid2
[251] J. Manwell *et al.*, *Hybrid2: a hybrid system simulation model: theory manual*. Citeseer, 1998.
[252] L. K. Gan, "Improving the performance of hybrid wind-diesel-battery systems," 2017.
[253] A. A. Kazem, M. T. Chaichan, and H. A. Kazem, "Dust effect on photovoltaic utilization in Iraq: Review article," *Renewable and Sustainable Energy Reviews,* vol. 37, pp. 734-749, 2014.
[254] D. C. S. , Emad H. K. Al-ani, Dr. Timothy Martin, " Land Use and Vegetation Cover for Iraq," in *ERDAS 8.7* vol. 33.7 MB, alliraq_landuse_landcover_modis232, Ed., ed. IRAQ: Ministry of Agriculture Department of AEZ Map Specialist Soil& Water GIS &Remote 2006.
[255] HAZUS-MH, "Multi-hazard Loss Estimation Methodology: Hurricane Model," *Department of Homeland Security FEMA Washington, D.C.,* 2003.
[256] J. Silva, C. Ribeiro, and R. Guedes, "Roughness length classification of Corine Land Cover classes," in *Proceedings of the European Wind Energy Conference, Milan, Italy*, 2007, vol. 710, p. 110.
[257] F. V. Hansen, "Surface roughness lengths," DTIC Document1993.
[258] A. Holtslag, "Estimates of diabatic wind speed profiles from near-surface weather observations," *Boundary-Layer Meteorology,* vol. 29, no. 3, pp. 225-250, 1984.
[259] E. Simiu and R. H. Scanlan, *Wind effects on structures*. Wiley, 1996.
[260] J. Wiernga, "Representative roughness parameters for homogeneous terrain," *Boundary-Layer Meteorology,* vol. 63, no. 4, pp. 323-363, 1993.
[261] L. C. I. (LCI). (2012). *0.5 km MODIS-based Global Land Cover Climatology*. Available: http://landcover.usgs.gov/global_climatology.php
[262] E. Bou-Zeid, M. B. Parlange, and C. Meneveau, "On the parameterization of surface roughness at regional scales," *Journal of the atmospheric sciences,* vol. 64, no. 1, pp. 216-227, 2007.
[263] S. A. Hsu, "Measurement of shear stress and roughness length on a beach," *Journal of Geophysical Research,* vol. 76, no. 12, pp. 2880-2885, 1971.
[264] E. Bou‐Zeid, C. Meneveau, and M. B. Parlange, "Large‐eddy simulation of neutral atmospheric boundary layer flow over heterogeneous surfaces: Blending height and effective surface roughness," *Water Resources Research,* vol. 40, no. 2, 2004.
[265] J. F. Barlow, "Progress in observing and modelling the urban boundary layer," *Urban Climate,* vol. 10, pp. 216-240, 2014.
[266] B. Valor. Professional information about meteorological conditions in the world [Online]. Available: http://www.ogimet.com/home.phtml.en
[267] E. Stellwagen. (2016).

Forecasting 101: A Guide to Forecast Error Measurement Statistics and How to Use Them. Available: http://www.forecastpro.com/Trends/forecasting101August2011.html
[268] T. Chai and R. R. Draxler, "Root mean square error (RMSE) or mean absolute error (MAE)?–Arguments against avoiding RMSE in the literature," *Geoscientific Model Development,* vol. 7, no. 3, pp. 1247-1250, 2014.
[269] F. Bautista, D. Bautista, and C. Delgado-Carranza, "Calibration of the equations of Hargreaves and Thornthwaite to estimate the potential evapotranspiration in semi-arid and subhumid tropical climates for regional applications," *Atmósfera,* vol. 22, no. 4, pp. 331-348, 2009.
[270] A. C. Cameron and F. A. J. J. o. e. Windmeijer, "An R-squared measure of goodness of fit for some common nonlinear regression models," vol. 77, no. 2, pp. 329-342, 1997.
[271] J. Millward-Hopkins, A. Tomlin, L. Ma, D. Ingham, and M. Pourkashanian, "Assessing the potential of urban wind energy in a major UK city using an analytical model," *Renewable energy,* vol. 60, pp. 701-710, 2013.
[272] D. Allen, A. Tomlin, C. Bale, A. Skea, S. Vosper, and M. Gallani, "A boundary layer scaling technique for estimating near-surface wind energy using numerical weather prediction and wind map data," *Applied Energy,* vol. 208, pp. 1246-1257, 2017.
[273] A. S. Bahaj, L. Myers, and P. A. B. James, "Urban energy generation: Influence of micro-wind turbine output on electricity consumption in buildings," *Energy and Buildings,* vol. 39, no. 2, pp. 154-165, 2007/02/01/ 2007.
[274] K. Adam, V. Hoolohan, J. Gooding, T. Knowland, C. S. Bale, and A. S. Tomlin, "Methodologies for city-scale assessment of renewable energy generation potential to inform strategic energy infrastructure investment," *Cities,* vol. 54, pp. 45-56, 2016.
[275] T. Ouarda *et al.*, "Probability distributions of wind speed in the UAE," *Energy Conversion and Management,* vol. 93, pp. 414-434, 2015.
[276] J. Wieringa, "Shapes of annual frequency distributions of wind speed observed on high meteorological masts," in *Boundary Layer Studies and Applications*: Springer, 1989, pp. 85-110.
[277] D.L.Bricker, "Weibull Distribution," ed: The University of Iowa.
[278] US.NRC. (2017). *Capacity factor (net)*. Available: https://www.nrc.gov/reading-rm/basic-ref/glossary/capacity-factor-net.html
[279] (2017). *SENWEI ENERGY TECHNOLOGY INC*. Available: http://www.windpowercn.com/
[280] Z. M. Salameh, B. S. Borowy, and A. R. J. I. t. o. E. c. Amin, "Photovoltaic module-site matching based on the capacity factors," vol. 10, no. 2, pp. 326-332, 1995.
[281] M. I. Blanco, "The economics of wind energy," *Renewable and sustainable energy reviews,* vol. 13, no. 6-7, pp. 1372-1382, 2009.
[282] D. Gielen, "Renewable energy technologies: cost analysis series," *Sol Photovolt,* vol. 1, no. 1, p. 52, 2012.
[283] W. A. D. Parsons Brinckerhoff, "Small-scale Generation Cost Update," Department of Energy and Climate Change, London2015, Available: https://www.gov.uk/government/uploads/system/uploads/attachment_data/file/456187/DECC_Small-Scale_Generation_Costs_Update_FINAL.PDF.
[284] (2012). *Table of imported goods covered by the Tariff Law*. Available: http://www.customs.mof.gov.iq/en
[285] E. W. E. Association, *The economics of wind energy*. EWEA, 2009.
[286] A. Kaabeche, M. Belhamel, and R. Ibtiouen, "Optimal sizing method for stand-alone hybrid PV/wind power generation system," *Revue des Energies Renouvelables (SMEE'10) Bou Ismail Tipaza,* pp. 205-213, 2010.
[287] M. A. Mohamed, A. M. Eltamaly, and A. I. Alolah, "PSO-based smart grid application for sizing and optimization of hybrid renewable energy systems," *PloS one,* vol. 11, no. 8, p. e0159702, 2016.

[288] t. C. B. o. Iraq, "Iraq Interest Rate 2004-2018," 2018.
[289] T. w. bank. Inflation, consumer prices (annual %) [Online]. Available: https://data.worldbank.org/indicator/FR.INR.RINR
[290] !!! INVALID CITATION !!!
[291] A. Albani, M. Ibrahim, and K. Yong, "The feasibility study of offshore wind energy potential in Kijal, Malaysia: the new alternative energy source exploration in Malaysia," *Energy Exploration & Exploitation,* vol. 32, no. 2, pp. 329-344, 2014.
[292] A. Albani and M. Ibrahim, "An assessment of wind energy potential for selected sites in Malaysia using feed-in tariff criteria," *Wind Engineering,* vol. 38, no. 3, pp. 249-259, 2014.
[293] PVGIS. (2016). *PVgis photovoltaic calculator for Africa, Mediterranean Basin and Asia*. Available: http://re.jrc.ec.europa.eu/pvgis/apps4/pvest.php?lang=en&map=africa
[294] E. European Commission, "EUROPEAN ENERGY AND TRANSPORT. Scenarios on energy efficiency and renewables," Luxemburg2006.
[295] L. Bluesun Solar Energy Tech. Co. (2019). *Solar System*. Available: www.bluesunpv.com/?fbclid=IwAR2yf3Pw4TtOZ-LMCM1Wb1smrM3THW0GLd_3UpEiY4LeJxF7n4SazCPJfy0
[296] OECD, N. E. Agency, and I. E. Agency, *Projected Costs of Generating Electricity 2010*. 2010.
[297] Homer pro 3.12. (2019, 10 June). *The output of the PV array calculation*. Available: https://www.homerenergy.com/products/pro/docs/3.12/how_homer_calculates_the_pv_array_power_output.html
[298] S. P. Sukhatme and J. Nayak, *Solar energy*. McGraw-Hill Education, 2017.
[299] N/A, "2011 ASHRAE Handbook - Heating, Ventilating, and Air-Conditioning Applications (SI Edition)," ed: American Society of Heating, Refrigerating and Air-Conditioning Engineers, Inc. (ASHRAE), p. 35.2.
[300] E. Skoplaki, A. Boudouvis, and J. Palyvos, "A simple correlation for the operating temperature of photovoltaic modules of arbitrary mounting," *Solar Energy Materials and Solar Cells,* vol. 92, no. 11, pp. 1393-1402, 2008.
[301] G. Modelling, "Assimilation Office (GMAO)," *MERRA-2 tavgM_2d_ocn_Nx: 2d, monthly mean, time-averaged, single-level, assimilation, ocean surface diagnostics,* vol. 5.
[302] R. Mueller, T. Behrendt, A. Hammer, and A. Kemper, "A new algorithm for the satellite-based retrieval of solar surface irradiance in spectral bands," *Remote Sensing,* vol. 4, no. 3, pp. 622-647, 2012.
[303] R. Mueller, C. Matsoukas, A. Gratzki, H. Behr, and R. Hollmann, "The CM-SAF operational scheme for the satellite based retrieval of solar surface irradiance—A LUT based eigenvector hybrid approach," *Remote Sensing of Environment,* vol. 113, no. 5, pp. 1012-1024, 2009.
[304] C. Smith, R. Crook, and P. Forster, "Changes in solar PV output due to water vapour loading in a future climate scenario," *EU PVSEC Proceedings,* pp. 2102-2105, 2015.
[305] P. Arul, V. K. Ramachandaramurthy, and R. Rajkumar, "Control strategies for a hybrid renewable energy system: A review," *Renewable and sustainable energy reviews,* vol. 42, pp. 597-608, 2015.
[306] N. A. Ahmed, A. Al-Othman, and M. J. E. P. S. R. AlRashidi, "Development of an efficient utility interactive combined wind/photovoltaic/fuel cell power system with MPPT and DC bus voltage regulation," vol. 81, no. 5, pp. 1096-1106, 2011.
[307] X. Liu, P. Wang, and P. C. J. I. T. o. s. g. Loh, "A hybrid AC/DC microgrid and its coordination control," vol. 2, no. 2, pp. 278-286, 2011.
[308] S. S. B. S. systems. *Battery Storage systems*. Available: http://www.stealthenergy.co.uk/stealth-tile-system/stealthenergytm-growatt-inverter/so-far-solar/index.shtml
[309] S. p. change. (2017). *Battery Storage Knowledge Bank*. Available: https://www.spiritenergy.co.uk/kb-batteries-understanding-batteries

[310] "SUNTREE ELECTRIC GROUP Co., Ltd.."
[311] J. Lean, "Solar Irradiance Reconstruction. IGBP PAGES/World Data Center for Paleoclimatology, Data Contribution Series# 2004-035. NOAA/NGDC Paleoclimatology Program, Boulder CO, USA, 2004," ed.
[312] N. Nahle. (2009.). *CORRELATION BETWEEN SOLAR IRRADIANCE AND GLOBAL TEMPERATURE*. Available: http://www.biocab.org/Solar_Irradiance_is_Actually_Increasing.html#top
[313] E. T. SL, "Dashboard of engage portal from efergy," ed, 2018.
[314] E. T. SL. (2018). *online energy Monitor 3-phase kit*. Available: https://efergy.com/engage-online-monitoring/
[315] L. K. Gan, J. K. Shek, M. A. J. E. C. Mueller, and Management, "Hybrid wind–photovoltaic–diesel–battery system sizing tool development using empirical approach, life-cycle cost and performance analysis: A case study in Scotland," vol. 106, pp. 479-494, 2015.
[316] L. Goldie-Scot, "A Behind the Scenes Take on Lithium-ion Battery Prices," Available: https://about.bnef.com/blog/behind-scenes-take-lithium-ion-battery-prices/
[317] A. J. Pimm, T. T. Cockerill, and P. G. Taylor, "Time-of-use and time-of-export tariffs for home batteries: Effects on low voltage distribution networks," *Journal of Energy Storage,* vol. 18, pp. 447-458, 2018.
[318] S. Sinha and S. Chandel, "Review of recent trends in optimization techniques for solar photovoltaic–wind based hybrid energy systems," *Renewable and Sustainable Energy Reviews,* vol. 50, pp. 755-769, 2015.
[319] W. M. Seong *et al.*, "Abnormal self-discharge in lithium-ion batteries," *Energy & Environmental Science,* vol. 11, no. 4, pp. 970-978, 2018.
[320] B. University. (2018-11-16). *BU-802b: What does Elevated Self-discharge Do?* Available: https://batteryuniversity.com/learn/article/elevating_self_discharge
[321] B. Lawson. (2005). *Battery Performance Characteristics*. Available: https://www.mpoweruk.com/performance.htm
[322] H. p. 3.13. (2019). *Salvage value*. Available: https://www.homerenergy.com/products/pro/docs/3.13/salvage_value.html
[323] S. Saitta. *Standardization vs. normalization*. Available: http://www.dataminingblog.com/standardization-vs-normalization/
[324] B. Lin and Z. Jiang, "Designation and influence of household increasing block electricity tariffs in China," *Energy Policy,* vol. 42, pp. 164-173, 2012.